frontiers | Research Topics

Clinic-oriented multifunctional biomaterials: From rational design to applications

Edited by
Meng Tian, Ye Cao, Yang Kang, Huixu Xie and Qianbin Wang

Published in
Frontiers in Bioengineering and Biotechnology

ISSN 1664-8714
ISBN 978-2-8325-4067-1
DOI 10.3389/978-2-8325-4067-1

About Frontiers

Frontiers is more than just an open access publisher of scholarly articles: it is a pioneering approach to the world of academia, radically improving the way scholarly research is managed. The grand vision of Frontiers is a world where all people have an equal opportunity to seek, share and generate knowledge. Frontiers provides immediate and permanent online open access to all its publications, but this alone is not enough to realize our grand goals.

Frontiers journal series

The Frontiers journal series is a multi-tier and interdisciplinary set of open-access, online journals, promising a paradigm shift from the current review, selection and dissemination processes in academic publishing. All Frontiers journals are driven by researchers for researchers; therefore, they constitute a service to the scholarly community. At the same time, the *Frontiers journal series* operates on a revolutionary invention, the tiered publishing system, initially addressing specific communities of scholars, and gradually climbing up to broader public understanding, thus serving the interests of the lay society, too.

Dedication to quality

Each Frontiers article is a landmark of the highest quality, thanks to genuinely collaborative interactions between authors and review editors, who include some of the world's best academicians. Research must be certified by peers before entering a stream of knowledge that may eventually reach the public - and shape society; therefore, Frontiers only applies the most rigorous and unbiased reviews. Frontiers revolutionizes research publishing by freely delivering the most outstanding research, evaluated with no bias from both the academic and social point of view. By applying the most advanced information technologies, Frontiers is catapulting scholarly publishing into a new generation.

What are Frontiers Research Topics?

Frontiers Research Topics are very popular trademarks of the *Frontiers journals series*: they are collections of at least ten articles, all centered on a particular subject. With their unique mix of varied contributions from Original Research to Review Articles, Frontiers Research Topics unify the most influential researchers, the latest key findings and historical advances in a hot research area.

Find out more on how to host your own Frontiers Research Topic or contribute to one as an author by contacting the Frontiers editorial office: frontiersin.org/about/contact

Clinic-oriented multifunctional biomaterials: From rational design to applications

Topic editors

Meng Tian — Sichuan University, China

Ye Cao — Institute of Blood Transfusion, Chinese Academy of Medical Sciences and Peking Union Medical College, China

Yang Kang — Sun Yat-sen University, China

Huixu Xie — Sichuan University, China

Qianbin Wang — University of Massachusetts Amherst, United States

Citation

Tian, M., Cao, Y., Kang, Y., Xie, H., Wang, Q., eds. (2023). *Clinic-oriented multifunctional biomaterials: From rational design to applications*. Lausanne: Frontiers Media SA. doi: 10.3389/978-2-8325-4067-1

Table of contents

frontiers | Frontiers in Bioengineering and Biotechnology

TYPE Editorial
PUBLISHED 21 November 2023
DOI 10.3389/fbioe.2023.1338945

OPEN ACCESS

EDITED AND REVIEWED BY
Hasan Uludag,
University of Alberta, Canada

*CORRESPONDENCE
Meng Tian,
tianmeng@scu.edu.cn

RECEIVED 15 November 2023
ACCEPTED 16 November 2023
PUBLISHED 21 November 2023

CITATION
Tian M (2023), Editorial: Clinic-oriented multifunctional biomaterials: from rational design to applications.
Front. Bioeng. Biotechnol. 11:1338945.
doi: 10.3389/fbioe.2023.1338945

Editorial: Clinic-oriented multifunctional biomaterials: from rational design to applications

Meng Tian*

Department of Neurosurgery and Neurosurgery Research Laboratory, West China Hospital, Sichuan University, Chengdu, China

KEYWORDS

clinic, oriented, biomaterials, rational design, application

Editorial on the Research Topic
Clinic-oriented multifunctional biomaterials: from rational design to applications

Although great success has been achieved in the development of various biomaterials, there are only a few products that can meet the requirements of clinical applications. Thus, rational design and fabrication of multifunctional biomaterials that are capable of better meeting the needs in the clinic are promising for practical application. Recently, a great quantity of biomaterials have been engineered for practical applications in view of clinical use, which could be in terms of preparation, evaluation, or clinical trials.

In this Research Topic, we collected of 11 articles, including 8 articles and 3 reviews, contributed by 82 researchers worldwide. The original research articles involved multiple biomaterials: nanolipogel, membrane, hydrogel, stent, red blood cell substitute, tracheal allograft, titanium prosthesis, and multi-layered drug delivery system. These biomaterials were rationally designed and provide enormous references for their clinical applications.

There are three review articles in this Research Topic. In their review article, Newman et al. described features of microfluidic technology with a focus on blood-contacting applications, where material hemocompatibility was discussed in the context of interactions with blood components, from the initial absorption of plasma proteins to the activation of cells and factors and the contribution of these interactions to the coagulation cascade and thrombogenesis. Finally, they reviewed the techniques for improving microfluidic channel hemocompatibility through material surface modifications, including bioactive and biopassive coatings, and future directions. In another review article, Huang et al. focused on recent progress in the use of hydrogels in mimicking the hematopoietic niche for the efficient expansion of hematopoietic stem cells, where biomimetic strategies and the combination use of hydrogel matrices and microfluidics, including the emerging organ-on-a-chip technology, are summarized. They also provided a brief description of novel stimulus-responsive hydrogels that are used to establish an intelligent dynamic cell microenvironment. Regenerating periodontal tissue is a huge clinical challenge because of the structural complexity and the poor self-healing capability of periodontal tissue, in which the homing of endogenous stem cells may bring promising treatment strategies in the future. In the third review article, Meng et al. summarized the stimulating strategies for endogenous cell homing, such as the combination of cytokines and chemokines, and the implantation of tissue-engineered scaffolds.

In this Research Topic, all of the original research presented crucial aspects regarding preparation, evaluation, and potential clinical translation applications. Zeng et al. combined a bioengineering approach and a cryopreservation technique to fabricate a neo-trachea using a pre-epithelialized cryopreserved tracheal allograft. Using rat heterotopic and orthotopic implantation models, they confirmed that tracheal cartilage has sufficient mechanical properties to bear neck movement and compression, indicating that pre-epithelialization with respiratory epithelial cells can prevent fibrosis obliteration and maintain lumen/airway patency and showing that a pedicled adipose tissue flap can be easily integrated with a tracheal construct to achieve neovascularization. Yang et al. prepared an antibacterial polypropylene/polyurethane composite membrane through a hot-pressing membrane-forming technology for invisible orthodontics application. The membranes were conferred with favorable transparency (~70% in the visible light range) and excellent antibacterial ability. Kong et al. prepared a red blood cell substitute composed of polymerized human cord hemoglobin assisted with ascorbic acid that alleviates oxidative stress for blood transfusion.

Two articles have been collected related to improving drug delivery. Nanolipogel emerges as a potential system to encapsulate and deliver hydrophilic drugs while suppressing their initial burst release. However, there is a lack of characterization of their drug release mechanism. Melvin Liew et al. used different molecular weights of poly (ethylene glycol) diacrylate to vary the mesh size of the nanogel core, drawing inspiration from the macromolecular crowding effect in cells, which can be viewed as a mesh network of undefined sizes. The multi-layered drug delivery system has promising potential to achieve controlled release. However, existing technologies face difficulties regulating the number of layers and layer–thickness ratio. Zheng et al. utilized layer-multiplying co-extrusion technology to modulate the layer–thickness ratio and drug release to expand their application.

Another two articles have been published to focus on *in vivo* implantation evaluation. The ultrathin-strut drug-eluting stent (DES) has shown better clinical results than thin- or thick-strut DES. Hahn et al. investigated whether re-endothelialization was different among three types of commercial DES, and their results showed that re-endothelialization after stent implantation was related to smooth muscle cells (SMC) coverage and SMC layer differentiation, in which ultrathin-strut DES exhibited significantly faster and denser re-endothelialization. Currently, there is no ideal material available for posterior scleral reinforcement (PSR) to prevent the progression of high myopia. Xu et al. evaluated the safety and biological reactions of robust regenerated silk fibroin hydrogels as potential grafts for PSR in animal experiments.

Last, we highlight one article collected that reported a clinical trial. Total wrist arthroplasty is an effective treatment for end-stage wrist arthritis from all causes. However, wrist prostheses are still prone to complications such as prosthesis loosening and periprosthetic fractures after total wrist arthroplasty. Cai et al. designed and developed a personalized three-dimensional printed microporous titanium artificial wrist prosthesis (3DMT-Wrist) for the treatment of end-stage wrist joint and investigated its safety and effectiveness.

In conclusion, the current Research Topic reports different types of biomaterials and their broad applications, providing new chances for meeting requirements toward clinical translation.

Author contributions

MT: Writing–original draft, Writing–review and editing.

Funding

The author(s) declare that no financial support was received for the research, authorship, and/or publication of this article.

Conflict of interest

The author declares that the research was conducted in the absence of any commercial or financial relationships that could be construed as a potential conflict of interest.

Publisher's note

frontiers | Frontiers in Bioengineering and Biotechnology

TYPE Review
PUBLISHED 13 October 2022
DOI 10.3389/fbioe.2022.1017613

OPEN ACCESS

EDITED BY
Jianxun Ding,
Changchun Institute of Applied Chemistry (CAS), China

REVIEWED BY
Lei Hu,
Beijing Stomatological Hospital, Capital Medical University, China
Xiaoxiao Cai,
Sichuan University, China
Zhen Geng,
Shanghai University, China
Jiabin Zhang,
Sun Yat-Sen University, China
Lei Sui,
Tianjin Medical University, China

*CORRESPONDENCE
Huixu Xie,
aitian007@126.com

SPECIALTY SECTION
This article was submitted to Biomaterials, a section of the journal Frontiers in Bioengineering and Biotechnology

RECEIVED 12 August 2022
ACCEPTED 03 October 2022
PUBLISHED 13 October 2022

CITATION
Meng L, Wei Y, Liang Y, Hu Q and Xie H (2022), Stem cell homing in periodontal tissue regeneration.
Front. Bioeng. Biotechnol. 10:1017613.
doi: 10.3389/fbioe.2022.1017613

Stem cell homing in periodontal tissue regeneration

Lingxi Meng[1], Yige Wei[1], Yaxian Liang[1], Qin Hu[2] and Huixu Xie[1]*

[1]State Key Laboratory of Oral Diseases, Department of Head and Neck Oncology Surgery, National Clinical Research Center for Oral Diseases, West China Hospital of Stomatology, Sichuan University, Chengdu, China, [2]Faculty of Dentistry, The University of Hong Kong, Hong Kong, China

The destruction of periodontal tissue is a crucial problem faced by oral diseases, such as periodontitis and tooth avulsion. However, regenerating periodontal tissue is a huge clinical challenge because of the structural complexity and the poor self-healing capability of periodontal tissue. Tissue engineering has led to advances in periodontal regeneration, however, the source of exogenous seed cells is still a major obstacle. With the improvement of *in situ* tissue engineering and the exploration of stem cell niches, the homing of endogenous stem cells may bring promising treatment strategies in the future. In recent years, the applications of endogenous cell homing have been widely reported in clinical tissue repair, periodontal regeneration, and cell therapy prospects. Stimulating strategies have also been widely studied, such as the combination of cytokines and chemokines, and the implantation of tissue-engineered scaffolds. In the future, more research needs to be done to improve the efficiency of endogenous cell homing and expand the range of clinical applications.

KEYWORDS

periodontal regeneration, endogenous stem cell, cell homing, regenerative medicine, stimulation strategies

1 Introduction

Periodontal tissue is a kind of complex tissue composed of both soft tissue like periodontal ligament (PDL) and gingiva, as well as hard tissue such as alveolar bone and cementum. It plays a crucial role in supporting teeth, bearing occlusal forces, and maintaining oral mucosa integrity. When faced with the destruction of periodontal tissue, negative effects such as tooth loss, and physical and mental health damage could happen (Darveau, 2010; Kinane et al., 2017). The existing clinical treatment methods, such as guided tissue/bone regeneration (GTR/GBR) can improve the clinical efficacy of various tissue defects (Bottino et al., 2012; Xu et al., 2019). However, the effect on periodontal regeneration is not as satisfying, especially in the recovery of physiological structure and function. The ideal result of periodontal therapy is to regenerate the cementum-periodontium-bone system while achieving this goal remains a huge challenge. However, the insufficiency of stem/progenitor cells seems to be the primary limitation for periodontal membrane and alveolar bone reconstruction.

With the development and improvement of cell therapy, researchers have found various stem cells for periodontal regeneration. Mesenchymal stem cells (MSCs) and periodontal ligament stem cells (PDLSCs) are most studied, together with other stem cells

such as dental pulp stem cells (DPSCs) and induced pluripotent stem cells (iPSC) (Huang et al., 2009b; Kwon et al., 2018). Those stem cells are routinely isolated, cultured, and amplified *in vitro* and relatedly applied. However, exogenous stem cell transplantation still has various disadvantages, for example, the complicated technology of *in vitro* operation, high-cost *ex vivo* cell culture, and even the potential ethical and safety risks (Lee et al., 2016; Pacelli et al., 2017; Safina and Embree, 2022).

Stem cell homing is a physiologic process which been studied since the 1970s. The fact that intravenously injected HSPCs can find their way home to the marrow was first found in clinical transplant settings. To address the shortcomings of cell transplantation, researchers turned to the homing of endogenous stem cells, attempting to heal wounds by activating the self-repairing capacity by recruiting endogenous stem cells to the defect area (Chen et al., 2010; Ahmed et al., 2021). Stem-cell-homing involves a series of physiological processes including cell recognition, migration, proliferation, and differentiation, and ultimately achieves tissue regeneration, which plays a huge role under certain conditions and has achieved remarkable therapeutic effects (Liesveld et al., 2020). In this method, biomaterials were utilized for bioactive factors delivery as well as the host's inherent regenerative potential activating (Safina and Embree, 2022; Xin et al., 2022; Yao and Lv, 2022; Zhao et al., 2022). By mobilizing appropriate stem/progenitor cells to specific spaces for tissue repair through cell-material interactions at the defect site, the endogenous regeneration process can be mimicked (Andreas et al., 2014; Mao et al., 2022). The possible advantages of this strategy in promoting periodontal regeneration are as follows: firstly, it provides a solution to some of the limitations of stem cell transplantation, and transforms periodontal regeneration treatment methods into a clinically valid way; secondly, it gives full play to the potential of host self-repair and regeneration, making periodontal tissue regeneration safer; moreover, compared with the introduction of exogenous stem cells, it is simpler and less expensive to treat periodontal diseases and other diseases (Abdulghani and Mitchell, 2019; Safina and Embree, 2022). To make better use of the stem cell homing technique to restore the periodontal defect, this paper reviews the research status of the stem cell homing technique.

2 Brief history of cell homing for tissue engineering

Stem cell homing was originally defined as the process of endothelialization through blood vessels and migration of hematopoietic stem cells (HSCs) after transplantation, and finally, HSCs colonize in the bone marrow and restart hematopoiesis, in which many cytokines and chemokines are involved (Ji et al., 2015; Zhu et al., 2015). Blood lineages are considered to be risen from hematopoietic stem and progenitor cells (HSPCs), which then migrate to the bone marrow niche through homing for further proliferation and differentiation (Li et al., 2018a; Blokzijl-Franke et al., 2021; Ranzoni et al., 2021). The homing mechanism of HSPCs is relevant to stem cell transplantation therapy and has been investigated by many researchers (Morrison and Scadden, 2014; Li et al., 2018a; Liesveld et al., 2020), though the specific mechanism of HSPCs homing was not elucidated. While researchers considered that specific cells or cytokines may mediate this process, thus enabling the homing of HSCs (Li et al., 2018a).

Recently, the tissue engineering technique has expanded the meaning of stem cell homing as the process in which endogenous stem cells mainly migrate directionally and across the vascular endothelium to target tissues, and then colonize and survive (Ji et al., 2015; Zhu et al., 2015). *In vivo*, stem cells are located in various stem cell niches and are exposed to a large number of complex and manageable biomaterials, including chemokines, cytokines, growth factors, the extracellular matrix (ECM), and so on (Chen et al., 2011; Yang et al., 2020) (Figure 1).

Tissue regeneration, also known as *in situ* tissue engineering, has emerged over the past 20 years because of its remarkable advantages. This technique mimics the human wound healing process and aims to repair or regenerate tissue by recruiting endogenous stem cells to the defections *via* targeted specific bionic scaffolds and/or bioactive cues that stimulate the host's biological substance and repairing capacity (Ji et al., 2015; Safina and Embree, 2022). To make the endogenous stem cells migrate toward a specific tissue, these endogenous stem cells must recognize the biomolecules that mediate homing first and manipulate their activity to catalyze the homing process (Chen et al., 2011). The possible mechanism might rely on the development of the scaffold system which is implanted into the damaged area (Lee et al., 2016; Abdulghani and Mitchell, 2019). The proper microenvironment created by the implanted scaffold will then promote the host stem cells to recruit and move through the vascular network or tissue interstitial space to the damaged tissue or organ, where the stem cells then proliferate, differentiate, and form tissue within the scaffold which eventually degrades, leaving only regenerated tissue (Zheng et al., 2019; Chu et al., 2022).

In regenerative medicine, there is growing evidence proving that cell recruitment could stimulate self-repair ability in hosts and harness the born regenerative capacity of tissues. It was regarded as a promising cell-based therapy and has been used to regenerate heart tissue, cartilage tissue, and bone tissue *in situ* already (Chen et al., 2011; Cai et al., 2018). In terms of articular cartilage repair, it has been demonstrated that intra-articular and peri-articular MSCs are involved in the cartilage repair process, but due to their limited number, they are unable to achieve the desired repair effect and require stem cells from other sites to recruit to the injured site for repair and to facilitate this process, chemotactic agents are required (Yang et al., 2020; Zhang et al., 2020). Lee et al. (2010)utilized poly-ε-caprolactone and hydroxyapatite to create an

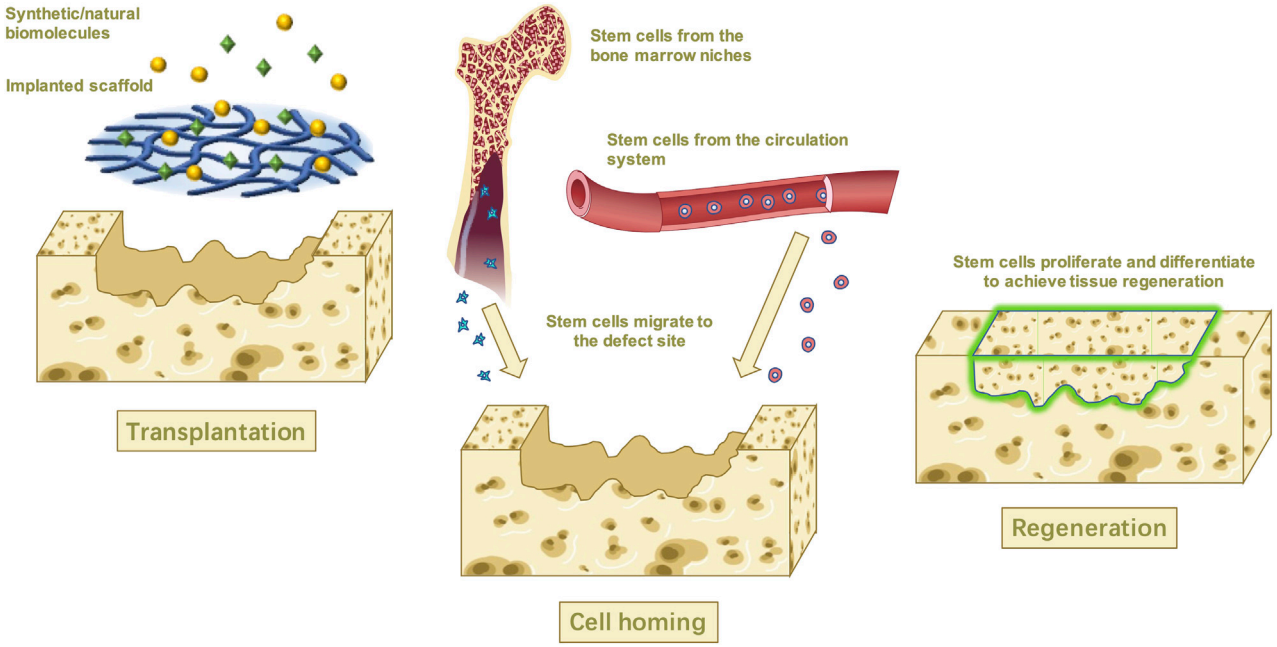

FIGURE 1
In situ tissue engineering uses biological molecular and scaffolds to recruit the stem cells from the niches while promoting proliferation and differentiation and achieving tissue regeneration in the end.

anatomically correct TGF-β3-containing biological scaffold. The results suggest that for such complex tissues, the regeneration may happen *via* endogenous cell homing instead of cell transplantation. In addition, endogenous stem cell homing technology has shown great potential in the cardiovascular field, aiming at repairing heart-damaged tissues in myocardial infarction (MI) and ischemic heart disease, and is considered one of the most promising therapeutic strategies (Pacelli et al., 2017; Li et al., 2018b). Shafiq et al. (2018) developed specific cardiac patches, which can promote the mobilization and recruitment of endogenous MSCs to the defected area in acute MI models. The experimental results showed that this new cardiac patch together with suitable scaffold materials is a good choice for promoting *in situ* vascular regeneration and deserves to be promoted.

For periodontal regeneration, though the injured periodontium possesses a weak ability for self-healing, it can be significantly promoted when proper treatment and guidance are added (Xu et al., 2019). Increasing evidence demonstrates that directing endogenous stem cells to defected areas contributes to the regenerative and immunomodulating function since the resident MSCs play a key role in periodontal regeneration. Except for MSCs, PDL also contains PDLSCs and osteogenic progenitor cells which can regenerate cementum, bone, and the PDL tissue itself together with MSCs (Cai et al., 2018; Yamamoto et al., 2018; Xu et al., 2019). Additionally, a variety of factor-loaded scaffolds for periodontal regeneration have been fabricated. Yu et al. (2022) constructed a biphasic scaffold combining intrafibrillarly mineralized collagen (IMC) and concentrated growth factor (CGF) to synergist regeneration of periodontal tissues. In animal experiments, PDLSCs, BMSCs, and induced pluripotent stem cells showed the potential to stimulate the formation of new periodontal tissues (Ji et al., 2015). Consequently, the application of cell homing could eliminate clinical constraints associated with periodontal wounds (Cai et al., 2018). Wang et al. (2016) constructed a cell-free stromal cell-derived factor-1α (SDF-1α)-scaffold-parathyroid hormone system which can stimulate the proliferation of $CD90^{+}CD34^{-}$stromal cells and promote the regeneration of damaged tissues in a rat periodontal defect model. Liang et al. (2021) also used rats to apply SDF-1 topically and exendin-4 (EX-4) systemically. The experimental results showed that combined SDF-1/EX-4 treatment could promote the recruitment of MSCs *in vivo*, induce early osteoclastogenesis, and promote the expression of osteogenic proteins, which results in both the quantity and quality improvement of regenerated bone. Although the cell homing for periodontal regeneration is still at the experimental stage, it has great potential to facilitate bone-ligament-cementum regeneration in the treatment of periodontal diseases, such as periodontitis, providing a safe, effective and cost-effective alternative therapy (Liu et al., 2019a; Xu et al., 2019).

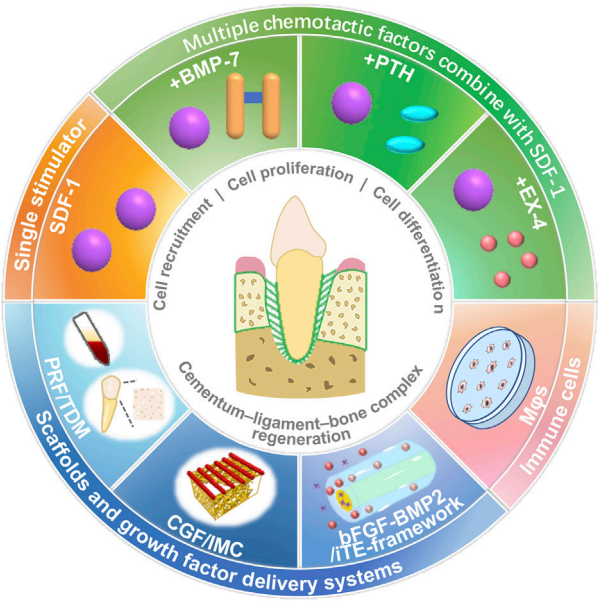

FIGURE 2
Stimulation strategies, such as chemokines, cytokines, scaffolds, and immune cells, for stem cell homing and periodontal tissue regeneration.

3 Main strategies for the regeneration of periodontal tissues by endogenous stem cells homing

In periodontal tissue regeneration and repair, endogenous stem cells mainly used include BMSCs and PDLSCs, which can migrate to the defect site and stimulate their proliferation and differentiation by adopting appropriate strategies, such as chemokines, and using tissue-engineered scaffolds (Figure 2; Table 1).

3.1 The sources of endogenous stem cell

To repair periodontal tissues, reparative cells can be acquired from stem niches (Kimura et al., 2014; Liu et al., 2015; Yin et al., 2017). Mainly BMSCs and PDLSCs were studied. PDLSCs are the first choice for studying cell delivery for periodontal regenerative purposes, while bone marrow-derived cells also contribute to it because of the insufficiency of the stem cells in PDL tissue (Yin et al., 2017).

3.1.1 MSCs derived from bone marrow

Multipotent MSCs can be proliferated both *in vitro* and *in vivo*, which then differentiate into mesodermal tissues of different functions, including bone, cartilage, tendons, fat, and nerves (Pittenger et al., 1999). As a consequence, MSCs have been proposed as potentially useful tissue-engineering seeding cells. Several studies have found that BMSCs can be the origin of cementoblasts, osteoblasts, and periodontal fibroblasts, in addition to secreting extracellular matrix from PDLs, cementum, and alveolar bone (Kawaguchi et al., 2004; Hasegawa et al., 2006).

Immunohistochemistry was used to quantify the engraftment of MSCs in the defect by Liu et al. (2015). A sequential section approach was used to identify MSCs (CD29+/CD45−), which showed that the number of MSC transplanted with SDF-1 significantly increased.

He et al. (2019) selected rat BMSCs to investigate Mφ polarization and endogenous stem cell recruitment which enhance periodontal regeneration. It has been shown that the homing of BMSCs was significantly improved both *in vitro* and *in vivo*.

3.1.2 PDLSCs from odontogenic tissues

Recently, subsequent attempts were made to harvest MSCs from odontogenic tissues, such as periodontal ligaments (Seo et al., 2004), gingiva (Zhang et al., 2009), the dental follicle (Morsczeck et al., 2005), the dental pulp (Gronthos et al., 2000), apical papilla (Sonoyama et al., 2008), and human exfoliated tissue deciduous teeth (Miura et al., 2003; Hynes et al., 2012). From human-impacted third molars, Seo et al. (2004) successfully isolated PDLSC, which can differentiate into multiple periodontal tissues. (Liu et al., 2008; Huang et al., 2009a; Park et al., 2011).

PDLSCs, located around the blood vessels of periodontal tissues and having the characteristics of mesenchymal stem cells, are one of the most practically applied multipotency stem cells in the field of periodontal tissue repair and regeneration. Liang et al. (2021) tested PDLSCs and confirmed that the proliferation and migration of PDLSCs. In other research, the effects of growth factors on controlling the fate of PDLSCs are studied (Ding et al., 2020).

3.1.3 Non-hematopoietic stromal cells derived from hosts

$CD90^+CD34^-$ stromal cells have also been studied for recruitment. CD90, also referred to as Thy-1, represents stem and progenitor cells on the cell surface, which makes $CD90^+CD34^-$ stromal cells to be considered non-hematopoietic stromal cells. A previous study also showed that MSCs, including PDLSCs, could express CD73, CD90, and CD105 while not CD14, CD34, and CD45 (Dominici et al., 2006). Therefore, according to previous studies, $CD90^+CD34^-$stromal cells were considered as MSCs (Wang et al., 2016).

Several studies have shown that adult stem cells with CD90 expression have high osteogenic differentiation potential (Chung et al., 2013). In the study by Wang et al. (2016), stromal cells with $CD90^+CD34^-$ staining were analyzed quantitatively

TABLE 1 Stem cells and the stimulation strategies in the research for periodontal regeneration.

Stem cells	Recruitment stimulation	Proliferation stimulation	Differentiation stimulation	Scaffolds	*In vivo* model	Regeneration periodontal tissues	References
PDLSCs	SDF-1	—	BMP-7	Neutralized type I collagen solution	Beagle dog tooth avulsion models	PDL tissue	Zhu et al. (2015)
MSC/HSC	SDF-1	—	—	Absorbable collagen membranes	Rat mandibular bone defect models	Periodontal bone	Liu et al. (2015)
CD90+CD34−stromal cells	PTH/SDF-1	—	—	Medical collagen repair membranes	Rat periodontal defect models	Bone, cementum and functional PDL	Wang et al. (2016)
BMSCs	SDF-1	—	BMP-7	An artificial scaffold made from PCL and HA hybrid	Rat orthotopic/ectopic tooth regeneration models	PDL and new bone	Kim et al. (2010)
PDLSCs	SDF-1	—	EX-4	Medical collagen membranes	Rat periodontal defect models	Periodontal bone	Liang et al. (2021)
BMSCs	SDF-1	—	IL-4/Mφs	High-stiffness TG-gels	Rat periodontal defect models	Bone, cementum and soft tissue	He et al. (2019)
BMSCs/PDLSCs	PRF	PRF	PRF/TDM	Fabrication of canine TDM and PRF membrane	Beagle dog periodontal defect models	Cementum–PDL complex and tooth root	Ji et al. (2015)
BMSCs/PDLSCs	CGF/IMC	CGF/IMC	CGF/IMC	Hierarchical CGF/IMC bilayer architecture	Rat periodontal defect models	Bone, cementum and PDL	Yu et al. (2022)
BMSCs	SDF-1	—	—	Commercially available gelatin sponge	Rat periodontal defect models	PDL and new bone	Cai et al. (2018)
PDLSCs/MSCs	bFGF/iTE-framework	bFGF/iTE-framework	BMP-2/iTE-framework	iTE-framework	Rat periodontal defect models	Bone, cementum and PDL	Ding et al. (2020)

using immunofluorescence double staining. The results showed that host-derived $CD90^+CD34^-$stromal cells were recruited and transplanted into the defect. Ding et al. (2020) also used the framework to recruit $CD90^+CD34^-$ stromal cells. The *in vivo* research results showed significant promotion of the recruitment of host-derived $CD90^+CD34^-$ stromal cells at the early stage of wound healing, favoring tissue repair and regeneration.

3.1.4 Multiple sources derived stem cells

Some researchers studied the recruiting and regulating fate of PDLSCs and BMSCs together (Ji et al., 2015; Yu et al., 2022). According to Ji et al. (2015), PDLSCs and BMSCs were tested *in vitro* with canine platelet-rich fibrin (PRF) and treated dentin matrix (TDM). An orthotopic transplantation model using Beagle dogs was developed to regenerate roots with a tooth-PDL-alveolar interface by cell homing in a canine orthotopic model, combined with the use of PRF membranes and TDM. *In vitro*, PRF significantly stimulated the recruitment and proliferation of PDLSCs and BMSCs. The *in vivo* results similarly illustrated that roots connected to the alveolar bone by cementum-PDL complexes can be regenerated by implanting PRF and TDM in the alveolar microenvironment, possibly through the homing of BMSCs and PDLSCs.

3.2 The strategies of stem cell homing

Currently, the main chemotactic strategies used include: 1) the use of chemotactic agents, such as sdf-1, and the combination of the two; 2) the use of scaffold materials loaded with biological factors; 3) regulatory assistance through macrophages. They are described as follows:

3.2.1 Local application of SDF-1

SDF-1, also known as C–X–C motif ligand 12 (CXCL12), is a promising candidate for *in situ* tissue engineering among various

cytokines and chemokines. Previous studies have shown that during the healing process of impaired tissues [brain (Ardelt et al., 2013), heart (Wang et al., 2012; Hajjar and Hulot, 2013; Cavalera and Frangogiannis, 2014), muscle (Brzoska et al., 2012), skin (Yang et al., 2013), and bone (Ji et al., 2013)], elevated levels of SDF-1 at the site of injury can recruit stem/precursor cells from the cardiovascular system and local tissues, and promote their proliferation and differentiation at the site of damage, leading to organ repair and regeneration (Brzoska et al., 2012; Wang et al., 2012; Hajjar and Hulot, 2013; Yang et al., 2013).

In the study of Liu et al. (2015), it has been verified that SDF-1 promoted the proliferation, migration, and differentiation of PDLSCs *in vitro*. After that, they further confirmed the effect of local application of SDF-1 on stem/progenitor cell homing and periodontal bone regeneration *in vivo* through a rat mandibular defect model. Host-derived CD29+/CD45− MSCs were confirmed to be triggered to home and graft into periodontal bone defects by loading SDF-1 into collagen membrane scaffolds. As a result of SDF-1 treatment, MSCs were significantly increased and CD45 + HSCs were engrafted.

The same results were obtained by Adelina S. (Cai et al., 2018) using an SDF-1α loaded gelatin sponge (Spongostan®) for rats with mandibular bone defects. At the same time, a possible explanation has been proposed regarding the enhanced periodontal regeneration caused by SDF-1α stimulation: first, bone marrow-derived osteogenic progenitor cells present in the flowing blood may be recruited to the defected area by the SDF-1α/CXCR4 axis in response to the local release of SDF-1α (Otsuru et al., 2008; Ji et al., 2013). The recruited cells play an important role in periodontal regeneration by expressing their multilineage differentiation capacity, as well as secreting promoting cytokines and growth factors (Bryan et al., 2005). Furthermore, SDF-1α may also induce other progenitor cells in the bone marrow such as HSCs and endothelial progenitor cells to migrate to the defect sites *via* the SDF-1α/CXCR4 axis, creating a proangiogenic environment (Hattori et al., 2003; Petit et al., 2007).

3.2.2 SDF-1 in combination with other chemotactic factors

The main effect of SDF-1 is to actively direct endogenous cell homing. However, its promoting effect on the proliferation and differentiation of stem cells is limited. Therefore, combining other active molecules, such as bone morphogenetic protein 7 (BMP-7), parathyroid hormone (PTH), and EX-4, to improve the efficiency of tissue regeneration has been studied.

BMP-7 could modulate osteogenesis and bone cell differentiation potently. A preclinical study assessed its effects on the regeneration of periodontal bone defects and improvement of cementum regeneration (Cook et al., 1995; Giannobile et al., 1998; Ripamonti et al., 2001). Groundbreaking research into the regeneration of PDL tissue *via* cell homing with SDF1 and BMP-7 was carried out by Kim et al. (2013) in 2010. BMP-7 may be responsible for orthotopic mineralization and formation of the newly formed alveolar bone in rat extraction sockets. The observed putative periodontal ligament also suggests that SDF1 and/or BMP-7 can recruit multiple cell lineages. On this basis, Zhu et al. (2015) further studied the application of SDF1 and BMP-7 in the tooth trauma model frequently. Zhu et al. (2015) hypothesized that SDF1 and BMP-7 may recruit endogenous cells to the root surface to replace the unavailable original PDL cells after avulsed teeth were delayed. During the experiment, avulsed roots coated with SDF1 and BMP-7 were put into the prepared alveolar bone socket. By directing stem cells to the space between replanted roots and the adjacent alveolar bone, SDF1 and BMP-7 were proven to establish the integrated PDL-like structure.

PTH has been used as an optional treatment for bone defects. In periodontal tissue repair, when a large number of endogenous progenitor cells are mobilized directly to the peripheral blood, they will return to the defect site and participate in tissue regeneration, along which PTH is considered a promising periodontal tissue repair agent (Barros et al., 2003; Bashutski et al., 2010; Tokunaga et al., 2011). As a crucial factor for stem cell homing, the chemotactic properties of SDF-1α may be limited by the N-terminal cleavage of the cell surface protein CD26/dipeptidyl peptidase-IV (DPP-IV) at position 2 proline (Christopherson et al., 2002; Christopherson et al., 2004). PTH, known as a DPP-IV inhibitor, has been confirmed recently to enhance the SDF-1α-driven homing of CXCR4 + stem cells in the ischemic heart recently (Huber et al., 2011). In a rat periodontal defect model, Wang et al. (2016) confirmed that PTH/SDF-1α cotherapy was able to induce CD90 + $CD34^-$stromal cell migration and enhance the chemotactic ability of SDF-1α, and accelerate periodontal tissue regeneration.

EX-4, as a full agonist of the glucagon-like peptide-1 receptor (GLP-1R), could promote both migration and proliferation of MSCs (Zhou et al., 2015; Zhang et al., 2016; Sharma et al., 2018; Yap and Misuan, 2019). Recently, studies on EX-4 have proved its capability to inhibit adipogenic stem/precursor cell differentiation while promoting osteogenic differentiation and bone formation. (Feng et al., 2016; Meng et al., 2016; Luciani et al., 2018). Moreover, the quantity of CXCR4+ MSCs was increased by EX-4 *via* PI3K/AKT-SDF-1/CXCR4 signaling pathway (Zhou et al., 2015). Liang et al. (2021) demonstrated that the combination of SDF-1/EX-4 enhanced the proliferation and migration of PDLSCs *in vitro*, together with the recruitment of MSCs, inducement of early osteoclastogenesis, expression of osteoblast protein in new bone formation, as long as the formation of new bone *in vivo*. Therefore, the combination of SDF-1/EX-4 could provide a new strategic option for periodontal bone regeneration *in situ*.

3.2.3 Chemotaxis effect of scaffold and its role as growth factor carriers

Scaffold biomaterials should be designed to mimic the natural extracellular environment as much as possible to affect cell behavior and control cell fate *in vivo*. In the present study, many scaffold materials can not only act as carriers but also play a role in recruiting stem cells and promoting their proliferation and differentiation.

Choukroun et al. (2001) reported in 2001 that PRF could promote the recruitment, proliferation, and differentiation of stem cells by releasing several growth factors, such as transforming growth factor-β(TGF-β), platelet-derived growth factor (PDGF), epidermal growth factor (EGF). TDM, a natural acellular matrix scaffold, could retain essential non-collagenous proteins and growth factors for the regeneration of apical periodontal tissue (Li et al., 2008; Smith et al., 2012). Both PRF and processed TDM are depots of various growth factors that can promote cell homing. Ji et al. (2015) confirmed that PRF can recruit BMSCs and PDLSCs. In addition, the proliferation of PDLSCs and BMSCs was also stimulated *in vitro*, which is consistent with other studies (Ehrenfest et al., 2010; Chang and Zhao, 2011). The results also demonstrated that TDM was able to direct the differentiation of seed cells (Ma et al., 2008; Wu et al., 2008; Li et al., 2011; Guo et al., 2012; Yang et al., 2012). Treated as one unit, PRF/TDM's potential to stimulate the differentiation of PDLSCs and BMSCs was confirmed *in vitro*. *In vivo*, the experimental results showed that it is essential for endogenous tooth root regeneration by using PRF as bioactive cues, and TDM as an inductive scaffold, together with tooth socket microenvironments.

In addition to scaffold materials of biological origin, synthetic scaffold materials also have similar effects. Ding et al. (2020) developed a super assembly framework (SAF) in which bFGF and BMP-2 were designed to facilitate regeneration of the local cementum-ligament-bone complex in a sequential manner. The in *situ* tissue engineering framework (iTE-framework) not only showed improved physicochemical properties, but also was shown to promote the proliferation, migration, and osteogenic differentiation of PDLSCs *in vitro*. A rat periodontal defect model is created for *in vivo* experiment. The results showed that both the formation of new bone and the regeneration of PDL and cementum tissue could be promoted by the iTE framework significantly.

3.2.4 The role of immunomodulation in stem cell recruitment

Microenvironments can influence cell homing by influencing the properties of stem cells. Since there are already many well-established drugs targeting the immune microenvironment in treating periodontitis, it is a promising strategy to combine these existing therapeutic agents and cytokines to enhance the immune microenvironment and promote cell homing and tissue formation, thus achieving higher levels of immune regulation and tissue repair (Yang et al., 2021).

In correlative studies (Abbott et al., 2004), exogenous SDF-1 was found to be insufficient to stimulate stem cell recruitment without injury for periodontal regeneration. A combination of inflammation and SDF-1 may increase stem cell recruitment in the healing process (Chen et al., 2013). In further studies conducted by Li et al. (2018a), it was confirmed that VCAM-1 + macrophage-like cells are important for both homing and retention of HSPCs. In the field of periodontal defect regeneration, He et al. (2019) studied the effect of "macrophage regulation" in periodontal tissue regeneration. It was hypothesized that high-stiffness TG gels modulate Mφ polarization and promote endogenous stem cell recruitment by modulating IL-4 and SDF-1α production. Immunofluorescence staining and histological examination showed that IL-4 could promote the polarization of Mφs into the M2 phenotype, and further promote the osteogenic differentiation of successfully homed BMSCs.

In the future, further studies on the role of immunomodulation in stem cell homing are needed to address these uncertain issues and reach scientific conclusions.

3.3 Scaffolds contributing to stem cell regulation

3.3.1 Natural scaffold materials

Natural scaffold materials have good biocompatibility and bioactivity, and can also be loaded with a variety of biological factors, effectively promoting the reconstruction of periodontal tissues.

Collagen, as a natural protein, is obtained from the skin, bones, and ligaments of animals and is widely used in tissue engineering scaffolds due to its superior biocompatibility, biodegradability, and weak antigenicity (Reyes and García, 2004; Xiong et al., 2009). In the study of recruiting endogenous stem cells for periodontal tissue regeneration, collagen membrane or collagen solution is often used as a tissue engineering scaffold and plays a role in transporting chemokines and recruiting endogenous stem cells (Liu et al., 2015; Zhu et al., 2015; Wang et al., 2016; Liang et al., 2021). A commercial product, gelatin sponge (Spongostan ®) (Cai et al., 2018), was also used as a carrier for the delivery of SDF-1α.

TDM is a kind of natural matrix scaffold that is decellularized and retains multiple bioactive molecules, including non-collagenous proteins and growth factors (Smith et al., 2012) that are crucial for the formation of periodontal tissue around tooth roots (Li et al., 2008). Several studies have shown that PDLSCs treated with dentin non-collagenous proteins exhibit several signs of differentiation into cementoblasts. In their previous studies, TDM demonstrated a role as an inductive microenvironment and scaffold for tooth root regeneration (Guo et al., 2012; Yang et al., 2012). TDM, compared with nature dentin, has similarities in structure and

mechanical characteristics but is more cost-effective. By regulating molecules in a mechanically-suitable environment, it is expected to trigger regenerative processes not only structurally but also physiologically. There was evidence that TDM can direct the differentiation of seeded cells (Ma et al., 2008; Wu et al., 2008; Li et al., 2011; Guo et al., 2012; Yang et al., 2012). The study by Ji et al. (2015) mentioned above demonstrated the effect of TDM in periodontal tissue regeneration.

Another scaffold material of natural origin was prepared by Yu et al. (2022). With biomimetic self-assembly and microstamping techniques, they constructed a parallel hierarchy of mineralized IMC layers and unmineralized collagenized-CGF layers. With special micro-structure, mechanical characteristics, and growth-factor-rich microenvironment, the differential biphasic scaffold simulates the periodontal hard/soft tissue interface perfectly. This solves the obvious disadvantage that monophasic scaffolds cannot be used effectively for regenerating complex multiphasic tissues, such as periodontal tissues (Dan et al., 2014; Cho et al., 2016). This biomimetic IMC scaffold modulates and determines the fate of PDLSC and BMSCs. Even though it cannot secrete growth factors, the osteoid microenvironment can serve as a biofactor-rich microenvironment that facilitates cell osteogenesis (Liu et al., 2019b). CGF is rich in endogenous growth factors, including TGF-β1, VEGF, PDGF-BB, IGF-1, and bFGF. The CGF substrate superstructure with parallel-aligned gaps may also be responsible for the oriented migration of stem cells (Liu et al., 2013). *In vitro* experiments demonstrated that PDLSCs were successfully differentiated into PDL/osteogenesis using the biphasic scaffold containing CGF/IMC. After implantation in rat periodontal defects, multilineage differentiation could be effectively achieved by recruiting host stem cells into soft and hard periodontal tissues.

3.3.2 Composite scaffolds

Natural scaffold materials have good biocompatibility and bioactivity, but synthetic scaffold materials usually have more controllable degradation rates and physical and mechanical properties. To overcome the disadvantages of the above materials when used alone, as well as simulate complex periodontal tissues, a new direction in the development of scaffold materials in recent years is to combine two or more materials to obtain good physical and chemical properties while improving their biocompatibility and bioactivity.

Unlike previous approaches that relied primarily on hard materials like collagen, silk, or PLGA, the primary scaffold relies on soft materials (Young et al., 2002; Modino and Sharpe, 2005; Ikeda et al., 2009). The mechanical stiffness of polycaprolactone (PCL) and hydroxyapatite (HA) hybrid has good load-bearing properties (Woodfield et al., 2005). Rapid prototyping methods such as 3D bioprinting may offer additional advantages such as precise control, interconnectivity, as well as anatomical dimensions (Woodfield et al., 2005; Lee et al., 2009). Kim et al. (2010), anatomically shaped human layer scaffold and rat incisor scaffold from a hybrid of PCL and HA *via* 3D layer-by-bioprinting channels. The collagen solution loaded with SDF1 and BMP-7 was also injected into the scaffold microchannel by a micropipette. Next, the rat model was used for orthotopic/ectopic tooth regeneration without cell transplantation. Quantitatively, the combination of SDF1/BMP-7 significantly improved the cell's chances of homing into the microchannels of human molar scaffolds compared to scaffolds without growth factors. Besides recruitment of cells into the microchannels, the regeneration of putative PDL and new alveolar bone also supports the claim that cell homing is effective.

Other composite scaffolds, such as a three-dimensional (3D) scaffold of high-stiffness Transglutaminase cross-linked gelatin (TG-gel) constructed by He et al. (2019) and framework (SAF) which can sequentially release bFGF and BMP-2 constructed by Ding et al. (2020), also showed great potential for *in situ* periodontal tissue regeneration.

4 Application of endogenous stem cells homing in periodontal tissue regeneration

Periodontal tissue is a complex tissue composed of PDL, alveolar bone, cementum, and gingiva, which together play an important role in supporting teeth, masticatory forces, and maintaining the mucosa of the oral masticatory. In addition to controlling the inflammation in the periodontal tissues caused by periodontitis (Pihlstrom et al., 2005; Darveau, 2010; Kinane et al., 2017), periodontal therapy aims to regenerate the cementum-ligament-bone complexes (Phillips et al., 2000). The traditional method is stem cell transplantation (Liu et al., 2008), which is unsatisfactory for a complete and stable restoration of periodontal tissue. The use of *in situ* tissue engineering for periodontal regeneration has recently gained popularity. Specifically, scaffolds are used to deliver chemotactic agents to maximize the host's intrinsic potential, mobilize appropriate progenitor cells into an area designated for tissue repair, and mimic endogenous regenerative processes (Chen et al., 2015; Martino et al., 2015; Lee et al., 2017). Therefore, the method can regenerate and repair a variety of periodontal tissues, including periodontal ligaments, alveolar bone, cementum, and periodontal ligament fibers (Table 1).

4.1 Hard tissue (alveolar bone and cementum) regeneration

In severe cases of periodontitis, the alveolar bone could be resorbed, resulting in tooth loss. During periodontal therapy, the main goal is to regenerate bone. Tissue engineering techniques have opened up new possibilities for regenerating periodontal bone. Liu et al. (2015) performed *in vitro* experiments using a

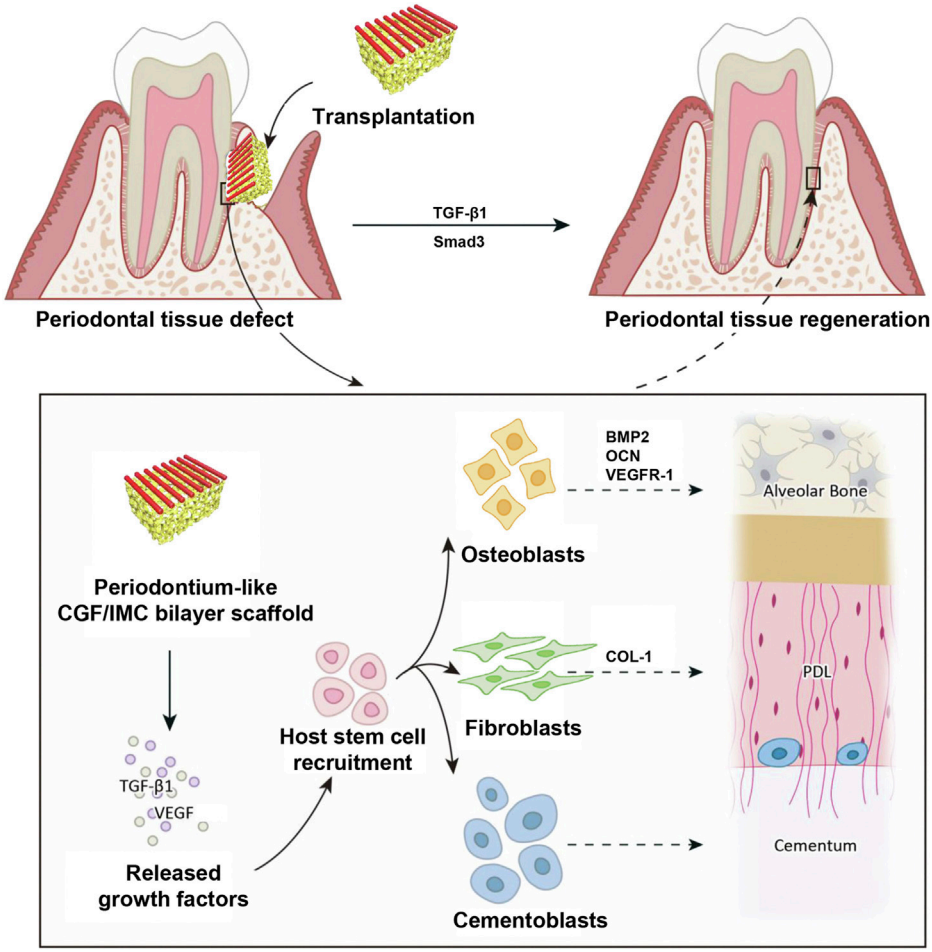

FIGURE 3
Potential mechanisms of periodontal hard/soft tissue regeneration by the hierarchical CGF/IMC bilayer architecture. Reprinted from ref (Yu et al. (2022)).

Wistar rat model of mandibular buccal bone defects. The effects of SDF-1 on bone formation were assessed. At the early stage of degradation, old bone was resorbed through osteoclastogenesis facilitated by SDF-1, and collagen scaffold formation was accelerated by MMP-9, making space for new bone and other tissue. The anti-inflammatory properties of SDF-1 could reduce the inflammatory response, promote vascularization, recruit MSCs and HSCs to the wound for healing processes, and ultimately enhancing bone regeneration. Even though it is still unclear which mechanism governs bone regeneration, the study confirms that loading SDF-1 into collagen scaffolds shows great potential as *in situ* tissue engineering strategy in periodontal bone regeneration.

It is insufficient to apply SDF-1 alone for favorable bone regeneration (Cipitria et al., 2017). Hence, other growth factors should be combined to boost periodontal bone regeneration. An *in vitro* and *in vivo* study conducted by Liang et al. (2021) showed that SDF-1/EX-4 combination treatment enhanced PDLSC proliferation and migration, as well as *in vitro* mineral deposition production and early osteoclastogenesis. The osteogenic protein expression in a rat periodontal bone defect model has also been upregulated. This strategy therefore improves the quantity and quality of regenerated bone and provides a new tool for periodontal bone regeneration *in situ*.

4.2 Soft tissue (periodontal ligament) regeneration

In dental trauma, tooth avulsion is one of the most common but severe cases (Andreasen et al., 1994). After the tooth was avulsed, the fibers of its PDL were torn, which would render immediate but

severe injury to the periodontal soft tissue. To survive after avulsed teeth are replanted, regeneration of PDL is essential.

By coating the root surface with SDF-1 and BMP-7, Wenting Zhu et al. (2015) succeeded in generating a PDL-like neo-tissue between the surrounding alveolar bone and the replanted root surface. Since the collagen fibers were inserted deep into the cementum and adjacent bone perpendicularly, neo-tissue displayed periodontium-like characteristics. In essence, it was possible to restore the integrity of the periodontal structure of the teeth. Using this method, it would be possible to determine whether avulsed teeth could be rescued after they had been given up clinically.

4.3 Reparation of complex multiphase periodontal tissues

The disease of periodontitis involves both periodontal ligaments and alveolar bone, which causes inflammation of gingival tissues, the loss of periodontal attachment, and ultimately leads to tooth loss (Pihlstrom et al., 2005). To limit inflammation within the periodontal tissues and control the progression of periodontitis, the main goal of periodontal therapy is to restore these lost tissues to their original morphology, structure, and function. Due to the complex mineralized/non-mineralized layered structure of periodontal tissues (Woo et al., 2021), regenerative repair is a challenging task for dentists (Bartold et al., 2000) once the loss of hard tissue and soft tissue occurs. While stem cell-based cell delivery therapy shows great promise in periodontal wound healing, culture-expanded stem cells require complex procedures and are expensive to apply. (Chen et al., 2010; Chen et al., 2012b). Endogenous regeneration techniques can stimulate potential self-repair mechanisms in the host by promoting endogenous stem cell recruitment and adaptation to the lesion site (Chen et al., 2011). Compared to complex and expensive *ex-vivo* manipulation techniques, these options enhanced safety, affordability, and flexibility, making them increasingly popular in periodontal regenerative medicine (Chen et al., 2010).

Using the rat periodontal fenestration defects model, Wang et al. (2016) explored the effects of a cell-free system that combined PTH systemic application to SDF-1α-scaffold on periodontal tissue regeneration *in vivo*, while co-presentation of IL -4 and SDF-1α in high-stiffness TG-gels on periodontal regeneration was studied by He et al. (2019). Two experiments both led to satisfactory soft tissue and hybrid tissue regeneration.

Due to the difficulty of regenerating complex multiphase tissues by monophasic scaffolds (Dan et al., 2014; Cho et al., 2016), Yu et al. (2022) constructed a biomimetic tissue-specific functional structure to regenerate periodontal tissues (Figure 3). In the hierarchical biphasic architecture, IMC scaffolds could be used for osteogenic differentiation, while CGF fibers exhibited fibroblastic differentiation potential. After implanting the critical-sized intact defect in a rat model, the host stem cells could be recruited effectively, which then achieve multilineage differentiation into periodontal tissues. As the PDL fibers were inserted into the newly formed bone tissue, the CGF/IMC biphasic scaffold successfully reconstructed complete and functional periodontium after 8 weeks of implantation.

5 Conclusion and prospects

The repair of periodontal defects is a difficult problem of international concern. The existing traditional clinical treatment methods, such as GTR and GBR, fail to restore the physiological structure and function of teeth and periodontal tissues effectively. With the rapid advancements in cell therapy, stem cell transplantation has become the main focus and means of promoting tooth and periodontal regeneration. However, *in vitro* culture of stem cells requires strict conditions, complex procedures, and faces a huge risk of clinical application. The use of *in vivo* endogenous stem cell migration to promote tissue regeneration is expected to solve the difficulties of stem cells *in vitro* and reduce the risk of clinical application, which has a broad research prospect and clinical application space.

Stem cell homing involves a series of physiological processes such as cell adhesion, migration, proliferation, and remodeling, and requires appropriate scaffold materials as well as a certain microenvironment. Current research mainly includes *in vitro* cell experiments and *in vivo* animal experiments, while does not involve clinical trials yet. At present, the chemotactic strategies mainly use a variety of chemotactic agents, such as SDF-1, BMP-7, EX-4, PRF, to encourage the migration and proliferation of endogenous stem cells, as well as the differentiation into periodontal tissues. Some scaffold materials are also involved in chemotaxis. Additionally, the application of immune cells (such as macrophages) in cell homing has also been studied.

However, despite the validated role of stem cell homing in periodontal tissue regeneration, there are still significant limitations of the strategy. Firstly, the stem cell sources are hard to define, and the mechanisms by which chemotactic strategies promote stem cell homing have not been fully elucidated. Additionally, the property of endogenous stem cells may be affected under certain physiological conditions such as inflammation and aging, which will limit the effect of stem cell homing strategy. On the other hand, the currently used animal models are comparatively limited and lack *in vivo* findings in mammals. Meanwhile, due to the maturity of the technology itself, it has not been put into clinical trials.

In the future, the regulation of endogenous stem cell fate by different chemotactic agents and the combination of chemotactic agents and scaffold materials will remain the key point of research. Further understanding of homing mechanisms and

development of methods to enhance this phenomenon may have further clinical benefits. At the same time, more advanced detection techniques are required to identify the source of recruited stem cells. In addition, improving the animal experimental model of periodontal tissue engineering is also the focus of future research. Only by clarifying the mechanism and obtaining reliable results on a suitable animal model can the transformation from basic experiments to clinical applications be achieved as soon as possible.

Author contributions

Conceived and designed the topic: HX and LM. Wrote the original draft: LM, YW, and HX. Analyzed the data: LM, YW, and YL. Prepared the figures LM, YW, YL, and QH. HX, YW, YL, QH, and LM edited the manuscript. All authors read and approved the final manuscript.

Funding

This work was supported by Medical Science and Technology Project of Sichuan Provincial Health Commission (No. 21PJ059), and Science and Technology Application Fundamental Project of Sichuan Province (No. 2022YFS0124).

Conflict of interest

The authors declare that the research was conducted in the absence of any commercial or financial relationships that could be construed as a potential conflict of interest.

The reviewer, XC, declared a shared affiliation with the authors LM, YW, YL, and HX, to the handling editor at the time of review.

Publisher's note

References

Abbott, J. D., Huang, Y., Liu, D., Hickey, R., Krause, D. S., and Giordano, F. J. (2004). Stromal cell-derived factor-1 alpha plays a critical role in stem cell recruitment to the heart after myocardial infarction but is not sufficient to induce homing in the absence of injury. *Circulation* 110, 3300–3305. doi:10.1161/01.Cir.0000147780.30124.Cf

Abdulghani, S., and Mitchell, G. R. (2019). Biomaterials for *in situ* tissue regeneration: A review. *Biomolecules* 9, 750. doi:10.3390/biom9110750

Ahmed, G. M., Abouauf, E. A., AbuBakr, N., Fouad, A. M., Dörfer, C. E., and Fawzy El-Sayed, K. M. (2021). Cell-based transplantation versus cell homing approaches for pulp-dentin complex regeneration. *Stem Cells Int.* 2021, 1–23. doi:10.1155/2021/8483668

Andreas, K., Sittinger, M., and Ringe, J. (2014). Toward *in situ* tissue engineering: Chemokine-guided stem cell recruitment. *Trends Biotechnol.* 32, 483–492. doi:10.1016/j.tibtech.2014.06.008

Andreasen, J. O., Andreasen, F. M., and Andersson, L. (1994). *Textbook and color atlas of traumatic injuries to the teeth*. Hoboken, Wiley-Blackwell: John Wiley & Sons.

Ardelt, A. A., Bhattacharyya, B. J., Belmadani, A., Ren, D. G., and Miller, R. J. (2013). Stromal derived growth factor-1 (CXCL12) modulates synaptic transmission to immature neurons during post-ischemic cerebral repair. *Exp. Neurol.* 248, 246–253. doi:10.1016/j.expneurol.2013.06.017

Barros, S. P., Silva, M. A. D., Somerman, M. J., and Nociti, F. H. (2003). Parathyroid hormone protects against periodontitis-associated bone loss. *J. Dent. Res.* 82, 791–795. doi:10.1177/154405910308201006

Bartold, P. M., McCulloch, C. A. G., Narayanan, A. S., and Pitaru, S. (2000). Tissue engineering: A new paradigm for periodontal regeneration based on molecular and cell biology. *Periodontol. 2000* 24, 253–269. doi:10.1034/j.1600-0757.2000.2240113.x

Bashutski, J. D., Eber, R. M., Kinney, J. S., Benavides, E., Maitra, S., Braun, T. M., et al. (2010). Teriparatide and osseous regeneration in the oral cavity. *N. Engl. J. Med. Overseas. Ed.* 363, 2396–2405. doi:10.1056/NEJMoa1005361

Blokzijl-Franke, S., Ponsioen, B., Schulte-Merker, S., Herbomel, P., Kissa, K., Choorapoikayil, S., et al. (2021). Phosphatidylinositol-3 kinase signaling controls survival and stemness of hematopoietic stem and progenitor cells. *Oncogene* 40, 2741–2755. doi:10.1038/s41388-021-01733-5

Bottino, M. C., Thomas, V., Schmidt, G., Vohra, Y. K., Chu, T.-M. G., Kowolik, M. J., et al. (2012). Recent advances in the development of GTR/GBR membranes for periodontal regeneration--a materials perspective. *Dent. Mat.* 28, 703–721. doi:10.1016/j.dental.2012.04.022

Bryan, D., Walker, K. B., Ferguson, M., and Thorpe, R. (2005). Cytokine gene expression in a murine wound healing model. *Cytokine* 31, 429–438. doi:10.1016/j.cyto.2005.06.015

Brzoska, E., Kowalewska, M., Markowska-Zagrajek, A., Kowalski, K., Archacka, K., Zimowska, M., et al. (2012). Sdf-1 (CXCL12) improves skeletal muscle regeneration via the mobilisation of Cxcr4 and CD34 expressing cells. *Biol. Cell.* 104, 722–737. doi:10.1111/boc.201200022

Cai, X., Yang, F., Walboomers, X. F., Wang, Y., Jansen, J. A., van den Beucken, J., Plachokova, A. S., et al. (2018). Periodontal regeneration via chemoattractive constructs. *J. Clin. Periodontol.* 45, 851–860. doi:10.1111/jcpe.12928

Cavalera, M., and Frangogiannis, N. G. (2014). Targeting the chemokines in cardiac repair. *Curr. Pharm. Des.* 20, 1971–1979. doi:10.2174/13816128113199990449

Chang, Y. C., and Zhao, J. H. (2011). Effects of platelet-rich fibrin on human periodontal ligament fibroblasts and application for periodontal infrabony defects. *Aust. Dent. J.* 56, 365–371. doi:10.1111/j.1834-7819.2011.01362.x

Chen, F. M., Lu, H., Wu, L. A., Gao, L. N., An, Y., and Zhang, J. (2013). Surface-engineering of glycidyl methacrylated dextran/gelatin microcapsules with thermo-responsive poly(N-isopropylacrylamide) gates for controlled delivery of stromal cell-derived factor-1α. *Biomaterials* 34, 6515–6527. doi:10.1016/j.biomaterials.2013.05.014

Chen, F. M., Wu, L. A., Zhang, M., Zhang, R., and Sun, H. H. (2011). Homing of endogenous stem/progenitor cells for *in situ* tissue regeneration: Promises, strategies, and translational perspectives. *Biomaterials* 32, 3189–3209. doi:10.1016/j.biomaterials.2010.12.032

Chen, F. M., Zhang, J., Zhang, M., An, Y., Chen, F., and Wu, Z. F. (2010). A review on endogenous regenerative technology in periodontal regenerative medicine. *Biomaterials* 31, 7892–7927. doi:10.1016/j.biomaterials.2010.07.019

Chen, F. M., Zhao, Y. M., Jin, Y., and Shi, S. T. (2012b). Prospects for translational regenerative medicine. *Biotechnol. Adv.* 30, 658–672. doi:10.1016/j.biotechadv.2011.11.005

Chen, J. D., Zhang, Y. J., Pan, P. P., Fan, T. T., Chen, M. M., and Zhang, Q. Q. (2015). *In situ* strategy for bone repair by facilitated endogenous tissue engineering. *Colloids Surfaces B Biointerfaces* 135, 581–587. doi:10.1016/j.colsurfb.2015.08.019

Cho, H., Tarafder, S., Fogge, M., Kao, K., and Lee, C. H. (2016). Periodontal ligament stem/progenitor cells with protein-releasing scaffolds for cementum formation and integration on dentin surface. *Connect. Tissue Res.* 57, 488–495. doi:10.1080/03008207.2016.1191478

Choukroun, J., Adda, F., Schoeffler, C., and Vervelle, A. (2001). *Une opportunite´ en paro-implantologie: Le PRF*. Implantodontie 42, 55–62.

Christopherson, K. W., Hangoc, G., and Broxmeyer, H. E. (2002). Cell surface peptidase CD26/dipeptidylpeptidase IV regulates CXCL12/stromal cell-derived factor-1 alpha-mediated chemotaxis of human cord blood CD34(+) progenitor cells. *J. Immunol.* 169, 7000–7008. doi:10.4049/jimmunol.169.12.7000

Christopherson, K. W., Hangoc, G., Mantel, C. R., and Broxmeyer, H. E. (2004). Modulation of hematopoietic stem cell homing and engraftment by CD26. *Science* 305, 1000–1003. doi:10.1126/science.1097071

Chu, G., Zhang, W., Han, F., Li, K., Liu, C., Wei, Q., et al. (2022). The role of microenvironment in stem cell-based regeneration of intervertebral disc. *Front. Bioeng. Biotechnol.* 10, 968862. doi:10.3389/fbioe.2022.968862

Chung, M. T., Liu, C. J., Hyun, J. S., Lo, D. D., Montoro, D. T., Hasegawa, M., et al. (2013). CD90 (Thy-1)-Positive selection enhances osteogenic capacity of human adipose-derived stromal cells. *Tissue Eng. Part A* 19, 989–997. doi:10.1089/ten.tea.2012.0370

Cipitria, A., Boettcher, K., Schoenhals, S., Garske, D. S., Schmidt-Bleek, K., Ellinghaus, A., et al. (2017). *In-situ* tissue regeneration through SDF-1 alpha driven cell recruitment and stiffness-mediated bone regeneration in a critical-sized segmental femoral defect. *Acta Biomater.* 60, 50–63. doi:10.1016/j.actbio.2017.07.032

Cook, S. D., Salkeld, S. L., and Rueger, D. C. (1995). Evaluation of recombinant human osteogenic protein-1 (rhOP-1) placed with dental implants in fresh extraction sites. *J. Oral Implantol.* 21, 281–289.

Dan, H. X., Vaquette, C., Fisher, A. G., Hamlet, S. M., Xiao, Y., Hutmacher, D. W., et al. (2014). The influence of cellular source on periodontal regeneration using calcium phosphate coated polycaprolactone scaffold supported cell sheets. *Biomaterials* 35, 113–122. doi:10.1016/j.biomaterials.2013.09.074

Darveau, R. P. (2010). Periodontitis: A polymicrobial disruption of host homeostasis. *Nat. Rev. Microbiol.* 8, 481–490. doi:10.1038/nrmicro2337

Ding, T., Li, J., Zhang, X., Du, L., Li, Y., Li, D., et al. (2020). Super-assembled core/shell fibrous frameworks with dual growth factors for *in situ* cementum-ligament-bone complex regeneration. *Biomater. Sci.* 8, 2459–2471. doi:10.1039/d0bm00102c

Dominici, M., Le Blanc, K., Mueller, I., Slaper-Cortenbach, I., Marini, F. C., Krause, D. S., et al. (2006). Minimal criteria for defining multipotent mesenchymal stromal cells. The International Society for Cellular Therapy position statement. *Cytotherapy* 8, 315–317. doi:10.1080/14653240600855905

Ehrenfest, D. M. D., Doglioli, P., de Peppo, G. M., Del Corso, M., and Charrier, J. B. (2010). Choukroun's platelet-rich fibrin (PRF) stimulates *in vitro* proliferation and differentiation of human oral bone mesenchymal stem cell in a dose-dependent way. *Archives Oral Biol.* 55, 185–194. doi:10.1016/j.archoralbio.2010.01.004

Feng, Y. Y., Su, L., Zhong, X., Wei, G. H., Xiao, H. P., Li, Y. B., et al. (2016). Exendin-4 promotes proliferation and differentiation of MC3T3-E1 osteoblasts by MAPKs activation. *J. Mol. Endocrinol.* 56, 189–199. doi:10.1530/jme-15-0264

Giannobile, W. V., Ryan, S., Shih, M. S., Su, D. L., Kaplan, P. L., and Chan, T. C. K. (1998). Recombinant human osteogenic protein-1 (OP-1) stimulates periodontal wound healing in class III furcation defects. *J. Periodontology* 69, 129–137. doi:10.1902/jop.1998.69.2.129

Gronthos, S., Mankani, M., Brahim, J., Robey, P. G., and Shi, S. (2000). Postnatal human dental pulp stem cells (DPSCs) *in vitro* and *in vivo*. *Proc. Natl. Acad. Sci. U. S. A.* 97, 13625–13630. doi:10.1073/pnas.240309797

Guo, W. H., Gong, K., Shi, H. G., Zhu, G. X., He, Y., Ding, B. F., et al. (2012). Dental follicle cells and treated dentin matrix scaffold for tissue engineering the tooth root. *Biomaterials* 33, 1291–1302. doi:10.1016/j.biomaterials.2011.09.068

Hajjar, R. J., and Hulot, J. S. (2013). Myocardial delivery of stromal cell-derived factor 1 in patients with ischemic heart disease safe and promising. *Circ. Res.* 112, 746–747. doi:10.1161/circresaha.113.300902

Hasegawa, N., Kawaguchi, H., Hirachi, A., Takeda, K., Mizuno, N., Nishimura, M., et al. (2006). Behavior of transplanted bone marrow-derived mesenchymal stem cells in periodontal defects. *J. Periodontology* 77, 1003–1007. doi:10.1902/jop.2006.050341

Hattori, K., Heissig, B., and Rafii, S. (2003). The regulation of hematopoietic stem cell and progenitor mobilization by chemokine SDF-1. *Leukemia Lymphoma* 44, 575–582. doi:10.1080/1042819021000037985

He, X. T., Li, X., Xia, Y., Yin, Y., Wu, R. X., Sun, H. H., et al. (2019). Building capacity for macrophage modulation and stem cell recruitment in high-stiffness hydrogels for complex periodontal regeneration: Experimental studies *in vitro* and in rats. *Acta Biomater.* 88, 162–180. doi:10.1016/j.actbio.2019.02.004

Huang, C. Y. C., Pelaez, D., Bendala, J. D., Garcia-Godoy, F., and Cheung, H. S. (2009a). Plasticity of stem cells derived from adult periodontal ligament. *Regen. Med.* 4, 809–821. doi:10.2217/RME.09.55

Huang, G. T. J., Gronthos, S., and Shi, S. (2009b). Mesenchymal stem cells derived from dental tissues vs. Those from other sources: Their biology and role in regenerative medicine. *J. Dent. Res.* 88, 792–806. doi:10.1177/0022034509340867

Huber, B. C., Brunner, S., Segeth, A., Nathan, P., Fischer, R., Zaruba, M. M., et al. (2011). Parathyroid hormone is a DPP-IV inhibitor and increases SDF-1-driven homing of CXCR4(+) stem cells into the ischaemic heart. *Cardiovasc. Res.* 90, 529–537. doi:10.1093/cvr/cvr014

Hynes, K., Menicanin, D., Gronthos, S., and Bartold, P. M. (2012). Clinical utility of stem cells for periodontal regeneration. *Periodontol. 2000* 59, 203–227. doi:10.1111/j.1600-0757.2012.00443.x

Ikeda, E., Morita, R., Nakao, K., Ishida, K., Nakamura, T., Takano-Yamamoto, T., et al. (2009). Fully functional bioengineered tooth replacement as an organ replacement therapy. *Proc. Natl. Acad. Sci. U. S. A.* 106, 13475–13480. doi:10.1073/pnas.0902944106

Ji, B., Sheng, L., Chen, G., Guo, S., Xie, L., Yang, B., et al. (2015). The combination use of platelet-rich fibrin and treated dentin matrix for tooth root regeneration by cell homing. *Tissue Eng. Part A* 21, 26–34. doi:10.1089/ten.tea.2014.0043

Ji, W., Yang, F., Ma, J. L., Bouma, M. J., Boerman, O. C., Chen, Z., et al. (2013). Incorporation of stromal cell-derived factor-1 alpha in PCL/gelatin electrospun membranes for guided bone regeneration. *Biomaterials* 34, 735–745. doi:10.1016/j.biomaterials.2012.10.016

Kawaguchi, H., Hirachi, A., Hasegawa, N., Iwata, T., Hamaguchi, H., Shiba, H., et al. (2004). Enhancement of periodontal tissue regeneration by transplantation of bone marrow mesenchymal stem cells. *J. Periodontology* 75, 1281–1287. doi:10.1902/jop.2004.75.9.1281

Kim, K., Lee, C. H., Kim, B. K., and Mao, J. J. (2010). Anatomically shaped tooth and periodontal regeneration by cell homing. *J. Dent. Res.* 89, 842–847. doi:10.1177/0022034510370803

Kim, K. S., Kim, H. S., Park, J. M., Kim, H. W., Park, M. K., Lee, H. S., et al. (2013). Long-term immunomodulatory effect of amniotic stem cells in an Alzheimer's disease model. *Neurobiol. Aging* 34, 2408–2420. doi:10.1016/j.neurobiolaging.2013.03.029

Kimura, Y., Komaki, M., Iwasaki, K., Sata, M., Izumi, Y., and Morita, I. (2014). Recruitment of bone marrow-derived cells to periodontal tissue defects. *Front. Cell. Dev. Biol.* 2, 19. doi:10.3389/fcell.2014.00019

Kinane, D. F., Stathopoulou, P. G., and Papapanou, P. N. (2017). Periodontal diseases. *Nat. Rev. Dis. Prim.* 3, 17038. doi:10.1038/nrdp.2017.38

Kwon, S. G., Kwon, Y. W., Lee, T. W., Park, G. T., and Kim, J. H. (2018). Recent advances in stem cell therapeutics and tissue engineering strategies. *Biomater. Res.* 22, 36. doi:10.1186/s40824-018-0148-4

Lee, C. H., Cook, J. L., Mendelson, A., Moioli, E. K., Yao, H., and Mao, J. J. (2010). Regeneration of the articular surface of the rabbit synovial joint by cell homing: A proof of concept study. *Lancet* 376, 440–448. doi:10.1016/s0140-6736(10)60668-x

Lee, C. H., Marion, N. W., Hollister, S., and Mao, J. J. (2009). tissue formation and vascularization in anatomically shaped human joint condyle ectopically *in vivo*. *TISSUE Eng. PART A* 15, 3923–3930. doi:10.1089/ten.tea.2008.0653

Lee, J. S., Jin, Y., Park, H. J., Yang, K., Lee, M. S., Yang, H. S., et al. (2017). *In situ* bone tissue engineering with an endogenous stem cell mobilizer and osteoinductive nanofibrous polymeric scaffolds. *Biotechnol. J.* 12, 1700062. doi:10.1002/biot.201700062

Lee, S. J., Yoo, J. J., and Atala, A. (2016). Chapter 1 - fundamentals of *in situ* tissue regeneration. *situ tissue Regen.* 2016, 3–17. doi:10.1016/B978-0-12-802225-2.00001-5

Li, D., Xue, W., Li, M., Dong, M., Wang, J., Wang, X., et al. (2018a). VCAM-1(+) macrophages guide the homing of HSPCs to a vascular niche. *Nature* 564, 119–124. doi:10.1038/s41586-018-0709-7

Li, R., Guo, W. H., Yang, B., Guo, L. J., Sheng, L., Chen, G., et al. (2011). Human treated dentin matrix as a natural scaffold for complete human dentin tissue regeneration. *Biomaterials* 32, 4525–4538. doi:10.1016/j.biomaterials.2011.03.008

Li, Y. C., Jin, F., Du, Y., Ma, Z. W., Li, F., Wu, G., et al. (2008). Cementum and periodontal ligament-like tissue formation induced using bioengineered dentin. *Tissue Eng. Part A* 14, 1731–1742. doi:10.1089/ten.tea.2007.0268

Li, Z., Shen, D., Hu, S., Su, T., Huang, K., Liu, F., et al. (2018b). Pretargeting and bioorthogonal click chemistry-mediated endogenous stem cell homing for heart repair. *ACS Nano* 12, 12193–12200. doi:10.1021/acsnano.8b05892

Liang, Q., Du, L., Zhang, R., Kang, W., and Ge, S. (2021). Stromal cell-derived factor-1/Exendin-4 cotherapy facilitates the proliferation, migration and osteogenic differentiation of human periodontal ligament stem cells *in vitro* and promotes periodontal bone regeneration *in vivo*. *Cell. Prolif.* 54, e12997. doi:10.1111/cpr.12997

Liesveld, J. L., Sharma, N., and Aljitawi, O. S. (2020). Stem cell homing: From physiology to therapeutics. *Stem Cells* 38, 1241–1253. doi:10.1002/stem.3242

Liu, H. R., Li, M. Q., Du, L. Q., Yang, P. S., and Ge, S. H. (2015). Local administration of stromal cell-derived factor-1 promotes stem cell recruitment and bone regeneration in a rat periodontal bone defect model. *Mater. Sci. Eng. C* 53, 83–94. doi:10.1016/j.msec.2015.04.002

Liu, J., Ruan, J., Weir, M. D., Ren, K., Schneider, A., Wang, P., et al. (2019a). Periodontal bone-ligament-cementum regeneration via scaffolds and stem cells. *Cells* 8, 537. doi:10.3390/cells8060537

Liu, W. T., Wei, Y., Zhang, X. H., Xu, M. M., Yang, X. P., and Deng, X. L. (2013). Lower extent but similar rhythm of osteogenic behavior in hBMSCs cultured on nanofibrous scaffolds versus induced with osteogenic supplement. *Acs Nano* 7, 6928–6938. doi:10.1021/nn402118s

Liu, Y., Luo, D., Yu, M., Wang, Y., Jin, S. S., Li, Z. X., et al. (2019b). Thermodynamically controlled self-assembly of hierarchically staggered architecture as an osteoinductive alternative to bone autografts. *Adv. Funct. Mat.* 29, 1806445. doi:10.1002/adfm.201806445

Liu, Y., Zheng, Y., Ding, G., Fang, D. J., Zhang, C. M., Bartold, P. M., et al. (2008). Periodontal ligament stem cell-mediated treatment for periodontitis in miniature swine. *STEM CELLS* 26, 1065–1073. doi:10.1634/stemcells.2007-0734

Luciani, P., Fibbi, B., Mazzanti, B., Deledda, C., Ballerini, L., Aldinucci, A., et al. (2018). The effects of Exendin-4 on bone marrow-derived mesenchymal cells. *Endocrine* 60, 423–434. doi:10.1007/s12020-017-1430-2

Ma, Z. F., Li, S., Song, Y. L., Tang, L., Ma, D. D., Liu, B. L., et al. (2008). The biological effect of dentin noncollagenous proteins (DNCPs) on the human periodontal ligament stem cells (HPDLSCs) *in vitro* and *in vivo*. *Tissue Eng. Part A* 14, 2059–2068. doi:10.1089/ten.tea.2008.0021

Mao, Y., Chen, Y., Li, W., Wang, Y., Qiu, J., Fu, Y., et al. (2022). Physiology-Inspired multilayer nanofibrous membranes modulating endogenous stem cell recruitment and osteo-differentiation for staged bone regeneration. *Adv. Healthc. Mat.* 2022, e2201457. doi:10.1002/adhm.202201457

Martino, M. M., Briquez, P. S., Maruyama, K., and Hubbell, J. A. (2015). Extracellular matrix-inspired growth factor delivery systems for bone regeneration. *Adv. Drug Deliv. Rev.* 94, 41–52. doi:10.1016/j.addr.2015.04.007

Meng, J. R., Ma, X., Wang, N., Jia, M., Bi, L., Wang, Y. Y., et al. (2016). Activation of GLP-1 receptor promotes bone marrow stromal cell osteogenic differentiation through beta-catenin. *Stem Cell. Rep.* 6, 579–591. doi:10.1016/j.stemcr.2016.02.002

Miura, M., Gronthos, S., Zhao, M. R., Lu, B., Fisher, L. W., Robey, P. G., et al. (2003). Shed: Stem cells from human exfoliated deciduous teeth. *Proc. Natl. Acad. Sci. U. S. A.* 100, 5807–5812. doi:10.1073/pnas.0937635100

Modino, S. A. C., and Sharpe, P. T. (2005). Tissue engineering of teeth using adult stem cells. *ARCHIVES ORAL Biol.* 50, 255–258. doi:10.1016/j.archoralbio.2005.01.002

Morrison, S. J., and Scadden, D. T. (2014). The bone marrow niche for haematopoietic stem cells. *Nature* 505, 327–334. doi:10.1038/nature12984

Morsczeck, C., Gotz, W., Schierholz, J., Zellhofer, F., Kuhn, U., Mohl, C., et al. (2005). Isolation of precursor cells (PCs) from human dental follicle of wisdom teeth. *MATRIX Biol.* 24, 155–165. doi:10.1016/j.matbio.2004.12.004

Otsuru, S., Tamai, K., Yamazaki, T., Yoshikawa, H., and Kaneda, Y. (2008). Circulating bone marrow-derived osteoblast progenitor cells are recruited to the bone-forming site by the CXCR4/stromal cell-derived factor-1 pathway. *Stem Cells* 26, 223–234. doi:10.1634/stemcells.2007-0515

Pacelli, S., Basu, S., Whitlow, J., Chakravarti, A., Acosta, F., Varshney, A., et al. (2017). Strategies to develop endogenous stem cell-recruiting bioactive materials for tissue repair and regeneration. *Adv. Drug Deliv. Rev.* 120, 50–70. doi:10.1016/j.addr.2017.07.011

Park, J. Y., Jeon, S. H., and Choung, P. H. (2011). Efficacy of periodontal stem cell transplantation in the treatment of advanced periodontitis. *Cell. Transpl.* 20, 271–286. doi:10.3727/096368910X519292

Petit, I., Jin, D., and Rafii, S. (2007). The SDF-1-CXCR4 signaling pathway: A molecular hub modulating neo-angiogenesis. *Trends Immunol.* 28, 299–307. doi:10.1016/j.it.2007.05.007

Phillips, C. L., Bradley, D. A., Schlotzhauer, C. L., Bergfeld, M., Libreros-Minotta, C., Gawenis, L. R., et al. (2000). Oim mice exhibit altered femur and incisor mineral composition and decreased bone mineral density. *Bone* 27, 219–226. doi:10.1016/s8756-3282(00)00311-2

Pihlstrom, B. L., Michalowicz, B. S., and Johnson, N. W. (2005). Periodontal diseases. *Lancet* 366, 1809–1820. doi:10.1016/s0140-6736(05)67728-8

Pittenger, M. F., Mackay, A. M., Beck, S. C., Jaiswal, R. K., Douglas, R., Mosca, J. D., et al. (1999). Multilineage potential of adult human mesenchymal stem cells. *Science* 284, 143–147. doi:10.1126/science.284.5411.143

Ranzoni, A. M., Tangherloni, A., Berest, I., Riva, S. G., Myers, B., Strzelecka, P. M., et al. (2021). Integrative single-cell RNA-seq and ATAC-seq analysis of human developmental hematopoiesis. *Cell. Stem Cell.* 28, 472–487.e7. e7. doi:10.1016/j.stem.2020.11.015

Reyes, C. D., and García, A. J. (2004). $\alpha_2\beta_1$integrin-specific collagen-mimetic surfaces supporting osteoblastic differentiation. *J. Biomed. Mat. Res. A* 69, 591–600. doi:10.1002/jbm.a.30034

Ripamonti, U., Crooks, J., Petit, J. C., and Rueger, D. C. (2001). Periodontal tissue regeneration by combined applications of recombinant human osteogenic protein-1 and bone morphogenetic protein-2. A pilot study in Chacma baboons (*Papio ursinus*). *Eur. J. Oral Sci.* 109, 241–248. doi:10.1034/j.1600-0722.2001.00041.x

Safina, I., and Embree, M. C. (2022). Biomaterials for recruiting and activating endogenous stem cells *in situ* tissue regeneration. *Acta Biomater.* 143, 26–38. doi:10.1016/j.actbio.2022.03.014

Seo, B. M., Miura, M., Gronthos, S., Bartold, P. M., Batouli, S., Brahim, J., et al. (2004). Investigation of multipotent postnatal stem cells from human periodontal ligament. *Lancet* 364, 149–155. doi:10.1016/S0140-6736(04)16627-0

Shafiq, M., Zhang, Y., Zhu, D., Zhao, Z., Kim, D. H., Kim, S. H., et al. (2018). *In situ* cardiac regeneration by using neuropeptide substance P and IGF-1C peptide eluting heart patches. *Regen. Biomater.* 5, 303–316. doi:10.1093/rb/rby021

Sharma, D., Verma, S., Vaidya, S., Kalia, K., and Tiwari, V. (2018). Recent updates on GLP-1 agonists: Current advancements & challenges. *Biomed. Pharmacother.* 108, 952–962. doi:10.1016/j.biopha.2018.08.088

Smith, A. J., Scheuen, B. A., Takahashi, Y., Ferracane, J. L., Shelton, R. M., and Cooper, P. R. (2012). Dentine as a bioactive extracellular matrix. *Archives Oral Biol.* 57, 109–121. doi:10.1016/j.archoralbio.2011.07.008

Sonoyama, W., Liu, Y., Yamaza, T., Tuan, R. S., Wang, S., Shi, S., et al. (2008). Characterization of the apical papilla and its residing stem cells from human immature permanent teeth: A pilot study. *J. Endod.* 34, 166–171. doi:10.1016/j.joen.2007.11.021

Tokunaga, K., Seto, H., Ohba, H., Mihara, C., Hama, H., Horibe, M., et al. (2011). Topical and intermittent application of parathyroid hormone recovers alveolar bone loss in rat experimental periodontitis. *J. Periodontal Res.* 46, 655–662. doi:10.1111/j.1600-0765.2011.01386.x

Wang, F., Du, L. Q., and Ge, S. H. (2016). PTH/SDF-1 alpha cotherapy induces CD90+CD34-stromal cells migration and promotes tissue regeneration in a rat periodontal defect model. *Sci. Rep.* 6, 30403. doi:10.1038/srep30403

Wang, K., Zhao, X. H., Kuang, C. Y., Qian, D. H., Wang, H., Jiang, H., et al. (2012). Overexpression of SDF-1 alpha enhanced migration and engraftment of cardiac stem cells and reduced infarcted size via CXCR4/PI3K pathway. *Plus One* 7, e43922. doi:10.1371/journal.pone.0043922

Woo, H. N., Cho, Y. J., Tarafder, S., and Lee, C. H. (2021). The recent advances in scaffolds for integrated periodontal regeneration. *Bioact. Mater.* 6, 3328–3342. doi:10.1016/j.bioactmat.2021.03.012

Woodfield, T. B. F., Van Blitterswijk, C. A., De Wijn, J., Sims, T. J., Hollander, A. P., and Riesle, J. (2005). Polymer scaffolds fabricated with pore-size gradients as a model for studying the zonal organization within tissue-engineered cartilage constructs. *TISSUE Eng.* 11, 1297–1311. doi:10.1089/ten.2005.11.1297

Wu, J., Jin, F., Tang, L., Yu, J., Xu, L., Yang, Z., et al. (2008). Dentin non-collagenous proteins (dNCPs) can stimulate dental follicle cells to differentiate into cementoblast lineages. *Biol. Cell.* 100, 291–302. doi:10.1042/bc20070092

Xin, L., Zheng, X., Chen, J., Hu, S., Luo, Y., Ge, Q., et al. (2022). An acellular scaffold facilitates endometrial regeneration and fertility restoration via recruiting endogenous mesenchymal stem cells. *Adv. Healthc. Mat.* 2022, e2201680. doi:10.1002/adhm.202201680

Xiong, X., Ghosh, R., Hiller, E., Drepper, F., Knapp, B., Brunner, H., et al. (2009). A new procedure for rapid, high yield purification of Type I collagen for tissue engineering. *Process Biochem.* 44, 1200–1212. doi:10.1016/j.procbio.2009.06.010

Xu, X. Y., Li, X., Wang, J., He, X. T., Sun, H. H., and Chen, F. M. (2019). Concise review: Periodontal tissue regeneration using stem cells: Strategies and translational considerations. *Stem Cells Transl. Med.* 8, 392–403. doi:10.1002/sctm.18-0181

Yamamoto, T., Ugawa, Y., Kawamura, M., Yamashiro, K., Kochi, S., Ideguchi, H., et al. (2018). Modulation of microenvironment for controlling the fate of periodontal ligament cells: The role of rho/ROCK signaling and cytoskeletal dynamics. *J. Cell. Commun. Signal.* 12, 369–378. doi:10.1007/s12079-017-0425-3

Yang, B., Chen, G., Li, J., Zou, Q., Xie, D., Chen, Y. L., et al. (2012). Tooth root regeneration using dental follicle cell sheets in combination with a dentin matrix - based scaffold. *Biomaterials* 33, 2449–2461. doi:10.1016/j.biomaterials.2011.11.074

Yang, B., Pang, X., Li, Z., Chen, Z., and Wang, Y. (2021). Immunomodulation in the treatment of periodontitis: Progress and perspectives. *Front. Immunol.* 12, 781378. doi:10.3389/fimmu.2021.781378

Yang, D. Z., Sun, S. J., Wang, Z. G., Zhu, P. F., Yang, Z. L., and Zhang, B. (2013). Stromal cell-derived factor-1 receptor CXCR4-overexpressing bone marrow mesenchymal stem cells accelerate wound healing by migrating into skin injury areas. *Cell. Reprogr.* 15, 206–215. doi:10.1089/cell.2012.0046

Yang, Z., Li, H., Yuan, Z., Fu, L., Jiang, S., Gao, C., et al. (2020). Endogenous cell recruitment strategy for articular cartilage regeneration. *Acta Biomater.* 114, 31–52. doi:10.1016/j.actbio.2020.07.008

Yao, D., and Lv, Y. (2022). A cell-free difunctional demineralized bone matrix scaffold enhances the recruitment and osteogenesis of mesenchymal stem cells by promoting inflammation resolution. *Biomater. Adv.* 139, 213036. doi:10.1016/j.bioadv.2022.213036

Yap, M. K. K., and Misuan, N. (2019). Exendin-4 from *Heloderma suspectum* venom: From discovery to its latest application as type II diabetes combatant. *Basic Clin. Pharmacol. Toxicol.* 124, 513–527. doi:10.1111/bcpt.13169

Yin, Y., Li, X., He, X. T., Wu, R. X., Sun, H. H., and Chen, F. M. (2017). Leveraging stem cell homing for therapeutic regeneration. *J. Dent. Res.* 96, 601–609. doi:10.1177/0022034517706070

Young, C. S., Terada, S., Vacanti, J. P., Honda, M., Bartlett, J. D., and Yelick, P. C. (2002). Tissue engineering of complex tooth structures on biodegradable polymer scaffolds. *J. Dent. Res.* 81, 695–700. doi:10.1177/154405910208101008

Yu, M., Luo, D., Qiao, J., Guo, J., He, D., Jin, S., et al. (2022). A hierarchical bilayer architecture for complex tissue regeneration. *Bioact. Mat.* 10, 93–106. doi:10.1016/j.bioactmat.2021.08.024

Zhang, Q. Z., Shi, S. H., Liu, Y., Uyanne, J., Shi, Y. F., Shi, S. T., et al. (2009). Mesenchymal stem cells derived from human gingiva are capable of immunomodulatory functions and ameliorate inflammation-related tissue destruction in experimental colitis. *J. Immunol.* 183, 7787–7798. doi:10.4049/jimmunol.0902318

Zhang, S., Hu, B., Liu, W., Wang, P., Lv, X., Chen, S., et al. (2020). Articular cartilage regeneration: The role of endogenous mesenchymal stem/progenitor cell recruitment and migration. *Semin. Arthritis Rheum.* 50, 198–208. doi:10.1016/j.semarthrit.2019.11.001

Zhang, Y., Chen, S., Liu, B. C., Zhou, H., Hu, S. Y., Zhou, Y., et al. (2016). Exendin-4 promotes proliferation of adipose-derived stem cells through ERK and JNK signaling pathways. *Vitro Cell. Dev. Biol. -Animal.* 52, 598–606. doi:10.1007/s11626-016-0003-7

Zhao, Y., Zhao, S., Ma, Z., Ding, C., Chen, J., and Li, J. (2022). Chitosan-based scaffolds for facilitated endogenous bone Re-generation. *Pharm. (Basel)* 15, 1023. doi:10.3390/ph15081023

Zheng, C., Chen, J., Liu, S., and Jin, Y. (2019). Stem cell-based bone and dental regeneration: A view of microenvironmental modulation. *Int. J. Oral Sci.* 11, 23. doi:10.1038/s41368-019-0060-3

Zhou, H., Li, D. D., Shi, C., Xin, T., Yang, J. J., Zhou, Y., et al. (2015). Effects of Exendin-4 on bone marrow mesenchymal stem cell proliferation, migration, and apoptosis *in vitro*. *Sci. Rep.* 5, 12898. doi:10.1038/srep12898

Zhu, W., Zhang, Q., Zhang, Y., Cen, L., and Wang, J. (2015). PDL regeneration via cell homing in delayed replantation of avulsed teeth. *J. Transl. Med.* 13, 357. doi:10.1186/s12967-015-0719-2

frontiers | Frontiers in Bioengineering and Biotechnology

TYPE Review
PUBLISHED 24 November 2022
DOI 10.3389/fbioe.2022.1049965

OPEN ACCESS

EDITED BY
Yang Kang,
Sun Yat-sen University, China

REVIEWED BY
Betül Çelebi Saltik,
Hacettepe University, Turkey
Yuting Wang,
Seventh Affiliated Hospital, Sun Yat-sen University, China

*CORRESPONDENCE
Feiqiu Wen,
fwen62@126.com
Sixi Liu,
sixi_liu@163.com
Gerile Oudeng,
gerile.oudeng@connect.polyu.hk

†These authors have contributed equally to this work and share first authorship

SPECIALTY SECTION
This article was submitted to Biomaterials, a section of the journal Frontiers in Bioengineering and Biotechnology

RECEIVED 21 September 2022
ACCEPTED 07 November 2022
PUBLISHED 24 November 2022

CITATION
Huang X, Wang Y, Wang T, Wen F, Liu S and Oudeng G (2022), Recent advances in engineering hydrogels for niche biomimicking and hematopoietic stem cell culturing.
Front. Bioeng. Biotechnol. 10:1049965.
doi: 10.3389/fbioe.2022.1049965

Recent advances in engineering hydrogels for niche biomimicking and hematopoietic stem cell culturing

Xiaochan Huang[1†], Yuting Wang[1,2†], Tianci Wang[1], Feiqiu Wen[1,2*], Sixi Liu[1*] and Gerile Oudeng[1*]

[1]Department of Hematology and Oncology, Shenzhen Children's Hospital, Shenzhen, Guangdong, China, [2]Shenzhen Children's Hospital, China Medical University, Shenzhen, Guangdong, China

Hematopoietic stem cells (HSCs) provide a life-long supply of haemopoietic cells and are indispensable for clinical transplantation in the treatment of malignant hematological diseases. Clinical applications require vast quantities of HSCs with maintained stemness characteristics. Meeting this demand poses often insurmountable challenges for traditional culture methods. Creating a supportive artificial microenvironment for the culture of HSCs, which allows the expansion of the cells while maintaining their stemness, is becoming a new solution for the provision of these rare multipotent HSCs. Hydrogels with good biocompatibility, excellent hydrophilicity, tunable biochemical and biophysical properties have been applied in mimicking the hematopoietic niche for the efficient expansion of HSCs. This review focuses on recent progress in the use of hydrogels in this specialized application. Advanced biomimetic strategies use for the creation of an artificial haemopoietic niche are discussed, advances in combined use of hydrogel matrices and microfluidics, including the emerging organ-on-a-chip technology, are summarized. We also provide a brief description of novel stimulus-responsive hydrogels that are used to establish an intelligent dynamic cell microenvironment. Finally, current challenges and future perspectives of engineering hydrogels for HSC biomedicine are explored.

KEYWORDS

hydrogels, hematopoietic stem cells, *in vitro* expansion, niche biomimicking, cell microenvironment

1 Introduction

Hematopoietic stem cells (HSCs) are self-renewing pluripotent stem cells. HSCs can differentiate into all types of blood cell in the body (Wilkinson et al., 2020). In the clinical treatment of hematopoietic diseases, transplantation of HSCs from healthy donors into patients can reconstitute hematopoiesis and the immune system in recipients (Chatterjee et al., 2021). There is a considerable demand for HSCs in clinical transplantation, gene therapy, and basic stem cell research (Wilkinson and Nakauchi, 2020). However, the lack of readily accessible HSC sources poses a barrier to the more widespread clinical and

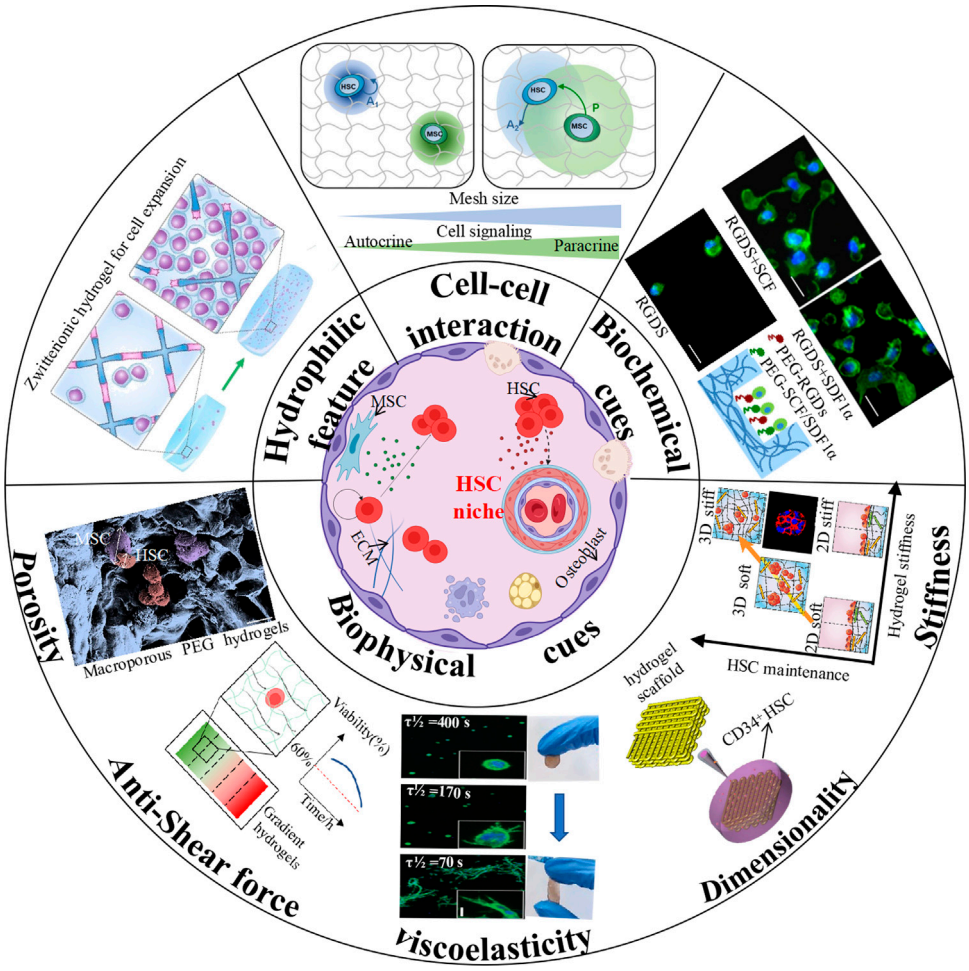

FIGURE 1
Schematic illustration of hydrogel engineering strategies for hematopoietic niche recapitulation. (Cell-cell interaction: (Gilchrist et al., 2019b) Copyright © 2019. Reproduced with permission from John Wiley and Sons; Biochemical cues: (Cuchiara et al., 2013) Copyright © 2019. Reproduced with permission from John Wiley and Sons; Stiffness: (Gvaramia et al., 2017) Copyright © 2017. Reproduced with permission from Elsevier; Dimensionality: (Zhou et al., 2020) Copyright © 2020. Reproduced with permission from Springer Nature; Viscoelasticity-Left: (Chaudhuri et al., 2016) Copyright © 2015. Reproduced with permission from Springer Nature; Viscoelasticity-Right: (Liang et al., 2022) Copyright © 2022. Reproduced with permission from American Chemical Society; Anti-shear force: (Mahadik et al., 2014) Copyright © 2013. Reproduced with permission from John Wiley and Sons; Porosity: (Raic et al., 2014) Copyright © 2014. Reproduced with permission from Elsevier; Hydrophilic feature: (Bai et al., 2019) Copyright © 2019. Reproduced with permission from Springer Nature.

research use of these cells (Liu et al., 2022). The *in vitro* expansion of primitive pluripotent HSC populations promises to represent an effective solution to overcome this shortage (Liu et al., 2022).

HSCs used in transplantation are mainly derived from umbilical cord blood. These cells can be used with a relatively low risk of immune rejection, while the number of cells that can be recovered is limited (Ballen et al., 2013; Cohen et al., 2020).

In-depth studies regarding the molecular mechanism of self-renewal and differentiation in HSCs have explored various methods for HSCs expansion *ex vivo,* for example, supplementing hematopoietic stimulating factors, the addition of small molecule compounds into the suspension culture medium, and co-culture of HSCs and their supporting cells to maintain cell growth enhance the cellular connections (Zimran et al., 2021). However, it is difficult to are difficult to replicate cell–cell and cell–extracellular matrix (ECM) interactions that occur in the natural niche of the bone marrow (BM) using conventional two-dimensional (2D) culture methods (Langhans, 2018; Liu et al., 2022). To achieve a better *in vitro* hematopoietic microenvironment, research has focused on creating three-dimensional (3D) culture conditions *in vitro* (Huang et al., 2017). Hydrogel biomaterials have excellent biocompatibility, share some of the physical properties of the natural matrix, and provide a flexible solution to introduce biochemical and biophysical triggers. Ongoing efforts to establish an engineered BM-like niche for the *in vitro* expansion of HSCs is primarily focused on refining hydrogel-based culture methods (Yin and Cao, 2021).

This review summarizes hydrogel-based engineering methods used for recreation of the hematopoietic microenvironment for the purpose of the *in vitro* expansion of HSCs (Figure 1). We briefly describe the basic physiological characteristics of the hematopoietic niche, challenges culturing HSCs *ex vivo*, and recent culture approaches, followed by an overview of the engineering strategies used for replicating the natural hematopoietic niche. We also discuss new technologies for establishing an "intelligent microenvironment." Finally, challenges and perspectives in the development of the hydrogel-based culture platforms for clinical application are evaluated.

2 The hematopoietic niche

In 1978, Schofield introduced the concept of the "niche", which refers to the HSC microenvironment in the BM (Chatterjee et al., 2021). The niche provides indispensable factors for the self-renewal and differentiation of HSCs, controls the quiescence and stemness characteristics of HSCs, and regulates cell fate (Rasheed, 2022). In early studies, the hematopoietic niche was classified as the endosteal niche and perivascular niche based on the distribution of cell populations (Zhao and Li, 2016). The endosteal niche contains osteoblasts and osteoclasts at the endosteum. These cells regulate homing and the maintenance of quiescence in HSCs (Ingavle et al., 2019). The perivascular niche, formed in the vicinity of blood vessels, can promote the interaction of HSCs with endothelial, perivascular, and mesenchymal stem cells (MSCs) (Silberstein and Lin, 2013; Barnhouse et al., 2021). With increasing molecular mechanism studies, more and more cellular constituents have been identified in BM niche. Current research has showed that it is possible for different types of hematopoietic stem cells and progenitor cells (HSPCs) to have their own special niche created by multiple cell types. (Morrison and Scadden, 2014).

The HSC pool is highly heterogeneous in function and molecules it contains, which has increased the possibility that "specialized" niches are existed for "specialized" HSCs. This could also be inferred from the physiological distribution characteristics of HSCs. It has been reported that almost all HSC cells are in near range sinusoid vessels and are supported by the factors, such as Stem Cell Factor (SCF), C-X-C motif chemokine 12 (CXCL-12), and pleiotrophin, synthesized by leptin Receptor$^+$ (LepR$^+$) MSCs and endothelial cells (Christodoulou et al., 2020). Few HSCs are distributed in the BM, and <20% are located within 10 μ m from the BM intima (Lo Celso et al., 2009). These small HSC populations may be directly or indirectly regulated by factors near the bone surface (Cao et al., 2019; Zhao et al., 2019). In addition, some important factors for maintenance of HSCs are not synthesized in the BM, such as thrombopoietin (TPO), which is generated by the liver and transported to the BM through the blood (Nakamura-Ishizu et al., 2014). Therefore, the hematopoietic niche is composed of multiple components including different cells, biomolecules, and matrix, in which each component of HSCs has an important regulatory role.

2.1 Cellular compounds

2.1.1 Osteoblasts

Osteoblasts are particularly common in the trabecular bone of the endosteum and are important in regulating HSC maintenance (Calvi et al., 2003; Zhang et al., 2003). Primitive HSPCs primarily home and engraft in the endosteal niche, which is rich in immature osteoblasts and osteoblastic progenitor cells (Levesque et al., 2010). Along with other cytokines, these immature osteoblasts secrete angiopoietin-1 (Arai et al., 2004), osteopontin (Stier et al., 2005), and CXCL12 to support HSC quiescence and self-renewal (Matteini et al., 2021). In contrast, mature osteoblasts induce the proliferation of HSCs (Choi et al., 2015).

Osteoblasts were one of the first non-hematopoietic BM cells reported to participate in HSPC regulation (Nilsson et al., 2001). Early studies showed that osteoblasts differentiated from human BM stromal cells could produce hematopoietic cytokines and support the HSC maintenance (Calvi et al., 2003; Zhang et al., 2003). More recent studies showed that conditional deletion of CXCL12 or SCF in osteoblasts did not affect the frequency of HSC in BM, which indicates that although these two factors are necessary niche factors for maintaining HSC, osteoblasts do not support the maintenance of HSCs through these niche factors (Greenbaum et al., 2013; Crane et al., 2017). It has been reported that osteoblasts can promote the maintenance of early lymphoid progenitor cells by secreting extremely low levels of CXCL12. It is worth mentioning that most lymphoid cells are located in the perisinusoidal niche in which they rely on CXCL12, and Transforming Growth Factor (TGF-β), synthesized by LEPR$^+$ cells (Shen et al., 2021).

2.1.2 Endothelial cells

Nutrient arteries entering the cortical bone divide into descending and ascending branches. These extend axially along the central cavity containing the BM, giving off radial branches. These enter the endosteal region of the cortical bone in a small network of Sca1$^+$ arterioles and capillaries. These vessels anastomose with Sca1$^-$ venous sinuses (approximately 50–100 μm in diameter). These venous sinuses drain into the central longitudinal vein running in the BM (Ramasamy, 2017; Owen-Woods and Kusumbe, 2022).

Sca1$^+$ arterial endothelial cells are present in transitional vessels (or type H vessels), arterioles and arteries (Langen et al., 2017). Type H vessels represent a specific subset of capillaries localizing exclusively to the endosteal region of the BM. They enhance angiogenesis and osteogenesis by transducing signals to osteoprogenitor cells (Spencer et al., 2014). Both H-type vessels and arterioles exhibit low permeability, protecting HSCs from high levels of reactive oxygen species (ROS). This phenomenon prevents the overactivation of the progenitor cells that could cause the loss of stemness (Kunisaki et al., 2013; Silberstein and Lin, 2013; Spencer et al.,

2014). Sca1$^-$ sinusoidal endothelial cells represent the main endothelial components of L-type vessels (Langen et al., 2017). In contrast to the arteriolar system, around the sinusoids ROS levels are relatively high. This enhances the migratory capacity and activation of HSCs (Itkin et al., 2016). Nonetheless, some reports suggested that sinusoidal endothelial cells may also contribute to the maintenance of HSC quiescence (Acar et al., 2015).

2.1.3 Mesenchymal stem cells

BM-derived MSCs have excellent potential for self-renewal and multilineage differentiation. They can form osteocytes, fat cells, cartilage, muscle cells, nerves, liver cells, and form the substrate cells supporting hematopoiesis (Pievani et al., 2021). MSCs secrete a variety of cytokines, hematopoietic and non-hematopoietic growth factors, and chemokines. Together, these modulate the BM microenvironment and regulate the proliferation and differentiation of HSCs. It appears that the secretion of CXCL12 by MSCs can induce the CXC12-CXCR4 mediated homing and retention of HSCs, while the production of stem cell growth factor (SCF) is responsible for cell survival and proliferation (Mannino et al., 2022). The simultaneous transplantation of MSCs and HSCs can promote HSCs homing, promote hematopoietic reconstruction, and reduce graft rejection (Jing et al., 2010). MSCs secrete multiple biomolecules by interacting with HSCs to support their growth and further to promote the hematopoietics. Meanwhile, MSCs inhibit the immunogenicity and immunomodulatory and reduce the incidence of graft-versus-host disease (GVHD). Co-transplantation of MSCs and HSCs has been applied in clinical and achieved positive results. Because MSCs are relatively easy to obtain without major ethical and legal issues their potential to support the *in vitro* expansion of HSCs can be easily studied.

2.1.4 Adipocytes

Adipocytes are the most abundant cells in the BM of adults and are commonly seen in close contact with hematopoietic cells. Before birth the bone marrow cavity does not contain any fat cells but the amount of bone marrow adipose tissue (BMAT) increases with age and eventually occupies up to 50% of the BM cavity (Hardouin et al., 2014). Traditionally, adipocytes were thought to negatively regulate HSC function in the BM microenvironment (Naveiras et al., 2009). However, emerging evidence suggests that adipocytes may promote the maintenance of HSCs. Mattiucci (Matteini et al., 2021) demonstrated that BM-MSCs can differentiate into BM adipocytes expressing specific cytokines. Amongst these Interleukin-3 appear to support HSC survival.

2.1.5 Progeny of hematopoietic stem cells

In addition to the stromal niche components, various progenies of HSCs including macrophages, neutrophils, regulatory T cells, and megakaryocytes, also participate in the regulation of the hematopoietic niche in the BM (Pinho and Frenette, 2019; Torres et al., 2022). Macrophages can regulate HSC migration; Bone marrow macrophages promote the retention of HSCs by regulating osteolineage cells and MSCs, thus antagonizing the excretion of HSC from BM mediated by SNS (Méndez-Ferrer et al., 2010; Chow et al., 2011). Macrophages clear senescent neutrophils and change the function of CXCL12 antibody reticular cells and retain HSCs in BM (Casanova-Acebes et al., 2013). Neutrophils derived from the bone marrow can promote endothelial cell regeneration after transplantation by secreting TNF, thus accelerating hematopoietic recovery (Bowers et al., 2018). Studies have shown that allogeneic hematopoietic stem cells co-locate with FoxP3$^+$ regulatory T cells in the endothelial area after transplantation and can survive for 1 month without immunosuppressive drugs (Fujisaki et al., 2011; Hirata et al., 2018). However, depletion of Tregs cells leads to the rapid loss of allogeneic hematopoietic stem cells, indicating that FoxP3$^+$ Tregs provide immune privilege for HSC (Fujisaki et al., 2011). Megakaryocytes maintain HSC quiescence by secreting CXCL4 (Bruns et al., 2014), TGF-β (Zhao et al., 2014), and TPO (Nakamura-Ishizu et al., 2014).

2.2 Cytokines

Cytokines are small protein molecules secreted by a variety of cells. By interacting with specific receptors they regulate the biological behavior of other cells. SCF, CXCL12, and thrombopoietin (TPO) are essential growth factors for HSCs (Yucel and Kocabas, 2018). SCF, also known as KIT ligand, exists in membrane binding and dissolving configurations (Asada et al., 2017). Both forms bind to the c-kit receptor, a tyrosine kinase, on the surface of HSCs, and promote HSC expansion. TPO is expressed mainly in the liver and kidneys and is a soluble factor necessary for the survival and proliferation of CD34$^+$ HSPCs (Chatterjee et al., 2021). CXCL12 (also known as SDF-1) is secreted by several cells in HSC niche. CAR cells found in perivascular regions represent the main sources of CXCL12 (Mendelson and Frenette, 2014; Kosan and Godmann, 2016). The CXCL12/CXCR4 signaling cascade plays an essential role in the homing, mobilization, and retention of HSCs (Verma et al., 2020).

2.3 Neural regulation

There is evidence to show that the autonomic nervous system (ANS) and SNS can regulate the fate of HSCs (Maryanovich et al., 2018). ANS signals are important for the circadian mobilization of HSCs in the BM niche (García-García et al., 2019). SNS fibers respond to Granulocyte Colony-Stimulating Factors (G-CSF) and release norepinephrine, which activates β3-adrenergic receptors to control rhythmic changes in CXCL2 expression (Asada et al., 2013; Matteini et al., 2021). Non-myelinating

Schwann cells promote HSC quiescence and maintenance by activating TGF-β and Suppressor of Mothers Against Decapentaplegic (SMAD)-induced signaling pathways (Mannino et al., 2022). However, studies on the regulating mechanism of sensory fibers on HSC behaviors in the BM niche are very limited in recent. One study reported that nociceptive receptors of the sensory neuropeptides lcitonin gene-related peptide could regulate G-CSF-induced HSC mobilization (Gao et al., 2021).

2.4 Niche extracellular environment

The ECM is a scaffold network that contains embedded HSCs and stromal cells. It is rich in collagen, laminin, and elastin, and contains a mixture of cytokines regulating proliferation and differentiation behaviors (Bello et al., 2018). This network is composed of two main classes of macromolecules: gel matrix components and fibrous protein components. The gel matrix components form gel-like structures composed of polysaccharides, amino sugars, and a range of protein constituents. In contrast, fibrous proteins primarily include collagen and elastic proteins and form a 2D or 3D structure with tunable stiffness and elasticity. This provides spatial support for the survival of HSCs and regulates their growth through interactions with integrin molecules present on the surface of HSCs (Chatterjee et al., 2021). The most studied fibrous proteins of the natural niche are fibronectin and laminin, which can bind to integrins and regulate the migration and homing behavior of HSCs. For example, studies have shown that BM laminins promote adhesion and migration of human HSCs through interaction with the integrin α_6 receptor for homing (Gu et al., 2003). Stiffer endosteal environments support the differentiation of HSCs into primitive myeloid progenitors, while softer substrates promote differentiation along the erythroid lineage. The adherence and motility of HSPCs is significantly higher on harder surfaces.

3 Hematopoietic stem cell culture *ex vivo*

3.1 Challenges of hematopoietic stem cell culture *ex vivo*

Two main types of HSCs were defined: long-term (LT)-HSCs, which are deeply quiescent in niches to maintain self-renewal and multilineage differentiation potential throughout their lives, and short-term (ST)-HSCs, which are maintained in more active niches with limited self-renewal potential (Choi et al., 2015). The main goal of *ex vivo* culture of HSCs is to expand the number of HSCs and HSPCs with a high capability of self-replicating and self-maintenance. However, few normal HSCs are in the cell cycle and undergo asymmetric mitosis. The asymmetric mitosis of HSCs is highly self-replicating and self-sustaining. After several mitoses, the cells stop entering the S phase and turn to the quiescent phase G_0, therefore, it is difficult to effectively expand them *ex vivo*. If HSCs are induced to undergo symmetrical mitosis through gene mutation, that is, the cells expand indefinitely without differentiation, this will inevitably lead to malignant transformation of the cells, with a loss in the ability to self-renewal and self-maintenance. During cell culture, supplementation with inappropriate cytokines or long-term culturing can promote both proliferation and differentiation of cells and destroy the asymmetric mitosis of the cells. Therefore, long-term culture may obtain a large absolute number of $CD34^+$ cells or nuclei cells; it also easily to lead to the differentiation and exhaustion of the early progenitor cells and only produces numerous HSPCs without hematopoietic reconstitution function.

Heterogeneity of HSCs is another important reason for the difficulty in their expansion *in vitro*. *Ex vivo* expansion methods of HSCs reported in the literatures are often quite different. Even under the same conditions of cytokine combination, the expansion ability and transplantation ability of cells are still significantly differ. The heterogeneity of HSCs also makes it challenging to understand the comprehensive signaling mechanism that defines the balance between homeostasis and self-renewal of among cells. Recent evidence has added new insights into the plasticity of BM niche and mitochondrial network, which synergistically determine the fate of HSCs. However, these new discoveries also increase the complexity and introduce a highly dynamic interrelationship in studies of HSC fate. Therefore, research on the complex mechanisms controlling the fate of HSCs remains limited.

3.2 Recent approaches to hematopoietic stem cell culture *ex vivo*

Compared with haplotype hematopoietic stem cell transplantation (haplo HSCT), umbilical cord blood stem cell transplantation (UCBT) can be easily obtained from CB resources. UCBT has high tolerance to human leukocyte antigen HLA mismatch, a high colony forming potential of HSCs and HSPCs, and a low incidence and recurrence rate of graft versus host disease (GVHD) following transplantation. Furthermore, HSCs are ideal vector cells for gene therapy. The long-term self-renewal and self-maintenance abilities of HSCs are conducive to the long-term expression of the target therapeutic genes *in vivo*. However, insufficient amounts limit the clinical application. *Ex vivo* expansion of HSCs is the basis both for the clinical promotion of UCBT and gene therapy. Therefore, many efforts have been focused on improving HSCs expansion methods.

Supplementing with the hematopoietic stimulators is a typical method for HSC expansion. Cytokines are one of the

first molecular stimulators for HSC expansion *ex vivo*. After 5–8 days of culturing of human CB $CD34^+CD38^-$ cells in serum free medium containing Fms Related Tyrosine Kinase 3 (Flt-3), SCF, Interleukin (IL)-3, IL-6 and G-CSF, the number of colony forming units (CFU) increased 100 -fold, and the number of long-term culture-initiating cells (LTC-IC) increased 4-fold (Conneally et al., 1997). The addition of Fibroblast Growth Factor 1 (FGF1) and FGF2 to the serum free medium during the co-culture of HSCs and osteoblast supported the expansion and regeneration of HSCs *in vitro* (Yeoh et al., 2006). Notch signaling pathway is an important pathway for HSC fate and lymphocyte generation. An engineered Delta-like ligand $Delta1^{Ext-IgG}$ (DXI) was used to activate the Notch signal pathway in human CB $CD34^+$ cells to achieve clinically significant *in vitro* expansion of ST-HSPCs with and shorten the implantation time of neutrophils following transplantation (Delaney et al., 2005; Delaney et al., 2010). In addition, TNF Superfamily Member 15 (TNFSF15), the Wnt signaling pathway and Prostaglandin E2 (PGE2) were used *ex vivo* to expand the long-term reconstruction ability of HSPCs (Ding et al., 2020).

The addition of small molecule compounds such as copper chelator tetraethylenediamine (TEPA), nicotinamide, stem regin-1 and valproic acid, which simultaneously expand ST- and LT-HSCs, provide effective schemes for HSC amplification *in vitro* (Zimran et al., 2021). U1M171, an HSC agonist, is one of the most promising small molecules for HSC expansion in recent years (Fares et al., 2014). In 2014, Guy Sauvageau and Peter W zandstra (Fares et al., 2014; Pabst et al., 2014) were the first to show that UM171 can significantly expand umbilical CB stem cells and enhance multilineage hematopoietic reconstruction in rats. In 2019, the team published Phase I/II clinical trial results (NCT02668315) on the safety and feasibility of a single UM171 expanded umbilical CB graft in The Lancet Haematology (Cohen et al., 2020). The minimum dose of rapidly implanted umbilical CB cells in this clinical trail was 0.52×10^5 $CD34^+$ cells, which has relatively low chronic GVHD and recurrence risk due to rapid T cell reconstruction.

MSCs are the main cell component of hematopoietic microenvironment and plays an important role in the growth, proliferation, and differentiation of HSCs. MSCs support and promote hematopoiesis by interacting with HSCs and secreting various cytokines, or expressing, and through the expression of adhesion molecules and ECM proteins related to adhesion and homing of HSCs. *In vitro* experiments have shown that MSCs plays an important role in the maintenance and expansion of $CD34^+$ BM cells, but do not affect the erythroid differentiation ability (Lau et al., 2017). At present, great progress has been made in the research of MSC-promoting hematopoietic reconstitution following HSCT. MSC and HSC co transplantation supports the growth of HSCs and significantly improves megakaryocyte and platelet formation. In addition, MSCs may also play a role in epigenetic regulation during HSC differentiation (Zakrzewski et al., 2019).

Static culture systems, such as culture plates and flasks, generally require repeated processing of HSCs regarding fluid change. Furthermore, due to ineffective mixing, the non-homogeneous of compounds may result in differences in the initial stimulation of cultured cells. The continuous perfusion bioreactor is a fully closed dynamic culture automation device to create 3D constructed microenvironments with different cellular or biomechanical features (Bhaskar et al., 2018). For example, Martin's group developed a perfusion bioreactor system analogue, which partially recapitulated the structural and compositional features of the human osteoblastic niche. Human purified CB-derived were cultured in the bioreactor; after 1 week culture, number of the $CD34^+$ cells and colonies numbers significantly increased. Perfusion bioreactor systems provided important evidence for dynamic control of the expansion quality during *ex vivo* HSC culture (Bourgine et al., 2018).

The hematopoietic niche is composed of biophysical and biochemical factors, which play a key role in the static, self-renewal, implantation, migration, differentiation, and other behaviors of HSCs. HSCs in the niche are affected by the mechanical force matrix, physical or chemical stimulations from stromal cells and the environment, as well as the cytokines distributed in the 3D niche space. Biomaterials with adjustable physical, mechanical, and chemical properties can easily be modified by different biological molecules, which opens up new opportunities for controlling the bionics of the niche. Compared with inorganic or metal biomaterials, hydrogels are organic materials with excellent biocompatibility. *In vivo*, the hematopoietic niche is a 3D environment dominated by hydrophilic and amphiphilic cell membrane lipids. Hydrogels have good hydrophilicity and rich functional groups; it is easy to modify the hydrophobic groups and various biomolecules. Their controllable physical and chemical characteristics, such as hardness, porosity, elasticity, and functionalization of key cytokines, can be beneficial in creating an environment closer to the niche.

4 Engineering hydrogels based on niche physiology

When HSCs detach from their niche microenvironment, the cells easily exhaust and differentiate. 2D culturing is not consistent with the spatial feature of natural niches. The intricated chemical and physical cues inside niche are crucial to regulate HSCs behavior. Therefore, 3D culturing of HSCs has been extensively researched recently; hydrogel biomaterials with excellent biocompatibility have been gradually employed for establishing a 3D environment for HSCs. (Yan et al., 2022) (Maji and Lee, 2022).

Hydrogels with good hydrophilicity capacity can swell in aqueous media, minimize non-specific protein adsorption, and

TABLE 1 Engineering hydrogel strategies of biomimetic hematopoietic niche and *in vitro* HSC culture.

Hydrogel composition	Engineering strategies	Key findings	Comments	Ref.
Puramatrix gel	3D coculture of human BM-derived $CD34^+$ with human placenta-derived MSCs	Hydrogel-based 3D culture of MSCs mimicked a functional hematopoietic niche for quiescent HSC maintenance and simultaneous multilineage hematopoiesis *via* the CXCR4-SDF1α axis, integrin beta1-mediated adhesion interactions, and a hypoxia gradient.	This study illustrates the specific pathways that supports the quiescence and pluripotent capability of HSCs in hydrogel-based MSC coculture system.	Sharma et al. (2012)
Collagen	3D coculture of HSCs with MSCs derived either from BM or UC	MSCs supported the migration of HSCs into the collagen hydrogel and promoted clonal expansion of HSC populations with higher ration of primitive $CD34^+CD38^-$ phenotype	3D coculture system of HSCs and BM-MSCs in collagen scaffold resembles the endosteal niche and allows dissecting two subpopulations of HSCs.	Leisten et al. (2012)
PEG-DA	Photopolymerization; RGDS, SCF, and SDF-1α were covalently immobilized onto the surfaces of hydrogels	Cell adhesion and spreading was enhanced by immobilizing biomolecules on hydrogel surfaces.	This study does not demonstrate that the hydrogel-based culture system can promote the *in vitro* expansion of HSCs and maintaining pluripotent potential.	Cuchiara et al. (2013)
Collagen	Microfluidic; Opposite-gradient populations of HSCs and osteoblasts	The hydrogel construct with stable multicellular gradients was created in a manner independent of cell size and hydrogel density and enabled the modulation of microenvironmental signals on HSC fate.	The microfluidic generation of gradient hydrogels with heterotypic microenvironment helps to study the impact of microenvironmental signals on HSC fate.	Mahadik et al. (2014)
Type I collagen gel	Microfluidic BM on-a-chip; photolithography; Engineered BM was formed in a PDMS device *in vivo* and then cultured in a microfluidic system	The BM on-a-chip replicated a functional hematopoietic niche *in vitro*, supporting HSCs in normal *in vivo*-like proportions for at least 1 week.	The *in vivo* engineering strategy enables the reconstitution of hematopoietic niche physiology and function restoration of natural BM.	Torisawa et al. (2014)
Methacrylamide-functionalized gelatin (GelMA) hydrogel	Microfluidic; PEGylated SCF were covalently immobilized within GelMA hydrogel *via* photochemistry	The GelMA hydrogels with immobilized SCF selectively maintained primitive HSCs and generated more GEMM colonies while soluble SCF induced lineage specification.	The study shows the effect of the local presentation of soluble vs. matric-immobilized biomolecules on HSC proliferation and lineage differentiation.	Mahadik et al. (2015)
PEG-DA	Photopolymerization; SCF, IFNγ, RGDS and connecting segment I were conjugated into hydrogels.	HSCs expanded 97-fold and 104-fold with the supplement of SCF and IFNγ respectively, and retained good differential capability.	Bioactive molecules modified on hydrogels promotes the recapitulation of functional HSC niche.	Cuchiara et al. (2016)
Collagen	Primary HSCs were cocultured with lineage positive (Lin^+) niche cells on collagen hydrogels with varying hydrogel densities and HSC: Lin^+ ratios	HSC-generated autocrine signals that dominate in the low-diffusive hydrogel matrix promoted the proliferation of early hematopoietic progenitors, while niche cell-generated paracrine signals that dominate in the high-diffusion hydrogel environment enhanced myeloid differentiation.	The effect of collagen hydrogels on autocrine and paracrine signaling between HSCs and niche cells depends on the hydrogel diffusivity and niche cell density.	Mahadik et al. (2017)
Methacrylated hyaluronic acid (HAMA)	*In-situ* radical crosslinking; HA/GO hydrogels were fabricated by methacrylated hyaluronic and methacrylated graphene oxide (GO).	HA/GO hydrogels exhibited excellent water absorption ability and elastic moduli. HA/GO-0.05 hydrogel showed a higher expansion of $CD34^+$ cells compared to HA, HA/GO-0.1, HA/GO-0.2.	The incorporation of nanomaterials can enhance the biophysical properties of hydrogels to promote the proliferation of HSCs.	Guo et al. (2017)
HAMA-methacrylated gelatin	Photo-crosslinking; SCF was physically encapsulated within HA/gelatin double network (HGDN) hydrogel to achieve a slow-release rate	The HGDN hydrogels achieved a sustained release of SCF to reduce the consumption of SCF. This cost-effective protocol could support the proliferation of HSCs and generate more multipotent colony-forming units.	SCF-loaded HGDN hydrogel provides a cost-effective *ex vivo* culture strategy for HSCs	Zhang et al. (2018)
Star-shaped poly (carboxybetaine acrylamide)	Click reaction; modified with polypeptide crosslinkers containing alternating K and E amino acid sequences and metalloproteinase	The zwitterionic hydrogel showed excellent hydrophilicity and ROS scavenging capability, leading to a 73-fold increase in long-term HSCs and hematopoietic reconstitution in mice up to 24 weeks.	The zwitterionic hydrogels with excellent hydrophilicity and anti-fouling properties hold great promise in realizing the long-term *in vitro* expansion of multipotent HSCs.	Bai et al. (2019)

(Continued on following page)

TABLE 1 (*Continued*) Engineering hydrogel strategies of biomimetic hematopoietic niche and *in vitro* HSC culture.

Hydrogel composition	Engineering strategies	Key findings	Comments	Ref.
Hyaluronic acid/carbon nanotubes antioxidant hydrogel	Photo-crosslinking; functionalized CNTS were incorporated into hydrogels	The HA/CNT hydrogels exhibited concentration-dependent antioxident activities to significantly enhanced the expansion of HSCs.	The antioxidant hybrid hydrogels provide a microenvironment with low ROS level for *in vitro* proliferation of HSCs.	Zhang et al. (2019b)
Thiolated HA, thiolated gelatin, PEGDA crosslinker	Microfluidic BM on-a-chip; 4 niche cell populations were encapsulated in the ECM-derived hydrogel, each in its own chamber of a microfluidic device	The microfluidic BM on-a-chip was deconstructed into four distinct but integrated niche constructs. Healthy and malignant human HSCs showed selective homing to specific niche on this device.	It provides a tool to study the interactions of normal and malignant HSCs with niche cells, which facilitate to delineate the HSC-niche signaling pathways.	Aleman et al. (2019)
Gelatin-alginate	3D bioprinting; hydrogel scaffold for HSCs and UC-MSCs coculture	$CD34^+CD38^-$ cells expanded 33.57-fold and $CD34^+CD184^+$ cells expanded 16.66-fold after 10 days of coculture with engineered scaffolds	The study demonstrates the feasibility of 3D bioprinting in constructing HSPC and MSC coculture environments.	Zhou et al. (2020)
Collagen	Microfluidic BM on-a-chip; Top channel: human $CD34^+$ cells and BMSCs in a fibrin gel; bottom channel: HUVECs	The vascularized human BM chip supported the differentiation and maturation of multiple blood cell lineages while improving the maintenance of $CD34^+$ progenitors.	BM on-a-chip with physiological function can be utilized to study the pathophysiology of hematological diseases and BM toxicity of drugs.	Chou et al. (2020)
PEG-DA/MA	Cryogelation; Iron nanoparticle are embedded in polymer solutions by pulsed laser ablation in liquids	PEG-iron nanocomposite hydrogels showed constant iron release to enhance erythroid differentiation.	This study proposes a strategy to guide erythroid differentiation in an *ex vivo* HSC culture model	Brandle et al. (2020)
Alginate-Puramatrix	Chemical crosslink; droplet-based microfluidics; Double layered hydrogel beads (inner: MSCs in alginate; outer: HSCs in Puramatrix) were cultured in DMEM with 10% FBS without additional supplements.	Human BM-derived $CD34^+$ cells survived, maintained, and expanded over 8 weeks in microdroplet.	This study presents a novel and economical protocol for the encapsulation, maintenance, and expansion of primary HSCs.	Carreras et al. (2021)

inhibit collagen capsule formation, thus preventing undesirable differentiations of HSCs (Zhang et al., 2015; Erathodiyil et al., 2020). In addition, the hematopoietic niche consists of a series of ECMs and interacting components (Winkler et al., 2020). Engineered hydrogels can be developed to contain interconnected polymer networks to spatially mimic the ECM networks and the cell–cell contacts in the natural niche. Stiffness can be achieved by regulating the degree of polymer cross-links (Rosales and Anseth, 2016; Tang et al., 2021; Maji and Lee, 2022). Such structures render hydrogels high permeable, supporting nutrient exchange between cells and the environment (Liu et al., 2019).

To better replicate cell–matrix interactions and improve the responsiveness of hydrogels to microenvironmental changes, they can be chemically and mechanically modified. These modifications enable the production of hydrogels with adjustable viscoelastic, mechanical, degradation, and cell adhesion characteristics, as desired (Zhang and Khademhosseini, 2017; Prince and Kumacheva, 2019; Caldwell et al., 2020; Liang et al., 2022). Aside from the provision of an artificial niche in cell cultures, hydrogels can also be used in the experimental studies of cellular behaviors and cell–material interactions (Costa et al., 2022). Various components can be introduced into engineered hydrogels to help the mimic the hematopoietic niche for the expansion of HSCs and the regulation of cellular behavior. These modifications of hydrogels are examined in the following sections. Recent engineering hydrogel strategies of the biomimetic hematopoietic niche and *in vitro* cultures are summarized in Table 1. Information on the characterization and functional assessments of cultured HSCs on these hydrogel-based studies are supplemented in Table 2.

4.1 Polymers for matrix networks

Hydrogels are fabricated by covalently or non-covalently cross-linking polymer chains dispersed in an aqueous solution. These 3D hydrogels are constructed by chemical cross-linking (Zhang and Khademhosseini, 2017; Yin and Cao, 2021) (Figure 2A), photo cross-linking (Nezhad-Mokhtari et al., 2019) (Figure 2B) and atom-transfer radical polymerization (Bai et al. (2019)) (Figure 2C). Depending on the source of polymers, hydrogels are classified into natural, synthetic, and hybrid polymers (Maji and Lee, 2022). As the name indicates, natural hydrogels contain polymers derived from biological sources. These matrices commonly contain alginate, hyaluronic acid (HA), chitosan, collagen, gelatin, and fibrin. Natural polymers are inherently biocompatible with living cells (Bao et al., 2019; Jiang et al., 2020; Peers et al., 2020); however, their practical use is limited by batch-to-batch compositional inconsistency, poorly controlled polymerization

TABLE 2 Some hydrogel-based studies for *in vitro* HSC culture and expansion.

HSC source	HSC phenotype	Culture maintenance	Functional assessment/other HSC-related analysis	Ref.
Human BM HSCs	$CD34^+$	7 days	*In vitro* CFU assay, Long-term culture initiating cell assay, *In vivo* study of secondary transplantation in NOD/SCID mice	Sharma et al. (2012)
Human UCB-HSCs	$CD34^+$	14 days	Viability assay, cell division tracking, flow cytometry, histomorphological analysis	Leisten et al. (2012)
Murine 32D cells, myeloid progenitor cells	—	6 days	Evaluation of cell adhesion and spreading	Cuchiara et al. (2013)
Murine BM HSCs	LSK HSCs	3 days	Viability assay	Mahadik et al. (2014)
Murine BM HSCs	LSK HSCs, progenitor cells (Lin^-Sca1^+, Lin^-cKit^+, Lin^-CD34^+, Lin^-CD135^+)	7 days	Viability assay, BM transplant in irradiated mice	Torisawa et al. (2014)
Murine BM HSCs	LSK HSCs	7 days	Viability assay, *in vitro* CFU assay	Mahadik et al. (2015)
Murine BM HSCs	LSK HSCs	14 days	Viability assay, CFU assay	Cuchiara et al. (2016)
Murine BM HSCs	LSK HSCS	2 days	Viability assay, CFU assay	Mahadik et al. (2017)
Human UCB HSCs	$CD34^+$	10 days	CFU assay	Guo et al. (2017)
Human UCB HSCs	$CD34^+$	14 days	CFU assay	Zhang et al. (2018)
Human UCB- and BM- derived HSCs	$CD34^+CD38^-CD45RA^-CD49f^+CD90^+$	24 days	*In vitro* CFU assay, *in vivo* study of secondary transplantation in NSG mice, Limiting dilution analysis	Bai et al. (2019)
Human UCB HSCs	$CD34^+$	10 days	Viability assays, CFU assay	Zhang et al. (2019b)
Human BM HSCs	$CD34^+$	5 days	Viability assay	Aleman et al. (2019)
Human UCB HSCs	$CD34^+$	10 days	Viability assay	Zhou et al. (2020)
Human peripheral blood-derived HSCs	$CD34^+$	14 days	CFU assay	Chou et al. (2020)
Human UCB HSCs	$CD34^+$	7 days	Flow cytometric analysis	Brandle et al. (2020)
Human BM HSCs	$CD34^+$	8 weeks	Viability assay	Carreras et al. (2021)

kinetics, and chain configuration (Echalier et al., 2017). These limitations can be overcome by using of bioengineered versions of natural polymers. These synthetic alternatives facilitate the controlled polymerization of the hydrogels (Zhao et al., 2016; Zhan et al., 2022). Polyethylene glycol (PEG), polylactic acid, polyvinyl alcohol, and polyurethane are synthetic polymers commonly utilized in tissue engineering and *in vitro* cell culture (Gjorevski et al., 2016). Hybrid hydrogels combine the best features of natural and synthetic polymers. Most research and practical use applications rely on these hybrid systems (Afewerki et al., 2019). Changing the composition and ratio of the incorporated polymers affects both the biocompatibility and mechanical properties (e.g., stiffness and degradation time), thus influencing cell fate and behavior (Wolf et al., 2015; Zhang et al., 2016). For example, keratin/PEG composite hydrogels exhibit a high compressive modulus of 45 kPa and long-term stability in physiological buffer solutions and cell culture media (Yue et al., 2018).

4.2 Regulation of bioactive molecules

The BM microenvironment contains various biologically active components, such as cell adhesion molecules, growth factors, cytokines, enzymes, and other signaling molecules. These represent specific signaling pathways and regulate diverse cellular processes, including proliferation, differentiation, migration, and apoptosis (Hastings et al., 2019; Winkler et al., 2020). Non-modified synthetic polymers and most natural polymers (e.g., alginate and

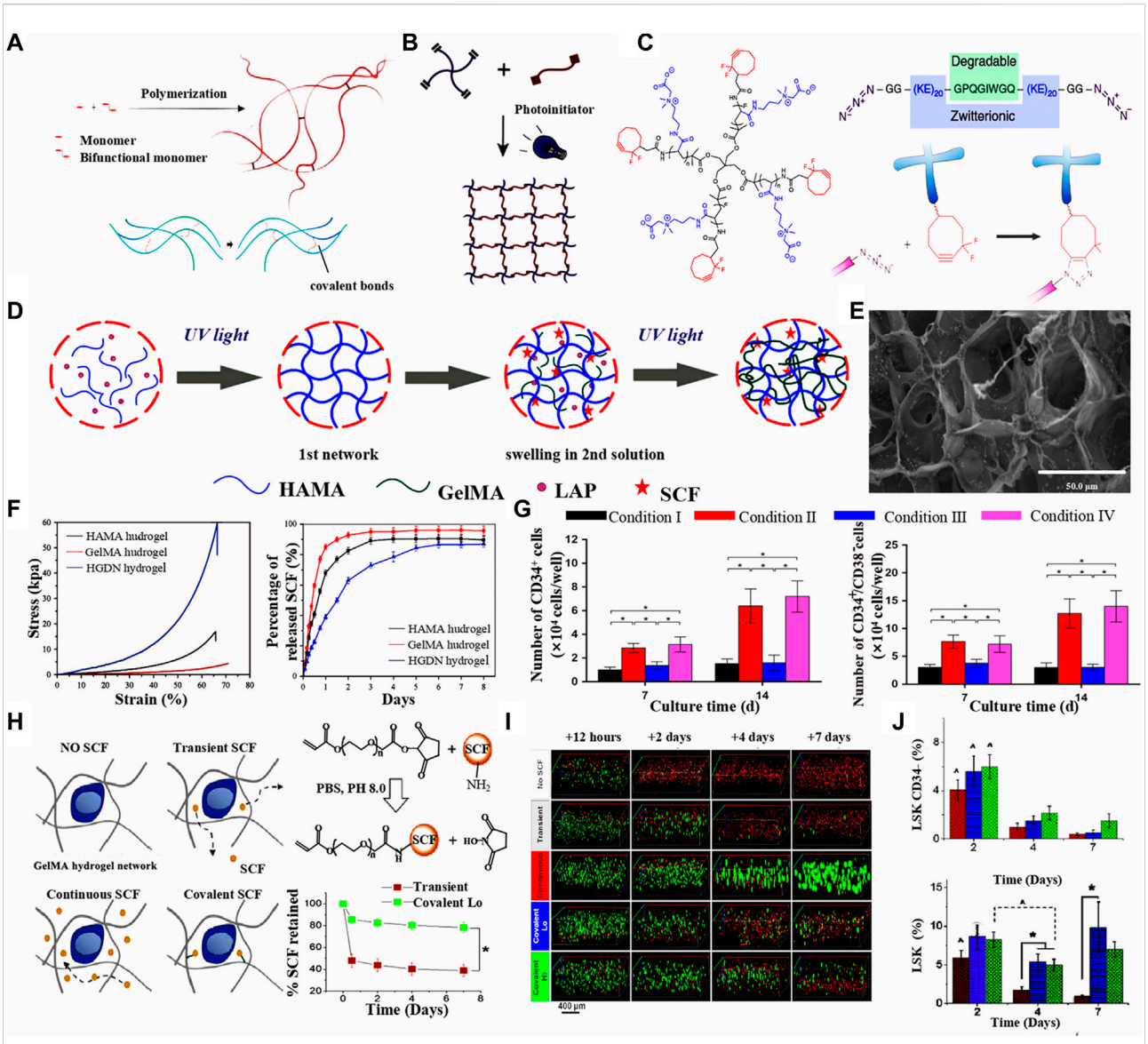

FIGURE 2
(A) Scheme of chemical crosslinking of hydrogel. Upper: (Yin and Cao, 2021) Copyright © 2021. Reproduced with permission from Elsevier. Lower: (Zhang and Khademhosseini, 2017) Copyright © 2017. Reproduced with permission from The American Association for the Advancement of Science. **(B)** Scheme of photo crosslinking. (Nezhad-Mokhtari et al., 2019) Copyright © 2019. Reproduced with permission from Elsevier. **(C)** Schemes of poly (carboxybetaine acrylamide) with a star-shape; polypeptide crosslinkers with KE sequences as the metalloproteinase degradable sites; The hydrogel synthesis basing on the step-growth polymerization mechanism of Huisgen cycloaddition. (Bai et al., 2019) Copyright © 2019. Reproduced with permission from Springer Nature. **(D)** Fabrication of the HGDN double network hydrogel and the physical loading of SCF. **(E)** Scanning electron microscopy images of the SCF-loaded HGDN double network hydrogel. **(F)** Stress-strain curves and SCF releases analysis of the HAMA, GelMA and HGDN hydrogels. **(G)** Percentages of CD34+ and CD34+CD38- phenotype of cells culture for 7 and 14 days. (Zhang et al., 2018) Figure 2D-G: Copyright © 2017. Reproduced with permission from John Wiley and Sons. **(H)** Different methods or SCF modification in hydrogels (left); SCF release curve of the transient and covalent modification of SCF. **(I)** Florescence images of the phenotype of cells cultured hydrogels with different release mode of SCF. **(J)** Percentage of LSK and CD34+ phenotype of cells culture in the SCF-loaded hydrogels with different culture time. (Mahadik et al., 2015) Figure 2H-J: Copyright © 2015. Reproduced with permission from Elsevier.

chitosan) lack these bioactive molecules (Maji and Lee, 2022). Therefore, considerable effort has been devoted to developing hydrogel polymers containing biomolecules necessary for the creation of a cellular microenvironment that enables the precise control of cellular behaviors (Caldwell et al., 2020). These biomolecules can be incorporated by non-covalent means, such as physical entanglement (Bovone et al., 2021), electrostatic interactions (Sivakumaran et al., 2013; Wang et al., 2018), or through covalent tethering (Zhang and Khademhosseini, 2017; Bovone et al., 2021). Incorporating

biomolecules *via* non-covalent weak interactions is more conducive towards the controlled release of nutrients and regulatory molecules.

Zhang group (Zhang et al., 2018) fabricated a HA/gelatin double network (HGDN) hydrogel that is physically loaded with stem SCF. The HA methacrylate (HAMA) hydrogel was fabricated by pouring the pre-gel HAMA solution and the photo-initiator phenyl-2,4,6-trimethylbenzoyl phosphonate lithium (LAP) into a round mold, which was then irradiated solution with ultraviolet light for a fast cross-linking. The HAMA network was then immersed in the GelMA solution with LAP until swelling equilibrium was reached and then photo-cross-linked to form a double network Figure 2D. This double network hydrogel is combined a fragile network and a double network and exhibits high mechanical strength and sustained release of SCF (Figure 2E, F). After 14 days of culturing, the total number of nucleated cells in the SCF-loaded HGDN hydrogel was approximately 3-fold higher than that of cells in the non-loading hydrogel, and the proportion of $CD34^+$ $CD38^-$ cells was slightly higher in the non-SCF treated group (Figure 2G). A CFU assay showed SCF-loaded HGDN hydrogels had more primitive CFU-GEMM (granulocyte, erythrocyte, monocyte, megakaryocyte) phenotype compared to the cells in plated with SCF. The HGDN hydrogel retained the SCF release for 6 days. Chemical incorporation of biomolecules through covalent, ionic, or metallic binding is widely used in the construction of 3D hydrogel networks (Xin et al., 2019; Chimene et al., 2020). Mahadik et al. (2015) demonstrated a methacrylamide-functionalized gelatin (GelMA) hydrogel covalently modified with SCF for culturing of primary HSCs isolated from the BM of mice. SCF was linked to the PEG-N-hydroxysuccinimide (NHS) ester and reacted with GelMA hydrogel precursor in solution (Figure 2H). When comparing the performance of the continuous SCF and covalent SCF in GelMA hydrogels, continuous SCF greatly increased the cell number after 7 days of culture and quickly reduced the cell number in longer culture, while reducing the maintenance of the initial LSK phenotype and primitive $CD34^-$ LSK cells (Figures 2I, J). In contrast, covalent SCF showed increased maintenance of the 2 cell populations. At day 7, CFU colonies had increased for cells treated with covalent SCF, and the cell expansion reached 3 which was higher than that of day 1.

Cuchiara et al. (2013) covalently immobilized the cell adhesion peptide RGDS, the cell growth factor SCF, and the stromal derived factor 1a (SDF1α) on the surface of a PEG hydrogel to control the adhesion and spreading of HSCs. An anchorage-independent hematopoietic cell line, named 32D clone 3 cells were seeded into the PEG-diacrylate (DA) hydrogel wells modified with the above compounds. The number of adherent 32D cells was higher in the 25 $\mu g\,cm^{-2}$ CF and SDF1α modified hydrogel well compared with other concentration, in addition to a larger adhere area (450 μm^{-2}). Sustained activation of CXCR4 receptor in the 32D cells shows the effect of biomolecules on 32D cell migration in the modified PEG-DA hydrogel. A concept of biological cues introduced into the hydrogel well for HSC culture was revealed, while experiment on the measurement of more HSC biomarkers has been limited.

This research group also fabricated a HSPC culture substrate with the derivatives of PEG-DA hydrogels. PEG-DA hydrogel wells were fabricated *via* a microfabrication patterning technology assisted by a photomask and photoresist. Proteins and peptides including the key cytokines, SCF, interferon-g (IFNg) and RGDS connecting segment 1, were chemically modified onto PEG with certain ratios to form the PEG-protein and PEG-RGDS composite. The composite was immobilized on the well surface *via* a photo-induced linking reaction. C-kit^+ cells collected from mouse BM cells were cultured in the PEG-DA hydrogel wells. After 2-week culture, the cell number increased by 11.6–19.0% for cells 3D encapsulated in hydrogel, which is higher than that in 2D culture, and 53.8% cells remined c-kit^+ without an observed loss. Encapsulated c-kit^+ cells could form all colonies which had similar results to that of 2D culture. However, 3D culture exhibited a larger number of multilineage HSPC-derived colonies than that of 2D culture. These experiments demonstrated that cytokines encapsulated in a 3D scaffold better replicated the cell–matrix interactions and showed advantages in controlling diffusion in cultures designed for LT-HSC expansion compared with the 2D hydrogel (Cuchiara et al., 2016) (Figures 3A,B). SCF is a key component of the native HSC niche and needs to be continuously and abundantly supplied in the medium when HSCs are cultured *in vitro*. Mahadik et al. (2015) reported the use of a composite hydrogel created by chemically immobilizing SCF within a degradable GelMA hydrogel matrix. Convective mixing of different precursor solutions of hydrogels was applied to creat a gradient environment in 3D hydrogels, which could influence cell aggregation and migration, or produce channels to transfer growth factors in gradient concentrations. By adjusting the geometry and the mixing models of the channels, they intend to use the device to develop a complex 3D culture environment that more closely mimics the elements of cell populations, matrix, and biological molecules within the BM. They observed single LSKs and Lin^+ BM cells and found that using the spectral deconvolution methods could identify the LSKs ($cKit^+$ $Sca1^+$) from mature BM (Lin^+) cells. The covalent incorporation ensured that the GelMA hydrogel retained its SCF content for longer than 7 days. The stable provision of this critical growth factor was sufficient to support the proliferation and lineage differentiation of HSCs.

In summary, modifying 3D hydrogels through the incorporation of important functional biomolecules *via* chemical or physical means can create a complex growth environment for HSC culture that more closely approximates the natural niche and allows the precise regulation of cell behavior to achieve extensive expansion of cells, while reducing undesired differentiation.

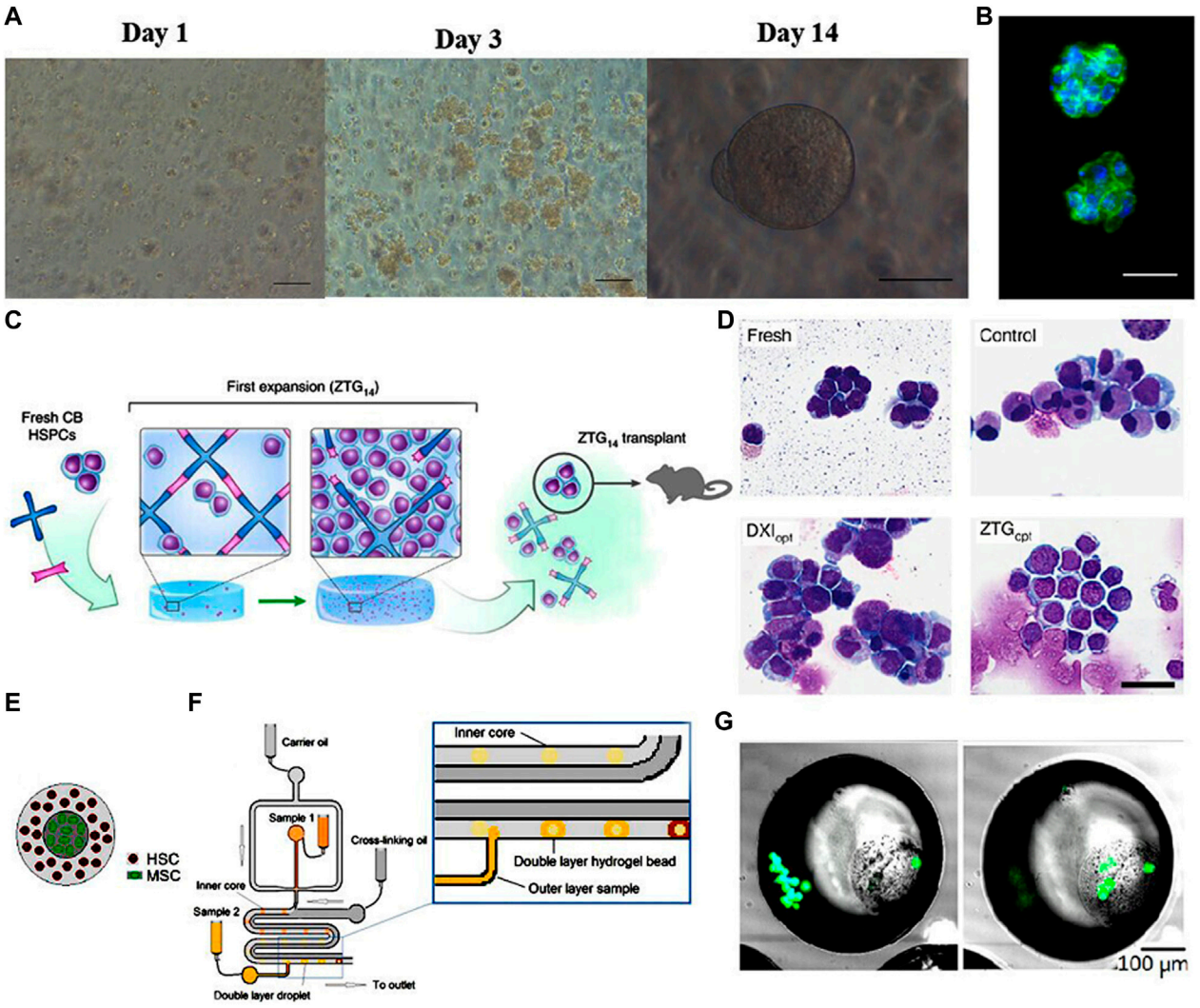

FIGURE 3
(A) Phase contrast images of HSCs encapsulated within bioactive PEG hydrogels at days 1, 3, and 14 showing the proliferation and round shape retention of HSCs. Scale bar: 100 mm (day 1, day 3), 50 mm (day 14). **(B)** DAPI (blue) and phalloidin (green) staining of HSCs after 14 days expansion showing the cell morphology retention and gel structure integrity. Scale bar: 25 mm. (Cuchiara et al., 2016) Figure 3A, B: Copyright © 2015. Reproduced with permission from John Wiley and Sons. **(C)** Schematic illustration of the zwitterionic hydrogels with superhydrophilicity and volumetric swelling. **(D)** Photomicrograph of Wright-Giemsa-stained HSCs showing the significant expansion of the primitive HSC population in zwitterionic hydrogels. Scale bar: 30 μm. (Bai et al., 2019) Figure 3C, D: Copyright © 2019. Reproduced with permission from Springer Nature. **(E)** Schematic representation of the double layered hydrogel bead with HSCs on the outer core and MSCs on the inner core. **(F)** Schematic illustration of the double layered structure fabrication process using droplet-based microfluidic. **(G)** Fluorescent staining of viable MSCs and HSCs show that both types of cells are successfully encapsulated in the double layered structure. (Carreras et al., 2018) Figure 3E-G: Copyright © 2018. Reproduced with permission from Elsevier.

4.3 Regulating the biophysical features

Several groups have reported the beneficial effects of the biophysical characteristics of hydrogels during the culture of MSCs and embryonic stem cells (Lu et al., 2014; Wong et al., 2021; Costa et al., 2022). Based on prior experimental observation, hydrogels with tunable biophysical characteristics were developed to mimic the native spatial architecture of the hematopoietic niche (Zhang P. et al., 2019; Wong et al., 2021). The most important physical properties include the matrix architecture of the microenvironment, which can be appropriately modified by engineering changes (Vining and Mooney, 2017; Zhang Y. et al., 2019). The behavior of HSCs can be regulated by adjusting the stiffness, dimensionality, architectural features, viscoelasticity, and shear forces in hydrogel matrices.

Physiological compounds of the HSC niche vary in stiffnesses; for example, the stiffness of soft marrow or

adipose tissue is lower than 1kPa, cell membranes is 1–3 kPa, and non-mineralized bone is >34 kPa (Patel et al., 2005; Discher et al., 2009; Chowdhury et al., 2010). Choi and Harley (2012) fabricated a polyacrylamide (PA) hydrogel substrate coated by collagen with varying stiffness to investigate the effect of substrate stiffness on the HSC behaviors. Elastic moduli of the PA hydrogel were adjusted by changing the ratio of the acrylamide and bis-acrylamide polymers to obtain a suitable cross-linking degree. They found that within the stiffness range of 0.01480–0.0442 kPa, varying the stiffness of the substrate, by altering its density, improved the viability of HSCs. The shape and spread area of 32D cells showed a similar trend to than of primary HSPCs when cultured on hydrogel with different stiffness. However, when the stiffness exceeded this range, the viability of the cells decreased with increasing substrate density. Additionally, the spreading of HSCs was enhanced significantly with the increased stiffness of the substrate. The effect of receptor-ligand interactions on HSPC behavior was also quantified, and it was observed that substrate stiffness significantly impacted the cytoskeletal distribution and density of HSPCs. Therefore, accurate control of hydrogel stiffness is important to ensure cell viability. Furthermore, HSCs cultured in a 3D hydrogel environment preserved their naïve state and rounded morphology better than when maintained on top of a 2D surface composed of the same components.

Hydrogel scaffolds containing macropores approximate the "spongy" architecture of natural trabecular bones. The resulting complex internal structure replicates the natural ECM of the hematopoietic niche and promotes the uniform diffusion of soluble factors by regulating their concentration and depletion (Raic et al., 2014). The pores can also aid the propagation of autocrine and paracrine signals involved in cell–cell communication (Raic et al., 2014; Gilchrist et al., 2019a; Gilchrist et al., 2019b). In one study, the poroelestic properties and Young's modulus (E) of the GelMA hydrogels were controlled by adjusting the photo-initiator concentration and degree of methacrylamide functionalization (DOF). HSPCs and MSCs were both extracted from the tibia and femur BM of mice and were co-cultured in GelMA hydrogels with a high E value. After 7 days of culture, the hematopoietic population increased to the 11.11 ± 3.18% of the total, which is higher than that of a hydrogel with a low E value. This may be related to reduced myeloid differentiation of the cells. The percentage of quiescent (G0) LT-HSCs or HSCs to the initial HSPCs was highest for cells co-cultured in high E value hydrogel. This demonstrates that autocrine and paracrine signaling can be modulated by tuning the seeding density and poroelastic properties of the hydrogel matrix. Small mesh-sized pores resulted in slow diffusion, which reduced cell-to-cell communication, increasing the importance of autocrine regulatory dominated pathways. Under these conditions the quiescence of the primitive HSC population was better preserved (Gilchrist et al., 2019).

The viscoelasticity of hydrogels means that the stress relaxation characteristics of the matrix can be influenced by external pressure. These changes force cells to remodel the matrix through cell–ECM interactions (Tang et al., 2021). Chaudhuri et al. (2016) developed alginate hydrogels with tunable viscoelastic properties to adjust the differentiation of MSCs by modulating the nanoscale architecture of the matrix. They reported that at an elastic modulus of 17 kPa, the hydrogel showed fast stress relaxation and promoted MSCs to differentiate, resulting in the production of a mineralized collagen-1-rich matrix that showed some similarities to the structure of natural bone. Regulation of viscoelasticity can also affect mechanical stresses and substance diffusion (Chaudhuri, 2017). However, to date, most studies have relied on controlling the elasticity of the hydrogel during its preparation, rather than the adjusting the viscoelasticity dynamically (Chaudhuri et al., 2016). The modulation of hydrogel viscoelasticity may provide new insights to aid in the creation of an optimal microenvironment for the growth of HSCs. In the 3D hydrogel microenvironment, liquid movements result in a shear force being exerted over the HSCs (Rodell et al., 2013). Furthermore, hydrogel-based microfluidic systems are in development for high throughput cultures of HSCs. As microdroplets are formed in these systems, shear forces will change (Xia et al., 2017; Zhan et al., 2022). Studies have shown that shear stresses within the hydrogel suspension could reduce the survival of HSCs (Hosseinizand et al., 2016). Mahadik et al. (2014) fabricated a microfluidic multicellular gradient hydrogel platform and observed that the viability of MSCs and HSCs was not significantly influenced by flow characteristics. HSCs are exposed to a certain degree of shear force in their natural niche, so under ideal conditions this would need to be recreated in artificial matrices. Thus, shear forces in hydrogels need to be adjusted to a point where they support cell growth rather than reduce viability.

Zwitterionic materials have attracted attention recently due to their structural similarity to naturally occurring cell membrane lipids. Bai et al. (2019) developed zwitterionic polycarboxybetaine-based hydrogels modified with polypeptide cross-linkers. These exhibited enhanced hydration and swelled up markedly in aqueous solutions, which had an anti-fouling effect and improved biocompatibility (Figure 3C). HSCs cultured in this optimized zwitterionic hydrogel could undergo massive expansion without loss of their stemness (Figure 3D). A systematic study on expansion of primitive human HSCs using a zwitterionic hydrogel reported the construction of a uniform 3D zwitterionic hydrogel network (hereinafter referred to as ZTG hydrogel) through the click chemical reaction between alkyne terminated four arm polycarboxylated betaine acrylamide (pCBAA) and azide modified polypeptide polymerization (Azide–GG-(KE) 20-GPQGIWGQ-(KE) 20-GG Azide) to simulate the 3D environment dominated by hydrophilic and zwitterionic cell membrane lipids of HSPCs

in vivo. ZTG hydrogel maintained the high expression of CD34 during the whole culture period, in which 93.7 ± 2% of the expanded cells were $CD34^+$. Substantial expansion of primitive $CD34^+$ BM- and CB-derived HSPCs for 24 days achieved 73-fold of increase in the number of LT-HSCs. The researchers also used limited dilution analysis (LDA) to detect the amplification frequency of medium and LT-HSCs; after 24–30 weeks of transplantation, the amplification frequency of LT-HSCs cultured in ZTOpt mode was much higher than that of other culture methods. Both LDA and secondary transplantation experiments showed that LT-HSC cells with long-term hematopoietic function could be cultured and expanded by ZTG. The LT-HSCs expanded in ZTG hydrogel were injected into immune-deficient NSG mice for primary and secondary BM transplantation. The experimental results showed that in HSPCs derived from CB, $CD34^+$ was effectively amplified in ZTG hydrogel; the expanded HSPCs were used for BM transplantation, which also showed good amplification performance *in vivo*.

In the past, strategies for the *in vitro* expansion of HSCs mostly focused on the role of the ECM, while the effects of the metabolism of the HSCs themselves has received very little attention (Kohli and Passegue, 2014). Reactive oxygen species (ROS) produced by HSCs during proliferation is one of the key factors causing overactivation of the cells and results in the loss of hematopoietic potential (Suda et al., 2011). Incorporating ROS scavenging components into hydrogels represents a novel approach to maintain the quiescent status of HSCs. Gilchrist et al. (2021) encapsulated difficult-to-preserve HSPCs in a maleimide-functionalized gelatin (GelMAL) hydrogel containing added dithiol cross-linkers to absorb ROS. Bai et al. (2019) prepared 3D zwitterionic hydrogels that were unique in suppressing excess ROS production by inhibiting oxygen-related metabolism. Cells maintained in this environment showed reduced differentiation, thereby promoting their self-renewal.

4.4 Biomimicking cell–cell interactions

Cell–cell interactions within the hematopoietic niche provide both soluble factors and direct cell–cell contact, which are critical in determining the fate of HSCs (Walenda et al., 2010). Although supplementation with a cocktail of cytokines can increase the expansion of $CD34^+$ HSCs (Li et al., 2019), cell–cell interactions during the co-culture of HSCs and MSCs can synergistically enhance cytokine-induced cell proliferation (Schmal et al., 2016). These observations prompted experiments in which various niche cells, such as MSCs and endothelial cells, were co-cultured with HSCs to investigate how the presence of another cell population affected the maintenance of stemness or the induction of desired lineage differentiation (Xiao et al., 2022). The results showed that MSCs and endothelial cells are the most important feeder cells in HSC cultures, as these cells produce more supporting factors than other BM stromal cells (Xiao et al., 2022). Although MSCs are relatively rare in the BM, they secrete several critical cytokines and growth factors, including CXCL12, which direct chemotaxis, survival, proliferation, and promote SFC. Furthermore, key differentiation factors, such as Flt3-ligand, TPO, and IL-6, are all produced primarily by BM-MSCs (Lo Iacono et al., 2017; Sarvar et al., 2022). Human umbilical vein endothelial cells (HUVECs) have also been used as feeder cells to support the proliferation and differentiation of HSCs *in vitro*. They express some of the same surface markers and transcription factors found in HSCs, including CD31, CD34, Runx1, and GATA-2 (Kuan et al., 2017; Li et al., 2019).

Co-culturing HSCs with MSCs or HUVECs provides important cell–cell interactions. However, because both MSCs and HUVECs are adherent cells, their interactions with HSCs on a 2D surface are suboptimal (Bello et al., 2018). To improve the cell–cell interactions in co-culturing, hydrogels were used to create an artificial matrix in which adhesion molecules present on MSCs and HUVECs interacted in a 3D spatial area with the HSCs, resulting in improved HSC proliferation (Tibbitt and Anseth, 2009).

Leisten et al. (2012) reported a collagen-based 3D microenvironment for co-culture of human BM or umbilical cord derived progenitor cells (HPCs) with MSCs. MSCs were embedded in the collagen hydrogel (denoted as niche II) and HPCs were seeded in the collagen-free suspension (denoted as niche I). After 14 days culture, HSCs migrated along the collagen fibers niche II and formed cobblestone-like cluster of 10 cells. After 14 days of culture, HPCs in the BM-MSC contained in niche II had a highest number of $CD34^+$ cells, while the lowest number of $CD34^+$ cells was observed in umbilical cord (UC)-MSC niche II, indicating that UC-MSC stimulated HPC differentiation. In niche II, expression of the pan-leukocyte marker CD45, and CD13 were observed, whilst CD56 was poorly expressed in niche II and myeloid differentiation was increased. The researchers established a collagen hydrogel-based artificial HSC niche with two statuses: HPCs in niche I are a proliferative and contained cell population of $CD34^+/CD38^-$ maturing myeloid cells ($CD38^+$, $CD13^+$, CAE^+), while HPCs in niche II contained high numbers of primitive $CD34^+/CD38^-$ phenotype cells beginning myeloid ($CD13^+$, CAE^+) differentiation, resembling the endosteal part of the BM niche. These authors also reported that UC-MSCs were not appropriate feeder cells as they caused extensive differentiation and a complete loss of primitive HSC phenotype (Leisten et al., 2012). Hydrogels can contain a complex diffusion system with an anisotropic distribution of molecules that is more similar to the natural niche, potentially allowing a more precise regulation of cellular behavior (Gurkan et al., 2014). Tuning of the mesh size in hydrogels can precisely regulate cell–cell interactions between co-cultured HSCs and MSCs; this approach allows the balancing

of autocrine and paracrine signals (Gilchrist et al., 2019). The co-culture of Lin^+ BM niche cells and HSCs in different hydrogel matrices showed that proliferation rate and myeloid differentiation of HSCs closely depended on the rate of diffusion in the matrix (Mahadik et al., 2017). Integrating hydrogels with microfluidic technology resulted in a novel 3D artificial hematopoietic niche (Carreras et al., 2018; Carreras et al., 2021). In this double-layered model, alginate embedded MSCs were place in the middle of hydrogel beads. This core was surrounded by an outer layer of Puramatrix encapsulated HSCs. Figures 3E,F HSCs embedded in these double layered beads maintained their stemness even after 8 weeks of culture (Figure 3G).

4.5 Optimization: Integrating functional nanomaterials

Organic polymers used as hydrogel sources have distinct advantages due to the superior biocompatibility of their natural matrix (Guvendiren and Burdick, 2013). Unfortunately, these polymers lack the necessary physical features and properties to create a viable culture system (Billiet et al., 2012). Recently, inorganic nanomaterials with excellent mechanical strength, abundant functional groups, good optical properties, and a large surface area have gained increasing use in tissue engineering (Billiet et al., 2012). To improve the mechanical properties and extend the application of biologically derived hydrogels in the production of cultured HSCs, organic–inorganic 3D hybrid hydrogels were prepared *via* the physical or chemical cross-linking of biopolymers with functional nanomaterials in an aqueous phase (Motealleh and Kehr, 2017). These nanomaterial-containing hybrid hydrogels exhibited improved mechanical, electronic, and optical characteristics. Their stimulus-response properties and biocompatibility are also very promising (Gaharwar et al., 2014; Kehr et al., 2015; Motealleh and Kehr, 2017; Sharma et al., 2018; Guillet et al., 2019; Deng et al., 2021).

Zhang P. et al. (2019) fabricated a HAMA hydrogel *via* the esterification of MA and HA. The macromolecular ROS scavenger, carbon nanotubes (CNTs) were loaded into the HAMA hydrogel by mixing the CNTs suspension with HAMA and LAP in pre-gel solution and followed by a photo-cross-linking. CNT hybrid hydrogels showed better hydrophilicity because of the abundant carboxyl groups from the CNTs. CNTs also improved the modulus of the hydrogels from 5.0 to 7.5 kPa. Isolated $CD34^+$ cells were cultured on the hydrogels supplied with the cytokine cocktail. HSC release of ROS decreases the survival of HSCs and causes the activation of HSCs. In the CNT-loaded HAMA hydrogel, ROS triggers the biodegradation of polysaccharides in the hydrogel, releasing the CNTs to scavenge ROS. The percentage of $CD34^+CD38^-$ and $CD34^+$ cells increased in the CNT hybrid hydrogel after 10 days of culture. CNT hybrid hydrogels also significantly promoted the total CFU, CFU-GM, and CFU-GEMM compared with non-CNT loaded hydrogels, indicating that integrating nanomaterials with antioxidant properties is beneficial for the hematopoietic function of HSCs. Another study combined methacrylated graphene oxide (MeGO) with HA hydrogels, which significantly increased the water absorption and elastic modulus of the hybrid material. The composite MeGO-HA matrix supported the proliferation of $CD34^+$ cells, whilst maintaining their primitive $CD34^+CD38^-$ phenotype, especially in a version containing 0.05% w/v MeGO (Guo et al., 2017). To promote the differentiation of HSCs into red blood cells, Brandle et al. (2020) developed an iron nanoparticle composite PEG hydrogel, which ensured the gradual release of iron, inducing some erythroid differentiation. However, they failed to achieve the desired level of differentiation due to iron overload in the 3D PEG-iron nanocomposite scaffolds.

5 Fabrication technologies to create a hydrogel-based artificial niche

5.1 Hydrogel coating on 2D substrates

Culturing HSCs on the 2D surface of polystyrene flasks is still the most widely used traditional culture method (Ribeiro-Filho et al., 2019). This approach has low costs, the flasks are easy to handle and the cells can be harvested with ease (Bello et al., 2018). However, the hydrophobicity of these plastic substrates can induce attachment and the excessive production of ROS, resulting in unintended differentiation and the rapid loss of stemness (Bai et al., 2019; Erathodiyil et al., 2020). It has been demonstrated that culturing cells on plastic surfaces coated with hydrophilic hydrogels inhibited this unnecessary differentiation (Cuchiara et al., 2016; Bai et al., 2019; Liu et al., 2021). Choi and Harley prepared type I collagen-coated polyacrylamide substrates of varying stiffness by altering the total polymer content and the density of cross-linkers. The spreading and morphology of HSCs was significantly influenced by the 2D hydrogel coating of the polyacrylamide surface (Choi and Harley, 2012). However, using a 2D environment for the culture of HSCs is substantially different from the 3D architecture of their natural niche. This leads to a non-physiological flattened spreading pattern with abnormal polarity that causes the loss of their multilineage differentiation potential (Caliari and Burdick, 2016). Compelling evidence suggests that 3D systems enhance cell-microenvironment interactions by improving mechano-sensing by HSCs resulting in increased proliferation and the maintenance of repopulating capacity even after long periods in culture (Cuchiara et al., 2016; Gvaramia et al., 2017; Gilchrist et al., 2019). Thus, current research trends are focusing on the development of optimized 3D hydrogel systems (Jensen and Teng, 2020).

5.2 3D hydrogel encapsulation

To better mimic the 3D hematopoietic microenvironment, the encapsulation of HSCs into a synthetic 3D hydrogel space has been extensively studied (Bello et al., 2018). As mentioned above, these hydrogels can contain natural or synthetic polymers, or a combination of the two. Some of the most commonly utilized natural hydrogels include HA, collagen, alginate, and chitosan, while synthetic hydrogels commonly include PEG, polyethylene oxide (PEO), and poly-l-lactic acid (Maji and Lee, 2022).

Traditional bulk hydrogels are usually relatively large and lack micropores, resulting in slow degradation and limited substance diffusion (Hsu et al., 2019). Micron-sized hydrogels, termed microgels, are expected to solve these problems. These microgels can act as a culture unit for a single cell or may contain a co-culture of multiple cells. Alternatively, the hydrogel can also be assembled into larger scaffolds (Carreras et al., 2018; Caldwell et al., 2020; Carreras et al., 2021). Carreras et al. (2021) reported the use of a droplet microfluidic device contained with double-layered hydrogel beads for the long-term culturing of human HSCs ($CD34^+$ cells). They presented a 3D niche biomimetic model by fabricating an engineered double-layered bead with an alginate-based inner layer and a Puramatrix-based out layer. Numbers of $CD34^+$ cells significantly increased at weeks 6–7, reaching to a maximum level at week 7 of approximately 4-fold that of week 1–2; it then gradually declining at week 8. At week 4, most cells were functional and remained in an undifferentiated status; however, there was a slight CD20 and CD38 signal for lymphoid differentiation, and CD33 signal for myeloid differentiation, as well as $CD34^+/HLA^-DR^+$ for an intermediate stem cell population. The results indicated this biomimetic niche model had good potential for the long-term culture of HSCs and maintenance on functional cell numbers.

The above methods enabled the microencapsulation of co-cultured HSCs and MSCs with a population distribution approximating that of the natural niche. Encapsulating cells in 3D hydrogels has been demonstrated to regulate stem cell fate decisions by supporting tunable ligand incorporation, the delivery of soluble factors, and mechano-sensing (Gvaramia et al., 2017; Kim et al., 2019; Gilchrist et al., 2021).

5.3 Hydrogel-integrated microfluidic systems

Microfluidic technology has emerged as a powerful tool in the reconstruction of the cellular microenvironment. This approach enables the creation of micro-sized droplets matching the diameter of the cells and permits the precise microscale manipulation of fluid flow and the modulation of the concentration of various factors (Whitesides, 2006; Sackmann et al., 2014; An et al., 2019). However, conventional microfluidics manipulations usually take place in 2D environments (An et al., 2019). Incorporating hydrogel matrices into microfluidic systems enables the construction of 3D spatial environments and the provision of different biophysical and biochemical features mimicking the natural microenvironment (Liu et al., 2019).

The use of microfluidic systems can rapidly establish a concentration gradient of various chemical compounds, facilitating the precise control of culture conditions and experimental investigation of the effects of individual factors (An et al., 2019). Chemical gradients are created in microfluidic channels *via* both flow and diffusion (Kim et al., 2010). T- or Y-shaped channels also allow the mixing of two fluid streams entering from two separate inlets and converging at the intersection (An et al., 2019). Mahadik et al. (2015) reported the use of the PEG-SCF functionalized GelMA hydrogel; PEG functionalized SCF retains the natural biological activity of SCF, and >80% of PEG functionalized SCF can be stably incorporated and retained in the GelMA hydrogel within 7 days. Mouse BM HSCs were cultured in hydrogels with four SCF presentation modes (No SCF, transient SCF, continuous SCF, concurrent SCF). The effects of continuous and covalent SCF presentation patterns on the fate of HSCs were examined by surface antigen expression and CFU analysis. After 7 days, the total number of cells under both conditions increased significantly; however, the maintenance of LSK and $CD34^-$LSK components decreased significantly under continuous SCF conditions, while in the hydrogel containing covalently fixed SCF, they remained unchanged over time. In GelMA hydrogel containing covalent fixation, the CFU-GEMM score was significantly higher than that of continuous SCF, indicating that the maintenance of more primitive hematopoietic progenitor cell population was improved. They also mixed two pre-polymer solutions (5% w/v GelMA; 5% w/v GelMA $^+$ 400 ng/ml PEG-SCF) through a microfluidic device using a computer-controlled syringe pump to form a GelMA hydrogel containing a covalently fixed SCF gradient, and observed that HSCs expanded with the SCF content gradient. SCF embedded in this 3D environment promoted the proliferation and the maintenance of primitive HSCs in a dose-dependent manner.

In addition to chemical gradients, microfluidics can also generate cellular gradients to mimic the complex multicellular microenvironment. Mahadik et al. (2014) used a traditional staggered herringbone shaped microfluidic mixer to generate a 3D collagen hydrogel containing adjustable, reverse gradient cells and biomaterial properties from two hydrogel precursor suspensions. To check the effect of flow through the mixer on cell viability, a 1-mg/ml collagen suspension containing MC3T3-E1 osteoblasts or mouse BM LSK cells was directly put into the glass dish (control) or entered the dish through the microfluidic mixer (device). For these 2 cell types, high relative viability was observed in the first 24 h of culture, which remained high after 3 days of culture (>60%). The mixer was then used to prepare the reverse gradient hydrogel of the above 2 cells in the 1 mg/ml collagen hydrogel. The relative gradient (2:1–1:2) of LSK and osteoblasts was quantified by fluorescence analysis of the whole structure. The relative gradient of mixed cells was similar to that of

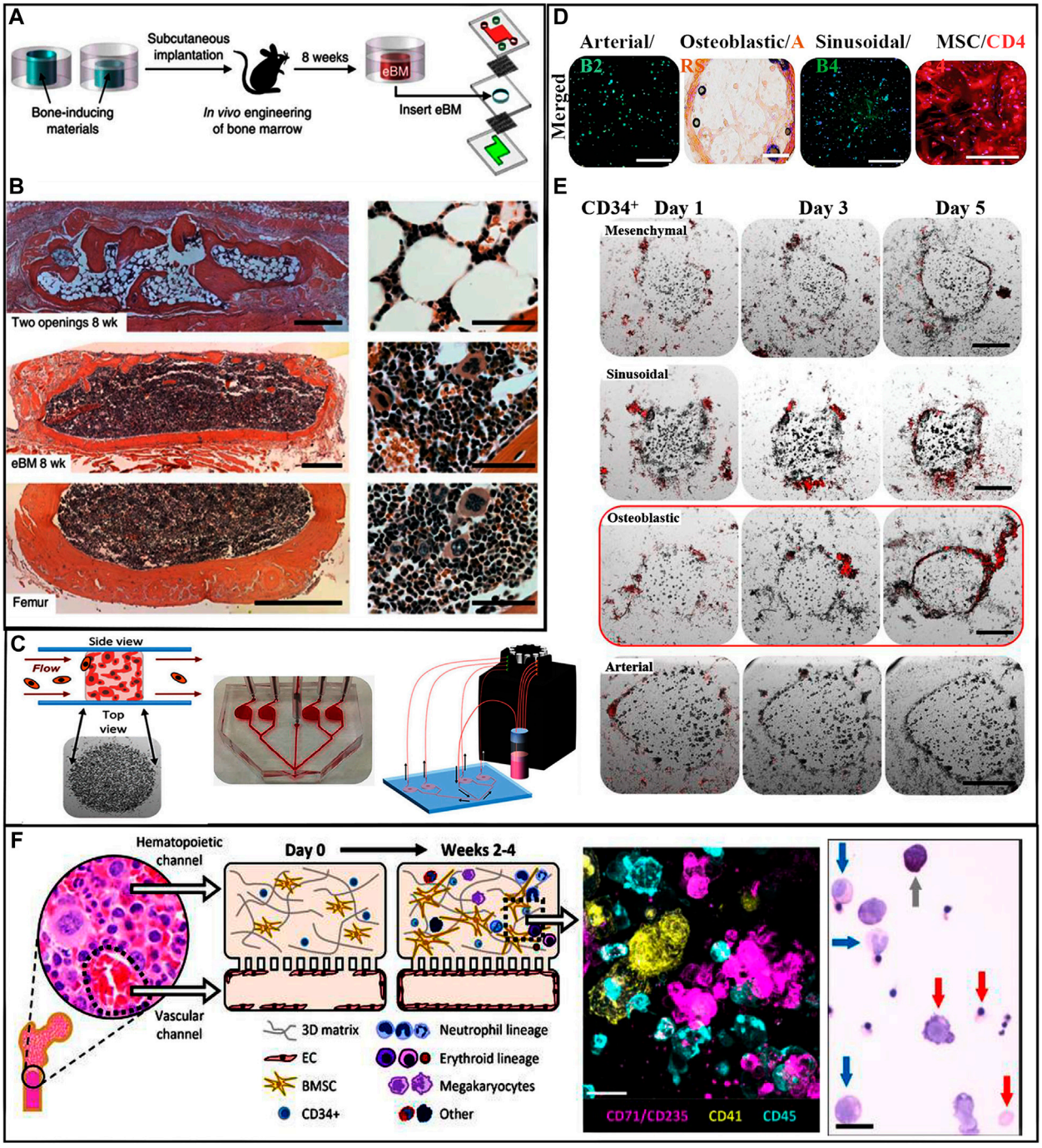

FIGURE 4
(A) Schematic of workflow to fabricate BM on-a-chip, in which eBM is formed in mouse and is then cultured in a microfluidic system. **(B)** Images show the establishment of eBM with in vivo-like histological BM structure. (Top) Hematoxylin-and-eosin-stained sections of the post-implanted eBM formed in the PDMS device with two opening. (Center) Histological sections of the post-implanted eBM formed in the PDMS device with one lower opening. (Bottom) Cross-section of BM in a normal adult mouse femur. Scale bars: 500 and 50 μm for low and high magnification views, respectively. (Torisawa et al., 2014) Figure 4A, B: Copyright © 2014. Reproduced with permission from Springer Nature. **(C)** Niche-on-chip microfluidic chip. (Left) Side and top view depictions of the niche constructs in the device chambers. (Center) Schematic of multi-niche-on-chip device. (Right) Schematic of operational recirculating multi-niche-on-a-chip systems. **(D)** Live/dead viability staining of each niche construct type. Scale bars: 100 μm. **(E)** Fluorescent images of niche-on-a-chip lodging/retention experiments using CD34+ HSCs. Scale bar: 250 μm. (Aleman et al., 2019) Figure 4C-E: Copyright © 2019. Reproduced with permission from John Wiley and Sons. **(F)** Schematic illustration of the vascularized BM on-a-chip with CD34+ progenitors and MSCs in the top gel channel and a vascular lining in the bottom channel. Immunofluorescence image of a vertical cross-section through the upper channel of the BM chip. Scale bar: 20 μm. Wright-Giemsa staining image of cells from the BM chip showing multilineage differentiation. Scale bar: 20 μm. (Chou et al., 2020). Copyright © 2020. Reproduced with permission from Springer Nature.

single cell hydrogel with opposite gradient, indicating that the relative gradient of mixed cells was generated. Single LSK and $Lin^+(GFP^+)$ BM cells mixed in a single hydrogel were imaged using a multiphoton microscope. The spectral deconvolution method could identify LSK cells from mature BM (Lin^+) cells. The multiple gradient hydrogel constructs developed here provide the potential for HSC fate manipulation and tracking analysis in 3D microenvironment models, and will become a powerful tool for studying cell–microenvironment interactions (Choi et al., 2015).

The human organ chip is a transformative biomedical technology that was voted as one of the "Top Ten Emerging Technologies" in 2016 (Domingues et al., 2017). In one application, scientists established a BM on-a-chip based on the integrations of hydrogels and a microfluidic system. The hydrogel element contained various encapsulated niche cells (Sieber et al., 2018; Chatterjee et al., 2021). This BM on-a-chip approach represents a sophisticated model of the living BM with cellular diversity and complex functionality, and was subsequently approved by the Food and Drug Administration (Liu et al., 2019). BM toxicity, radiation resistance, and drug testing can be conducted using these artificial BM models, replacing experimentation on animals (Chou et al., 2020).

These organ on-a-chip models closely approximate the environment of the natural BM. Torisawa et al. (2014) developed a BM on-a-chip system and tested whether HSCs cultured on these chips can maintain their capacity to self-renew and differentiate into multiple lineages. They fabricated a polydimethylsiloxane microdevice contained a central cavity filled with collagen, bone morphogenetic proteins, and demineralized bone powder. These devices were implanted into mice for a period of 4–8 weeks. On removal, the central cavity contained a well-developed BM compartment. These recovered BM chips were transferred into a microfluidic system for further observation (Figure 4A). After 7 days of *in vitro* culture, the amount and distribution of HSPCs and HSCs remained similar to those of the fresh BM (Torisawa et al., 2014) (Figure 4B). Aleman et al. (2019) created another version of the BM on-a-chip; the HA and gelatin hydrogel microenvironment was subdivided into four major hematopoietic areas, a periarterial, a perisinusoidal, a mesenchymal, and an osteoblastic niche (Figures 4C,D). In this system, healthy and malignant human HSCs showed unique and selective homing behavior into specific niches (Figure 4E). Chou et al. (2020) created a vascularized human BM on-a-chip system that consisted of two chambers connected by a porous membrane. The top "hematopoietic" chamber, representing the intraosseous niche, was filled with human $CD34^+$ HSCs and BM-derived MSCs in fibrin gels. The bottom "vascular" chamber was lined by HUVECs and perfused with culture medium containing supportive cytokines (Figure 4F). Culturing HSCs within this *in vitro* model preserved stemness and supported myeloerythroid proliferation and differentiation (Chou et al., 2020). Research on the validation of the effectiveness of HSCs developed in these artificial environments is currently being carried out in living animals. The HSC populations expanded in the engineered environments *in vitro* are transplanted into mice for evaluation of their safety and their ability to reconstitute BM function (Baena et al., 2021). It is anticipated that future BM on-a-chip systems will be sophisticated enough to allow the validation and characterization of *in vitro* expanded HSCs without the need to sacrifice live animals.

5.4 Stimulus-responsive hydrogel-based multifunctional hematopoietic stem cell culture platform

Stimulus-responsive hydrogels are promising tools that can sense signals coming from niche cells and/or cytokines in the matrix and respond to these signals by changes in conductive, chemical, or temperature characteristics. These "intelligent" microenvironments can adapt to the requirements of the cells growing within (Jiang et al., 2020; Deng et al., 2021). For example, an enzyme-responsive 3D hydrogel was developed containing conjugated polypeptides that could be hydrolyzed by the matric metalloproteases (MMPs) secreted by encapsulated HSCs. As HSC numbers expanded, their increased cumulative MMP production gradually cleaved the polypeptides in the matrix, facilitating the swelling of the hydrogel, thus providing a larger space for further increases in HSC number. In addition, the enzyme sensitive nature of the hydrogel also simplified the rapid harvesting of cells. By exposing the whole hydrogel compartment to exogenous MMPs, this resulted in the degradation of the matrix, so the encased cells could be easily collected (Bai et al., 2019). Although hydrogel-based 3D environments allow the successful expansion of HSCs, harvesting the encapsulated cells remains challenging (Bodenberger et al., 2017; Yin and Cao, 2021). Commonly the expanded cells are collected after mechanical disassembly or chemical dissociation of the matrix. However, these processes can damage the cells. Kwak and Lee, 2020 reported an inverted colloidal crystal hydrogel scaffold that was created from poly(N-isopropylacrylamide). The volume of this hydrogel shrank or swelled significantly depending on changes in the temperature within a physiological range (4–37°C). Due to this reversible thermoresponsive behavior of the hydrogel spheroids containing embedded cells could be created in a single step and the expanded cells could be rapidly recovered afterwards by controlling the volume of the hydrogel. By changing the temperature, the encapsulated HSCs could be selectively separated from spheroids.

Stimulus responsive hydrogels can be combined with biosensor technology to directly monitor key markers of living cells cultured in the biomimetic environment. This approach allows for the long-term tracking and monitoring of the encapsulated cells (Jiang et al., 2020; Deng et al., 2021). Lee et al., 2016 reported a 3D capacitance biosensor that worked in alginate hydrogels containing MSCs. This system allowed the real time monitoring of cell proliferation, migration, and

differentiation, by measuring dynamic changes in capacitance and conductance. Because HSCs can easily lose their stemness during in vitro culture, the ability to monitor their differentiation and stemness markers, preferably in real time, has considerable advantages (De Leon et al., 2020; Allenby and Woodruff, 2022).

While current hydrogel methods enable the massive expansion of encapsulated cells, they are seldom equipped to sense and monitor cell characteristics (Fedi et al., 2022). Instead, the detection of biomarkers still relies on conventional fluorescence or immunological detection techniques requiring the extraction of cells from the matrix. Under these conditions, the real-time state of the bionic culture environment cannot be continuously monitored (Lim et al., 2007; Gilchrist et al., 2021). Stimulus-responsive hydrogels will provide new approaches in developing a comprehensive platform for the expansion and simultaneous monitoring of the state of encapsulated HSCs, potentially optimizing yield and quality.

6 Prospects and challenges

Hydrogel biomaterials show excellent biosafety, offer flexible possibilities for chemical modifications and biofunctionalization, and have been successfully used for the *in vitro* expansion of primitive HSCs. A combination of various chemical modifications, the addition of biomaterials, and advancements in technologies—such as microfluidics and organ on-a-chip—make it possible to establish hydrogel-based microenvironments with exquisite architecture and adjustable physical features that closely mimic the natural hematopoietic niche. Aside from their clinical relevance, these systems also facilitate studies on the behavior and fate of HSCs. However, due to the extraordinarily complex physiology of the natural hematopoietic niche, replicating it *in vitro* using engineered hydrogel-based systems still holds many challenges. Various features of the natural hematopoietic environment, such as the presence of other cells, biochemical cues, varying stiffness, and topography, are distributed in a heterogeneous environment and direct the behavior and fate of HSCs though multiple mechanisms. In contrast, most hydrogel-based culture systems exhibit isotropy and lack the anisotropic properties of the tissue microenvironment. Although the integration of hydrogels in microfluidic systems enabled the dynamic co-existence of two distinct cell populations, the gap between these and the natural niche remains wide. BM on-a-chip technology is a promising and powerful tool for *ex-vivo* HSC culture and the monitoring and scientific exploration of the hematopoietic process. However, in their current iteration, they can only accommodate no more than two distinct cell populations. In addition, their complex manufacturing and high costs currently limit their large-scale production for clinical applications.

In general, hydrogel have uniform internal structures, which differs significantly from the architecture of a natural niche (Zimmermann et al., 2019). 3D printing of biomaterials is powerful emerging tool for the fabrication of sophisticated and highly organized 3D hydrogel structures (Ong et al., 2018; Olate-Moya et al., 2020; Moore et al., 2021). Composite hydrogels with enhanced shape fidelity can facilitate the printing of scaffolds with mechanical and architectural details closely resembling the features of the *in vivo* niche (Zhou et al., 2020). A composite hydrogel composed of 4% methylcellulose and 2% alginate that also contained encapsulated BM niche cells was used to bioprint a scaffold to mimic the perivascular area of the BM (Moore et al., 2021). However, 3D printing for artificial niche mimicking is a new technology that requires further exploration.

The natural hematopoietic niche contains a viscoelastic matrix, while most hydrogels are primarily elastic materials. These artificial matrices cannot relax under strain forces. In contrast, the natural viscoelastic matrix is mechanically yielding, and the matrix can be dynamically remodeled. The development of better viscoelastic hydrogels, replicating the conditions for cell–ECM interactions *in vivo*, could significantly improve the outcomes of culturing HSCs *in vitro*.

7 Conclusion

HSCs from CB play an important role in clinical transplantation. CB provides an alternative source for allogeneic HSCT patients lacking HLA-matched donors (Rocha, 2016). Compared with BM and mobilized peripheral blood stem cells, CB has lower requirements on HLA matching, increased donor availability, and low rates of chronic GVHD. However, due to the limited number of HSCs and HSPCs within a single umbilical CB unit, the implantation of neutrophils is delayed, which increases the risk of early infection and transplant-related mortality. Therefore, increasing research has been devoted to the exploration of new techniques for functional HSC expansion *in vitro*. However, there are very limited to normal HSCs that undergo asymmetric mitosis. HSCs are very sensitive to the environment, which means after leaving the niche, stimulation from the external environment, such as mechanical force or redox reaction, can easily cause their differentiation and loss of the expression of original phenotype markers.

In the previous, Section 2, we discussed the complexity of the BM niche and the correlation of several elements of this niche in HSC physiology. Recent HSC culture methods such as adding cytokines, small molecule compounds and perfusion reactor in the laboratory, have been introduced. In addition, building a 3D culture environment that is closer to the HSC niche in terms of space and biological interaction has gradually become a new trend in the study of HSC expansion *in vitro*. The chemical and engineering strategies and techniques for improving the niche of biomimetic hematopoiesis were summarized. The potential of stimulus-responsive hydrogels in the establishment of an intelligent microenvironment was also described. Finally, the

remaining challenges in the use of the hydrogel culture platform and the broad prospects for development were reviewed. The improved artificial microenvironment for HSC amplification *in vitro* and the bionic BM for testing the safety and effectiveness of HSC treatment are exciting developments, providing new solutions for the increasing use of hydrogel-based HSC culture platforms in clinical applications and scientific research. However, due to the complexity of the niche, in the current technology, it remains difficult to artificially reconstruct all these elements into functional BM. The development of an effective bioengineering strategy requires further research on the molecular mechanism of HSC behavior in the niche and the progression of biomaterial technology.

Author contributions

XH: conceptualization, methodology, writing-original draft, data curation, and writing-review; YW: writing-original draft and writing-review; FW: supervision and funding acquisition; TW: writing-review; SL: investigation, supervision, and funding acquisition; GO: conceptualization, supervision, writing-reviewing and editing.

Funding

This work was supported by Shenzhen Fund for Guangdong Provincial High-Level Clinical Key Specialties (No. SZGSP012) Shenzhen Key Medical Discipline Construction Fund (No. SZXK034) and Guangdong High-level Hospital Construction Fund.

Conflict of interest

The authors declare that the research was conducted in the absence of any commercial or financial relationships that could be construed as a potential conflict of interest.

Publisher's note

All claims expressed in this article are solely those of the authors and do not necessarily represent those of their affiliated organizations, or those of the publisher, the editors and the reviewers. Any product that may be evaluated in this article, or claim that may be made by its manufacturer, is not guaranteed or endorsed by the publisher.

References

Acar, M., Kocherlakota, K. S., Murphy, M. M., Peyer, J. G., Oguro, H., Inra, C. N., et al. (2015). Deep imaging of bone marrow shows non-dividing stem cells are mainly perisinusoidal. *Nature* 526 (7571), 126–130. doi:10.1038/nature15250

Afewerki, S., Sheikhi, A., Kannan, S., Ahadian, S., and Khademhosseini, A. (2019). Gelatin-polysaccharide composite scaffolds for 3D cell culture and tissue engineering: Towards natural therapeutics. *Bioeng. Transl. Med.* 4 (1), 96–115. doi:10.1002/btm2.10124

Ahmed, E. M. (2015). Hydrogel: Preparation, characterization, and applications: A review. *J. Adv. Res.* 6 (2), 105–121. doi:10.1016/j.jare.2013.07.006

Aleman, J., George, S. K., Herberg, S., Devarasetty, M., Porada, C. D., Skardal, A., et al. (2019). Deconstructed microfluidic bone marrow on-a-Chip to study normal and malignant hemopoietic cell-niche interactions. *Small* 15 (43), 1902971. doi:10.1002/smll.201902971

Allenby, M. C., and Woodruff, M. A. (2022). Image analyses for engineering advanced tissue biomanufacturing processes. *Biomaterials* 284, 121514. doi:10.1016/j.biomaterials.2022.121514

An, S., Han, S. Y., and Cho, S. W. (2019). Hydrogel-integrated microfluidic systems for advanced stem cell engineering. *BioChip J.* 13 (4), 306–322. doi:10.1007/s13206-019-3402-5

Arai, F., Hirao, A., Ohmura, M., Sato, H., Matsuoka, S., Takubo, K., et al. (2004). Tie2/Angiopoietin-1 signaling regulates hematopoietic stem cell quiescence in the bone marrow niche. *Cell* 118 (2), 149–161. doi:10.1016/j.cell.2004.07.004

Asada, N., Katayama, Y., Sato, M., Minagawa, K., Wakahashi, K., Kawano, H., et al. (2013). Matrix-embedded osteocytes regulate mobilization of hematopoietic stem/progenitor cells. *Cell Stem Cell* 12 (6), 737–747. doi:10.1016/j.stem.2013.05.001

Asada, N., Kunisaki, Y., Pierce, H., Wang, Z., Fernandez, N. F., Birbrair, A., et al. (2017). Differential cytokine contributions of perivascular haematopoietic stem cell niches. *Nat. Cell Biol.* 19 (3), 214–223. doi:10.1038/ncb3475

Baena, A. R. Y., Manso, B. A., and Forsberg, E. C. (2021). Cfu-S assay: A historical single-cell assay that offers modern insight into clonal hematopoiesis. *Exp. Hematol.* 104, 1–8. doi:10.1016/j.exphem.2021.10.003

Bai, T., Li, J., Sinclair, A., Imren, S., Merriam, F., Sun, F., et al. (2019). Expansion of primitive human hematopoietic stem cells by culture in a zwitterionic hydrogel. *Nat. Med.* 25 (10), 1566–1575. doi:10.1038/s41591-019-0601-5

Ballen, K. K., Gluckman, E., and Broxmeyer, H. E. (2013). Umbilical cord blood transplantation: The first 25 Years and beyond. *Blood* 122 (4), 491–498. doi:10.1182/blood-2013-02-453175

Bao, Z., Xian, C., Yuan, Q., Liu, G., and Wu, J. (2019). Natural polymer-based hydrogels with enhanced mechanical performances: Preparation, structure, and property. *Adv. Healthc. Mat.* 8 (17), 1900670. doi:10.1002/adhm.201900670

Barnhouse, V., Petrikas, N., Crosby, C., Zoldan, J., and Harley, B. (2021). Perivascular secretome influences hematopoietic stem cell maintenance in a gelatin hydrogel. *Ann. Biomed. Eng.* 49 (2), 780–792. doi:10.1007/s10439-020-02602-0

Bello, A. B., Park, H., and Lee, S. H. (2018). Current approaches in biomaterial-based hematopoietic stem cell niches. *Acta Biomater.* 72, 1–15. doi:10.1016/j.actbio.2018.03.028

Bhaskar, B., Owen, R., Bahmaee, H., Rao, P. S., and Reilly, G. C. (2018). Design and assessment of a dynamic perfusion bioreactor for large bone tissue engineering scaffolds. *Appl. Biochem. Biotechnol.* 185 (2), 555–563. doi:10.1007/s12010-017-2671-5

Billiet, T., Vandenhaute, M., Schelfhout, J., Van Vlierberghe, S., and Dubruel, P. (2012). A review of trends and limitations in hydrogel-rapid prototyping for tissue engineering. *Biomaterials* 33 (26), 6020–6041. doi:10.1016/j.biomaterials.2012.04.050

Bodenberger, N., Kubiczek, D., Trösch, L., Gawanbacht, A., Wilhelm, S., Tielker, D., et al. (2017). Lectin-mediated reversible immobilization of human cells into a glycosylated macroporous protein hydrogel as a cell culture matrix. *Sci. Rep.* 7, 6151. doi:10.1038/s41598-017-06240-w

Bourgine, P. E., Klein, T., Paczulla, A. M., Shimizu, T., Kunz, L., Kokkaliaris, K. D., et al. (2018). *In vitro* biomimetic engineering of a human hematopoietic niche with functional properties. *Proc. Natl. Acad. Sci. U. S. A.* 115 (25), E5688–e5695. doi:10.1073/pnas.1805440115

Bovone, G., Dudaryeva, O. Y., Marco-Dufort, B., and Tibbitt, M. W. (2021). Engineering hydrogel adhesion for biomedical applications via chemical design of the junction. *ACS Biomater. Sci. Eng.* 7 (9), 4048–4076. doi:10.1021/acsbiomaterials.0c01677

Bowers, E., Slaughter, A., Frenette, P. S., Kuick, R., Pello, O. M., and Lucas, D. (2018). Granulocyte-derived TNFα promotes vascular and hematopoietic regeneration in the bone marrow. *Nat. Med.* 24 (1), 95–102. doi:10.1038/nm.4448

Brandle, K., Bergmann, T. C., Raic, A., Li, Y., Million, N., Rehbock, C., et al. (2020). Iron nanoparticle composite hydrogels for studying effects of iron ion release on red blood cell *in vitro* production. *ACS Appl. Bio Mat.* 3 (8), 4766–4778. doi:10.1021/acsabm.0c00297

Bruns, I., Lucas, D., Pinho, S., Ahmed, J., Lambert, M. P., Kunisaki, Y., et al. (2014). Megakaryocytes regulate hematopoietic stem cell quiescence through CXCL4 secretion. *Nat. Med.* 20 (11), 1315–1320. doi:10.1038/nm.3707

Caldwell, A. S., Aguado, B. A., and Anseth, K. S. (2020). Designing microgels for cell culture and controlled assembly of tissue microenvironments. *Adv. Funct. Mat.* 30 (37), 1907670. doi:10.1002/adfm.201907670

Caliari, S. R., and Burdick, J. A. (2016). A practical guide to hydrogels for cell culture. *Nat. Methods* 13 (5), 405–414. doi:10.1038/nmeth.3839

Calvi, L. M., Adams, G. B., Weibrecht, K. W., Weber, J. M., Olson, D. P., Knight, M. C., et al. (2003). Osteoblastic cells regulate the haematopoietic stem cell niche. *Nature* 425 (6960), 841–846. doi:10.1038/nature02040

Cao, H., Cao, B., Heazlewood, C. K., Domingues, M., Sun, X., Debele, E., et al. (2019). Osteopontin is an important regulative component of the fetal bone marrow hematopoietic stem cell niche. *Cells* 8 (9), 985. doi:10.3390/cells8090985

Carreras, P., Chaves, R. C., Gallardo, M., Ortiz, A., Lopez, J. M., and Sia, S. K. (2018). Microengineering double layer hydrogel structures towards the recapitulation of the hematopoietic stem cell niche. *Sci. Bull. (Beijing).* 63 (20), 1319–1323. doi:10.1016/j.scib.2018.09.003

Carreras, P., González, I., Gallardo, M., Ortiz-Ruiz, A., Morales, M. L., Encinas, J., et al. (2021). Long-term human hematopoietic stem cell culture in microdroplets. *Micromachines* 12 (1), 90. doi:10.3390/mi12010090

Casanova-Acebes, M., Pitaval, C., Weiss, L. A., Nombela-Arrieta, C., Chèvre, R., N, A. G., et al. (2013). Rhythmic modulation of the hematopoietic niche through neutrophil clearance. *Cell* 153 (5), 1025–1035. doi:10.1016/j.cell.2013.04.040

Chatterjee, C., Schertl, P., Frommer, M., Ludwig-Husemann, A., Mohra, A., Dilger, N., et al. (2021). Rebuilding the hematopoietic stem cell niche: Recent developments and future prospects. *Acta Biomater.* 132, 129–148. doi:10.1016/j.actbio.2021.03.061

Chaudhuri, O., Gu, L., Klumpers, D., Darnell, M., Bencherif, S. A., Weaver, J. C., et al. (2016). Hydrogels with tunable stress relaxation regulate stem cell fate and activity. *Nat. Mat.* 15 (3), 326–334. doi:10.1038/nmat4489

Chaudhuri, O. (2017). Viscoelastic hydrogels for 3D cell culture. *Biomater. Sci.* 5 (8), 1480–1490. doi:10.1039/c7bm00261k

Chimene, D., Kaunas, R., and Gaharwar, A. K. (2020). Hydrogel bioink reinforcement for additive manufacturing: A focused review of emerging strategies. *Adv. Mat.* 32 (1), 1902026. doi:10.1002/adma.201902026

Choi, J. S., and Harley, B. A. (2012). The combined influence of substrate elasticity and ligand density on the viability and biophysical properties of hematopoietic stem and progenitor cells. *Biomaterials* 33 (18), 4460–4468. doi:10.1016/j.biomaterials.2012.03.010

Choi, J. S., Mahadik, B. P., and Harley, B. A. (2015). Engineering the hematopoietic stem cell niche: Frontiers in biomaterial science. *Biotechnol. J.* 10 (10), 1529–1545. doi:10.1002/biot.201400758

Chou, D. B., Frismantas, V., Milton, Y., David, R., Pop-Damkov, P., Ferguson, D., et al. (2020). On-chip recapitulation of clinical bone marrow toxicities and patient-specific pathophysiology. *Nat. Biomed. Eng.* 4 (4), 394–406. doi:10.1038/s41551-019-0495-z

Chow, A., Lucas, D., Hidalgo, A., Méndez-Ferrer, S., Hashimoto, D., Scheiermann, C., et al. (2011). Bone marrow $CD169^{+}$ macrophages promote the retention of hematopoietic stem and progenitor cells in the mesenchymal stem cell niche. *J. Exp. Med.* 208 (2), 261–271. doi:10.1084/jem.20101688

Chowdhury, F., Na, S., Li, D., Poh, Y. C., Tanaka, T. S., Wang, F., et al. (2010). Material properties of the cell dictate stress-induced spreading and differentiation in embryonic stem cells. *Nat. Mat.* 9 (1), 82–88. doi:10.1038/nmat2563

Christodoulou, C., Spencer, J. A., Yeh, S. A., Turcotte, R., Kokkaliaris, K. D., Panero, R., et al. (2020). Live-animal imaging of native haematopoietic stem and progenitor cells. *Nature* 578 (7794), 278–283. doi:10.1038/s41586-020-1971-z

Cohen, S., Roy, J., Lachance, S., Delisle, J. S., Marinier, A., Busque, L., et al. (2020). Hematopoietic stem cell transplantation using single um171-expanded cord blood: A single-arm, phase 1-2 safety and feasibility study. *Lancet Haematol.* 7 (2), e134–e145. doi:10.1016/s2352-3026(19)30202-9

Conneally, E., Cashman, J., Petzer, A., and Eaves, C. (1997). Expansion *in vitro* of transplantable human cord blood stem cells demonstrated using a quantitative assay of their lympho-myeloid repopulating activity in nonobese diabetic-scid/scid mice. *Proc. Natl. Acad. Sci. U. S. A.* 94 (18), 9836–9841. doi:10.1073/pnas.94.18.9836

Costa, B. N. L., Adão, R. M. R., Maibohm, C., Accardo, A., Cardoso, V. F., and Nieder, J. B. (2022). Cellular interaction of bone marrow mesenchymal stem cells with polymer and hydrogel 3D microscaffold templates. *ACS Appl. Mat. Interfaces* 14 (11), 13013–13024. doi:10.1021/acsami.1c23442

Crane, G. M., Jeffery, E., and Morrison, S. J. (2017). Adult haematopoietic stem cell niches. *Nat. Rev. Immunol.* 17 (9), 573–590. doi:10.1038/nri.2017.53

Cuchiara, M. L., Coskun, S., Banda, O. A., Horter, K. L., Hirschi, K. K., and West, J. L. (2016). Bioactive poly (ethylene glycol) hydrogels to recapitulate the HSC niche and facilitate HSC expansion in culture. *Biotechnol. Bioeng.* 113 (4), 870–881. doi:10.1002/bit.25848

Cuchiara, M. L., Horter, K. L., Banda, O. A., and West, J. L. (2013). Covalent immobilization of stem cell factor and stromal derived factor 1α for *in vitro* culture of hematopoietic progenitor cells. *Acta Biomater.* 9 (12), 9258–9269. doi:10.1016/j.actbio.2013.08.012

De Leon, S. E., Pupovac, A., and McArthur, S. L. (2020). Three-dimensional (3D) cell culture monitoring: Opportunities and challenges for impedance spectroscopy. *Biotechnol. Bioeng.* 117 (4), 1230–1240. doi:10.1002/bit.27270

Delaney, C., Heimfeld, S., Brashem-Stein, C., Voorhies, H., Manger, R. L., and Bernstein, I. D. (2010). Notch-mediated expansion of human cord blood progenitor cells capable of rapid myeloid reconstitution. *Nat. Med.* 16 (2), 232–236. doi:10.1038/nm.2080

Delaney, C., Varnum-Finney, B., Aoyama, K., Brashem-Stein, C., and Bernstein, I. D. (2005). Dose-dependent effects of the Notch ligand Delta1 on ex vivo differentiation and in vivo marrow repopulating ability of cord blood cells. *Blood.* 106 (8), 2693–2699. doi:10.1182/blood-2005-03-1131

Deng, Z., Yu, R., and Guo, B. (2021). Stimuli-responsive conductive hydrogels: Design, properties, and applications. *Mat. Chem. Front.* 5 (5), 2092–2123. doi:10.1039/d0qm00868k

Ding, Y., Gao, S., Shen, J., Bai, T., Yang, M., Xu, S., et al. (2020). TNFSF15 facilitates human umbilical cord blood haematopoietic stem cell expansion by activating Notch signal pathway. *J. Cell. Mol. Med.* 24 (19), 11146–11157. doi:10.1111/jcmm.15626

Discher, D. E., Mooney, D. J., and Zandstra, P. W. (2009). Growth factors, matrices, and forces combine and control stem cells. *Science* 324 (5935), 1673–1677. doi:10.1126/science.1171643

Domingues, M. J., Cao, H., Heazlewood, S. Y., Cao, B., and Nilsson, S. K. (2017). Niche extracellular matrix components and their influence on HSC. *J. Cell. Biochem.* 118 (8), 1984–1993. doi:10.1002/jcb.25905

Echalier, C., Jebors, S., Laconde, G., Brunel, L., Verdie, P., Causse, L., et al. (2017). Sol-gel synthesis of collagen-inspired peptide hydrogel. *Mat. TodayKidlingt.* 20 (2), 59–66. doi:10.1016/j.mattod.2017.02.001

Erathodiyil, N., Chan, H. M., Wu, H., and Ying, J. Y. (2020). Zwitterionic polymers and hydrogels for antibiofouling applications in implantable devices. *Mat. TodayKidlingt.* 38, 84–98. doi:10.1016/j.mattod.2020.03.024

Fares, I., Chagraoui, J., Gareau, Y., Gingras, S., Ruel, R., Mayotte, N., et al. (2014). Pyrimidoindole derivatives are agonists of human hematopoietic stem cell self-renewal. *Science* 345 (6203), 1509–1512. doi:10.1126/science.1256337

Fedi, A., Vitale, C., Giannoni, P., Caluori, G., and Marrella, A. (2022). Biosensors to monitor cell activity in 3D hydrogel-based tissue models. *Sensors* 22 (4), 1517. doi:10.3390/s22041517

Fujisaki, J., Wu, J., Carlson, A. L., Silberstein, L., Putheti, P., Larocca, R., et al. (2011). *In vivo* imaging of Treg cells providing immune privilege to the haematopoietic stem-cell niche. *Nature* 474 (7350), 216–219. doi:10.1038/nature10160

Gaharwar, A. K., Peppas, N. A., and Khademhosseini, A. (2014). Nanocomposite hydrogels for biomedical applications. *Biotechnol. Bioeng.* 111 (3), 441–453. doi:10.1002/bit.25160

Gao, X., Zhang, D., Xu, C., Li, H., Caron, K. M., and Frenette, P. S. (2021). Nociceptive nerves regulate haematopoietic stem cell mobilization. *Nature* 589 (7843), 591–596. doi:10.1038/s41586-020-03057-y

García-García, A., Korn, C., García-Fernández, M., Domingues, O., Villadiego, J., Martín-Pérez, D., et al. (2019). Dual cholinergic signals regulate daily migration of hematopoietic stem cells and leukocytes. *Blood* 133 (3), 224–236. doi:10.1182/blood-2018-08-867648

Gilchrist, A. E., Lee, S., Hu, Y., and Harley, B. A. (2019). Soluble signals and remodeling in a synthetic gelatin-based hematopoietic stem cell niche. *Adv. Healthc. Mat.* 289553, e1900751. doi:10.1002/adhm.201900751

Gilchrist, A. E., Serrano, J. F., Ngo, M. T., Hrnjak, Z., Kim, S., and Harley, B. A. C. (2021). Encapsulation of murine hematopoietic stem and progenitor cells in a thiol-crosslinked maleimide-functionalized gelatin hydrogel. *Acta Biomater.* 131, 138–148. doi:10.1016/j.actbio.2021.06.028

Gjorevski, N., Sachs, N., Manfrin, A., Giger, S., Bragina, M. E., Ordóñez-Morán, P., et al. (2016). Designer matrices for intestinal stem cell and organoid culture. *Nature* 539 (7630), 560–564. doi:10.1038/nature20168

Greenbaum, A., Hsu, Y.-M. S., Day, R. B., Schuettpelz, L. G., Christopher, M. J., Borgerding, J. N., et al. (2013). CXCL12 in early mesenchymal progenitors is required for haematopoietic stem-cell maintenance. *Nature* 495 (7440), 227–230. doi:10.1038/nature11926

Guillet, J. F., Valdez-Nava, Z., Golzio, M., and Flahaut, E. (2019). Electrical properties of double-wall carbon nanotubes nanocomposite hydrogels. *Carbon* 146, 542–548. doi:10.1016/j.carbon.2019.01.090

Guo, W., Pan, X., Zhang, Y., Cai, H., and Zhang, W. (2017). A hyaluronic acid/graphene oxide hydrogel for enhanced *ex vivo* expansion of cord blood-derived $CD34^+$ cells. *Mat. Lett.* 205, 253–256. doi:10.1016/j.matlet.2017.06.023

Gurkan, U. A., El Assal, R., Yildiz, S. E., Sung, Y., Trachtenberg, A. J., Kuo, W. P., et al. (2014). Engineering anisotropic biomimetic fibrocartilage microenvironment by bioprinting mesenchymal stem cells in nanoliter gel droplets. *Mol. Pharm.* 11 (7), 2151–2159. doi:10.1021/mp400573g

Guvendiren, M., and Burdick, J. A. (2013). Engineering synthetic hydrogel microenvironments to instruct stem cells. *Curr. Opin. Biotechnol.* 24 (5), 841–846. doi:10.1016/j.copbio.2013.03.009

Gu, Y. C., Kortesmaa, J., Tryggvason, K., Persson, J., Ekblom, P., Jacobsen, S. E., et al. (2003). Laminin Isoform-Specific Promotion of Adhesion and Migration of Human Bone Marrow Progenitor Cells. *Blood.* 101 (3), 877–885. doi:10.1182/blood-2002-03-0796

Gvaramia, D., Muller, E., Muller, K., Atallah, P., Tsurkan, M., Freudenberg, U., et al. (2017). Combined influence of biophysical and biochemical cues on maintenance and proliferation of hematopoietic stem cells. *Biomaterials* 138, 108–117. doi:10.1016/j.biomaterials.2017.05.023

Hardouin, P., Pansini, V., and Cortet, B. (2014). Bone marrow fat. *Jt. Bone Spine* 81 (4), 313–319. doi:10.1016/j.jbspin.2014.02.013

Hastings, J. F., Skhinas, J. N., Fey, D., Croucher, D. R., and Cox, T. R. (2019). The extracellular matrix as a key regulator of intracellular signalling networks. *Br. J. Pharmacol.* 176 (1), 82–92. doi:10.1111/bph.14195

Hirata, Y., Furuhashi, K., Ishii, H., Li, H. W., Pinho, S., Ding, L., et al. (2018). CD150(high) bone marrow Tregs maintain hematopoietic stem cell quiescence and immune privilege via adenosine. *Cell Stem Cell* 22 (3), 445–453. doi:10.1016/j.stem.2018.01.017

Hosseinizand, H., Ebrahimi, M., and Abdekhodaie, M. J. (2016). Agitation Increases Expansion of Cord Blood Hematopoietic Cells and Promotes Their Differentiation into Myeloid Lineage. *Cytotechnology.* 68 (4), 969–978. doi:10.1007/s10616-015-9851-3

Hsu, R. S., Chen, P. Y., Fang, J. H., Chen, Y. Y., Chang, C. W., Lu, Y. J., et al. (2019). Adaptable microporous hydrogels of propagating NGF-gradient by injectable building blocks for accelerated axonal outgrowth. *Adv. Sci.* 6 (16), 1900520. doi:10.1002/advs.201900520

Huang, G., Li, F., Zhao, X., Ma, Y., Li, Y., Lin, M., et al. (2017). Functional and biomimetic materials for engineering of the three-dimensional cell microenvironment. *Chem. Rev.* 117 (20), 12764–12850. doi:10.1021/acs.chemrev.7b00094

Ingavle, G., Vaidya, A., and Kale, V. (2019). Constructing three-dimensional microenvironments using engineered biomaterials for hematopoietic stem cell expansion. *Tissue Eng. Part B Rev.* 25 (4), 312–329. doi:10.1089/ten.TEB.2018.0286

Itkin, T., Gur-Cohen, S., Spencer, J. A., Schajnovitz, A., Ramasamy, S. K., Kusumbe, A. P., et al. (2016). Distinct bone marrow blood vessels differentially regulate haematopoiesis. *Nature* 532 (7599), 323–328. doi:10.1038/nature17624

Jensen, C., and Teng, Y. (2020). Is it time to start transitioning from 2D to 3D cell culture? *Front. Mol. Biosci.* 7, 33. doi:10.3389/fmolb.2020.00033

Jiang, Y., Wang, Y., Li, Q., Yu, C., and Chu, W. (2020). Natural polymer-based stimuli-responsive hydrogels. *Curr. Med. Chem.* 27 (16), 2631–2657. doi:10.2174/0929867326666191122144916

Jing, D., Fonseca, A. V., Alakel, N., Fierro, F. A., Muller, K., Bornhauser, M., et al. (2010). Hematopoietic stem cells in Co-culture with mesenchymal stromal cells-modeling the niche compartments *in vitro*. *Haematologica* 95 (4), 542–550. doi:10.3324/haematol.2009.010736

Kehr, N. S., Atay, S., and Ergün, B. (2015). Self-assembled monolayers and nanocomposite hydrogels of functional nanomaterials for tissue engineering applications. *Macromol. Biosci.* 15 (4), 445–463. doi:10.1002/mabi.201400363

Kim, H., Bae, C., Kook, Y. M., Koh, W. G., Lee, K., and Park, M. H. (2019). Mesenchymal stem cell 3D encapsulation technologies for biomimetic microenvironment in tissue regeneration. *Stem Cell Res. Ther.* 10 (1), 51. doi:10.1186/s13287-018-1130-8

Kim, S., Kim, H. J., and Jeon, N. L. (2010). Biological applications of microfluidic gradient devices. *Integr. Biol.* 2 (11-12), 584–603. doi:10.1039/c0ib00055h

Kohli, L., and Passegue, E. (2014). Surviving change: The metabolic journey of hematopoietic stem cells. *Trends Cell Biol.* 24 (8), 479–487. doi:10.1016/j.tcb.2014.04.001

Kosan, C., and Godmann, M. (2016). Genetic and epigenetic mechanisms that maintain hematopoietic stem cell function. *Stem Cells Int.* 2016, 1–14. doi:10.1155/2016/5178965

Kuan, I. I., Liang, K. H., Wang, Y. P., Kuo, T. W., Meir, Y. J. J., Wu, S. C. Y., et al. (2017). EpEX/EpCAM and Oct4 or Klf4 alone are sufficient to generate induced pluripotent stem cells through STAT3 and HIF2α. *Sci. Rep.* 7 (1), 41852–41914. doi:10.1038/srep41852

Kunisaki, Y., Bruns, I., Scheiermann, C., Ahmed, J., Pinho, S., Zhang, D., et al. (2013). Arteriolar niches maintain haematopoietic stem cell quiescence. *Nature* 502 (7473), 637–643. doi:10.1038/nature12612

Kwak, J. G., and Lee, J. (2020). Thermoresponsive inverted colloidal crystal hydrogel scaffolds for lymphoid tissue engineering. *Adv. Healthc. Mat.* 9 (6), 1901556. doi:10.1002/adhm.201901556

Langen, U. H., Pitulescu, M. E., Kim, J. M., Enriquez-Gasca, R., Sivaraj, K. K., Kusumbe, A. P., et al. (2017). Cell-matrix signals specify bone endothelial cells during developmental osteogenesis. *Nat. Cell Biol.* 19 (3), 189–201. doi:10.1038/ncb3476

Langhans, S. A. (2018). Three-dimensional *in vitro* cell culture models in drug discovery and drug repositioning. *Front. Pharmacol.* 9, 6. doi:10.3389/fphar.2018.00006

Lau, S. X., Leong, Y. Y., Ng, W. H., Ng, A. W. P., Ismail, I. S., Yusoff, N. M., et al. (2017). Human mesenchymal stem cells promote CD34(+) hematopoietic stem cell proliferation with preserved red blood cell differentiation capacity. *Cell Biol. Int.* 41 (6), 697–704. doi:10.1002/cbin.10774

Lee, S. M., Han, N., Lee, R., Choi, I. H., Park, Y. B., Shin, J. S., et al. (2016). Real-time monitoring of 3D cell culture using a 3D capacitance biosensor. *Biosensors and Bioelectronics.* 77, 56–61. doi:10.1016/j.bios.2015.09.005

Leisten, I., Kramann, R., Ferreira, M. S. V., Bovi, M., Neuss, S., Ziegler, P., et al. (2012). 3D Co-culture of hematopoietic stem and progenitor cells and mesenchymal stem cells in collagen scaffolds as a model of the hematopoietic niche. *Biomaterials* 33 (6), 1736–1747. doi:10.1016/j.biomaterials.2011.11.034

Levesque, J. P., Helwani, F. M., and Winkler, I. G. (2010). The endosteal 'osteoblastic' niche and its role in hematopoietic stem cell homing and mobilization. *Leukemia* 24 (12), 1979–1992. doi:10.1038/leu.2010.214

Liang, Y., Li, M., Yang, Y., Qiao, L., Xu, H., Guo, B., et al. (2022). pH/Glucose dual responsive metformin release hydrogel dressings with adhesion and self-healing via dual-dynamic bonding for athletic diabetic foot wound healing. *ACS Nano.* 16 (2), 3194–3207. doi:10.1021/acsnano.1c11040

Li, J. H., Wu, C. T., Chu, P. K., and Gelinsky, M. (2020). 3D printing of hydrogels: Rational design strategies and emerging biomedical applications. *Mater. Sci. Eng. R Rep.* 140, 100543. doi:10.1016/j.mser.2020.100543

Li, Q., Zhao, D., Chen, Q., Luo, M., Huang, J., Yang, C., et al. (2019). Wharton's jelly mesenchymal stem cell-based or umbilical vein endothelial cell-based serum-free coculture with cytokines supports the *ex vivo* expansion/maintenance of cord blood hematopoietic stem/progenitor cells. *Stem Cell Res. Ther.* 10 (1), 376–379. doi:10.1186/s13287-019-1502-8

Lim, M., Ye, H., Panoskaltsis, N., Drakakis, E. M., Yue, X., Cass, A. E., et al. (2007). Intelligent bioprocessing for haemotopoietic cell cultures using monitoring and design of experiments. *Biotechnol. Adv.* 25 (4), 353–368. doi:10.1016/j.biotechadv.2007.02.002

Liu, B., Tao, C., Wu, Z., Yao, H., and Wang, D. A. (2022). Engineering strategies to achieve efficient *in vitro* expansion of haematopoietic stem cells: Development and improvement. *J. Mat. Chem. B* 10 (11), 1734–1753. doi:10.1039/d1tb02706a

Liu, H., Wang, Y., Cui, K., Guo, Y., Zhang, X., and Qin, J. (2019). Advances in hydrogels in organoids and organs-on-a-chip. *Adv. Mat.* 31 (50), 1902042. doi:10.1002/adma.201902042

Liu, J. J., Qu, S. X., Suo, Z. G., and Yang, W. (2021). Functional hydrogel coatings. *Natl. Sci. Rev.* 8 (2), nwaa254. doi:10.1093/nsr/nwaa254

Lo Celso, C., Fleming, H. E., Wu, J. W., Zhao, C. X., Miake-Lye, S., Fujisaki, J., et al. (2009). Live-animal tracking of individual haematopoietic stem/progenitor cells in their niche. *Nature* 457 (7225), 92–96. doi:10.1038/nature07434

Lo Iacono, M., Anzalone, R., La Rocca, G., Baiamonte, E., Maggio, A., and Acuto, S. (2017). Wharton's jelly mesenchymal stromal cells as a feeder layer for the *ex vivo* expansion of hematopoietic stem and progenitor cells: A review. *Stem Cell Rev. Rep.* 13 (1), 35–49. doi:10.1007/s12015-016-9702-4

Lu, D., Luo, C., Zhang, C., Li, Z., and Long, M. (2014). Differential regulation of morphology and stemness of mouse embryonic stem cells by substrate stiffness and topography. *Biomaterials* 35 (13), 3945–3955. doi:10.1016/j.biomaterials.2014.01.066

Mahadik, B. P., Bharadwaj, N. A., Ewoldt, R. H., and Harley, B. A. (2017). Regulating dynamic signaling between hematopoietic stem cells and niche cells via a hydrogel matrix. *Biomaterials* 125, 54–64. doi:10.1016/j.biomaterials.2017.02.013

Mahadik, B. P., Haba, S. P., Skertich, L. J., and Harley, B. A. C. (2015). The use of covalently immobilized stem cell factor to selectively affect hematopoietic stem cell activity within a gelatin hydrogel. *Biomaterials* 67, 297–307. doi:10.1016/j.biomaterials.2015.07.042

Mahadik, B. P., Wheeler, T. D., Skertich, L. J., Kenis, P. J., and Harley, B. A. (2014). Microfluidic generation of gradient hydrogels to modulate hematopoietic stem cell culture environment. *Adv. Healthc. Mat.* 3 (3), 449–458. doi:10.1002/adhm.201300263

Maji, S., and Lee, H. (2022). Engineering hydrogels for the development of three-dimensional *in vitro* models. *Int. J. Mol. Sci.* 23 (5), 2662. doi:10.3390/ijms23052662

Mannino, G., Russo, C., Maugeri, G., Musumeci, G., Vicario, N., Tibullo, D., et al. (2022). Adult stem cell niches for tissue homeostasis. *J. Cell. Physiol.* 237 (1), 239–257. doi:10.1002/jcp.30562

Maryanovich, M., Takeishi, S., and Frenette, P. S. (2018). Neural regulation of bone and bone marrow. *Cold Spring Harb. Perspect. Med.* 8 (9), a031344. doi:10.1101/cshperspect.a031344

Matteini, F., Mulaw, M. A., and Florian, M. C. (2021). Aging of the hematopoietic stem cell niche: New tools to answer an old question. *Front. Immunol.* 12, 738204. doi:10.3389/fimmu.2021.738204

Mendelson, A., and Frenette, P. S. (2014). Hematopoietic stem cell niche maintenance during homeostasis and regeneration. *Nat. Med.* 20 (8), 833–846. doi:10.1038/nm.3647

Méndez-Ferrer, S., Michurina, T. V., Ferraro, F., Mazloom, A. R., Macarthur, B. D., Lira, S. A., et al. (2010). Mesenchymal and haematopoietic stem cells form a unique bone marrow niche. *Nature* 466 (7308), 829–834. doi:10.1038/nature09262

Moore, C. A., Siddiqui, Z., Carney, G. J., Naaldijk, Y., Guiro, K., Ferrer, A. I., et al. (2021). A 3D bioprinted material that recapitulates the perivascular bone marrow structure for sustained hematopoietic and cancer models. *Polymers* 13 (4), 480. doi:10.3390/polym13040480

Morrison, S. J., and Scadden, D. T. (2014). The bone marrow niche for haematopoietic stem cells. *Nature* 505 (7483), 327–334. doi:10.1038/nature12984

Motealleh, A., and Kehr, N. S. (2017). Nanocomposite hydrogels and their applications in tissue engineering. *Adv. Healthc. Mat.* 6 (1), 1600938. doi:10.1002/adhm.201600938

Nakamura-Ishizu, A., Takubo, K., Fujioka, M., and Suda, T. (2014). Megakaryocytes are essential for HSC quiescence through the production of thrombopoietin. *Biochem. Biophys. Res. Commun.* 454 (2), 353–357. doi:10.1016/j.bbrc.2014.10.095

Naveiras, O., Nardi, V., Wenzel, P. L., Hauschka, P. V., Fahey, F., and Daley, G. Q. (2009). Bone-marrow adipocytes as negative regulators of the haematopoietic microenvironment. *Nature* 460 (7252), 259–263. doi:10.1038/nature08099

Nezhad-Mokhtari, P., Ghorbani, M., Roshangar, L., and Rad, J. S. (2019). Chemical gelling of hydrogels-based biological macromolecules for tissue engineering: Photo-and enzymatic-crosslinking methods. *Int J Biol Macromol.* 139, 760–772. doi:10.1016/j.ijbiomac.2019.08.047

Nilsson, S. K., Johnston, H. M., and Coverdale, J. A. (2001). Spatial localization of transplanted hemopoietic stem cells: Inferences for the localization of stem cell niches. *Blood* 97 (8), 2293–2299. doi:10.1182/blood.v97.8.2293

Olate-Moya, F., Arens, L., Wilhelm, M., Mateos-Timoneda, M. A., Engel, E., and Palza, H. (2020). Chondroinductive alginate-based hydrogels having graphene oxide for 3D printed scaffold fabrication. *ACS Appl. Mat. Interfaces* 12 (4), 4343–4357. doi:10.1021/acsami.9b22062

Ong, C. S., Yesantharao, P., Huang, C. Y., Mattson, G., Boktor, J., Fukunishi, T., et al. (2018). 3D bioprinting using stem cells. *Pediatr. Res.* 83 (1), 223–231. doi:10.1038/pr.2017.252

Owen-Woods, C., and Kusumbe, A. (2022). Fundamentals of bone vasculature: Specialization, interactions and functions. *Semin. Cell Dev. Biol.* 123, 36–47. doi:10.1016/j.semcdb.2021.06.025

Pabst, C., Krosl, J., Fares, I., Boucher, G., Ruel, R., Marinier, A., et al. (2014). Identification of small molecules that support human leukemia stem cell activity *ex vivo*. *Nat. Methods* 11 (4), 436–442. doi:10.1038/nmeth.2847

Patel, P. N., Smith, C. K., and Patrick, C. W., Jr. (2005). Rheological and recovery properties of poly(ethylene glycol) diacrylate hydrogels and human adipose tissue. *J. Biomed. Mat. Res. A* 73 (3), 313–319. doi:10.1002/jbm.a.30291

Peers, S., Montembault, A., and Ladavière, C. (2020). Chitosan hydrogels for sustained drug delivery. *J. Control. Release* 326, 150–163. doi:10.1016/j.jconrel.2020.06.012

Pievani, A., Savoldelli, R., Poelchen, J., Mattioli, E., Anselmi, G., Girardot, A., et al. (2021). Harnessing mesenchymal stromal cells for the engineering of human hematopoietic niches. *Front. Immunol.* 12, 631279. doi:10.3389/fimmu.2021.631279

Pinho, S., and Frenette, P. S. (2019). Haematopoietic stem cell activity and interactions with the niche. *Nat. Rev. Mol. Cell Biol.* 20 (5), 303–320. doi:10.1038/s41580-019-0103-9

Prince, E., and Kumacheva, E. (2019). Design and applications of man-made biomimetic fibrillar hydrogels. *Nat. Rev. Mat.* 4 (2), 99–115. doi:10.1038/s41578-018-0077-9

Raic, A., Rödling, L., Kalbacher, H., and Lee-Thedieck, C. (2014). Biomimetic macroporous PEG hydrogels as 3D scaffolds for the multiplication of human hematopoietic stem and progenitor cells. *Biomaterials* 35 (3), 929–940. doi:10.1016/j.biomaterials.2013.10.038

Ramasamy, S. K. (2017). Structure and functions of blood vessels and vascular niches in bone. *Stem Cells Int.* 2017, 1–10. doi:10.1155/2017/5046953

Rasheed, A. (2022). Niche regulation of hematopoiesis: The environment is "micro, " but the influence is large. *Arterioscler. Thromb. Vasc. Biol.* 42 (6), 691–699. doi:10.1161/atvbaha.121.316235

Ribeiro-Filho, A. C., Levy, D., Ruiz, J. L. M., Mantovani, M. D. C., and Bydlowski, S. P. (2019). Traditional and advanced cell cultures in hematopoietic stem cell studies. *Cells* 8 (12), 1628. doi:10.3390/cells8121628

Rocha, V. (2016). Umbilical cord blood cells from unrelated donor as an alternative source of hematopoietic stem cells for transplantation in children and adults. *Semin Hematol.* 53 (4), 237–245. doi:10.1053/j.seminhematol.2016.08.002

Rodell, C. B., Kaminski, A. L., and Burdick, J. A. (2013). Rational design of network properties in guest-host assembled and shear-thinning hyaluronic acid hydrogels. *Biomacromolecules* 14 (11), 4125–4134. doi:10.1021/bm401280z

Rosales, A. M., and Anseth, K. S. (2016). The design of reversible hydrogels to capture extracellular matrix dynamics. *Nat. Rev. Mat.* 1 (2), 15012–15015. doi:10.1038/natrevmats.2015.12

Sackmann, E. K., Fulton, A. L., and Beebe, D. J. (2014). The present and future role of microfluidics in biomedical research. *Nature* 507 (7491), 181–189. doi:10.1038/nature13118

Sarvar, D. P., Effatpanah, H., Akbarzadehlaleh, P., and Shamsasenjan, K. (2022). Mesenchymal stromal cell-derived extracellular vesicles: Novel approach in hematopoietic stem cell transplantation. *Stem Cell Res. Ther.* 13 (1), 202–210. doi:10.1186/s13287-022-02875-3

Schmal, O., Seifert, J., Schäffer, T. E., Walter, C. B., Aicher, W. K., and Klein, G. (2016). Hematopoietic stem and progenitor cell expansion in contact with mesenchymal stromal cells in a hanging drop model uncovers disadvantages of 3D culture. *Stem Cells Int.* 2016, 1–13. doi:10.1155/2016/4148093

Sharma, G., Thakur, B., Naushad, M., Kumar, A., Stadler, F. J., Alfadul, S. M., et al. (2018). Applications of nanocomposite hydrogels for biomedical engineering and environmental protection. *Environ. Chem. Lett.* 16 (1), 113–146. doi:10.1007/s10311-017-0671-x

Sharma, M. B., Limaye, L. S., and Kale, V. P. (2012). Mimicking the functional hematopoietic stem cell niche *in vitro*: Recapitulation of marrow physiology by hydrogel-based three-dimensional cultures of mesenchymal stromal cells. *Haematologica* 97 (5), 651–660. doi:10.3324/haematol.2011.050500

Shen, B., Tasdogan, A., Ubellacker, J. M., Zhang, J., Nosyreva, E. D., Du, L., et al. (2021). A mechanosensitive peri-arteriolar niche for osteogenesis and lymphopoiesis. *Nature* 591 (7850), 438–444. doi:10.1038/s41586-021-03298-5

Sieber, S., Wirth, L., Cavak, N., Koenigsmark, M., Marx, U., Lauster, R., et al. (2018). Bone marrow-on-a-chip: Long-term culture of human haematopoietic stem cells in a three-dimensional microfluidic environment. *J. Tissue Eng. Regen. Med.* 12 (2), 479–489. doi:10.1002/term.2507

Silberstein, L. E., and Lin, C. P. (2013). A new image of the hematopoietic stem cell vascular niche. *Cell Stem Cell* 13 (5), 514–516. doi:10.1016/j.stem.2013.10.012

Sivakumaran, D., Maitland, D., Oszustowicz, T., and Hoare, T. (2013). Tuning drug release from smart microgel-hydrogel composites via cross-linking. *J. Colloid Interface Sci.* 392, 422–430. doi:10.1016/j.jcis.2012.07.096

Spencer, J. A., Ferraro, F., Roussakis, E., Klein, A., Wu, J., Runnels, J. M., et al. (2014). Direct measurement of local oxygen concentration in the bone marrow of live animals. *Nature* 508 (7495), 269–273. doi:10.1038/nature13034

Stier, S., Ko, Y., Forkert, F., Lutz, C., Neuhaus, T., Grunewald, E., et al. (2005). Osteopontin is a hematopoietic stem cell niche component that negatively regulates stem cell pool size. *J. Exp. Med.* 201 (11), 1781–1791. doi:10.1084/jem.20041992

Suda, T., Takubo, K., and Semenza, G. L. (2011). Metabolic regulation of hematopoietic stem cells in the hypoxic niche. *Cell Stem Cell* 9 (4), 298–310. doi:10.1016/j.stem.2011.09.010

Tang, S. C., Richardson, B. M., and Anseth, K. S. (2021). Dynamic covalent hydrogels as biomaterials to mimic the viscoelasticity of soft tissues. *Prog. Mat. Sci.* 120, 100738. doi:10.1016/j.pmatsci.2020.100738

Tibbitt, M. W., and Anseth, K. S. (2009). Hydrogels as extracellular matrix mimics for 3D cell culture. *Biotechnol. Bioeng.* 103 (4), 655–663. doi:10.1002/bit.22361

Torisawa, Y. S., Spina, C. S., Mammoto, T., Mammoto, A., Weaver, J. C., Tat, T., et al. (2014). Bone marrow-on-a-chip replicates hematopoietic niche physiology *in vitro*. *Nat. Methods* 11 (6), 663–669. doi:10.1038/nmeth.2938

Torres, L. S., Asada, N., Weiss, M. J., Trumpp, A., Suda, T., Scadden, D. T., et al. (2022). Recent advances in "sickle and niche" research - tribute to Dr. Paul S Frenette. *Stem Cell Rep.* 17 (7), 1509–1535. doi:10.1016/j.stemcr.2022.06.004

Verma, D., Zanetti, C., Godavarthy, P. S., Kumar, R., Minciacchi, V. R., Pfeiffer, J., et al. (2020). Bone marrow niche-derived extracellular matrix-degrading enzymes

influence the progression of B-cell acute lymphoblastic leukemia. *Leukemia* 34 (6), 1540–1552. doi:10.1038/s41375-019-0674-7

Vining, K. H., and Mooney, D. J. (2017). Mechanical forces direct stem cell behaviour in development and regeneration. *Nat. Rev. Mol. Cell Biol.* 18 (12), 728–742. doi:10.1038/nrm.2017.108

Walenda, T., Bork, S., Horn, P., Wein, F., Saffrich, R., Diehlmann, A., et al. (2010). Co-culture with mesenchymal stromal cells increases proliferation and maintenance of haematopoietic progenitor cells. *J. Cell. Mol. Med.* 14 (1-2), 337–350. doi:10.1111/j.1582-4934.2009.00776.x

Wang, W., Zhao, Y., Bai, H., Zhang, T., Ibarra-Galvan, V., and Song, S. (2018). Methylene blue removal from water using the hydrogel beads of poly (vinyl alcohol)-sodium alginate-chitosan-montmorillonite. *Carbohydr. Polym.* 198, 518–528. doi:10.1016/j.carbpol.2018.06.124

Whitesides, G. M. (2006). The origins and the future of microfluidics. *Nature* 442 (7101), 368–373. doi:10.1038/nature05058

Wilkinson, A. C., Igarashi, K. J., and Nakauchi, H. (2020). Haematopoietic stem cell self-renewal *in vivo* and *ex vivo*. *Nat. Rev. Genet.* 21 (9), 541–554. doi:10.1038/s41576-020-0241-0

Wilkinson, A. C., and Nakauchi, H. (2020). Stabilizing hematopoietic stem cells *in vitro*. *Curr. Opin. Genet. Dev.* 64, 1–5. doi:10.1016/j.gde.2020.05.035

Winkler, J., Abisoye-Ogunniyan, A., Metcalf, K. J., and Werb, Z. (2020). Concepts of extracellular matrix remodelling in tumour progression and metastasis. *Nat. Commun.* 11 (1), 5120–5219. doi:10.1038/s41467-020-18794-x

Wolf, M. T., Dearth, C. L., Sonnenberg, S. B., Loboa, E. G., and Badylak, S. F. (2015). Naturally derived and synthetic scaffolds for skeletal muscle reconstruction. *Adv. Drug Deliv. Rev.* 84, 208–221. doi:10.1016/j.addr.2014.08.011

Wong, S. W., Lenzini, S., Giovanni, R., Knowles, K., and Shin, J. W. (2021). Matrix biophysical cues direct mesenchymal stromal cell functions in immunity. *Acta Biomater.* 133, 126–138. doi:10.1016/j.actbio.2021.07.075

Xia, B., Jiang, Z., Debroy, D., Li, D., and Oakey, J. (2017). Cytocompatible cell encapsulation via hydrogel photopolymerization in microfluidic emulsion droplets. *Biomicrofluidics* 11 (4), 044102. doi:10.1063/1.4993122

Xiao, Y., McGuinness, C. S., Doherty-Boyd, W. S., Salmeron-Sanchez, M., Donnelly, H., and Dalby, M. J. (2022). Current insights into the bone marrow niche: From biology *in vivo* to bioengineering *ex vivo*. *Biomaterials* 286, 121568. doi:10.1016/j.biomaterials.2022.121568

Xin, S., Chimene, D., Garza, J. E., Gaharwar, A. K., and Alge, D. L. B. s. (2019). Clickable PEG hydrogel microspheres as building blocks for 3D bioprinting. *Biomater. Sci.* 7 (3), 1179–1187. doi:10.1039/c8bm01286e

Yan, L., Yang, X., Zhao, Y., Wu, Y., Moutloali, R. M., Mamba, B. B., et al. (2022). Bio-inspired mineral-hydrogel hybrid coating on hydrophobic PVDF membrane boosting oil/water emulsion separation. *Sep. Purif. Technol.* 285, 120383. doi:10.1016/j.seppur.2021.120383

Yeoh, J. S., van Os, R., Weersing, E., Ausema, A., Dontje, B., Vellenga, E., et al. (2006). Fibroblast growth factor-1 and -2 preserve long-term repopulating ability of hematopoietic stem cells in serum-free cultures. *Stem Cells* 24 (6), 1564–1572. doi:10.1634/stemcells.2005-0439

Yin, S., and Cao, Y. (2021). Hydrogels for large-scale expansion of stem cells. *Acta Biomater.* 128, 1–20. doi:10.1016/j.actbio.2021.03.026

Yucel, D., and Kocabas, F. (2018). Developments in hematopoietic stem cell expansion and gene editing technologies. *Adv. Exp. Med. Biol.* 1079, 103–125. doi:10.1007/5584_2017_114

Yue, K., Liu, Y., Byambaa, B., Singh, V., Liu, W., Li, X., et al. (2018). Visible light crosslinkable human hair keratin hydrogels. *Bioeng. Transl. Med.* 3 (1), 37–48. doi:10.1002/btm2.10077

Zakrzewski, W., Dobrzyński, M., Szymonowicz, M., and Rybak, Z. (2019). Stem cells: Past, present, and future. *Stem Cell Res. Ther.* 10 (1), 68. doi:10.1186/s13287-019-1165-5

Zhan, Z., Liu, Z. Y., Nan, H. C., Li, J. J., Xie, Y., and Hu, C. Z. (2022). Heterogeneous spheroids with tunable interior morphologies by droplet-based microfluidics. *Biofabrication* 14 (2), 025024. doi:10.1088/1758-5090/ac5e12

Zhang, H. J., Sun, T. L., Zhang, A. K., Ikura, Y., Nakajima, T., Nonoyama, T., et al. (2016). Tough physical double-network hydrogels based on amphiphilic triblock copolymers. *Adv. Mat.* 28 (24), 4884–4890. doi:10.1002/adma.201600466

Zhang, J., Niu, C., Ye, L., Huang, H., He, X., Tong, W. G., et al. (2003). Identification of the haematopoietic stem cell niche and control of the niche size. *Nature* 425 (6960), 836–841. doi:10.1038/nature02041

Zhang, P., Sun, F., Tsao, C., Liu, S., Jain, P., Sinclair, A., et al. (2015). Zwitterionic gel encapsulation promotes protein stability, enhances pharmacokinetics, and reduces immunogenicity. *Proc. Natl. Acad. Sci. U. S. A.* 112 (39), 12046–12051. doi:10.1073/pnas.1512465112

Zhang, P., Zhang, C., Li, J., Han, J., Liu, X., and Yang, H. (2019a). The physical microenvironment of hematopoietic stem cells and its emerging roles in engineering applications. *Stem Cell Res. Ther.* 10 (1), 327. doi:10.1186/s13287-019-1422-7

Zhang, Y., Pan, X., Shi, Z., Cai, H., Gao, Y., and Zhang, W. (2018). Sustained release of stem cell factor in a double network hydrogel for *ex vivo* culture of cord blood-derived $CD34^+$ cells. *Cell Prolif.* 51 (2), e12407. doi:10.1111/cpr.12407

Zhang, Y. S., and Khademhosseini, A. (2017). Advances in engineering hydrogels. *Science* 356 (6337), eaaf3627. doi:10.1126/science.aaf3627

Zhang, Y., Tong, Y., Pan, X., Cai, H., Gao, Y., and Zhang, W. (2019b). Promoted proliferation of hematopoietic stem cells enabled by a hyaluronic acid/carbon nanotubes antioxidant hydrogel. *Macromol. Mat. Eng.* 304 (4), 1800630. doi:10.1002/mame.201800630

Zhao, M., and Li, L. (2016). Dissecting the bone marrow HSC niches. *Cell Res.* 26 (9), 975–976. doi:10.1038/cr.2016.71

Zhao, M., Perry, J. M., Marshall, H., Venkatraman, A., Qian, P., He, X. C., et al. (2014). Megakaryocytes maintain homeostatic quiescence and promote post-injury regeneration of hematopoietic stem cells. *Nat. Med.* 20 (11), 1321–1326. doi:10.1038/nm.3706

Zhao, M., Tao, F., Venkatraman, A., Li, Z., Smith, S. E., Unruh, J., et al. (2019). N-Cadherin-Expressing bone and marrow stromal progenitor cells maintain reserve hematopoietic stem cells. *Cell Rep.* 26 (3), 652–669. doi:10.1016/j.celrep.2018.12.093

Zhao, X., Lang, Q., Yildirimer, L., Lin, Z. Y., Cui, W. G., Annabi, N., et al. (2016). Photocrosslinkable gelatin hydrogel for epidermal tissue engineering. *Adv. Healthc. Mat.* 5 (1), 108–118. doi:10.1002/adhm.201500005

Zhou, D. Z., Chen, L. D., Ding, J. J., Zhang, X. X., Nie, Z. G., Li, X. D., et al. (2020). A 3D engineered scaffold for hematopoietic progenitor/stem cell Co-culture *in vitro*. *Sci. Rep.* 10 (1), 11485. doi:10.1038/s41598-020-68250-5

Zimmermann, R., Hentschel, C., Schron, F., Moedder, D., Buttner, T., Atallah, P., et al. (2019). High resolution bioprinting of multi-component hydrogels. *Biofabrication* 11 (4), 045008. doi:10.1088/1758-5090/ab2aa1

Zimran, E., Papa, L., and Hoffman, R. (2021). *Ex vivo* expansion of hematopoietic stem cells: Finally transitioning from the lab to the clinic. *Blood Rev.* 50, 100853. doi:10.1016/j.blre.2021.100853

frontiers | Frontiers in Bioengineering and Biotechnology

TYPE Original Research
PUBLISHED 10 January 2023
DOI 10.3389/fbioe.2022.1119720

OPEN ACCESS

EDITED BY
Meng Tian,
Sichuan University, China

REVIEWED BY
Jianxun Ding,
Changchun Institute of Applied Chemistry (CAS), China
Huixu Xie,
Sichuan University, China
He Liu,
Jilin University, China

*CORRESPONDENCE
Sheng Lu,
drlusheng@163.com
Yongqing Xu,
xuyongqingkm@163.net

SPECIALTY SECTION
This article was submitted to Biomaterials, a section of the journal Frontiers in Bioengineering and Biotechnology

RECEIVED 09 December 2022
ACCEPTED 22 December 2022
PUBLISHED 10 January 2023

CITATION
Cai X, Wang B, Zhang B, Zhang Y, Wang T, Lin W, Huang Y, Chen B, Zhou S, Lu S and Xu Y (2023), Safety and efficacy of a novel three-dimensional printed microporous titanium prosthesis for total wrist arthroplasty in the treatment of end-stage wrist arthritis.
Front. Bioeng. Biotechnol. 10:1119720.
doi: 10.3389/fbioe.2022.1119720

Safety and efficacy of a novel three-dimensional printed microporous titanium prosthesis for total wrist arthroplasty in the treatment of end-stage wrist arthritis

Xingbo Cai[1,2], Bin Wang[1,2], Bihuan Zhang[1,2], Yue Zhang[1,2], Teng Wang[2], Wei Lin[2], Youjun Huang[3], Bingquan Chen[3], Siyuan Zhou[3], Sheng Lu[4]* and Yongqing Xu[2]*

[1]Graduate School, Kunming Medical University, Kunming, China, [2]Department of Orthopedics, 920th Hospital of Joint Logistics Support Force, PLA, Kunming, China, [3]Suzhou MicroPort OrthoRecon Co., Suzhou, China, [4]Department of Orthopedics, The First People's Hospital of Yunnan Province, Kunming, China

Background: Total wrist arthroplasty is an effective treatment for end-stage wrist arthritis from all causes. However, wrist prostheses are still prone to complications such as prosthesis loosening and periprosthetic fractures after total wrist arthroplasty. This may be due to the wrist prosthesis imprecise matching with patient's bone. In this study, we designed and developed a personalized three-dimensional printed microporous titanium artificial wrist prosthesis (3DMT-Wrist) for the treatment of end-stage wrist joint, and investigated its safety and effectiveness.

Methods: Total wrist arthroplasty was performed using 3DMT-Wrist in 14 cases of arthritis between February 2019 and December 2021. Preoperative and postoperative visual analog scale scores, QuickDASH scores, wrist range of motion, and wrist grip strength were evaluated. Data were statistically analyzed using the paired samples *t*-test.

Results: After 19.7 ± 10.7 months of follow-up, visual analog scale decreased from 66.3 ± 8.9 to 6.7 ± 4.4, QuickDASH scores decreased from 47.4 ± 7.3 to 28.2 ± 7.6, grip strength increased from 5.6 ± 1.4 to 17.0 ± 3.3 kg. The range of motion improved significantly in palmar flexion (30.1° ± 4.9° to 44.9° ± 6.5°), dorsal extension (15.7° ± 3.9° to 25.8° ± 3.3°), ulnar deviation (12.2° ± 3.9° to 20.2° ± 4.3°) and radial deviation (8.2° ± 2.3° to 16.2 ± 3.1). No dislocation or loosening of the prosthetic wrist joint was observed.

Conclusion: Total wrist arthroplasty using 3DMT-Wrist is a safe and effective new treatment for various types of end-stage wrist arthritis; it offers excellent pain relief and maintains the range of motion.

KEYWORDS

3D-printed microporous titanium artificial wrist joint, artificial wrist joint prosthesis, end-stage carpal arthritis, long-term follow up, total wrist arthroplasty

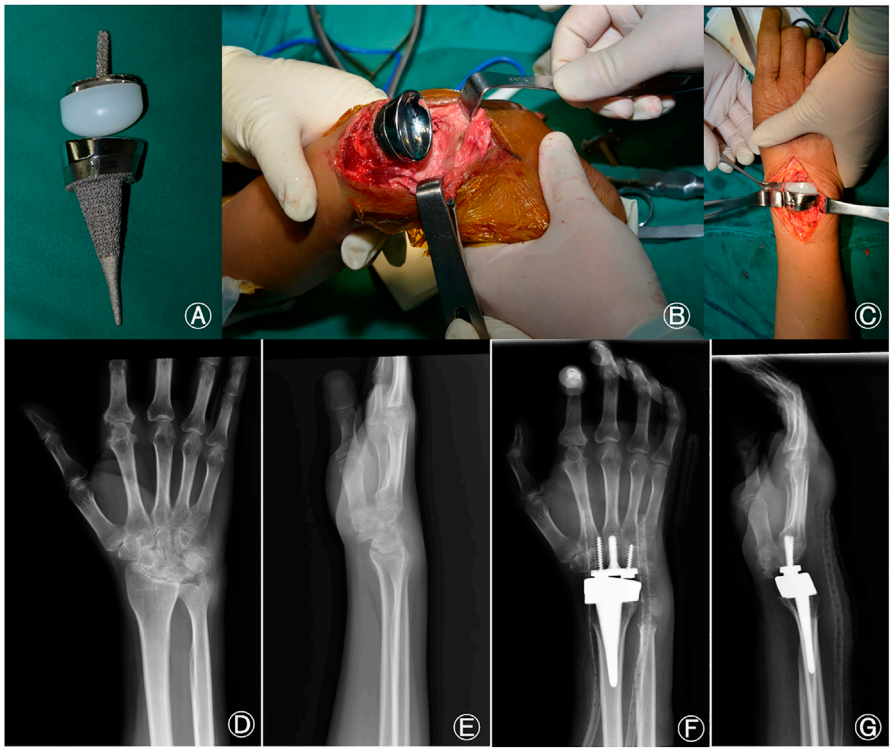

FIGURE 1
(A) Microporous titanium total wrist joint prosthesis, **(B)** Intraoperative carpal and radial osteotomy have been completed and the radial component is being installed. **(C)** Polyethylene has been inserted into the carpal component and the artificial wrist joint has been reset, **(D)** Preoperative posteroanterior radiographs of the wrist, **(E)** Preoperative lateral radiographs of the wrist, **(F)** Posteroanterior radiographs of the wrist at 1 month after TWA, **(G)** Lateral radiographs at 1 month after TWA. TWA, total wrist arthroplasty.

1 Introduction

Total wrist arthroplasty (TWA) has been performed for more than 40 years, and has offered good results in terms of pain relief and improvement of range of motion (ROM) and wrist function; however, the carpal component tends to loosen and subside on long-term follow-up. The first-generation Swanson silastic wrist prosthesis was developed in 1967, and offers the longest available follow-up data for over 15 years; however, silicone is prone to fracture and this procedure has a revision rate of 15%–41% (Damert, 2019). In the 1970s, the second generation of wrist prosthesis was developed by Meuli (Sulzer, acquired by Zimmer) and Volz (Howmedica, acquired by Stryker). These titanium prostheses had a bifurcated design and required bone cement for fixation. Unfortunately, it was demonstrated a high failure rate (Srnec et al., 2018). The third generation of artificial wrist prostheses were developed in 2000; these were mainly biaxial artificial wrist joints, biaxial total wrist implants (DePuy), and universal total wrist implants (KMI). These implants had a prosthetic coating, polyethylene components, and involved screw fixation; however, the main components still required bone cement fixation (Berber et al., 2018; Elbuluk et al., 2018; Reigstad and Røkkum, 2018; Srnec et al., 2018). The fourth generation prosthetic wrist joints emerged in 2003. These included the ReMotion (Stryker) and Maestro (Zimmer Biomet) systems, and involved biologic fixation without the need of cement (Herzberg et al., 2012; Bidwai et al., 2013; Boeckstyns et al., 2013; Sagerfors et al., 2015). This represented a significant improvement over previous generation. In this context, studies have reported better results with the fourth generation of artificial wrist joints (Bidwai et al., 2013; Froschauer et al., 2021). In contrast to wrist fusion, TWA preserves wrist mobility and provides effective pain relief (Fischer et al., 2020; Berber et al., 2020; Matsui et al., 2020; Zhu et al., 2021). However, the carpal component still tends to loosen on long-term follow-up (Reigstad et al., 2017).

Additive manufacturing, often known as three-dimensional (3D) printing or prototyping, can convert 3D digital models into functioning components regardless of their geometry

TABLE 1 General information (*n* = 14).

Characteristic		No.	%
Sex	Female	7	50.0
	Male	7	50.0
Disease Type	Osteoarthritis	10	71.4
	Traumatic arthritis	1	7.1
	Rheumatoid arthritis	3	21.4
Follow-up (month)	19.7 ± 10.7		
Age (years)	45.2 ± 13.5 (23–70)		

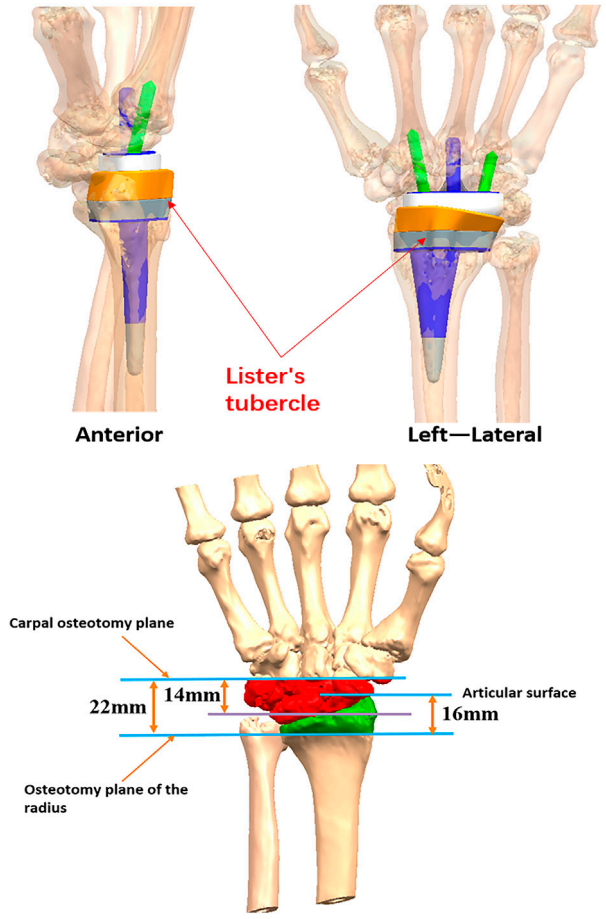

FIGURE 2
Preoperative wrist joint prosthesis design.

(Raheem et al., 2021). Selective laser melting metal 3D printing technology is able to construct complex free-form surfaces, print parts with proper toughness and elastic modulus, and even surface coating layer (Yang et al., 2021). Owing to these properties, 3D printing technology has been employed in the field of hand surgery research for artificial lunar bone replacement and good results have been obtained in the treatment of advanced Kienböck's disease (Ma et al., 2020). Trabecular bone grows within the grid of these implants and permeates throughout the porous structure. In addition, the body identifies human bones and microporous titanium as one structure, leading to good osteogenesis (Núñez et al., 2013). In the field of TWA research, customized artificial wrist prostheses have not been made using 3D-printed personalized microporous titanium. This study therefore aimed to investigate the safety and feasibility of developing a personalized 3D-printed microporous titanium artificial wrist prosthesis (3DMT-Wrist) system for the treatment of end-stage wrist arthritis.

2 Materials and methods

2.1 Case selection criteria

Patients fulfilling the following criteria were included in this study: 1) diagnosed with rheumatoid arthritis, osteoarthritis, or deformity of the wrist with significant pain and limitation of movement (or combined with ulnar displacement instability of the radial wrist joint); 2) requiring total wrist fusion (including fusion of the radial wrist and midcarpal joints) with low requirements for life quality; 3) having severe ischemic necrosis of the wrist bones with an advanced stage of joint collapse; and 4) having good general condition, with good function of the heart, liver, kidney, brain, and other organs.

The following patients were excluded: 1) those with poor general condition and serious complications, 2) having *tuberculosis* or septic infection of the wrist joint, and 3) those demonstrating poor compliance or the inability to perform relevant postoperative functional rehabilitation exercises.

2.2 General information

This study included 14 patients who underwent TWA using the individualized 3DMT-Wrist system at our hospital between February 2019 and December 2021 (Table 1). They were seven men and seven women in the study; they had an average age of 45.2 ± 13.5 (23–70) years. Overall, 3, 1, and 10 cases had rheumatoid arthritis, an open segmental defect caused by gunshot injury, and osteoarthritis, respectively. Patients were evaluated both preoperatively and postoperatively, based on findings on wrist radiography and

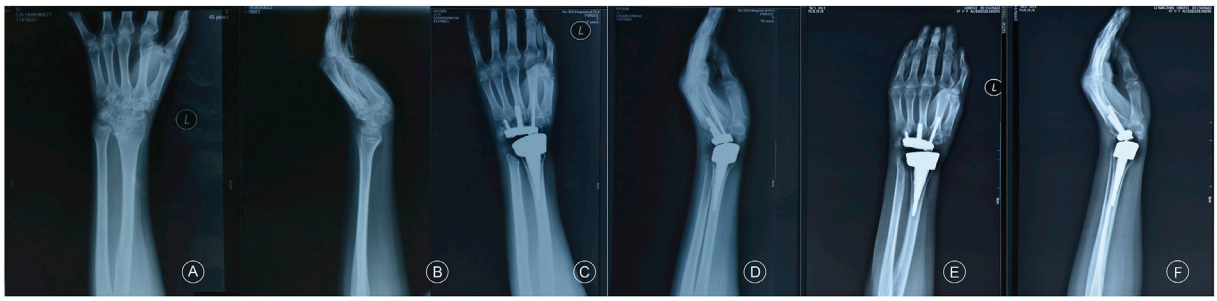

FIGURE 3
Osteoarthritis of the left wrist joint in a female patient aged 46 years. **(A,B)**: preoperative anteroposterior and lateral radiographs, **(C,D)**: postoperative anteroposterior and lateral radiographs at 6 months, **(E,F)**: postoperative anteroposterior and lateral radiographs at 12 months.

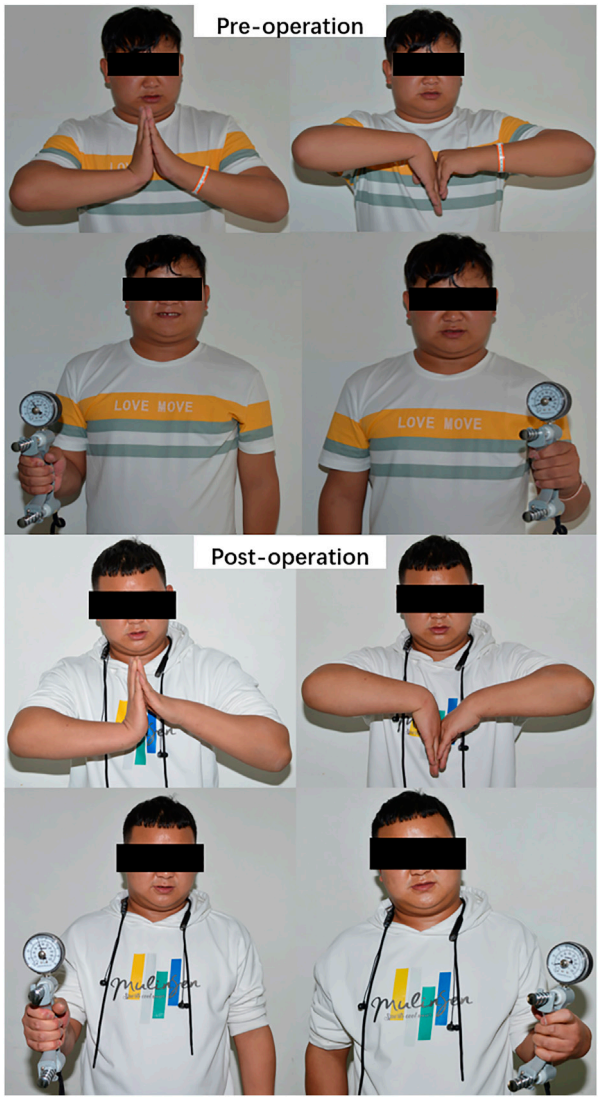

FIGURE 4
A patient with rheumatoid wrist arthritis with 24 months of follow-up after 3DMT-Wrist TWA.

computed tomography, pain levels, and wrist function. The level of wrist pain was evaluated based on the visual analog scale (VAS) scores and wrist function, which was evaluated based on the QuickDASH score, wrist grip strength, and wrist ROM (palmar flexion, dorsal extension, ulnar and radial deviation, pronation, and supination). Grip strength measurements were performed by a resident surgeon using the JAMAR hydraulic hand dynamometer (Sammons Preston, United States); the ROM was recorded using a goniometer. Radiographs were obtained at 1, 3, 6, and 12 months postoperatively. At least 2 mm of movement around the prosthesis-bone interface on serial radiographs were considered to be indicative of implant loosening; two surgeons performed the examination consistently.

2.3 Design and research of the individualized microporous titanium artificial wrist joint

The 3DMT-Wrist was developed by our research team in collaboration with MicroPort OrthoRecon Co. As shown in Figure 1A, the microporous titanium artificial wrist joint consisted of three parts: carpal and radial components and a polyethylene joint ball. The 3DMT-Wrist body material is Ti6Al4V and was manufactured by a metal 3D printer (SLMS310, Xi'an Plastica Additive Technology Co., China). The joint ball material is highly cross-linked ultra-high molecular weight polyethylene, which is manufactured by mechanical processing. The carpal component included a carpal platform, a central carpal column, screws on the left and right sides, a cylindrical projection on the carpal platform, and a carpal stem of Ti6Al4V with a diameter of 5 mm (which was fixed by inserting into the waist of the capitate); it had a 1-mm-thick porous surface to facilitate bone growth. Screws with a diameter of 4.0 mm could be placed in the screw holes on both sides of the carpal stem; in order to achieve fixation of the carpal component, radial and ulnar screws were aimed at the second and fourth metacarpal, respectively.

The polyethylene joint ball had a semi-ellipsoidal shape and was 40 mm long and 18 mm wide. It was prepared in three different sizes based on the height; the sizes were as follows: 12.5 mm (size I), 17.5 mm (size II), and 22.5 mm (size III). The polyethylene joint ball formed an elliptical joint with the radial component to maximize restoration of the wrist joint motion pattern.

The radial component consisted of a radial shank and an articular socket composed of Ti6Al4V and a CoCrMo alloys, respectively. The length of the radial shank was 65 mm and the proximal diameter was either 5 mm (size S#) or 7 mm (size L#); the ulnar deviation angle was approximately 15°. The surface of the radial stalk was porous and had a thickness of 1 mm to facilitate bone growth; the articular fossa was polished to reduce friction between the articular surfaces.

For clinical application, bilateral wrist joints, distal forearms, and metacarpals were first scanned by computed tomography; anatomical data relating to the wrist joints were obtained by mirroring the flip image. These data were provided to the company (which qualified based on biomechanical testing results) and the hospitals for use (Figure 2).

TABLE 2 Comparison of VAS score, quick dash score, grip strength before surgery and final follow-up[a].

Measurement	Before surgery	Final follow-up	t	*p*-value
VAS Score	66.3 ± 8.9	6.7 ± 4.4	19.71	<0.001
Quick DASH Score	47.4 ± 7.3	28.2 ± 7.6	16.18	<0.001
Grip Strength (kg)	5.6 ± 1.4	17.0 ± 3.3	−22.0	<0.001

[a]Data are shown as mean ± SD. Comparison between preoperative condition and final flow-up.

2.4 Surgical method

The affected limb was exsanguinated using a tourniquet after general or brachial plexus anesthesia; the tourniquet pressure was then maintained during surgery. An 8-cm incision was placed from the root of the third metacarpal to the distal radius *via* the Lister's tuberosity; the skin and subcutaneous tissue were incised. The dorsal carpal capsule was lifted from the distal radius to the base of the metacarpal and the ulnar head was removed using biting forceps. The wrist was palmar flexed and the osteotomy line was marked on the distal radius using an electric knife; the median nerve was then protected using a periosteal stripper. The distal radius was osteotomized with a pendulum saw and reamed based on the individual medullary contour; as shown in Figure 1B, this was followed by insertion of the radial component. The thickness of the artificial carpal joint polyethylene and carpal component was measured to determine the thickness of the carpal bone to be osteotomized; after marking, the required segment was removed using a pendulum saw. The medullary cavity of the third metacarpal was then drilled from the center of the capitate section using an electric drill and the position was confirmed *via* radiographic fluoroscopy. The carpal stem was then driven in after reaming and fixed using screws on both sides. The radial stem was inserted, followed by insertion of polyethylene into the carpal component; as shown in Figure 1C, the artificial wrist joint was reset and moved to observe the ROM and check for the likelihood of dislocation. The procedure was confirmed to be satisfactory after fluoroscopic inspection of the artificial wrist joint. The tourniquet was then released, hemostasis was ensured, and the wound was irrigated. The *in-situ* suture of the U-shaped tissue flap was handled with care during the procedure to prevent dorsal dislocation of the wrist joint. The operation was completed after suturing of the incision and application of vacuum sealing drainage over the incision site.

2.5 Postoperative management

The cast was removed after 2 weeks and active and passive exercises were performed; the degree of dorsal extension was increased by 3–5° every 3 days to gradually increase the ROM. Cefazolin (1 g) was administered intravenously after surgery along with Aescuven Forte, which was administered orally. In this context, postoperative edema may occur easily after surgery to the wrist, as the soft tissue layer on the dorsal aspect is thin (with only tendons and no muscle coverage).

2.6 Postoperative imaging evaluation

Radiographs were obtained at 1, 3, 6, and 12 months after surgery.

2.7 Statistical analysis

The SPSS version 19.0 statistical software package was used for data analysis. Measurement data, including the VAS and QuickDASH scores, grip strength, and wrist mobility, were evaluated based on the ROM. Preoperative and postoperative data were compared using the paired *t*-test; $p < .05$ was considered statistically significant. All data have been presented as means with standard deviation.

2.8 Study design

Our study had a before–after design, in which the patients' VAS and QuickDASH scores were assessed based on questionnaires administered before and after surgery. Data pertaining to wrist ROM and grip strength were obtained by physical measurement. Allocation concealment was not performed; blinding of treatment allocation was not possible owing to the nature of the interventions. This study was approved by the local ethics committee before patient enrolment.

3 Results

The mean age of the patients was 45.2 ± 13.5 (23–70) years, and the cohort had a male-to-female ratio of 1:1. Among the 14 patients, 10, 3, and 1 were diagnosed with osteoarthritis, rheumatoid arthritis, and traumatic arthritis, respectively. None experienced prosthesis loosening or dislocation or required revision surgery during the study period. One patient with a history of a gunshot wound in the wrist experienced occasional postoperative wrist and back pain due to severe trauma and surrounding soft tissue injury. All patients were followed up for 19.7 ± 10.7 (7–41) months (Figures 3, 4). At the final follow-up (Table 2), the VAS score decreased from 66.3 ± 8.9 to 6.7 ± 4.4 (t = 19.71, $p < 0.05$), and the QuickDASH score decreased from 47.4 ± 7.3 to 28.2 ± 7.6 (t = 16.18, $p < 0.05$). The grip strength increased from 5.6 ± 1.4 kg to 17.0 ± 3.3 kg (t = −22.0, $p < 0.05$) and the ROM improved significantly for palmar flexion, dorsal extension, and ulnar and radial deviation, with no significant differences for pronation or supination. The palmar flexion angle improved from 30.1° ± 4.9° to 44.9° ± 6.5° (t = −8.4, $p < 0.05$), the

TABLE 3 Comparison of ROM before surgery and final follow-up[a].

Activity direction	Before surgery	Final follow-up	t	*p*-value
Palmar Flexion	30.1 ± 4.9	44.9 ± 6.5	−8.4	<0.001
Dorsal Extension	15.7 ± 3.9	25.8 ± 3.3	−11.9	<0.032
UInar Deviation	12.2 ± 3.9	20.2 ± 4.3	−4.9	<0.001
Radial Deviation	8.2 ± 2.3	16.2 ± 3.1	−14.2	<0.001
Pronation	79.4 ± 3.3	81.6 ± 3.0	−1.7	0.099
Supination	80.9 ± 4.0	80.8 ± 3.5	0.048	0.964

[a]Data are shown as mean ± SD. Comparison between preoperative condition and final flow-up.

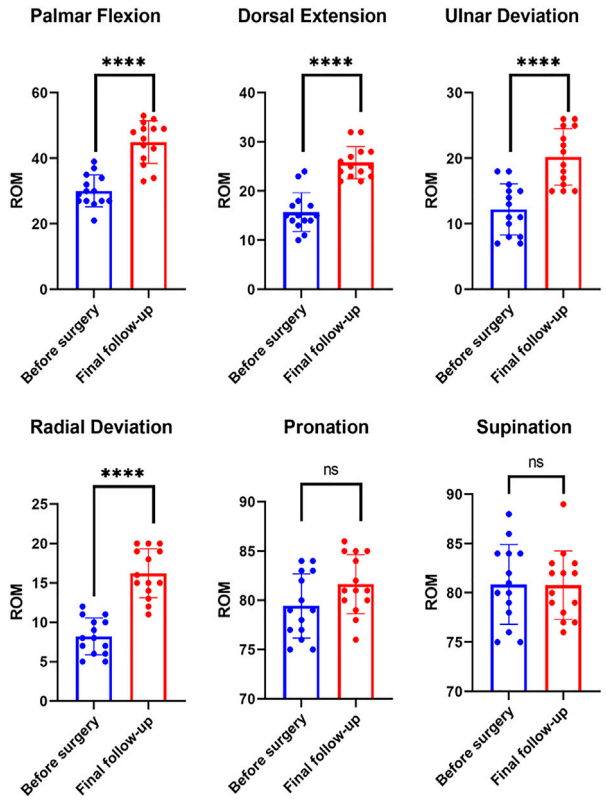

FIGURE 5
Comparison of ROM observed before surgery and at final follow-up. ROM, range of motion.

dorsal extension angle improved from 15.7° ± 3.9° to 25.8° ± 3.3° (t = −11.9, $p < 0.05$), the ulnar deviation angle increased from 12.2° ± 3.9° to 20.2° ± 4.3° (t = −4.9, $p < 0.05$), and the radial deviation angle increased from 8.2° ± 2.3° to 16.2° ± 3.1° (t = −14.2, $p < 0.05$). There was no statistical difference for pronation and supination ($p > 0.05$) (Table 3; Figure 5). Evaluation at the final follow-up showed no loosening or dislocation of the wrist in any patient. The preoperative and postoperative radiographs are shown in Figures 1D–G, 6.

4 Discussion

In this study, the 14 participants who had undergone TWA with the 3DMT-Wrist system showed a decrease in VAS scores from 66.3 ± 8.9 to 6.7 ± 4.4 at 1.6 years after surgery; the QuickDASH scores also decreased from 47.4 ± 7.3 to 28.2 ± 7.6. These findings suggest that TWA using the 3DMT-Wrist system offered significant pain relief and improved function and ROM of the wrist joint. Except for in one patient with a history of a gunshot wound to the wrist (who had occasional dorsal wrist pain after surgery due to severe trauma and surrounding soft tissue damage), wrist pain had disappeared in all cases. The grip strength increased from 5.6 ± 1.4 kg to 17.0 ± 3.3 kg, probably reflecting the reduction in wrist pain; loosening of the prosthesis or joint dislocation were not observed on the radiographs. It is worth noting that all patients who underwent TWA using the 3DMT-Wrist system demonstrated excellent pronation and supination ability; this was mostly because ulnar head excision was performed in all cases to remove inflammatory tissue from the distal radioulnar joint and ease wrist pain. In this context, the most recent follow-up did not reveal ulnar impingement.

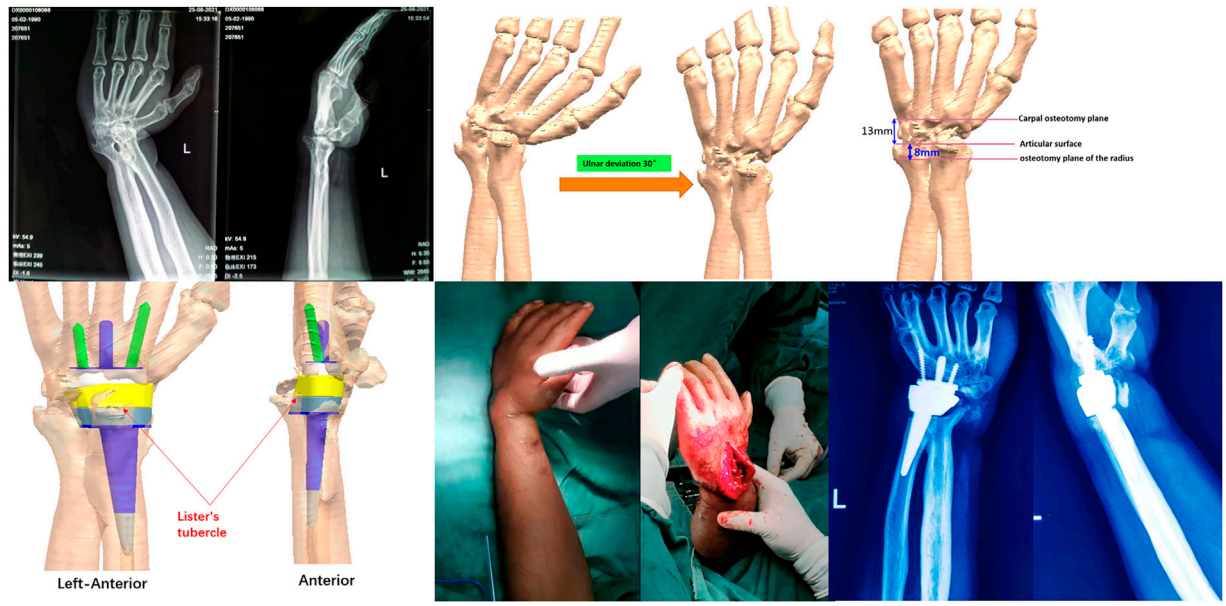

FIGURE 6
A complicated case with non-development of the carpal bones owing to a donkey bite at the age of 3 years. The patient demonstrated loss of wrist and forearm movement, but experienced pain relief and could move the wrist following personalized total wrist arthroplasty.

Our study showed that the 3DMT-Wrist system can offer the following ROM: palmar flexion by 44.9° ± 6.5°, dorsal extension by 25.8° ± 3.3°, ulnar deviation by 20.2° ± 4.3°, radial deviation by 16.2° ± 3.1°, pronation by 81.6° ± 3.0°, and supination by 80.8° ± 3.5°. Brumfield et al. (Brumfield and Champoux, 1984) found that patients with a wrist joint ROM of 10° palmar flexion and 35° dorsal extension were capable of performing most daily activities. Palmer et al. (Palmer et al., 1985) measured functional wrist motion in 10 normal individuals using triaxial electrical goniometry. They assessed wrist motion by asking the participants to perform 52 standardized tasks; the results showed that normal wrist ROM included 5° flexion, 30° dorsal extension, 10° radial deviation, and 15° ulnar deviation. In this context, a recent study showed that daily hand activities can be accomplished at 60% of the maximum ROM of the wrist (Nadeem et al., 2022). This indicates that the ROM offered by the 3DMT-Wrist system is adequate for all requirements of daily life.

Implant loosening is evaluated by continuous radiographs, and is characterized by permeability around the stem or migration by at least 2 mm from the stem profile to the implanted tantalum bead. Data from a study that performed 10-year follow-up after placement of fourth-generation total wrist prostheses (Table 4) have indicated the overall cumulative implant survival rate (with revision as the primary outcome) to be 92%. On including radiologically loosened implants that had not been fixed, the overall implant survival rate was found to be 75% (Fischer et al., 2020). Five-year survival rates of up to 90%–97% have been observed with Maestro or ReMotion implants. In this context, Biax and Maestro implants have been withdrawn from the market as they are no longer economically viable and the Universal II has been updated to the Freedom version (Harlingen et al., 2011). In a study, the cumulative implant survival for Biax, Remotion, and Maestro implants was found to be 81%, 94%, and 95%, respectively, after 5 years of follow-up; the corresponding rates of radiographic loosening were 26%, 18%, and 2%, respectively (Sagerfors et al., 2015).

The ReMotion system includes a titanium plasma-coated CoCr stem for press-fit fixation in the cranial and radial bones, two CoCr carpal screws, and an ovoid CoCr metal-ultra high molecular weight polyethylene joint (Herzberg et al., 2012). The Motec prosthesis has a sandblasted calcium phosphate-coated titanium stem for cementless screw fixation of the capitate/third metacarpal and radius and a metal-on-metal ball-and-socket joint made of CoCr; a small amount of bone

TABLE 4 Reported results and survival with the cementless fourth-generation TWA implants.

Outcomes	Remotion	Universal 2	Remotion	Universal 2	Motec wrist	New total wrist arthroplasty
Number	69	69	87	95	57	20
Mean follow-up (years)	10	9	7	4.4	8	5.7
ROM	Flexion 0 (−10 to 10) Extension (−10 to 10) Radial Deviation 5 (−10–15) Ulnar Deviation 0 (−5–10) Pronation 0 (−5 to 5) Supination 0 (−10 to 10) Results are shown as median (interquartile range).	Pre-operation: 34° flexion and 36° extension Post-operation:37°flexion and 29°extension	Flexion0 (−10 to 10) Extension 5 (−5–15) Radial deviation 0 (−5 to5) Ulnar deviation 0 (−5–10) Pronation0 (−5 to 5) Supination 5 (−5–10) Results are shown as median (interquartile range).	Dorsiflexion 29 palmar flexion 21	AROM 97–126 Supination 81-83; Pronation 82 -83	Flexion-extension: 42.3
VAS	NA	NA	-2.0 Postoperation minus preoperation	8.1 to 5.4	34 to 8	57.9 to 4.5
DASH						
Pre-operative	NA	NA	NA	61	39	NA
Post-operative	NA	NA	NA	46	25	61.2 Post-operative 1.5year
PRWHE[a]	-35.5	NA	-37.5	NA	NA	NA
Complications	Radial component polyethylene	NA	Loosening of the prosthesis	Persistent wrist pain; joint stiffness	Loose distal component, infection, misalignment	Loose carpal components
Kaplan-Meier cumulative survival (%)	94%	78%	99%	91%	86%	NA
Grip strength (Kg)						
Pre-operative	NA	NA	Statistically significant difference between postoperative and preoperative	4.8	21	NA
Post-operative	6	NA		10	24	NA
Principal Investigator	Fischer et al. https://doi.org/10.1016/j.jhsa.2020.02.006	Gil JA et al. https://doi.org/10.1007%2Fs11999-017-5445-z	Sagerfors et al. https://doi.org/10.1016/j.jhsa.2015.09.016 Badge	Badge et al. https://doi.org/10.1302/0301-620x.98b12.37121	Reigstad et al. https://doi.org/10.1016/j.jhsa.2017.06.097	Ward et al. https://doi.org/10.2106/jbjs.h.01614

[a]PRWHE, score was analyzing by Postoperative minus preoperative.

cement is required for TWA (Thillemann et al., 2016). In their study, Holm-Glad et al. (Holm-Glad et al., 2022) observed statistically significant increases in blood Cr and Co levels in participants who had undergone TWA with the metal-on-metal Motec prosthesis. Notably, the 3DMT-Wrist system consists of Ti6Al4V carpal and radial components and a polyethylene joint ball; the radial component consists of a Ti6Al4V shank and a CoCrMo articular socket. The surfaces of the carpal and radial stems have a microporous structure measuring 1 mm in thickness; as they are synthesized in one piece by metal 3D printing, there are no issues related to the loss of coating. In addition, the joint interface of the 3DMT-Wrist system comprises metal-on-polyethylene; metal debris should not therefore be generated during activity.

The 3DMT-Wrist system appeared to offer good clinical results. This may be attributed to the personalization of the implant; the osteotomy position and center of rotation of the native joint were planned individually prior to surgery with the aim of maximal restoration of the biomechanical characteristics of the wrist. In addition, the shape of the osteotomy surface was consistent with that of the radius; this minimized the pressure of the prosthesis on the osteotomy plane. The congruence was maintained with the aim of reducing complications such as prosthesis loosening and sinking. Compared to the fourth generation Motec prosthesis, the 3DMT-Wrist radial component is better shaped to match the inner wall of the cortical bone; this improves stability and strength of the radial component until adequate bone growth occurs. This also prevents early loosening due to differences in elastic modulus between the prosthesis and cancellous bone.

Our study has a number of limitations. First, it had a small sample size. In this context, the 3DMT-Wrist system is newly designed, and is not related to the four generations of total wrist joint prostheses currently in use; the duration of follow-up was therefore limited in addition to the sample size. However, follow-up will be continued and further cases will be included to increase the sample size and validate the results of this study. In this context, Krukhaug et al. found no difference in TWA outcomes between high- and low-volume centers in Norway (Krukhaug et al., 2011). Second, the current study did not to compare outcomes of the novel system with those in current use; this is mainly because TWA has recently gained popularity in China and no available total wrist prostheses have been designed and manufactured in the country. Third, the duration of follow-up was inadequate and no cases required revision; however, the patients will be continuously followed-up in future.

In conclusion, the novel 3D-printed microporous titanium artificial wrist joint prosthesis can significantly relieve wrist pain and improve function with good fixation and ROM. The developed prosthesis demonstrated no dislocation or need for revision after 1.6 years' follow up; this suggests that the novel design has considerable potential for clinical application.

Data availability statement

The original contributions presented in the study are included in the article/supplementary material, further inquiries can be directed to the corresponding authors.

Ethics statement

The studies involving human participants were reviewed and approved by the Ethics Committee of 920th Hospital of Joint Logistics Support Force, PLA [ER 2019-018 (other)-02]. The patients/participants provided their written informed consent to participate in this study. Written informed consent was obtained from the individual(s) for the publication of any potentially identifiable images or data included in this article.

Author contributions

YX, SL, and XC contributed to the conception of the study; XC, BW, BZ, YZ, TW, and WL performed the experiment; XC, BW, and BZ contributed significantly to analysis and manuscript preparation; XC, BW, BZ, and YZ performed the data analyses and wrote the manuscript; YH, BC, and SZ helped perform the analysis with constructive discussions.

Funding

The work was partially supported by: 920th Hospital of Joint Logistics Support Force, PLA (2020YGB04); Yunnan Provincial Clinical Orthopaedic Trauma Medical Center (ZX20191001); Yunnan Orthopedics and Sports Rehabilitation Clinical Medicine Research Center (202102AA310068); Yunnan Key Laboratory of Digital Orthopaedics, Yunnan Provincial Science and Technology Department (202005AG070004); LU,WEIJIA WILLIAM expert workstation of Yunnan Province (202005AF150038); Yunnan Provincial Digital Orthopaedic Innovation Team (202105AE160015); Health Commission of Yunnan Province (L-2019006); Yunnan Province Science and Technology Department (202001AS070028); Yunnan Province Science and Technology Program Major Project (202102AA310042).

Acknowledgments

We would like to thank YH, BC, and SZ for their assistance in design and manufacture of wrist prostheses in this research. We would also like to thank BW for his assistance in photo collection.

Conflict of interest

YH, BC, and SZ were employed by Suzhou MicroPort OrthoRecon Co.

The remaining authors declare that the research was conducted in the absence of any commercial or financial relationships that could be construed as a potential conflict of interest.

Publisher's note

All claims expressed in this article are solely those of the authors and do not necessarily represent those of their affiliated organizations, or those of the publisher, the editors and the reviewers. Any product that may be evaluated in this article, or claim that may be made by its manufacturer, is not guaranteed or endorsed by the publisher.

References

Berber, O., Garagnani, L., and Gidwani, S. (2018). Systematic review of total wrist arthroplasty and arthrodesis in wrist arthritis. *J. Wrist Surg.* 7 (5), 424–440. doi:10.1055/s-0038-1646956

Berber, O., Gidwani, S., Garagnani, L., Spiteri, M., Riley, N., McNab, I., et al. (2020). Salvage of the failed total wrist arthroplasty: A systematic review. *J. Wrist Surg.* 9 (5), 446–456. doi:10.1055/s-0040-1713728

Bidwai, A. S., Cashin, F., Richards, A., and Brown, D. J. (2013). Short to medium results using the remotion total wrist replacement for rheumatoid arthritis. *Hand Surg.* 18 (2), 175–178. doi:10.1142/s0218810413500202

Boeckstyns, M. E., Herzberg, G., and Merser, S. (2013). Favorable results after total wrist arthroplasty: 65 wrists in 60 patients followed for 5–9 years. *Acta Orthop.* 84 (4), 415–419. doi:10.3109/17453674.2013.823588

Brumfield, R. H., and Champoux, J. A. (1984). A biomechanical study of normal functional wrist motion. *Clin. Orthop. Relat. Res.* 187, 23–25. doi:10.1097/00003086-198407000-00004

Damert, H. G. (2019). Total wrist arthroplasty-a review. *Orthopade* 48 (5), 402–412. doi:10.1007/s00132-019-03725-6

Elbuluk, A. M., Milone, M. T., Capo, J. T., Bosco, J. A., and Klifto, C. S. (2018). Trends and demographics in the utilization of total wrist arthroplasty. *J. Hand Surg. Asian Pac* 23 (4), 501–505. doi:10.1142/s2424835518500492

Fischer, P., Sagerfors, M., Jakobsson, H., and Pettersson, K. (2020). Total wrist arthroplasty: A 10-year follow-up. *J. Hand Surg. Am.* 45 (8), 780.e1–780.e10. doi:10.1016/j.jhsa.2020.02.006

Froschauer, S. M., Holzbauer, M., Hager, D., Kwasny, O., and Duscher, D. (2021). Proximal row carpectomy with total scapoidectomy vs. Conventional carpal resection for ReMotion total wrist arthroplasty. *J. Clin. Med.* 10 (9), 1865. doi:10.3390/jcm10091865

Harlingen, D. v., Heesterbeek, P. J. C., and J de Vos, M. (2011). High rate of complications and radiographic loosening of the biaxial total wrist arthroplasty in rheumatoid arthritis: 32 wrists followed for 6 (5–8) years. *Acta Orthop.* 82 (6), 721–726. doi:10.3109/17453674.2011.636669

Herzberg, G., Boeckstyns, M., Sorensen, A. I., Axelsson, P., Kroener, K., Liverneaux, P., et al. (2012). Remotion" total wrist arthroplasty: Preliminary results of a prospective international multicenter study of 215 cases. *J. Wrist Surg.* 1 (1), 17–22. doi:10.1055/s-0032-1323642

Holm-Glad, T., Rokkum, M., Rohrl, S. M., Roness, S., Godang, K., and Reigstad, O. (2022). A randomized controlled trial comparing two modern total wrist arthroplasties: Improved function with stable implants, but high complication rates in non-rheumatoid wrists at two years. *Bone Jt. J.* 104-b (10), 1132–1141. doi:10.1302/0301-620x.104b10.bjj-2022-0201.r2

Krukhaug, Y., Lie, S. A., Havelin, L. I., Furnes, O., and Hove, L. M. (2011). Results of 189 wrist replacements. A report from the Norwegian Arthroplasty Register. *Acta Orthop.* 82 (4), 405–409. doi:10.3109/17453674.2011.588858

Ma, Z. J., Liu, Z., Shi, Q., Li, T., Liu, Z., Yang, Z., et al. (2020). Varisized 3D-printed lunate for kienbock's disease in different stages: Preliminary results. *Orthop. Surg.* 12 (3), 792–801. doi:10.1111/os.12681

Matsui, Y., Minami, A., Kondo, M., Ishikawa, J., Motomiya, M., and Iwasaki, N. (2020). A minimum 5-year longitudinal study of a new total wrist arthroplasty in patients with rheumatoid arthritis. *J. Hand Surg. Am.* 45 (3), 255.e1–255.e7. doi:10.1016/j.jhsa.2019.06.011

Nadeem, M., Loss, J. G., Li, Z. M., and Seitz, W. H. (2022). Ulnar extension coupling in functional wrist kinematics during hand activities of daily living. *J. Hand Surg.* 47 (2), 187.e1–187.e13. e113. doi:10.1016/j.jhsa.2021.03.026

Núñez, F. A., Arguelles, A. A., Lozano, L. L., Popescu, D., MaculeF.and Suso, V. S. (2013). Use of trabecular metal in total knee arthroplasty in severely and morbidly obese patients (BMI > 35 kg/m2). *Acta Ortop. Mex.* 27 (2), 97.

Palmer, A. K., Werner, F. W., Murphy, D., and Glisson, R. (1985). Functional wrist motion: A biomechanical study. *J. Hand Surg. Am.* 10 (1), 39–46. doi:10.1016/s0363-5023(85)80246-x

Raheem, A. A., Hameed, P., Whenish, R., Elsen, R. S., G, A., Jaiswal, A. K., et al. (2021). A review on development of bio-inspired implants using 3D printing. *Biomimetics (Basel)* 6 (4), 65. doi:10.3390/biomimetics6040065

Reigstad, O., Holm-Glad, T., Bolstad, B., Grimsgaard, C., Thorkildsen, R., and Rokkum, M. (2017). Five-to 10-year prospective follow-up of wrist arthroplasty in 56 nonrheumatoid patients. *J. Hand Surg. Am.* 42 (10), 788–796. doi:10.1016/j.jhsa.2017.06.097

Reigstad, O., and Røkkum, M. (2018). Wrist arthroplasty using prosthesis as an alternative to arthrodesis: Design, outcomes and future. *J. Hand Surg. Eur.* 43 (7), 689–699. doi:10.1177/1753193418784707

Sagerfors, M., Gupta, A., Brus, O., and Pettersson, K. (2015). Total wrist arthroplasty: A single-center study of 219 cases with 5-year follow-up. *J. Hand Surg. Am.* 40 (12), 2380–2387. doi:10.1016/j.jhsa.2015.09.016

Srnec, J. J., Wagner, E. R., and Rizzo, M. (2018). Total wrist arthroplasty. *JBJS Rev.* 6 (6), e9. doi:10.2106/jbjs.rvw.17.00123

Thillemann, J. K., Thillemann, T. M., Munk, B., and Kroner, K. (2016). High revision rates with the metal-on-metal Motec carpometacarpal joint prosthesis. *J. Hand Surg. Eur.* 41 (3), 322–327. doi:10.1177/1753193415595527

Yang, X., Ma, W., Gu, W., Zhang, Z., Wang, B., Wang, Y., et al. (2021). Multi-scale microstructure high-strength titanium alloy lattice structure manufactured via selective laser melting. *RSC Adv.* 11 (37), 22734–22743. doi:10.1039/d1ra02355a

Zhu, X. M., Perera, E., Gohal, C., Dennis, B., Khan, M., and Alolabi, B. (2021). A systematic review of outcomes of wrist arthrodesis and wrist arthroplasty in patients with rheumatoid arthritis. *J. Hand Surg. Eur.* 46 (3), 297–303. doi:10.1177/1753193420953683

frontiers | Frontiers in Bioengineering and Biotechnology

TYPE Original Research
PUBLISHED 17 January 2023
DOI 10.3389/fbioe.2023.1113236

OPEN ACCESS

EDITED BY
Jianxun Ding,
Changchun Institute of Applied Chemistry (CAS), China

REVIEWED BY
Huizhi Chen,
Guangdong Medical University, China
Haibo Yang,
Tongji University, China

*CORRESPONDENCE
Ye Cao,
caoyecy@126.com
Bertrand Czarny,
bczarny@ntu.edu.sg

SPECIALTY SECTION
This article was submitted to Biomaterials, a section of the journal Frontiers in Bioengineering and Biotechnology

RECEIVED 01 December 2022
ACCEPTED 05 January 2023
PUBLISHED 17 January 2023

CITATION
Liew WJM, Wong YS, Parikh AN, Venkatraman SS, Cao Y and Czarny B (2023), Cell-mimicking polyethylene glycol-diacrylate based nanolipogel for encapsulation and delivery of hydrophilic biomolecule.
Front. Bioeng. Biotechnol. 11:1113236.
doi: 10.3389/fbioe.2023.1113236

Cell-mimicking polyethylene glycol-diacrylate based nanolipogel for encapsulation and delivery of hydrophilic biomolecule

Wen Jie Melvin Liew[1], Yee Shan Wong[2], Atul N. Parikh[3], Subbu S. Venkatraman[4], Ye Cao[5]* and Bertrand Czarny[1,6]*

[1]School of Materials Science and Engineering, Nanyang Technological University, Singapore, Singapore, [2]Biomedical Engineering, School of Engineering, Temasek Polytechnic, Singapore, Singapore, [3]Biomedical Engineering and Materials Science and Engineering, University of California, Davis, Davis, CA, United States, [4]School of Materials Science and Engineering, National University of Singapore, Singapore, Singapore, [5]Institute of Blood Transfusion, Chinese Academy of Medical Sciences and Peking Union Medical College, Chengdu, China, [6]Lee Kong Chian School of Medicine, Nanyang Technological University, Singapore, Singapore

Lipid based nanoparticulate formulations have been widely used for the encapsulation and sustain release of hydrophilic drugs, but they still face challenges such as high initial burst release. Nanolipogel (NLG) emerges as a potential system to encapsulate and deliver hydrophilic drug while suppressing its initial burst release. However, there is a lack of characterization of the drug release mechanism from NLGs. In this work, we present a study on the release mechanism of hydrophilic Dextran-Fluorescein Isothiocyanate (DFITC) from Poly (ethylene glycol) Diacrylate (PEGDA) NLGs by using different molecular weights of PEGDA to vary the mesh size of the nanogel core, drawing inspiration from the macromolecular crowding effect in cells, which can be viewed as a mesh network of undefined sizes. The effect is then further characterized and validated by studying the diffusion of DFITC within the nanogel core using Fluorescence Recovery after Photobleaching (FRAP), on our newly developed cell derived microlipogels (MLG). This is in contrast to conventional FRAP works on cells or bulk hydrogels, which is limited in our application. Our work showed that the mesh size of the NLGs can be controlled by using different Mw of PEGDA, such as using a smaller MW to achieve higher crosslinking density, which will lead to having smaller mesh size for the crosslinked nanogel, and the release of hydrophilic DFITC can be sustained while suppressing the initial burst release, up to 10-fold more for crosslinked PEGDA 575 NLGs. This is further validated by FRAP which showed that the diffusion of DFITC is hindered by the decreasing mesh sizes in the NLGs, as a result of lower mobile fractions. These findings will be useful for guiding the design of PEGDA NLGs to have different degree of suppression of the initial burst release as well as the cumulative release, for a wide array of applications. This can also be extended to other different types of nanogel cores and other nanogel core-based nanoparticles for encapsulation and release of hydrophilic biomolecules.

KEYWORDS

cell-mimicking, nanolipogel, encapsulation, delivery, hydrophilic biomolecules

1 Introduction

The majority of nanoparticle-based formulations for delivery of hydrophilic drugs and biomolecules exhibits a "burst" release of the encapsulated contents upon administration in a couple of hours (Huang and Brazel, 2001). In most drug delivery applications, burst release is undesirable due to the shorter duration of action, which leads to higher dosage frequency to achieve the therapeutic effect; in addition, and more importantly, the burst may lead to local and systemic toxicity (Huang and Brazel, 2001). For chronic conditions, higher dosage frequency will result in a huge burden from the higher treatment cost and may result in liver toxicity (Sequeira et al., 2019). Thus, there is a need for better systems to control the burst release of hydrophilic therapeutics, and to achieve the desired sustained effect. Lipid based nanoparticles, such as liposomes, have been evaluated for the delivery of hydrophilic cargos (Wang and Wang, 2013). Liposomes give a modifiable alternative to other delivery systems, as its properties can be altered to suit various needs, such as improved systemic circulation, targeted delivery and biocompatibility, by using method such as PEGylation (Blume et al., 1993). Liposomes can also hold both hydrophobic molecules within the bilayer, as well as hydrophilic molecules in the aqueous core (Torchilin, 2005). However, liposomes still suffer from several shortcomings, which include the burst release of hydrophilic cargo (Samad et al., 2007; Kraft et al., 2014; Ye and Venkatraman, 2019) and the immunogenicity issues associated with repeated administration. (Wang et al., 2007; Schellekens et al., 2013; Zhang et al., 2016). Therefore, there is a lot of research activity related to the suppression of the burst release.

One of those approaches taken was using nanolipogel (NLG), in which the hydrophilic small-molecule drugs or biomolecules are encapsulated within the gelated core of the NLG, surrounded by a lipid bilayer (Ramanathan et al., 2016; Guo et al., 2018; Cao et al., 2020). Current studies have demonstrated that NLGs has successfully been used to encapsulate and suppress the burst release of hydrophilic drugs and biomolecules, such as doxorubicin hydrochloride (Yu et al., 2018), Dextran-Fluorescein Isothiocyanate (DFITC) (Anselmo et al., 2015), maraviroc and tenofovir disoproxil fumarate (Ramanathan et al., 2016). However, the release mechanisms were not studied in detail and the diffusion characteristics were not characterized. In those examples, the initial burst release was shown to be suppressed to various degrees but the release was monitored for only 8 h (Yu et al., 2018) or only up to 3 days (Ramanathan et al., 2016). There is also a lack of characterization of the diffusion of encapsulated drug within the nanogel core of the NLGs, which gives limited insight into the design of NLG delivery system.

Therefore, we adopted the design of PEGDA NLG (Cao et al., 2020) for a mechanistic study on the release of encapsulated biomolecule, where inspiration was drawn from the concept of macromolecular crowding phenomenon in cells (Ellis, 2001; Zhou et al., 2008; Soleimaninejad et al., 2017). It is known that the intracellular diffusion of proteins, or other biomolecules, in the cytoplasm can be hindered by a phenomenon loosely termed as "macromolecular crowding", where intracellular organelles and macromolecules exhibit a crowding effect to hinders the diffusion of intracellular proteins. Building upon this concept, the NLG system possesses a nanogel core surrounded by a lipid bilayer, in which these structure mimics the crowding effect in cells, hindering the release of hydrophilic biomolecules, as depicted in Figure 1. The encapsulated biomolecules will be held within the mesh network of the nanogel core, in which it could be tailored to give different crosslinking densities and mesh sizes, restricting the diffusion of the encapsulated biomolecules (Cao et al., 2020). From this, we are able to vary the mesh size and crosslinking density of the PEGDA NLG by using different MW of PEGDA, for a mechanistic study on the diffusion and release of encapsulated biomolecule. Some of the commonly used method for diffusion studies include Fluorescence Recovery After Photobleaching (FRAP), Single Particle Tracking (SPT) and Fluorescence Correlation Spectroscopy (FCS), with FRAP being the most used method (Mika and Poolman, 2011; Schavemaker et al., 2018). However, SPT is limited by its high sensitivity to background fluorescence and FCS is more suited for giant-unilamellar vesicles (GUV), which isn't suited for our application. On the other hand, FRAP has attained higher level of success in studying macromolecular mobility, especially in cells (Mika and Poolman, 2011), which can be fitted to our diffusion study by developing cell derived microlipogels (MLG). Hence, we have chosen to perform FRAP as our method for a mechanistic study into the diffusion and release of encapsulated biomolecule in PEGDA NLG. For that, we have newly developed the method of using cell derived MLGs to perform FRAP, to overcome the difficulty in performing FRAP on NLGs. This is also a novel approach, as compared to conventional methods of FRAP that are done on cells (Mika and Poolman, 2011; Schavemaker et al., 2018) or bulk hydrogel (Cha et al., 2011).

In this study, we fabricated NLGs with PEGDA of three different molecular weights (575 Da, 2000 Da and 4,000 Da) to mimic the cellular macromolecular crowding effect and systemically investigate the diffusion mechanism of hydrophilic cargos within the nanogel core in NLGs with varied extent of macromolecular crowding through different crosslinking densities. PEGDA is known to be biocompatible, non-toxic, immunologically inert and has been used in various biomolecule delivery studies (Sabnis et al., 2009; Durst et al., 2011; Liu et al., 2017;

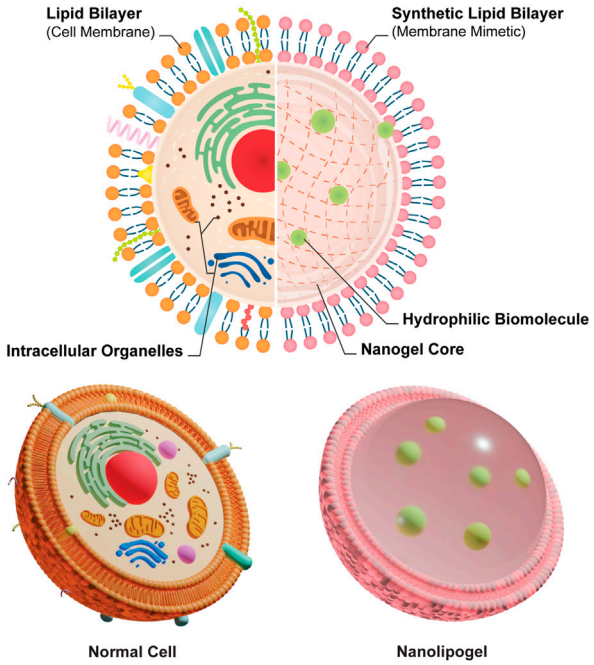

FIGURE 1
Schematics of the comparison between normal cell and cell mimetic nanolipogels.

Stillman et al., 2020). Also, the PEG moiety is degradable *in vitro* and *in vivo* without toxic by-products (Browning et al., 2014; Stillman et al., 2020). Dextran-Fluorescein Isothiocyanate (DFITC) is used as a hydrophilic molecule for the release studies. Fluorescence Recovery after Photobleaching (FRAP) have been done to study the diffusion of encapsulated molecules and the mechanism for release, using cell derived MLGs that we have developed.

2 Materials and methods

2.1 Materials

L-α-phosphatidylcholine (Egg, Chicken) (EPC) was procured from Avanti Polar Lipids, Inc. PEGDA (MW: 575Da, 2000Da, 4000Da), DFITC (MW: 150000Da), Iron (III) Chloride Hexahydrate, Ammonium Thiocyanate, Lithium phenyl-2,4,6-trimethylbenzoylphosphinate (LAP), chloroform (ethanol stabilized), Tetramethylrhodamine Isothiocyanate-Dextran (DRITC), Sodium Chloride (NaCl), Potassium Chloride (KCl), Triton™ X-100 were obtained from Sigma–Aldrich (Singapore). PELCO NetMesh™ TEM support Grids are obtained from Ted Pella, Inc. Nuclepore™ Polycarbonate Track-Etched Membranes are obtained from Fisher Scientific Pte Ltd. Spectra/Por® Biotech Cellulose Ester (CE) Membrane (1000 kDa) were procured from Thermo Fisher Scientific. Primary Human Dermal Fibroblasts (HDFs, ATTC® PCS-201-010TM, US) were kindly gifted from Prof. Ng Kee Woei's research group.

2.2 Fabrication of DFITC-loaded PEGDA NLG

PEGDA NLGs were prepared using the thin film hydration method (Zhang, 2017). In brief, EPC was dissolved in chloroform and added into a round bottom flask. The lipid solution was dried using a rotary evaporator at 150 rpm for 1 h, in a water bath at 40°C. The resulting lipid thin film was hydrated at 37°C with solution containing PEGDA hydrogel precursor, DFITC (3 mg/ml) and LAP (0.5 mg/ml), dissolved in phosphate buffered saline (PBS). The thin film was hydrated using a rotary evaporator (without the use of a vacuum pump), at 200 rpm for 1 h. The resulting multilamellar vesicles (MLV) solution was then extruded through polycarbonate membranes of decreasing pore sizes (800 nm, 400 nm, 200 nm) until large unilamellar vesicle (LUVs) of a desired size of between 150 nm and 180 nm are obtained. The LUVs were then purified using ultracentrifugation at 300,000 G and 4°C for 1 h. The resulting pellet was resuspended in fresh PBS. The un-crosslinked NLGs were then exposed to ultraviolet (UV) light of 365 nm (VL-8. L, Vilber, 1-2 mW/cm^2) for 5 min to form crosslinked NLGs *via* photo-polymerization. Bare liposomes are fabricated the same way, with the lipid thin film hydrated with only PBS.

2.3 Characterization of PEGDA NLG nanoparticles

2.3.1 Size and zeta potential

The size, zeta potential and polydispersity index (PDI) of the PEGDA NLG nanoparticles were measured using Malvern Nanosizer 2000. The hydrodynamic size of the samples, together with the PDI, are determined through the measurement of the light intensity fluctuations from the Brownian motion of the particles in suspension, using Dynamic Light Scattering (DLS). Samples are diluted 75x in distilled water before measurement with the Nanosizer. In order to affirm the formation of the nanogel core, crosslinked NLG samples are added with 1% Triton™ X-100 before DLS measurements.

2.3.2 Morphology of NLGs

Cryogenic transmission electron microscopy (TEM) was used to image the bare liposomes, un-crosslinked and crosslinked NLG samples' morphology with their spherical integrity intact. In cryogenic TEM, the samples were quickly frozen to prevent any structural collapse that may happen in slow drying. 3 μL of sample was pipette onto the TEM copper grids and blotted for 1.5 s, then plunged into liquid nitrogen cooled liquid ethane, using the Cryoplunge® three system (Gatan, Inc. United States). This was done at near 100% humidity to produce amorphous ice around the sample to reduce beam induced damage during imaging, while maintaining native conformation. The frozen sample on the grid is then stored in liquid nitrogen prior to imaging on the Carl Zeiss Libra® 120 Plus electron microscope. The images were taken at 31,500 times magnification at low dose, while maintaining the TEM holder at below −170°C using liquid nitrogen.

2.3.3 Drug encapsulation and release

One of the most important factors to consider when using liposomes for delivery system is the encapsulation efficiency of the vesicles, which is the fraction of total drug used during fabrication that would eventually be encapsulated within the liposomal samples, as shown in Eq (1) below,

$$Encapsulation\,Efficiency\,(\%) = \frac{Amount\,of\,Drug\,Encapsulated}{Total\,Amount\,of\,Drug\,Used} \times 100 \quad (1)$$

The amount of encapsulated drug can be quantified by breaking the un-crosslinked NLG samples and test for the concentration of DFITC. Liposomal samples were first dissolved in absolute ethanol to dissolve the lipid bilayer. The solution was then diluted 5 times with PBS and tested for fluorescence intensity of DFITC using Tecan Microplate reader (Excitation: 490 nm and Emission: 520 nm). The results were then compared against a calibration curve prepared with known concentrations of DFITC dissolved in the same ratio of PBS and ethanol.

The release of DFITC was monitored over a period of 14 days. Un-crosslinked and crosslinked NLG samples were placed in Spectra/Por® cellulose ester dialysis bag (1000kD, MWCO). To achieve sink condition, the bagged samples were suspended in 40 times the volume of PBS with .05% sodium azide and the release bottles were shaken in a 37°C incubator with the speed of 100 rpm. Each sample was done in triplicates for accurate representation. At each time points (Day 1, 3, 7, 10, 14), 1 ml from the release buffer was extracted to test for amount of DFITC released by testing the fluorescence intensity of the sample against a set of known standards, using Tecan Microplate reader. Fresh PBS with .05% sodium azide was replaced after every time point.

2.3.4 Stewart Assay

Stewart Assay was used to quantify the amount of lipid in the samples. The assay quantifies the phospholipids presence based on the formation of complex between phospholipids and ammonium

ferrothiocyanate, after extraction by chloroform (Stewart, 1980). Briefly, un-crosslinked NLG samples were dissolved in chloroform and Stewart reagent was added at a 1:1 ratio. Stewart reagent was prepared beforehand by dissolving ammonium thiocyanate and Iron (III) Chloride hexahydrate in DI water. The mixture was then vortexed and then centrifuged at 500 g to separate the two-phase mixture. The organic phase was extracted and its absorbance at 495 nm was tested using Tecan Microplate reader. The measurements were compared against a calibration graph prepared by measuring increasing concentrations of phospholipids. Lipid loss can be calculated using the following equation,

$$Lipid\ loss = \frac{P_0 - P_{lipo}}{P_0} \tag{2}$$

Where P_0 is the total amount of phospholipid used and P_{lipo} is the amount of phospholipid in NLG samples, measured using Stewart Assay.

2.3.5 Mesh size calculation

The mesh size, or distance between two crosslinking points, of the nanogel core was calculated using the equations based on Flory-Rehner theory (Peppas et al., 2006),

$$\frac{1}{\bar{M}_c} = \frac{2}{\bar{M}_n} - \frac{\left(\frac{\bar{v}}{V_1}\right)\left[\ln\left(1 - v_{2,s}\right) + v_{2,s} + \chi_1 v_{2,s}^2\right]}{\left(v_{2,s}^{1/3} - \frac{v_{2,s}}{2}\right)} \tag{3}$$

Where $\bar{M}_c$ is the molecular weight of the polymer chain between two neighboring crosslinking points, $\bar{v}$ is the specific volume of the polymer, $\bar{M}_n$ is the molecular weight of the polymer chains, V_1 is the molar volume of solvent, χ_1 is the interaction parameter between the polymer and solvent (.426 for PEG in water) (Truong et al., 2012) and $v_{2,s}$ is the polymer volume fraction in swollen state. $v_{2,s}$ is calculated from the dry mass and wet mass of the NLGs, based on the following relationship (Melekaslan et al., 2004),

$$v_{2,s} = \left[1 + \frac{\left(\frac{wet\ mass}{dry\ mass}\right)\rho_{polymer}}{\rho_{solvent}}\right]^{-1} \tag{4}$$

Where $\rho_{polymer}$ and $\rho_{solvent}$ are the density of polymer and solvent used for swelling, respectively. Following that, the mesh size (ξ) can be correlated with Flory characteristic ratio (C_n) (PEG: 4.0), molecular weight of repeating unit (M_r) and C-C bond length (L) by (Peppas et al., 2006),

$$\xi = v_{2,s}^{-1/3}\left(\frac{2C_n\bar{M}_c}{M_r}\right)^{1/2} l \tag{5}$$

ξ provided an insight into the diffusional constraints on release from the nanogel core of NLG system. In this work, the wet and dry masses of the fabricated un-crosslinked NLGs (measured after lyophilization), were measured and used to calculate the mesh sizes.

2.3.6 Fluorescence recovery after photobleaching (FRAP)

In order to monitor the diffusion of particles within the nanogel core in NLGs, FRAP was employed. In brief, a region of interest (ROI) (μm^2) of fluorescence species within the nanogel core was photobleached by exposure to a high intensity laser for a sufficient amount of time. The fluorescence recovery was observed by capturing still images at fixed intervals.

In order to have micrometer size microlipogels (MLG), gentle hydration was explored for the fabrication of MLGs for FRAP. However, we failed to achieve the MLG based on conventional liposome preparation methods. So we explored the preparation of cell membrane based MLGs by an adapted hypo-osmotic method (Jeewantha and Slivkin, 2018), which was used to harvest the cell membrane ghosts of human dermal fibroblasts and encapsulate PEGDA with DRITC. Briefly, cultured HDFs were collected, washed with PBS and resuspended in .6% NaCl for 30 min at 4°C. The swollen cells were then recovered from the hypotonic cell suspension by centrifugation at 5000 *g* for 5 min. The supernatant was discarded and the recovered swollen cells in the pellet were resuspended in PBS solution containing PEGDA of varying molecular weights, LAP and DRITC, similar to the solution used in fabrication of PEGDA NLG, at 37°C for 60 min. After incubation, equal amount of hypertonic 1.5 M KCl was added to the cell suspension to restore the integrity of the HDF cell membrane, incubated at 37°C for 30 min. The gel precursor loaded HDF cells were then centrifuged and washed with PBS at 120000 g for 15 min at 4°C. Following that, the vesicles are UV crosslinked at 365 nm and the resulting cdMLGs were imaged with confocal microscopy to confirm its formation.

FRAP was then performed on the MLGs using a single-mode laser source of 532 nm (100mW, Coherent Inc. Santa Clara, CA), with a 20 μm diameter circular spot being photobleached. Fluorescence micrographs were then captured at 3 s interval for 8–10 mins to monitor the fluorescence recovery. The obtained data was then normalized and accounted for fading (Kang et al., 2015). The diffusion coefficient were estimated using the Soumpasis Equation as below (Kang et al., 2012),

$$D = 0.224\frac{r^2}{\tau_{1/2}} \tag{6}$$

Where D is the diffusion coefficient ($\mu m^2/s$), r being the radius of the bleached spot and $\tau_{1/2}$ is the half-life of the recovery, or time taken for the recovery to reached 50% of the mobile fraction.

2.4 Statistical analysis

OriginPro 2018 was used to perform analysis of variance (ANOVA) to determine the statistical significance for mobile fractions for all PEGDA MW. A *p*-value of smaller than .05 is considered to be significantly different ($^*p < .05$).

3 Results

3.1 Particle characterisation

As observed in Table 1. all un-crosslinked and crosslinked NLGs showed similar hydrodynamic sizes of about 170 nm and 185 nm respectively, with PDI lower than .15, reflecting homogeneity and narrow size distribution. In Figure 2A, a comparison is shown between the size distribution graph from the DLS measurement of crosslinked NLG and when crosslinked NLGs are added with 1% Triton™ X-100, which showed an additional peak at about 10 nm, apart from the expected nanogel peak around 200 nm. This

10.3389/fbioe.2023.1113236

TABLE 1 Characterisation of Bare Liposome, uncrosslinked PEGDA NLG and crosslinked PEGDA NLG (n = 3).

PEGDA Mw (Da)		Bare liposome	575	2000	4,000
Uncrosslinked NLG	**Size (nm)**	160.5 ± 2.8	165.6 ± 5.4	169.4 ± 2.6	163.8 ± 3.3
	PDI	.085 ± .006	.155 ± .007	.109 ± .010	.107 ± .021
Crosslinked NLG	**Size (nm)**	–	170.5 ± 5.7	200.3 ± 2.6	188.8 ± 4.2
	PDI	–	.117 ± .001	.141 ± .004	.137 ± .089
Lipid Loss (%)		10.24 ± 1.22	9.70 ± .40	12.67 ± 1.03	20.29 ± 2.14

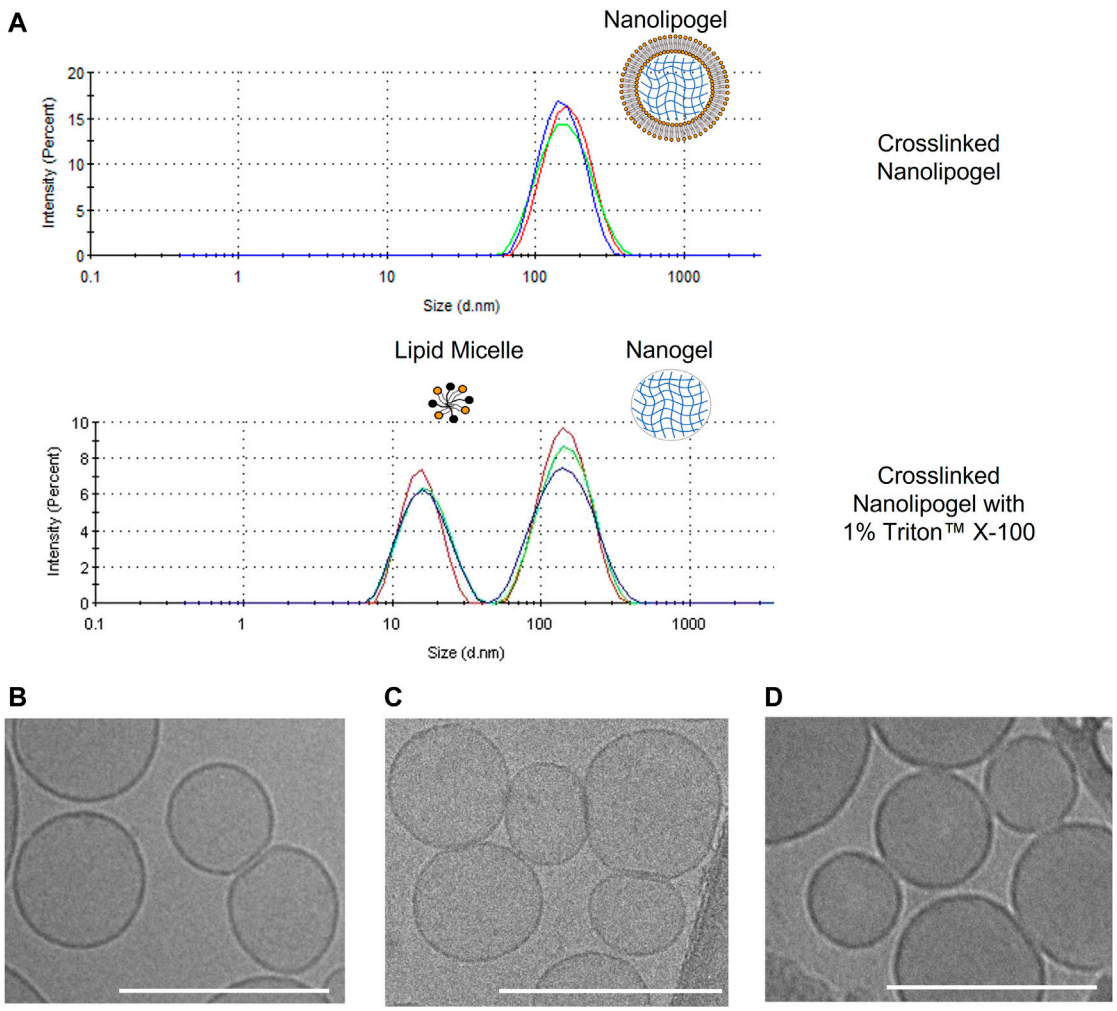

FIGURE 2
(A) DLS size distribution graphs of crosslinked PEGDA NLG and crosslinked PEGDA NLG with 1% Triton™ X-100; Cryogenic-TEM images of **(B)** Bare Liposomes, **(C)** PEGDA 575 uncrosslinked NLGs, **(D)** PEGDA 575 crosslinked NLGs. Unmarked scale bars in the figures represent 200 nm.

additional micelle peak is a result of the Triton™ X-100 stripping off the lipid bilayer from the NLGs, leading to the lipids forming micelles in the aqueous environment. Thus, it showed that the NLGs have a structure with a lipid bilayer surrounding a crosslinked nanogel core.

Cryogenic TEM is then employed to observe the morphologies of bare liposome, un-crosslinked and crosslinked NLG samples. As seen in Figure 2B, bare liposomes are of nano-spherical shape, consistent with DLS data above. Furthermore, encapsulating PEGDA and DFITC within the core in both un-crosslinked and crosslinked NLGs, in

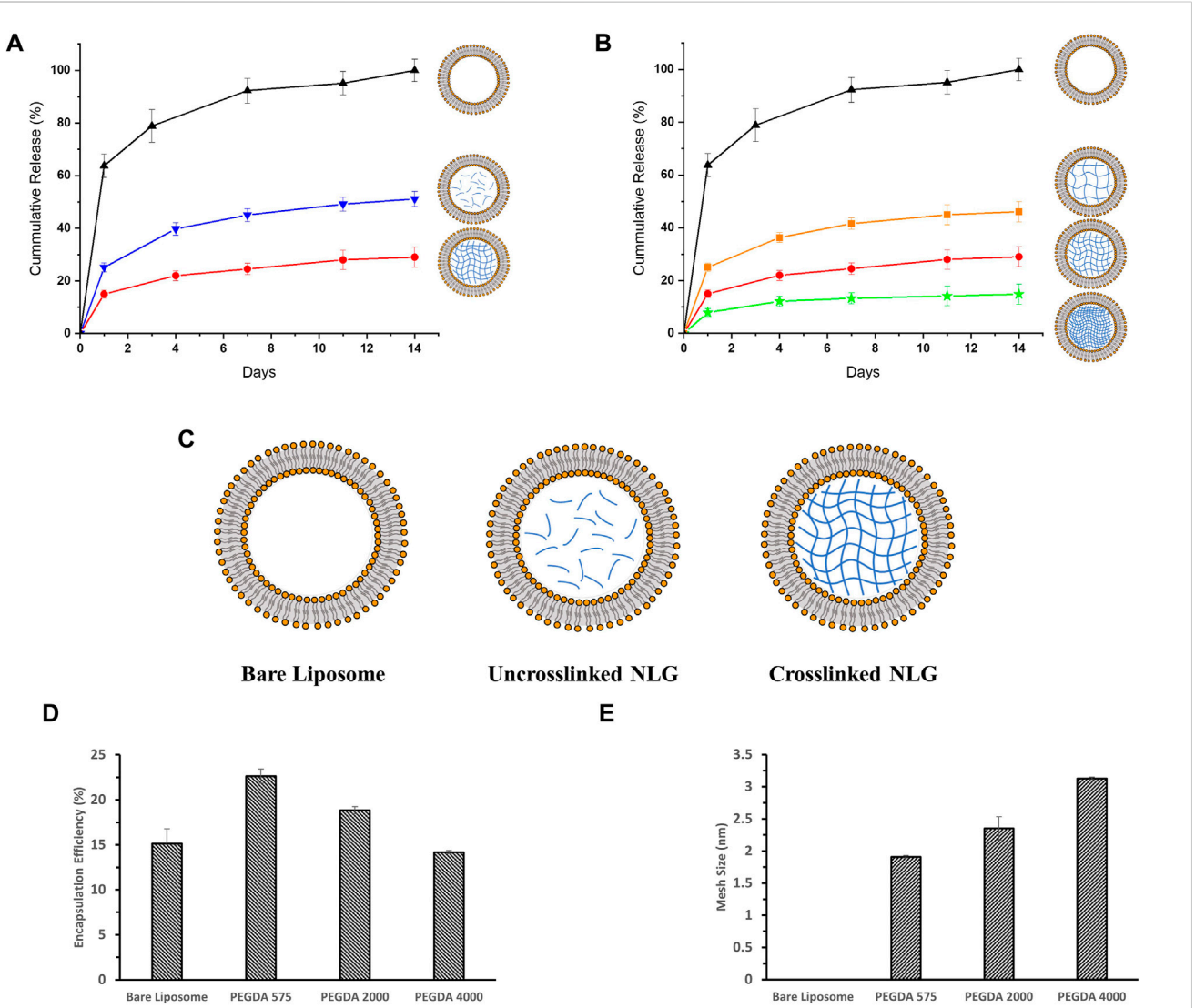

FIGURE 3
In-vitro release profiles for DFITC encapsulated in **(A)** Bare Liposome (Black, Triangle), Uncrosslinked PEGDA 2000 NLG (Blue, Inverted Triangle) and Crosslinked PEGDA 2000 NLG (Red, Circle), **(B)** Bare Liposomes (Black, Triangle), Crosslinked PEGDA 4000 NLG (Orange, Square), Crosslinked PEGDA 2000 NLG (Red, Circle) and Crosslinked PEGDA 575 NLG (Green, Star); **(C)** schematic showing the structural differences between Bare Liposome, Uncrosslinked NLG and Crosslinked NLG; **(D)** encapsulation efficiency and **(E)** mesh size of each PEGDA NLG.

Figures 2C, D respectively, does not cause any significant change in both shape and size.

3.2 *In vitro* release studies

PEGDA of three different molecular weights (575 Da, 2000 Da and 4,000 Da) were used to fabricate NLGs and study the difference in drug release profiles, as shown in Figure 3.

DFITC was encapsulated into PEGDA NLGs to observe the encapsulation efficiency (EE) and release from PEGDA NLGs. As shown in Figure 3D, increasing PEGDA Mw decreases EE and at the same time increases the lipid loss, as shown in Table 1, during fabrication. During which, it was observed that agitation was needed for complete hydration of lipid film for higher PEGDA Mw NLGs, and the pressure needed for extrusion of higher PEGDA Mw NLGs was slightly higher, thus resulting in higher lipid loss and fewer liposome formation. The release of DFITC from PEGDA NLG was then monitored over 14 days at physiological relevant conditions. As shown in Figure 3A, there was burst release of DFITC from bare liposomes, up to 65% on Day 1 and complete release was observed on Day 7. This indicates that the membrane partitioning does not limit the rate of release of DFITC to a huge extent. In comparison, both crosslinked and un-crosslinked NLGs fabricated with PEGDA are able to suppress the initial burst release of DFITC, up to 5-fold and 2-fold more, respectively. Both formulations were also showed to be able to sustain the release over a longer period of time, where the PEGDA NLGs provides better control on the release of DFITC. Furthermore, the Mw of PEGDA, which acts as the macromolecular crowding agent, can be varied to give different mesh sizes and thus different degree of burst release suppression. As the encapsulated molecules are entrapped within the nanogel core in NLG, the mesh size will hinder the diffusion of the molecules through it to varying degrees, as it controls the diffusional path length and steric interactions with the encapsulated molecules (Cao et al., 2020).

It can be seen that un-crosslinked NLGs also show suppression of initial burst release in Figure 3A, down to about 25% in Day 1. This suppression is likely due to the 'crowding effect' caused by the presence of PEGDA polymer chains in the core of the liposomes, which disrupts the diffusion of encapsulated DFITC. Therefore, crosslinking of the PEGDA core will further retard the diffusion within the core, resulting in up to 2-fold greater suppression of initial release, as compared to bare liposomes. Next, the effect of crosslinking density in the PEGDA core was examined. According to Figure 3E, PEGDA 575 NLGs shows the smallest mesh size among the three NLGs with different Mw. The smaller mesh size in PEGDA 575 translates to higher crosslinking density (Li and Mooney, 2016), thus allowing it to better entrap encapsulated molecules, such as DFITC in this work. It is noteworthy that when the mesh size are much smaller than the size of DFITC, which is about 9.0 nm (Bu and Russo, 1994; Wen et al., 2013), the mesh size will effectively immobilize the DFITC molecules within the network (Li and Mooney, 2016). Therefore, diffusion of DFITC molecules will then be likely due to reptation only (Peppas et al., 2000). From Figure 3B, we can also see that the suppression of initial burst release is more noteworthy for PEGDA 575 NLG as compared to PEGDA 2000 NLG and PEGDA 4000 NLG, with almost a 10-fold difference from bare liposomes. In addition, the release for DFITC was also slowed to a greater extent of 15% over 14 days for PEGDA 575 NLG, as compared to 20% for PEGDA 2000 NLGs and 40% for PEGDA 4000 NLGs.

Up until now, our results proved that modulation of the release of encapsulated biomolecule can be achieved by varying the mesh size of nanogels; Mw and concentration of PEGDA used in the formation of NLGs have impact on the crosslinking density and therefore mesh size of the NLGs (Cao et al., 2020). The observed trend in cargo release is then validated by performing FRAP on the MLGs, to provide insight on the diffusion across the nanogel core of the NLGs.

3.3 FRAP results of MLG

In order to characterize the suppression of burst release in PEGDA NLG and validate the trends in release profile of the PEGDA NLGs, FRAP was performed to understand how the diffusion coefficient of encapsulated molecules varies in different nanogel cores of the NLGs. In FRAP, the irreversible photobleaching is followed by an observable overall recovery of fluorescence, which is due to the diffusion of the neighboring fluorescent species molecules into the photobleached area and the photobleached species molecules out of the area, as a result of the constant ensemble diffusion in the nanogel core (Mika and Poolman, 2011). By observing the recovery of fluorescence, which is a direct result of the constant diffusion of encapsulated fluorophore in the nanogel core, we can correlate that to the diffusion coefficient of the encapsulated fluorophore. However, due to limitations of the size of the photobleaching spot required, micrometer sized MLGs are needed for the study. Fabrication of micrometer sized GUVs commonly involves electroformation (Le Berre et al., 2008) as well as gel-assisted formation (Weinberger et al., 2013). Even though the use of electroformation technique produces GUVs with fewer structural defects and gives high yield (Patil and Jadhav, 2014), it is less efficient for PBS-based solutions due to screening of electric field effect in the solution and electrostatic forces on the phospholipid layers (Li et al., 2016; Lefrançois et al., 2018). Furthermore, purification after GUV formations without leakage of encapsulated solution is also an issue, in order for UV crosslinking of MLGs. Similarly, gel assisted formation of GUVs has some limitations for our work as it involves the swelling of the PVA gel in the PEGDA solutions, after which the phospholipid layer will detach to form GUVs(Weinberger et al., 2013). However, little is known on how the swelling effect will affect the encapsulation of PEGDA and DFITC into the GUV and a certain degree of agitation is necessary to improve the detachment of GUV from PVA surfaces (Weinberger et al., 2013), which presents a risk for leakage of encapsulated materials.

Therefore, we established a new method for MLG formation based on loaded erythrocytes as drug carriers (Jeewantha and Slivkin, 2018), to study the diffusion coefficient of encapsulated molecules using FRAP. Briefly, human dermal fibroblasts were lysed and loaded with PEGDA solutions together with Tetramethylrhodamine Isothiocyanate-Dextran (DRITC), then purified for photo-crosslinking and imaged under a laser confocal microscope. DRITC was used in place of DFITC in order to be bleached by the laser source of the microscope. As seen in Figures 4A–C, vesicles of about 20 μm diameter are consistently fabricated and are loaded with rhodamine tagged dextran. The MLGs were then photobleached with high intensity laser of 532 nm and the intensity recovery was monitored at 3 s intervals. After accounting for fading and background fluorescence, the intensity was plotted as seen in Figure 4D, and the diffusion coefficient, D, for each formulation were estimated and shown in Figure 4E. From Figures 4D, E, it can be seen that the diffusion coefficient of all three samples were comparable of between .333–.407 $\mu m^2/s$. However, what is strikingly different is the mobile fraction, as shown in Figure 4F, which decreases with decreasing Mw of PEGDA. This is in line with the trend in in vitro release studies and mesh size data where the lower PEGDA NLGs shows a larger suppression of the initial burst release. A lower mobile fraction implies that the encapsulated molecules are more tightly trapped within the NLGs and its release is suppressed to a larger extent. The FRAP data thus, lends further support to the foregoing notion that a smaller PEGDA Mw produce NLGs with finer mesh size of the nanogel core, giving a smaller mobile fraction and resulting into greater hinderance to the release of the encapsulated molecular cargo.

It is in order here to note that while a direct positive correlation exists between the mesh size produced by lower molecular weight PEGDA and the mobile fraction, diffusion constants remain unaffected by the mesh size. This then suggests that the effective viscosity and fluidity of the aqueous phase medium of the encapsulated bulk is not affected by the well-hydrated PEGDA gel. We reason that the changes in mobile fraction reflect that a greater proportion of DFITC (i.e., cargo) molecules become immobile because of surface interactions with the finer mesh.

4 Discussion

Lipid based nanoparticles, such as liposomes, provides a modifiable alternative for drug delivery systems to improve systemic circulation and biocompatibility. However, it also comes with its own limitations that includes initial burst release of encapsulated hydrophilic molecules and immunogenicity issues. In our work, we introduced PEGDA NLGs with a cell mimicking and tunable design that can be fabricated easily with a one pot method. PEGDA is chosen as the macromolecular crowding agent as it is non-toxic, biocompatible and without harmful degradation by-product (Sabnis et al., 2009; Durst et al., 2011; Browning et al., 2014; Liu et al., 2017; Stillman et al., 2020). In the NLG structure, the nanogel

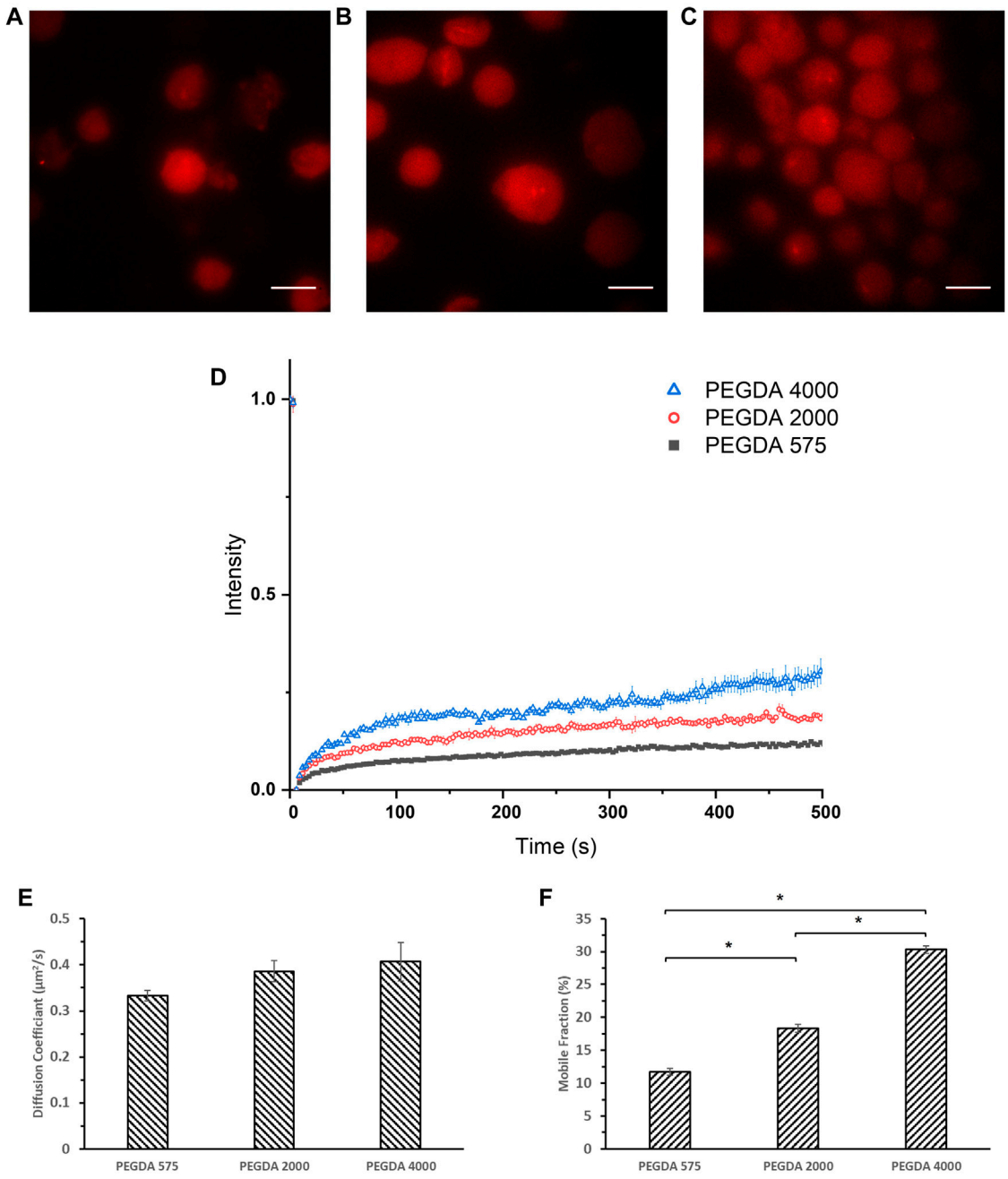

FIGURE 4
Confocal images of **(A)** crosslinked PEGDA 575 MLG, **(B)** crosslinked PEGDA 2000 MLG, **(C)** crosslinked PEGDA 4000 MLG and **(D)** FRAP recovery curves of crosslinked PEGDA 575 MLG (Black Square), PEGDA 2000 MLG (Red Circle), PEGDA 4000 MLG (Blue Triangle). Unmarked scale bars in the figures represent 20 μm; **(E)** Diffusion Coefficients and **(F)** Mobile Fractions of PEGDA 575, 2000, 4,000 MLGs (*$p < .05$).

core surrounded by a phospholipid bilayer serves to mimic the natural structure of cells where the cytoplasm is surrounded by the cell membrane, as depicted in Figure 1. In this regard, PEGDA NLG is used as a model system to establish the macromolecular crowding effect and it is being utilized to investigate how the extent of crowding would impact the diffusion coefficient of the drug molecules or biomolecules. PEGDA NLGs can be fabricated with different Mw of PEGDA to encapsulate hydrophilic biomolecules and sustained its release while suppressing its initial burst release. PEGDA solution with DFITC was used to hydrate a thin film of Egg PC, allowing for the self-assembly of lipids into lipid vesicles, encapsulating PEGDA and DFITC. Serial extrusions of the multilamellar vesicles through polycarbonate filter membrane allows for uniformed large unilamellar vesicles (LUV). After purification of the LUVs *via* ultra-centrifugation, the aqueous cores were photo crosslinked to form nanogel cores within the lipid bilayer. This template can be used for different Mw of PEGDA, with homogenous and controlled size being achievable.

We have also shown that the one pot fabrication method can be used to fabricate homogeneous PEGDA NLG nanoparticles, with PDI of less than .2, for encapsulation of hydrophilic cargos such as DFITC. Further,

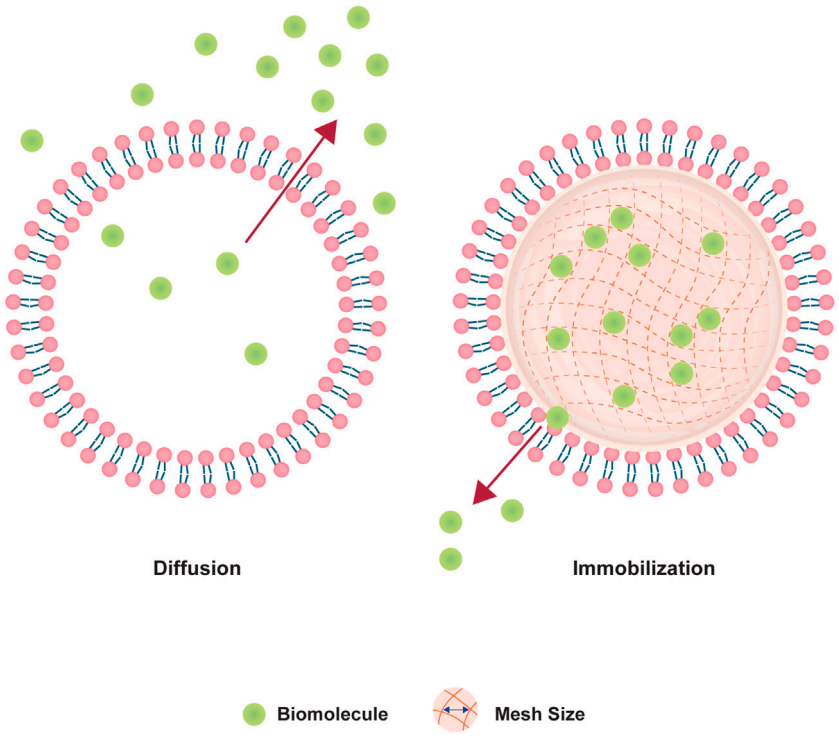

FIGURE 5
Schematic depicting the effect of crosslinking nanogel core on diffusion of encapsulated biomolecule.

cryogenic TEM images of the NLG nanoparticles in Figure 2 confirmed the spherical and core shell structures, with sizes that are consistent with DLS data in Table 1. In order to sustain the release of DFITC, DFITC was introduced together with PEGDA during hydration and the aqueous PEGDA core was then photo-crosslinked to obtain a nanogel core, encapsulating the DFITC. Both crosslinked and un-crosslinked nanogel cores hindered the diffusion of DFITC and resulted in a suppression of initial burst release and sustained release. That was shown in Figure 3, where bare liposomes showed burst release of DFITC of about 65% on the first day while PEGDA NLGs have shown to reduce the initial burst release down to 25% for un-crosslinked PEGDA 2000 NLG and 15% for PEGDA 2000 crosslinked NLGs. This trend is also present in PEGDA 575 NLG and PEGDA 4000 NLG, as shown in Supplementary Figure S1, where crosslinked NLGs showed greater suppression of initial burst release and sustained release. In term of the mesh size effect, crosslinked PEGDA NLGs of lower Mw showed greater suppression of initial burst release, as corresponded to mesh size data in Figure 3E, where mesh size is the smallest for PEGDA 575 NLG, which is only 80% of the mesh size of PEGDA 2000 NLG and 60% of PEGDA 4000 NLG's mesh size. In un-crosslinked NLGs, the presence of PEGDA polymer chains within the core provides a certain degree of steric hindrance on the diffusion by having a crowding effect on the encapsulated biomolecules. Even though the uncrosslinked PEGDA could possibly be diffusing out of the NLG at the same time, it does not result in accelerated release of encapsulated DFITC will still suppress the initial burst release and sustain the release, as shown in the release profiles in Figure 3 and Supplementary Figures S1, S2. In the NLGs where the nanogel cores are crosslinked, the diffusion of the encapsulated biomolecules is hindered by the mesh network of the nanogel by steric hindrance, especially when the mesh size is similar to or smaller than the size of the biomolecule (Li and Mooney, 2016; Cao et al., 2020), as depicted in Figure 5.

As diffusion is key in our study in the release of DFITC from PEGDA NLGs, FRAP was conducted on the particles to understand its diffusion kinetics. Here we introduced a novel method to fabricate micrometer sized PEGDA MLGs, by lysing and loading human dermal fibroblasts. Confocal images in Figure 4 confirmed that MLGs were able to be fabricated with sizes around 20 μm consistently. The MLGs were then photobleached and monitored for fluorescence recovery. From the recovery curves in Figure 4D, the diffusion coefficient and mobile fraction was determined and presented in Figures 4E, F which showed that the mobile fraction decreases as Mw of PEGDA decreases. This correlates with the mesh size data to validate the greater suppression of initial burst release for lower PEGDA Mw NLGs, where the smaller mesh sizes coincide with lower mobile fractions, or spaces where the encapsulated DFITC can diffuse in. Although FRAP was conducted on cell membrane coated MLG as compared to EPC coated NLGs for release studies, the difference between cell membrane and EPC will not significantly affected the diffusion studies performed using FRAP as the ROI monitored for photobleaching and recovery is only selected within the nanogel core. Residual macromolecular substances and organelles are also limited to the membrane layer, and even if there are traces of them within the microgel core, the predominant effect is still the fine mesh

size of the crosslinked gel core immobilizing the encapsulated cargo, which are of much bigger scale than any trace interactions with the residual organelles.

Taking the data together, we have shown that PEGDA NLGs can be easily fabricated and are able to encapsulate hydrophilic biomolecules and suppress its initial burst release. PEGDA NLG system also provides a tunable core by using different Mw PEGDA, in which it could be varied and/or crosslinked, to suppress the initial release and sustain its release to different extends. When compared together, as shown in Supplementary Figure S2, it can be seen that the degree of suppression of initial burst release and accumulated release of encapsulated DFITC differs for all formulations, allowing for a wide range of options to select from for the most suitable formulation for a multitude of different applications, where different rates of release are required. For instance, PEGDA 575 NLGs, which only release 15% of the encapsulated DFITC, can be used in immune response applications or in tumour chemotherapy, where the encapsulated biomolecules or even drug, can be kept within the core and be only released after ingestion by inflammatory cells such as resident macrophages (Rooijen and Sanders, 1994). Lysosomal phospholipases in macrophages disrupts the bilayer of the NLG, and the PEGDA nanogel core will undergo phagocytosis and endocytosis (Rooijen and Sanders, 1994; Anselmo et al., 2015), delivering the encapsulated biomolecule. In addition, it can also be observed in Supplementary Figure S2 that the suppression of burst release is similar between uncrosslinked PEGDA 2000 NLG and crosslinked PEGDA 4000 NLG, and between uncrosslinked PEGDA 575 NLG and crosslinked PEGDA 2000 NLG. This opens up the possibility to choose between a crosslinked NLG or a uncrosslinked NLG where a certain release profile is required. In the aforementioned immune response or tumour chemotherapy, we can possibly have a uncrosslinked PEGDA NLG of smaller MW than 575 that may give the same burst release suppression and cumulative release but allows for a much distinct release after the lipid bilayer is ingested by inflammatory cells, as the encapsulated biomolecule are not immobilized by a crosslinked nanogel's mesh network. On the other hand, for PEGDA 2000 and 4,000 NLGs, the slowed release of 40% may be applied to renal fibrosis treatment by delivering mRNA or cytokines like IL-10 (Nastase et al., 2018), or ocular applications such as delivery to the back of the eye for treating ischemic retinopathies and macular edema (Ozaki et al., 1997; Kompella et al., 2010), where a much slower release over a longer period of time is desired.

Nonetheless, there remains other areas of interest that can be studied, giving us a more complete understanding on the encapsulation, diffusion and release of biomolecules in NLGs, such as the influence from the membrane, if any. EPC was selected in this study for a neutrally charged model membrane system for the introduction of PEGDA nanogel core as it is relatively inert, stable during photopolymerization of NLGs and EPC liposomes has good stability (Yavlovich et al., 2009; Corrales Chahar et al., 2018). Adding of cholesterol, which is present in cell membranes, may be used to further study the membrane properties such as membrane fluidity, permeability or radiation protection (Gaber et al., 2002; Chibowski and Szcześ, 2016). Other phospholipids may also be explored, such as dipalmitoylphosphatidylcholine (DPPC), which will confer temperature sensitivity due to its gel-to-lipid crystalline phase transition at 41°C (Yatvin et al., 1978), or phosphatidylethanolamine (PE) for pH responsiveness (Litzinger and Huang, 1992; Singh et al., 2013). Charged lipids like 1,2-dioleoyl-3-trimethylammoniopropane (DOTAP) and 1,2-distearoyl-sn-glycero-3-phospho- (1′-rac-glycerol) (DSPG) can also be studied for other membrane properties such as increased cellular uptake or skin permeation (Maione-Silva et al., 2019), which may also affect the release of encapsulated biomolecules from such NLGs due to possible interactions with the membrane. These give other avenues to study the membrane effects on encapsulation and release of encapsulated biomolecules.

5 Conclusion

In this work, we have successfully characterized the diffusion and release of encapsulated hydrophilic biomolecule from cell mimicking PEGDA NLGs, using a novel method of cell derived microlipogels to conduct FRAP studies. Our findings can be translated into designing a promising system with a tunable core for better control of the release of hydrophilic biomolecules. Through the release studies, we can show that the PEGDA nanogel cores used in the study is able to hinder the diffusion of encapsulated biomolecules and suppress its release, while sustaining its release up to 14 days. Our experiments also proved that crosslinking the NLGs will give even greater suppression than un-crosslinked cores, and thus by changing the Mw of PEGDA, we can control both the burst release suppression as well as the subsequent sustained release. Lower MW PEGDA NLG has a smaller mesh size, due to higher crosslinking density, which will hinder and immobilize the encapsulated hydrophilic biomolecule to a greater extend. We have successfully validated this using FRAP on cell derived MLGs which show a lower mobile fraction for smaller MW PEGDA MLGs. Taken together, our developed method to characterize the nanogel core of PEGDA NLGs shows great promise and potential to guide the design of a delivery system for hydrophilic biomolecules. We expect our approach to be extendable to other forms of NLGs with different nanogel cores, encapsulating different biomolecule cargos as well as different coating using different phospholipids for specific targeting for cells or tissue sites.

Data availability statement

The original contributions presented in the study are included in the article/Supplementary Material, further inquiries can be directed to the corresponding authors.

Author contributions

Topic and experiments were conceptualized by WL and YC Initial draft and figures were prepared by WL Data analysis was done by WL and reviewed by YC, YW, AP, and BC Project funding acquisition and supervision were done by BC Manuscript was reviewed and edited by YC, YW, SV, AP, and BC. The submitted manuscript were vetted and approved by all authors.

Acknowledgments

We acknowledge the grant support from Ministry of Education (MOE) Tier 1 (RG40/19) and Nanyang Technological University start up grant from School of Material Science and Engineering. We

would like to acknowledge the Facility for Analysis, Characterisation, Testing and Simulation (FACTS), Nanyang Technological University, Singapore, for use of their electron microscopy/X-ray facilities. We thank Tay Yee Yan from FACTS for his expertise on cryogenic TEM. We would also like to thank Cho Nam-Joon for the usage of his confocal microscopy facilities. We would also like to acknowledge Khoo Ee Von for her help with the Figures in the manuscript.

Conflict of interest

The authors declare that the research was conducted in the absence of any commercial or financial relationships that could be construed as a potential conflict of interest.

Publisher's note

Supplementary material

The Supplementary Material for this article can be found online at: https://www.frontiersin.org/articles/10.3389/fbioe.2023.1113236/full#supplementary-material

References

Anselmo, A. C., Zhang, M., Kumar, S., Vogus, D. R., Menegatti, S., Helgeson, M. E., et al. (2015). Elasticity of nanoparticles influences their blood circulation, phagocytosis, endocytosis, and targeting. *ACS Nano* 9 (3), 3169–3177. doi:10.1021/acsnano.5b00147

Blume, G., Cevc, G., Crommelin, M. D. J. A., Bakker-Woudenberg, I. A. J. M., Kluft, C., and Storm, G. (1993). Specific targeting with poly(ethylene glycol)-modified liposomes: Coupling of homing devices to the ends of the polymeric chains combines effective target binding with long circulation times. *Biochimica Biophysica Acta (BBA) - Biomembr.* 1149 (1), 180–184. doi:10.1016/0005-2736(93)90039-3

Browning, M. B., Cereceres, S. N., Luong, P. T., and Cosgriff-Hernandez, E. M. (2014). Determination of the *in vivo* degradation mechanism of PEGDA hydrogels. *J. Biomed. Mater Res. A* 102 (12), 4244–4251. doi:10.1002/jbm.a.35096

Bu, Z., and Russo, P. S. (1994). Diffusion of dextran in aqueous (hydroxypropyl) cellulose. *Macromolecules* 27 (5), 1187–1194. doi:10.1021/ma00083a017

Cao, Y., Wong, Y. S., Ben Mabrouk, A., Anita, V., Jie Liew, M. W., Tan, Y. F., et al. (2020). Nanolipogels as a cell-mimicking platform for controlled release of biomacromolecules. *Nanoscale Adv.* 2 (3), 1040–1045. doi:10.1039/D0NA00093K

Cha, C., Jeong, J. H., Shim, J., and Kong, H. (2011). Tuning the dependency between stiffness and permeability of a cell encapsulating hydrogel with hydrophilic pendant chains. *Acta Biomater.* 7 (10), 3719–3728. doi:10.1016/j.actbio.2011.06.017

Chibowski, E., and Szcześ, A. (2016). Zeta potential and surface charge of DPPC and DOPC liposomes in the presence of PLC enzyme. *Adsorption* 22 (4), 755–765. doi:10.1007/s10450-016-9767-z

Corrales Chahar, F., Díaz, S. B., Ben Altabef, A., Gervasi, C., and Alvarez, P. E. (2018). Characterization of interactions of eggPC lipid structures with different biomolecules. *Chem. Phys. Lipids* 210, 60–69. doi:10.1016/j.chemphyslip.2017.11.013

Durst, C. A., Cuchiara, M. P., Mansfield, E. G., West, J. L., and Grande-Allen, K. J. (2011). Flexural characterization of cell encapsulated PEGDA hydrogels with applications for tissue engineered heart valves. *Acta Biomater.* 7 (6), 2467–2476. doi:10.1016/j.actbio.2011.02.018

Ellis, R. J. (2001). Macromolecular crowding: An important but neglected aspect of the intracellular environment. *Curr. Opin. Struct. Biol.* 11 (1), 114–119. doi:10.1016/S0959-440X(00)00172-X

Gaber, M., Abd el Halim, N., and Khalil, W. (2002). Antioxidant activity of ascorbic acid against peroxidation of phosphatidylcholine liposomes exposed to gamma radiation: A synergistic interaction. *Rom. J. Biophys.* 12 (3-4), 103–115.

Guo, P., Liu, D., Subramanyam, K., Wang, B., Yang, J., Huang, J., et al. (2018). Nanoparticle elasticity directs tumor uptake. *Nat. Commun.* 9 (1), 130. doi:10.1038/s41467-017-02588-9

Huang, X., and Brazel, C. S. (2001). On the importance and mechanisms of burst release in matrix-controlled drug delivery systems. *J. Control. Release* 73 (2), 121–136. doi:10.1016/S0168-3659(01)00248-6

Jeewantha, H. M. A., and Slivkin, A. I. (2018). The terpene-indole alkaloids loaded erythrocytes as a drug carrier: Design and assessment. *Russ. Open Med. J.* 7 (4), e0406. doi:10.15275/rusomj.2018.0406

Kang, M., Andreani, M., and Kenworthy, A. K. (2015). Validation of normalizations, scaling, and photofading corrections for FRAP data analysis. *PLOS ONE* 10 (5), e0127966. doi:10.1371/journal.pone.0127966

Kang, M., Day, C. A., Kenworthy, A. K., and DiBenedetto, E. (2012). Simplified equation to extract diffusion coefficients from confocal FRAP data. *Traffic* 13 (12), 1589–1600. doi:10.1111/tra.12008

Kompella, U. B., Kadam, R. S., and Lee, V. H. (2010). Recent advances in ophthalmic drug delivery. *Ther. Deliv.* 1 (3), 435–456. doi:10.4155/tde.10.40

Kraft, J. C., Freeling, J. P., Wang, Z., and Ho, R. J. Y. (2014). Emerging research and clinical development trends of liposome and lipid nanoparticle drug delivery systems. *J. Pharm. Sci.* 103 (1), 29–52. doi:10.1002/jps.23773

Le Berre, M., Yamada, A., Reck, L., Chen, Y., and Baigl, D. (2008). Electroformation of giant phospholipid vesicles on a silicon substrate: Advantages of controllable surface properties. *Langmuir* 24 (6), 2643–2649. doi:10.1021/la703391q

Lefrançois, P., Goudeau, B., and Arbault, S. (2018). Electroformation of phospholipid giant unilamellar vesicles in physiological phosphate buffer. *Integr. Biol.* 10 (7), 429–434. doi:10.1039/c8ib00074c

Li, J., and Mooney, D. J. (2016). Designing hydrogels for controlled drug delivery. *Nat. Rev. Mater.* 1 (12), 16071. doi:10.1038/natrevmats.2016.71

Li, Q., Wang, X., Ma, S., Zhang, Y., and Han, X. (2016). Electroformation of giant unilamellar vesicles in saline solution. *Colloids Surfaces B Biointerfaces* 147, 368–375. doi:10.1016/j.colsurfb.2016.08.018

Litzinger, D. C., and Huang, L. (1992). Phosphatodylethanolamine liposomes: Drug delivery, gene transfer and immunodiagnostic applications. *Biochimica Biophysica Acta (BBA) - Rev. Biomembr.* 1113 (2), 201–227. doi:10.1016/0304-4157(92)90039-D

Liu, S., Yeo, D. C., Wiraja, C., Tey, H. L., Mrksich, M., and Xu, C. (2017). Peptide delivery with poly(ethylene glycol) diacrylate microneedles through swelling effect. *Bioeng. Transl. Med.* 2 (3), 258–267. doi:10.1002/btm2.10070

Maione-Silva, L., de Castro, E. G., Nascimento, T. L., Cintra, E. R., Moreira, L. C., Cintra, B. A. S., et al. (2019). Ascorbic acid encapsulated into negatively charged liposomes exhibits increased skin permeation, retention and enhances collagen synthesis by fibroblasts. *Sci. Rep.* 9 (1), 522. doi:10.1038/s41598-018-36682-9

Melekaslan, D., Kasapoglu, F., Ito, K., Yagci, Y., and Okay, O. (2004). Swelling and elasticity of hydrogels based on poly(ethylene oxide) macroinimer. *Polym. Int.* 53 (3), 237–242. doi:10.1002/pi.1334

Mika, J. T., and Poolman, B. (2011). Macromolecule diffusion and confinement in prokaryotic cells. *Curr. Opin. Biotechnol.* 22 (1), 117–126. doi:10.1016/j.copbio.2010.09.009

Nastase, M. V., Zeng-Brouwers, J., Wygrecka, M., and Schaefer, L. (2018). Targeting renal fibrosis: Mechanisms and drug delivery systems. *Adv. Drug Deliv. Rev.* 129, 295–307. doi:10.1016/j.addr.2017.12.019

Ozaki, H., Hayashi, H., Vinores, S. A., Moromizato, Y., Campochiaro, P. A., and Oshima, K. (1997). Intravitreal sustained release of VEGF causes retinal neovascularization in rabbits and breakdown of the blood– retinal barrier in rabbits and primates. *Exp. Eye Res.* 64 (4), 505–517. doi:10.1006/exer.1996.0239

Patil, Y. P., and Jadhav, S. (2014). Novel methods for liposome preparation. *Chem. Phys. Lipids* 177, 8–18. doi:10.1016/j.chemphyslip.2013.10.011

Peppas, N. A., Hilt, J. Z., Khademhosseini, A., and Langer, R. (2006). Hydrogels in biology and medicine: From molecular principles to bionanotechnology. *Adv. Mater.* 18 (11), 1345–1360. doi:10.1002/adma.200501612

Peppas, N. A., Huang, Y., Torres-Lugo, M., Ward, J. H., and Zhang, J. (2000). Physicochemical foundations and structural design of hydrogels in medicine and biology. *Annu. Rev. Biomed. Eng.* 2, 9–29. doi:10.1146/annurev.bioeng.2.1.9

Ramanathan, R., Jiang, Y., Read, B., Golan-Paz, S., and Woodrow, K. A. (2016). Biophysical characterization of small molecule antiviral-loaded nanolipogels for HIV-1 chemoprophylaxis and topical mucosal application. *Acta Biomater.* 36, 122–131. doi:10.1016/j.actbio.2016.02.034

Rooijen, N. V., and Sanders, A. (1994). Liposome mediated depletion of macrophages: Mechanism of action, preparation of liposomes and applications. *J. Immunol. Methods* 174 (1), 83–93. doi:10.1016/0022-1759(94)90012-4

Sabnis, A., Rahimi, M., Chapman, C., and Nguyen, K. T. (2009). Cytocompatibility studies of an *in situ* photopolymerized thermoresponsive hydrogel nanoparticle system using human aortic smooth muscle cells. *J. Biomed. Mater. Res. Part A* 91A (1), 52–59. doi:10.1002/jbm.a.32194

Samad, A., Sultana, Y., and Aqil, M. (2007). Liposomal drug delivery systems: An update review. *Curr. Drug Deliv.* 4 (4), 297–305. doi:10.2174/156720107782151269

Schavemaker, P. E., Boersma, A. J., and Poolman, B. (2018). How important is protein diffusion in prokaryotes? *Front. Mol. Biosci.* 5, 93. doi:10.3389/fmolb.2018.00093

Schellekens, H., Hennink, W. E., and Brinks, V. (2013). The immunogenicity of polyethylene glycol: Facts and fiction. *Pharm. Res.* 30 (7), 1729–1734. doi:10.1007/s11095-013-1067-7

Sequeira, J. A. D., Santos, A. C., Serra, J., Estevens, C., Seiça, R., Veiga, F., et al. (2019). Subcutaneous delivery of biotherapeutics: Challenges at the injection site. *Expert Opin. Drug Deliv.* 16 (2), 143–151. doi:10.1080/17425247.2019.1568408

Singh, A., Iyer, A. K., Amiji, M., and Ganta, S. (2013). "14 - multifunctional nanosystems for cancer therapy," in *Biomaterials for cancer therapeutics*. Editor K. Park (Sawston, Cambridge: Woodhead Publishing), 387–413.

Soleimaninejad, H., Chen, M. Z., Lou, X., Smith, T. A., and Hong, Y. (2017). Measuring macromolecular crowding in cells through fluorescence anisotropy imaging with an AIE fluorogen. *Chem. Commun.* 53 (19), 2874–2877. doi:10.1039/C6CC09916E

Stewart, J. C. M. (1980). Colorimetric determination of phospholipids with ammonium ferrothiocyanate. *Anal. Biochem.* 104 (1), 10–14. doi:10.1016/0003-2697(80)90269-9

Stillman, Z. S., Jarai, B. M., Raman, N., Patel, P., and Fromen, C. A. (2020). Degradation Profiles of Poly(ethylene glycol) diacrylate (PEGDA)-based hydrogel nanoparticles. *Polym. Chem.* 11 (2), 568–580. doi:10.1039/c9py01206k

Torchilin, V. P. (2005). Recent advances with liposomes as pharmaceutical carriers. *Nat. Rev. Drug Discov.* 4 (2), 145–160. doi:10.1038/nrd1632

Truong, V., Blakey, I., and Whittaker, A. K. (2012). Hydrophilic and amphiphilic polyethylene glycol-based hydrogels with tunable degradability prepared by "click" Chemistry. *Biomacromolecules* 13 (12), 4012–4021. doi:10.1021/bm3012924

Wang, E. C., and Wang, A. Z. (2013). Nanoparticles and their applications in cell and molecular biology. *Integr. Biol.* 6 (1), 9–26. doi:10.1039/c3ib40165k

Wang, X., Ishida, T., and Kiwada, H. (2007). Anti-PEG IgM elicited by injection of liposomes is involved in the enhanced blood clearance of a subsequent dose of PEGylated liposomes. *J. Control. Release* 119 (2), 236–244. doi:10.1016/j.jconrel.2007.02.010

Weinberger, A., Tsai, F.-C., Koenderink, Gijsje H., Schmidt, Thais F., Itri, R., Meier, W., et al. (2013). gel-assisted formation of giant unilamellar vesicles. *Biophysical J.* 105 (1), 154–164. doi:10.1016/j.bpj.2013.05.024

Wen, H., Hao, J., and Li, S. K. (2013). Characterization of human sclera barrier properties for transscleral delivery of bevacizumab and ranibizumab. *J. Pharm. Sci.* 102 (3), 892–903. doi:10.1002/jps.23387

Yatvin, M. B., Weinstein, J. N., Dennis, W. H., and Blumenthal, R. (1978). Design of liposomes for enhanced local release of drugs by hyperthermia. *Science* 202(4374), 1290–1293. doi:10.1126/science.364652

Yavlovich, A., Singh, A., Tarasov, S., Capala, J., Blumenthal, R., and Puri, A. (2009). Design of liposomes containing photopolymerizable phospholipids for triggered release of contents. *J. Therm. Anal. Calorim.* 98 (1), 97–104. doi:10.1007/s10973-009-0228-8

Ye, C., and Venkatraman, S. (2019). The long-term delivery of proteins and peptides using micro/nanoparticles: Overview and perspectives. *Ther. Deliv.* 10 (5), 269–272. doi:10.4155/tde-2019-0016

Yu, L., Dong, A., Guo, R., Yang, M., Deng, L., and Zhang, J. (2018). DOX/ICG coencapsulated liposome-coated thermosensitive nanogels for NIR-triggered simultaneous drug release and photothermal effect. *ACS Biomaterials Sci. Eng.* 4 (7), 2424–2434. doi:10.1021/acsbiomaterials.8b00379

Zhang, H. (2017). in *Thin-film hydration followed by extrusion method for liposome PreparationLiposomes: Methods and protocols*. Editor G. G. M. D'Souza (New York, NY: Springer New York), 17–22.

Zhang, P., Sun, F., Liu, S., and Jiang, S. (2016). Anti-PEG antibodies in the clinic: Current issues and beyond PEGylation. *J. Control. Release* 244, 184–193. doi:10.1016/j.jconrel.2016.06.040

Zhou, H.-X., Rivas, G., and Minton, A. P. (2008). Macromolecular crowding and confinement: Biochemical, biophysical, and potential physiological consequences. *Annu. Rev. Biophysics* 37 (1), 375–397. doi:10.1146/annurev.biophys.37.032807.125817

frontiers | Frontiers in Bioengineering and Biotechnology

TYPE Original Research
PUBLISHED 23 February 2023
DOI 10.3389/fbioe.2023.1151975

OPEN ACCESS

EDITED BY
Huixu Xie,
Sichuan University, China

REVIEWED BY
Qianbin Wang,
University of Massachusetts Amherst, United States
Yang Kang,
Sun Yat-sen University, China

*CORRESPONDENCE
Rui Zhong,
zhongrui@ibt.pumc.edu.cn
Jiaxin Liu,
liujiaxin@ibt.pumc.edu.cn

SPECIALTY SECTION
This article was submitted to Biomaterials, a section of the journal Frontiers in Bioengineering and Biotechnology

RECEIVED 27 January 2023
ACCEPTED 13 February 2023
PUBLISHED 23 February 2023

CITATION
Kong W, Zhou W, He Z, Zhang X, Li S, Zhong R and Liu J (2023), Polymerized human cord hemoglobin assisted with ascorbic acid as a red blood cell substitute alleviating oxidative stress for blood transfusion.
Front. Bioeng. Biotechnol. 11:1151975.
doi: 10.3389/fbioe.2023.1151975

Polymerized human cord hemoglobin assisted with ascorbic acid as a red blood cell substitute alleviating oxidative stress for blood transfusion

Weichen Kong[1], Wentao Zhou[1], Zeng He[2], Xuejun Zhang[1], Shen Li[1], Rui Zhong[1]* and Jiaxin Liu[1]*

[1]Institute of Blood Transfusion, Chinese Academy of Medical Sciences and Peking Union Medical College, Chengdu, Sichuan, China, [2]Hospital of Chengdu Office of People's Government of Tibetan Autonomous Region, Chengdu, Sichuan, China

Introduction: Blood transfusion is widely used in clinical settings, where considerable efforts have been devoted to develop red blood cell substitutes to overcome blood shortage and safety concerns. Among the several kinds of artificial oxygen carriers, hemoglobin-based oxygen carriers are promising due to their inherent good oxygen-binding and -loading properties. However, difficulties in prone to oxidation, production of oxidative stress, and injury in organs limited their clinical utility. In this work, we report a red blood cell substitute composed of polymerized human cord hemoglobin (PolyCHb) assisted with ascorbic acid (AA) that alleviates oxidative stress for blood transfusion.

Methods: In this study, the in vitro impacts of AA on the PolyCHb were evaluated by testing the circular dichroism, methemoglobin (MetHb) contents and oxygen binding affinity before and after the addition of AA. In the *in vivo* study, guinea pigs were subjected to a 50% exchange transfusion with PolyCHb and AA co-administration, followed by the collection of blood, urine, and kidney samples. The hemoglobin contents of the urine samples were analyzed, and histopathologic changes, lipid peroxidation, DNA peroxidation, and heme catabolic markers in the kidneys were evaluated.

Results: After treating with AA, there was no effect on the secondary structure and oxygen binding affinity of the PolyCHb, while the MetHb content was kept at 55%, which was much lower than that without AA treating. Moreover, the reduction of PolyCHbFe3+ was significantly promoted, and the content of MetHb could be reduced from 100% to 51% within 3 h. *In vivo* study results showed that PolyCHb assisted with AA inhibited the formation of hemoglobinuria, upgraded the total antioxidant capacity and downgraded the superoxide dismutase activity of kidney tissue, and lowered the expression of biomarkers for oxidative stress, e.g., malondialdehyde (ET vs ET+AA: 4.03±0.26 μmol/mg vs 1.83±0.16 μmol/mg), 4-hydroxy-2-nonenal (ET vs ET+AA: 0.98±0.07 vs 0.57±0.04), 8-hydroxy 2 deoxyguanosine(ET vs ET+AA: 14.81±1.58 ng/ml vs 10.91±1.36 ng/ml), heme oxygenase 1 (ET vs ET+AA: 1.51±0.08 vs 1.18±0.05) and ferritin (ET vs ET+AA: 1.75±0.09 vs 1.32±0.04). The kidney histopathology results also demonstrated that kidney tissue damage was effectively alleviated.

Conclusion: In conclusion, these comprehensive results provide evidence for the potential role of AA in controlling oxidative stress and organ injury in the kidneys induced by PolyCHb, and suggest that PolyCHb assisted with AA has promising application for blood transfusion.

KEYWORDS

PolyCHb, ascorbic acid, oxidative stress, kidney, Guinea pigs

1 Introduction

Blood transfusion is widely used in clinical settings such as trauma, severe anemia, and selective operation with massive blood loss. Among the blood components from healthy donors, the packed red blood cell is essential for maintaining the oxygen transportation function. Due to concerns about blood-borne diseases and the availability of fresh red blood cells, considerable efforts have been devoted to develop red blood cell substitutes to overcome blood shortage and safety concerns (Pape and Habler, 2007). In this regard, several artificial oxygen carriers have been reported (Khan et al., 2020). Among them, hemoglobin-based oxygen carriers (HBOCs) derived from native or re-combinational hemoglobin (Hb) through chemical modification (Alayash, 2014) are one of the most attractive category. Because of their inherent good oxygen binding and loading properties, they have become the mainstream of this field. To date, several kinds of HBOCs have undergone preclinical studies and clinical trials, suggesting that they are promising oxygen-bridging agents in many conditions (Buehler et al., 2010). However, difficulties in prone to oxidation, production of oxidative stress, and injury in organs limited their clinical utility. Thus, some strategies have been proposed, such as controlling oxidative stress by adding heme scavengers or antioxidants to the administration of HBOC.

Ascorbic acid (AA) is a first-line clinical antioxidant, widely used in a variety of situations. For example, AA has been successfully used in sickle cell disease patients and toxin-induced met-hemoglobin patients who are known to have a large amount of free ferrous and ferric Hb in circulation (Silva et al., 2013; Dhibar et al., 2018). Likewise, to alleviate the oxidative stress side effect of HBOC (Alayash, 2019), AA treatment has gained attraction to maintain infused HBOC in the reduced oxidative form (Dunne et al., 2006; Cooper et al., 2008). However, previous studies usually used rats as the animal models to evaluate their efficacy, which probably made it confused as rats bear a different antioxidant status due to their quick synthesis of endogenous ascorbic acid (Nandi et al., 1997). Among all the mammalian species, only some species, including humans, non-human primates, fruit bats, and guinea pigs are not able to synthesize endogenous AA due to an evolutionary loss of the hepatic L-gluconolactone oxidase gene (Chatterjee, 1973). The loss of endogenous AA production and subsequent the reliance on dietary intake for AA have shifted the anti-oxidative balance from plasma toward the tissue in these species (Buehler and Alayash, 2010). Therefore, it is important to consider the antioxidant status differences between different species and its impact on the study of the efficacy and safety of HBOC.

Herein, polymerized human cord hemoglobin (PolyCHb) as one kind of HBOCs was prepared by chemical cross-linking, and then *in vitro* and *in vivo* studies were performed, in which guinea pig was used as animal model to mimic the condition of human being that lacks endogenous AA production. In addition, although HBOC-induced oxidative stress can be found in several organs, such as the liver, kidney, heart, and lung (Buehler and D'Agnillo, 2010) etc., the primary safety problem of acellular Hb is the kidney, which is primarily responsible for excreting smaller degradation fragments of infused HBOC (Keipert et al., 1992). Thus, oxidative stress was mainly assayed in the kidney. In specific, guinea pigs were subjected to a 50% exchange transfusion (ET) with PolyCHb(ET group), and AA was co-administrated with PolyCHb at the end of ET (ET + AA group). By evaluating the formation of hemoglobinuria, kidney tissue oxidation stress, and pathological injury, the effects of PolyCHb assisted with AA on oxidative stress were investigated.

2 Materials and methods

2.1 Chemicals, antibodies, and kits

Human serum albumin solution was purchased from Baxter (Vienna, Austria). Vitamin C (AA) injection was supplied by Shenya Animal Healthcare (Shanghai, China). Mouse monoclonal antibodies to heme oxygenase 1 (HO-1, #MA1-112) and mouse monoclonal antibodies to L-ferritin (#MA5-14733) were purchased from Thermo Fisher Scientific (Rockford, United States). Rabbit monoclonal antibody to ß-Actin (#AC026) was purchased from Abclonal (Wuhan, China). Rabbit monoclonal antibody to nuclear factor erythroid 2-related factor 2 (Nrf2, # ab92946), rabbit monoclonal antibodies 4-hydroxy-2-nonenal (4-HNE, #ab46545), goat anti-mouse IgG H&L (HRP) (#ab6789), goat anti-rabbit IgG H&L (HRP) (#ab6721), a catalase (CAT) activity assay kit (#ab83464), a glutathione peroxidase (GPx) assay kit (#ab102530), and an 8-hydroxy 2 deoxyguanosine (8-OHdG) assay kit (#ab201734) were purchased from Abcam (Cambridge, MA, United States). A total antioxidant capacity (T-AOC) assay kit (#A015-2-1) and superoxide dismutase (SOD) kit (#A001-3-1) were obtained from Jiancheng Biotech. (Nanjing, China). A malondialdehyde (MDA) kit (#S0131S) was supplied by Beyotime Biotechnology (Shanghai, China). An enhanced chemiluminescence (ECL) kit (#PF001) was a product from Affinity Biosciences (Changzhou, China).

2.2 Preparation of PolyCHb

PolyCHb used in this study was prepared as reported previously (Zhou et al., 2015). Generally, red blood cells were separated from human cord blood (donated by Sichuan Neo-life Stem Cell Biotech

INC., Sichuan, China), then stroma-free hemoglobin was derived from the red blood cells by hypnotic hemolysis. The prepared Hb was polymerized with glutaraldehyde, followed by filtration to the membrane with a molecular weight cut off at 100 kDa. The prepared PolyPHb solution was added into phosphate buffer solution (PBS) to a final concentration of 8.0 gHb/L, and bubbled with nitrogen for 10 min for oxygenation. The study protocol was approved by the Institute of Blood Transfusion Ethics Committee (Registration number:2016018).

2.3 CD analysis

The CD of Circular Dichroism analyzer (J-815, JASCO, Japan) was used to monitor the changes of PolyCHb secondary structure before and after AA addition. Add 30 μL PolyCHb sample solution to 3 mL 0.05 mol/L PBS solution with pH 7.5 in the cuvette for CD analysis, and then obtain CD spectrum (190–250 nm).

2.4 Oxygen binding affinity assay

The oxygen binding affinity of PolyCHb sample solutions before and after AA addition were detected by HEMOX-ANALYZER (TCS Scientific Corp.). The oxygen balance curve was measured at 37°C in PBS buffer solution with pH 7.4. The oxygen balance curve was used to obtain the value of P50, which was defined as the oxygen partial pressure related to the half ratio of oxygen saturated hemoglobin, and was considered as a sign of the oxygen affinity of PolyCHb samples.

2.5 *In vitro* antioxidant assay

PolyCHb solution (with100 μmol/L Hb concentration) containing different AA contents were prepared in 0.2 mol/L phosphate buffer saline with 100 μmol/L H_2O_2 (pH 7.4 PBS). By changing the AA addition amounts, the mole ratios in PolyCHb solutions between AA and PolyCHb were adjusted to be 0, 1, 2, and 3, respectively. The antioxidant reaction was started with the AA addition at the temperature of 37°C. The MetHb contents in PolyCHb solutions were tested every half an hour until 4 h.

2.6 Reduction of PolyCHbFe^{3+} assay

Preparation of PolyCHbFe^{3+}: Dilute PolyCHb sample 40 times with PBS, add 0.1 M potassium ferricyanide solution with 1.5 times molar concentration of heme, and detect every 10 min until PolyCHb has been completely oxidized, and the content of PolyCHbFe^{3+} will not increase. Then use ultrafiltration centrifuge tube to repeatedly ultrafiltration for 6 times, and filter by 0.22 μM membrane, and calculate the prepared PolyCHbFe^{3+} heme concentration again.

By changing the AA addition amounts, the mole ratios in PolyCHbFe^{3+} solutions between AA and PolyCHbFe^{3+} were adjusted to be 0, 1, 2, and 3, respectively. The reduction reaction was started with the AA addition at the temperature of 37°C. The MetHb contents in PolyCHbFe^{3+} solutions were tested every hour until 12 h.

2.7 MetHb content measurement

The oxidation degrees of PolyCHb sample solutions were illustrated by the MetHb content, which was measured by the published equations (Benesch et al., 1973). Calculate the hemoglobin oxidation rate constant (Kox) according to the following formula:

$$Y = Y_{max}\left(1 - e^{-kt}\right) + Y_0$$

Where, t represents the measurement time point, Y represents the sample's methemoglobin content, Y_{max} represents the highest methemoglobin content during the experiment, Y_0 represents the initial value of methemoglobin, and K represents the sample's oxidation rate. For oxidation reaction, the calculated K value is expressed in Koxidation, which is called K_{ox} for short. For the reduction reaction, the calculated K value is negative, so the reduction reaction can be understood as a "negative oxidation" reaction, and its absolute value is taken to represent the reduction rate Kreduction, or K_{re} for short.

2.8 Animals and surgical procedures

Male Hartley guinea pigs weighing 300–400 g were purchased from Chengdu Dossy experimental animals Co., Ltd. (Chengdu, China). Each guinea pig was assigned to the sham group ($n = 5$), ET group ($n = 5$), or ET + AA treatment group ($n = 5$). All animals were kept in standard conditions for 1 week as the acclimation period and they had free access to food and water. Then, the animals were restricted to food for 12 h and restricted to water for 2 h and anesthetized by IP injection of 40 mg/kg sodium pentobarbital. After shaving, a midline incision was made at the anterior neck, followed by blunt dissection to expose the right common carotid artery and the left external jugular vein. A tunnel under the skin was built using an anesthetic puncture trocar from the back of the neck to the edge of the midline incision. A PE50 tube filled with saline containing 500 IU/mL heparin was nested in the trocar and embedded in the tunnel by extracting the trocar. The outer end of the tube was connected to the heparin cap, and the inner end of the tube was intubated to each vessel. Immediately after the surgery, the animals were administrated a subcutaneous dose of meloxicam (1 mg/kg) and then were individually housed to recover for 24 h. The animal study protocol was approved by the Institutional Ethics Committee of the Institute of Blood Transfusion, Chinese Academy of Medical Sciences, and Peking Union Medical College (protocol code 2018032, approved on 31 Aug 2018).

2.9 Exchange transfusion operation

Fully conscious, heparinized animals underwent 50% ET with PolyCHb solution (Hb concentration 6%, human albumin 4%; the PolyCHb and human albumin were mixed immediately before ET). The blood was collected through the arterial catheter, and the PolyCHb solution was transfused through the venous catheter by syringe pumps simultaneously at a rate of 1 mL/min. The total blood volume of a guinea pig was calculated as 0.07 (milliliters per gram) × body weight

(grams) (Ancill, 1956). Immediately after ET, AA injection solution was injected to the body *via* the venous catheter, by a 1 mL disposable syringe. The dosage of AA is calculated by multiplying the target concentration (2 mmol/L) with the blood volume. Blood samples (300 μL) were obtained from the arterial catheter pre-transfusion together at 0 and 4 h after ET. The guinea pigs were individually housed in metabolism cages for 4 h pre- and post-ET to collect the urine samples. The animals were sacrificed 4 h post-ET and the kidneys were dissected and rinsed with pre-cold saline. One kidney was cut in half and frozen immediately in liquid nitrogen, and the other kidney was fixed in 10% paraformaldehyde.

2.10 Blood/urine testing

Whole blood, collected immediately pre- and post-ET, was measured by an automated blood counter system (BC-5800, Mindray Corp., China) to record the drop in hematocrit. Urine samples were used to analyze 1) the concentration of hemoglobin (BC-5800, Mindray Corp., China) and 2) wavelength scans (DU800, Beckman) to calculate the percentage of ferric Hb, using equations for the spectrophotometric analysis of hemoglobin mixtures (Benesch et al., 1973). All urine samples (diluted five times by 0.01M, pH 7.2 PBS) and plasma samples (diluted 20 times by 0.01 M, pH 7.2 PBS) from the whole blood collected at 0- and 4-h post-ET were used to check the PolyCHb polymer distribution (HPLC platform Waters e2695 separation module and Waters e2498 UV detector). The stationary phase was Zenix SEC-300 (300 × 7.5 mm) column, the mobile phase was 0.1 M phosphate buffer, pH 6.5, the flow rate was 0.5 mL/min, and the absorbance was monitored at 410 nm.

2.11 Histopathology

The kidneys were fixed in 10% paraformaldehyde immediately after harvest, embedded in paraffin after dehydrating, and then 5 μm sections were cut and stained following standard hematoxylin and eosin procedures. The tissue sections were scored by a certified veterinary pathologist using semiquantitative grading criteria modified from an established one (Eadon et al., 2020). Generally, changes were recorded by the veterinary pathologist by observing the percentages of kidney parenchyma affected and then sort them to different terms (absent, mild, moderate, or diffuse). Final determinations were categorized on a scale from 0 to 3, with 0 corresponding to absence or <5% of kidney affected; 1− mild or 5%–25% of the kidney affected; 2−moderate or 26%–50% of the kidney affected; and 3−diffuse or >50% of the kidney affected.

2.12 Antioxidant assay

Colorimetric assay kits were used for measuring the T-AOC, CAT, SOD, and GPx activity in renal tissue homogenates. All assay procedures performed were according to the manufacturer's instructions. The T-AOC is expressed as mmol/g protein and all the enzyme activities are expressed as U/mg protein.

2.13 Lipid and DNA peroxidation assay

Lipid peroxidation was assessed using a colorimetric assay kit, by measuring free MDA as decomposition products of lipid peroxides, and DNA peroxidation was measured using an enzyme-linked immunoassay kit that measures 8-OHdG as a marker of DNA peroxides. All assay procedures were performed according to the manufacturers' instructions. The values of the MDA and 8-OHdG were calculated as μmol/mg and ng/mL, respectively.

2.14 Western blotting

Kidney tissue (cross-sectional cut through the center of the kidney, 200 mg) was homogenized in ice-cold lysis buffer (50 μM Tris-HCl, pH 7.4, 150 μM NaCl, 0.25% deoxycholic acid, 1% NP-40, 1 mM EDTA), containing Halt Protease Inhibitors Cocktail (Thermo Fisher Scientific). Homogenates were incubated for 10 min on ice and then centrifuged at 10,000 g for 10 min. Supernatants were divided into several aliquots and stored at −80°C. The protein concentration of the aliquots was analyzed by the BCA method. The proteins were separated *via* gel electrophoresis and then transferred onto PVDF membranes. The membranes were blocked in Tris-buffered saline (pH 7.4) containing 0.01% Tween-20% and 5% skim milk. Next, they were incubated with antibodies to Nrf2, HO-1, Ferritin, and 4-HNE at 4°C overnight with gentle shaking. The proteins were visualized using the ECL kit. Equal loading was confirmed by re-probing the blots with a rabbit polyclonal antibody to *ß*-Actin. Finally, the relative intensities were calculated as a densitometric ratio between the sample and *ß*-Actin by the ImageJ program (V1.8).

2.15 Statistical analysis

All parameters obtained from each group were expressed as the means ± S.E.M. for the data in each group. For comparison of the urine Hb and blood hematocrit between the ET and ET + AA groups, unpaired Student's t-tests were performed. For all the statistical comparisons among the three groups, ordinary one-way ANOVA tests with Tukey *post hoc* analysis were used. All the statistical calculations were processed by Graph Pad Prism 8.0 software (Graph Pad Software, CA, United States). A $p < 0.05$ was taken as the level of statistical significance (mark: * $p < 0.05$; ** $p < 0.01$; *** $p < 0.001$). The number of replicates in the characterization of PolyCHb is three. The number of replicates in the Western blotting was four, and the number of replicates in all other experiments in this study was five.

3 Results

3.1 CD analysis

The effects of antioxidant reaction by AA on the secondary structures of PolyCHb were investigated by the CD analysis and the results were shown in Figure 1. As reported previously, there were two negative peaks and one positive peak at the wavelength of 208,

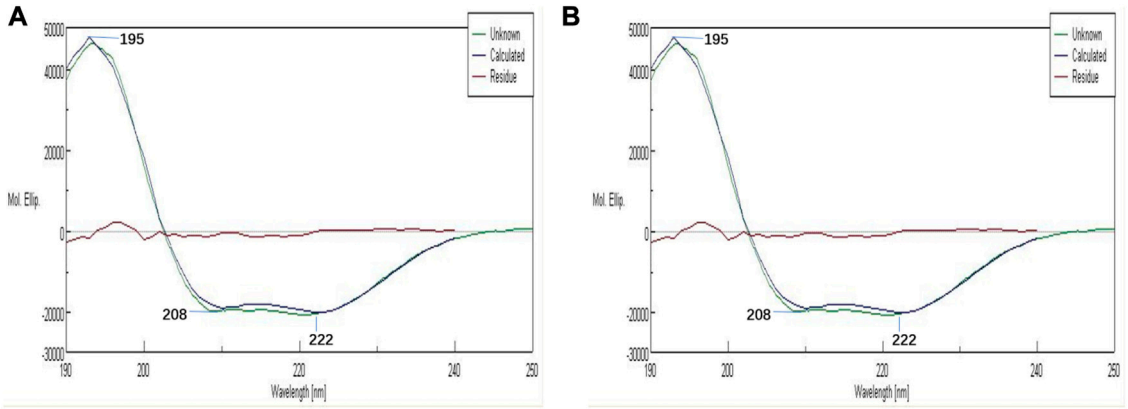

FIGURE 1
CDs of PolyCHb before **(A)** and after**(B)** AA addition.

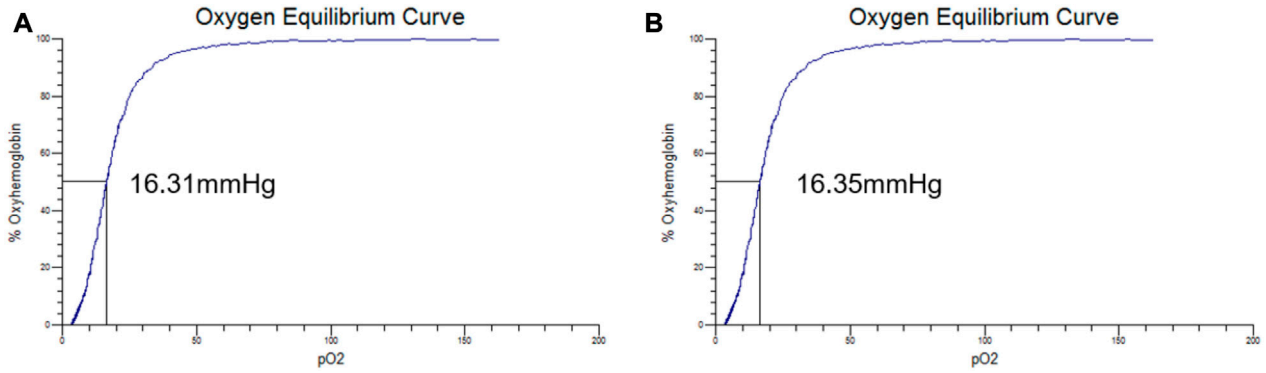

FIGURE 2
The oxygen equilibrium curve of PolyCHb, **(A)**, before AA addition, **(B)**, 72 h after AA addition.

222, and 195 nm in Figure 1A. As for the PolyCHb solution 72 h after AA addition, Figure 1B showed that the CD analysis curve presented almost no differences with that of PolyCHb solution before AA addition. Thus, it could be concluded that there was no effect of AA antioxidant reactions on the secondary structure of the PolyCHb molecules.

3.2 Oxygen binding affinity assay

The oxygen equilibrium curves of PolyCHb solution before and 72 h after AA addition are shown in Figures 2A, B. It could be seen that the curves before and after the AA addition were almost the same, and the P50 values presented in the two curves were about 16.31 ± 0.25 and 16.35 ± 0.31 mmHg, and Hill coefficient (Hill co) characterizing the synergistic effect between subunits of Hb solution obtained from the oxygenation curve was 2.65 ± 0.14 and 2.63 ± 0.12 (n = 3), which suggested that the AA addition did not alter the oxygen binding affinity of PolyCHb.

3.3 *In vitro* antioxidant assay

As shown in Figure 3A, in the presence of H_2O_2 and absence of AA, the MetHb contents in PolyCHb solution increased from the initial value 49.75% to more than 65.00%, indicating the oxidant effect of H_2O_2 for PolyCHb. After addition of AA, the MetHb contents gradually decreased with the AA content increasing. When the AA addition amounts increased to 300 μM, the MetHb content nearly kept constantly, and the Kox was significantly lower than other groups (Figure 3B). Therefore, it could be suggested that AA plays an activity similar to catalase, reducing the oxidation of H_2O_2 to hemoglobin.

3.4 Reduction of PolyCHbFe^{3+} assay

As shown in Figure 4A, the prepared PolyCHbFe^{3+} is light brown in appearance, and the content of MetHb is 99.3% ± 1.35%. Full-wavelength scanning diagram (Figure 4B) showed that PolyCHbFe^{2+} has characteristic absorption peaks at 541 and

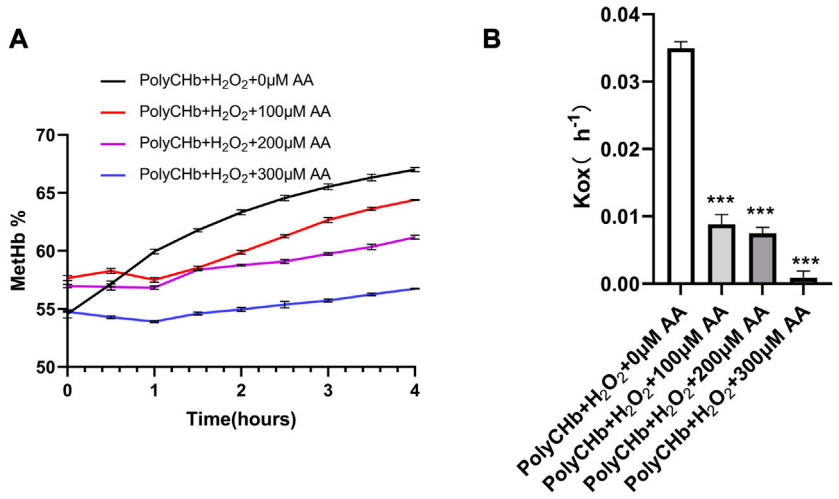

FIGURE 3
Intervention of AA on PolyCHbFe^{2+} oxidation under H_2O_2 at 37°C, **(A)**, the content of MetHb before and after AA addition, **(B)**, the Kox before and after AA addition, Values are expressed as mean ± SEM, n = 3.

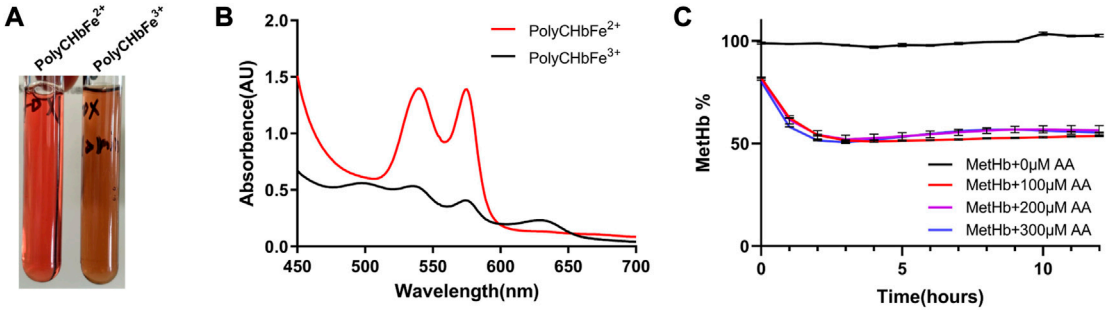

FIGURE 4
A), the appearance of PolyCHbFe^{2+} and PolyCHbFe^{3+}, **(B)**, the full-wavelength scanning diagram of PolyCHbFe^{2+} and PolyCHbFe^{3+}, **(C)**, the content of MetHb before and after AA addition. Values are expressed as mean ± SEM, n = 3.

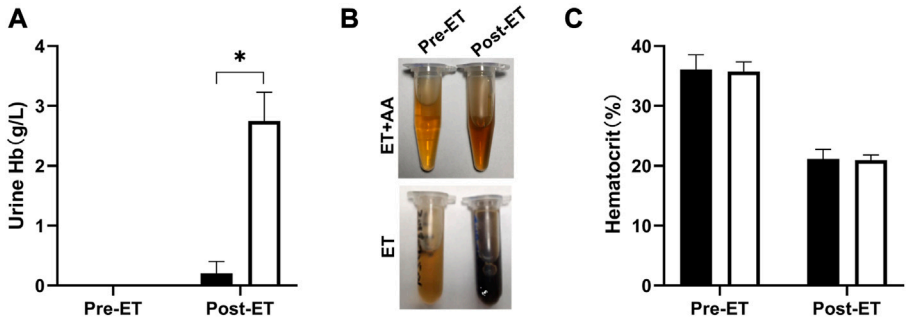

FIGURE 5
Hemoglobin levels of urine samples and hematocrit pre-ET and post-ET. **(A)** Urine Hb concentration of one animal in the ET + AA group (filled open bars) and ET group (open bars). **(B)** Picture of urine samples in the two groups. The upper picture is from one animal in the ET + AA group, the lower picture is from the ET group. In each picture, the left tube contains urine pre-ET, the right tube contains urine post-ET. **(C)** Hct drop after exchange transfusion in the ET + AA group. Values are expressed as mean ± SEM, n = 5.

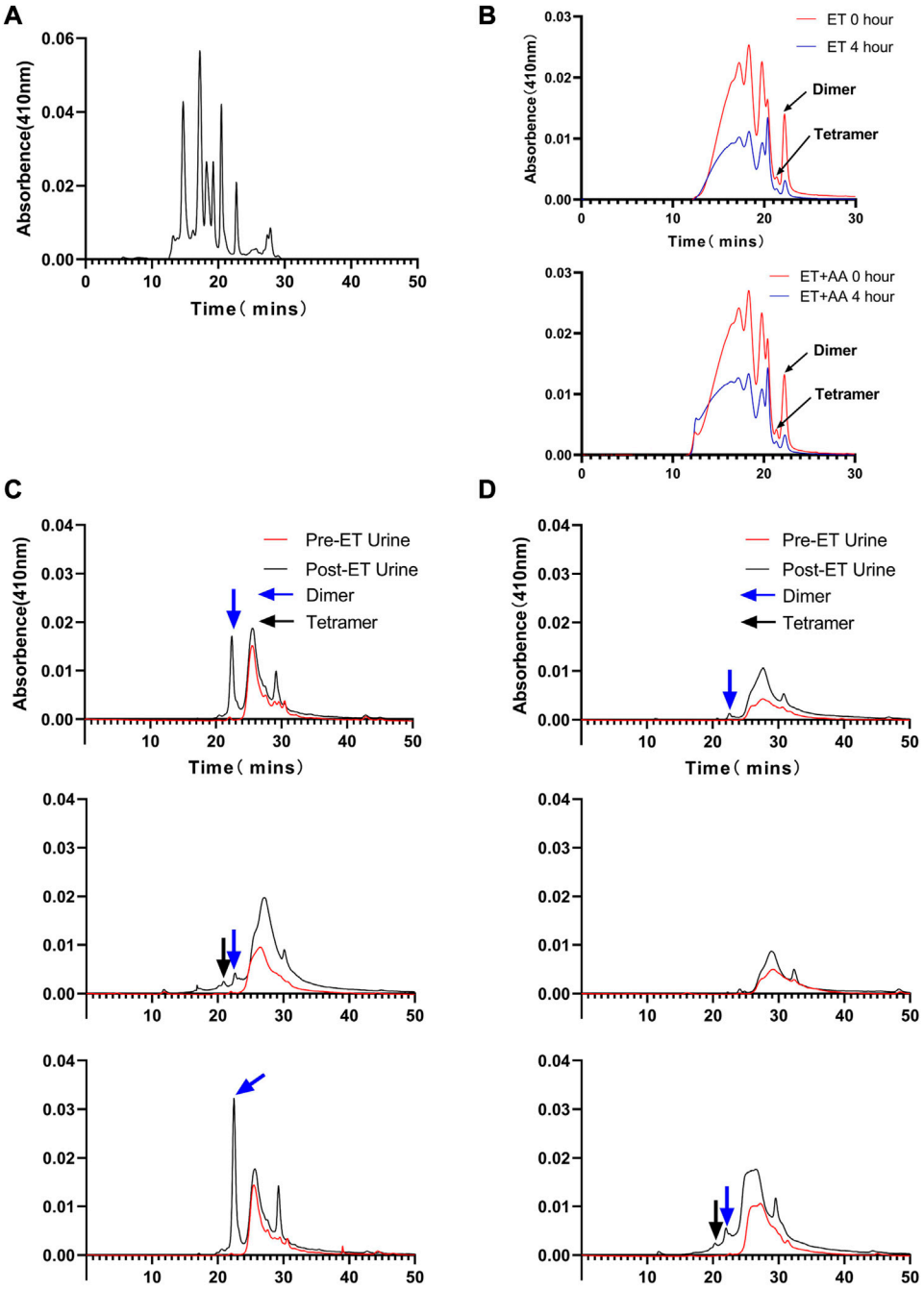

FIGURE 6
Size-exclusion chromatography distribution of heme in urine samples collected from ET group and ET + AA group. **(A)** Markers ran in parallel with samples. **(B)** Results of 0 and 4 h post-ET plasma samples; the upper panel is from one animal in the ET group, the lower panel is from one animal in the ET + AA group. **(C)** Results of three samples collected from single animals in the ET + AA group. **(D)** Results of three samples collected from single animals in the ET group.

576 nm, and the prepared PolyCHbFe^{3+} has characteristic absorption peaks at 500 and 630 nm. Compared with the group without AA, after adding 100、200、300 μM AA, the reduction of PolyCHbFe^{3+} was significantly promoted, and the content of MetHb could be reduced from nearly 100% to 51% within 3 h (Figure 4C). This suggests that AA has a strong reduction effect on the oxidized PolyCHb.

3.5 Ascorbic acid inhibits the formation of PolyCHb-induced hemoglobinuria

Urine samples from individual animals were collected 4 h pre- and post-ET separately. All the urine samples collected pre-ET were clear, and no hemoglobin was detected by the blood analyzer. For the post-ET urine samples in the ET + AA group, one urine sample

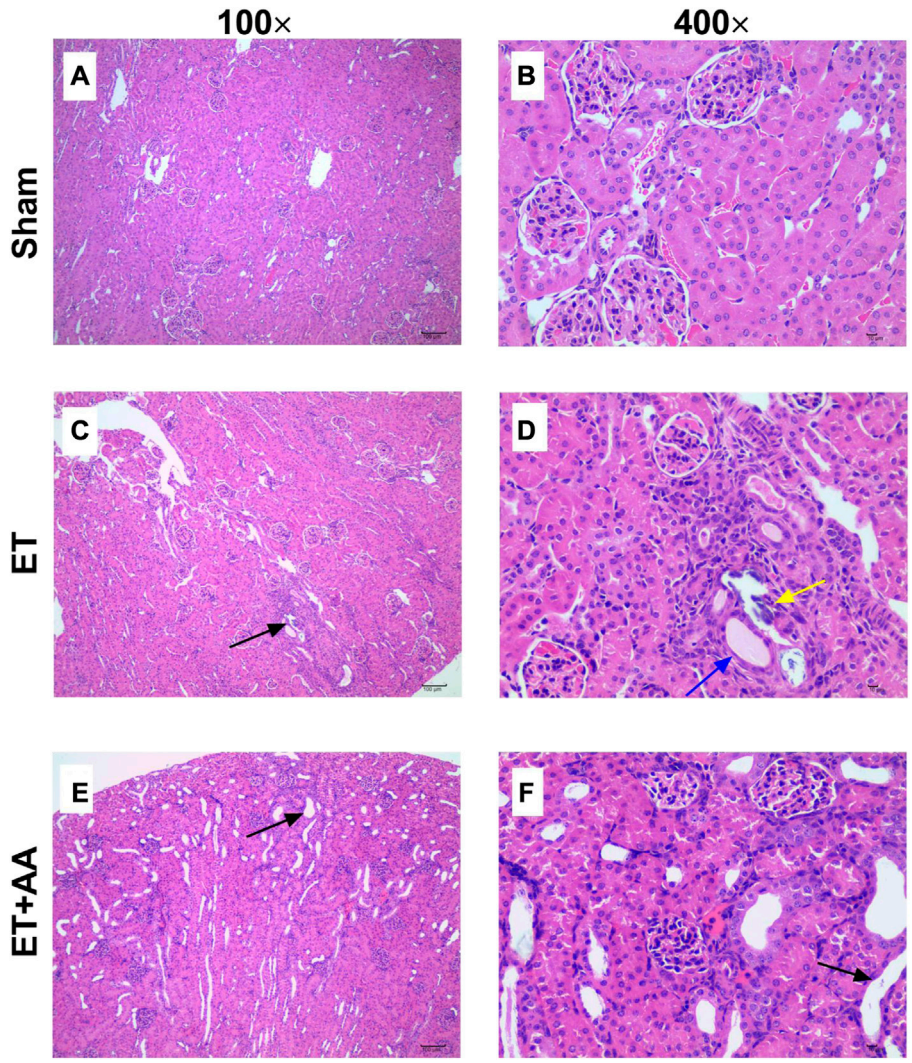

FIGURE 7
Kidney histopathological evaluation of guinea pigs in the sham, ET, and ET + AA groups. Hematoxylin and eosin-stained kidney harvested in the sham **(A,B)**, ET **(C,D)**, and ET + AA **(E,F)** groups. Magnification at ×100 **(A,C,E)** and ×400 **(B,D,F)**. In the sham group, there was no histopathological changes. In the ET group, there was local tubular epithelial necrosis [**(C)**, black arrow], glomerular micro thrombosis [**(D)**, black arrow], tubular epithelial necrosis [**(D)**, yellow arrow], and squamous epithelium [**(D)**, blue arrow]. In the ET + AA group, mild dilation of renal tubules [**(E)**, black arrow)] and flat epithelial cells [**(F)**, black arrow] can be observed.

contained 1 g/L Hb, and the other four samples contained no Hb. Instead, Hb in urine samples in ET group increased significantly (2.75 ± 0.48 g/L). The color of all the collected urine samples was dark brown, indicating the presence of ferric hemoglobin. (Figures 5A, B); the percentage of ferric Hb was 90.20% ± 1.3%. The size-exclusion chromatography distribution curve showed that before ET, all the urine samples collected in the two groups contained trace amounts of hemoglobin in the form of dimer and degradants, although it was not detectable by the blood analyzer (Figure 5A). Compared with the markers (Figure 6A), after ET, the Hb concentration in the urine samples increased in the ET group. The major form of excreted Hb was still dimer and degradants, with a slight increase in tetramer (Figures 6C, D). It can be concluded that after the PolyCHb infusion, there was an increase in filtered hemoglobin to the kidney proximal tubular. The size-exclusion chromatography curves of infused PolyCHb in the plasma demonstrated that all the different polymer portions showed a synchronous degradation during the 4-h metabolic course (Figure 6B). The post-ET urine samples contained no significantly increased tetramer (64 kDa) or biomacromolecule with a bigger molecular weight. It can be concluded that the polymers in the infused PolyCHb were stable *in vivo*, and there was neither a quick breakdown of the polymers nor an accumulation of dimers in the circulation. The AA co-administration eliminated the phenomenon of hemoglobinuria. In addition, the ET operation was accompanied by a loss of red blood cells, which play an important role in the recycling of ascorbic acid from its oxidized forms, the ascorbate free radical and dehydroascorbic acid (May et al., 2004). Here, the drop in hematocrit was identical between the two groups (from 35.74% ± 1.61% to 20.96% ± 0.86% in the ET

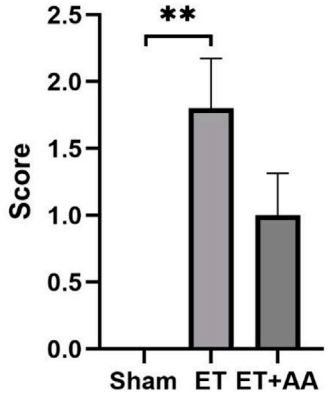

FIGURE 8
Histopathology scores of the kidneys in the sham, ET, and ET + AA groups. Values are expressed as mean ± SEM, n = 5.

group vs. from 36.12% ± 2.44% to 21.14% ± 1.62% in the ET + AA group) (Figure 5C), therefore, the difference between ET group and ET + AA group has nothing to do with the loss of red blood cells during ET.

3.6 Histopathology

Microscopic observation by 100 times and 400 times magnification showed the existence of histopathological change in the ET and ET + AA groups, whereas there was no microscopic change in the sham operation group (Figures 7A, B). The histopathology scores in the ET and ET + AA group were 1.8 ± 0.37 and 1.0 ± 0.32 respectively. (Figure 8).

In detail, in the sham group, the capsule of renal tissue was intact, and the boundary between cortex and medulla was clear. The glomerular structure of the cortical area was normal, and there was no obvious expansion of the capillaries and no basement membrane thickening. The renal tubular epithelial cells have normal morphology, uniform cytoplasmic staining, large and round nuclei, and no obvious degeneration and necrosis. There was no obvious fibrous tissue proliferation or inflammatory cell infiltration in the renal stroma. The structure of the medullary collecting duct was complete and clear, and no obvious pathological changes were found. However, in three cases (3/5) of ET group (Figures 7C, D), some glomerular structures in the cortex were abnormal, with capillary dilation, and a small number of lumens were filled with uniform, unstructured and slightly stained microthrombosis. In four cases (4/5), a small amount of renal tubular degeneration was found, with a slight expansion of renal tubules, flat epithelial cells, swelling of nuclei, and loss of some nuclei. One case (1/5) had local degeneration and necrosis of the renal tubular epithelium, necrosis and abscission of renal tubular epithelial cells in the necrotic area, and regeneration of renal tubular cells. Finally, In the ET + AA group (Figures 7E, F), three cases (3/5) had a small amount of local tubular degeneration, with a slight expansion of renal tubules, flat epithelial cells, swollen nuclei, and partial loss of nuclei. One case (1/5) showed local degeneration and necrosis of the renal tubular epithelium and necrosis and abscission of the renal tubular epithelial cells in the necrotic area.

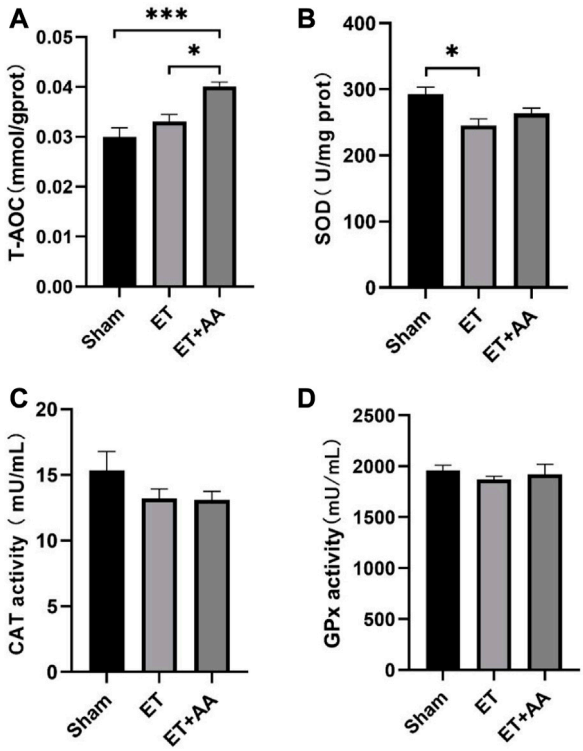

FIGURE 9
T-AOC and enzyme activities of kidney tissue 4 h post-ET in the sham, ET, and ET + AA group. **(A)** Total Antioxidant Capacity. **(B)**, SOD activity. **(C)**, CAT activity. **(D)**, GPx activity. Values are expressed as mean ± SEM, n = 5.

3.7 Ascorbic acid increases the total antioxidant capacity of kidneys in exchange transfused Guinea pigs

It is reported that the infusion of polymerized bovine Hb may affect the functional state of the antioxidant defense system (Rentsendorj et al., 2016), so it is speculated that PolyCHb should have a similar effect. To determine the effect of PolyCHb on the renal antioxidant enzyme response, the antioxidant enzyme activities and the T-AOC of the kidney tissue 4 h after PolyCHb exposure were measured. Compared to the sham and ET groups, the T-AOC in the ET + AA group was significantly increased (Figure 9A). SOD activity in the ET group was suppressed (Figure 9B), and CAT activity and GPx activity were not interrupted (Figures 9C, D). The detailed data are listed in the Supplementary Table S1.

3.8 Ascorbic acid alleviates the lipid and DNA peroxidation of the kidney

Lipid peroxidation is characterized by the oxidative degradation of polyunsaturated fatty acids attacked by free radicals. MDA is one of the

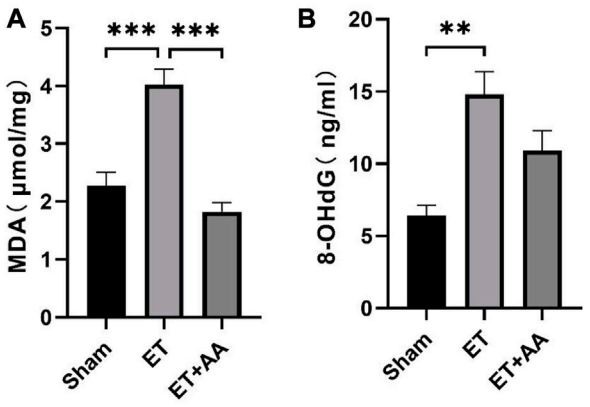

FIGURE 10
Kidney MDA and 8-OHdG levels pre- and post-ET in the sham, ET, and ET + AA groups. **(A)**, MDA levels, **(B)**, 8-OHdG levels. Values are expressed as mean ± SEM, n = 5.

commonly used biomarkers for lipid peroxidation (Frijhoff et al., 2015). In our previous research, MDA was increased in the organs of rats when they were exposed to PolyCHb. In this study, MDA increments were found in the ET group, indicating peroxidation in the kidneys of guinea pigs exposed to PolyCHb. Compared to the ET group, the MDA in the ET + AA group dropped to the base line (Figure 10A). 4-HNE is a lipid peroxidation product of n-6 polyunsaturated fatty acid, and measurement of 4-HNE-modified protein adducts has become a reliable biomarker of *in vivo* oxidative stress (Poli et al., 2008). In this study, it was found that there was no detectable 4-HNE in the sham group. However, in the ET group, there was a dramatic increase in the 4-NHE levels when they were exposed to PolyCHb. In the ET + AA group, the levels of 4-HNE were significantly lower compared to those of the ET group (Figure 11A), which indicates the effectiveness of AA on polyCHb-induced lipid peroxidation. 8-OHdG is the product of free radical-induced DNA oxidative damage and is a biomarker for oxidative stress. Similar to the results of MDA, the 8-OHdG levels increased in the kidney when PolyCHb was infused. AA can inhibit the formation of 8-OHdG when co-administrated with PolyCHb (Figure 10B). The detailed data are listed in Supplementary Table S1.

3.9 Ascorbic acid attenuates oxidative stress in the kidney of Guinea pigs exchange transfused with PolyCHb

It is reported that kidney exposure to Hb can activate heme catabolism pathway (i.e., HO-1, ferritin) (Butt et al., 2010) to enhance heme metabolism. The Western Blot results of 4-HNE, Ferritin and HO-1 are shown in Figure 11E, and the results were expressed by the relative expression of target protein, and the relative expression of target protein = the integral optical density (IOD) of target protein/the integral optical density (IOD) of internal reference. Figure 11B showed that Nrf2 expression increased in the ET group compared to the sham and ET + AA groups. HO-1 and

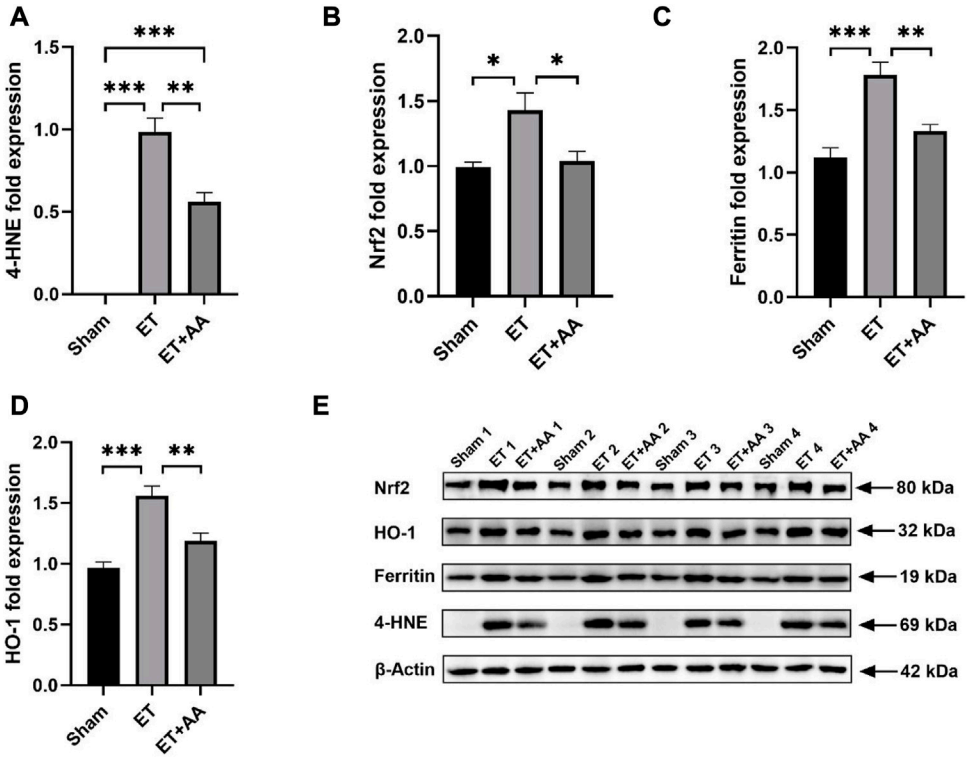

FIGURE 11
Effect of ascorbic acid on alleviating oxidative stress in the kidneys of guinea pigs. **(A–D)** Graphic representation of the fold expressions of 4-HNE, Nrf2, ferritin, and HO-1, respectively. **(E)** Image of the Western blotting assay. Values are expressed as mean ± SEM, n = 4

ferritin expression increased in the kidney tissue in the ET group, and AA lowered their expression levels to the baseline. (Figures 11C, D). Thus, it can be deduced that in the ET group, there was a higher degree of oxidative stress, and the system upregulated the Nrf2 to prepare to further strengthen the activity of antioxidant enzymes. The detailed data are listed in the Supplementary Table S1.

4 Discussion

Hemoglobin functions as an oxygen supplier through the process of combining and releasing oxygen [$HbFe^{2+}+O_2 \rightleftarrows HbFe^{2+}(O_2)$]. In this process, hemoglobin can also be oxidized to MetHb, which generates superoxide ions. Therefore, it should pay attention to the autoxidation of hemoglobin on the HBOC research. In this study, PolyCHb was prepared from HbF by chemical crosslinking, and the results of adding AA to PolyCHb indicated that there was no effect of AA antioxidant reactions on the secondary structure of the PolyCHb molecules and the oxygen binding affinity of PolyCHb. In addition, AA plays an activity similar to catalase, reducing the oxidation of H_2O_2 to hemoglobin and has a strong reduction effect on the oxidized PolyCHb, which plays an important role in maintaining the status of reduced hemoglobin in the body.

In vivo study, AA was used as a small molecular antioxidant to evaluate the effect of hemoglobin oxidation on renal stress in guinea pig exchange model. AA co-administration with PolyCHb was compared with the sham group and the ET group in terms of renal oxidative stress. It has been proved that PolyCHb infusion causes oxidative stress and damage to the kidney of guinea pigs. Furthermore, it was also found that AA had a significant effect on controlling the oxidative stress in the kidneys and inhibiting the formation of hemoglobinuria after PolyCHb infusion.

Under normal physiology conditions, Hb is packed in the red blood cells and protected by enzymes such as CAT, GSH, and GPx to prevent oxidation (Rifkind et al., 2014). Transfusion of HBOC into the blood circulation can "create a potentially dangerous oxidative environment by generating redox oxygen radicals" (Buehler and Alayash, 2010), and actually, oxidative stress is a major safety concern for the clinical application of HBOC. Different from the control of Hb auto-oxidation in the RBC, the control of circulating HBOC in plasma is not directly enzymatic but instead controlled by small molecule reducing agents, such as AA, and GSH (Buehler and Alayash, 2010). Under such circumstances, "endogenous plasma-reducing systems may be easily overwhelmed by the infusion of a high-dose of HBOC" (D'Agnillo, 2013). Exchange transfusion in this study caused a heavy exposure of PolyCHb in the blood circulation. The PolyCHb solutions used in this study contained less than 3% dimer, and hemoglobinuria did not occur when it was transfused to rats in our previous studies. However, in this study, hemoglobinuria formed post-ET in the guinea pigs in the ET group. This difference between rats and guinea pigs confirms the necessity of using guinea pigs in the preclinical study of PolyCHb. In addition to our findings, other studies have also demonstrated that when transfused with polymerized bovine Hb, hemoglobinuria could also be found in guinea pigs (Boretti et al., 2009; Butt et al., 2010). Considering that guinea pigs are prone to form hemoglobinuria when exposed to HBOC, together with the fact that there was no hemoglobinuria in the ET + AA group, AA showed a solid effect on eliminating the formation of hemoglobinuria in this study. This effect is of great significance to the clinical application of HBOC. The reason is that if hemoglobinuria occurs during the clinical application of HBOC, it is difficult for doctors to find out the reason, because it may be due to the dimer in HBOC, or hemolysis or rhabdomyolysis. Thus, from a clinical point of view, if AA is further confirmed to inhibit the formation of hemoglobinuria in clinical trials, hemoglobinuria will not be a major concern when using PolyCHb.

Acellular hemoglobin is particularly prone to oxidation and then denaturation, accompanied by heme release and free radical formation (Reeder, 2010), especially dimers are extremely prone to oxidation (Marden et al., 1995). In this study, the urine samples of the ET group were confirmed to contain ferric Hb dimers. The dimers in urine were filtered from the circulation through glomeruli and then taken up by proximal tubular cells. Further, they were excreted when the tubular reabsorption capacity was exceeded. In the process of heme catabolism, heme oxygenase (HO) is a rate-limiting enzyme, which can be upregulated by heme and hypoxia. There are two isoforms of HO—HO-1 and HO-2. HO-1 is the inducible isoform, expressed at a low level in the kidney under basal conditions, but its expression is regulated by a wide variety of physiologic and pathophysiologic stimuli (Drummond et al., 2019), and it plays a protective role in the heme protein-mediated renal injury (Nath et al., 1995). Additionally, the nuclear factor erythroid 2-related factor 2 (Nrf2)-Kelch-like ECH-associated protein 1 (KEAP1) regulatory pathway plays a vital role in protecting cells and tissues from oxidative damage (Panieri et al., 2020). The mechanism of Nrf2 in the defense against oxidative stress is that it can activate the expression of antioxidant enzymes and HO-1 (Rubio-Navarro et al., 2019). In this study, PolyCHb infusion in the ET group was accompanied by the elevation of Nrf2. AA treatment lowered the level of Nrf2, indicating the body's response to PolyCHb infusion by activating the anti-oxidative system. The enzyme activity had no significant alarm 4 h post-ET; we assume that this is because it takes a period of time from the upregulation of Nrf2 to the activation of downstream enzyme expression. Observation more than 4 h after ET will help to find further relationship.

As AA can eliminate the hemoglobinuria in this study, the difference of HO-1 and ferritin between the ET and ET + AA groups proved that AA upregulated the Hb reabsorption capacity of proximal tubular cells, and the filtered dimers were reabsorbed in the renal tubules. In contrast, in the ET group without AA prevention, filtered dimers were not fully reabsorbed and were pooled in the bladder. HO catalyzes the degradation of heme into biliverdin, iron, and CO, and it is an important molecular in protecting against acute heme protein-induced nephrotoxicity and other forms of acute tissue injury (Nath et al., 2001; Tracz et al., 2007). HO-1 upregulation is often accompanied by ferritin induction, aim to trap iron released from Hb subunit and limit oxidative stress (D'Agnillo, 2013). Another study demonstrated that HO-1 induction was beneficial for protecting the kidneys from injury by *in vitro* and preclinical models (Nath and Agarwal, 2020). In this study, the expressions of HO-1 and ferritin in the ET group was higher than that in sham group, indicating the presence of metabolic stress for heme in this group. AA treatment lowered the expressions of HO-1 and ferritin in the ET + AA group, and decreased other oxidative biomarkers, including MDA, 4-HNE, and 8-OHdG. Along with the histopathological

changes, AA showed an exact protection role in alleviating the oxidative stress in kidneys when co-administrated with PolyCHb.

As an electron donor, AA is a potent water-soluble antioxidant. Its antioxidant effect has been demonstrated in many applications. For example, AA has been widely used for the reduction of lipid peroxidation in cancer treatment (Reang et al., 2021), oxidative damage induced by degenerative diseases, and other stimulations (Ghosh et al., 1996; Panda et al., 2000). Another beneficial characteristic of AA is the wide-ranging safety, and it is safe when even used at high doses. When using HBOC, the difference between AA-producing animals and non-AA-producing animals also indicates the important role of AA in previous studies. Additionally, this study inspired and confirmed that the selection of animal species is important during the preclinical study of PolyCHb. Usually, rats are the most commonly used animal in the standard pre-clinical toxicology evaluation of HBOC (Newmark, 2014), but guinea pigs should be added to the evaluation list to focus on the evaluation of oxidative stress and renal side effects of the acellular Hb-based blood substitute.

There are still several limitations of this study. Firstly, although we proved that AA could prevent the formation of methemoglobinuria after PolyCHb infusion, the exact mechanism should be further investigated. Secondly, the optional dosing and co-administration method of AA together with PolyCHb infusion needs to be further studied in detail. Finally, more test time points, for example, 8, 12, 24, and 48 h, should be added to confirm the changes during the dynamic time course and the best AA prevention strategy.

Data availability statement

The original contributions presented in the study are included in the article/Supplementary Material, further inquiries can be directed to the corresponding author.

Ethics statement

The studies involving human participants were reviewed and approved by Ethics Review Committee of Institute of Blood Transfusion, Chinese Academy of Medical Sciences. Written informed consent for participation was not required for this study in accordance with the national legislation and the institutional requirements. The animal study was reviewed and approved by Ethics Review Committee of Institute of Blood Transfusion, Chinese Academy of Medical Sciences.

Author contributions

JL and WK conceptualized the study and designed the experiments; WZ and SL developed the PolyCHb solution and applied for the funding; WK and XZ performed the experiments and analyzed the data; WK wrote the manuscript; RZ, ZH, and XZ made the manuscript revisions. All authors have read and agreed to the published version of the manuscript.

Funding

This study was supported by grants from the CAMS Innovation Fund for Medical Sciences (CIFMS), No. 2017-I2M-3-021 and No. 2021-I2M-1-060.

Acknowledgments

We would like to acknowledge the Chengdu Lilai Biomedicine Experiment Center for the assis-tance in the preparation of the histopathology samples and in determining the results.

Conflict of interest

The authors declare that the research was conducted in the absence of any commercial or financial relationships that could be construed as a potential conflict of interest.

Publisher's note

Supplementary material

The Supplementary Material for this article can be found online at: https://www.frontiersin.org/articles/10.3389/fbioe.2023.1151975/full#supplementary-material

References

Alayash, A. I. (2014). Blood substitutes: Why haven't we been more successful? *Trends Biotechnol.* 32 (4), 177–185. doi:10.1016/j.tibtech.2014.02.006

Alayash, A. I. (2019). Mechanisms of toxicity and modulation of hemoglobin-based oxygen carriers. *Shock* 52, 41–49. doi:10.1097/shk.0000000000001044

Ancill, R. J. (1956). The blood volume of the normal Guinea-pig. *J. Physiol.* 132 (3), 469–475. doi:10.1113/jphysiol.1956.sp005539

Benesch, R. E., Benesch, R., and Yung, S. (1973). Equations for the spectrophotometric analysis of hemoglobin mixtures. *Anal. Biochem.* 55 (1), 245–248. doi:10.1016/0003-2697(73)90309-6

Boretti, F. S., Buehler, P. W., D'Agnillo, F., Kluge, K., Glaus, T., Butt, O. I., et al. (2009). Sequestration of extracellular hemoglobin within a haptoglobin complex decreases its hypertensive and oxidative effects in dogs and Guinea pigs. *J. Clin. Invest.* 119 (8), 2271–2280. doi:10.1172/jci39115

Buehler, P. W., and Alayash, A. I. (2010). Oxidation of hemoglobin: Mechanisms of control *in vitro* and *in vivo*. *Transfus. Altern. Transfus. Med.* 9 (4), 204–212. doi:10.1111/j.1778-428X.2007.00081.x

Buehler, P. W., D'Agnillo, F., and Schaer, D. J. (2010). Hemoglobin-based oxygen carriers: From mechanisms of toxicity and clearance to rational drug design. *Trends Mol. Med.* 16 (10), 447–457. doi:10.1016/j.molmed.2010.07.006

Buehler, P. W., and D'Agnillo, F. (2010). Toxicological consequences of extracellular hemoglobin: Biochemical and physiological perspectives. *Antioxid. Redox Signal* 12 (2), 275–291. doi:10.1089/ars.2009.2799

Butt, O. I., Buehler, P. W., and D'Agnillo, F. (2010). Differential induction of renal heme oxygenase and ferritin in ascorbate and nonascorbate producing species transfused with modified cell-free hemoglobin. *Antioxid. Redox Signal* 12 (2), 199–208. doi:10.1089/ars.2009.2798

Chatterjee, I. B. (1973). Evolution and the biosynthesis of ascorbic acid. *Science* 182 (4118), 1271–1272. doi:10.1126/science.182.4118.1271

Cooper, C. E., Silaghi-Dumitrescu, R., Rukengwa, M., Alayash, A. I., and Buehler, P. W. (2008). Peroxidase activity of hemoglobin towards ascorbate and urate: A synergistic protective strategy against toxicity of hemoglobin-based oxygen carriers (HBOC). *Biochim. Biophys. Acta* 1784 (10), 1415–1420. doi:10.1016/j.bbapap.2008.03.019

D'Agnillo, F. (2013). "Redox activity of cell-free hemoglobin: Implications for vascular oxidative stress and endothelial dysfunction," in *Hemoglobin-based oxygen carriers as red cell substitutes and oxygen therapeutics*. Editors H. W. Kim and A. G. Greenburg (Berlin, Heidelberg: Springer Berlin Heidelberg), 665–682. doi:10.1007/978-3-642-40717-8_35

Dhibar, D. P., Sahu, K. K., Jain, S., Kumari, S., and Varma, S. C. (2018). Methemoglobinemia in a case of paint thinner intoxication, treated successfully with vitamin C. *J. Emerg. Med.* 54 (2), 221–224. doi:10.1016/j.jemermed.2017.10.035

Drummond, H. A., Mitchell, Z. L., Abraham, N. G., and Stec, D. E. (2019). Targeting heme oxygenase-1 in cardiovascular and kidney disease. *Antioxidants* 8 (6), 181. doi:10.3390/antiox8060181

Dunne, J., Caron, A., Menu, P., Alayash, A. I., Buehler, P. W., Wilson, M. T., et al. (2006). Ascorbate removes key precursors to oxidative damage by cell-free haemoglobin *in vitro* and *in vivo*. *Biochem. J.* 399 (3), 513–524. doi:10.1042/bj20060341

Eadon, M. T., Schwantes-An, T. H., Phillips, C. L., Roberts, A. R., Greene, C. V., Hallab, A., et al. (2020). Kidney histopathology and prediction of kidney failure: A retrospective cohort study. *Am. J. Kidney Dis.* 76 (3), 350–360. doi:10.1053/j.ajkd.2019.12.014

Frijhoff, J., Winyard, P. G., Zarkovic, N., Davies, S. S., Stocker, R., Cheng, D., et al. (2015). Clinical relevance of biomarkers of oxidative stress. *Antioxid. Redox Signal* 23 (14), 1144–1170. doi:10.1089/ars.2015.6317

Ghosh, M. K., Chattopadhyay, D. J., and Chatterjee, I. B. (1996). Vitamin C prevents oxidative damage. *Free Radic. Res.* 25 (2), 173–179. doi:10.3109/10715769609149922

Keipert, P. E., Gomez, C. L., Gonzales, A., Macdonald, V. W., and Winslow, R. M. (1992). The role of the kidneys in the excretion of chemically modified hemoglobins. *Biomater. Artif. Cells Immobil. Biotechnol.* 20 (2-4), 737–745. doi:10.3109/10731199209119712

Khan, F., Singh, K., and Friedman, M. T. (2020). Artificial blood: The history and current perspectives of blood substitutes. *Discov. (Craiova)* 8 (1), e104. doi:10.15190/d.2020.1

Marden, M. C., Griffon, N., and Poyart, C. (1995). Oxygen delivery and autoxidation of hemoglobin. *Transfus. Clin. Biol.* 2 (6), 473–480. doi:10.1016/s1246-7820(05)80074-6

May, J. M., Qu, Z. C., and Cobb, C. E. (2004). Human erythrocyte recycling of ascorbic acid: Relative contributions from the ascorbate free radical and dehydroascorbic acid. *J. Biol. Chem.* 279 (15), 14975–14982. doi:10.1074/jbc.M312548200

Nandi, A., Mukhopadhyay, C. K., Ghosh, M. K., Chattopadhyay, D. J., and Chatterjee, I. B. (1997). Evolutionary significance of vitamin C biosynthesis in terrestrial vertebrates. *Free Radic. Biol. Med.* 22 (6), 1047–1054. doi:10.1016/S0891-5849(96)00491-1

Nath, K. A., Balla, J., Croatt, A. J., and Vercellotti, G. M. (1995). Heme protein-mediated renal injury: A protective role for 21-aminosteroids *in vitro* and *in vivo*. *Kidney Int.* 47 (2), 592–602. doi:10.1038/ki.1995.75

Nath, K. A., Vercellotti, G. M., Grande, J. P., Miyoshi, H., Paya, C. V., Manivel, J. C., et al. (2001). Heme protein-induced chronic renal inflammation: Suppressive effect of induced heme oxygenase-1. *Kidney Int.* 59 (1), 106–117. doi:10.1046/j.1523-1755.2001.00471.x

Nath, M., and Agarwal, A. (2020). New insights into the role of heme oxygenase-1 in acute kidney injury. *Kidney Res. Clin. Pract.* 39 (4), 387–401. doi:10.23876/j.krcp.20.091

Newmark, J. A. (2014). Toxicology and safety determination for a novel therapeutic dual carbon monoxide and oxygen delivery agent. *J. Clin. Toxicol.* 04 (4). doi:10.4172/2161-0495.1000206

Panda, K., Chattopadhyay, R., Chattopadhyay, D. J., and Chatterjee, I. B. (2000). Vitamin C prevents cigarette smoke-induced oxidative damage *in vivo*. *Free Radic. Biol. Med.* 29 (2), 115–124. doi:10.1016/s0891-5849(00)00297-5

Panieri, E., Buha, A., Telkoparan-Akillilar, P., Cevik, D., Kouretas, D., Veskoukis, A., et al. (2020). Potential applications of NRF2 modulators in cancer therapy. *Antioxidants (Basel)* 9 (3), 193. doi:10.3390/antiox9030193

Pape, A., and Habler, O. (2007). Alternatives to allogeneic blood transfusions. *Best. Pract. Res. Clin. Anaesthesiol.* 21 (2), 221–239. doi:10.1016/j.bpa.2007.02.004

Poli, G., Schaur, R. J., Siems, W. G., and Leonarduzzi, G. (2008). 4-hydroxynonenal: A membrane lipid oxidation product of medicinal interest. *Med. Res. Rev.* 28 (4), 569–631. doi:10.1002/med.20117

Reang, J., Sharma, P. C., Thakur, V. K., and Majeed, J. (2021). Understanding the therapeutic potential of ascorbic acid in the battle to overcome cancer. *Biomolecules* 11 (8), 1130. doi:10.3390/biom11081130

Reeder, B. J. (2010). The redox activity of hemoglobins: From physiologic functions to pathologic mechanisms. *Antioxid. Redox Signal* 13 (7), 1087–1123. doi:10.1089/ars.2009.2974

Rentsendorj, O., Zhang, X., Williams, M. C., Buehler, P. W., and D'Agnillo, F. (2016). Transcriptional suppression of renal antioxidant enzyme systems in Guinea pigs exposed to polymerized cell-free hemoglobin. *Toxics* 4 (1), 6. doi:10.3390/toxics4010006

Rifkind, J. M., Mohanty, J. G., and Nagababu, E. (2014). The pathophysiology of extracellular hemoglobin associated with enhanced oxidative reactions. *Front. Physiol.* 5, 500. doi:10.3389/fphys.2014.00500

Rubio-Navarro, A., Vázquez-Carballo, C., Guerrero-Hue, M., García-Caballero, C., Herencia, C., Gutiérrez, E., et al. (2019). Nrf2 plays a protective role against intravascular hemolysis-mediated acute kidney injury. *Front. Pharmacol.* 10, 740. doi:10.3389/fphar.2019.00740

Silva, D. G. H., Belini Junior, E., de Almeida, E. A., and Bonini-Domingos, C. R. (2013). Oxidative stress in sickle cell disease: An overview of erythrocyte redox metabolism and current antioxidant therapeutic strategies. *Free Radic. Biol. Med.* 65, 1101–1109. doi:10.1016/j.freeradbiomed.2013.08.181

Tracz, M. J., Alam, J., and Nath, K. A. (2007). Physiology and pathophysiology of heme: Implications for kidney disease. *J. Am. Soc. Nephrol.* 18 (2), 414–420. doi:10.1681/asn.2006080894

Zhou, W., Li, S., Hao, S., Liu, J., Wang, H., and Yang, C. (2015). An optimal polymerization process for low mean molecular weight HBOC with lower dimer. *Artif. Cells, Nanomedicine, Biotechnol.* 43 (3), 148–151. doi:10.3109/21691401.2014.934455

frontiers | Frontiers in Bioengineering and Biotechnology

TYPE Original Research
PUBLISHED 05 May 2023
DOI 10.3389/fbioe.2023.1196521

OPEN ACCESS

EDITED BY
Meng Tian,
Sichuan University, China

REVIEWED BY
Donghai Li,
Sichuan University, China
Yang Kang,
Sun Yat-sen University, China

*CORRESPONDENCE
Peirong Yu,
peirongyu@mdanderson.org
Qixu Zhang,
qzhang5@mdanderson.org

†PRESENT ADDRESSES
Ning Zeng,
Plastic Surgery Department, Tongji Hospital, Tongji Medical College, Huazhong University of Science and Technology, Wuhan, China
Youbai Chen,
Department of Plastic and Reconstructive Surgery, Chinese PLA General Hospital, Beijing, China
Mengqing Zang,
Department of Plastic Surgery, Plastic Surgery Hospital, Chinese Academy of Medical Sciences and Peking Union Medical College, Beijing, China

‡These authors have contributed equally to this work and share first authorship

RECEIVED 29 March 2023
ACCEPTED 26 April 2023
PUBLISHED 05 May 2023

CITATION
Zeng N, Chen Y, Wu Y, Zang M, Largo RD, Chang EI, Schaverien MV, Yu P and Zhang Q (2023), Pre-epithelialized cryopreserved tracheal allograft for neo-trachea flap engineering.
Front. Bioeng. Biotechnol. 11:1196521.
doi: 10.3389/fbioe.2023.1196521

Pre-epithelialized cryopreserved tracheal allograft for neo-trachea flap engineering

Ning Zeng†‡, Youbai Chen†‡, Yewen Wu, Mengqing Zang†, Rene D. Largo, Edward I. Chang, Mark V. Schaverien, Peirong Yu* and Qixu Zhang*

Department of Plastic Surgery, The University of Texas MD Anderson Cancer Center, Houston, TX, United States

Background: Tracheal reconstruction presents a challenge because of the difficulty in maintaining the rigidity of the trachea to ensure an open lumen and in achieving an intact luminal lining that secretes mucus to protect against infection.

Methods: On the basis of the finding that tracheal cartilage has immune privilege, researchers recently started subjecting tracheal allografts to "partial decellularization" (in which only the epithelium and its antigenicity are removed), rather than complete decellularization, to maintain the tracheal cartilage as an ideal scaffold for tracheal tissue engineering and reconstruction. In the present study, we combined a bioengineering approach and a cryopreservation technique to fabricate a neo-trachea using pre-epithelialized cryopreserved tracheal allograft (ReCTA).

Results: Our findings in rat heterotopic and orthotopic implantation models confirmed that tracheal cartilage has sufficient mechanical properties to bear neck movement and compression; indicated that pre-epithelialization with respiratory epithelial cells can prevent fibrosis obliteration and maintain lumen/airway patency; and showed that a pedicled adipose tissue flap can be easily integrated with a tracheal construct to achieve neovascularization.

Conclusion: ReCTA can be pre-epithelialized and pre-vascularized using a 2-stage bioengineering approach and thus provides a promising strategy for tracheal tissue engineering.

KEYWORDS

tracheal tissue engineering, tracheal cryopreservation, partial decellularization, pre-epithelialization, vascularization

Introduction

Tracheal defects can result from congenital disease, trauma, tumors, or the treatment thereof (Grillo and Mathisen, 1990; Gandhi et al., 1999; Rendina et al., 1999; Mitchell et al., 2001; American Cancer Society, 2002; Grillo, 2004). Tracheal defects as long as 5 cm can be closed primarily, but anastomotic complications and mortality rates increase as the defect length increases (Mitchell et al., 2001). Longer defects that cannot be closed primarily require reconstruction with a tracheal conduit. In tracheal reconstruction, the rigidity of the trachea must be maintained to ensure an open lumen, and the luminal lining must be

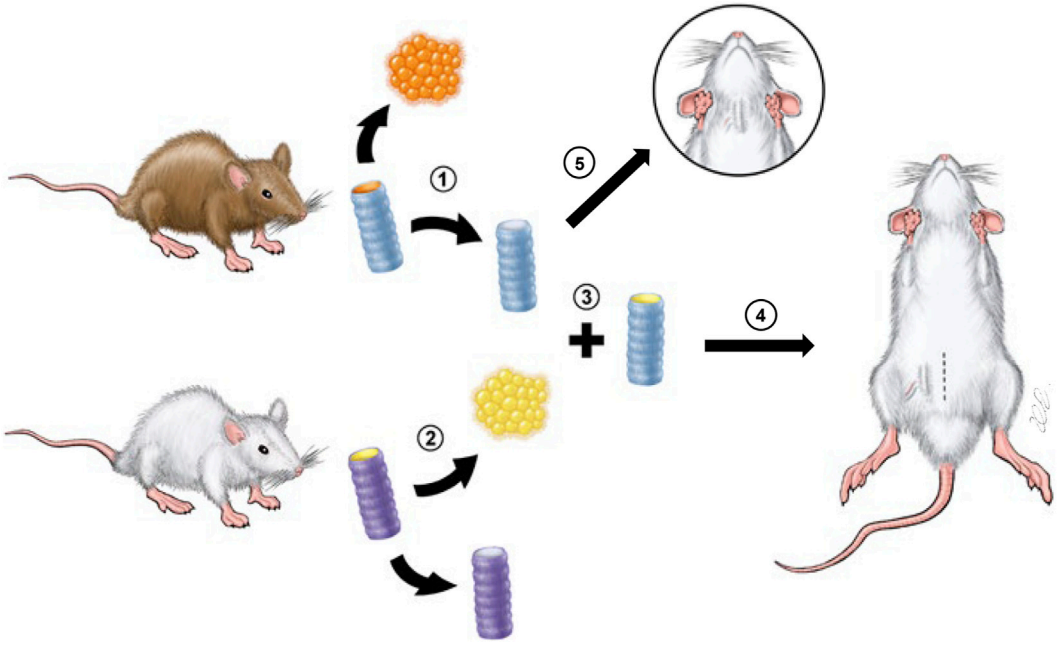

GRAPHICAL ABSTRACT
Scheme of the experimental design. 1, CTA derived from donor Brown Norway rats was de-epithelialized to create DeCTA. 2, RECs were isolated from syngeneic recipient Lewis rats. 3, DeCTA was pre-epithelialized to create ReCTA. 4, In the heterotopic implantation model, ReCTA was subcutaneously implanted into the groin area, and an adipose tissue flap pedicled by superficial epigastric blood vessels was used for neovascularization. 5, In the orthotopic implantation model, DeCTA was implanted into the neck to reconstruct a 4-ring tracheal defect.

intact to secrete mucus and protect against infection. These unique requirements have challenged reconstructive surgeons for decades. Efforts to reconstruct longer and/or circumferential tracheal defects have been largely unsuccessful. Therefore, patients with extensive tracheal involvement typically are not surgical candidates, or they may require total laryngectomy and possibly mediastinal tracheostomy, which is associated with a high mortality rate. Obviously, successful tracheal reconstruction would extend the surgical indications for cure and offer patients a good quality of life.

Tracheal reconstruction has evolved from the simple implantation of prosthetic materials to the use of autologous soft tissue flaps with supporting materials to the use of entirely tissue-engineered tracheas (Pan et al., 2022a; Pan et al., 2022b; Tsou et al., 2023; Hiwatashi et al., 2022; Liu CS et al., 2022). Although prosthesis materials have evolved from stainless steel to porous materials with better biocompatibility, a prosthesis alone always fails to re-epithelialize, leading to infection and rejection (Cull et al., 1990; Teramachi et al., 1997; Matloub and Yu, 2006). Tracheal repair with a segment of small bowel with or without a cartilage graft has been attempted in dogs and goats, but these reconstructions failed or resulted in high mortality rates (up to 70%) because of airway collapse and obstruction due to mucus production (Letang et al., 1990; Mukaida et al., 1998). Other autologous tissues, such as free periosteal, muscular, esophageal, bronchial, and aortic grafts, have also been used for tracheal reconstruction, but merely to maintain airway patency (Letang et al., 1990; Cavadas, 1998; Matloub and Yu, 2006). Chemically fixed cadaveric tracheal allografts have been used to repair short, partial (i.e., noncircumferential) tracheal defects caused by benign stenosis (Cull et al., 1990; Anderl and Haid, 2005), but such reconstructions are prone to resorption and loss of rigidity, leading to airway collapse, and obviously are not suitable for extensive defects (Beldholm et al., 2003).

To date, only a few clinical applications of large-scale tracheal reconstruction have been relatively successful (Genden and Laitman, 2023). On the basis of a series of animal experiments (Matloub and Yu, 2006; Zang et al., 2010), we developed an approach in which an autologous skin flap is used to line the lumen of a prosthesis which is used as a support scaffold for the repair of large tracheal defects, and we investigated its use in 7 cancer patients. However, this approach is very complicated; it is suitable only for strictly selected patients, and it should be attempted only by skillful microsurgeons (Yu et al., 2006; 2011; Ghali et al., 2015). Macchiarini et al. (2008) performed the first reconstruction with a tissue-engineered trachea [a completely decellularized tracheal scaffold seeded with the patient's own bone marrow (BM)-derived stem cells and respiratory epithelial cells (RECs)] in 2008 (Macchiarini et al., 2008). However, the uncertain cartilage regeneration in this approach and the issue around the clinical sets makes it very difficult to implement (Vogel, 2013; Delaere and Van Raemdonck, 2014; Gonfiotti et al., 2014; Kojima and Vacanti, 2014). In other studies, we found that stem cells seeded on the surface of an acellular tracheal matrix scaffold appeared to have hardly migrated into the cartilage lacunae or differentiated there (Zang et al., 2012; Zang et al., 2013), thus, the scaffold may require some modification to improve the migration of chondrocytes across the collagen matrix boundary into the center of the scaffold (Xu et al., 2017). Realizing the pitfalls of using a completely decellularized tracheal scaffold for tracheal tissue engineering, Jungebluth et al. (2011) switched to using a synthetic tube-type

prosthetic scaffold for clinical tracheal reconstruction. Unfortunately, most of the patients who received the synthetic tracheas died shortly after their implantation.

The optimal method of tracheal reconstruction would be to replace the native trachea with another trachea via composite tissue allotransplantation. However, traditional organ transplantation requires life-long immunosuppression, whose potential severe side effects, including opportunistic infections, end-organ toxicity, and neoplasms, render the technique unsuitable for many applications. A breakthrough in clinical tracheal allotransplantation without immunosuppression was achieved in 2010, when Delaere et al. (2010) used a 2-stage microsurgical approach to orthotopically transfer a vascularized tracheal flap comprising a fresh viable cartilage allograft covered with a buccal mucosa isograft. The success of the case indicated that the epithelium, perichondrium, and mucosal and submucosal glands are the major antigenic structures of the trachea (and thus responsible for transplant rejection), whereas tracheal cartilage is an immune-privileged tissue; its avascularity and dense matrix enable it to evade host immune recognition (Sykes, 2010; Huey et al., 2012). However, recipient cells are slow to repopulate the mucosal lining, and this has hindered the widespread clinical use of the approach (Delaere et al., 2012). Nevertheless, the experience of Delaere et al. (2012) demonstrates that in orthotopically implanted fresh tracheal allograft (FTA), the cartilage can have restored function after its re-epithelialization by recipient buccal mucosa and requires no immunosuppression.

Inspired by the clinical trials of Delaere et al. (2010) (Sykes, 2010; Delaere et al., 2012; Huey et al., 2012), researchers have started subjecting tracheal allografts to "partial decellularization" (in which only the epithelium and its antigenicity are removed), rather than complete decellularization, to maintain the tracheal cartilage as an ideal scaffold for tracheal tissue engineering and reconstruction. The transplantation of cryopreserved tracheal allografts (CTAs) has been investigated for decades (Sotres-Vega et al., 2006; Nakanishi, 2009), but most of these allografts (Nakanishi, 2009), as well as many partially decellularized scaffolds (Hysi et al., 2014; Hysi et al., 2015; Den Hondt et al., 2016; De Wolf et al., 2017; Den Hondt et al., 2017; Cui et al., 2021; Wang et al., 2021), were not pre-epithelialized with real RECs. Therefore, only the short allografts achieved satisfactory results *in vivo*, whereas the longer ones failed to maintain patency, mostly because of proliferating fibroblasts that originated from the lamina propria and was caused by a lack of proper REC coverage (Hysi et al., 2015).

Combining a bioengineering approach and a cryopreservation technique, we aimed to fabricate a neo-trachea using pre-epithelialized CTA (ReCTA). We hypothesized that, after its vascularization *in vivo*, our engineered neo-trachea flap can evade host immune recognition without the need for immunosuppression and retain both cartilage and epithelium function. To test our hypothesis, we first partially decellularized CTA, removing only the epithelium while preserving chondrocytes. We then cultured RECs in the lumen of the tracheal scaffold for pre-epithelialization. We then heterotopically and orthotopically implanted the engineered neo-trachea into rodent models to examine its viability and rigidity (Graphical Abstract). The findings of the present study may inform the development of a platform for designing and fabricating neo-trachea flap that can be used to reconstruct longer tracheal defects.

Materials and methods

Tracheal cryopreservation and partial decellularization

All procedures were approved by MD Anderson's Institutional Animal Care and Use Committee and met all requirements of the Animal Welfare Act.

We used 8- to 10-week-old male Brown Norway rats (Harlan Laboratories, Indianapolis, IN; n = 21) weighing 250 g each to provide donor tracheas for tracheal allograft scaffolds. Each mouse's trachea was harvested and processed under sterile conditions. The entire length of the trachea was harvested and carefully stripped of overlying soft tissue. The trachea was then divided into 2 segments of approximately 8 rings each and frozen as described previously (Sotres-Vega et al., 2006). Briefly, the samples were immersed in protective medium (DMEM containing 20% FBS, 10% DMSO, 0.1 M trehalose, 0.1 M sucrose, 100 μg/mL penicillin, and 100 μg/mL streptomycin) and frozen at 4°C for 60 min, then frozen to −80°C at a controlled rate of −1°C/min, and finally stored at −196°C for 1 month. The samples were thawed in a 37°C water bath and rinsed in DMEM for further use. For decellularization, the samples were washed in sterile phosphate-buffered saline (PBS) at 4°C (except as indicated otherwise) with agitation at 80 rpm for 2–12 h. The resultant de-epithelialized CTA (DeCTA) samples were then characterized using the following methods.

Immunohistochemical analysis

FTA, CTA, and DeCTA were fixed in 10% formalin, embedded in paraffin, and sliced into 5-μm sections. The sections were deparaffinized, rehydrated, washed in distilled water, and mounted on slides. The sections were subjected to histological hematoxylin and eosin (H&E) staining, 4′-6-diamidino-2-phenylindole (DAPI) staining, Masson trichrome staining, and Safranin O staining. For immunohistochemical staining, the sections were placed in antigen retrieval citrate buffer (Biogenex, Fremont, CA) in a steamer at 95°C for 10 min. Endogenous peroxidases were blocked by incubation with Peroxide Block (Innogenex, San Ramon, CA), and nonspecific binding was blocked with normal goat serum (Vector Laboratories, Burlingame, CA). The sections were incubated overnight with primary antibodies against MHC-1, MHC-II, OX62, collagen II, and collagen IV (all at 1: 200; Abcam, Cambridge, MA) at 4°C. The sections were washed, and biotinylated secondary antibody was applied for 30 min, followed by treatment with streptavidin-horseradish peroxidase complex (Vectastain ABC Kit, Vector Laboratories) and diaminobenzidine solution (DAB Kit, Vector) and counterstaining with hematoxylin. The sections were dehydrated, mounted, and imaged using an IX71 microscope (Olympus, Center Valley, PA).

Sulfated glycosaminoglycan content

The sulfated glycosaminoglycan (GAG) content of native tissues and decellularized samples was quantified using an Alcian blue colorimetric assay kit (sGAG Dye Binding Assay, ALPCO, Salem,

NH). Samples were lyophilized, papain-digested, and then incubated with Alcian blue dye. Absorbance of the samples at 600–620 nm was measured with a DU 730 UV/Vis Spectrophotometer (Beckman Coulter) using chondroitin sulfate (Sigma, St. Louis, MO) as the standard. GAG content was normalized to the initial dry weight of the samples.

Scanning electron microscopy

For scanning electron microscopy (SEM), samples were fixed in a solution containing 3% glutaraldehyde plus 2% paraformaldehyde in 0.1 M cacodylate buffer, pH 7.3, washed with 0.1 M cacodylate buffer, pH 7.3, post-fixed with 1% cacodylate-buffered osmium tetroxide, washed with 0.1 M cacodylate buffer, and then washed with distilled water. Next, the samples were sequentially treated with Millipore-filtered 1% aqueous tannic acid, washed with distilled water, treated with Millipore-filtered 1% aqueous uranyl acetate, and then rinsed thoroughly with distilled water. The samples were dehydrated with a graded series of increasing concentrations of ethanol, transferred to a graded series of increasing concentrations of hexamethyldisilazane, and air-dried overnight. The samples were mounted on double-stick carbon tabs (Ted Pella, Inc., Redding, CA), which were previously mounted on aluminum specimen mounts (Electron Microscopy Sciences, Fort Washington, PA). The samples received a 25-nm coating of platinum alloy under vacuum using a Balzer MED 010 evaporator (Technotrade International, Manchester, NH) and were then immediately flash carbon-coated under vacuum. The samples were transferred to a desiccator for examination at a later date. Samples were imaged and examined using a JSM-5910 scanning electron microscope (JEOL USA, Inc., Peabody, MA) at an accelerating voltage of 5 kV.

Transmission electron microscopy

For transmission electron microscopy (TEM), samples were fixed with a solution containing 3% glutaraldehyde plus 2% paraformaldehyde in 0.1 M cacodylate buffer, pH 7.3, washed in 0.1 M sodium cacodylate buffer, treated with 0.1% Millipore-filtered cacodylate-buffered tannic acid, post-fixed with 1% buffered osmium, and then stained *en bloc* with 1% Millipore-filtered uranyl acetate. The samples were dehydrated in increasing concentrations of ethanol, filtered, and embedded in LX-112 medium. The samples were polymerized in a 60°C oven for approximately 3 days. Ultrathin sections were cut in an Ultracut microtome (Leica, Deerfield, IL), stained with uranyl acetate and lead citrate in an EM Stainer (Leica), and examined using a JEM 1010 transmission electron microscope (JEOL USA, Inc.) at an accelerating voltage of 80 kV. Digital images were obtained using an AMT Imaging System (Advanced Microscopy Techniques Corp., Danvers, MA).

Contact assay

To determine whether DeCTA is cytotoxic, we performed a contact assay in which the scaffold was co-cultured with BM-derived mesenchymal stem cells (BM-MSCs). Briefly, we isolated BM-MSCs from 8- to 10-week-old male Lewis rats (Harlan Laboratories, Indianapolis, IN) weighing 250 g each using our established protocol (Zang et al., 2012; Zang et al., 2013). BM-MSCs were cultured in medium and harvested at passage 3. The cells were seeded in a petri dish, and then DeCTA was placed in the same petri dish. On day 3, the cells were washed with PBS 3 times. Then, the cells were exposed to 2 μM calcein AM and ethidium homodimer-1 using the LIVE/DEAD Viability/Cytotoxicity Kit (Molecular Probes, Carlsbad, CA) according to the manufacturer's instructions. Briefly, the samples were washed with PBS 3 times and then incubated with the staining reagents in PBS for 30 min at 37°C before the staining solution was replaced. The samples were washed with PBS 3 times before they were viewed using an IX81 confocal microscope (Olympus).

Chondrocyte isolation and culture

Chondrocytes were isolated from DeCTA using methods we described previously (Zang et al., 2011; Zang et al., 2013). Briefly, cartilage sheets from 3 DeCTA samples were minced into pieces of approximately 1 mm^3 and digested in 0.1% collagenase type II (Worthington Biochemical Corp., Lakewood, NJ) in DMEM with 4.0 g/L glucose (Hyclone, Waltham, MA) on a shaker for 21 h at 37°C. The resultant cell suspension was centrifuged at 200 g for 8 min, and the cell pellet was resuspended in growth medium consisting of DMEM with 4.0 g/L glucose supplemented with 10% FBS (Atlanta Biologicals, Lawrenceville, GA) and 1% antibiotics (100 U/mL penicillin G, 100 μg/mL streptomycin sulfate, and 250 ng/mL amphotericin B; Hyclone). Then, the cells were plated at a density of 10,000 cells/cm^2 and incubated at 37°C with media changes every 3 days. At 80% confluence, the cells were detached with 0.05% trypsin-EDTA (Gibco, Carlsbad, CA), plated in 2-well chamber slides for culturing, and stained with Alcian blue (Sigma).

Chondrocyte proliferation was measured with CellQuanti-MTT Cell Viability Assay Kits (BioAssay Systems, Hayward, CA) according to the manufacturer's instructions. Chondrocytes isolated from DeCTA were placed in 96-well tissue culture plates at a density of 10,000 cells/cm^2 in 100 μL of medium. The cells were washed and treated with a 1:5 ratio of 3(4,5-dimethylthiazol-2Yl)-2,5-diphenyltetrazolium bromide (MTT) to culture media 1, 3, and 7 days after seeding. Following incubation at 37°C for 2 h, MTT was taken up by active cells and reduced inside the mitochondria to insoluble purple formazan granules. The cells were subsequently lysed, and the formazan granules were solubilized in dimethyl sulfoxide on a shaker. The supernatant was transferred to fresh 96-well plates to reduce background contamination, and the optical density was read at 540 nm using a photometric plate reader (BioTek, Oklahoma City, OK).

REC isolation and culture

Tracheal RECs were isolated from Lewis rats using methods we described previously (Zang et al., 2012; Zang et al., 2013). Briefly, RECs were dissociated from the tracheal mucosal lining with 2 mg/mL pronase (Roche Applied Science, Indianapolis, IN) in Ham's F-12 medium overnight (12 h) at 4°C. Cells were collected by centrifugation at 500 g for 10 min. Cell pellets were re-suspended in

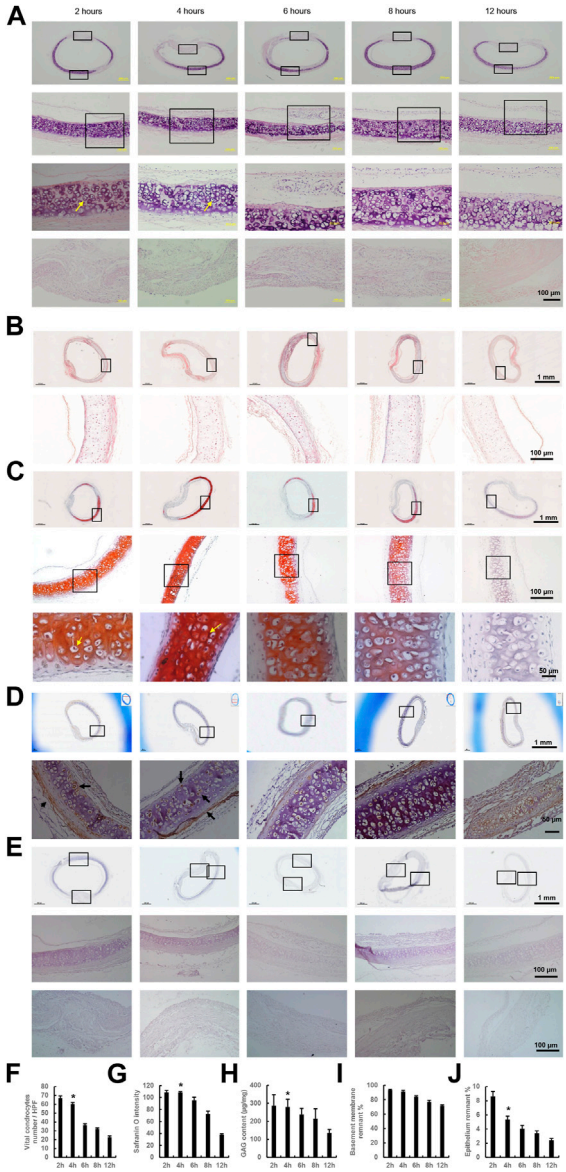

FIGURE 1
Preparation of DeCTA. **(A)** H&E staining revealed chondrocyte nuclei and lacunar structures in DeCTA after 2, 4, 6, 8, and 12 h of washing with cold PBS; however, the number of normal chondrocytes decreased significantly after 6 h of washing with cold PBS. First (top) row, images of H&E-stained DeCTA. Second row, magnified views of the areas demarcated by the upper black boxes in the first row. Third row, magnified views of the areas demarcated by the black boxes in the second row; the yellow arrows indicate chondrocyte nuclei. Fourth (bottom) row, magnified views of the membrane areas demarcated by the lower black boxes in the first row. **(B,C)** Masson trichrome staining **(B)** and Safranin O staining **(C)** indicated a high density of collagen in the cartilage surrounding the chondrocytes after 4 h of washing with cold PBS; this density gradually diminished with additional washing. In panel **(B)**, the images in the bottom row are magnified views of the areas demarcated by the black boxes in the top row. In panel **(C)**, the images in the bottom row are magnified views of the areas demarcated by the black boxes in the middle row, which themselves are magnified views of the areas demarcated by the black boxes in the top row; yellow arrows indicate chondrocyte nuclei. **(D)** Collagen IV was strongly expressed in basement membrane, lacunar structures and perichondrium after 2 and 4 h of washing with cold PBS, its expression decreased slightly with additional washing. Images in the bottom row are magnified views of the areas demarcated by the

(*Continued*)

FIGURE 1 (Continued)
black boxes in the top row; black arrows indicate positive staining. **(E)** At all time points, DeCTA showed no OX62 staining, indicating that de-epithelialization completely removed OX62-positive dendritic cells, the most potent antigen-presenting cells within epithelium. Images in the middle and bottom rows are magnified views of the areas demarcated by the black boxes in the top row. **(A–E)** In contrast to the retained chondrocytes, more than 90% of RECs and the submucosa were removed from the tracheal epithelium after 4 h of washing with cold PBS. **(F)** The numbers of normal chondrocytes decreased significantly after 6 h of washing. $*p < 0.05$ vs. 6, 8 and 12 h. **(G)** The intensity of Safranin O staining decreased significantly after 8 h of washing. $*p < 0.05$ vs. 8 and 12 h. **(H)** GAG content decreased significantly after 8 h of washing. $*p < 0.05$ vs. 8 and 12 h. **(I)** The percentage of remnant basement membrane did not differ significantly across time points. **(J)** The percentage of remnant epithelium decreased significantly after 4 h of washing. $*p < 0.05$ vs. 2 h. ANOVA was used for comparisons among multiple groups, as appropriate. N = 3 biological replicates.

DMEM/Ham's F-12 medium (Sigma) supplemented with 10 μg/mL insulin (Sigma), 0.1 μg/mL hydrocortisone (Sigma), 0.1 μg/mL cholera toxin (Sigma), 5 μg/mL transferrin (BD, Franklin Lakes, NJ), 50 μM phosphoethanolamine (Sigma), 80 μM ethanolamine (Sigma), 25 ng/mL epidermal growth factor (BD), 70 μg/mL bovine pituitary extract (United States Biological, Swampscott, MA), 3 mg/mL bovine serum albumin (Sigma), and 5 nM retinoic acid (Sigma). Epithelial cells at passage 0 were centrifuged with a Shandon Cytospin (GMI, Inc., Ramsey, MN) and stained with antibodies against cytokeratin peptide 17, beta tubulin IV, mucin 5AC, and P63 (all at 1:200; Sigma) to identify their components. We found that the percentage of cells expressing the markers of rat respiratory tract epithelial differentiation decreased during subculture. Because most cells became fibroblast-like cells in passage 2, we used only freshly isolated RECs for cell seeding in the ensuing experiments.

Creation of ReCTA

RECs were seeded into the lumen of DeCTA at a density of 1×10^5 cells/cm^2. Acland artery clamps were used to seal the lumen ends, and DeCTA was cultivated in epithelial cell growth medium. Twenty-four hours later, the pre-epithelialized DeCTA (i.e., ReCTA) was stained with calcein AM and ethidium homodimer-1 using the LIVE/DEAD Viability/Cytotoxicity Kit as described above. SEM was used to assess cell morphology.

In vivo evaluation of ReCTA in a heterotopic implantation model

To assess the neovascularization and survival of ReCTA *in vivo*, we heterotopically implanted ReCTA and other tracheal grafts into 8- to 10-week-old male Lewis rats. Rats were anesthetized and maintained with isoflurane (0.5%–2%, 3–5 L/min) and oxygen during surgery.

In the heterotopic implantation model, rats received FTA, CTA, DeCTA, ReCTA, or fresh isograft trachea (FIT) (n = 6/group). FTA, CTA, DeCTA, and ReCTA were allografts from Brown Norway rats. FIT was from Lewis rats. Both FTA and FIT were rinsed with PBS to remove additional mucus and blood and then preserved in PBS. CTA was quickly thawed in a 37°C water bath, simply rinsed with PBS to

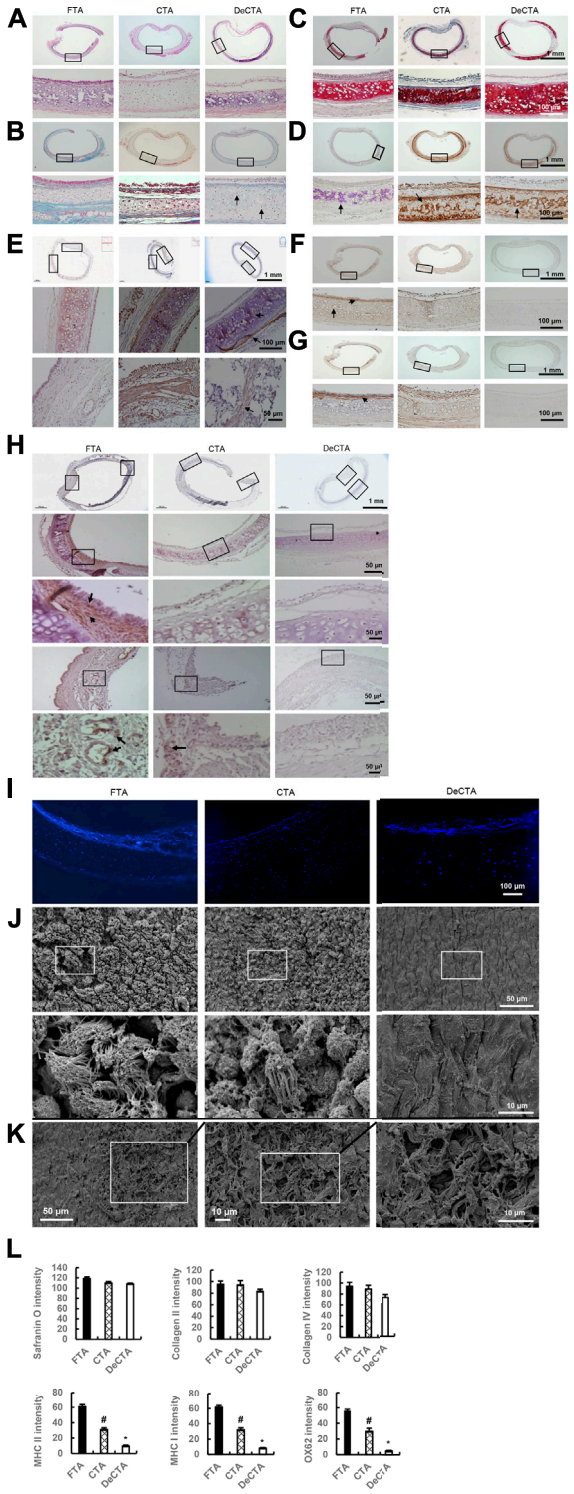

FIGURE 2
Characterization of DeCTA. **(A)** H&E staining showed that chondrocytes were well preserved, most of the epithelium was removed, and the basement membrane was maintained in DeCTA. Compared with that in FTA or CTA, cartilage in DeCTA had some slight calcification, but this difference was not significant. Most of the epithelium in CTA was preserved. **(B)** Masson trichrome staining showed that DeCTA had numerous normal chondrocytes with clear nuclei in lacunar structures, which were surrounded by dense collagen (blue). The chondrocytes in FTA, CTA, and DeCTA had similar features. Black arrows indicate chondrocyte nuclei. **(C,D)** Safranin O

(*Continued*)

FIGURE 2 (Continued)
staining **(C)** and collagen II staining **(D)** showed that FTA, CTA, and DeCTA all had cartilage with a dense collagen matrix. The images in the bottom rows of **(A–D)** are magnified views of the areas demarcated by the black boxes in the top rows of those panels. **(E)** Collagen IV, an important component of basement membrane, was distributed in the basement membrane, lacunar structures and perichondrium in FTA, CTA, and DeCTA. The images in the middle and bottom rows are magnified views of the areas demarcated by the black boxes in the top row; black arrows indicate positive staining of collagen IV. **(F–H)** Compared with that in FTA, MHC I **(F)**, MHC II **(G)**, and OX62 **(H)** staining were significantly decreased in CTA and even absent from DeCTA. OX62-positive dendritic cells (black arrows), which are important antigen-presenting cells, were distributed in the subepithelial layer around vascular structures in FTA. In panels **(F,G)**, the images in the bottom rows are magnified views of the areas demarcated by the black boxes in the top rows. In **(H)**, the images in the third (middle) and fifth (bottom) rows are magnified views of the areas demarcated by the black boxes in the second and fourth rows, respectively, which are themselves magnified views of the areas demarcated by the black boxes in the first (top) row. Black arrows indicate positive staining. **(I)** DAPI staining showed that chondrocytes were present in FTA, CTA, and DeCTA. **(J)** SEM analysis confirmed that the epithelium was removed and the basement membrane remained intact in DeCTA. The images in the bottom row are magnified views of the areas demarcated by the black boxes in the top row. **(K)** SEM revealed several areas of basement membrane pinpoint defects, which resulted in the exposure of underlying collagen fibrils, after 6 h of washing with cold PBS. The average size of these areas of destruction was about 0.01 mm^2. **(L)** Safranin O, collagen II, and collagen IV staining intensity did not differ significantly among FTA, CTA, and DeCTA. Compared with FTA, both CTA and DeCTA had significantly diminished MHC I, MHC II, and OX62 staining intensity. $^{\#}p < 0.05$ vs. FTA; $^{*}p < 0.01$ vs. FTA and CTA. ANOVA was used for comparisons among multiple groups, as appropriate. N = 3 biological replicates.

remove cryoprotectants, and then preserved in PBS. DeCTA was prepared as described above. ReCTA was prepared as described above; briefly, RECs isolated from one Lewis rat trachea were suspended with REC growth media and injected into the lumen of one DeCTA scaffold (8 rings), and then both ends of the scaffold were sealed with Acland arterial clamps, and the scaffold was implanted immediately to avoid longer ischemia. The warm ischemia time was within 4 h for all grafts before implantation. In each animal, one graft was carefully implanted under the fat pad of the adipose tissue flap pedicled by the superficial epigastric blood vessel in the groin area. Animals were monitored for clinical signs of inflammation or rejection for 30 days and then humanely killed for graft explantation.

In vivo evaluation of DeCTA in an orthotopic implantation model

In the orthotopic implantation model, a 5 mm section of trachea (3-4-ring) was removed from each Lewis rat and replaced with a tracheal graft of the same size. Rats received FIT or DeCTA (n = 5/group). Rats were anesthetized with IM ketamine/xylazine. A 2 cm midline cervical incision was made in line with the trachea. The strap muscles were divided and the entire trachea was exposed. The vascular structures and the recurrent laryngeal nerves were sharply dissected away from the trachea. A 3-4-ring segment was removed and the graft was interposed between the recipient tracheal defects and anastomosed after ensuring adequate hemostasis and clean tracheal edges (Supplementary Figure S1).

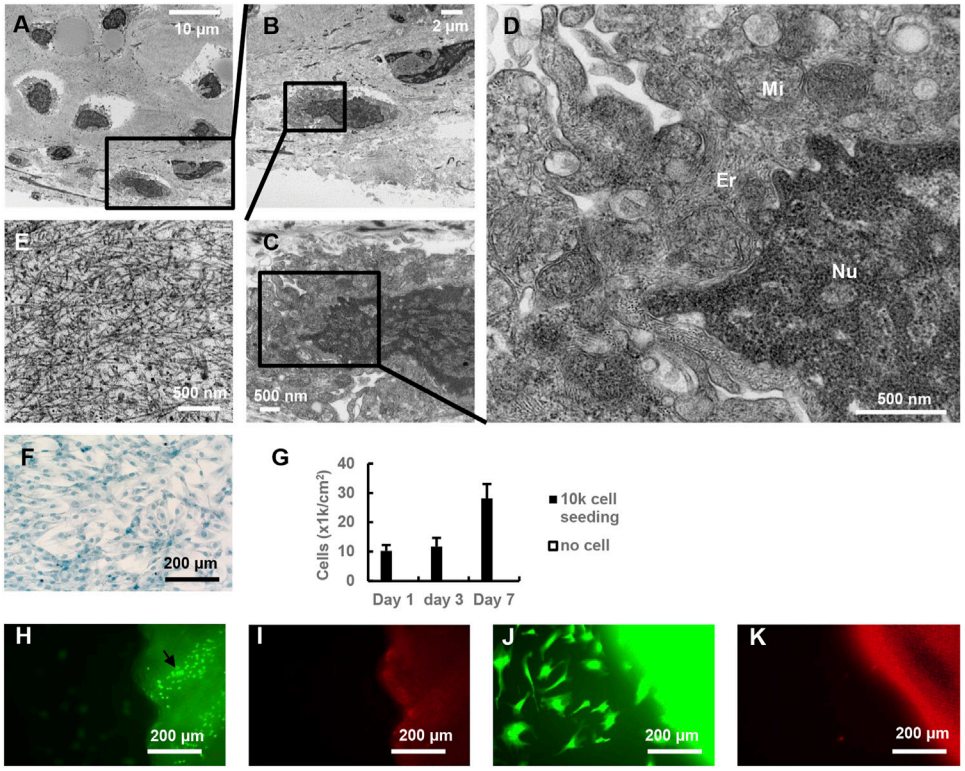

FIGURE 3
Characterization of chondrocytes in DeCTA. **(A–D)** TEM showed supermicroscopic structures of normal chondrocytes in DeCTA. Mi, mitochondria; Er, endoplasmic reticulum; Nu, nucleus. **(E)** Dense extracellular matrix surrounding chondrocytes in lacunae. **(F)** Alcian blue–stained chondrocytes isolated from DeCTA and cultured at day 3. **(G)** MTT assay showed chondrocyte proliferation from day 1–7. **(H)** Live/dead staining showed living chondrocytes (black arrows) in DeCTA. Few vital epithelium cells were detected. Calcein AM staining appears as green fluorescence. **(I)** Live/dead staining showed few dead cells in DeCTA. EthD-1 staining appears as red fluorescence. **(J)** Live/dead staining showed living BM-MSCs seeded on DeCTA. **(K)** No dead BM-MSCs were detected in DeCTA. N = 3 biological replicates.

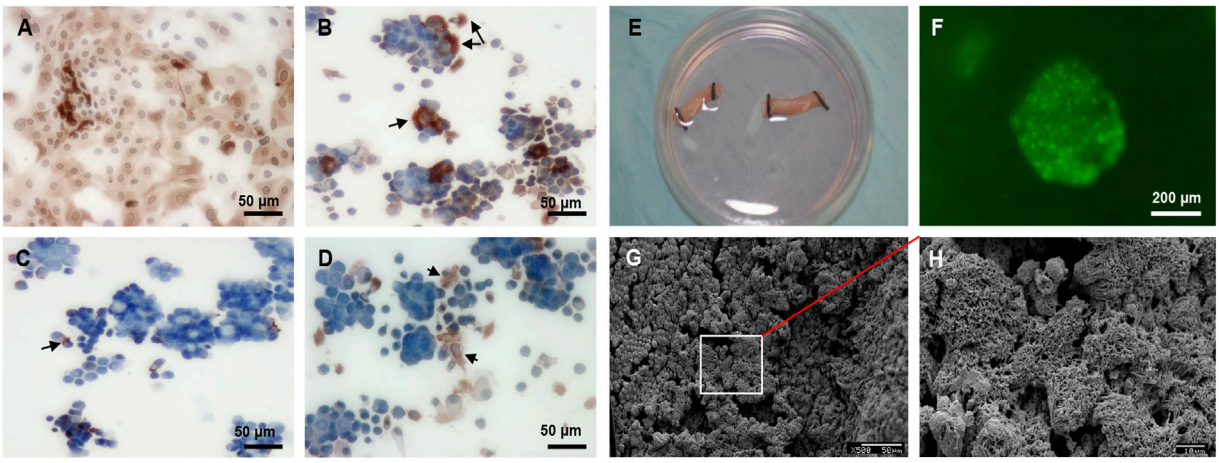

FIGURE 4
REC culture and seeding in DeCTA. **(A)** RECs were positive for cytokeratin peptide 17. **(B)** Beta tubulin IV–positive ciliated columnar cells. Black arrows indicate cilia. **(C)** Black arrows indicate P63-positive basal cells. **(D)** Black arrows indicate mucin 5AC–positive goblet cells. **(E)** RECs were seeded into DeCTA. **(F)** Live/dead staining showed clusters of healthy RECs adhered to DeCTA. **(G)** SEM revealed that RECs adhered to and re-epithelialized DeCTA with 1 day of culturing. **(H)** Magnified view of the area demarcated by the white box in panel **(G)** N = 3 biological replicates.

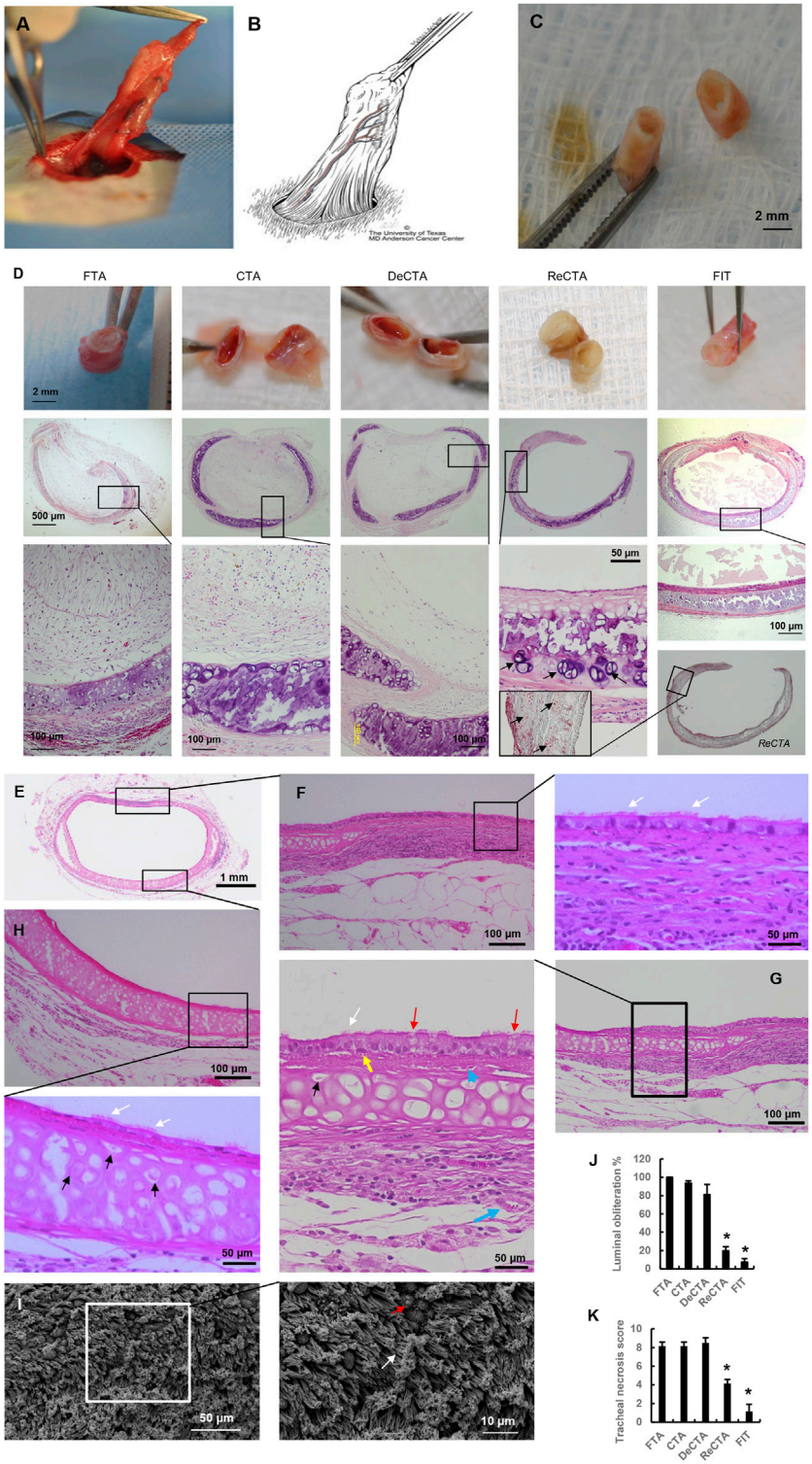

FIGURE 5
In vivo assessment of heterotopically implanted ReCTA. **(A)** ReCTA was neovascularized by a pedicled adipose tissue flap subcutaneously in the groin area 30 days postoperatively. **(B)** Scheme of the pedicled adipose tissue flap based on the superficial epigastric blood vessels in the groin area. Its micro-branches anastomosed with ReCTA to provide the blood supply. **(C)** ReCTA retained luminal patency 30 days postoperatively. **(D)** Histological analysis showed that fibrosis obliterated FTA, CTA, and DeCTA. There was calcification necrosis in the center of the cartilage. Unlike FTA, CTA, and DeCTA, both ReCTA and FIT retained luminal patency and structural integrity with complete epithelial cell coverage. There was some calcification necrosis in the center of the cartilage in ReCTA; however, lots of vital chondrocytes (black arrows) were in the cartilage, especially in the periphery. **(E–I)** Histological features of explanted ReCTA 30 days postoperatively. Both the membrane part **(F,G)** and cartilage part **(H)** of ReCTA were completely epithelialized by RECs, which included cilia cells (white arrows), basal cells (yellow arrows), and goblet cells (red arrows). Microvascular blood vessels (blue arrows) grew in both the subepithelium and adventitia. Vital chondrocytes with clear nuclei (black arrows) were distributed in the cartilage, especially in the periphery.
(*Continued*)

FIGURE 5 (Continued)
SEM revealed healthy cilia (white arrows) and goblet cells (red arrows) in the epithelium **(I)**. **(J)** Compared with FTA, CTA, and DeCTA, both ReCTA and FIT had significantly lower percentages of luminal obliteration. *$p < 0.05$ vs. FTA, CTA, and DeCTA. **(K)** Compared with FTA, CTA, and DeCTA, both ReCTA and FIT had significantly lower tracheal graft necrosis scores. *$p < 0.05$ vs. FTA, CTA, and DeCTA. ANOVA was used for comparisons among multiple groups, as appropriate.

Animals were monitored for clinical signs of respiratory distress for 3 months and then humanely killed for graft explantation.

Immunohistochemical analysis of *in vivo* explants

Specimens cut from the centers of the heterotopic explants were fixed in 10% neutral buffered formalin and embedded in paraffin. Sections cut from the paraffin-embedded samples were subjected to histological H&E staining and immunohistochemical staining with antibodies against CD68, CD4, and CD8 (all at 1:200, Abcam). Positively stained cells were counted to evaluate the host immunological response. SEM was used to examine the luminal surface of the explanted specimens. The degree of tracheal luminal obliteration was calculated by dividing the area of fibrosis by the total area of lumen. The H&E-stained sections were scanned at ×4 magnification, and the area of the obliterated lumen and the total area of lumen were measured using the ImageJ software program (NIH, Bethesda, MD) (Zhao et al., 2013). Histopathologic variables were scored from 0 to 3 to calculate the tracheal necrosis score modified from a method described previously (Iyikesici et al., 2009; Candas et al., 2016) (Supplementary Table S1). Orthotopic explants were dissected latitudinally and longitudinally to examine the anastomosis site stenosis and the viability of the entire explant.

Statistical analysis

Data were presented as means ± standard deviations. Data were analyzed using one-way analysis of variance (ANOVA) with SigmaStat 4.0 (Systat Software, San Jose, California). *p*-values of less than 0.05 were considered significant.

Results

Characterization of DeCTA

Integrity was preserved in all trachea samples during washing with PBS. H&E staining showed that DeCTA initially had chondrocyte nuclei and lacunar structures, however, normal chondrocyte numbers significantly decreased after 6–12 h of washing in cold PBS (Figures 1A, F). Masson trichrome and Safranin O staining indicated that the density of the extracellular matrix surrounding chondrocytes remained high after 4 h of washing but gradually decreased with additional washing (Figures 1B, C, G). Consistent with the histological analysis, GAG content in the tracheal matrix remained high after 2 and 4 h of washing (Figure 1H). Tracheal basement membrane was also well preserved after 2 and 4 h of washing (Figures 1A–C, I). Collagen IV, the major component of basement membrane, was strongly expressed in basement membrane and lacunar structures after 2 and 4 h of washing but gradually decreased thereafter (Figure 1D). The absence of OX62 staining indicated that dendritic cells, the most potent antigen-presenting cells within epithelium, were completely removed during de-epithelialization (Figure 1E). In contrast to its effect on chondrocytes, a 4-h wash with cold PBS removed more than 90% of epithelial cells and the submucosa from the trachea samples, while the left epithelium (~5.35% ± 0.49%) was lacking normal structure (Figures 1A–C, J). These results suggested that a 4-h wash with cold PBS sufficiently removed epithelium from CTA but did not remove its chondrocytes, extracellular matrix content, and tracheal rigidity. Therefore, the DeCTA that resulted from the 4-h wash with PBS was selected for ensuing experiments.

To further characterize DeCTA, we compared it with FTA and CTA. H&E, Masson trichrome, and DAPI staining revealed high percentage of viable chondrocytes were preserved in both CTA (~84.3 ± 3.4% normal chondrocytes ratio of CTA/FTA) and DeCTA (~61.2 ± 2.9% normal chondrocytes ratio of CTA/FTA) as well as in FTA (Figures 2A, B, I). Safranin O, collagen II, and collagen IV staining intensity did not differ significantly among FTA, CTA, and DeCTA (Figures 2C–E, L). Compared with that in FTA, staining for MHC I, MHC II, and OX62 were significantly decreased in CTA and even absent in DeCTA (Figures 2F–H, L). SEM analysis confirmed that the epithelium was removed, whereas the basement membrane remained intact, in DeCTA (Figure 2J). However, a 6-h wash with PBS resulted in partial basement membrane destruction with exposure of the underlying collagen fibrils (Figure 2K). SEM analysis revealed pinpoint defects in the basement membrane that were undetectable with regular histological analysis.

Chondrocyte was further evaluated using TEM analysis. Chondrocytes in the cartilage of DeCTA had clear supermicroscopic structures, including nuclei, mitochondria, and endoplasmic reticulum (Figures 3A–E). These normal structures are vital to cellular biological functionality. Coinciding with this finding, MTT assay revealed that chondrocytes isolated from DeCTA were able to proliferate (Figures 3F, G). Live/dead staining of BM-MSCs cocultured with DeCTA demonstrated not only viable chondrocytes in cartilage but also healthy BM-MSCs surrounding cartilage, which suggests that DeCTA is non-toxic and has histocompatibility. Particularly, very few viable epithelium cells were detected in DeCTA (Figures 3H–K).

Pre-epithelialization of DeCTA

RECs were successfully cultured and then identified with immunohistochemical staining. Most RECs were positive for cytokeratin peptide 17 at passage 0 (Figure 4A). RECs at passage 0 included beta tubulin IV–positive ciliated columnar cells (Figure 4B), P63-positive basal cells (Figure 4C), and mucin 5AC–positive goblet cells (Figure 4D). Healthy ciliated columnar

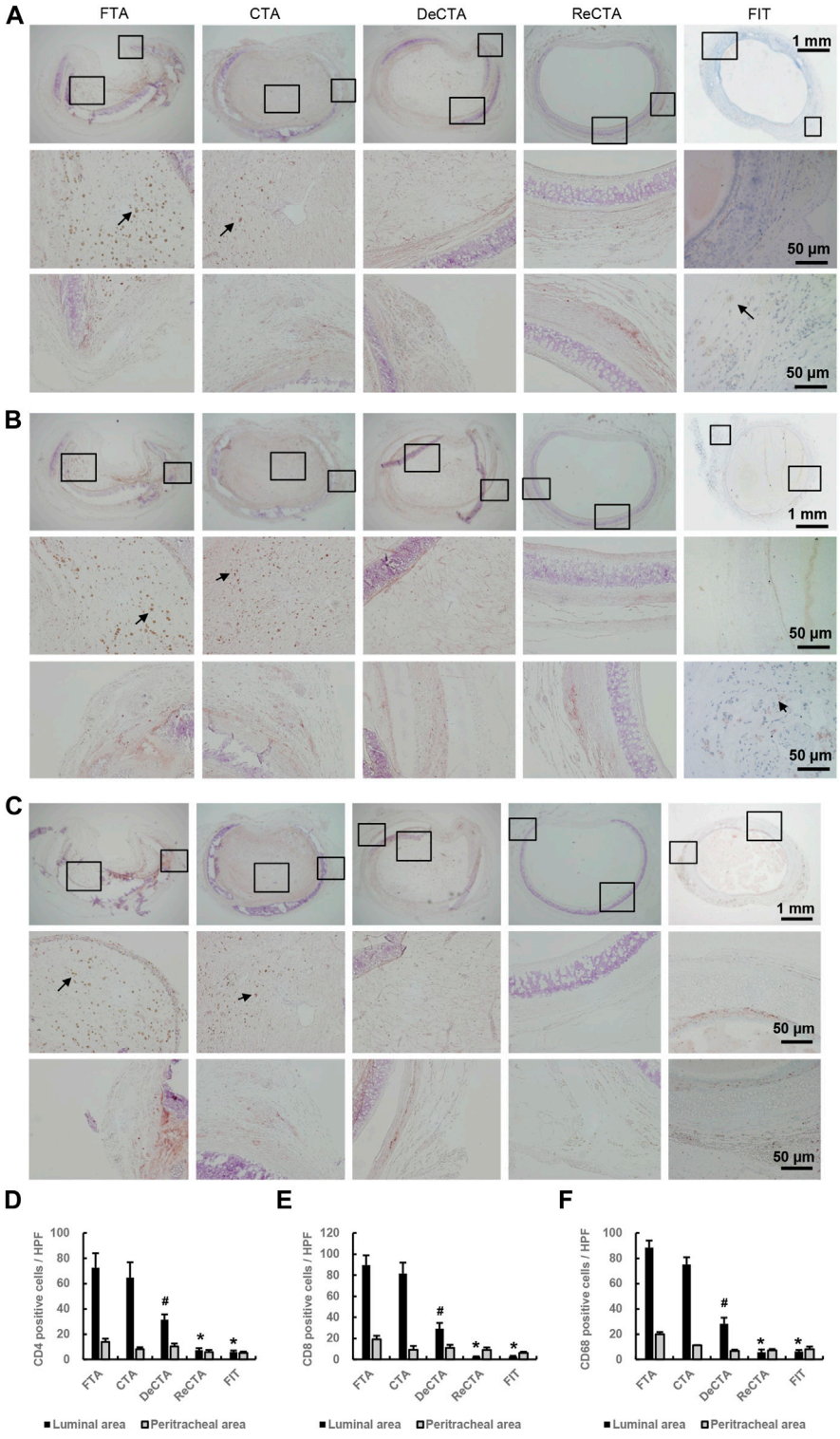

FIGURE 6
Infiltration of inflammatory cells in tracheal allografts. **(A–C)** Immunohistochemical staining revealed $CD4^+$ T cells **(A)**, $CD8^+$ T cells **(B)**, and $CD68^+$ macrophages **(C)** infiltrating the lumens of FTA and CTA but detected few of these immune cells in DeCTA, ReCTA, or FIT. In panels **(A–C)**, images in the middle (showing lumen) and bottom rows (showing cartilage and adventitia) are magnified views of the areas demarcated by the black boxes in the top rows; black arrows indicate the infiltrating cells. **(D–F)** Compared with FTA and CTA, DeCTA, ReCTA, and FIT had significantly fewer $CD4^+$ cells **(D)**, $CD8^+$ T cells **(E)**, and $CD68^+$ macrophages **(F)** infiltrating their luminal and peritracheal areas. $^{\#}p < 0.05$ vs. FTA, CTA; $^{*}p < 0.01$ vs. FTA, CTA. ANOVA was used for comparisons among multiple groups, as appropriate.

10.3389/fbioe.2023.1196521

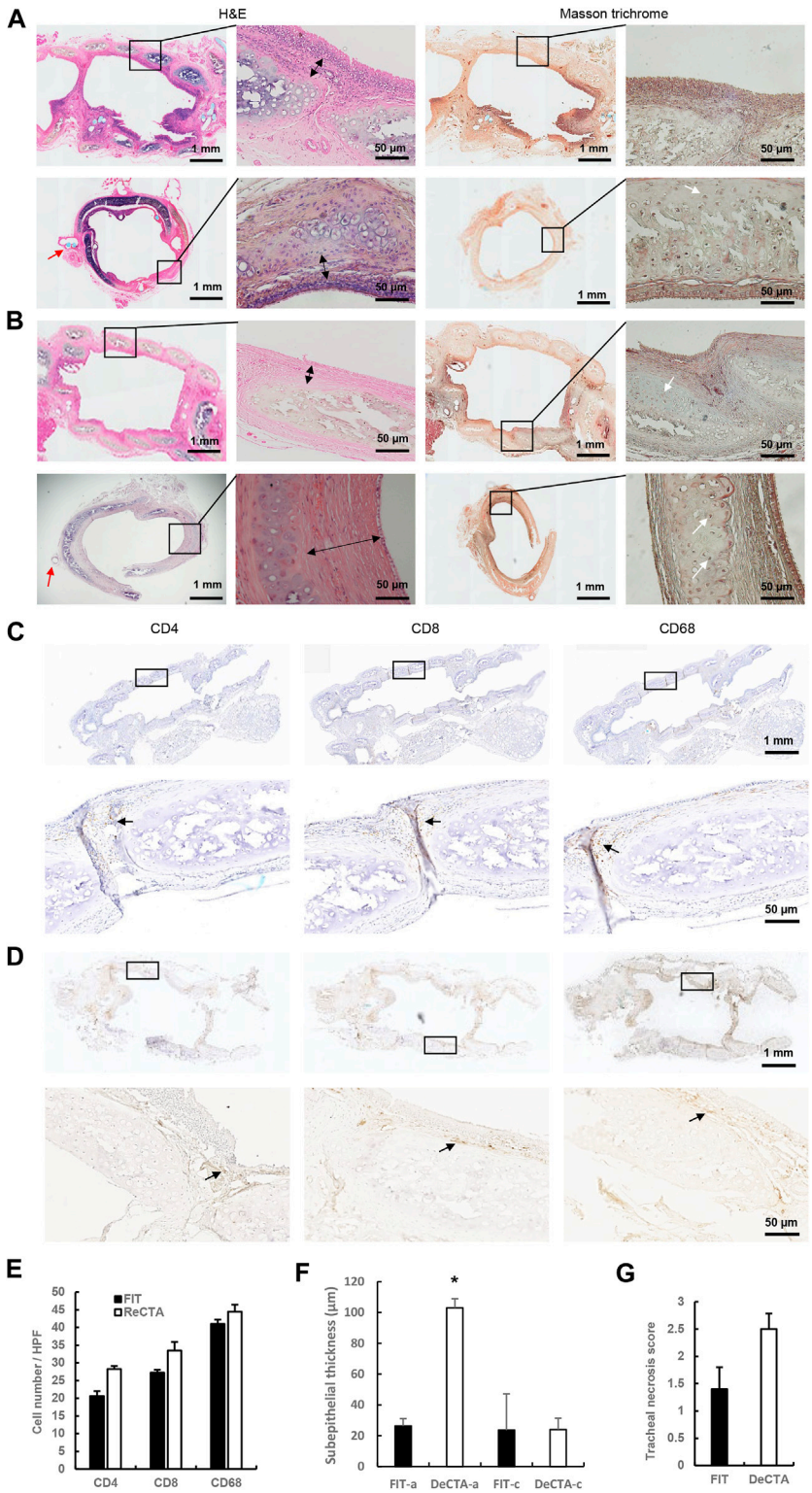

FIGURE 7
In vivo assessment of orthotopically implanted DeCTA 3 months postoperatively. **(A,B)** H&E and Masson trichrome staining showed that both FIT **(A)** and DeCTA **(B)** retained luminal patency with complete structural integrity and strong mechanic features and were completely covered by epithelial cells. Top row, images of longitudinal sections; bottom row, images of cross sections of the anastomosis sites. White arrows indicate vital chondrocytes; red arrows indicate surgical sutures; double-headed arrows indicate subepithelial thicknesses. **(C,D)** Both FIT **(C)** and DeCTA **(D)** showed infiltration of a few $CD4^+$ T cells, $CD8^+$ T cells, and $CD68^+$ macrophages (black arrows) in the subepithelial area. Images in the bottom rows show magnified views of the areas demarcated by the black boxes in the top rows. **(E–G)** The necrosis scores **(G)** and inflammatory cell numbers **(E)** for DeCTA and FIT did not differ significantly; however, DeCTA had significantly higher subepithelial thickness at the anastomosis site **(F)**. $*p < 0.05$ vs. anastomosis site of FIT. FIT-a, anastomosis site of FIT; DeCTA-a, anastomosis site of DeCTA; FIT-c, graft center of FIT; DeCTA-c, graft center of DeCTA. ANOVA was used for comparisons among multiple groups, as appropriate.

cells functioned normally to move cell clusters (Supplementary Video S1). Live/dead staining revealed that RECs adhered to DeCTA well (Figures 4E, F). SEM showed that DeCTA cocultured with RECs was successfully epithelialized in the luminal surface (~81.3 ± 5.6%), yielding ReCTA (Figures 4G, H).

In vivo assessment of heterotopically implanted ReCTA

ReCTA maintained normal rigidity with some slight contracting 30 days postoperatively. It was integrated with and vascularized by the surrounding adipose tissue flap (Figures 5A, B). Under surgical microscope observation, its lumen was patent, and the neo-trachea had preserved elasticity and strength to resist compression (Figure 5C; Supplementary Video S2). In contrast, FTA, CTA, and DeCTA were obliterated and severely contracted, resulting in deformity (Figure 5D). Histological analysis confirmed that ReCTA maintained normal structural integrity and had epithelium, cartilage, and luminal patency. In all grafts, the periphery of the cartilage had a high percentage of viable chondrocytes (~31.8% ± 9.5%), indicating that cartilage maximally evaded host immune recognition (Figure 5D). FTA, CTA, and DeCTA were almost completely obliterated by lamina propria hyperplasia, which was characterized by epithelium loss in FTA and CTA and abundant fibroblasts in FTA, CTA, and DeCTA, while only varied subepithelium thickness was observed in ReCTA (~70.5 ± 15 μm). H&E staining and SEM analysis revealed cilia in the ReCTA epithelium, especially in the posterior wall of tracheal membrane fascia area, where the blood supply was easily established earlier than in other parts (Figures 5E–I). Besides ciliated cells, both basal cells and goblet cells, which are responsible for epithelial proliferation and mucus secretion, respectively, were distributed along the epithelium (Figures 5E–I). In FIT, the entire lining was covered by normal pseudostratified columnar epithelium with cilia, whereas in ReCTA the entire lining was covered by a monolayer of epithelial cells, of which only about 15.0% ± 2.3% had cilia. Partial cartilage necrosis and calcification were present in the centers of all grafts, but compared with FTA, CTA, and DeCTA, both ReCTA and FIT had significantly lower luminal obliteration ratios and tracheal necrosis scores (Figures 5J, K).

Immunohistochemistry revealed significant immunorejection in FTA and CTA (Figures 6A–C). Compared with DeCTA, ReCTA, and FIT, both FTA and CTA had dramatically more $CD4^+$ T-cell, $CD8^+$ T-cell, and $CD68^+$ macrophage infiltration in the lumen and adventitial areas (Figures 6D–F), indicating that the rejection was initiated by the epithelium. Antigen-presenting cells, such as macrophages and dendritic cells, could have presented the alloantigen to T cells, activating them. The consequent molecular signaling cascade resulted in severe inflammation and cellular proliferation, which further caused graft obliteration and loss of function (Figure 6). Compared with FTA and CTA, DeCTA had less T cell and macrophage infiltration, suggesting that its obliteration was mainly initiated by wound healing and fibrosis rather than immunorejection (Figure 6). The numbers of infiltrating $CD4^+$, $CD8^+$, and $CD68^+$ cells in ReCTA and FIT did not differ significantly, indicating that ReCTA did not stimulate immunorejection (Figure 6).

In vivo assessment of orthotopically implanted DeCTA

To evaluate if the cartilage rigidity of DeCTA can endure tracheal movement *in vivo*, we compared orthotopic implants of DeCTA and FIT, which were placed in 5 rats each. One rat implanted with DeCTA died 9 days postoperatively because of airway obstruction and collapse at the trachea anastomosis site, but the remaining 4 rats implanted with DeCTA survived until they were humanely killed 3 months postoperatively. Explanted DeCTA showed luminal patency as well as rigidity with elasticity and strength. Histological analysis showed that, like FIT, DeCTA had a normal tracheal structure. As in the heterotopic implantation model, partial cartilage calcification necrosis occurred in the centers of the grafts. However, there was a considerable percentage of viable chondrocytes (~32.1% ± 6.5%) distributed in the periphery, and these cells sufficiently supported the trachea's structural integrity and functionality, enabling its adaptation to neck movement. Unlike in the heterotopic implantation model, the tracheal lining had a high percentage of cilia cells (~86.0% ± 8.6%), indicating that it was completely covered by the cells and that host epithelial cells successfully migrated from the anastomosis site and proliferated to cover the grafts (Figures 7A, B). In both FIT and DeCTA, the anastomosis area had $CD68^+$ macrophages, $CD4^+$ T cells, and $CD8^+$ T cells (Figures 7C, D), albeit in significantly smaller numbers than those in FTA and CTA in the heterotopic implantation model (Figures 7C, D). The numbers of these cells in DeCTA and FIT in the orthotopic implantation model did not differ significantly (Figure 7E). The subepithelium at the anastomosis site was thicker in DeCTA than in FIT; however, the subepithelial thicknesses at the centers of the grafts did not differ significantly (Figures 7A, B, F). Subepithelial thickness did not affect luminal patency during the 3-month observation period, and the tracheal necrosis scores for DeCTA and FIT did not differ significantly (Figure 7G).

Discussion

The goal of tracheal reconstruction is to provide a non-collapsible airway with a stable epithelial lining and reliable, well-vascularized tissue coverage (Yu et al., 2006; Delaere et al., 2010; Yu et al., 2011; Rendina and Patterson, 2022; Yang et al., 2023). To achieve this goal, in the present study, we applied a partially decellularized tracheal scaffold to provide airway support and successfully covered its lumen with RECs to provide a functional respiratory lining. Our findings demonstrate that heterotopically implanted engineered neo-tracheas can be successfully neovascularized with an adipo-fascial flap and that orthotopically implanted neo-tracheas can have long-term survival with full function. This proof-of-concept study provides a new strategy for tracheal tissue engineering and could be clinically translated to reconstruct longer tracheal defects.

Completely removing epithelium from tracheal allografts while retaining an intact basement membrane and viable cartilage presents a challenge. Liu et al. (2000) recently reevaluated their previous studies over the past 2 decades and found that chemical detergent could effectively remove most of the epithelium and mixed glands from dog trachea. Compared with fresh tracheal cartilage, the de-epithelialized tracheal cartilage had significantly less GAG and collagen II, but the viable chondrocyte ratio was about 50%, and in a dog orthotopic

transplantation model, the remaining chondrocytes played key roles in preserving the patency and rigidity of the resultant allograft and preventing the development of granulation tissue during the initial transplantation period, thereby supporting the graft's long-term survival (Lu et al., 2018). The authors concluded that maintaining cartilage viability is necessary for successful immunosuppressant-free allotransplantation; however, the chemical detergent inevitably damaged chondrocytes during de-epithelialization (Liu L et al., 2002). Liu et al. (2021) and Liu et al. (2022) also reported that a modified detergent-based decellularization protocol eliminated all cell populations except chondrocytes in mouse trachea. Although the number of vital chondrocytes, which was initially small (~2.00% ± 3.46%), increased after implantation (~25.97% ± 10.99%), chondrocyte viability was still poor overall, and this may have been associated with the higher mortality rate of the host animals (~58%). Hence, chondrocyte viability plays a critical role in maintaining the biomechanical properties necessary to prevent stenosis or collapse in tracheal replacement (Liu et al., 2021; Liu Y et al., 2022). To protect tracheal chondrocytes in their study, Aoki et al. used a brief (3-h) detergent-based treatment with sodium dodecyl sulfate to remove only the epithelium and maintain the structural integrity of porcine tracheal grafts while keeping most of the cartilage alive *in vitro* (Aoki et al., 2019). In another series of studies, Hysi et al., 2014 heterotopically and orthotopically transplanted epithelium-denuded CTA into rabbit and porcine models. Rather than using a chemical-based method, they successfully applied a mechanical/surgical-based approach to remove the tracheal mucosa and obtain an epithelium-denuded tracheal allograft with preserved viable cartilage (Hysi et al., 2014; Hysi et al., 2015; De Wolf et al., 2017). Our findings are consistent with these previous reports. We found that the rat tracheal epithelium with most of its antigenicity could be easily removed after cryopreservation; even simply washing the trachea with cold PBS could remove most of the epithelium. Our SEM and histological analyses showed that most of the basement membrane was maintained, which is key to re-epithelialization (Delaere and Van Raemdonck, 2014), and our live/dead cell assay and histological and TEM analyses showed that cartilage viability was maintained, as evidenced by the high percentage of viable chondrocytes (~61.2% ± 2.9%). Our *in vivo* studies confirmed that the resultant DeCTA had the biomechanical properties the graft required to resist compression and remain patent. However, vital chondrocytes were predominantly distributed around the periphery of DeCTA, which indicated that cryoprotectants did not permeate the tracheal graft entirely, especially at its center. Although the remaining vital chondrocytes and surrounding dense extracellular matrix sufficiently maintained the tracheal structural integrity both *in vitro* and *in vivo*, additional studies are warranted to develop novel permeating and non-permeating cryoprotectants and to improve both the cryopreservation program [for example, by using vitrification cryopreservation (Yong et al., 2020)] and the partial de-epithelialization procedure to maximize the viability of tracheal cartilage (Sotres-Vega et al., 2006; Nakanishi, 2009; Zang et al., 2011; Delaere and Van Raemdonck, 2014).

Cryopreservation not only enables the long-term storage of viable allografts but also induces an immunomodulatory effect to improve allograft survival. Studies have shown that both the reduced antigenicity of the trachea (i.e., that conveyed by MHC I and II) that results from the partially denuded epithelium and the degeneration of chondrocytes by cryopreservation contribute to the immunomodulatory effect (Nakanishi, 2009). In other studies, cartilage sufficiently maintained tracheal rigidity in orthotopically implanted CTA (Sotres-Vega et al., 2006; Nakanishi, 2009), whereas the remaining epithelium (10%–40%) was rejected and gradually replaced by recipient epithelium (Mukaida et al., 1998; Genden et al., 2003). These results suggest that successful CTA implantation depends in part on the immune privilege of the cartilage. The experimental use of CTA for shorter defects has shown some success, but its use for longer defects has been largely unsuccessful (Nakanishi, 2009), primarily because the host epithelium cannot proliferate rapidly enough to entirely cover the exposed graft and prevent its fibrosis, stenosis, infection, and/or collapse (Hysi et al., 2015). This occurred in the heterotopic implantation experiments in the present study. Although CTA had significantly reduced antigenicity, the remaining epithelium still stimulated immunorejection, as evidenced by the high numbers of $CD4^+$ T cells, $CD8^+$ T cells, and $CD68^+$ macrophages infiltrating the lumens of the implants. In contrast, in DeCTA, the complete removal of the epithelium resulted in significantly fewer of those immune cells in the lumen; however, the lumen was still completely obliterated by fibrosis. Therefore, the successful transplantation of CTA and DeCTA requires appropriate epithelium cover to prevent immunorejection and lamina propria hyperplasia and ensure functional recovery (Delaere et al., 2010; Delaere and Van Raemdonck, 2014; Hysi et al., 2015). To further delineate the characterization of the immunological response on CTA and DeCTA, more details of macrophages subtypes infiltration (e.g., M1 and M2 macrophages) and their functionality need to be investigated in the next step.

A bioengineering approach could significantly enhance the pre-epithelialization of the tracheal bioscaffold, but the outcomes of such an approach depend on the cell types and seeding procedure used. In the first successful clinical use of tracheal allotransplantation, buccal mucosa was used to cover the fresh tracheal allograft (Delaere et al., 2010). However, the slow repopulation of the tracheal lining by grafted recipient oral mucosa cells significantly hinders the wide application of this therapy, and mucosa by itself cannot replace the full function of real RECs (Delaere et al., 2010; Delaere et al., 2012). Therefore, researchers have turned to a tissue-engineering approach to pre-epithelialize tracheal grafts with RECs (Aoki et al., 2019). However, the use of RECs to prepopulate de-epithelialized tracheal allograft or DeCTA for transplantation has not been reported (Liu et al., 2000; Hysi et al., 2014; Hysi et al., 2015; De Wolf et al., 2017; Lu et al., 2018). In the present study, we successfully isolated RECs from syngeneic donor rats and cultured them. The cultured RECs included cilia cells, basal cells, and goblet cells, all of which play important roles in effecting the full functional recovery of the neo-trachea. RECs seeded in the DeCTA lumen *in vitro* adhered and grew because the basement membrane was intact after de-epithelialization. Complete preservation of the basement membrane is important to epithelium healing because RECs cannot grow properly if the basement membrane is damaged (Delaere and Van Raemdonck, 2014). Without the coverage of the RECs, fibroblast hyperplasia would occur, resulting in subepithelial lamina propria tissue thickening and lethal stenosis (Hysi et al., 2015; Liu Y et al., 2022). In the heterotopic implantation model in the present study, RECs completely covered the lumens of explanted ReCTA, and these grafts had not only tracheal patency (with the smallest obliteration ratio among all grafts) but also functional epithelial cells. Moreover,

SEM and histological analyses revealed healthy cilia cells growing in the epithelium. It is well known that cilia are crucial to the removal of sputum to prevent and reduce infection. Histological analysis showed that more cilia cells grew in the posterior wall of the tracheal membrane area than in the cartilage area, possibly because vascularization occurred more easily in the membrane area, which has only soft tissue. Although cilia, basal, and goblet cells were all maintained in ReCTA, in most areas, they constituted only a monolayer epithelium, which was much thinner than the pseudostratified columnar epithelium in FIT. Contributing to this may have been the static culture system we used for the pre-epithelialization of ReCTA. To improve epithelialization, researchers must develop and optimize more comprehensive, cutting-edge culturing strategies; for example, dynamic organ culturing using a bioreactor could be employed to enhance tracheal scaffold epithelialization (Aoki et al., 2019). However, this would require achieving a delicate balance between the duration of the *in vitro* culturing of RECs on DeCTA and the duration of cartilage ischemia to avoid excessive chondrocyte apoptosis. An ideal strategy for achieving this goal could be an *in vivo* engineering approach in which heterotopic vascularization is simultaneously incorporated with the induction of REC proliferation and maturation on DeCTA after its initial adhesion *in vitro*.

In previous studies, de-epithelialized tracheal allograft showed a significant loss of chondrocyte viability after implantation in both long-term dog and short-term rabbit orthotopic implantation models (Hysi et al., 2015; Lu et al., 2018). In the present study, we also found that chondrocyte viability decreased after both short-term heterotopic and long-term orthotopic implantation. As Tanaka et al. (2003) reported, this reduced chondrocyte viability may be closely related to the fact that the relative ischemia of the cartilage during the initial revascularization phase could provoke apoptosis and subsequent dystrophic cartilage calcification. Because the tracheal graft is prone to ischemia, the neovascularization of the neo-trachea must be established as early as possible. Researchers have attempted numerous strategies to enhance the neovascularization of tracheal implants. Because the trachea lacks a dominant vasculature, it cannot be transferred with microvascular anastomosis; rather, its blood supply must be derived secondarily from wrapping flaps. Local pedicled flaps [e.g., sternohyoid muscle flaps (Luo et al., 2013)] and distal pedicled flaps [e.g., omentum flaps (Masaoka et al., 2002)] have been used to wrap tracheal grafts and constructs to form neo-trachea flap to provide a blood supply. In orthotopic models, such flaps are fabricated either immediately or in 2 stages; in the latter case, they are first prefabricated in a heterotypical position and then transferred to the orthotopic position in the neck (Sykes, 2010). Because neck and/or tracheal movement can dramatically affect the anastomosis between the vascular branch of the flap and the tracheal graft, 2-stage fabrication, such as that used in the present study, is most commonly used. With its pedicle of superficial epigastric arteries and veins, the neo-trachea flap fabricated in the groin position can be transferred to the neck as a vascularized composite free flap. Because the rat model we used allowed the orthotopic transfer of only a short tracheal graft, whose survival could be achieved through its vascularization with the adjacent recipient trachea, we did not perform a 2-stage transfer in the orthotopic model in the present study. The presence of viable epithelial cells and chondrocytes in neo-trachea indicated that neovascularization occurred shortly after heterotopic and orthotopic implantation. Besides flaps, angiogenic growth factors, such as VEGF or bFGF, have been applied directly to tracheal grafts and constructs to improve neovascularization (Sung and Won, 2001; Nakamura et al., 2019). Other approaches, such as those employing MSCs, have been used to enhance epithelium regeneration and graft vascularization (Han et al., 2011). An "all-in-one" approach incorporating the abovementioned methods could be used to promote earlier neovascularization in tracheal constructs in further studies.

In the present study, one of the rats with orthotopically implanted DeCTA died postoperatively from airway obstruction and collapse, indicating that the approach needs to be refined to further improve cartilage vitality and tracheal integrity. In the rats with orthotopic implants, the thickened subepithelium at the anastomosis site may have been caused by surgical injury and the exposure of the lining in the early postoperative stages, which may have stimulated cellular hyperplasia. However, in terms of graft epithelialization, the mechanical strength of the cartilage, luminal patency, and the overall survival rates of the animals, our results are promising as those of previous studies of orthotopically implanted tracheal allografts in rodent models (Candas et al., 2016; Liu et al., 2021). Our heterotopic implantation studies demonstrated the successful pre-epithelialization and neovascularization of the neo-trachea, whereas our orthotopic implantation studies demonstrated that the cartilage of DeCTA had sufficient biomechanical strength to bear neck movement and compression to ensure normal airway function. These findings provide a proof-of-concept for applying ReCTA for tracheal tissue engineering. These findings also demonstrate that the implantation of small grafts of ReCTA presents few technical challenges, which should enable us to rapidly and efficiently advance our technique to testing in large animal models, in which we will ultimately use 2-stage transplantation to reconstruct longer tracheal defects.

Conclusion

DeCTA effectively had no epithelial allo-antigenicity and had a well-maintained 3-dimensional architecture, an intact basement membrane, vital chondrocytes, and cartilage with structural integrity and strong mechanical properties. DeCTA was also non-cytotoxic, having no side effects on RECs' morphology or adhesion, indicating that it has potential as a bioscaffold for tracheal tissue engineering by providing a mimetic niche *in vivo*. Our findings in heterotopic and orthotopic implantation models confirmed that the tracheal cartilage of ReCTA has immune privilege and has sufficient mechanical properties to bear neck movement and compression; indicated that the pre-epithelialization of DeCTA, resulting in ReCTA can prevent fibrosis obliteration and maintain lumen/airway patency in neo-trachea; and showed that a pedicled adipose tissue flap can be easily integrated with ReCTA to achieve neovascularization. In conclusion, a 2-stage bioengineering approach can be used to create and prevascularize ReCTA to form neo-trachea flap, whose intact basement membrane and viable chondrocytes contribute to its structural integrity, thus providing a promising tracheal reconstruction strategy that warrants further testing in large animal models. Ultimately, ReCTA could be translated to the clinic for the reconstruction of large tracheal defects.

Data availability statement

The original contributions presented in the study are included in the article/Supplementary Material, further inquiries can be directed to the corresponding authors.

Ethics statement

The animal study was reviewed and approved by Institutional Animal Care and Use Committee at the University of Texas MD Anderson Cancer Center.

Author contributions

NZ: investigation, formal analysis. YC: investigation, formal analysis. YW: investigation. MZ: investigation. RL: investigation. EC: investigation. MS: investigation, PY: supervision, resources, formal analysis, writing-review and editing. QZ: conceptualization, supervision, investigation, formal analysis, writing-original draft, review and editing. All authors contributed to the article and approved the submitted version

Funding

This work was supported by the Kyte Fund through MD Anderson's Department of Plastic Surgery. This work used MD Anderson's High Resolution Electron Microscopy Facility, which is supported by the NIH through MD Anderson's Cancer Center Support Grant (CA016672).

Acknowledgments

We thank Joseph Munch in MD Anderson's Research Medical Library for editing the manuscript; Michael Gallagher in MD Anderson's Department of Medical Graphics and Photography for editing the graphical abstract; Zhenbo Han in MD Anderson's Department of Molecular and Cellular Oncology for help with immunostaining imaging; and Kenneth Dunner, Jr., in MD Anderson's High Resolution Electron Microscopy Facility for assistance with SEM and TEM imaging.

Conflict of interest

The authors declare that the research was conducted in the absence of any commercial or financial relationships that could be construed as a potential conflict of interest.

Publisher's note

All claims expressed in this article are solely those of the authors and do not necessarily represent those of their affiliated organizations, or those of the publisher, the editors and the reviewers. Any product that may be evaluated in this article, or claim that may be made by its manufacturer, is not guaranteed or endorsed by the publisher.

Supplementary material

The Supplementary Material for this article can be found online at: https://www.frontiersin.org/articles/10.3389/fbioe.2023.1196521/full#supplementary-material

SUPPLEMENTARY VIDEO S1
Isolation of RECs. Cilia drive the movement of healthy cell clusters.

SUPPLEMENTARY VIDEO S2
ReCTA harvested 30 days after its heterotopic implantation. The graft had strong mechanical properties, enabling it to bear compression.

References

American Cancer Society (2002) *Cancer facts and figures 2002*. American Cancer Society: Atlanta, GA, 3.

Anderl, H., and Haid, B. (2005). Total reconstruction of the trachea: A 22-year follow-up. *Plast. Reconstr. Surg.* 115 (2), 548–552. doi:10.1097/01.prs.0000148418.73596.74

Aoki, F. G., Varma, R., Marin-Araujo, A. E., Lee, H., Soleas, J. P., Li, A. H., et al. (2019). De-epithelialization of porcine tracheal allografts as an approach for tracheal tissue engineering. *Sci. Rep.* 9 (1), 12034. doi:10.1038/s41598-019-48450-4

Beldholm, B. R., Wilson, M. K., Gallagher, R. M., Caminer, D., King, M. J., and Glanville, A. (2003). Reconstruction of the trachea with a tubed radial forearm free flap. *J. Thorac. Cardiovasc Surg.* 126 (2), 545–550. doi:10.1016/s0022-5223(03)00357-x

Candas, F., Gorur, R., Haholu, A., Yildizhan, A., Yucel, O., Ay, H., et al. (2016). Is tracheal transplantation possible with cryopreserved tracheal allograft and hyperbaric oxygen therapy? An experimental study. *Ann. Thorac. Surg.* 101 (3), 1139–1144. doi:10.1016/j.athoracsur.2015.09.018

Cavadas, P. C. (1998). Tracheal reconstruction using a free jejunal flap with cartilage skeleton: Experimental study. *Plast. Reconstr. Surg.* 101 (4), 937–942. doi:10.1097/00006534-199804040-00008

Cui, P., Liu, P., Li, S., and Ma, R. (2021). De-epithelialized heterotopic tracheal allografts without immunosuppressants in dogs: Long-term results for cartilage viability and structural integrity. *Ann. Otol. Rhinol. Laryngol.* 130 (5), 441–449. doi:10.1177/0003489420957357

Cull, D. L., Lally, K. P., Mair, E. A., Daidone, M., and Parsons, D. S. (1990). Tracheal reconstruction with polytetrafluoroethylene graft in dogs. *Ann. Thorac. Surg.* 50 (6), 899–901. doi:10.1016/0003-4975(90)91116-s

De Wolf, J., Brieu, M., Zawadzki, C., Ung, A., Kipnis, E., Jashari, R., et al. (2017). Successful immunosuppressant-free heterotopic transplantation of tracheal allografts in the pig. *Eur. J. Cardiothorac. Surg.* 52 (2), 248–255. doi:10.1093/ejcts/ezx116

Delaere, P. R., and Van Raemdonck, D. (2014). The trachea: The first tissue-engineered organ? *J. Thorac. Cardiovasc Surg.* 147 (4), 1128–1132. doi:10.1016/j.jtcvs.2013.12.024

Delaere, P., Vranckx, J., Verleden, G., De Leyn, P., and Van Raemdonck, D. (2010). Tracheal allotransplantation after withdrawal of immunosuppressive therapy. *N. Engl. J. Med.* 362 (2), 138–145. doi:10.1056/nejmoa0810653

Delaere, P. R., Vranckx, J. J., Meulemans, J., Vander Poorten, V., Segers, K., Van Raemdonck, D., et al. (2012). Learning curve in tracheal allotransplantation. *Am. J. Transpl.* 12 (9), 2538–2545. doi:10.1111/j.1600-6143.2012.04125.x

Den Hondt, M., Vanaudenaerde, B. M., Verbeken, E. K., and Vranckx, J. J. (2016). Tracheal tissue-engineering: *In-vivo* biocompatibility of mechanically-stripped allogenic rabbit trachea with autologous epithelial covering. *Acta Chir. Belg* 116 (3), 164–174. doi:10.1080/00015458.2016.1210844

Den Hondt, M., Vanaudenaerde, B. M., Maughan, E. F., Butler, C. R., Crowley, C., Verbeken, E. K., et al. (2017). An optimized non-destructive protocol for testing

mechanical properties in decellularized rabbit trachea. *Acta Biomater.* 60, 291–301. doi:10.1016/j.actbio.2017.07.035

Gandhi, S., Walsh, G. L., Komaki, R., Gokaslan, Z. L., Nesbitt, J. C., Putnam, J. B., Jr., et al. (1999). A multidisciplinary surgical approach to superior sulcus tumors with vertebral invasion. *Ann. Thorac. Surg.* 68 (5), 1778–1784. ; discussion 1784-5. doi:10.1016/s0003-4975(99)01068-1

Genden, E. M., and Laitman, B. M. (2023). Human tracheal transplantation. *Transplantation*. 2023 Feb 14. doi:10.1097/TP.0000000000004509

Genden, E. M., Iskander, A., Bromberg, J. S., and Mayer, L. (2003). The kinetics and pattern of tracheal allograft re-epithelialization. *Am. J. Respir. Cell. Mol. Biol.* 28 (6), 673–681. doi:10.1165/rcmb.2002-0214oc

Ghali, S., Chang, E. I., Rice, D. C., Walsh, G. L., and Yu, P. (2015). Microsurgical reconstruction of combined tracheal and total esophageal defects. *J. Thorac. Cardiovasc Surg.* 150 (5), 1261–1266. doi:10.1016/j.jtcvs.2011.10.100

Gonfiotti, A., Jaus, M. O., Barale, D., Baiguera, S., Comin, C., Lavorini, F., et al. (2014). The first tissue-engineered airway transplantation: 5-year follow-up results. *Lancet* 383 (9913), 238–244. doi:10.1016/s0140-6736(13)62033-4

Grillo, H. C., and Mathisen, D. J. (1990). Primary tracheal tumors: Treatment and results. *Ann. Thorac. Surg.* 49 (1), 69–77. doi:10.1016/0003-4975(90)90358-d

Grillo, H. (2004). "Primary tracheal neoplasms," in *Surgery of the trachea and bronchi* (Hamilton, Canada: BC Decker Inc.), 207–247.

Han, Y., Lan, N., Pang, C., and Tong, X. (2011). Bone marrow-derived mesenchymal stem cells enhance cryopreserved trachea allograft epithelium regeneration and vascular endothelial growth factor expression. *Transplantation* 92 (6), 620–626. doi:10.1097/tp.0b013e31822a4082

Hiwatashi, S., Iwai, R., Nakayama, Y., Moriwaki, T., and Okuyama, H. (2022) Successful tracheal regeneration using biofabricated autologous analogues without artificial supports. *Sci. Rep.* 12, 20279. doi:10.1038/s41598-022-24798-y

Huey, D. J., Hu, J. C., and Athanasiou, K. A. (2012). Unlike bone, cartilage regeneration remains elusive. *Science* 338 (6109), 917–921. doi:10.1126/science.1222454

Hysi, I., Wurtz, A., Zawadzki, C., Kipnis, E., Jashari, R., Hubert, T., et al. (2014). Immune tolerance of epithelium-denuded-cryopreserved tracheal allograft. *Eur. J. Cardiothorac. Surg.* 45 (6), e180–e186. doi:10.1093/ejcts/ezu133

Hysi, I., Kipnis, E., Fayoux, P., Copin, M. C., Zawadzki, C., Jashari, R., et al. (2015). Successful orthotopic transplantation of short tracheal segments without immunosuppressive therapy. *Eur. J. Cardiothorac. Surg.* 47 (2), e54–e61. doi:10.1093/ejcts/ezu444

Iyikesici, T., Tuncozgur, B., Sanli, M., Isik, A. F., Meteroglu, F., and Elbeyli, L. (2009). Two-piece cryopreserved tracheal allotransplantation: An experimental study. *Eur. J. Cardiothorac. Surg.* 36 (4), 722–726. doi:10.1016/j.ejcts.2009.04.050

Jungebluth, P., Alici, E., Baiguera, S., Blomberg, P., Bozóky, B., Crowley, C., et al. (2011). Retracted: Tracheobronchial transplantation with a stem-cell-seeded bioartificial nanocomposite: A proof-of-concept study. *Lancet* 378 (9808), 1997–2004. doi:10.1016/s0140-6736(11)61715-7

Kojima, K., and Vacanti, C. A. (2014). Tissue engineering in the trachea. *Anat. Rec. Hob.* 297 (1), 44–50. doi:10.1002/ar.22799

Letang, E., Sánchez-Lloret, J., Gimferrer, J. M., Ramírez, J., and Vicens, A. (1990). Experimental reconstruction of the canine trachea with a free revascularized small bowel graft. *Ann. Thorac. Surg.* 49 (6), 955–958. doi:10.1016/0003-4975(90)90875-7

Liu, C. S., Feng, B. W., He, S. R., Liu, Y. M., Chen, L., Chen, Y. L., et al. (2022). Preparation and evaluation of a silk fibroin-polycaprolactone biodegradable biomimetic tracheal scaffold. *J. Biomed. Mater Res. B Appl. Biomater.* 110 (6), 1292–1305. doi:10.1002/jbm.b.35000

Liu, Y., Nakamura, T., Yamamoto, Y., Matsumoto, K., Sekine, T., Ueda, H., et al. (2000). Immunosuppressant-free allotransplantation of the trachea: The antigenicity of tracheal grafts can be reduced by removing the epithelium and mixed glands from the graft by detergent treatment. *J. Thorac. Cardiovasc Surg.* 120 (1), 108–114. doi:10.1067/mtc.2000.106655

Liu, L., Dharmadhikari, S., Shontz, K. M., Tan, Z. H., Spector, B. M., Stephens, B., et al. (2021). Regeneration of partially decellularized tracheal scaffolds in a mouse model of orthotopic tracheal replacement. *J. Tissue Eng.* 12, 204173142110174. doi:10.1177/20417314211017417

Liu L, L., Dharmadhikari, S., Spector, B. M., Tan, Z. H., Van Curen, C. E., Agarwal, R., et al. (2022). Tissue-engineered composite tracheal grafts create mechanically stable and biocompatible airway replacements. *J. Tissue Eng.* 13, 204173142211087. doi:10.1177/20417314221108791

Liu Y, Y., Nakamura, T., Sekine, T., Matsumoto, K., Ueda, H., Yoshitani, M., et al. (2002). New type of tracheal bioartificial organ treated with detergent: Maintaining cartilage viability is necessary for successful immunosuppressant free allotransplantation. *Asaio J.* 48 (1), 21–25. doi:10.1097/00002480-200201000-00006

Lu, T., Huang, Y., Qiao, Y., Zhang, Y., and Liu, Y. (2018). Evaluation of changes in cartilage viability in detergent-treated tracheal grafts for immunosuppressant-free allotransplantation in dogs. *Eur. J. Cardiothorac. Surg.* 53 (3), 672–679. doi:10.1093/ejcts/ezx317

Luo, X., Liu, Y., Zhang, Z., Tao, R., Liu, Y., He, A., et al. (2013). Long-term functional reconstruction of segmental tracheal defect by pedicled tissue-engineered trachea in rabbits. *Biomaterials* 34 (13), 3336–3344. doi:10.1016/j.biomaterials.2013.01.060

Macchiarini, P., Jungebluth, P., Go, T., Asnaghi, M. A., Rees, L. E., Cogan, T. A., et al. (2008). Clinical transplantation of a tissue-engineered airway. *Lancet* 372 (9655), 2023–2030. doi:10.1016/s0140-6736(08)61598-6

Masaoka, T., Oizumi, H., Fujishima, T., Naruke, Y., Shiono, S., and Shimazaki, Y. (2002). Removal of cartilage rings prevents graft stenosis in extended tracheal allotransplantation with omentopexy and immunosuppression: An experimental study. *J. Heart Lung Transpl.* 21 (4), 485–492. doi:10.1016/s1053-2498(01)00370-9

Matloub, H. S., and Yu, P. (2006). Engineering a composite neotrachea in a rat model. *Plast. Reconstr. Surg.* 117 (1), 123–128. doi:10.1097/01.prs.0000185607.96476.44

Mitchell, J. D., Mathisen, D. J., Wright, C. D., Wain, J. C., Donahue, D. M., Allan, J. S., et al. (2001). Resection for bronchogenic carcinoma involving the carina: Long-term results and effect of nodal status on outcome. *J. Thorac. Cardiovasc Surg.* 121 (3), 465–471. doi:10.1067/mtc.2001.112832

Mukaida, T., Shimizu, N., Aoe, M., Andou, A., Date, H., and Moriyama, S. (1998). Origin of regenerated epithelium in cryopreserved tracheal allotransplantation. *Ann. Thorac. Surg.* 66 (1), 205–208. doi:10.1016/s0003-4975(98)00154-4

Nakamura, R., Katsuno, T., Kitamura, M., Yamashita, M., Tsuji, T., Suzuki, R., et al. (2019). Collagen sponge scaffolds containing growth factors for the functional regeneration of tracheal epithelium. *J. Tissue Eng. Regen. Med.* 13 (5), 835–845. doi:10.1002/term.2835

Nakanishi, R. (2009). Cryopreservation of the tracheal grafts: Review and perspective. *Organogenesis* 5 (3), 113–118. doi:10.4161/org.5.3.9494

Pan, S., Shen, Z., Xia, T., Pan, Z., Dan, Y., Li, J., et al. (2022a). Hydrogel modification of 3D printing hybrid tracheal scaffold to construct an orthotopic transplantation. *Am. J. Transl. Res.* 14 (5), 2910–2925.

Pan, S., Lu, Y., Li, J., and Shi, H. (2022b). The biological properties of the decellularized tracheal scaffolds and 3D printing biomimetic materials: A comparative study. *J. Biomed. Mater Res. A* 110 (5), 1062–1076. doi:10.1002/jbm.a.37352

Rendina, E. A., and Patterson, G. A. (2022). Tracheal replacement: A never-ending search. *Am. J. Transpl.* 22 (12), 2721–2722. doi:10.1111/ajt.17179

Rendina, E. A., Venuta, F., De Giacomo, T., Ciccone, A. M., Moretti, M., Ruvolo, G., et al. (1999). Sleeve resection and prosthetic reconstruction of the pulmonary artery for lung cancer. *Ann. Thorac. Surg.* 68 (3), 995–1001. ; discussion 1001-2. doi:10.1016/s0003-4975(99)00738-9

Sotres-Vega, A., Villalba-Caloca, J., Jasso-Victoria, R., Olmos-Zúñiga, J. R., Gaxiola-Gaxiola, M., Baltazares-Lipp, M., et al. (2006). Cryopreserved tracheal grafts: A review of the literature. *J. Invest. Surg.* 19 (2), 125–135. doi:10.1080/08941930600569779

Sung, S. W., and Won, T. (2001). Effects of basic fibroblast growth factor on early revascularization and epithelial regeneration in rabbit tracheal orthotopic transplantation. *Eur. J. Cardiothorac. Surg.* 19 (1), 14–18. doi:10.1016/s1010-7940(00)00624-2

Sykes, M. (2010). Immune evasion by chimeric trachea. *N. Engl. J. Med.* 362 (2), 172–174. doi:10.1056/nejme0908366

Tanaka, H., Maeda, K., and Okita, Y. (2003). Transplantation of the cryopreserved tracheal allograft in growing rabbits. *J. Pediatr. Surg.* 38 (12), 1707–1711. doi:10.1016/j.jpedsurg.2003.08.036

Teramachi, M., Okumura, N., Nakamura, T., Yamamoto, Y., Kiyotani, T., Takimoto, Y., et al. (1997). Intrathoracic tracheal reconstruction with a collagen-conjugated prosthesis: Evaluation of the efficacy of omental wrapping. *J. Thorac. Cardiovasc Surg.* 113 (4), 701–711. doi:10.1016/s0022-5223(97)70227-7

Tsou, K. C., Hung, W. T., Ju, Y. T., Liao, H. C., Hsu, H. H., and Chen, J. S. (2023). Application of aortic allograft in trachea transplantation. *J. Formos. Med. Assoc.* 29, S0929. doi:10.1016/j.jfma.2023.03.006

Vogel, G. (2013). Trachea transplants test the limits. *Science* 340 (6130), 266–268. doi:10.1126/science.340.6130.266

Wang, J., Zhang, H., Sun, Y., Liu, P., Li, S., and Cui, P. (2021). Mechanical properties of de-epithelialized tracheal allografts. *J. Thorac. Dis.* 13 (2), 1066–1074. doi:10.21037/jtd-20-2739

Xu, Y., Li, D., Yin, Z., He, A., Lin, M., Jiang, G., et al. (2017). Tissue-engineered trachea regeneration using decellularized trachea matrix treated with laser micropore technique. *Acta Biomater.* 58, 113–121. doi:10.1016/j.actbio.2017.05.010

Yang, M., Chen, J., Chen, Y., Lin, W., Tang, H., Fan, Z., et al. (2023). Scaffold-free tracheal engineering via a modular strategy based on cartilage and epithelium sheets. *Adv. Healthc. Mater* 12 (6), e2202022. doi:10.1002/adhm.202202022

Yong, K. W., Laouar, L., Elliott, J. A. W., and Jomha, N. M. (2020). Review of non-permeating cryoprotectants as supplements for vitrification of mammalian tissues. *Cryobiology* 96, 1–11. doi:10.1016/j.cryobiol.2020.08.012

Yu, P., Clayman, G. L., and Walsh, G. L. (2006). Human tracheal reconstruction with a composite radial forearm free flap and prosthesis. *Ann. Thorac. Surg.* 81 (2), 714–716. doi:10.1016/j.athoracsur.2004.12.009

Yu, P., Clayman, G. L., and Walsh, G. L. (2011). Long-term outcomes of microsurgical reconstruction for large tracheal defects. *Cancer* 117 (4), 802–808. doi:10.1002/cncr.25492

Zang, M., Chen, K., and Yu, P. (2010). Reconstruction of large tracheal defects in a canine model: Lessons learned. *J. Reconstr. Microsurg* 26 (6), 391–399. doi:10.1055/s-0030-1249605

Zang, M., Zhang, Q., Davis, G., Huang, G., Jaffari, M., Ríos, C. N., et al. (2011). Perichondrium directed cartilage formation in silk fibroin and chitosan blend scaffolds for tracheal transplantation. *Acta Biomater.* 7 (9), 3422–3431. doi:10.1016/j.actbio.2011.05.012

Zang, M., Zhang, Q., Chang, E. I., Mathur, A. B., and Yu, P. (2012). Decellularized tracheal matrix scaffold for tissue engineering. *Plast. Reconstr. Surg.* 130 (3), 532–540. doi:10.1097/prs.0b013e31825dc084

Zang, M., Zhang, Q., Chang, E. I., Mathur, A. B., and Yu, P. (2013). Decellularized tracheal matrix scaffold for tracheal tissue engineering: *In vivo* host response. *Plast. Reconstr. Surg.* 132 (4), 549e–559e. doi:10.1097/prs.0b013e3182a013fc

Zhao, Y., Steidle, J. F., Upchurch, G. R., Kron, I. L., and Lau, C. L. (2013). Prevention of the second stage of epithelial loss is a potential novel treatment for bronchiolitis obliterans. *J. Thorac. Cardiovasc Surg.* 145 (4), 940–947.e1. doi:10.1016/j.jtcvs.2012.07.098

frontiers | Frontiers in Bioengineering and Biotechnology

TYPE Original Research
PUBLISHED 23 May 2023
DOI 10.3389/fbioe.2023.1207858

OPEN ACCESS

EDITED BY
Meng Tian,
Sichuan University, China

REVIEWED BY
Donghai Li,
Sichuan University, China
Ye Cao,
Chinese Academy of Medical Sciences and Peking Union Medical College, China

*CORRESPONDENCE
Chang-Hwan Yoon,
kunson2@snu.ac.kr

RECEIVED 18 April 2023
ACCEPTED 08 May 2023
PUBLISHED 23 May 2023

CITATION
Hahn D, Lee D, Hyun W, Cho Y, Yoon C-H, Jeon K-H, Kang S-H, Youn T-J and Chae I-H (2023), Faster smooth muscle cell coverage in ultrathin-strut drug-eluting stent leads to earlier re-endothelialization.
Front. Bioeng. Biotechnol. 11:1207858.
doi: 10.3389/fbioe.2023.1207858

Faster smooth muscle cell coverage in ultrathin-strut drug-eluting stent leads to earlier re-endothelialization

Dongwoo Hahn[1], Donghoon Lee[2], Woonggyu Hyun[3], Yunnie Cho[3], Chang-Hwan Yoon[1]*, Ki-Hyun Jeon[1], Si-Hyuck Kang[1], Tae-Jin Youn[1] and In-Ho Chae[1]

[1]Division of Cardiology, Department of Internal Medicine, Seoul National University Bundang Hospital, Seongnam, Republic of Korea, [2]Cardiovascular center, Asan Chungmu Hospital, Asan, Republic of Korea, [3]College of Medicine, Seoul National University, Seoul, Republic of Korea

Background: The ultrathin-strut drug-eluting stent (DES) has shown better clinical results than thin- or thick-strut DES. We investigated if re-endothelialization was different among three types of DES: ultrathin-strut abluminal polymer-coated sirolimus-eluting stent (SES), thin-strut circumferential polymer-coated everolimus-eluting stent (EES), and thick-strut polymer-free biolimus-eluting stent (BES) to gain insight into the effect of stent design on promoting vascular healing.

Methods: After implanting three types of DES in the coronary arteries of minipigs, we performed optical coherence tomography (OCT) at weeks 2, 4, and 12 (n = 4, each). Afterward, we harvested the coronary arteries and performed immunofluorescence for endothelial cells (ECs), smooth muscle cells (SMCs), and nuclei. We obtained 3D stack images of the vessel wall and reconstructed the en face view of the inner lumen. We compared re-endothelialization and associated factors among the different types of stents at different time points.

Results: SES showed significantly faster and denser re-endothelialization than EES and BES at weeks 2 and 12. Especially in week 2, SES elicited the fastest SMC coverage and greater neointimal cross-sectional area (CSA) compared to EES and BES. A strong correlation between re-endothelialization and SMC coverage was observed in week 2. However, the three stents did not show any difference at weeks 4 and 12 in SMC coverage and neointimal CSA. At weeks 2 and 4, SMC layer morphology showed a significant difference between stents. A sparse SMC layer was associated with denser re-endothelialization and was significantly higher in SES. Unlike the sparse SMC layer, the dense SMC layer did not promote re-endothelialization during the study period.

Conclusion: Re-endothelialization after stent implantation was related to SMC coverage and SMC layer differentiation, which were faster in SES. Further investigation is needed to characterize the differences among the SMCs and explore methods for increasing the sparse SMC layer in order to improve stent design and enhance safety and efficacy.

KEYWORDS

drug-eluting stent (DES), optical coherence tomography, re-endothelialization, neointimal coverage, smooth muscle cell (SMC)

Highlights

· Neointimal coverage observed by optical coherence tomography and histologic coverage of vascular smooth muscle cells were almost complete after four weeks.
· However, histological re-endothelialization reached 50% at four weeks and 75% at 12 weeks after stent implantation.
· Re-endothelialization of stent struts at the late phase was associated with underlying neointimal smooth muscle cell phenotype.

Introduction

Since the introduction of angioplasty using balloons in 1977, bare-metal stents (BMS) in the 1980s, and drug-eluting stents (DES) in the 2000s, vascular healing of an injured coronary artery involving neointimal hyperplasia and re-endothelialization has been a major target to improve clinical efficacy after percutaneous coronary intervention (PCI) (Stefanini and Holmes, 2013; Fischman et al., 1994; Nicolas et al., 2022). In the process of PCI, endothelial cells (ECs) of blood vessels are inevitably damaged, and smooth muscle cells (SMCs) are activated in the subsequent recovery process, resulting in hyper-proliferation of intima tissue (Stefanini et al., 2017). Although antiproliferative agents that inhibit SMC proliferation significantly reduce restenosis, the risk of late stent thrombosis (LST) via suppression of endothelial regrowth remains a major concern after PCI, even with contemporary DES, such as thin-strut everolimus-eluting stents (EES), thick-strut polymer-free biolimus-eluting stents (BES), and ultra-thin strut biodegradable-polymer sirolimus-eluting stents (SES) (Taniwaki et al., 2016).

Intracoronary imaging, including intravascular ultrasound (IVUS) and optical coherence tomography (OCT), is used to clinically estimate the re-endothelialization of the strut surface and predict the risk of LST. OCT is the method of choice to characterize fibrous tissue, plaque, thrombus, and neointimal coverage, due to its axial resolution of 5–20 μm. Recently, it has been reported that the evaluation of strut coverage by OCT can be one of the factors for clinicians to decide the duration of dual antiplatelet therapy (Iliescu et al., 2017; Lee et al., 2018). However, it has been reported that neointimal coverage, which can be monitored by OCT, does not always include re-endothelialization of the vessel wall and fails to reveal the mechanism of clinical outcome difference among the stents. This grants closer histological observation after stent implantation over time (Torii et al., 2020). Therefore, it is necessary to investigate why contemporary stents show different clinical outcomes, particularly in terms of re-endothelialization, which is the true endpoint of vascular healing after stent implantation.

In this preclinical study, we investigated the relation between re-endothelialization, SMC pathophysiology, and neointimal coverage after stent implantation using quantitative histological examination and OCT data. Particularly, we compared the process of SMC differentiation and its effect on re-endothelialization after the implantation of EES, BES, and SES in the coronary artery of a porcine model.

Materials and methods

Animal care and use

The animal experimental procedures were approved by the Institutional Animal Care and Use Committee (IACUC) of Seoul National University Bundang Hospital (BA 1808-253/067-03) and performed in accordance with the Guide for the Care and Use of Laboratory Animals from the Institute of Laboratory Animals Resources. The day before the experiment, male minipigs (n = 12; body weight = 25–35 kg) were administered aspirin (300 mg) and clopidogrel (300 mg). On the day of the experiment, the pigs were premedicated with atropine sulfate (0.05 mg/kg, intramuscularly) and subsequently anesthetized with zoletil (5 mg/kg, intramuscularly) and xylazine (4.4 mg/kg, intramuscularly). Afterward, the pigs were intubated and ventilated with room air and sevoflurane. We inserted a 6 Fr sheath via the right femoral artery using an ultrasound-guided puncture.

Design

This study was conducted using three different stents: EES (Xience Sierra™, Abbott Vascular, United States), BES (Biofreedom™, Biosensors, United States), and SES (Genoss DES™, GENOSS, South Korea). The thin-strut EES has 81-μm-thick cobalt–chromium struts and a PVDF-HFP polymer-containing everolimus (Table 1). The thick-strut BES has 119-μm-thick stainless steel struts and releases biolimus A9 without a polymer. The ultrathin-strut SES has 70-μm-thick cobalt–chromium struts and a PLLA/PLGA biodegradable polymer-containing sirolimus.

These three stents were implanted in the three coronary arteries of 12 pigs. After stent implantation, the pigs were dosed with 100 mg aspirin and 75 mg clopidogrel daily. We assigned each of the four pigs to 2-, 4-, and 12-week post-stent implantation groups and compared the results from OCT and histology (Figure 1).

OCT imaging

Coronary angiography and OCT were performed using a Dragonfly® image catheter and C7-XR™ OCT system (Abbott, United States) after an intra-coronary injection of nitroglycerine before autopsy. From the OCT images, the cross-sectional area (CSA) of the coronary artery and stent strut apposition or coverage were evaluated using a dedicated imaging analysis program (OPTIS™ Imaging Systems software, Abbott Korea, Seoul, Korea).

Scanning electron microscopy

Samples were fixed in 10% neutral buffered formalin at room temperature. Dehydration treatment was performed using 50%–100% ethanol. Blood vessels were longitudinally cut, opened to expose the endothelium, and dried naturally. All samples were

TABLE 1 Characteristics of contemporary coronary drug-eluting stents tested in this study.

Stent	Drug	Stent material	Strut thickness (μm)	Polymer	Polymer type	Coating distribution	Polymer thickness
BES (Biofreedom™)	Biolimus A9	316 L	119	Polymer free	Polymer-free	Abluminal	Polymer-free
		Stainless steel					
EES (Xience Sierra™)	Everolimus	L-605	81	PVDF-HFP	Durable	Conformal	7–8 μm
		CoCr					
SES (Genoss-DES™)	Sirolimus	L-605	70	PLLA/ PGLA	Bioresorbable	Abluminal	<3 μm
		Co-Cr					

CoCr, cobalt–chromium; PGLA, poly(lactic-co-glycolic acid); PLLA, poly(L-lactic acid); PVDF-HFP, copolymer of vinylidene fluoride and hexafluoropropylene.

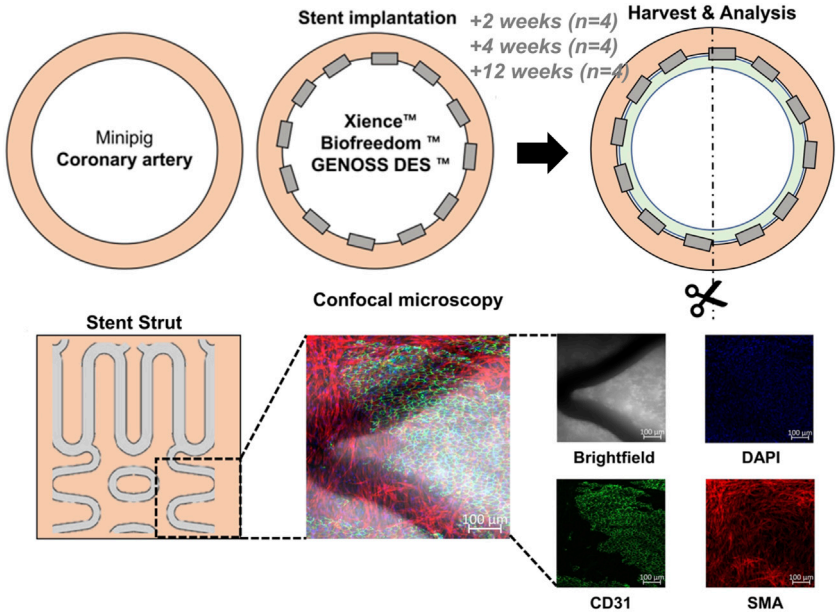

FIGURE 1
General schema of the experiment. Three different drug-eluting stents were implanted into the three coronary arteries (the left anterior descending artery, left circumflex artery, and right coronary artery) of a minipig. The arteries were harvested at 2, 4, and 12 weeks after stent implantation. Cells were analyzed under a confocal microscope after immunofluorescence staining with DAPI for nuclei, CD31 for endothelial cells, and smooth muscle actin (SMA) for smooth muscle cells. BES, Biofreedom™; EES, Xience Sierra™; SES, Genoss-DES™.

coated with gold to impart conductivity. The samples were imaged after selecting the magnification while appropriately adjusting the electron beam voltage and working distance by field-emission scanning electron microscopy (Sigma 500, Zeiss, Germany).

Histologic analysis

After the coronary arteries were harvested, endothelialization and neointima growth were evaluated by staining with antibodies against CD31, a glycoprotein expressed on ECs, alpha-smooth muscle actin (SMA-cy3), and nucleic acid (DAPI, 4,6-diamidino-2-phenylindole). Histological quantification was performed by obtaining three to six random field images from each coronary artery (Figure 1). Confocal microscopy was performed using a Zeiss LSM800 microscope (Carl Zeiss Korea, Seoul, Korea). Maximal intensity projection images were reconstructed from 100-fold magnification Z-stacked images. The total area of the stent strut and the area of the stent strut covered by ECs or SMCs were identified by immunofluorescence staining and quantified using the ImageJ program (Java-based image processing program, NIH, version 1.48s).

Statistical analysis

Continuous variables are reported as the mean ± standard deviation. One-way ANOVA and a statistical model constructed

10.3389/fbioe.2023.1207858

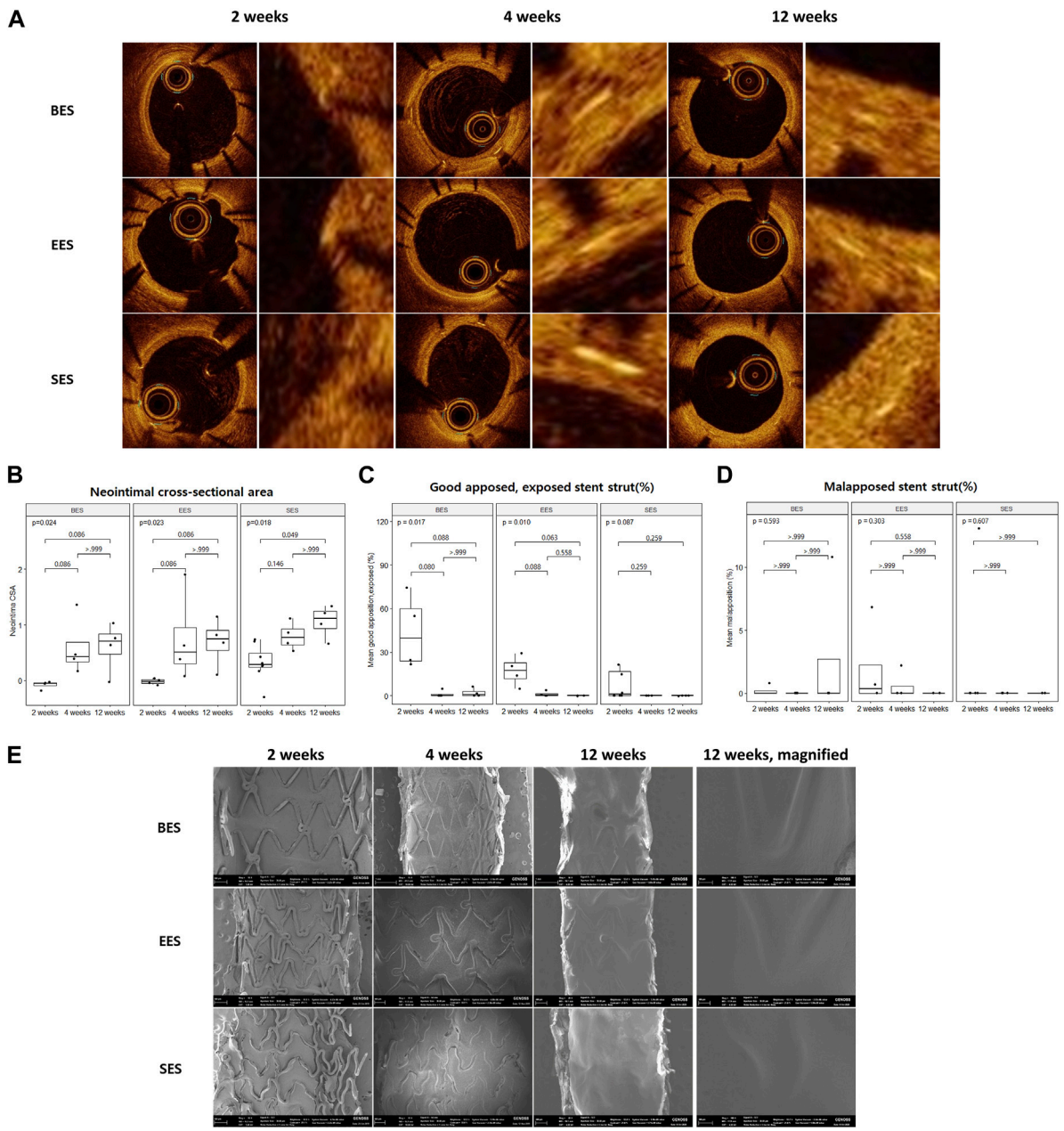

FIGURE 2
Neointimal coverage after stent implantation by optical coherence tomography and scanning electron microscopy. **(A)** Representative image of sequential optical coherence tomography images of stented coronary artery lumen at 2, 4, and 12 weeks after stent implantation. Images on the right pair show a magnified view of the neointimal area of the vessel wall. **(B)** Neointimal cross-sectional area, **(C)** % good apposition, exposed strut, and **(D)** % malapposed strut at three-time points. **(E)** Representative image of sequential scanning electron microscopic images of the stented vessel lumen at 2, 4, and 12 weeks after stent implantation. BES, Biofreedom™; EES, Xience Sierra™; SES, Genoss-DES™.

by generalized estimating equations with a variable number of repeated measures on every millimeter of OCT images and random field histologic images of each stent were applied. The main independent variable was the type of stent implanted, whereas the covariates included the major branches of the coronary artery where the stent was implanted. The dependent variables included the CSA of the stent, lumen, and neointima on OCT images, as well as the area of the stent strut, the area of the stent strut covered by ECs, or SMCs on histologic images. If there was significance among the three groups, Bonferroni's *post hoc* test was performed to find the statistical significance of the difference between one group and another. Statistical analyses were performed using R (R Foundation for Statistical Computing, Vienna, Austria; http://www.R-project.org, version 3.6.1). A two-sided p-value <0.05 was considered statistically significant.

TABLE 2 Optical coherence tomography analysis for each stent at 2, 4, and 12 weeks after implantations.

Time	Variable	BES	EES	SES	F-test *p*-value
2 weeks	Neointima CSA (mm^2)	−0.08 ± 0.07	−0.02 ± 0.05	0.32 ± 0.78	0.028[a]
	% Good apposed, covered	55.9 ± 25.4	81.0 ± 9.8	82.8 ± 34.1	0.303
	% Good apposed, exposed	43.9 ± 25.2	17.1 ± 10.3	15.6 ± 29.7	0.202
	% Malapposition	0.2 ± 0.4	1.9 ± 3.3	1.6 ± 4.6	0.781
4 weeks	Neointima CSA (mm^2)	0.60 ± 0.52	0.75 ± 0.80	0.80 ± 0.25	0.878
	% Good apposed, covered	98.8 ± 2.3	98.3 ± 3.0	100.0 ± 0.0	0.557
	% Good apposed, exposed	1.2 ± 2.3	1.2 ± 1.9	0.0 ± 0.0	0.576
	% Malapposition	0.0 ± 0.0	0.6 ± 1.1	0.0 ± 0.0	0.405
12 weeks	Neointima CSA (mm^2)	0.61 ± 0.45	0.69 ± 0.43	1.06 ± 0.29	0.279
	% Good apposed, covered	95.3 ± 6.0	10.0 ± 0.0	100.0 ± 0.0	0.143
	% Good apposed, exposed	2.0 ± 3.0	0.0 ± 0.0	0.0 ± 0.0	0.217
	% Malapposition	2.7 ± 5.4	0.0 ± 0.0	0.0 ± 0.0	0.405

BES, Biofreedom™; EES, Xience Sierra™; SES, Genoss-DES™; CSA, cross-sectional area; Mean ± SD.
[a]One-way ANOVA, with Bonferroni's *post hoc* test; BES vs. SES $p = 0.054$; BES vs. EES $p > 0.999$; SES vs. EES $p = 0.115$.

Results

Time-dependent vascular healing

All pigs survived the in-life phase of the study. All stents were evenly expanded at a 1:1 stent-to-vessel ratio. Angiography and OCT were performed immediately after stent implantation and at 2, 4, and 12 weeks (Figure 2A). No significant in-stent restenosis or stent thrombosis was observed by angiography or OCT throughout the study. CSA of the neointima gradually increased over time in all groups (Figure 2B). At week 2, the neointimal CSA in the SES group was significantly greater than in the BES and EES groups (Table 2). However, neointimal CSA showed no difference among the three stent groups at weeks 4 and 12 (Table 2). In terms of stent coverage, there was no statistical difference in the percentage of exposed and malapposed struts during the experimental period (Figures 2C, D; Table 2). Scanning electron microscopy also showed rapid neointimal growth and nearly complete stent coverage at week 12 after implantation in all stent groups (Figure 2E).

Using confocal microscopic images, we identified stent strut endothelialization and SMC coverage, as shown in Figures 3A–C. We found that endothelialization was slow and was not finished until week 12, whereas SMC coverage was fast and almost complete within 4 weeks (Figures 3D, E). Evaluation of cellularity using the DAPI (+) area on the strut showed that cellularity gradually decreased during the study period. Particularly, non-endothelial and non-SMCs, which were abundant at week 2, dramatically decreased at week 12 (Figure 3F).

The proportion of the area covered with ECs in the SES group was statistically greater than that in the BES and EES groups at week 2 (SES: 51.8 ± 41.6; BES: 13.3% ± 18.1%; EES: 19.7% ± 26.7%) (Figures 3A, D). At week 4, there was no significant difference in the proportion of the area covered with ECs among the three groups (Figures 3B, D). However, at week 12, the endothelial coverage area in the SES group (90.0% ± 15.1%) was significantly greater than that in the BES group (61.8% ± 35.2%, $p = 0.100$) or EES (62.2% ± 30.7%) (Figures 3C, D). The SMC coverage of the SES group progressed faster than that in BES and EES groups at week 2, but there was no difference in weeks 4 and 12 (Figure 3E). The area where only the nuclei were stained without endothelial or SMC marker staining was significantly smaller in the SES group compared to the BES group at week 4 (Figure 3F).

Delayed re-endothelialization compared to neointimal or SMC coverage

We observed full re-endothelialization on the neointima 12 weeks after stent implantation, and we found vessel wall defects of endothelium on neointima or even uncovered stent struts (Figure 4A). We evaluated the correlation between stent strut coverage from OCT analysis versus endothelialization and versus SMC coverage from histology. There was a correlation, but a gap between OCT and histologic quantification was observed. Specifically, 100% stent coverage observed by OCT was matched to around 55% in endothelialization and 75% in smooth muscle cells on the stent strut by histology (Figures 4B, C). Furthermore, there was a significant correlation between SMC coverage and re-endothelialization of stent struts at week 2 (Pearson's $r = 0.899$, $p < 0.001$). However, there was a very weak correlation at week 4 (Pearson's $r = 0.538$, $p < 0.001$) and no statistical significance at week 12 (Pearson's $r = 0.130$, $p = 0.377$) (Figure 4D).

Effect of smooth muscle cell morphology on re-endothelialization

We observed SMCs of different morphologies on the luminal side of the coronary arteries: no/rare, sparse (stellate), and dense (spindle) (Figure 5A). SMCs in normal vessels showed parallel

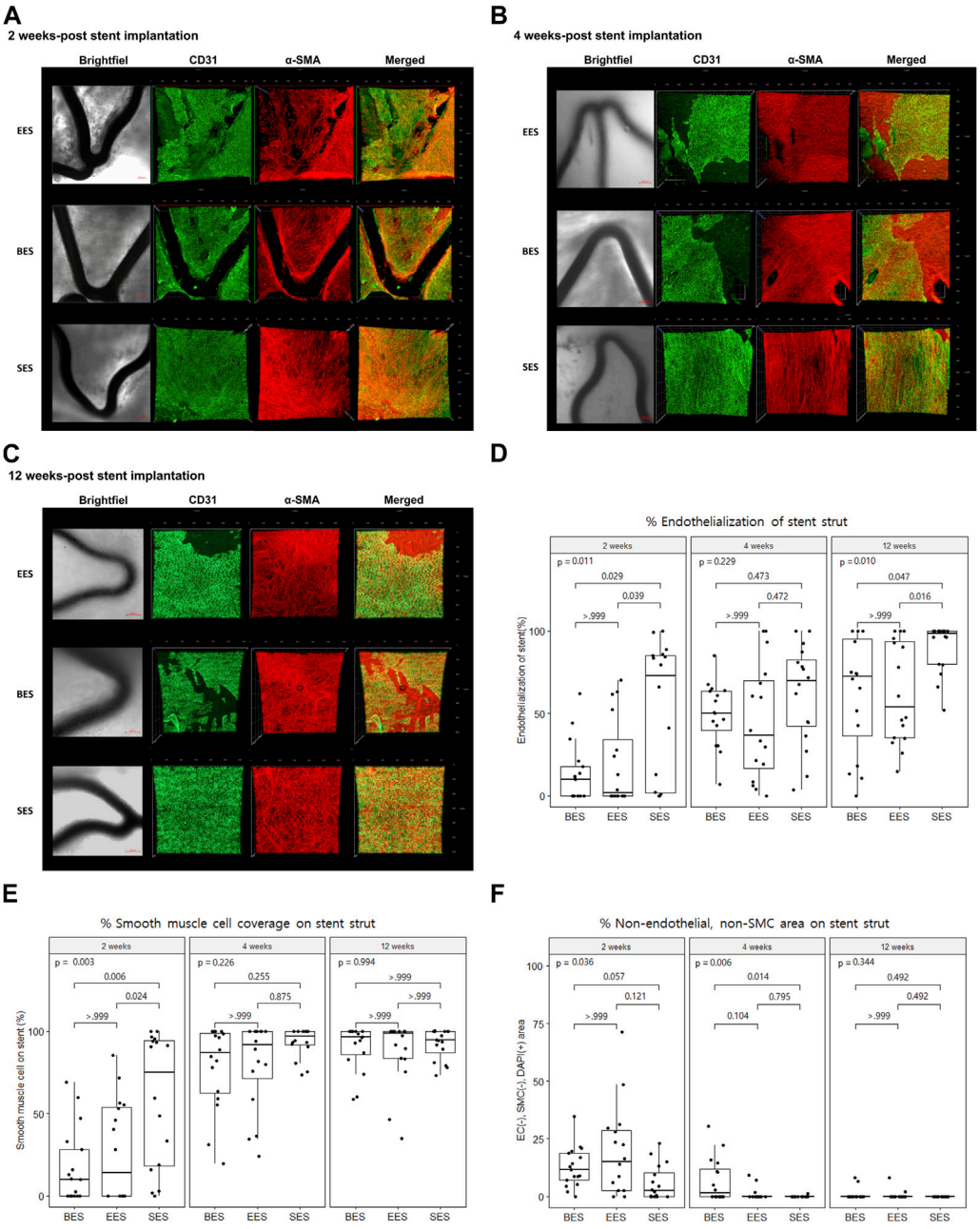

FIGURE 3
Re-endothelization and smooth muscle cell coverage after stent implantation by immunofluorescence. **(A–C)** Representative immunofluorescence images of stented coronary artery tissue depicting the endothelium (CD31, green), smooth muscle cell (α-smooth muscle actin, red), merged, and brightfield at 2, 4, and 12 weeks after stent implantation. Brightfield images show the stent strut (dark area). Scale bar = 100 μm. **(D)** % area of endothelial cells on different stent struts at 2, 4, and 12 weeks after stent implantation. **(E)** % area of smooth muscle cells on different stent struts at 2, 4, and 12 weeks after stent implantation. **(F)** % area of non-endothelial, non-smooth muscle cells on different stent struts at 2, 4, and 12 weeks after stent implantation. SMC, smooth muscle cell; BES, Biofreedom™; EES, Xience Sierra™; SES, Genoss-DES™.

alignment and vivid interconnecting muscle fibers (Figure 5B). However, sparse SMCs lost alignment but had connecting fibers. In contrast, dense SMCs showed high cellularity and poor development of interconnecting fibers. Throughout the experiment, the no/rare SMC area was decreased, whereas sparse SMC was increased (Figure 5C). However, the dense SMC area did not change. The no/rare SMC area was significantly lower in the SES group compared to the EES and BES groups at week 2 ($p = 0.005$). The sparse SMC area was significantly different at weeks 2 and 4, higher in the SES group ($p < 0.001$ and $p = 0.010$, respectively). Interestingly, the re-endothelialization on each SMC morphology layer was significantly different. On the no/rare SMC area, approximately 1% of the area showed re-endothelialization (Figure 5D; Table 3). Similarly, 13.5%–16.5% of the area showed

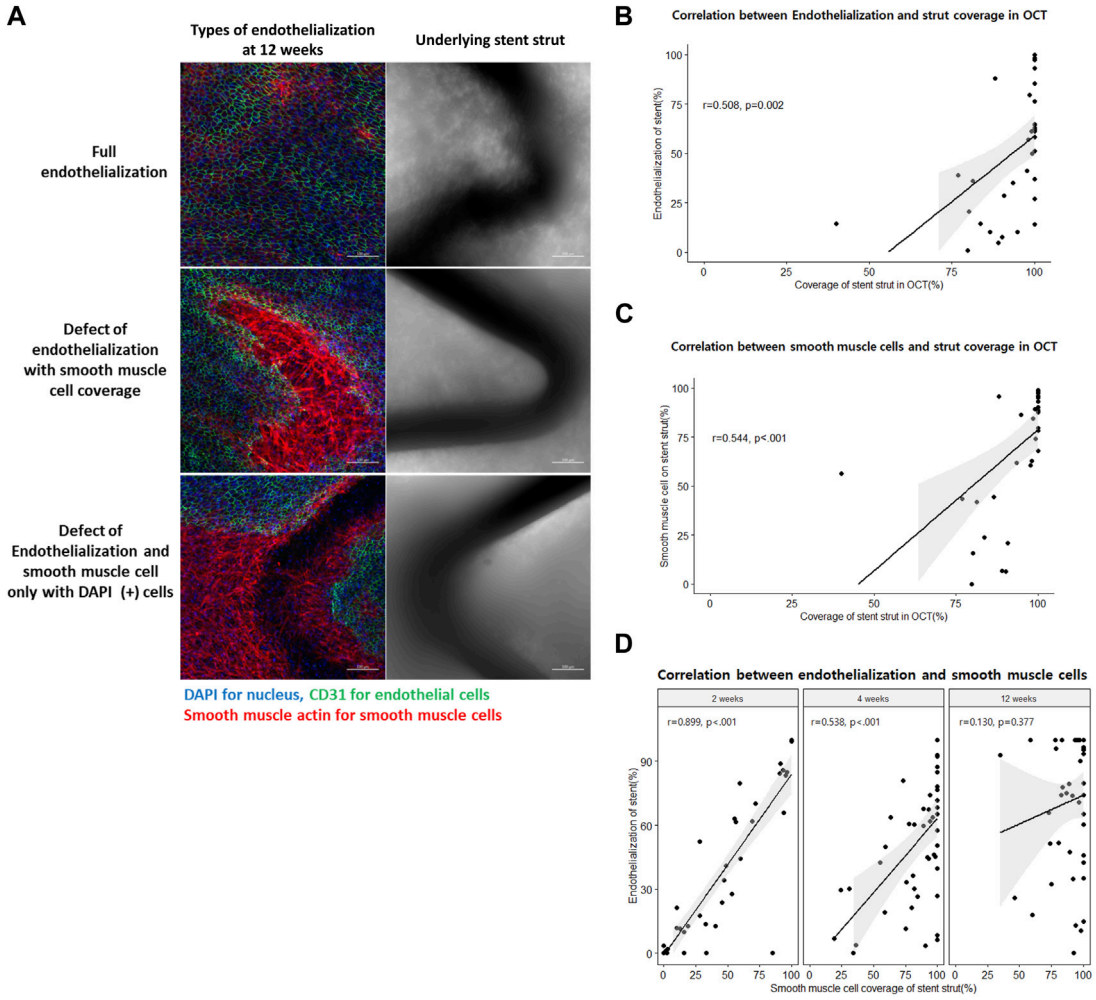

FIGURE 4
Delayed re-endothelialization and its predictors. **(A)** Different types of endothelialization at 12 weeks after stent implantation on the luminal side of the arterial wall by immunofluorescence. Scale bar = 100 μm (blue = nucleus, green = endothelial cells, and red = smooth muscle cells). **(B)** Correlation between the histologic endothelialization on the stent strut and optical coherence tomography (OCT)-defined covered stent strut. **(C)** Correlation between the histologic smooth muscle cell (SMC) coverage on the stent strut and OCT-defined covered stent strut. **(D)** Correlation between the histologic endothelialization and SMC coverage on the stent struts at 2, 4, and 12 weeks after stent implantations. OCT, optical coherence tomography; SMC, smooth muscle cells.

re-endothelialization in the dense SMC area. On the contrary, a significantly greater re-endothelialization area of 29.0%–61.3% was found in the sparse SMC area. Re-endothelialization increased as time passed only in the sparse SMC area. Particularly, re-endothelialization in the sparse SMC area was significantly higher in SES at weeks 2 and 4 (Figure 5D).

Discussion

This study demonstrates the difference between neointimal coverage and re-endothelialization of stents in the coronary artery and the effect of stent design on endothelialization after different types of DES implantation. Neointimal coverage of the stent struts was almost complete at 4 weeks after implantation, but re-endothelialization was not completed until week 12. Re-endothelialization seemed to be affected by the underlying SMC layer, particularly in the early phase of vascular healing, as there was a correlation between the appearance of the endothelium and the stent coverage of SMC until 4 weeks. In addition, we found no significant difference in the neointimal coverage of each type of stent tested in this study observed by the OCT. However, there was a significant difference in the endothelial coverage of the struts of each stent. The ultra-thin strut and abluminal biodegradable polymer SES showed the best re-endothelialization in the early and late phases of vascular healing. Re-endothelialization in the late phase of vascular healing seemed to be affected by the underlying SMC morphology as re-endothelialization progressed only on the sparse SMC area.

Stent thrombosis is caused by delayed healing of the coronary artery. It is also affected by persistent fibrin deposition, hypersensitivity, bifurcation lesions, and stent-strut malapposition (Joner et al., 2006). Especially after stent implantation, delayed re-endothelialization is an important factor in stent thrombosis (Finn et al., 2007; Otsuka et al., 2014). Finn et al. (2007) stated that

10.3389/fbioe.2023.1207858

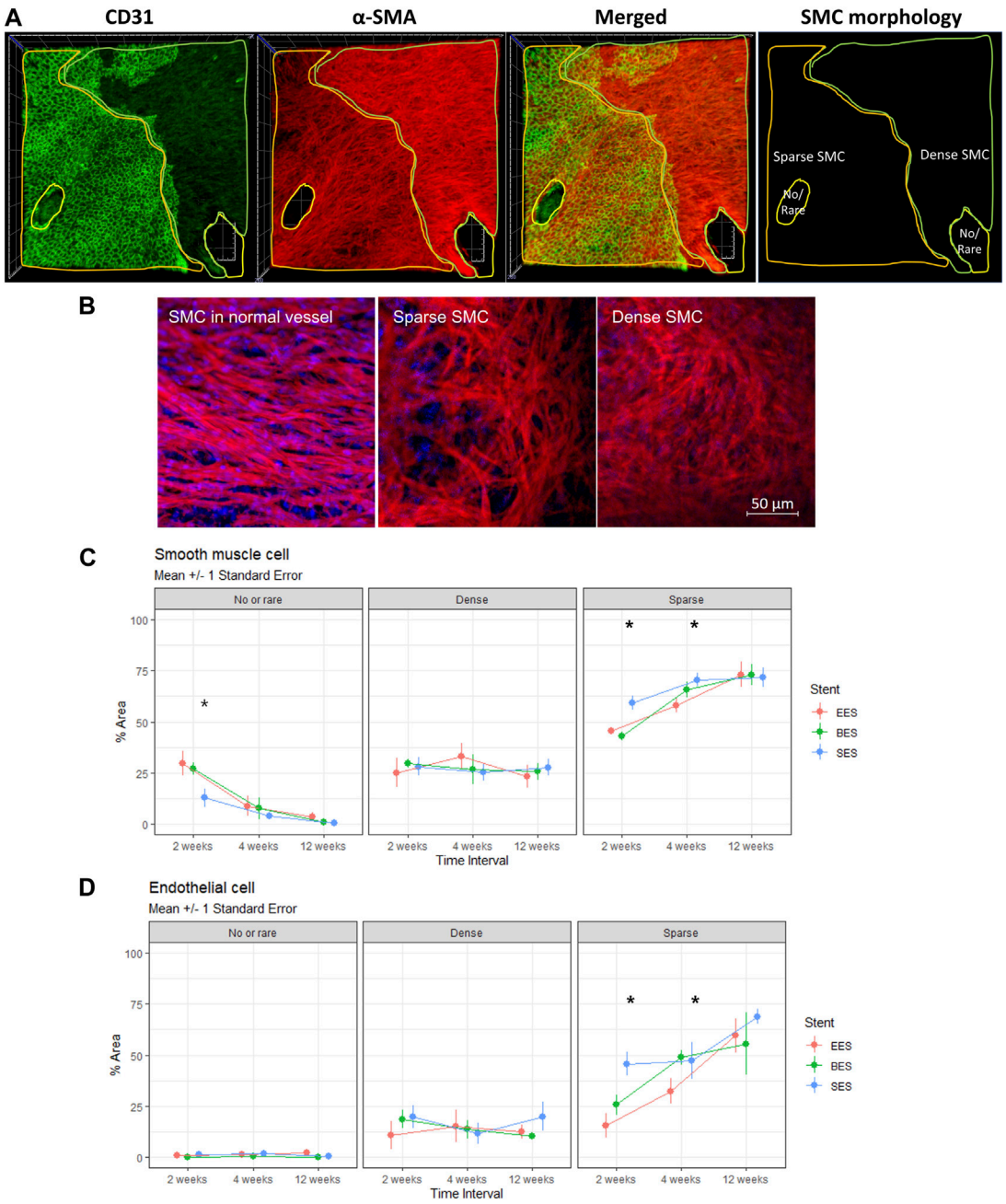

FIGURE 5
Morphology of smooth muscle cells and its effect on re-endothelialization. **(A)** Representative immunofluorescence image quantification of stented coronary artery tissue showing no/rare, dense (spindle), or sparse (stellate) SMC distribution on the luminal side of the stented coronary artery at 4 weeks after stent implantation. Endothelium (CD31, green), SMC (α-smooth muscle actin, red), merged, and SMC morphology distribution. Side of the rectangle = 800 µm. **(B)** Representative morphologic difference of SMC. Left panel, SMC in the normal vessel; mid panel, sparse SMC; right panel, dense SMC. **(C)** % area of no/rare, dense, or sparse SMC at 2, 4, and 12 weeks after stent implantations. *$p < 0.05$. **(D)** % area of endothelial cell distribution in the regions of no/rare, dense (spindle), or sparse (stellate) SMC distribution at 2, 4, and 12 weeks after stent implantation. *$p < 0.05$. BES, Biofreedom™ in green; EES, Xience Sierra™ in red; SES, Genoss-DES™ in blue; SMC, smooth muscle cells.

endothelial coverage of the stent strut is the most powerful histological predictor of stent thrombosis, and the ratio of uncovered stent strut is the best morphometric predictor of stent thrombosis. Early stent thrombosis (within 1 month) is primarily affected by interventional factors, such as under-expansion, stent edge dissection, plaque rupture, and medial fracture. However, most cases of LST (1–12 months) are affected by stent strut exposure due to delayed arterial healing (Nakazawa et al., 2011).

Imaging methods, such as IVUS or OCT, are used to clinically evaluate re-endothelialization of the stent strut and assess the risk of LST indirectly as it is impossible to evaluate re-endothelialization of the coronary arteries histologically. OCT offers the highest resolution

TABLE 3 Re-endothelialization rate by smooth muscle cell morphology underneath.

Time	Smooth muscle cell morphology	Re-endothelialization (%)	*p*-value by generalized estimating equation	
			Within	Between
2 weeks	No/rare	1.0 ± 3.2	Reference	<0.001*
	Dense	16.5 ± 14.6	<0.001*	
	Sparse	29.0 ± 23.1	<0.001*	
4 weeks	No/rare	1.3 ± 3.2	Reference	<0.001*
	Dense	13.5 ± 22.1	<0.001*	
	Sparse	42.8 ± 23.3	<0.001*	
12 weeks	No/rare	1.0 ± 3.4	Reference	<0.001*
	Dense	14.3 ± 17.4	<0.001*	
	Sparse	61.3 ± 26.0	<0.001*	

Mean ± SD. *$p < 0.05$ by generalization estimating equations with Bonferroni's *post hoc* test.

among all the currently available coronary imaging modalities (axial 10–20 μm and lateral 20–90 μm), which is ~10 times greater than that of IVUS (Taniwaki et al., 2016). Furthermore, OCT is an optimal approach to characterize fibrous tissue, plaque, thrombus, and neointimal coverage in the context of vascular healing. According to Lee et al. (2018), strut coverage can be evaluated by OCT, and the prescription of dual antiplatelet therapy (DAPT) for 3 months can be considered based on the results. Iliescu et al. (2017) argued that risk factors for stent thrombosis, such as stent malapposition and uncovered stent strut, can be evaluated using OCT, and DAPT can be discontinued based on the results. However, other studies showed that more stent thrombosis was found in the group with more advanced neointimal growth detected by OCT, suggesting that strut coverage findings in OCT and IVUS reflect just neointimal coverage, which does not imply complete endothelial cell coverage (Murakami et al., 2009). In the present study, we found that strut coverage evaluated by OCT should not be interpreted as complete re-endothelialization, which was far more delayed than neointimal coverage. Therefore, it can be dangerous to assess the risk of stent thrombosis based on strut coverage observed by OCT. As the period of DAPT after PCI should be determined based on the risk of bleeding and ischemic events, the optimal period of DAPT remains controversial. According to SMART CHOICE (Hahn et al., 2019) and STOPDAPT-2 trials (Watanabe et al., 2019), the efficacy of short DAPT was not inferior to longer DAPT in terms of cardiovascular and cerebrovascular outcomes. These studies suggest that single antiplatelet therapy can be an option to prevent thrombotic events despite incomplete re-endothelialization, as shown in the present study. However, the SMART-DATE trial showed that the risk of major adverse cardiac and cerebrovascular events in patients with acute coronary syndrome seemed to be higher in the 6-month DAPT group than in the 12-month or longer DAPT group (Hahn et al., 2018). Re-endothelialization in patients with acute coronary syndrome may be delayed, and thrombotic events may occur after the cessation of DAPT. Therefore, re-endothelialization in certain pathological conditions may show more variability. Further study is required to investigate the complex process of re-endothelialization.

One possible indication for re-endothelialization is SMC. There was a correlation between stent coverage of the SMC and re-endothelialization until 4 weeks after implantation. SMC coverage was much faster than re-endothelialization. Therefore, re-endothelialization seemed to require an underlying SMC layer, particularly in the early phase of vascular healing. In addition, the shape of the SMC on the surface of the stent strut changed from dense and spindle to sparse and stellate over time in the present study. SMC is known to change its shape and respond to damage once vascular damage occurs. Specifically, spindle-shaped SMCs are known to transform into a stellate shape by various factors, including miRNA, to promote the recovery of blood vessels (Davis-Dusenbery et al., 2011). The contractile phenotype of spindle shape is characterized by low proliferation. In contrast, the synthetic phenotype of stellate shape is characterized by increased proliferation, migration, and extracellular matrix production (Liu and Gomez, 2019). In the present study, the changes in SMC occurred gradually over 4 weeks and up to 12 weeks after stent implantation. When data for the entire period were analyzed, the sparse SMC layer showed a significantly higher rate of re-endothelialization than the dense SMC layer.

Stent design influences re-endothelialization and intimal hyperplasia (Soucy et al., 2010). Blood flow disturbance and shearing stress caused by the implanted stent affect endothelial growth (Hsiao et al., 2016). Analysis of endothelial cell recovery between DES showed that the thinner stent strut/polymer leads to more endothelial cell coverage. Stent design characteristics can affect thromboresistance, speed of neointimal coverage, and re-endothelialization, thus influencing the duration of DAPT after coronary intervention (Torii et al., 2020). The second-generation DES was shown to have less inflammation, fibrin deposition, and stent thrombosis than the first-generation DES with improved strut coverage (Otsuka et al., 2014). However, the antiproliferative agent used in DES inhibits the proliferation of vascular ECs and SMCs. In particular, mTOR inhibitors, also used in the present study, are known to inhibit the growth and repair of ECs by inhibiting the mTORC1 complex by binding to FKBP12, which causes incomplete re-endothelialization of stent struts (Habib and Finn, 2015). In the present study, SES showed the best initial neointimal growth on OCT and re-endothelialization at 2 weeks after implantation. The

ultrathin-strut and abluminal polymer might cause SMCs to proliferate and migrate faster on the stent strut, resulting in higher SMC coverage and re-endothelialization than the others. In addition, SES showed a significantly higher sparse SMC layer at weeks 2 and 4, which seemed to result in a higher re-endothelialization at weeks 2 and 12 in the present study. In line with this preclinical observation, a recent prospective registry of SES showed excellent clinical results (Youn et al., 2020). In contrast, the vascular healing represented by endothelialization by polymer-free BES was inferior to SES and similar to EES. BES was expected to improve vascular healing, as shown in a previous clinical study in patients with a high bleeding risk (Urban et al., 2015). However, the strut thickness of the BES might hinder the initial SMC and endothelial migration on the stent strut, finally leading to delayed re-endothelialization in the present study.

Limitations

This study had several limitations. First, the healing processes in humans and pigs are not the same. Neointimal responses are pronounced, and the time course of healing is five-to-six times longer in humans than in animals (Virmani et al., 2003). This study examined the re-endothelialization process up to 12 weeks after stent implantation in a porcine model, which may be equivalent to the healing process in humans beyond 1 year. However, our model is anatomically and physiologically similar to humans compared to other animals (Nakazawa et al., 2007). Second, we observed the process of re-endothelialization after a stent was implanted into a normal blood vessel without atherosclerosis. Therefore, the implantation of a DES into blood vessels with atherosclerosis or thrombus may differ from the observations in this study. Third, sirolimus, everolimus, and biolimus share the key mechanism to inhibit SMC growth as mTOR inhibitors. However, the three different kinds of mTOR inhibitors can have different effects on endothelialization independent of stent design.

Conclusion

Re-endothelialization after stent implantation was related to SMC coverage at the early phase and SMC layer differentiation at the late phase. Ultrathin-strut SES showed faster recovery than thin-strut EES or thick-strut BES. The pathophysiology of SMC and its characterization and modification should be further investigated to improve stent design to improve re-endothelialization and its clinical efficacy and safety.

Clinical perspectives

Clinical competencies

OCT is frequently used to clinically estimate re-endothelialization of stent struts, indirectly assessing the risk of stent thrombosis as it is impossible to test re-endothelialization of the coronary arteries histologically. In this study, we found that it is not the neointimal coverage observed on OCT that is critical, but that the SMC layer and its differentiation is essential for the re-endothelialization of the stented vascular wall. Therefore, the pathophysiology of SMC and its modification should be further investigated to improve stent design to improve re-endothelialization and its clinical efficacy and safety.

Translational outlook

In this study, the DES design affects the rapidity of SMC coverage and morphology of the SMC layer, leading to different re-endothelialization and vascular healing. Therefore, it is necessary to further renovate the coronary stent to enhance the initial proliferation and differentiation of SMC, which can improve re-endothelialization.

Data availability statement

The original contributions presented in the study are included in the article/supplementary material. Further inquiries can be directed to the corresponding author.

Ethics statement

The animal study was reviewed and approved by the Institutional Animal Care and Use Committee (IACUC) of Seoul National University Bundang Hospital.

Author contributions

All authors listed have made a substantial, direct, and intellectual contribution to the work and approved it for publication.

Funding

This work was supported by a grant from the Korean Health Technology R&D project, Ministry of Health and Welfare, Republic of Korea (Grant no. HI19C0655), and the Korea Medical Device Development Fund funded by the Korean Government (the Ministry of Science and ICT, the Ministry of Trade, Industry and Energy, the Ministry of Health and Welfare, and the Ministry of Food and Drug Safety) (KMDF RS-2020-KD000229 and RS-2020-KD000033).

Conflict of interest

The authors declare that the research was conducted in the absence of any commercial or financial relationships that could be construed as a potential conflict of interest.

Publisher's note

References

Davis-Dusenbery, B. N., Wu, C., and Hata, A. (2011). Micromanaging vascular smooth muscle cell differentiation and phenotypic modulation. *Arterioscler. Thromb. Vasc. Biol.* 31, 2370–2377. doi:10.1161/atvbaha.111.226670

Finn, A. V., Joner, M., Nakazawa, G., Kolodgie, F., Newell, J., John, M. C., et al. (2007). Pathological correlates of late drug-eluting stent thrombosis: Strut coverage as a marker of endothelialization. *Circulation* 115, 2435–2441. doi:10.1161/circulationaha.107.693739

Fischman, D. L., Leon, M. B., Baim, D. S., Schatz, R. A., Savage, M. P., Penn, I., et al. (1994). A randomized comparison of coronary-stent placement and balloon angioplasty in the treatment of coronary artery disease. *N. Engl. J. Med.* 331, 496–501. doi:10.1056/nejm199408253310802

Habib, A., and Finn, A. V. (2015). Endothelialization of drug eluting stents and its impact on dual anti-platelet therapy duration. *Pharmacol. Res.* 93, 22–27. doi:10.1016/j.phrs.2014.12.003

Hahn, J. Y., Song, Y. B., Oh, J. H., Cho, D. K., Lee, J. B., Doh, J. H., et al. (2018). 6-month versus 12-month or longer dual antiplatelet therapy after percutaneous coronary intervention in patients with acute coronary syndrome (SMART-DATE): A randomised, open-label, non-inferiority trial. *Lancet* 391, 1274–1284. doi:10.1016/s0140-6736(18)30493-8

Hahn, J. Y., Song, Y. B., Oh, J. H., Chun, W. J., Park, Y. H., Jang, W. J., et al. (2019). Effect of P2Y12 inhibitor monotherapy vs dual antiplatelet therapy on cardiovascular events in patients undergoing percutaneous coronary intervention: The SMART-CHOICE randomized clinical trial. *JAMA* 321, 2428–2437. doi:10.1001/jama.2019.8146

Hsiao, S. T., Spencer, T., Boldock, L., Prosseda, S. D., Xanthis, I., Tovar-Lopez, F. J., et al. (2016). Endothelial repair in stented arteries is accelerated by inhibition of Rho-associated protein kinase. *Cardiovasc Res.* 112, 689–701. doi:10.1093/cvr/cvw210

Iliescu, C. A., Cilingiroglu, M., Giza, D. E., Rosales, O., Lebeau, J., Guerrero-Mantilla, I., et al. (2017). Bringing on the light" in a complex clinical scenario: Optical coherence tomography-guided discontinuation of antiplatelet therapy in cancer patients with coronary artery disease (PROTECT-OCT registry). *Am. Heart J.* 194, 83–91. doi:10.1016/j.ahj.2017.08.015

Joner, M., Finn, A. V., Farb, A., Mont, E. K., Kolodgie, F. D., Ladich, E., et al. (2006). Pathology of drug-eluting stents in humans: Delayed healing and late thrombotic risk. *J. Am. Coll. Cardiol.* 48, 193–202. doi:10.1016/j.jacc.2006.03.042

Lee, S. Y., Kim, J. S., Yoon, H. J., Hur, S. H., Lee, S. G., Kim, J. W., et al. (2018). Early strut coverage in patients receiving drug-eluting stents and its implications for dual antiplatelet therapy: A randomized trial. *JACC Cardiovasc Imaging* 11, 1810–1819. doi:10.1016/j.jcmg.2017.12.014

Liu, M., and Gomez, D. (2019). Smooth muscle cell phenotypic diversity. *Arterioscler. Thromb. Vasc. Biol.* 39, 1715–1723. doi:10.1161/atvbaha.119.312131

Murakami, D., Takano, M., Yamamoto, M., Inami, S., Ohba, T., Seino, Y., et al. (2009). Advanced neointimal growth is not associated with a low risk of in-stent thrombus. Optical coherence tomographic findings after first-generation drug-eluting stent implantation. *Circ. J.* 73, 1627–1634. doi:10.1253/circj.cj-08-1166

Nakazawa, G., Finn, A. V., John, M. C., Kolodgie, F. D., and Virmani, R. (2007). The significance of preclinical evaluation of sirolimus-paclitaxel-and zotarolimus-eluting stents. *Am. J. Cardiol.* 100, 36M–44M. doi:10.1016/j.amjcard.2007.08.020

Nakazawa, G., Otsuka, F., Nakano, M., Vorpahl, M., Yazdani, S. K., Ladich, E., et al. (2011). The pathology of neoatherosclerosis in human coronary implants. *J. Am. Coll. Cardiol.* 57, 1314–1322. doi:10.1016/j.jacc.2011.01.011

Nicolas, J., Pivato, C. A., Chiarito, M., Beerkens, F., Cao, D., and Mehran, R. (2022). Evolution of drug-eluting coronary stents: A back-and-forth journey from the bench-to-bedside. *Cardiovasc Res.* 119, 631–646. doi:10.1093/cvr/cvac105

Otsuka, F., Vorpahl, M., Nakano, M., Foerst, J., Newell, J. B., Sakakura, K., et al. (2014). Pathology of second-generation everolimus-eluting stents versus first-generation sirolimus- and paclitaxel-eluting stents in humans. *Circulation* 129, 211–223. doi:10.1161/circulationaha.113.001790

Soucy, N. V., Feygin, J. M., Tunstall, R., Casey, M. A., Pennington, D. E., Huibregtse, B. A., et al. (2010). Strut tissue coverage and endothelial cell coverage: A comparison between bare metal stent platforms and platinum chromium stents with and without everolimus-eluting coating. *EuroIntervention* 6, 630–637. doi:10.4244/eijv6i5a105

Stefanini, G. G., Byrne, R. A., Windecker, S., and Kastrati, A. (2017). State of the art: Coronary artery stents - past, present and future. *EuroIntervention* 13, 706–716. doi:10.4244/eij-d-17-00557

Stefanini, G. G., and Holmes, D. R., JR. (2013). Drug-eluting coronary-artery stents. *N. Engl. J. Med.* 368, 254–265. doi:10.1056/nejmra1210816

Taniwaki, M., Radu, M. D., Zaugg, S., Amabile, N., Garcia-Garcia, H. M., Yamaji, K., et al. (2016). Mechanisms of very late drug-eluting stent thrombosis assessed by optical coherence tomography. *Circulation* 133, 650–660. doi:10.1161/circulationaha.115.019071

Torii, S., Jinnouchi, H., Sakamoto, A., Kutyna, M., Cornelissen, A., Kuntz, S., et al. (2020). Drug-eluting coronary stents: Insights from preclinical and pathology studies. *Nat. Rev. Cardiol.* 17, 37–51. doi:10.1038/s41569-019-0234-x

Urban, P., Meredith, I. T., Abizaid, A., Pocock, S. J., Carrie, D., Naber, C., et al. (2015). Polymer-free drug-coated coronary stents in patients at high bleeding risk. *N. Engl. J. Med.* 373, 2038–2047. doi:10.1056/nejmoa1503943

Virmani, R., Kolodgie, F. D., Farb, A., and Lafont, A. (2003). Drug eluting stents: Are human and animal studies comparable? *Heart* 89, 133–138. doi:10.1136/heart.89.2.133

Watanabe, H., Domei, T., Morimoto, T., Natsuaki, M., Shiomi, H., Toyota, T., et al. (2019). Effect of 1-month dual antiplatelet therapy followed by clopidogrel vs 12-month dual antiplatelet therapy on cardiovascular and bleeding events in patients receiving PCI: The STOPDAPT-2 randomized clinical trial. *JAMA* 321, 2414–2427. doi:10.1001/jama.2019.8145

Youn, Y. J., Yoo, S. Y., Lee, J. W., Ahn, S. G., Lee, S. H., Yoon, J., et al. (2020). Safety and efficacy of a new ultrathin sirolimus-eluting stent with abluminal biodegradable polymer in real-world practice. *Korean Circ. J.* 50, 317–327. doi:10.4070/kcj.2019.0258

frontiers | Frontiers in Bioengineering and Biotechnology

TYPE Original Research
PUBLISHED 14 June 2023
DOI 10.3389/fbioe.2023.1211688

OPEN ACCESS

EDITED BY
Huixu Xie,
Sichuan University, China

REVIEWED BY
Gang Li,
Soochow University, China
Meng Tian,
Sichuan University, China

*CORRESPONDENCE
Ao Rong,
Rongao@163.com
Xin Chen,
chenx@fudan.edu.cn
Yusu Ni,
niyusu@aliyun.com
Yi Jiang,
sxqy1995@qq.com

†These authors have contributed equally to this work

RECEIVED 25 April 2023
ACCEPTED 01 June 2023
PUBLISHED 14 June 2023

CITATION
Xu Y, Chen Q, Shao Z, Wei J, Zhu X, Rong A, Chen X, Ni Y and Jiang Y (2023), Evaluation of new robust silk fibroin hydrogels for posterior scleral reinforcement in rabbits.
Front. Bioeng. Biotechnol. 11:1211688.
doi: 10.3389/fbioe.2023.1211688

Evaluation of new robust silk fibroin hydrogels for posterior scleral reinforcement in rabbits

Yule Xu[1†], Qiaolin Chen[2†], Zhengzhong Shao[2], Jiahong Wei[1], Xuyou Zhu[3], Ao Rong[1,4*], Xin Chen[2*], Yusu Ni[5,6,7*] and Yi Jiang[4*]

[1]Department of Ophthalmology, Tongji Hospital, School of Medicine, Tongji University, Shanghai, China, [2]State Key Laboratory of Molecular Engineering of Polymers, Department of Macromolecular Science, Laborarory of Advanced Materials, Fudan University, Shanghai, China, [3]Department of Pathology, Tongji Hospital, School of Medicine, Tongji University, Shanghai, China, [4]Department of Ophthalmology, Shanghai Xin Shi Jie Eye Hospital, Shanghai, China, [5]Otology and Skull Base Surgery Department, Eye and ENT Hospital of Shanghai Medical School, Fudan University, Shanghai, China, [6]Key Laboratory of Hearing Medicine of National Health and Family Planning Commission, Shanghai, China, [7]Otorhinolaryngology Department of Affiliated Eye and ENT Hospital, State Key Laboratory of Medical Neurobiology, Fudan University, Shanghai, China

Background: Currently, there is no ideal material available for posterior scleral reinforcement (PSR) to prevent the progression of high myopia. In this study, we investigated robust regenerated silk fibroin (RSF) hydrogels as potential grafts for PSR in animal experiments to evaluate their safety and biological reactions.

Methods: PSR surgery was performed on the right eye of twenty-eight adult New Zealand white rabbits, with the left eye serving as a self-control. Ten rabbits were observed for 3 months, while 18 rabbits were observed for 6 months. The rabbits were evaluated using intraocular pressure (IOP), anterior segment and fundus photography, A- and B-ultrasound, optical coherence tomography (OCT), histology, and biomechanical tests.

Results: No complications such as significant IOP fluctuation, anterior chamber inflammation, vitreous opacity, retinal lesion, infection, or material exposure were observed. Furthermore, no evidence of pathological changes in the optic nerve and retina, or structural abnormalities on OCT, were found. The RSF grafts were appropriately located at the posterior sclera and enclosed in fibrous capsules. The scleral thickness and collagen fiber content of the treated eyes increased after surgery. The ultimate stress of the reinforced sclera increased by 30.7%, and the elastic modulus increased by 33.0% compared to those of the control eyes at 6 months after surgery.

Conclusion: Robust RSF hydrogels exhibited good biocompatibility and promoted the formation of fibrous capsules at the posterior sclera *in vivo*. The biomechanical properties of the reinforced sclera were strengthened. These findings suggest that RSF hydrogel is a potential material for PSR.

KEYWORDS

myopia, silk fibroin, biomaterial, posterior scleral reinforcement, biocompatibility

1 Introduction

Myopia is a prevalent ocular disease that has become a global public health issue. The prevalence of myopia in the United States and Europe is around 30%, while in Asian countries, it affects up to 60% of the general population (Saw et al., 2002; McBrien and Gentle, 2003). With increasing severity of myopia, the eyeball continues to elongate. High myopia is commonly defined as a spherical equivalent of ≥6.00 D and is frequently associated with pathologic myopia. Pathological myopia is one of the leading causes of low visual acuity and blindness worldwide, particularly in East Asia, making it a significant medical problem. The pathological changes include posterior scleral staphyloma, retinal choroidal atrophy, choroidal neovascularization, scleral structure and biomechanical streak, and peripheral retinal degeneration (Ohno-Matsui et al., 2016). Posterior staphylomas are a hallmark of high myopia and a significant cause of myopic maculopathy, which can lead to marked visual impairment (Hayashi et al., 2010; Fang et al., 2018).

The sclera is a fibrous and dynamic tissue that makes up the majority of the wall of eyeball. It is mainly composed of superimposed type 1 collagen lamellae with small amounts of elastic fibers embedded in a hydrated matrix of proteoglycans (Keeley et al., 1984; Rada et al., 1997). Thinning of the sclera at the posterior pole of the eye has long been recognized as an essential feature in the development of high myopia (Boote et al., 2020). Research has shown that the total collagen content in the sclera is reduced in high myopia, which can result in the sclera's deranged metabolism, leading to the weakening of its biomechanical properties. This, in turn, can allow for the continual expansion of the globe in the posterior direction (Gentle et al., 2003; McBrien and Gentle, 2003).

Posterior scleral reinforcement (PSR) involves strengthening the sclera at the posterior pole of the eye to halt the progression of high myopia. The technique was first reported by Shevelev in 1930 and was later modified by Snyder and Thompson (Shevelev, 1930; Snyder and Thompson, 1972; Thompson, 1978). Numerous studies have used various materials in animal experiments or clinical trials to assess the effectiveness and safety of PSR (Jacob-LaBarre et al., 1994; Yan et al., 2010; Huang et al., 2019). Some researchers have been satisfied with the surgical outcomes, while others have been disappointed with the results.

PSR materials are crucial for controlling the progression of high myopia and must exhibit both good biocompatibility and physical properties. PSR surgery has utilized various biological materials such as pericardium, donor sclera, umbilical cord, dura mater, and acellular allograft dermis, as well as non-biological synthetic materials like polyester fibers, polyester mesh sponges, and plasma-modified silicone grafts. Each material has its own advantages and limitations, and challenges to their use include issues such as insufficient availability of donor tissue, the risk of infection, pathogen transmission, and poor durability (Schepens and Acosta, 1991; Jacob-LaBarre et al., 1994; Dereli et al., 2020). Currently, there is no ideal PSR material available to strengthen the weak area of the sclera in the posterior pole and prevent the continuous elongation of the axial length associated with high myopia.

Silk fibroin (SF) is a fibrous protein primarily extracted from the cocoons of *Bombyx mori* silkworms. The amino acid sequence of SF contains repetitive Gly-Ala-Gly-Ala-Gly-Ser repeats, which self-assemble into an antiparallel β-sheet structure. These β-sheets are highly crystalline and essentially crosslink the protein by utilizing strong intra- and intermolecular hydrogen bonds, as well as strong van der Waals forces between stacked β-sheets, thereby improving the mechanical properties of SF (Zhou et al., 2001). Previous research has demonstrated that *in vivo*, only very mild inflammatory responses to SF occur (Wang Y et al., 2008). Regenerated silk fibroin (RSF) has been widely utilized as an excellent biomaterial for various biomedical applications, such as cartilage regeneration (Wang et al., 2006; Hong et al., 2020), artificial blood vessels (Lovett et al., 2007; Zhang et al., 2008; Li et al., 2019), drug delivery scaffolds (Wang X et al., 2008; Maity et al., 2020), ligament reconstruction (Bi et al., 2021; Yan et al., 2021), bone tissue engineering (Hofmann et al., 2007; Gambari et al., 2019), and skin tissue engineering (Bhardwaj et al., 2015). RSF can be fabricated into various forms of materials, including fibers, films, porous sponges, hydrogels, scaffolds, and nanomicrospheres (Kundu et al., 2013; Lu et al., 2015; Yan et al., 2015; Kapoor and Kundu, 2016; Choi et al., 2018). Due to its excellent biocompatibility, remarkable mechanical properties, and controllable biodegradation (Mottaghitalab et al., 2015), RSF holds great promise as a novel biological material for PSR.

In this study, we investigated a new robust RSF hydrogel as a patch for PSR in animal experiments to explore the safety and potential mechanism in preventing the progression of myopia.

2 Materials and methods

2.1 Fabrication of RSF hydrogels

All chemicals were received and used without further purification. The cocoons of *B. mori* silkworms were purchased from Jiangsu, China. $CaCl_2$ and formic acid (FA) were purchased from Sinopharm Chemical Reagent Co., Ltd. The water used in all experiments was deionized using a Millipore purification apparatus (resistivity >18.2 MΩ cm).

The preparation of the robust RSF hydrogels was conducted following the procedure that has been previously reported in our work (Chen et al., 2022). In brief, the degummed silk fibers were dissolved in FA with $CaCl_2$ ($CaCl_2$/RSF ratio of 0.5) at room temperature for 3 h to make a final RSF concentration of 0.15 g/mL. After defoaming, a transparent homogeneous solution was poured into Teflon molds, which were then immersed in deionized water to form robust RSF hydrogel. The water in which the RSF hydrogel was immersed was frequently replaced with fresh water until the pH of the immersion water was nearly neutral.

All RSF hydrogels were 1 mm thick and cut into 25 mm × 6 mm strips (Supplementary Figure S1). They were sterilized in 75% ethanol at 4°C before implantation.

2.2 Animals

A total of twenty-eight adult male New Zealand white rabbits weighing 2.3–2.5 kg were utilized in this study. They were randomly

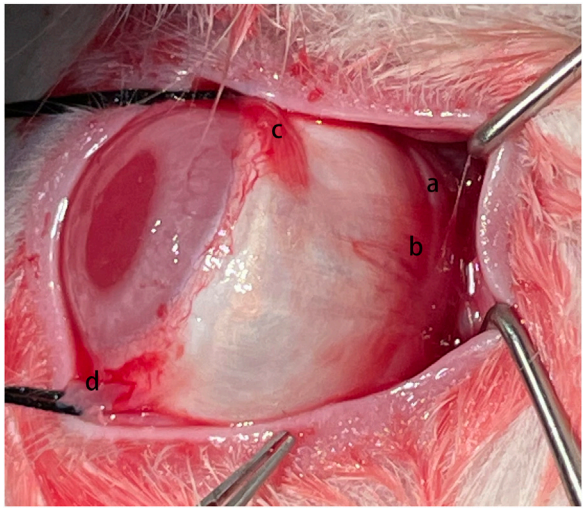

FIGURE 1
Surgical Procedure. The silk fibroin graft (a) was passed underneath the inferior oblique muscle (b), inferior rectus muscle (c), and lateral rectus muscle (d) sequentially.

allocated to group 1 (n = 10), group 2 (n = 10), and group 3 (n = 8). Ten rabbits (group 1) were monitored for 3 months, while 18 rabbits (groups 2 and 3) were monitored for 6 months. The right eye was selected as the treated eye, while the left eye served as the contralateral self-control. Prior to surgery, routine eye examinations were conducted, including intraocular pressure (IOP), anterior segment, fundus photography, A-ultrasound, B-ultrasound, and optical coherence tomography (OCT), to establish a baseline and exclude any pre-existing eye diseases. All experimental procedures were carried out in accordance with the Association for Research in Vision and Ophthalmology (ARVO) statement regarding the use of animals in ophthalmic and vision research. The study protocol was reviewed and approved by the Animal Treated Ethics Committee of Tongji Hospital Affiliated to Tongji University, China (authorized number: 2020-DW-006).

2.3 Surgical procedures

The PSR surgery was performed using a single strip, as previously described (Thompson, 1978). The animals were anesthetized by intravenous injection of 3% sodium pentobarbital solution at a dose of 1 mL/kg, along with topical proparacaine hydrochloride (Alcaine, 0.5%, Alcon-Couvreur, Puurs, Belgium). The surgery was conducted by an experienced doctor using an OPMI Lumera T surgical microscope (Carl Zeiss Meditec, Jena, Germany). A 180° conjunctival peritomy was carried out along the corneal limbus at the 4:00–10:00 clockwise position. A radial incision was made at each end of the peritomy, and traction sutures were placed under the inferior and external rectus muscles. With the help of traction sutures and muscle hooks, the strip was sequentially passed beneath the inferior oblique, inferior, and external rectus muscles. One end of the strip was secured to the sclera in the inferior-nasal quadrant using two 10–0 nylon sutures, and the other end was secured to the sclera in the superior temporal quadrant using the same technique. The strip was in good alignment with the outer surface of the posterior pole of the eye globe but was not tightened enough to compress it (Figure 1). Finally, the conjunctival incision was sutured with 10–0 nylon sutures. After surgery, all eyes were treated with levofloxacin eye drops (0.5% Cravit; Santen Pharmaceutical Co., Ltd. Osaka, Japan) four times daily for 1 week.

2.4 Postoperative clinical examinations

To assess the safety and biological reactions of the RSF scaffold material, postoperative clinical examinations were conducted at 1 week, 1 month, 3 months, and 6 months using a slit lamp (SL-1800; NIDEX Co., Ltd. Aichi, Japan) and a rebound tonometer (TAO11; Icare Finland Oy, Vantaa, Finland) to record the anterior segment and intraocular pressure (IOP). At 3 and 6 months after the surgery, A-ultrasound (Aviso; Quatel Medical Co., France) was used to measure the length of the ocular axis, B-ultrasound (Aviso; Quatel Medical Co., France) was utilized to detect vitreous changes and the relative position of the RSF scaffold graft material with the posterior sclera, and fundus photography was captured using a fundus camera (TRC-50DX; Topcon Co., Tokyo, Japan) to monitor the dynamic changes in retinal morphology and structure. Spectral domain OCT (Zeiss Cirrus HD-5000; Carl Zeiss Meditec, Dublin, CA) was also performed at the inferior optic nerve head (ONH) location (Figure 2A) to examine the microstructure and thickness of the retina, choroid, and sclera in the reinforcement area. The thicknesses of the retina, choroid, and sclera were measured using the proprietary software of the OCT machine. Five locations of the sectional HD images were averaged for thickness analysis (Figure 2C).

At 3 and 6 months after the surgery, all rabbits were sacrificed, and both eyeballs were immediately enucleated, grossly examined, and photographed. Ten rabbits in group 1 and 2 were randomly divided into subgroups A (n = 6), B (n = 2), and C (n = 2), respectively. Biomechanical testing was performed on eight rabbits in group 3 at 6 months after the surgery.

2.5 Histochemistry and immunohistochemistry

In subgroup A (n = 6), the eyes were fixed in 10% formalin for 48 h. The eyeballs were sectioned vertically through the central part of the reinforcement material and optic nerve, and then embedded in paraffin for light microscopy. Sections were cut at a thickness of 5 μm. Deparaffinized and rehydrated sections were stained with Hematoxylin & Eosin (HE), Masson's trichrome, and Verhoeff's Van Gieson to identify inflammation, vascularity, and formation of fibrous tissue, respectively.

The slides were observed under a light microscope (Eclipse E100; Nikon Co., Ltd. Japan) and the images were transferred into a computer using a digital video camera (DS-U3; Nikon Co., Ltd. Japan). Morphometric analysis was performed on five slides for each sample. Computer-aided analysis with ImageJ software (1.53 k, NIH, United States) was used to quantitatively assess the

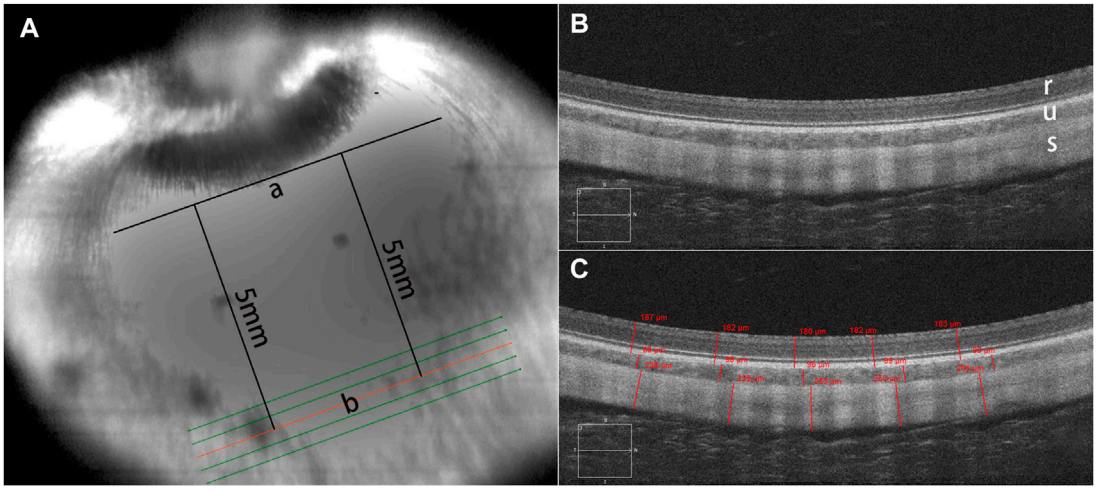

FIGURE 2
OCT scanning mode. Optical coherence tomography (OCT) was used to examine the microstructure of the retina, choroid, and sclera in the reinforcement area **(A)**. A tangent line (a) was marked at the lower edge of the optic nerve head (ONH) in the infrared (IR) image. The scanning direction was parallel to the tangent line, approximately 5 mm away from it. Enhanced-depth imaging (EDI) images were captured using the HD 5-Line Raster with a spacing of 0.25 mm, consisting of 6 mm parallel lines. There was no structural disorganization in the retinal layers, choroid, and sclera after posterior scleral reinforcement (PSR) surgery **(B)**. A sectional image (b) closest to 5 mm below the tangent line was used for thickness measurement. Five locations of the sectional HD images were averaged for thickness analysis **(C)**. In the images, r represents the retina, u represents the choroid, s represents the sclera.

percentage of collagen and elastic fiber area. All images were digitized to standardize the light intensity of the microscope and condenser height before the quantification process. The arithmetic mean of the percentage measured in the six fields of each slide was used for statistical analysis.

Evaluation of inflammation and vascularization was graded on a scale of 0–4 according to a modified grading system (Kassem et al., 2011; Dereli et al., 2020). The grading guidelines for inflammation and vascularization are listed in Supplementary Table S1.

Transforming growth factor beta (TGF-β) is the primary factor that drives fibrosis. For immunohistochemical staining, serial paraffin sections were deparaffinized and heated in a microwave oven for 15 min for antigen retrieval. After naturally cooling to room temperature and three washes (5 min each) in phosphate-buffered saline (PBS), sections were incubated with 3% hydrogen peroxide in distilled water for 25 min to block endogenous peroxidase, washed three times (5 min each) in PBS, and blocked in 3% BSA for 30 min at room temperature. Subsequently, the sections were incubated overnight with rabbit polyclonal anti-TGF-β1 antibody (GB13028; Servicebio, Wuhan, China) at a 1/100 dilution in a humidified chamber at 4°C. After washing with PBS, the sections were incubated with horseradish peroxidase-conjugated goat anti-rabbit IgG antibody (GB23303; Servicebio, Wuhan, China) at a 1/200 dilution for 50 min at room temperature. The sections were then stained with 3,3′-diaminobenzidine (K5007; DAKO, Denmark) and counterstained with hematoxylin for 3 min. Six randomly selected areas on each slide were evaluated under a light microscope (Eclipse E100; Nikon Co., Ltd., Japan). Photomicrographs were captured using a camera (DS-U3; Nikon Co., Ltd., Japan). ImageJ software was used to quantitatively assess the value of the average optical density (AOD) to estimate TGF-β1 expression.

All images were independently assessed by two researchers (JW and XZ), and a consensus agreement was reached.

2.6 Tunel staining

For TUNEL staining, the eyes from subgroup B ($n = 2$) were fixed in 4% paraformaldehyde for at least 24 h, followed by dehydration in 15% sucrose solution at 4°C and then transferred to 30% sucrose solution for further dehydration. The samples were embedded in Tissue-Tek (Sakura, Tokyo, Japan) and sectioned at 8 μm using a cryostat. Apoptotic cells were detected using a commercially available fluorescein (FITC) TUNEL Cell Apoptosis Detection Kit (G1501, Servicebio, Wuhan, China) according to the manufacturer's instructions. The samples were examined and imaged using a fluorescence microscope (Nikon Eclipse CI; Nikon Co., Ltd. Japan).

2.7 Transmission electron microscope

In subgroup C ($n = 2$), the eyes were fixed with 2% glutaraldehyde. Small sections of the wall in the reinforcement area and the optic nerve were cut, dehydrated, and embedded in Embed-812 (Electron Microscopy Sciences, Washington, PA, United States) for transmission electron microscopy (TEM). After polymerization, 60–80 nm thick sections were stained with uranium acetate and lead citrate and examined using an HT7800 transmission electron microscope (Hitachi, Ltd., Tokyo, Japan).

2.8 Biomechanical test

To evaluate the biomechanical effect of the RSF graft, stress-strain measurements were performed on the sclera of eight rabbits 6 months postoperatively. The rabbits were euthanized and their

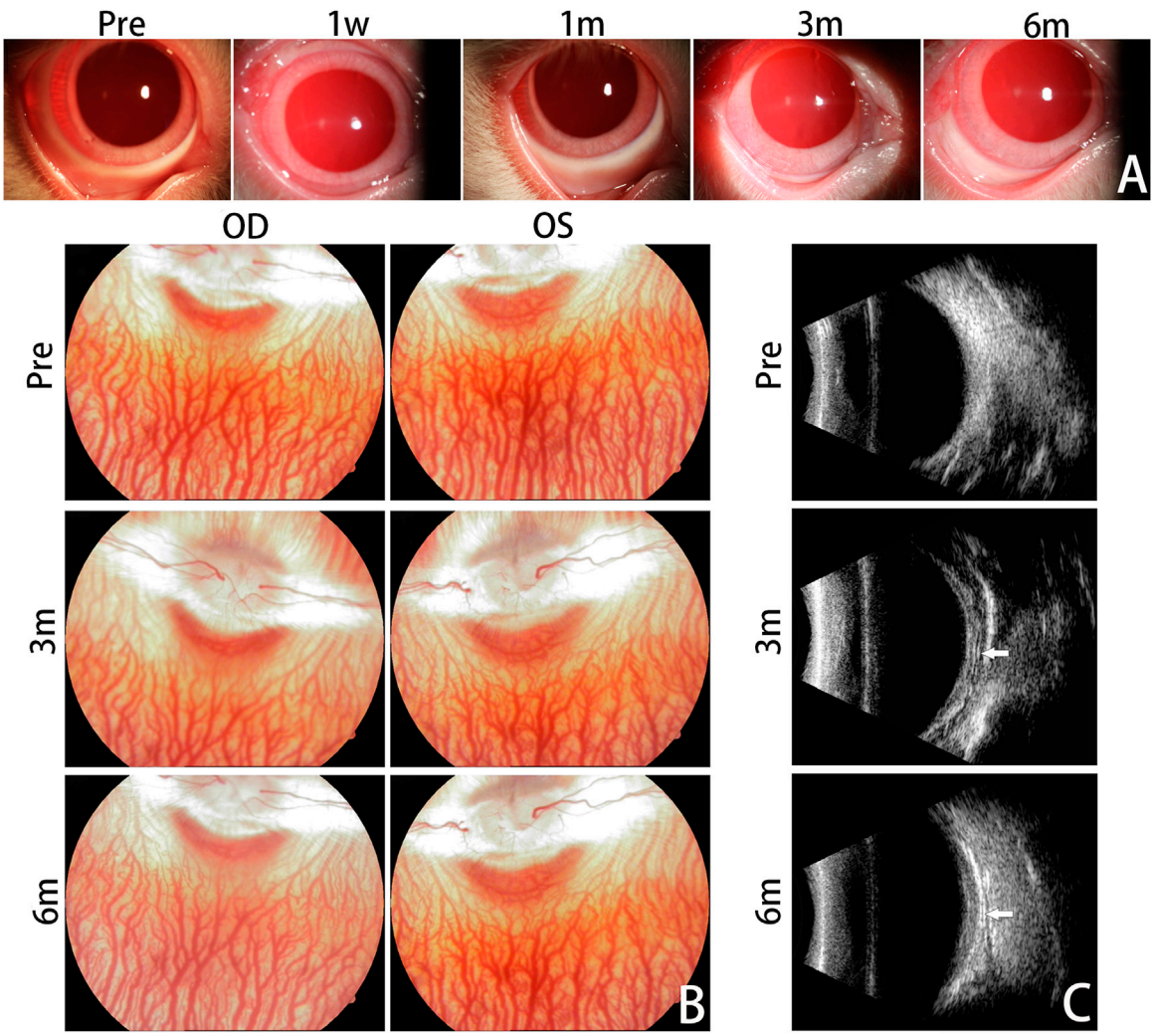

FIGURE 3
Clinical Evaluation. Anterior segment photographs are presented for the treated eyes before surgery and at 1 week, 1 month, 3 months, and 6 months after the surgery **(A)**. No significant complications emerged within the 6-month follow-up period. Mild conjunctival congestion was observed at 1 week postoperatively and had completely resolved by the first month. Fundus photographs were taken to monitor the dynamic changes of the vitreous body and retina **(B)**. No abnormal fundus changes were observed from 3 months to 6 months postoperatively, compared with pre-operation. Representative B-ultrasound images are displayed for the treated eyes before surgery and at 3 months and 6 months postoperatively **(C)**. The silk fibroin graft could be clearly observed and was characterized by an arcuate band (white arrows). OD, oculus dexter; OS, oculus sinister.

whole eyeballs were enucleated. The rabbit sclera adhered to the reinforcement material was harvested using a sharp blade and cut into a 2.5 mm wide and 15 mm long strip for measurement. The tissue adjacent to the strip was carefully removed. Scleral strips were also collected from the corresponding positions of the contralateral eye. The scleral thickness was measured at the center and on both sides of each sample using an electronic digital caliper from Guanglu Measuring Instrument Co., Ltd. in Guilin, China. These strips were clamped vertically at a distance of 8.0 mm between the jaws of an Instron 5943 System, a computer-controlled biomaterial tester from Instron Co., Ltd. in Massachusetts, USA. The strain was linearly increased at a velocity of 2 mm/min until the scleral strip ruptured. Ultimate stress was recorded as the stress on the tissue at the tearing point. The elasticity moduli of all the scleral strips were calculated using the testing system.

2.9 Statistical analysis

Data analysis was conducted using SPSS V.26.0 (SPSS Inc., Chicago, IL, United States). Continuous variables were presented as mean ± standard deviation (SD). When multiple measurements were taken from different parts of the same slide or image, the arithmetic mean was used for subsequent statistical analysis. Repeated-measures analysis of variance (ANOVA) was utilized to assess differences in different pre- and postoperative periods. A paired sample *t*-test was used to determine statistical differences between the treated and contralateral control eyes. An independent sample *t*-test was performed to compare data from 3 to 6 months after surgery. The Mann-Whitney U test was used to compare ranked data between groups. A significance level of $p < 0.05$ was considered statistically significant.

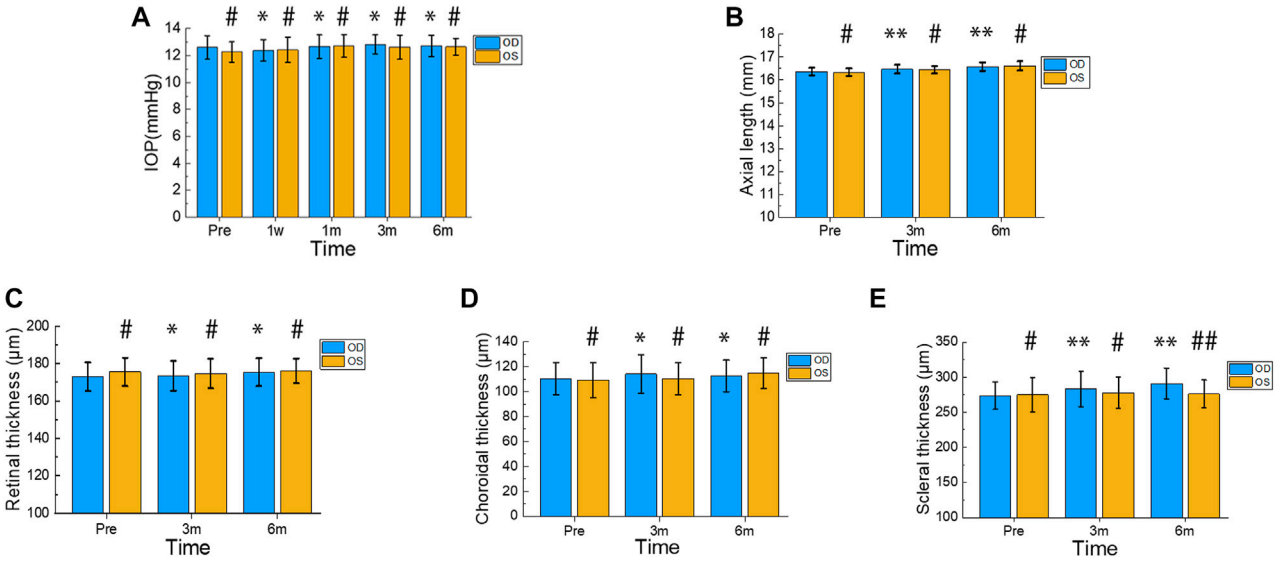

FIGURE 4
Changes in IOP, Axial Length, Retinal Thickness, Choroidal Thickness, and Scleral Thickness during Postoperative 6 Months. Intraocular pressure (IOP) was measured in the treated and contralateral eyes before surgery and at 1 week, 1 month, 3 months, and 6 months after surgery **(A)**. Axial length was assessed in the treated and contralateral eyes before surgery and at 3 months and 6 months after surgery **(B)**. The thickness of the retina, choroid, and sclera was measured in the treated and contralateral eyes before surgery as well as 3 and 6 months after surgery **(C–E)**. In the treated eyes group, differences in IOP before and after surgery were indicated by * or **. Differences in IOP between the treated and contralateral eyes at each time point were indicated by # or ##. Error bars represent the standard deviation. #$p > 0.05$, *$p > 0.05$, ##$p < 0.05$, **$p < 0.05$.

3 Results

3.1 Clinical evaluation

The treated eyes showed no signs of anterior chamber inflammation, with only mild conjunctival congestion observed in the early postoperative period, which completely resolved in all rabbits within the first month (Figure 3A). Corneas were normal and lenses were clear in all rabbits, with no observed vitreous or retinal lesions during the follow-up period (Figure 3B).

B-ultrasound images at 3 and 6 months postoperatively showed that the RSF graft was clearly visible as an arcuate hypo-echo space and high-echo band between the posterior sclera and orbital wall. The RSF graft was appropriately located and adhered well to the posterior sclera (Figure 3C).

Baseline OCT evaluation of retinal morphology showed that the experimental rabbit eyes had normal retinal anatomy. There were no structural disorganization or changes in the retinal layers, choroid, and sclera after PSR surgery (Figure 2B).

3.2 Changes of IOP

The changes in IOP after surgery are presented in Figure 4A. Compared to the preoperative IOP (12.61 ± 0.88 mmHg), there were no significant differences in the treated eyes at postoperative 1 week, 1 month, 3 months, and 6 months (12.38 ± 0.80 mmHg, 12.68 ± 0.87 mmHg, 12.84 ± 0.71 mmHg, and 12.72 ± 0.78 mmHg; p = 0.390, p = 0.794, p = 0.343, and p = 0.591, respectively). Moreover, there was no significant difference in IOP between the treatment group and the contralateral group at the same time points (12.28 ± 0.76 mmHg, 12.43 ± 0.94 mmHg, 12.72 ± 0.84 mmHg, 12.63 ± 0.91 mmHg, and 12.66 ± 0.66 mmHg; p = 0.231, p = 0.880, p = 0.892, p = 0.433, and p = 0.798, respectively).

3.3 Changes of AL

Figure 4B displays the changes in axial length. The treated eyes showed significant differences (p = 0.002 < 0.01, p < 0.001) in comparison to their preoperative axial length (16.37 ± 0.39 mm), with measurements of 16.47 ± 0.19 mm and 16.58 ± 0.87 mm at postoperative 3 months and 6 months, respectively. Moreover, no significant difference was observed in axial length between the treatment and contralateral groups at the same time point (16.34 ± 0.16 mm, 16.44 ± 0.16 mm, 16.61 ± 0.2 mm; p = 0.620, p = 0.640, p = 0.660). At 6 months after surgery, both the treated and control eyes exhibited an increase in axial length by 0.21 mm and 0.27 mm, respectively.

3.4 Changes about thickness of retina, choroid, and sclera

Figures 4C, D illustrate the changes in retinal and choroidal thickness, respectively. The treated eyes exhibited relatively gentle fluctuations in retinal and choroidal thickness during the postoperative period. Compared to the preoperative retinal thickness (172.89 ± 7.69 μm), the treated eyes showed no significant differences (173.50 ± 7.94 μm, 175.39 ± 7.49 μm; p =

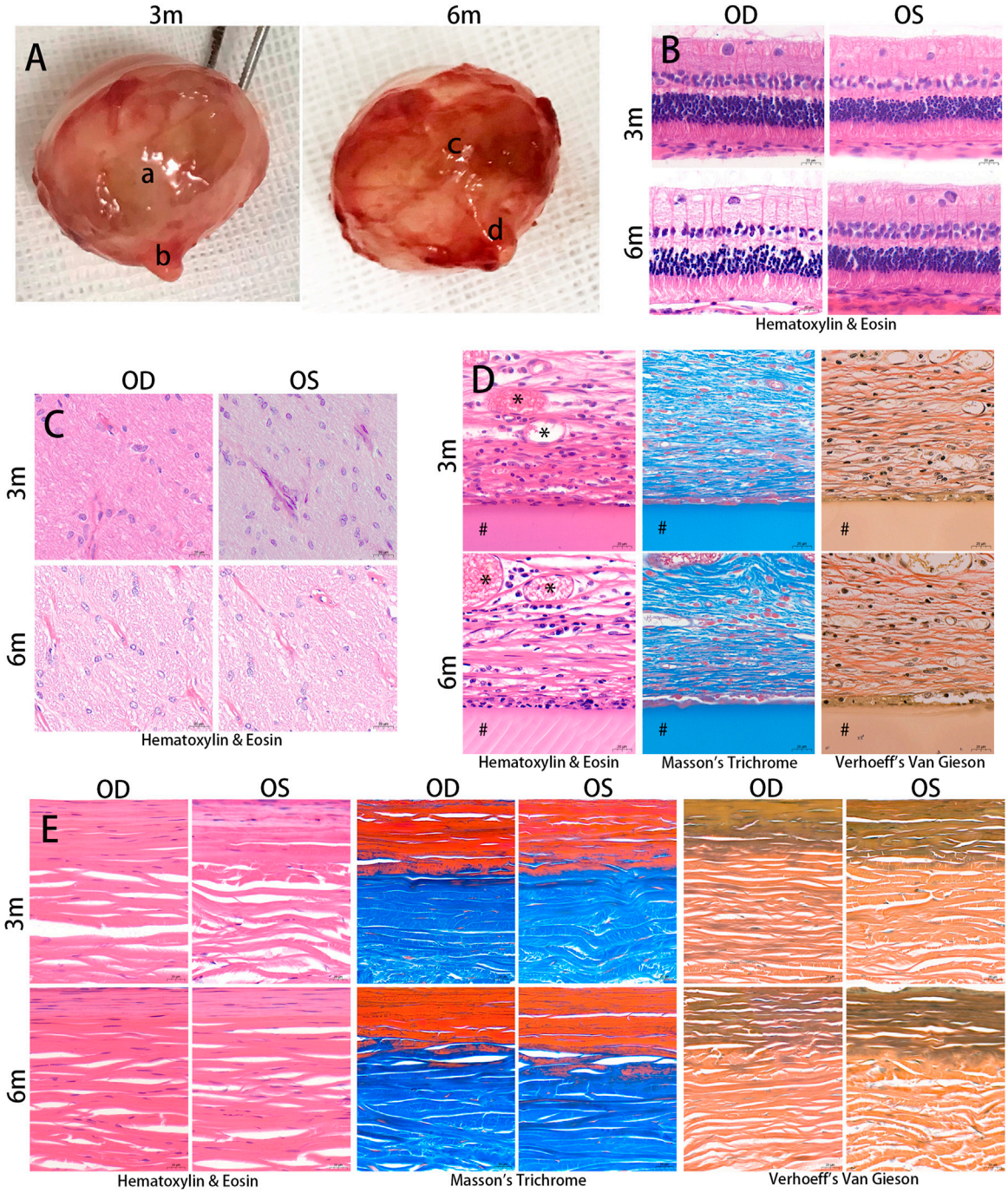

FIGURE 5
Histological examination. The eyeballs of the animals were enucleated and photographed at 3 and 6 months after the surgery **(A)**. Silk fibroin grafts were enclosed in a fibrous capsule (a, c). The optic nerves appeared normal in the treated eyes (b, d). The samples were embedded in paraffin and stained with Hematoxylin & Eosin, Masson's trichrome, and Verhoeff's Van Gieson. Hematoxylin & Eosin images showed no structural abnormalities or inflammatory cells in the retina and optic nerve in the treated and contralateral eyes at 3 months and 6 months postoperatively **(B, C)**. The silk fibroin graft (#) was surrounded by a fibrous capsule containing collagen and a number of inflammatory cells **(D)**. Vascular ingrowth (*) was evident in the fibrous capsule. The diameter of the scleral collagen fibrils varied in thickness **(E)**. OD, oculus dexter; OS, oculus sinister. Scale bar = 20 μm.

0.628, $p = 0.062$) at 3 and 6 months postoperatively. Furthermore, there were no significant differences in retinal thickness between the treated and contralateral eyes at the same time points (175.56 ± 7.52 μm, 174.67 ± 7.90 μm, 176.06 ± 6.65 μm; $p = 0.300$; $p = 0.661$, $p = 0.799$). The preoperative choroidal thickness was 110.39 ± 12.87 μm, and the postoperative choroidal thickness at 3 and 6 months was 114.17 ± 15.26 μm and 112.78 ± 12.77 μm, respectively. There were no significant differences between pre- and postoperative values ($p = 0.218$ and $p = 0.426$, respectively). Additionally, the treated eyes' choroidal thickness did not differ

significantly from that of the contralateral eyes at the same time points (109.28 ± 13.91 μm, 110.56 ± 12.99 μm, 115 ± 12.26 μm; p = 0.805, p = 0.450, p = 0.598).

Figure 4E shows the changes in scleral thickness over time. Compared to the preoperative scleral thickness (273.67 ± 19.46 μm), the treated eyes showed a significant increase (283.33 ± 25.25 μm, 290.94 ± 21.91 μm; p = 0.004, p < 0.001) at 3 and 6 months postoperatively. Six months after surgery, the treated eyes' scleral thickness increased by 17.27 μm. There were no significant differences in scleral thickness between the treated and contralateral eyes at the preoperative and 3-month time points (275 ± 24.36 μm, 277.94 ± 22.67 μm; p = 0.857, p = 0.505). However, the treated eyes' scleral thickness showed a statistically significant difference compared to the contralateral eyes' at 6 months postoperatively (276.17 ± 19.66 μm; p = 0.041).

3.5 Gross examination

Upon gross examination of the enucleated eye globes, it was observed that all grafts were surrounded by a fibrous capsule that could not be easily separated from the rabbit eyeball (Figure 5A). None of the grafts were displaced from the reinforced area at any point after PSR. When the fibrous capsule was incised, the RSF material remained intact for up to 3 months after surgery. However, after 6 months, the materials showed partial decomposition. The posterior edge of the RSF graft was located approximately 4 mm from the optic nerve, while the optic nerves appeared normal in all specimens. Both treated and untreated eyes appeared to be of similar size and shape.

3.6 HE, Masson's trichrome and Verhoeff's Van Gieson staining

Following implantation, histological examination of the HE staining revealed no evidence of pathological changes or structural abnormalities in the retina, choroid, and optic nerve (Figures 5B, C). The RSF graft was enclosed in a fibrous capsule containing collagen (Figure 5D). The RSF graft elicited a number of inflammatory cells, including plasma cells, lymphocytes, macrophages, neutrophils, and fibroblasts, which were observed around the graft. Vascular ingrowth was also evident at the graft periphery. The degree of inflammation and vascularization of the fibrous capsules surrounding the RSF graft is presented in Table 1. The inflammatory reaction at 3 months was slightly more evident than at 6 months, with a score of 1.67 ± 0.65 decreasing to 1.50 ± 0.52. However, there was no statistically significant difference between the two time points (p = 0.423). Mildly increased vascularity was observed in all treated eyes, while no inflammation or vascularization was observed in the contralateral eye.

The diameter and lamellae of the scleral collagen fibrils exhibited varying thicknesses (Figure 5E). Changes in the density of scleral collagen, as determined by Masson's trichrome and Verhoeff's Van Gieson staining, are presented in Table 2. At month 3, the percentage of collagen fiber area in the treated eyes was significantly higher than in the contralateral eyes, as measured by Masson's trichrome staining or Verhoeff's Van Gieson staining (51.57% ± 1.76% and 47.60% ± 1.81%, respectively, compared to 42.84% ± 2.19% and 42.25% ± 1.85% in the contralateral eyes; p < 0.001 and p = 0.002, respectively). The treated eyes also showed a significant difference in collagen fiber area compared to the contralateral eyes at month 6 (49.74% ± 4.12% and 48.17% ± 2.22%, respectively, compared to 44.37% ± 1.27% and 42.61% ± 1.29% in the contralateral eyes; p = 0.015 and p = 0.004, respectively). No significant changes were observed in the percentage of collagen fiber area with Masson's trichrome staining or Verhoeff's Van Gieson staining in the treated eyes between postoperative months 3 and 6 (p = 0.340 and p = 0.640, respectively).

The scleral elastic fibers are primarily located in the inner sclera as thin, long fiber networks. Changes in the density of scleral elastic fibers with Verhoeff's Van Gieson staining are presented in Table 2. In terms of the percentage of scleral elastic fiber area, no significant differences were observed between 3 and 6 months in both the treated and contralateral groups (p = 0.858 and p = 0.623, respectively). Similar results were obtained between the treated and contralateral eyes at 3 and 6 months postoperatively (p = 0.892 and p = 0.441, respectively).

Table 3 displays the changes in collagen fiber density of the fibrous capsule around the RSF graft with Masson's trichrome and Verhoeff's Van Gieson staining. At postoperative 6 months, a significant increase in the percentage of collagen fiber area with Masson's trichrome staining was observed in the treated eyes compared to postoperative 3 months (p < 0.001). Similar results were found in eyes stained with Verhoeff's Van Gieson stain (p < 0.001).

3.7 Over-expression of TGF-β1 detected through immunohistochemistry

To investigate the expression of TGF-β1 in the fibrous capsule surrounding the RSF graft, we performed immunohistochemical staining of paraffin sections of the eyeballs at 3 and 6 months postoperatively. The results of the immunohistochemical staining for TGF-β1 are shown in Figure 6, which revealed a significant upregulation of TGF-β1 expression in the treated groups. The AOD value was 0.219 ± 0.012 at 3 months and 0.221 ± 0.033 at 6 months in the treated eyes, as shown in Table 4. However, there was no statistically significant difference between the two time points (p = 0.857).

3.8 Apoptotic detection of retina

The TUNEL assay is a method used to detect fragmented DNA in apoptotic cells. In this study, nuclei were stained blue with DAPI, while apoptotic cells were labeled green with FITC. The absence of cellular apoptosis, as indicated by negative TUNEL results, suggests that there was no significant programmed cell death occurring in either the outer or inner nuclear layers of the retina in both the experimental and control eyes (Figure 7).

3.9 Ultrastructural TEM analyses of retina and optic nerve

The morphology of the retina and optic nerve was further analyzed using transmission electron microscopy (TEM).

TABLE 1 Inflammation and vascularization of the fibrous capsule around silk fibroin graft.

Animal no.	Inflammation score		Vascularity score	
	Treated eye	Contralateral eye	Treated eye	Contralateral eye
1[a]	2	0	3	0
2[a]	1	0	3	0
3[a]	2	0	3	0
4[a]	3	0	3	0
5[a]	1	0	3	0
6[a]	2	0	3	0
7[b]	2	0	3	0
8[b]	1	0	3	0
9[b]	1	0	3	0
10[b]	2	0	3	0
11[b]	2	0	3	0
12[b]	1	0	3	0

[a]Rabbit executed at month 3.
[b]Rabbit killed at month 6.

TABLE 2 Collagen and elastic fiber level in the sclera tissue.

Fiber area (%)	Treated eyes (n = 6)	Contralateral eyes (n = 6)	p-Value
Collagen fiber area at month 3 With Masson's trichrome staining Mean ± SD	51.57 ± 1.76	42.84 ± 2.19	<0.001[a]
Collagen fiber area at month 6 With Masson's trichrome staining Mean ± SD p-value	49.74 ± 4.12 0.340[b]	44.37 ± 1.27 0.167[b]	0.015[a]
Collagen fiber area at month 3 With Verhoeff's van gieson staining Mean ± SD	47.60 ± 1.81	42.25 ± 1.85	0.002[a]
Collagen fiber area at month 6 With Verhoeff's van gieson staining Mean ± SD p-value	48.17 ± 2.22 0.640[b]	42.61 ± 1.29 0.701[b]	0.004[a]
Elastic fiber area at month 3 With Verhoeff's van gieson staining Mean ± SD	25.46 ± 1.00	25.24 ± 3.35	0.892[a]
Elastic fiber area at month 6 With Verhoeff's van gieson staining Mean ± SD p-value	25.34 ± 1.27 0.858[b]	24.40 ± 2.31 0.623[b]	0.441[a]

[a]Paired-samples t-test.
[b]Independent t-test.

Figure 8 displays TEM images of the retina at 3 and 6 months after surgery, revealing no observable changes in any of the retinal layers of the treated eyes, including organelle swelling, nuclear shrinkage or condensation, and vacuolization (Figures 8A–F). In Figure 9, TEM images of the optic nerve at 3 and 6 months after surgery show that the myelin sheaths of the optic nerve were normal. Additionally,

TABLE 3 Collagen fiber level of the fibrous capsule around silk fibroin graft.

Collagen fiber level	3 months (n = 6)	6 months (n = 6)	p-Value
Collagen fiber area (%)			
With Masson's trichrome staining			
Mean ± SD	36.77 ± 1.61	46.91 ± 3.86	<0.001[a]
With EVG staining			
Mean ± SD	39.20 ± 1.88	44.76 ± 1.78	<0.001[a]

[a]Independent t-test.

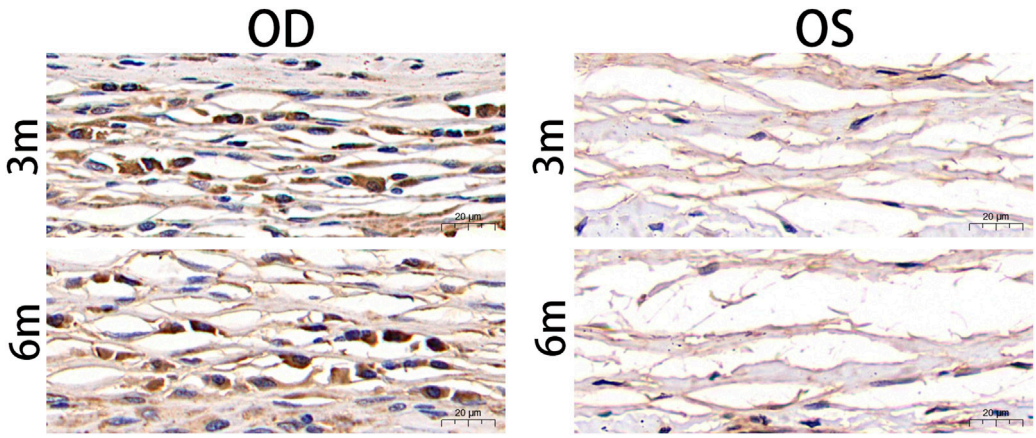

FIGURE 6
Postoperative photographs of the fibrous capsule around silk fibroin graft based on anti-TGF-β1 antibody immunohistochemical staining. TGF-β1 was significantly upregulated in the treated eyes 3 months and 6 months after surgery. TGF-β, transforming growth factor beta; OD, oculus dexter; OS, oculus sinister. Scale bar = 20 μm.

TABLE 4 Average optical density (AOD) of fibrous capsule to estimate the transforming growth factor beta1 (TGFβ1) expression.

Time	3 months (n = 6)	6months (n = 6)	p-Value
AOD			
Mean ± SD	0.219 ± 0.012	0.221 ± 0.033	0.857[a]

[a]Independent t-test.

there were no signs of disruption of axon fascicles, degeneration with axon swelling, lower axon numbers, or increased connective tissue septa in either the treated or contralateral groups.

3.10 Biomechanical evaluation of reinforced sclera

The biomechanical parameters of the reinforced sclera 6 months after surgery are presented in Table 5. The ultimate stress was 4.04 ± 1.45 MPa and 3.09 ± 1.00 MPa in the treated and control groups, respectively. There was a significant difference in ultimate stress between the two groups (p = 0.023), with a 30.7% increase in the treated group compared to the controls. The elastic modulus of the reinforced sclera was 19.00 ± 7.01 MPa in the treated group and 14.29 ± 5.27 MPa in the control group. Similarly, there was a significant difference in the elastic modulus between the two groups (p = 0.035), with a 33.0% increase in the treated group compared to the controls. These findings indicate that reinforced sclera has greater biomechanical stiffness than untreated eyes.

4 Discussion

SF is an attractive material for various biomedical applications due to its low immunogenicity, slow degradation profile, resistance to enzymatic cleavage, robust mechanical properties, and ease of processing into different forms (Minoura et al., 1990; Horan et al., 2005; Meinel et al., 2005; Farokhi et al., 2018). In our previous studies, we have confirmed that SF has high biocompatibility because of its unique structure (Ni et al., 2014; Ni et al., 2019). RSF hydrogels are three-dimensional polymer networks with a high water content that are typically formed by physical or chemical cross-linking (Wang and Zhang, 2015). However, traditional RSF hydrogels have a simple network structure, which limits their adaptability to complex environments. In recent years, functional RSF hydrogels with properties such as injectability, self-healing, adhesiveness, environmental responsiveness, electrical conductivity, and 3D printability have attracted researchers' attention (Zheng and Zuo, 2021). However, their applications are still limited due to their low mechanical strength. In this study, we applied a novel and robust RSF hydrogel and evaluated it as a patch for PSR in normal adult New Zealand white rabbits. In our previous work (Chen et al., 2022),

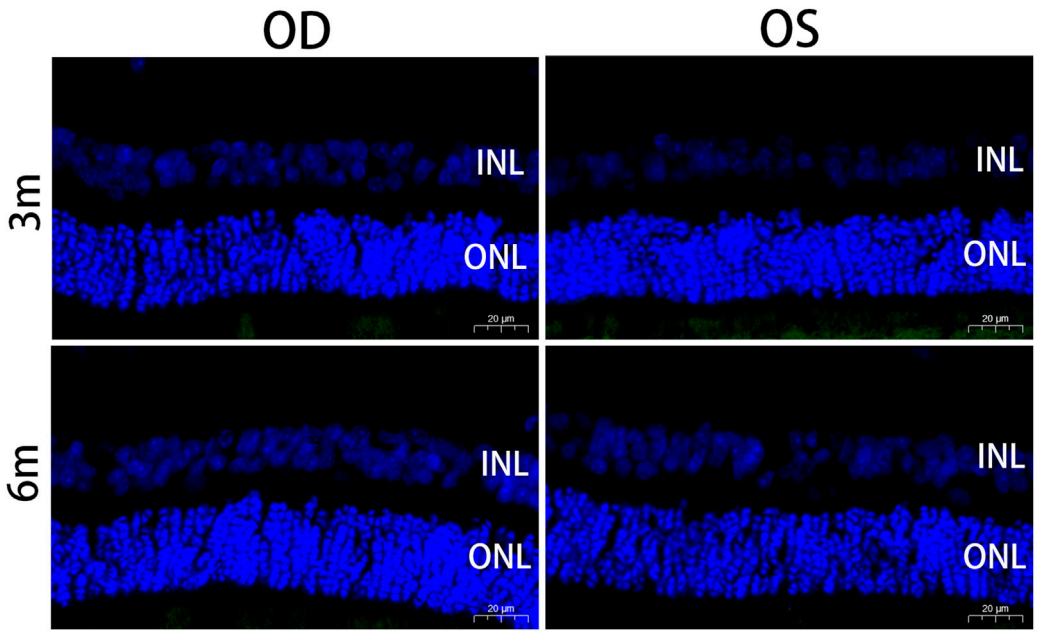

FIGURE 7
Apoptotic nuclei detected by TUNEL staining in the retina at 3 months and 6 months postoperatively. Positive apoptotic cells were labeled with FITC (green). Sections were counterstained with DAPI (blue). No cellular apoptosis was observed in the INL and ONL of the retina in the treated and contralateral eyes. OD, oculus dexter; OS, oculus sinister; INL, inner nuclear layer; ONL, outer nuclear layer. Scale bar = 20 μm.

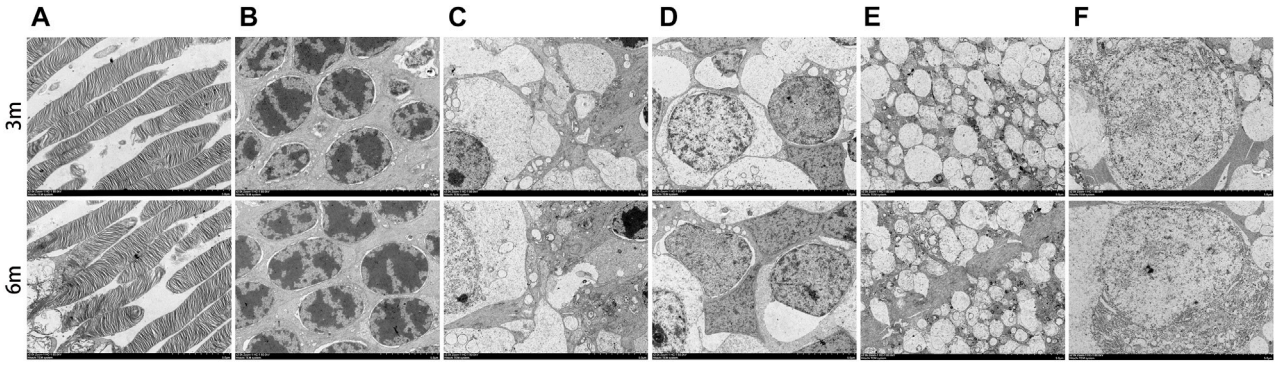

FIGURE 8
Ultrastructural transmission electron microscopy analyses of retina at 3 months and 6 months postoperatively. No signs of necrosis or apoptosis (including organelle swelling, nuclear shrinkage or condensation, and vacuolization) were found in all retinal layers of the treated eyes **(A–F)**. **(A)**, photoreceptor layer; **(B)**, outer nuclear layer; **(C)**, inner plexiform layer; **(D)**, inner nuclear layer; **(E)**, outer plexiform layer; **(F)**, retinal ganglion cell. Scale bar = 5 μm.

the characterization results of the RSF hydrogel (including mechanical and cytotoxicity properties) have been reported in detail. The mechanical properties can be adjusted by varying the concentration of RSF solution. When the RSF concentration increased from 0.075 to 0.15 g/mL, the compressive modulus of the hydrogel increased from 0.53 to 2.31 MPa, elastic modulus increased from 0.84 to 2.00 MPa, and the tensile strength increased from 0.23 to 0.54 MPa. In addition, the RSF hydrogel showed good biocompatibility by different testing methods, including incubation L929 cells with the hydrogel extracts, culturing L929 cells on the hydrogels surface, and implantation of the hydrogel into subcutaneous tissue of SD rats.

The study indicated that over a 6-month period, RSF hydrogels demonstrated good tolerance and biocompatibility when tested in rabbits. All implanted eyes remained healthy, and no intraocular or periorbital complications, such as infection or material exposure, were observed. Mild conjunctival congestion was observed early after the operation, which completely disappeared in the first month of the study. Additionally, there was no evidence of pathological changes in the optic nerve or retina, and no structural abnormalities

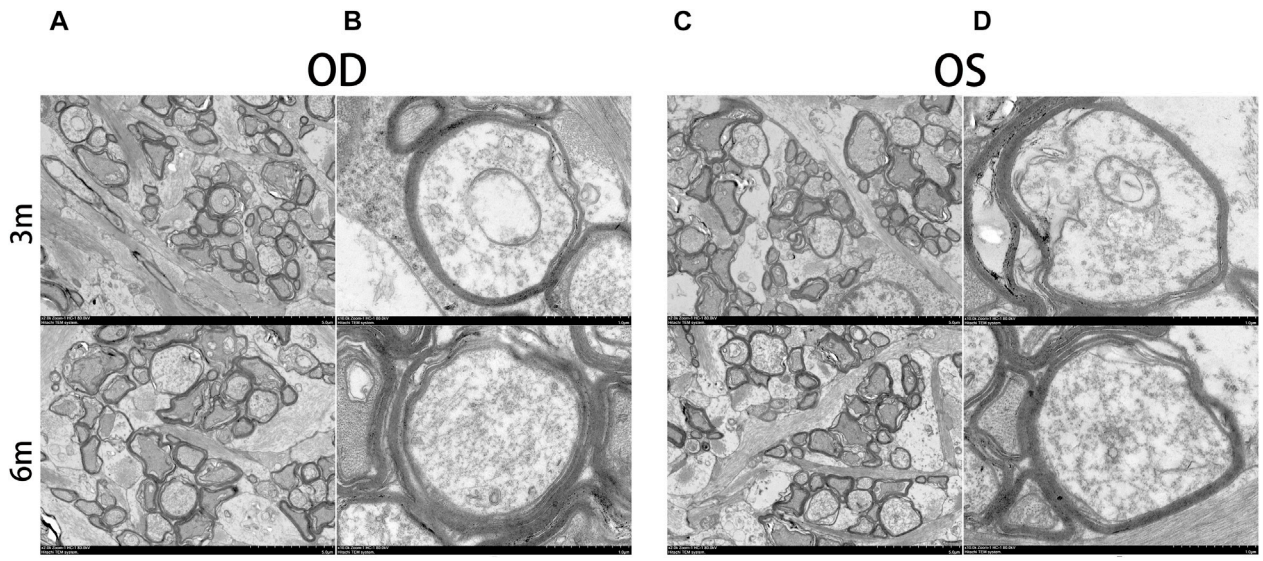

FIGURE 9
Ultrastructural transmission electron microscopy analyses of optic nerve at 3 months and 6 months postoperatively. No signs of disruption of axon fascicles, degeneration with axon swelling, lower axon numbers, and increases in connective tissue septa were found in the optic nerve of the treated and contralateral eyes. OD, oculus dexter; OS, oculus sinister. Scale bar = 5 μm **(A,C)**. Scale bar = 1 μm **(B,D)**.

TABLE 5 Biomechanical parameters of the sclera at month 6.

Biomechanical parameter	Treated eyes (n = 8)	Contralateral eyes (n = 8)	p-Value
Ultimate stress (MPa) Mean ± SD	4.04 ± 1.45	3.09 ± 1.00	0.023[a]
Elasticity modulus (MPa) Mean ± SD	19.00 ± 7.01	14.29 ± 5.27	0.035[a]

[a]Paired-samples t-test.

were observed in any layer of the retina on OCT. There were no significant intraocular pressure fluctuations during the postoperative observational period. The TUNEL assay was used to detect the DNA fragmentation characteristics of apoptotic cells (Gavrieli et al., 1992), and TUNEL-positive cells were not detected in the retinal sections of the treated eyes at 3 and 6 months postoperatively.

Despite the good biocompatibility of SF, it is still a heterogeneous protein in rabbits and may cause minimal foreign-body reactions. The development of a fibrous capsule around the RSF graft is a biological response to foreign proteins that cannot be eliminated, which isolates the foreign protein from the biological environment to minimize adverse effects. The fibrous capsules that surround long-term implants are typically characterized by the presence of macrophages, giant cells, lymphocytes, fibroblasts, a dense matrix of collagen, and fibrous tissue (Coleman et al., 1974). In our study, the RSF hydrogels were completely fixed inside the fibrovascular capsule, as demonstrated by B-ultrasound, gross, and histological examinations. The RSF graft was firmly attached to the posterior sclera over a wide area by the fibrovascular tissue, resulting in the formation of a sclera-fibrous tissue-material complex. The goal of scleral reinforcement surgery is to prevent global elongation, and the newly formed sclera-fibrous tissue-material complex may have superior biomechanical properties that can block the continuous elongation of the axial length and maintain a stable refractive status.

In our study, we observed infiltration of various inflammatory cells, including plasma cells, lymphocytes, macrophages, neutrophils, and fibroblasts, in the tissue around the RSF graft. The cell-mediated immune response to RSF can result in the synthesis of collagen lamellae, elastic fibers, and the extracellular matrix, leading to the formation of fiber wrapping around the graft. Macrophages and lymphocytes play important regulatory roles under fibrotic conditions by releasing cytokines. TGF-β is a key cytokine that is essential for inducing fibrosis (Biernacka et al., 2011). The immunohistochemistry results of this study showed higher expression levels of TGF-β1 at 3 and 6 months. Although all three isoforms (TGF-β1, 2, and 3) are expressed in fibrotic tissues, the development of tissue fibrosis is primarily attributed to TGF-β1 (Ask et al., 2008). Once TGF-β1 is activated, it promotes fibroblast-to-myofibroblast transition and regulates extracellular matrix remodeling.

The biomechanical properties of the reinforced sclera were found to be enhanced in this study. The ultimate stress of the reinforced sclera increased by 30.7%, and the elastic modulus increased by 33.0% compared to the control eyes. The treated

eyes had a significantly higher scleral collagen fiber content than the contralateral eyes at 3 and 6 months after surgery. Additionally, the scleral thickness of the treated eyes increased by 17.27 μm 6 months after surgery. Collagen fiber content and scleral thickness are crucial factors affecting the biomechanical properties of the sclera (Rada et al., 2006). Therefore, increasing collagen content and scleral thickness could potentially enhance the ultimate stress and elastic modulus of the sclera.

The degradation behavior of SF biomaterials is a crucial factor for their *in vivo* medical applications. A critical issue faced by researchers is whether the effect of PSR can be maintained for a longer time. Degradation of the implanted material after PSR surgery can result in the loss of the reinforcement effect (Xue et al., 2014). An ideal implant material should have a degradation rate that matches the healing or regeneration process at the implantation site. According to the United States Pharmacopeia's definition, silk is classified as a non-degradable biomaterial. However, silk is degradable and slowly absorbed *in vivo* over a long period. Different forms of SF may have highly variable degradation rates depending on factors such as structural and morphological features of the biomaterial, processing conditions, and characteristics of the biological environment at the implant site (Cao and Wang, 2009). Enzymes, especially proteolytic enzymes, play a significant role in the degradation of SF. B-mode ultrasound, computed tomography (CT), HE staining, and scanning electron microscopy are often used to evaluate the biodegradability of SF materials (Lu et al., 2015; Campos et al., 2020; Cai et al., 2021). In this study, although the material had partially decomposed at 6 months after surgery, it still acted as a graft for promoting cell migration and inducing the formation of extracellular matrix on the surface of the sclera. The reinforcement effect provided by the RSF graft was maintained for at least 6 months. Due to the slow degradation of SF, further investigation is necessary to determine the long-term biological reaction of PSR with RSF grafts.

A limitation of our study was that we did not use animal models of myopia to verify the effectiveness of RSF. Animal models of myopia have been established using guinea pigs, chicks, and mice, but their small eyeballs make them unsuitable for PSR. Therefore, rabbits were the most suitable animals for our study. In future studies, we plan to use rabbit models of myopia to evaluate the efficacy of RSF grafts in PSR. Additionally, our study did not include an examination of diopters and electrophysiological functions.

5 Conclusion

Our study has revealed that the RSF hydrogel exhibits excellent biocompatibility and is safe for all layers of the retina and optic nerve. The biomechanical properties of the reinforced sclera were improved, likely due to an increase in scleral collagen content and thickness. Additionally, the RSF hydrogel also facilitated the formation of a fibrous capsule around it. The newly formed sclera-fibrous tissue-material complex may possess superior biomechanical properties that can prevent the continuous elongation of the axial length and maintain a stable refractive status. Given its impressive biocompatibility and effectiveness, this novel robust RSF hydrogel holds great promise as a potential material for PSR surgery.

Data availability statement

The original contributions presented in the study are included in the article/Supplementary Material, further inquiries can be directed to the corresponding authors.

Ethics statement

The animal study was reviewed and approved by the Animal Treated Ethics Committee of Tongji Hospital Affiliated to Tongji University, Shanghai, China.

Author contributions

AR, XC, YN, and YJ conceived of the ideas and supervised all the aspects of this study. YX and YJ were responsible for animal husbandry and surgical manipulations. QC and ZS fabricated the regenerated silk fibroin hydrogels. JW and XZ conducted the histological, immunohistochemical, and histomorphometric analyses. YX performed the statistical analyses and wrote the manuscript. All authors contributed to the article and approved the submitted version.

Funding

This work was funded by the Science and Technology Committee of Changning District, Shanghai (CNKW 2020Y59), the Clinical Research Plan of SHDC (SHDC2020CR1043B), and the Clinical Research Program of Shanghai Tongji Hospital [ITJ(QN) 1904].

Acknowledgments

The authors would like to thank Yongmin Miao and Lingyun Ma for their valuable assistance in the ocular examinations.

Conflict of interest

The authors declare that the research was conducted in the absence of any commercial or financial relationships that could be construed as a potential conflict of interest.

Publisher's note

All claims expressed in this article are solely those of the authors and do not necessarily represent those of their

affiliated organizations, or those of the publisher, the editors and the reviewers. Any product that may be evaluated in this article, or claim that may be made by its manufacturer, is not guaranteed or endorsed by the publisher.

Supplementary material

The Supplementary Material for this article can be found online at: https://www.frontiersin.org/articles/10.3389/fbioe.2023.1211688/full#supplementary-material

References

Ask, K., Bonniaud, P., Maass, K., Eickelberg, O., Margetts, P. J., Warburton, D., et al. (2008). Progressive pulmonary fibrosis is mediated by TGF-β isoform 1 but not TGF-β3. *Int. J. Biochem. Cell Biol.* 40 (3), 484–495. doi:10.1016/j.biocel.2007.08.016

Bhardwaj, N., Sow, W. T., Devi, D., Ng, K. W., Mandal, B. B., and Cho, N.-J. (2015). Silk fibroin–keratin based 3D scaffolds as a dermal substitute for skin tissue engineering. *Integr. Biol.* 7 (1), 53–63. doi:10.1039/c4ib00208c

Bi, F., Chen, Y., Liu, J., Hu, W., and Tian, K. (2021). Bone mesenchymal stem cells contribute to ligament regeneration and graft-bone healing after anterior cruciate ligament reconstruction with silk-collagen scaffold. *Stem Cells Int.* 2021, 1–11. doi:10.1155/2021/6697969

Biernacka, A., Dobaczewski, M., and Frangogiannis, N. G. (2011). TGF-β signaling in fibrosis. *Growth factors.* 29 (5), 196–202. doi:10.3109/08977194.2011.595714

Boote, C., Sigal, I. A., Grytz, R., Hua, Y., Nguyen, T. D., and Girard, M. J. A. (2020). Scleral structure and biomechanics. *Prog. Retin. Eye Res.* 74, 100773. doi:10.1016/j.preteyeres.2019.100773

Cai, L., Gao, N., Sun, T., Bi, K., Chen, X., and Zhao, X. (2021). Application of an ultrasound semi-quantitative assessment in the degradation of silk fibroin scaffolds *in vivo*. *Biomed. Eng. Online* 20 (1), 48. doi:10.1186/s12938-021-00887-3

Campos, F., Bonhome-Espinosa, A. B., Chato-Astrain, J., Sánchez-Porras, D., García-García, Ó. D., Carmona, R., et al. (2020). Evaluation of fibrin-agarose tissue-like hydrogels biocompatibility for tissue engineering applications. *Front. Bioeng. Biotechnol.* 8, 596. doi:10.3389/fbioe.2020.00596

Cao, Y., and Wang, B. (2009). Biodegradation of silk biomaterials. *Int. J. Mol. Sci.* 10 (4), 1514–1524. doi:10.3390/ijms10041514

Chen, L., Sun, L. Y., Yao, J. R., Zhao, B. J., Shao, Z. Z., and Chen, X. (2022). Robust silk protein hydrogels made by a facile one-step method and their multiple applications. *ACS Appl. Bio Mat.* 5, 3086–3094. doi:10.1021/acsabm.2c00354

Choi, J. H., Kim, D. K., Song, J. E., Oliveira, J. M., Reis, R. L., and Khang, G. (2018). Silk fibroin-based scaffold for bone tissue engineering. *Adv. Exp. Med. Biol.* 1077, 371–387. doi:10.1007/978-981-13-0947-2_20

Coleman, D. L., King, R. N., and Andrade, J. D. (1974). The foreign body reaction: A chronic inflammatory response. *J. Biomed. Mat. Res.* 8 (5), 199–211. doi:10.1002/jbm.820080503

Dereli, C. G., Akcan, G., Can, M. E., Akdere Özge, E., Çaylı, S., Şimşek, G., et al. (2020). Surgical and immunohistochemical outcomes of scleral reconstruction with autogenic, allogenic and xenogenic grafts: An experimental rabbit model. *Curr. Eye Res.* 45 (12), 1572–1582. doi:10.1080/02713683.2020.1764976

Fang, Y., Yokoi, T., Nagaoka, N., Shinohara, K., Onishi, Y., Ishida, T., et al. (2018). Progression of myopic maculopathy during 18-year follow-up. *Ophthalmology* 125 (6), 863–877. doi:10.1016/j.ophtha.2017.12.005

Farokhi, M., Mottaghitalab, F., Samani, S., Shokrgozar, M. A., Kundu, S. C., Reis, R. L., et al. (2018). Silk fibroin/hydroxyapatite composites for bone tissue engineering. *Biotechnol. Adv.* 36 (1), 68–91. doi:10.1016/j.biotechadv.2017.10.001

Gambari, L., Amore, E., Raggio, R., Bonani, W., Barone, M., Lisignoli, G., et al. (2019). Hydrogen sulfide-releasing silk fibroin scaffold for bone tissue engineering. *Mat. Sci. Eng. C* 102, 471–482. doi:10.1016/j.msec.2019.04.039

Gavrieli, Y., Sherman, Y., and Ben-Sasson, S. A. (1992). Identification of programmed cell death *in situ* via specific labeling of nuclear DNA fragmentation. *J. Cell Biol.* 119 (3), 493–501. doi:10.1083/jcb.119.3.493

Gentle, A., Liu, Y., Martin, J. E., Conti, G. L., and McBrien, N. A. (2003). Collagen gene expression and the altered accumulation of scleral collagen during the development of high myopia. *J. Biol. Chem.* 278, 16587–16594. doi:10.1074/jbc.m300970200

Hayashi, K., Ohno-Matsui, K., Shimada, N., Moriyama, M., Kojima, A., Hayashi, W., et al. (2010). Long-term pattern of progression of myopic maculopathy: A natural history study. *Ophthalmology* 117 (8), 1595–1611. doi:10.1016/j.ophtha.2009.11.003

Hofmann, S., Hagenmüller, H., Koch, A. M., Müller, R., Vunjak-Novakovic, G., Kaplan, D. L., et al. (2007). Control of *in vitro* tissue-engineered bone-like structures using human mesenchymal stem cells and porous silk scaffolds. *Biomaterials* 28 (6), 1152–1162. doi:10.1016/j.biomaterials.2006.10.019

Hong, H., Seo, Y. B., Kim, D. Y., Lee, J. S., Lee, Y. J., Lee, H., et al. (2020). Digital light processing 3D printed silk fibroin hydrogel for cartilage tissue engineering. *Biomaterials* 232, 119679. doi:10.1016/j.biomaterials.2019.119679

Horan, R. L., Antle, K., Collette, A. L., Wang, Y., Huang, J., Moreau, J. E., et al. (2005). *In vitro* degradation of silk fibroin. *Biomaterials* 26 (17), 3385–3393. doi:10.1016/j.biomaterials.2004.09.020

Huang, W., Duan, A., and Qi, Y. (2019). Posterior scleral reinforcement to prevent progression of high myopia. *Asia-Pac. J. Ophthalmol.* 8 (5), 366–370. doi:10.1097/apo.0000000000000257

Jacob-LaBarre, J. T., Assouline, M., Byrd, T., and McDonald, M. (1994). Synthetic scleral reinforcement materials: I. Development and *in vivo* tissue biocompatibility response. *J. Biomed. Mat. Res.* 28 (6), 699–712. doi:10.1002/jbm.820280607

Kapoor, S., and Kundu, S. C. (2016). Silk protein-based hydrogels: Promising advanced materials for biomedical applications. *Acta Biomater.* 31, 17–32. doi:10.1016/j.actbio.2015.11.034

Kassem, R. R., Abdel-Hamid, M. A., and Khodeir, M. M. (2011). Effect of lyophilized amniotic membrane on the development of adhesions and fibrosis after extraocular muscle surgery in rabbits. *Curr. Eye Res.* 36 (11), 1020–1027. doi:10.3109/02713683.2011.601842

Keeley, F. W., Morin, J. D., and Vesely, S. (1984). Characterization of collagen from normal human sclera. *Exp. Eye Res.* 39 (5), 533–542. doi:10.1016/0014-4835(84)90053-8

Kundu, B., Rajkhowa, R., Kundu, S. C., and Wang, X. (2013). Silk fibroin biomaterials for tissue regenerations. *Adv. Drug Deliv. Rev.* 65 (4), 457–470. doi:10.1016/j.addr.2012.09.043

Li, H., Wang, Y., Sun, X., Tian, W., Xu, J., and Wang, J. (2019). Steady-state behavior and endothelialization of a silk-based small-caliber scaffold *in vivo*. Transplantation. *Polymers* 11 (8), 1303. doi:10.3390/polym11081303

Lovett, M., Cannizzaro, C., Daheron, L., Messmer, B., Vunjak-Novakovic, G., and Kaplan, D. L. (2007). Silk fibroin microtubes for blood vessel engineering. *Biomaterials* 28 (35), 5271–5279. doi:10.1016/j.biomaterials.2007.08.008

Lu, S., Wang, P., Zhang, F., Zhou, X., Zuo, B., You, X., et al. (2015). A novel silk fibroin nanofibrous membrane for guided bone regeneration: A study in rat calvarial defects. *Am. J. Transl. Res.* 7 (11), 2244–2253.

Maity, B., Samanta, S., Sarkar, S., Alam, S., and Govindaraju, T. (2020). Injectable silk fibroin-based hydrogel for sustained insulin delivery in diabetic rats. *ACS Appl. Bio Mat.* 3 (6), 3544–3552. doi:10.1021/acsabm.0c00152

McBrien, N. A., and Gentle, A. (2003). Role of the sclera in the development and pathological complications of myopia. *Prog. Retin. Eye Res.* 22 (3), 307–338. doi:10.1016/s1350-9462(02)00063-0

Meinel, L., Hofmann, S., Karageorgiou, V., Kirker-Head, C., McCool, J., Gronowicz, G., et al. (2005). The inflammatory responses to silk films *in vitro* and *in vivo*. *Biomaterials* 26 (2), 147–155. doi:10.1016/j.biomaterials.2004.02.047

Minoura, N., Tsukada, M., and Nagura, M. (1990). Physico-chemical properties of silk fibroin membrane as a biomaterial. *Biomaterials* 11 (6), 430–434. doi:10.1016/0142-9612(90)90100-5

Mottaghitalab, F., Hosseinkhani, H., Shokrgozar, M. A., Mao, C., Yang, M., and Farokhi, M. (2015). Silk as a potential candidate for bone tissue engineering. *J. Control. Release* 215, 112–128. doi:10.1016/j.jconrel.2015.07.031

Ni, Y., Jiang, Y., Wang, K., Shao, Z., Chen, X., Sun, S., et al. (2019). Chondrocytes cultured in silk-based biomaterials maintain function and cell morphology. *Int. J. Artif. Organs* 42 (1), 31–41. doi:10.1177/0391398818806156

Ni, Y., Jiang, Y., Wen, J., Shao, Z., Chen, X., Sun, S., et al. (2014). Construction of a functional silk-based biomaterial complex with immortalized chondrocytes *in vivo*. *J. Biomed. Mat. Res. Part A* 102 (4), 1071–1078. doi:10.1002/jbm.a.34763

Ohno-Matsui, K., Lai, T. Y. Y., Lai, C.-C., and Cheung, C. M. G. (2016). Updates of pathologic myopia. *Prog. Retin. Eye Res.* 52, 156–187. doi:10.1016/j.preteyeres.2015.12.001

Rada, J. A., Achen, V. R., Perry, C. A., and Fox, P. W. (1997). Proteoglycans in the human sclera. Evidence for the presence of aggrecan. *Invest. Ophthalmol. Vis. Sci.* 38 (9), 1740–1751.

Rada, J. A. S., Shelton, S., and Norton, T. T. (2006). The sclera and myopia. *Exp. Eye Res.* 82 (2), 185–200. doi:10.1016/j.exer.2005.08.009

Saw, S. M., Gazzard, G., Au Eong, K.-G., and Tan, D. T. H. (2002). Myopia: Attempts to arrest progression. *Br. J. .Ophthalmol.* 86 (11), 1306–1311. doi:10.1136/bjo.86.11.1306

Schepens, C. L., and Acosta, F. (1991). Scleral implants: An historical perspective. *Surv. Ophthalmol.* 35 (6), 447–453. doi:10.1016/0039-6257(91)90108-r

Shevelev, M. M. (1930). Operation against high myopia and sclera with aid of the transplantation of fascia lata on thinned sclera. *Russ. Oftalmol. J.* 11, 107–110.

Snyder, A. A., and Thompson, F. B. (1972). A simplified technique for surgical treatment of degenerative myopia. *Am. J. Ophthalmol.* 74 (2), 273–277. doi:10.1016/0002-9394(72)90544-2

Thompson, F. B. (1978). A simplified scleral reinforcement technique. *Am. J. Ophthalmol.* 86 (6), 782–790. doi:10.1016/0002-9394(78)90121-6

Wang, H., and Zhang, Y. (2015). Processing silk hydrogel and its applications in biomedical materials. *Biotechnol. Prog.* 31 (3), 630–640. doi:10.1002/btpr.2058

Wang, X., Zhang, X., Castellot, J., Herman, I., Iafrati, M., and Kaplan, D. L. (2008). Controlled release from multilayer silk biomaterial coatings to modulate vascular cell responses. *Biomaterials* 29 (7), 894–903. doi:10.1016/j.biomaterials.2007.10.055

Wang, Y., Blasioli, D. J., Kim, H.-J., Kim, H. S., and Kaplan, D. L. (2006). Cartilage tissue engineering with silk scaffolds and human articular chondrocytes. *Biomaterials* 27 (25), 4434–4442. doi:10.1016/j.biomaterials.2006.03.050

Wang, Y., Rudym, D. D., Walsh, A., Abrahamsen, L., Kim, H.-J., Kim, H. S., et al. (2008). *In vivo* degradation of three-dimensional silk fibroin scaffolds. *Biomaterials* 29 (24-25), 3415–3428. doi:10.1016/j.biomaterials.2008.05.002

Xue, A., Bao, F., Zheng, L., Wang, Q., Cheng, L., and Qu, J. (2014). Posterior scleral reinforcement on progressive high myopic young patients. *Optom. Vis. Sci.* 91 (4), 412–418. doi:10.1097/opx.0000000000000201

Yan, L.-P., Silva-Correia, J., Oliveira, M. B., Vilela, C., Pereira, H., Sousa, R. A., et al. (2015). Bilayered silk/silk-nanoCaP scaffolds for osteochondral tissue engineering: *In vitro* and *in vivo* assessment of biological performance. *Acta Biomater.* 12, 227–241. doi:10.1016/j.actbio.2014.10.021

Yan, Z., Chen, W., Jin, W., Sun, Y., Cai, J., Gu, K., et al. (2021). An interference screw made using a silk fibroin-based bulk material with high content of hydroxyapatite for anterior cruciate ligament reconstruction in a rabbit model. *J. Mat. Chem. B* 9 (26), 5352–5364. doi:10.1039/d1tb01006a

Yan, Z., Wang, C., Chen, W., and Song, X. (2010). Biomechanical considerations: Evaluating scleral reinforcement materials for pathological myopia. *Can. J. Ophthalmol.* 45 (3), 252–255. doi:10.3129/i09-279

Zhang, X., Baughman, C. B., and Kaplan, D. L. (2008). *In vitro* evaluation of electrospun silk fibroin scaffolds for vascular cell growth. *Biomaterials* 29 (14), 2217–2227. doi:10.1016/j.biomaterials.2008.01.022

Zheng, H., and Zuo, B. (2021). Functional silk fibroin hydrogels: Preparation, properties and applications. *J. Mat. Chem. B* 9 (5), 1238–1258. doi:10.1039/d0tb02099k

Zhou, C. Z., Confalonieri, F., Jacquet, M., Perasso, R., Li, Z. G., and Janin, J. (2001). Silk fibroin: Structural implications of a remarkable amino acid sequence. *Proteins* 44 (2), 119–122. doi:10.1002/prot.1078

frontiers | Frontiers in Bioengineering and Biotechnology

TYPE Original Research
PUBLISHED 23 June 2023
DOI 10.3389/fbioe.2023.1217938

OPEN ACCESS

EDITED BY
Qianbin Wang,
University of Massachusetts Amherst, United States

REVIEWED BY
Tairong Kuang,
Zhejiang University of Technology, China
Yang Kang,
Sun Yat-sen University, China

*CORRESPONDENCE
Guiting Liu,
liugt@scu.edu.cn
Rong Chen,
rongchen@scu.edu.cn

RECEIVED 06 May 2023
ACCEPTED 05 June 2023
PUBLISHED 23 June 2023

CITATION
Zheng H, Zhang C, Liu G, Chen R and Guo S (2023), The effect of layer thickness ratio on the drug release behavior of alternating layered composite prepared by layer-multiplying co-extrusion. *Front. Bioeng. Biotechnol.* 11:1217938. doi: 10.3389/fbioe.2023.1217938

The effect of layer thickness ratio on the drug release behavior of alternating layered composite prepared by layer-multiplying co-extrusion

Huiyu Zheng, Cong Zhang, Guiting Liu*, Rong Chen* and Shaoyun Guo

The State Key Laboratory of Polymer Materials Engineering, Polymer Research Institute of Sichuan University, Chengdu, China

Multi-layered drug delivery (MLDD) system has promising potential to achieve controlled release. However, existing technologies face difficulties in regulating the number of layers and layer-thickness ratio. In our previous works, layer-multiplying co-extrusion (LMCE) technology was applied to regulate the number of layers. Herein, we utilized layer-multiplying co-extrusion technology to modulate the layer-thickness ratio to expand the application of LMCE technology. Four-layered poly (ε-caprolactone)-metoprolol tartrate/poly (ε-caprolactone)-polyethylene oxide (PCL-MPT/PEO) composites were continuously prepared by LMCE technology, and the layer-thickness ratios for PCL-PEO layer and PCL-MPT layer were set to be 1:1, 2:1, and 3:1 just by controlling the screw conveying speed. The *in vitro* release test indicated that the rate of MPT release increased with decreasing the thickness of the PCL-MPT layer. Additionally, when PCL-MPT/PEO composite was sealed by epoxy resin to eliminate the edge effect, sustained release of MPT was achieved. The compression test confirmed the potential of PCL-MPT/PEO composites as bone scaffolds.

KEYWORDS

layered structures, interface, extrusion, drug release, scaffold

1 Introduction

Controlled release is the ultimate goal of drug delivery. Many strategies have been developed to fabricate drug delivery systems with desirable drug release behaviors, such as stimulus-responsive drug delivery systems (Antoniou et al., 2021), nano drug delivery systems (Birk et al., 2021) and multi-layered drug delivery systems (Abdul and Poddar, 2004). Among these, multi-layered drug delivery (MLDD) systems are garnering increasing attention due to their inherent flexibility and controllability in drug release, extensive applicability, and the potential for continuous preparation (Abdul and Poddar, 2004; Choi and Jeong, 2011; Choi et al., 2013). Nowadays, MLDD systems can be prepared by layer-by-layer (LBL) self-assembly technology (Alkekhia et al., 2020), microfluidic technology (Liu et al., 2018), electrospinning technology (Laha et al., 2017) and lamination (Mazel and Tchoreloff, 2021). Moreover, their release behaviors can be adjusted flexibly and controllably by manipulating the number of layers, layer thickness ratio and drug distribution (Heng,

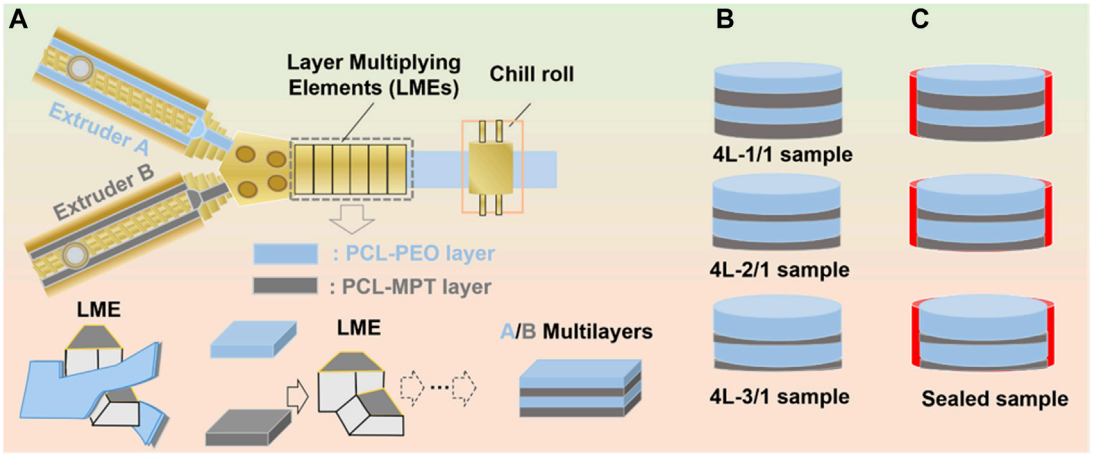

FIGURE 1
Schematic of layer-multiplying co-extrusion system **(A)**, prepared four-layered PCL-MPT/PEO composites with different layer-thickness ratio **(B)** and sealed PCL-MPT/PEO composites **(C)**.

2018; Cerea et al., 2020; Finsgar et al., 2021). For example, Rebeca Hernández et al. utilized LBL technology to construct alginate/chitosan multi-layered complex systems, in which tamoxifen was loaded in an intermediate position. The release of tamoxifen was regulated by varying the number of alternating layers (Criado-Gonzalez et al., 2019). In another study, Michael Kai Tsun To et al. prepared poly (lactic-co-glycolic acid)/alginate core-shell double-layer rifampicin delivery system by microfluidic technology (Wu et al., 2013). The release kinetics of rifampicin were adjusted by manipulating the thickness ratio of the core-shell structure, resulting in the achievement of a near-zero-order release pattern.

The design strategy of multi-layered structures has provided a versatile platform for the fabrication of drug delivery systems with programmed release behaviors. However, it is difficult for the existing preparation technology to realize the continuous preparation of multi-layered drug delivery systems with high layer numbers and wide layer thickness ratio at the same time. For instance, LBL technology can produce a high-layer number drug delivery system, but it encounters difficulties in achieving flexible regulation of layer thickness ratio and ensuring continuous preparation. On the other hand, the microfluidic technology can achieve flexible control of layer thickness ratio and continuous preparation of drug delivery systems. Nevertheless, it faces challenges in constructing layered structures with a high number of layers. Electrostatic spinning technology and laminating technology face difficulties in building high-leveler number of drug delivery systems. Our previous works developed layer-multiplying co-extrusion (LMCE) technology to continuously construct composites with thousands of alternating multi-layers (Ji et al., 2019; Zhang et al., 2019; Zheng et al., 2020). By this technology, the two components are each heat-processed and conveyed through a screw extruder and stacked as a two-layer product via a co-extrusion block. The number of layers of the product can be doubled with an application of layer multiplying elements (LMEs), and the layer thickness ratio of the two components can be adjusted by the ratio of screw extruder delivery rate. The LMCE technology has showed the potential of preparing multi-layered drug delivery systems with high layer number and wide layer thickness ratio. Motivated by this, we utilized LMCE technology to continuously construct alternating multi-layered drug delivery systems with a layer-thickness ratio of 1:1, including 128 layers, and investigated the effect of the number of layers on the drug release behavior (Liu et al., 2022; Zhang et al., 2022).

In this work, we further investigated the effect of layer thickness ratio on drug release behavior to expand the application of LMCE technology in the preparation of multi-layered drug delivery systems. Poly (ε-caprolactone) (PCL) worked as the loading layer of metoprolol tartrate (MPT), and PCL-polyethylene oxide (PEO) composite layer acted as the barrier layer. Three four-layered PCL-MPT/PEO composites with layer thickness ratios of 1:1, 2:1 and 3:1 for PCL-PEO layer and PCL-MPT layer, respectively, were prepared by LMCE technology (Figure 1A). *In vitro* release tests were carried out and the release mechanism was analyzed by the combination of scanning electron microscope and Raman spectroscopy. In addition, compression performance tests were performed to explore the potential of the PCL-MPT/PEO composites as tissue engineering scaffolds.

2 Materials and method

2.1 Materials

Poly (ε-caprolactone) (PCL, Mw = 80,000) was provided by Perstorp Co. Polyethylene oxide (PEO, Mw = 100,000) was purchased from Sumitomo Chemical Co. Metoprolol tartrate (MPT) and phosphate buffered solution (PBS) were supplied by Guangzhou Hanfang Pharmaceutical Co. and Zhongshan Golden Bridge Biotechnology Co., respectively.

TABLE 1 Weight ratio of PEO, PCL and MPT in PCL-MPT and PCL-PEO samples.

Abbreviation	PCL (w_t%)	PEO (w_t%)	MPT (w_t%)
PCL-MOT	90	0	10
PCL-PEO	50	50	0

2.2 Preparation of four-layered PCL-MPT/PEO composites by LMCE technology

PCL, PEO and MPT were dried in a vacuum oven at 40°C for 24 h, then mixed in a high mixer according to the mass ratio shown in Table 1. Subsequently, components were added to a twin-screw extruder (screw diameter: 20 mm, length diameter (L/D) ratio: 40) for melt extrusion and pelletizing. The two sections of extrusion screw and die temperatures were set at 40°C, 90°C, and 130°C, respectively, and the screw speed was 130 rpm. After pelletizing, the product was dried under vacuum for further application.

The dried PCL-MPT sample and PCL-PEO sample were added to two single-screw extruders of the LMCE equipment. The temperatures of screw section were set at 40°C, 90°C, and 130°C from inlet to outlet, respectively. The temperatures of co-extrusion block and layer multiplying elements (LMEs) were set at 130°C. The four-layered PCL-MPT/PEO composites were prepared by the connection between co-extrusion block and LMEs. The layer thickness ratio of PCL-MPT layer and PCL-PEO layer was adjusted by the screw speed ratio. In this work, three four-layered PCL-MPT/PEO composites with layer thickness ratios of 1:1, 2:1, and 3:1 for PCL-PEO layer and PCL-MPT layer, respectively, were prepared. A 10 mm diameter cutter was used to cut the PCL-MPT/PEO composites into small rounds with a diameter of 10 mm and a thickness of 2.0 mm (Figure 1B). The samples were named as shown in Table 2. Taking "4L-2/1" as an example, "4 L" indicated that the number of layers of samples was 4, "2/1" referred to the thickness ratio of PCL/PEO layer and PCL-MPT layer was 2:1.

2.3 The preparation of sealed samples

The surface PCL-PEO layer of pre-cut 4L-1/1, 4L-2/1 and 4L-3/1 samples was sealed with tape. Then samples were placed flat in a 20 mm diameter round plastic mold with the top PCL-MPT layer and the bottom PCL-PEO layer sealed with tape. Pre-configured epoxy resin was added around the samples drop by drop until the epoxy resin was level with the upper surface of the samples. The plastic mold was placed in a vacuum oven at 40°C for 7 days. Then cured samples were removed from the mold and the tape at the PCL-PEO layer was removed. Thus, sealed PCL-MPT/PEO composites were obtained (Figure 1C). The samples were named as 4L-1/1-1, 4L-2/1-1, and 4L-3/1-1.

2.4 Morphology observation

The multi-layered structures of samples were observed by a polarizing microscope (POM) (Olympus BX51). The morphology of 4L-1/1 sample soaked in PBS solution for 2 weeks was observed by scanning electron microscope (XL30FZG, Philips) with an accelerating voltage of 20 kV. Before testing, the samples were dried to constant weight in a vacuum oven at 40°C, then quenched in liquid nitrogen. The sections were vacuum gilded.

2.5 *In vitro* release test

The sample slices were immersed in 20 mL of PBS buffer and stirred at 100 rpm in an incubator at 37°C. The PBS buffer was removed completely at regular intervals and 20 mL of new PBS buffer was added. The dissolved concentration of MPT in PBS buffer was tested by UV-1750 UV-Vis spectrophotometer (Shimadzu, Japan) at 222 nm, and the applicable concentration range of the standard curve equation for MPT was 0.5–15.0 μg/mL, and the drug concentration and absorbance showed a good linear relationship ($R > 0.999$) in the applicable range. The experiment was repeated three times for all samples.

2.6 Raman spectroscopy

The 4L-1/1-1 samples were soaked in PBS buffer for 2, 4, and 8 h, respectively, then removed and dried with filter paper, quenched with liquid nitrogen. The cross-section of sample was observed by a DXRxi microlaser Raman spectrometer (Thermo Fisher, United States) equipped with an Olympus BX51 optical microscope (wavelength of 780 nm, resolution of 0.4 cm^{-1}, step size of 3 μm, 10 scans and exposure time of 2 Hz). The Raman curve of MPT was used as the standard curve, and the Correlation mode was selected to image different areas of the sample (area 50 μm × 50 μm).

2.7 The compression performance test

Samples were soaked in PBS buffer for 2 weeks, and then removed and dried with filter paper. Five samples were stacked and tested on a universal material testing machine (CM-4104, MTS Systems Co., United States) with a compression speed of 1 mm/min and a maximum compression strain of 60%. The test environment was 23°C and 55% humidity. Three samples were tested for each group and the results were averaged.

TABLE 2 The abbreviation of PCL-MPT/PEO composites.

Abbreviation	Layer number	Thickness ratio of PCL-PEO layer and PCL-MPT layer
4L-1/1	4	1:1
4L-2/1	4	2:1
4L-3/1	4	3:1

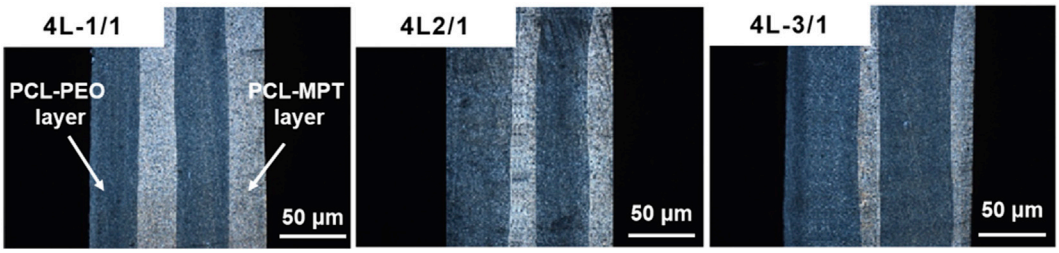

FIGURE 2
POM micrographs of PCL-MPT/PEO composites with different layer thickness ratios.

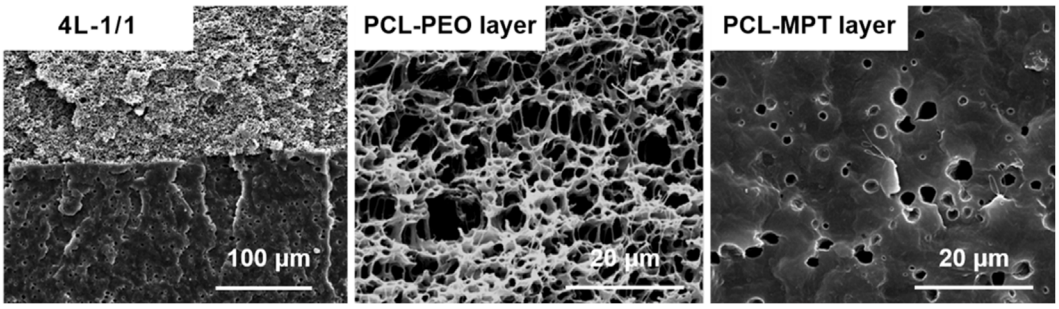

FIGURE 3
SEM images of 4L-1/1 sample after immersion for 2 weeks.

3 Results and discussion

3.1 Morphology observation

In this work, PCL-MPT/PEO composites with four-layered structure were continuously prepared by LMCE technology, the mechanism of which was described in detail in our previous work (Liu et al., 2022; Zhang et al., 2022). The two-layered PCL-MPT/PEO composites were prepared by the assembly of co-extrusion block, then four-layered PCL-MPT/PEO composites were obtained by an application of LMEs. The layer thickness ratio of PCL-MPT layer and PCL-PEO layer was adjusted by the screw speed ratio (Figure 1). The morphology of PCL-MPT/PEO composites was observed by POM and presented in Figure 2. The darker layer was the PCL-PEO layer and the brighter layer was the PCL-MPT layer. The four-layered PCL-MPT/PEO composites with layer thickness ratios of 1:1, 2:1, and 3:1 for PCL-PEO layer and PCL-MPT layer were successfully prepared by LMCE technology. Since the thickness of PCL-MPT/PEO composite was about 2 mm, the thickness of PCL-PEO layer of 4L-1/1, 4L-2/1, and 4L-3/1 sample was about 500, 330, and 250 μm, respectively. All the samples had a good layer structure, and the PCL-PEO layer and PCL-MPT layer were arranged in a continuous alternating pattern along the extrusion direction with a regular structure.

Before the evaluation of *in vitro* release, the 4L-1/1 sample was taken for SEM evaluation to observe the morphology of PCL-PEO layer and PCL-MPT layer after immersion in PBS for 2 weeks. As Figure 3 presented, interconnected pores in the PCL-PEO layer and a small number of isolated micropores (1–2 μm) in the PCL-MPT layer could be clearly observed. The pores in PCL-MPT layer were caused by the diffusion of MPT, and the pores in PCL-PEO layer were resulted by the dissolution of PEO. It could be considered that the diffusion of PEO was much faster than that of MPT.

3.2 *In vitro* drug release

The cumulative release and release rate profiles of PCL-MPT/PEO composites were shown in Figure 4A and Figure 4B, respectively. In the initial 24 h, MPT release rate increased with decreasing the thickness of PCL-MPT layer. The 24-h MPT release amount of 4L-1/1, 4L-2/1, and 4L-3/1 sample was about 40%, 46%, and 55%, respectively. The theory of diffusion kinetics showed that the larger the diffusion path of the drug in the carrier, the longer the time required for complete release (Siepmann and Siepmann, 2008). In the test of *in vitro* release, PCL-MPT/PEO composites were immersed in PBS solution. The MPT of surface PCL-MPT layer was released first, and the PEO of PCL-PEO layer was dissolved at the same time, which provided the diffusion channel for the MPT of inner PCL-MPT layer (Figure 4C). As the dissolution of PEO, which could form interconnected pores in the PCL-PEO layer, was much faster than that of MPT, the rate of MPT release of PCL-MPT/PEO composite was mainly determined by the diffusion of MPT in PCL-MPT layer. This phenomenon could explain

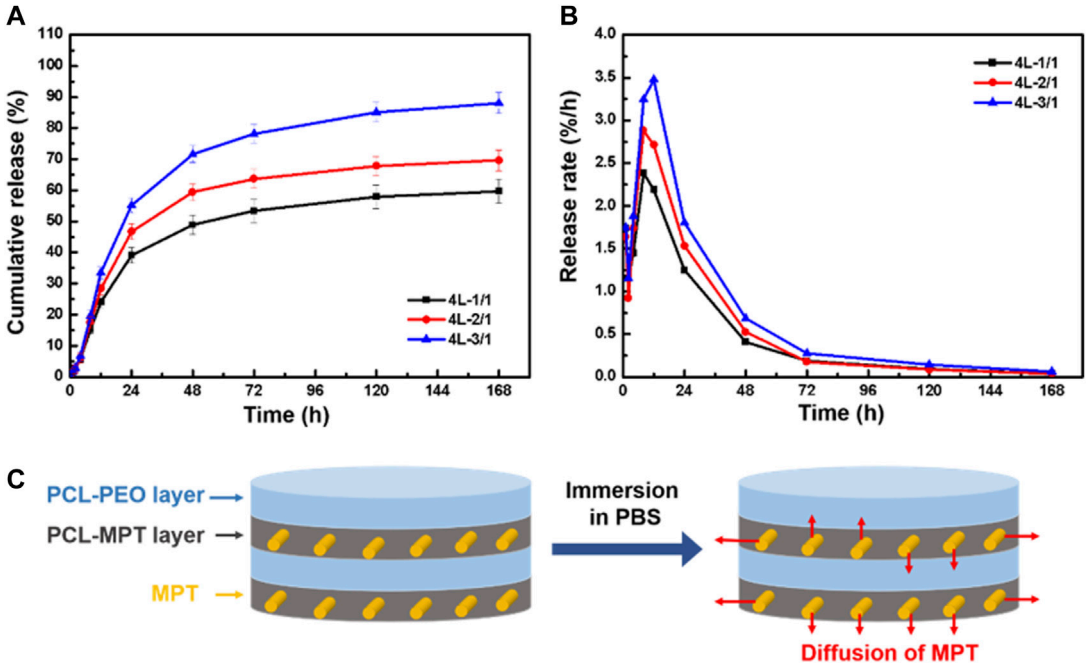

FIGURE 4
The cumulative release curve **(A)** and release rate curve **(B)** of PCL-MPT/PEO composites, and schematic of the diffusion of MPT in PCL-MPT/PEO composite after immersion in PBS **(C)**.

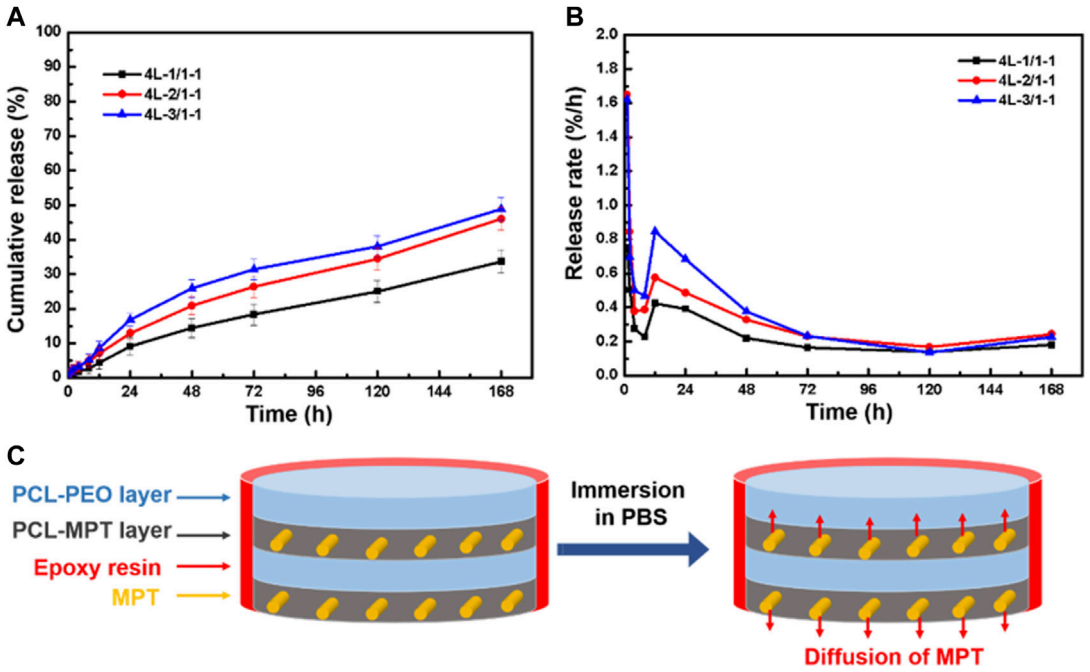

FIGURE 5
The cumulative release curve **(A)** and release rate curve **(B)** of sealed PCL-MPT/PEO composites, and schematic of the diffusion of MPT in sealed PCL-MPT/PEO composite after immersion in PBS **(C)**.

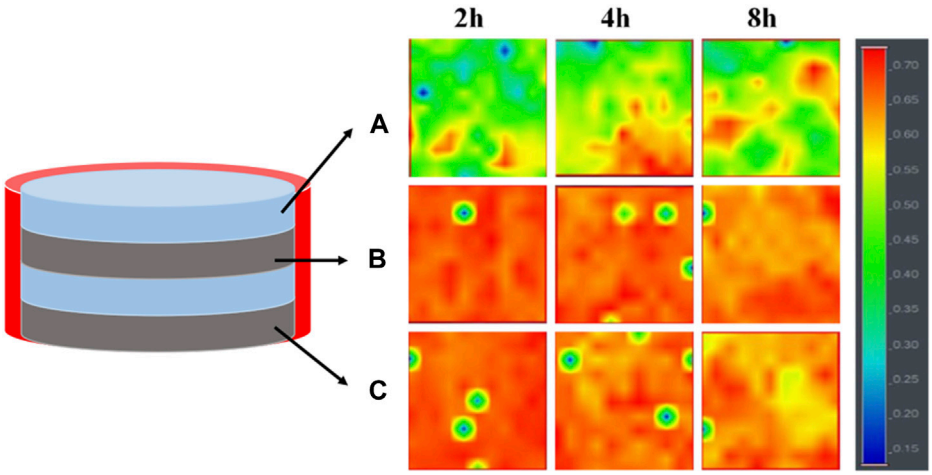

FIGURE 6
Raman spectroscopy imaging of the three different regions of 4L-1/1-1 sample immersed in PBS for different times: surface PCL-PEO layer **(A)**, inner PCL-MPT layer **(B)** and surface PCL-MPT layer **(C)**.

the observed increase in MPT release rate during the initial 24-h period as the thickness of the PCL-MPT layer decreases.

To eliminate the edge effect of sample on the MPT release, PCL-MPT/PEO composites were sealed by epoxy resin leaving the exposure of only the top and bottom surfaces. The cumulative release and release rate curves of sealed samples were presented in Figure 5A and Figure 5B, respectively. It could be seen that the MPT release rate of sealed samples were slower than that of unsealed samples. The 24-h MPT release amount of 4L-1/1-1, 4L-2/1-1, and 4L-3/1-1 sample was about 10%, 14%, and 18%, respectively. The thinner thickness of PCL-MPT layer led to the faster rate of MPT release, which was consist to MPT release behavior of unsealed samples. After the sample was sealed, MPT could only be released in the direction perpendicular to the layer plane, which prolonged the release path of MPT at the edge, resulting in a slower release rate of sealed sample compared to the unsealed sample (Figure 5C). The rate of MPT release gradually decreased from 1 to 8 h, which might be due to the diffusion of MPT in the surface PCL-MPT layer. The rate of MPT release increased from 8 to 12 h, which might be resulted by the diffusion of MPT in the inner PCL-MPT layer. After 48 h, the MPT release tended to be stable.

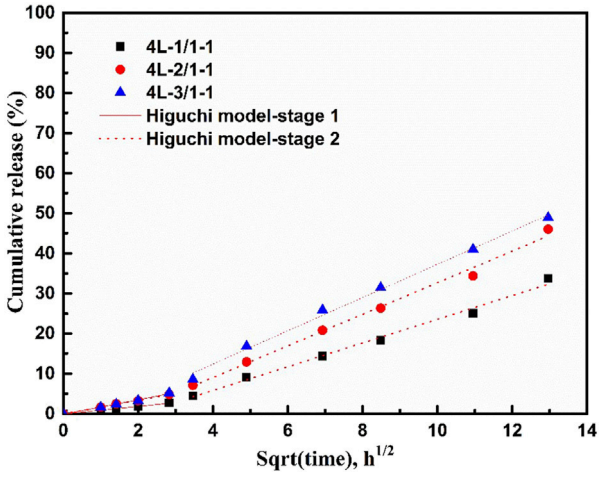

FIGURE 7
Fitting results of drug release profile of 4L-1/1-1, 4L-2/1-1, and 4L-3/1-1 samples.

3.3 Drug release mechanism

In order to elucidate the drug release mechanism of the sealed samples more clearly, 4L-1/1-1 samples soaked in PBS buffer for different times were subjected to Raman spectroscopy analysis (Figure 6). The results revealed that after 2 h of release, a minimal quantity of MPT from the inner PCL-MPT layer diffused into the surface PCL-PEO layer. Following 4 h of release, an increased dissolution of PEO and the formation of additional pores within the PCL-PEO layer were observed, consequently leading to a higher quantity of MPT diffusion into the surface PCL-PEO layer. At the same time, the MPT of surface PCL-MPT layer was continuously released. After 8 h of release, the MPT amount of inner PCL-MPT layer significantly decreased, which mainly diffused into the surface PCL-PEO layer. Consequently, the release of MPT occurred from both the surface PCL-MPT layer and the surface PCL-PEO layer, leading to an augmented MPT release rate during the subsequent 4-h period.

Combining the release curves (Figure 5) and Raman spectroscopy analysis (Figure 6), the release process of sealed samples could be divided into two stages. The first stage was mainly the release of MPT from surface PCL-MPT layer in the initial 8 h, and the second stage was the release of MPT form both surface PCL-MPT layer and surface PCL-PEO layer, the MPT of which was diffused from the inner PCL-MPT layer. In addition, the release profiles of the two stages of sealed PCL-MPT/PEO composites were almost consistent with Higuchi release model (Figure 7; Table 3) (Lu and Hagen, 2020; Karthikeyan et al.,

TABLE 3 Release kinetics parameters (k_1, k_2) and correlation coefficients, (Rc^2), for MPT released from 4L-1/1-1, 4L-2/1-1, and 4L-3/1-1 samples.

Specimen	First stage		Second stage	
	k_1	Rc^2	k_2	Rc^2
4L-1/1-1	0.97	0.99	2.96	0.99
4L-2/1-1	1.68	0.99	3.94	0.99
4L-3/1-1	1.82	0.99	4.15	0.99

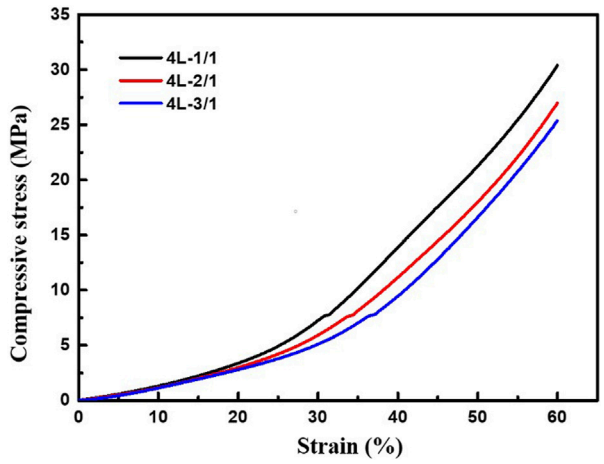

FIGURE 8
Compressive stress-strain curves of PCL-MPT/PEO composites with different layer thickness ratio.

2021). The Higuchi constant increased with decreasing the thickness of PCL-MPT layer, which was consistent with the analysis of MPT release rate.

3.4 Compression performance

For tissue engineering scaffolds, mechanical property evaluation, especially compression property study, was essential (Ghorbani et al., 2016). 4L-1/1, 4L-2/1, and 4L-3/1 sample after immersion in PBS for 2 weeks was taken for compression test, and the compressive stress-strain curves were presented in Figure 8. The compressive strength in 60% strain of 4L-1/1, 4L-2/1, and 4L-3/1 sample was about 30.4, 27.0, and 25.4 MPa, respectively. The compression modulus of 4L-1/1, 4L-2/1, and 4L-3/1 sample was about 15.5 MPa, 13.8 and 13.0 MPa, respectively (Table 4). The compressive strength of PCL-MPT/PEO composites decreased with increasing the thickness of PCL-PEO layer, which might be due to the fact that the forming of interconnected pores in PCL-PEO layer after immersion in PBS could disrupt the regularity of the composite structure and thus reduce the mechanical strength. The compressive performance of PCL-MPT/PEO composites suggested their potential as bone tissue scaffolds (Porter et al., 2000; Fu et al., 2013).

TABLE 4 Compressive properties of PCL-MPT/PEO composites.

Sample	4L-1/1	4L-2/1	4L-3/1
Compressive strength (MPa)	30.4 ± 0.8	27.0 ± 0.6	25.4 ± 0.9
Compression modulus (MPa)	15.5 ± 0.6	13.8 ± 0.5	13.0 ± 0.4

4 Conclusion

In this work, we continuously prepared four-layered PCL-MPT/PEO composites by LMCE technology, and the layer-thickness ratio for PCL-MPT layer and PCL-PEO layer was modulated by the screw speed ratio. To investigate the effect of layer-thickness ratio on the drug release behavior, four-layered PCL-MPT/PEO composites with thickness ratios of 1:1, 2:1 and 3:1 for PCL-PEO layer and PCL-MPT layer were prepared, respectively. *In vitro* release test results indicated that MPT release rate increased with decreasing the thickness of PCL-MPT layer in the initial 24 h, which could be contributed to the fact that the rate of MPT release of PCL-MPT/PEO composite was mainly determined by the diffusion of MPT in PCL-MPT layer. Further, PCL-MPT/PEO composites were sealed by epoxy resin to eliminate the edge effect on drug release. The MPT release rate of sealed samples were slower than that of unsealed samples, which could be resulted by the prolonged the release path of MPT at the edge of samples. Combining the release curves and Raman spectroscopy analysis, the release process of sealed samples could be divided into two stages, both of which were consistent with Higuchi release model. The sealed composites should possess the potential as controlled directional drug delivery system. In addition, the compression test confirmed the potential of four-layered composites as bone scaffold. This work should expand the application of LMCE technology in the preparation of multi-layered drug delivery systems.

Data availability statement

The original contributions presented in the study are included in the article/Supplementary Material, further inquiries can be directed to the corresponding authors.

Author contributions

HZ: Writing, experiment, art working CZ: experiment GL: Guiding experiments and writing RC: Guiding experiments and writing SG: Supervision. All authors contributed to the article and approved the submitted version.

Funding

This work was supported by National Natural Science Foundation of China (52103039).

Conflict of interest

The authors declare that the research was conducted in the absence of any commercial or financial relationships that could be construed as a potential conflict of interest.

Publisher's note

References

Abdul, S., and Poddar, S. S. (2004). A flexible technology for modified release of drugs: Multi layered tablets. *J. Control. Release* 97 (3), 393–405. doi:10.1016/s0168-3659(04)00186-5

Alkekhia, D., Hammond, P. T., and Shukla, A. J. A. R. o. B. E. (2020). Layer-by-Layer biomaterials for drug delivery. *Annu. Rev. Biomed. Eng.* 22 (1), 1–24. doi:10.1146/annurev-bioeng-060418-052350

Antoniou, A. I., Giofre, S., Seneci, P., Passarella, D., and Pellegrino, S. (2021). Stimulus-responsive liposomes for biomedical applications. *Drug Discov. Today* 26 (8), 1794–1824. doi:10.1016/j.drudis.2021.05.010

Birk, S. E., Boisen, A., and Nielsen, L. H. (2021). Polymeric nano- and microparticulate drug delivery systems for treatment of biofilms. *Adv. Drug Deliv. Rev.* 174, 30–52. doi:10.1016/j.addr.2021.04.005

Cerea, M., Foppoli, A., Palugan, L., Melocchi, A., Zema, L., Maroni, A., et al. (2020). Non-uniform drug distribution matrix system (NUDDMat) for zero-order release of drugs with different solubility. *Int. J. Pharm.* 581, 119217. doi:10.1016/j.ijpharm.2020.119217

Choi, D. H., and Jeong, S. H. J. J. o. P. I. (2011). Multi-layered matrix tablets with various tablet designs and release profiles. *J. Pharm. Investigation* 41 (5), 263–272. doi:10.4333/kps.2011.41.5.263

Choi, D. H., Kim, K. H., Park, J. S., Jeong, S. H., and Park, K. (2013). Evaluation of drug delivery profiles in geometric three-layered tablets with various mechanical properties, *in vitro-in vivo* drug release, and Raman imaging. *J. Control. Release* 172 (3), 763–772. doi:10.1016/j.jconrel.2013.08.301

Criado-Gonzalez, M., Fernandez-Gutierrez, M., San Roman, J., Mijangos, C., and Hernandez, R. (2019). Local and controlled release of tamoxifen from multi (layer-by-layer) alginate/chitosan complex systems. *Carbohydr. Polym.* 206, 428–434. doi:10.1016/j.carbpol.2018.11.007

Finsgar, M., Kovac, J., and Maver, U. (2021). The development and characterization of bioactive coatings for local drug delivery in orthopedic applications. *Prog. Org. Coatings* 158, 106350. doi:10.1016/j.porgcoat.2021.106350

Fu, Q., Saiz, E., Rahaman, M. N., and Tomsia, A. P. (2013). Toward strong and tough glass and ceramic scaffolds for bone repair. *Adv. Funct. Mater.* 23 (44), 5461–5476. doi:10.1002/adfm.201301121

Ghorbani, F., Nojehdehian, H., and Zamanian, A. (2016). Physicochemical and mechanical properties of freeze cast hydroxyapatite-gelatin scaffolds with dexamethasone loaded PLGA microspheres for hard tissue engineering applications. *Mater. Sci. Eng. C-Materials Biol. Appl.* 69, 208–220. doi:10.1016/j.msec.2016.06.079

Heng, P. W. S. (2018). Controlled release drug delivery systems. *Pharm. Dev. Technol.* 23 (9), 833. doi:10.1080/10837450.2018.1534376

Ji, X., Chen, D., Zheng, Y., Shen, J., Guo, S., and Harkin-Jones, E. (2019). Multilayered assembly of poly(vinylidene fluoride) and poly(methyl methacrylate) for achieving multi-shape memory effects. *Chem. Eng. J.* 362, 190–198. doi:10.1016/j.cej.2019.01.016

Karthikeyan, M., Deepa, M. K., Bassim, E., Rahna, C. S., and Raj, K. R. S. (2021). Investigation of kinetic drug release characteristics and *in vitro* evaluation of sustained-release matrix tablets of a selective COX-2 inhibitor for rheumatic diseases. *J. Pharm. Innovation* 16 (3), 551–557. doi:10.1007/s12247-020-09459-9

Laha, A., Sharma, C. S., and Majumdar, S. (2017). Sustained drug release from multi-layered sequentially crosslinked electrospun gelatin nanofiber mesh. *Mater. Sci. Eng. C-Materials Biol. Appl.* 76, 782–786. doi:10.1016/j.msec.2017.03.110

Liu, D., Zhang, H., Fontana, F., Hirvonen, J. T., and Santos, H. A. (2018). Current developments and applications of microfluidic technology toward clinical translation of nanomedicines. *Adv. Drug Deliv. Rev.* 128, 54–83. doi:10.1016/j.addr.2017.08.003

Liu, G., Zhang, C., Song, H., Pan, R., Chen, R., and Guo, S. (2022). Controlled metoprolol tartrate release from poly(ε-caprolactone)-poly(ε-caprolactone)/polyethylene oxide/metoprolol tartrate composites with alternating multi-layered structures prepared through layer-multiplying co-extrusion. *Compos. Part A Appl. Sci. Manuf.* 157, 106934. doi:10.1016/j.compositesa.2022.106934

Lu, T., and Hagen, T. J. J. o. C. R. (2020). A novel kinetic model to describe the ultra-fast triggered release of thermosensitive liposomal drug delivery systems. *J. Control. Release* 324, 669–678. doi:10.1016/j.jconrel.2020.05.047

Mazel, V., and Tchoreloff, P. (2021). Lamination of pharmaceutical tablets: Classification and influence of process parameters. *J. Pharm. Sci.* 111, 1480–1485. doi:10.1016/j.xphs.2021.10.025

Porter, B. D., Oldham, J. B., He, S. L., Zobitz, M. E., Payne, R. G., An, K. N., et al. (2000). Mechanical properties of a biodegradable bone regeneration scaffold. *J. Biomechanical Engineering-Transactions Asme* 122 (3), 286–288. doi:10.1115/1.429659

Siepmann, J., and Siepmann, F. (2008). Mathematical modeling of drug delivery. *Int. J. Pharm.* 364 (2), 328–343. doi:10.1016/j.ijpharm.2008.09.004

Wu, J., Kong, T., Yeung, K. W. K., Shum, H. C., Cheung, K. M. C., Wang, L., et al. (2013). Fabrication and characterization of monodisperse PLGA-alginate core-shell microspheres with monodisperse size and homogeneous shells for controlled drug release. *Acta Biomater.* 9 (7), 7410–7419. doi:10.1016/j.actbio.2013.03.022

Zhang, L., Xia, Q., Zhang, C., Wu, H., Liu, G., Chen, R., et al. (2022). Controlled directional drug release from poly(ε-caprolactone)/polyethylene oxide/metoprolol tartrate composites with multi-layered structures. *Compos. Part A Appl. Sci. Manuf.* 157, 106939. doi:10.1016/j.compositesa.2022.106939

Zhang, X., Xu, Y., Zhang, X., Wu, H., Shen, J., Chen, R., et al. (2019). Progress on the layer-by-layer assembly of multilayered polymer composites: Strategy, structural control and applications. *Prog. Polym. Sci.* 89, 76–107. doi:10.1016/j.progpolymsci.2018.10.002

Zheng, Y., Zeng, B., Yang, L., Shen, J., and Guo, S. (2020). Fabrication of thermoplastic polyurethane/polycaprolactone multilayered composites with confined distribution of MWCNTs for achieving tunable thermo- and electro-responsive shape-memory performances. *Industrial Eng. Chem. Res.* 59 (7), 2977–2987. doi:10.1021/acs.iecr.9b06247

frontiers | Frontiers in Bioengineering and Biotechnology

TYPE Original Research
PUBLISHED 07 July 2023
DOI 10.3389/fbioe.2023.1233398

OPEN ACCESS

EDITED BY
Qianbin Wang,
University of Massachusetts Amherst, United States

REVIEWED BY
Pengwu Xu,
Jiangnan University, China
Ruiqi Xie,
Southwest University, China

*CORRESPONDENCE
Rui Shu,
shurui@scu.edu.cn

RECEIVED 02 June 2023
ACCEPTED 28 June 2023
PUBLISHED 07 July 2023

CITATION
Yang F, Wu C, Jiang Y, Tan L and Shu R (2023), Development of an antibacterial polypropylene/polyurethane composite membrane for invisible orthodontics application. *Front. Bioeng. Biotechnol.* 11:1233398. doi: 10.3389/fbioe.2023.1233398

Development of an antibacterial polypropylene/polyurethane composite membrane for invisible orthodontics application

Feng Yang[1,2,3], Chenyi Wu[1], Yuanzhang Jiang[2,3], Lin Tan[2,3] and Rui Shu[1]*

[1]State Key Laboratory of Oral Diseases, Department of Pediatric Dentistry, West China School of Stomatology, Sichuan University, Chengdu, China, [2]State Key Laboratory of Polymer Materials Engineering, College of Biomass Science and Engineering, Sichuan University, Chengdu, China, [3]Research Center for Fiber Science and Engineering Technology, Yibin Institute of Industrial Technology, Sichuan University, Yibin, China

In virtue of the advantages, such as aesthetics, designability, convenient removal, and comfortable experience, invisible orthodontics (IO) have been widely recognized and accepted by the public. However, most of the membranes currently used for IO only meet the requirement of shape retention. Other vital functions, like antibacterial and antifouling activities, are neglected. Herein, antibacterial composite membranes (ACMs) containing polypropylene (PP), thermoplastic polyurethane (TPU) and poly (hexamethylene guanidine) hydrochloride-sodium stearate (PHMG-SS) were facilely manufactured through the hot-pressing membrane forming technology. ACMs were conferred with favorable transparency (~70% in the visible light range) and excellent antibacterial ability. Experiment results demonstrated that bactericidal rates of ACMs against *Staphylococcus aureus*, *Escherichia coli* and *Streptococcus mutans* were larger than 99.99%. Noticeably, the amount of protein adhered on the surface of ACMs was only 28.1 μg/cm^2, showing ideal antifouling performance. Collectively, the mutifunctional ACMs in the study are expected to be prominent alternatives for existing IO.

KEYWORDS

membrane, antibacterial, antibiofilm, antifouling, invisible orthodontics

1 Introduction

In recent decades, the health and whitening of teeth has received widespread attention (Sims et al., 2020). Orthodontics is becoming extensively popular as the most efficient and simplest treatment method for teeth restoration. Orthodontics can not only prevent teeth from oral problems (including periodontitis, caries, tooth loss, etc.), but also can achieve the effect of teeth whitening and improve the self-confidence of patients (Burden, 2007; Chaturvedula et al., 2021). At present, compared with traditional orthodontics, invisible orthodontics (IO) has gradually become the mainstream with its advantages of aesthetics comfort and ease of use. However, the antibacterial ability of the membrane used in traditional IO is insufficient or even missing, which makes it easy for microorganisms to accumulate, adhere and proliferate in oral environment (Schlafer et al., 2012). When wearing IO, the flow rate of saliva between IO and the dental mucosa will slow down, seriously affecting the self-cleaning of teeth and oral tissues, which will further lead to the growth of

bacteria (Kuramitsu et al., 2007; Kolenbrander et al., 2010). Therefore, the development of functional membrane with antibacterial and antifouling properties for the application of IO is of great significance for the prevention of bacterial adhesion and colonization, thereby promoting the oral health and safety during orthodontic treatment.

Among the several parameters affecting the clinical performance of IO, the membranes used for the manufacture of the IO play a crucial role (Bichu et al., 2023). According to literature reports, poly (methyl methacrylate) (PMMA), poly (ethylene terephthalate-1,4-cyclohexanedimethanol) (PETG), polypropylene (PP), thermoplastic polyurethane (TPU), polycarbonate (PC) and ethylene vinyl acetate (EVA) have been applied in IO fabrication (Gardner et al., 2003; Kwon et al., 2008; Zhang et al., 2011; Lombardo et al., 2017). However, the IO membranes prepared through conventional process usually have no antibacterial and low antifouling abilities. Therefore, various strategies have been adopted to prevent the growth and colonization of bacteria between IO and teeth, such as adding antibacterial agents, antibacterial coatings and constructing self-cleaning surfaces (Milionis et al., 2020; Zhang et al., 2020; Worreth et al., 2021). Xie et al. presented a strategy for modifying orthodontic devices, which took quaternary ammonium modified gold nanoclusters as an antibiotic reagent to prevent bacterial contamination and biofilm formation (Xie et al., 2020). Cheng reported an interpenetrating polymer network (IPN) structured antibacterial layer that was prepared on dental base materials containing quaternary ammonium salt monomers (HMDQAs), polyurethane dimethacrylate oligomers (BIHs) and functionalized SiO_2 nanoparticles, and this coating exhibited good transparency, excellent antibacterial activity and low cytotoxicity (Cheng et al., 2019). However, antibacterial coatings usually involve unstable fastness and influence on the physical properties of the substrate material, and the coating agents were often dissolved in toxic organic solvents, which were not environmentally friendly, and may further damage the surface structure of the coating substrate, and other related issues.

Polypropylene (PP) is considered an important polymer material due to its ease of processing, cheap price, high chemical resistance and good mechanical properties, which has been widely used in medical equipment, building materials, transportation and other fields (Zhao et al., 2021). As the demand for healthy life increasing, materials such as polymer membranes with antibacterial activity have attracted much attention in the medical and health fields, and their excellent antibacterial properties can alleviate or even solve the problem of infection and disease transmission (Huang et al., 2007). At present, the simplest processing method that can impart antibacterial capacity to PP is through the melt blending with antibacterial agents. Chen et al. fabricated antibacterial PP by incorporating silver nanoparticles, when the amount of silver nanoparticles reached 8wt%, 100% of *E. coli* and more than 99% of *S. aureus* were killed (Chen et al., 2020). Besides, dodecyl mercaptan functionalized silver nanoparticles were introduced into PP membrane by melt-blending, and the inhibition rates of the antibacterial PP membrane against *E. coli S. aureus* reached 100% and 84.6%, respectively (Cao et al., 2018). However, due to the non-polar nature of PP, it often faces the uneven dispersion when combined with inorganic powder, and also undergoes the weaknesses, such as poor wear resistance, low weather resistance, and difficult functionalization. Therefore, it is often compound with other polymer chips. Thermoplastic polyurethane (TPU) commonly exhibits excellent impact strength, flexibility and excellent wear resistance. It can improve the mechanical properties of the composites by blending with PP (Bakare et al., 2008). Therefore, by designing organic antibacterial PP/TPU composite membranes (ACMs) with low price and excellent processing performance, endowing them with excellent mechanical properties (such as breaking strength, tensile deformation, wear resistance, etc.), which can be applied for manufacturing invisible braces and other biomedical devices.

In present study, PP, TPU and organic PHMG-SS antibacterial agent were employed to prepare ACMs through the facile hot-pressing technology. The obtained ACMs were characterized in terms of mechanical, morphological and surface features. The results indicated that the ACMs exhibited favorable transparency, excellent antibacterial performance, protein adhesion resistance, and ideal cytotoxicity, and it is expected to be applied as the membrane substrate for IO.

2 Materials and methods

2.1 Materials

Polypropylene (PP) (S2040) was purchased from Shanghai Secco Petrochemical Co., Ltd., thermoplastic polyurethane (TPU) (Elastollan®, Mw~220000) was purchased from BASF (China) Co., Ltd., and poly (hexamethylene guanidine) hydrochloride-sodium stearate (PHMG-SS) antibacterial compound was prepared with reference to our previous literature (Zhang et al., 2021), potassium dihydrogen phosphate, sodium chloride, potassium chloride, agar powder, yeast extract powder and other reagents were from Chengdu Kelong Chemical Co., Ltd., and tryptone was from Beijing Aoboxing Biotechnology Co., Ltd.; *Staphylococcus aureus* (*S. aureus*, ATCC6538), *Escherichia coli* (*E. coli*, ATCC8739) were provided by the Functional Fiber Research Laboratory of Sichuan University, and *Streptococcus mutans* (*S. mutans*) was provided by West China Hospital of Sichuan University.

2.2 Preparation of ACMs

PP, TPU and PHMG-SS were dried for 12 h to remove moisture. PP and TPU with a total mass of 10 g (different proportions) were mixed for membrane formation through hot-pressing, and PHMG-SS was added during the membrane formation process with two ratios, including 0.5% and 1.0% relative to total mass. The parameter settings are as follows: lamination temperature ~210°C, lamination including preheating 3 min, precompression 3 min, and pressurization 5 min, exhaust ~2 times, and the applied pressure was 15 bar/cm^2. After the pressing, the mould was withdrawn, and the membranes were collected after cooling naturally at room temperature. Specifically, ACMs were denoted according to the compositions, and named as PxTy, where x, y represent the mass fraction of PP and TPU, for example, when the ratio of PP and TPU was 4:6, the amount of PHMG-SS added were 0, 0.5% and 1%, which were named P4T6, P4T6 (0.5%) and P4T6 (1%), accordingly.

2.3 Characterization of ACMs

The optical transparency of the ACMs was characterized by an UV-visible-near-infrared spectrometer (PerkinElmer 1,050, United States), and the surface wettability was measured by a contact angle goniometer (HARKE-SPCAX 1, China). The mechanical properties of ACMs were tested by a strength tester (YM06E, China). The sample width was 5 mm, the clamp distance was 10 mm, and the tensile speed was 10 mm/min. Each sample was tested five times, and the average values of breaking strength and elongation at break were recorded. The thermal stability of the ACMs was tested by thermogravimetry analysis (PerkinElmer TGA 8000, United States). The test temperature was ranging from 30°C to 800°C, and the heating rate was 10°C/min. The surface potential of the ACMs was tested by a solid/membrane surface ZETA potentiometer (Anton Paar, SurPASS2, Austria). Field emission scanning electron microscopy (SEM, SU3500, Japan) was used to characterize the surface and cross-sectional morphologies of the ACMs. Atomic Force Microscope (AFM, Dimension ICON, Germany) was used to observe the surface roughness of the ACMs, and NanoScope Analysis 1.8 was used for analysis.

2.4 Protein adsorption performance test

All membranes (1 cm × 1 cm) were pre-wetted in Phosphate Buffered Saline (PBS, pH = 7.4) buffer, and then placed in bovine serum albumin (BSA) solution at room temperature for 12 h. After being gently washed with PBS for 5 times, the membranes were placed in 1 mL of PBS and shaken at room temperature for 2 h to elute the protein adsorbed on the membranes surface. Then, the protein elution solution from each membrane was added to the 96-well plate containing the bicinchoninic acid (BCA) reagent and then left at room temperature for 30 min. The amount of adsorbed protein was determined by testing the absorbance at 562 nm by using a microplate reader (Multiskan FC, Thermo, United States). Each sample was tested five times.

2.5 Determination of minimum inhibitory concentration

The antibacterial test refers to the shaking method (Zhou et al., 2022). The bacteria were cultured in liquid culture medium at 37°C to logarithmic-phase, and the bacterial suspension was diluted to 10^5~10^6 CFU/mL with sterile PBS. Then 1, 5, and 10 mg of the ACMs were mixed with 1 mL of the diluted bacterial solution, and the blank control was the bacterial solution without ACMs. Afterwards, the mixtures were cultivated at 37°C for 12 h, and the bacteria solution were diluted to an appropriate concentration by 10-fold dilution method and spread onto the agar plates for the final colony counting.

2.6 Antibacterial kinetic test

Similar to above process, the bacteria were cultured to logarithmic-phase, then diluted to 10^5~10^6 CFU/mL with PBS, 10 mg of P4T6 (1%) membranes were added to bacterial solution for co-culture, and antibacterial tests were carried out with different contact periods (1 h, 2 h, 4 h, 8 h). 100 μL of the bacterial solution was diluted and spread onto the agar plates for the final colony counting and the number of recorded colonies was applied to calculate the antibacterial ratios.

2.7 Live and dead bacteria staining

The bacteria were cultured to logarithmic-phase, the ACMs were added to the bacterial solution for incubation at 37°C for 24 h, and the free-standing bacteria on the surface of the membrane were gently removed with PBS, and then the membranes were stored in the dark. SYTO 9 and PI were used to double-stain the membranes under dark conditions and the staining of bacteria were observed by confocal laser scanning microscope (CLSM) (Liu et al., 2022). Furthermore, the deposited bacteria after washing on the membranes were immobilized through 2.5% glutaraldehyde aqueous solution for 4 h, then dehydrated in ethanol gradient solutions (25%, 50%, 75%, 100%), and each gradient ethanol was placed for 15 min to achieve the dehydrated bacteria. Finally, the adhesion and structural of bacteria were observed by SEM.

2.8 Antibacterial stability test

In order to simulate the application environment of the human oral cavity, the ACMs were soaked in artificial saliva for different periods (6, 12 h) under 37°C, and then washed with distilled water, dried at room temperature. After that, the antibacterial effect was again investigated according to the above antibacterial test process.

2.9 Antibiofilm property (crystal violet staining)

The ACMs were completely immersed in the suspensions containing *S. aureus*, *E. coli* and *S. mutans* ($2*10^8$ CFU/mL, 1 mL) for 48 h to form biofilms on the surface. After the membranes were cleaned with PBS to remove the free-standing bacteria, 1 mL of methanol was added to fix them for 15 min in the dark. After that, the methanol was sucked off and evaporated naturally, then the ACMs were incubated with 0.1% crystal violet solution for 15 min, and the unbound crystal violet was washed away by PBS. Then, 1 mL of 95% ethanol was added to dissolve the crystal violet, and the absorbance of the dissolved crystal violet solution was measured at 490 nm using a microplate reader. Each sample was tested five times.

2.10 Cytotoxicity

According to the GB/T16886.5-2003 standard, mouse skeletal muscle cells L929 and cell counting kit-8 assay (CCK-8) were used to detect the cytotoxicity of the ACMs. Firstly, the ACMs were soaked in the DMEM medium containing 10% FBS and 1% penicillin streptomycin at 37°C for 12 h to obtain the ACMs extracts.

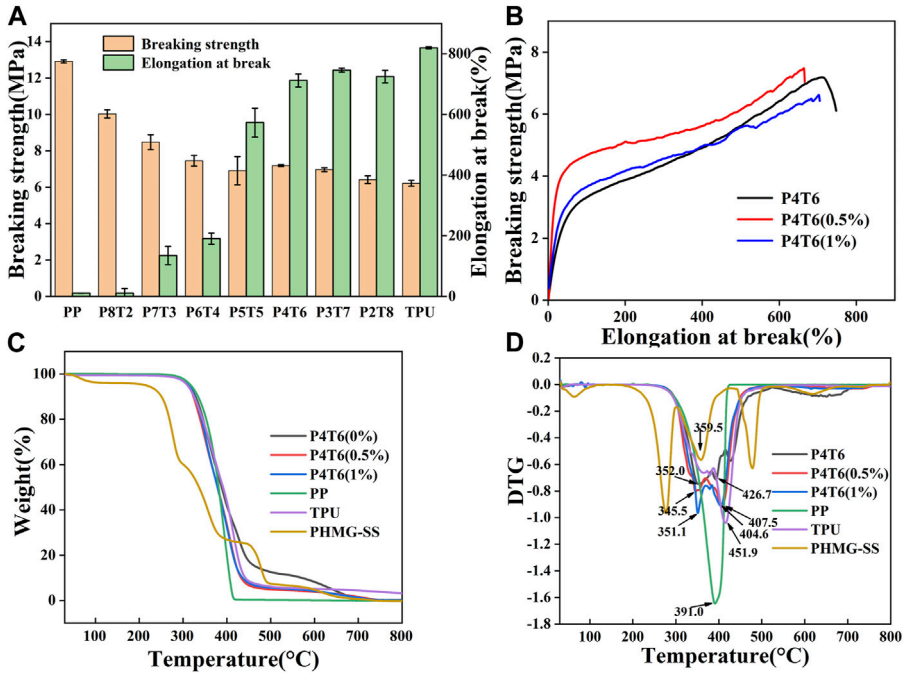

FIGURE 1
(A) Mechanical properties of composite membranes with different ratios; **(B)** Mechanical properties of the ACMs; TG **(C)** and DTG **(D)** curves of ACMs.

Simultaneously, L929 cells were seeded on a 96-well plate at 5,000 cells/well, and then cultured in a CO_2 incubator at 37°C for 12 h to allow the cells to adhere to the bottom. Then, the DMEM medium was replaced with the ACMs extracts, and the 96-well plates were placed in the incubator for further 3 days. After each day, 200 μL of CCK-8 was added into each well for incubation in the dark for 2 h. Finally, the absorbance values were recorded at a wavelength of 490 nm, and the formula for calculating cell viability was as follows:

$$\text{Cell Viability (\%)} = (A_W - A_B)/(A_N - A_B) \times 100$$

Among them, A_W, A_N, A_B are the absorbance value of the sample, negative control and blank control at wavelength of 490 nm, respectively. Each sample was tested five times.

3 Results and discussion

3.1 Characterization of ACMs

Due to the water absorption feature of TPU, if the moisture content is too high, a large number of bubbles will be generated during hot-pressing, which will negatively affect the membrane-forming process. Therefore, PP and TPU have been dried before pressing, and the contents of moisture are shown in Supplementary Table S1. The mechanical properties of composite membranes are summarized in Figure 1A, and it can be found that when P4T6 exhibits the relatively best mechanical properties in terms of tensile strain and strength which are 360.5% and 7.1 MPa, respectively. After adding PHMG-SS, the mechanical properties only slightly decrease (Figure 1B). The reason is that the addition of PHMG-SS may cause stress concentration, which lead to the decline of mechanical properties.

Figures 1C, D show the thermal analysis results of the ACMs. The maximum thermal decomposition temperature of the pure composite membrane exhibits two peaks, which are 352.0°C and 462.7°C, respectively, indicating that the membrane contains two substances (referring to PP and TPU). After the addition of PHMG-SS, both the decomposition temperature and the thermal stability decreased. The possible reason is that the SS components can accelerate the degradation of PP/TPU (Richert et al., 2019), but the ACMs still maintain good thermal stability which can satisfy the thermal sterilization process.

3.2 Surface topography analysis

From the SEM images of the surface and cross section of ACMs shown in Figure 2; Supplementary Figure S4, the surface of P4T6 is smooth, and the cross-section does not show obvious phase separation, indicating that the melt processing compatibility between TPU and PP. According to the measurement, the thickness of P4T6, P4T6 (0.5%), and P4T6 (1%) are 98.3, 98.0 and 93.9 μm, respectively, which indicate that PHMG-SS has no significant effect on film thickness. As the content of PHMG-SS increases, the surface of the membranes gradually becomes rougher, because PHMG-SS influences the interaction between PP and TPU macromolecular chains, and a small amount of unmelted PHMG-SS may also increase the surface roughness of the ACMs. This result

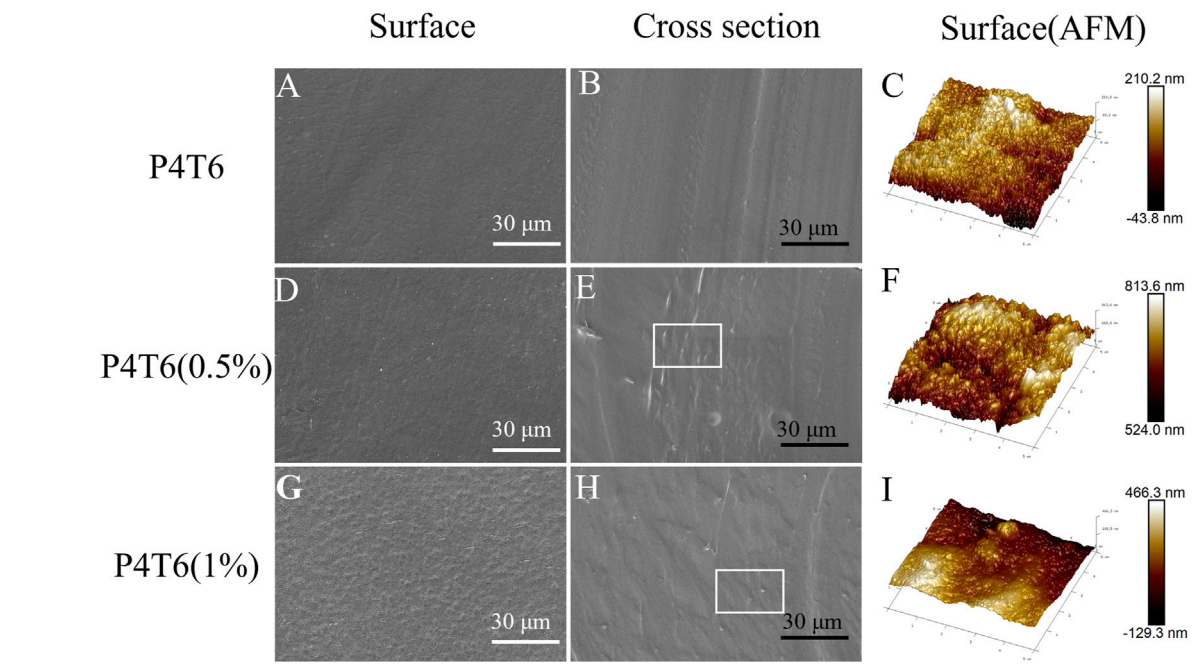

FIGURE 2
SEM images of the surfaces and cross-section of P4T6 **(A,B)**, P4T6 (0.5%) **(D,E)**, and P4T6 (1%) **(G,H)**, and AFM images of the surfaces of P4T6 **(C)**, P4T6 (0.5%) **(F)**, and P4T6 (1%) **(I)**.

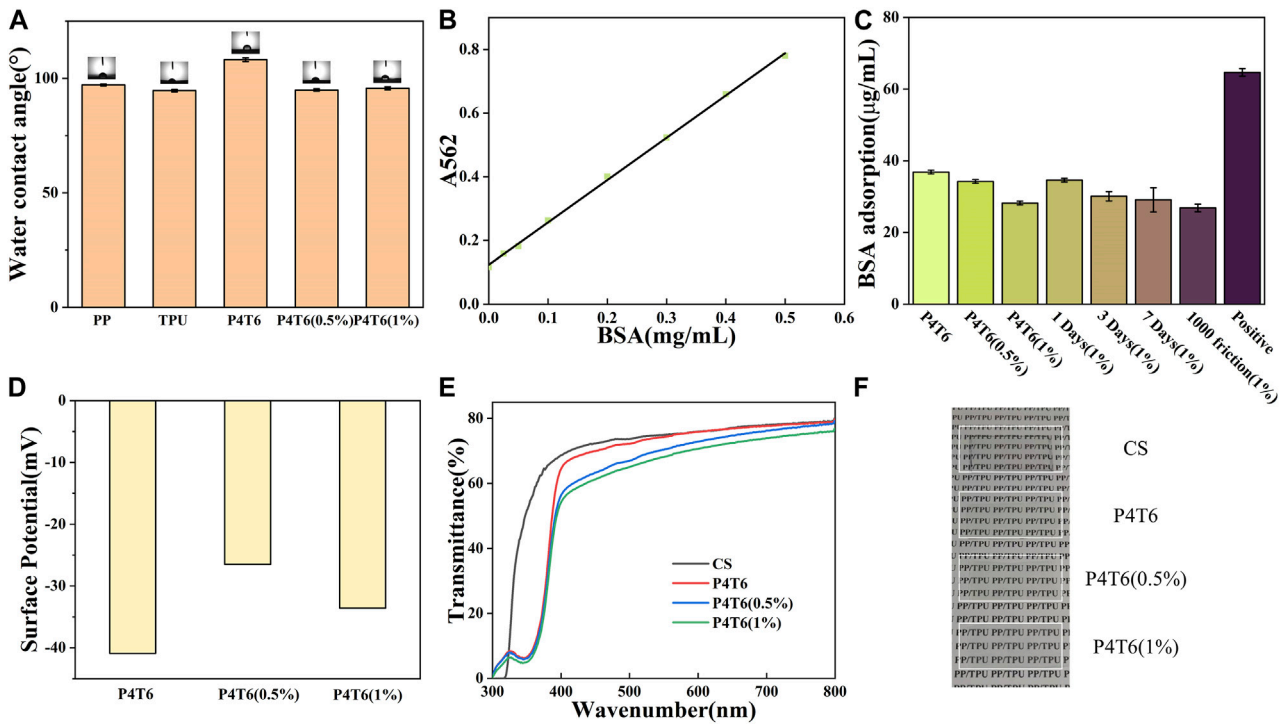

FIGURE 3
(A) Water contact angle of different membranes; **(B)** BSA standard curve; **(C)** BSA adsorption amounts; Surface potentials **(D)**, UV **(E)** and visible light **(F)** transmittance of the ACMs.

was further verified by AFM test. According to the images of AFM (Figures 2C, F, I), the Rq values of P4T6, P4T6 (0.5%), and P4T6 (1%) are 27.6, 32.1 and 40.2 nm, respectively, where Rq represents the root mean square roughness. The lower the Rq value, the smoother the surface of the membranes.

3.3 Surface wettability and antifouling performance

The water contact angle (WCA) is an important indicator of surface wettability. As shown in Figure 3A, the WCAs of pure PP and TPU are 97.1° and 94.6°, while that of P4T6 is 108.1°. Compared with pure PP and TPU, the WCA of their blender increase due to the increased roughness. When PHMG-SS was incorporated into the system, the hydrophobicity decreased, which can be attributed to the presence of hydrophilic guanidine groups in PHMG-SS. However, the WCA value (95.7°) of P4T6 (1%) is slightly higher than that (94.9°) of P4T6 (0.5%). The possible reason is the influence from the geometrical surface roughness and hydrophilic guanidine groups.

The static protein adsorption performance can reflect the antifouling performance of the ACMs. The BSA standard curve is shown in Figure 3B, and the fitting curve is $y = 1.33x + 1.23$. By substituting the absorbance of the BSA eluate of the ACMs into the standard curve, the BSA adsorption amounts of various membranes are summarized in Figure 3C. The protein adsorption capacity of the positive control (cellulose acetate membrane) is 64.6 mg/cm^2, while the protein adsorption capacities of other membranes are lower than 40 μg/cm^2, indicating good antifouling performance of the prepared membranes. The surface potentials are shown in Figure 3D, because both ACMs and protein are negatively charged, thus there exists electrostatic repulsion between them, so it shows good resistance to protein adhesion. The BSA adsorption amounts of P4T6, P4T6 (0.5%), and P4T6 (1%) are 36.8, 34.2 and 28.1 μg/cm^2, respectively. As the content of PHMG-SS increases, the antifouling performance also gradually increases, because the guanidine groups on PHMG-SS can combine with water molecules and form a hydration layer (Regev et al., 2022). Besides, the hydrophilic property of the membrane surface is also an important factor affecting protein adsorption, and the introduction of PHMG-SS leads to an increase in hydrophilicity (Yuan et al., 2021). In summary, the reduction of protein adsorption is attributed to the PHMG-SS. Considering the application scenario, friction resistance test was conducted for ACMs. As shown in Supplementary Figure S5, after 1,000 times of friction, the weight of the three samples still remains above 99%, showing excellent wear resistance. In addition, owning to long-term application in the oral environment, the antifouling properties of materials are highly susceptible to be affected. Hence, the antifouling stability of the resulting membranes was investigated. As shown in Figure 3C, there is no significant change in the amount of BSA adsorbed by the membranes after all the treatments, including the soaking in in artificial saliva for 1, 3, 7 Days, and after 1,000 times of friction, indicating their good stability.

The optical transparency of IO directly affects its aesthetics. In this study, the optical transparency of the ACMs was characterized by UV-visible spectroscopy. Considering the aesthetics of IO, we fabricated the ACMs with low roughness and good transparency, due to a relatively smoother surface can improve its transparency (Zhong et al., 2021)). Figure 3E shows the transmittance spectra of P4T6, P4T6 (0.5%) and P4T6 (1%). In fact, the transmittance curves of the three samples are very close at 300–800 nm, and reached 60% at 500 nm, which was similar to commercial sample (CS). In addition, as shown in Figure 3F, the words on the paper can be clearly seen through the ACMs. Therefore, the ACMs exhibit good optical transparency close to the commercial product, which can meet the transparency requirements of IO.

3.4 Characterization of antibacterial properties

As a common broad-spectrum antibacterial agent, PHMG shows good antibacterial properties against *S. aureus* and *E. coli* (Zheng et al., 2020). *S. mutans*, a bacterium that widely exits in environment, will secrete acidic substances to corrode tooth enamel, which is one of the main cariogenic bacteria. Therefore, the antibacterial properties of the membranes were investigated with *S. aureus*, *E. coli*, and *S. mutans*. The antibacterial results of P4T6 (0.5%) and P4T6 (1%) against the above three bacteria are shown in Figure 4A, and the MIC values of P4T6 (1%) against *S. aureus*, *E. coli* and *S. mutans* (~10^6 CFU/mL) are all less than 10 mg (reference to GB/T20944.3-2008). Both ACMs exhibit bactericidal rates of 99.999% for *E. coli* and *S. aureus*, and a bactericidal rate of 99.997% for *S. mutans*, indicating their extraordinary antibacterial properties. Overall, the antibacterial effect of ACMs against *E. coli* is better than *S. aureus* and *S. mutans*, which may be attributed to the thicker peptidoglycan layer of the cell walls of Gram-positive bacteria (*S. aureus* and *S. mutans*) than that of Gram-negative bacteria (*E. coli*), and this layer can protect them from antibacterial agents (Yang et al., 2021).

The adhesion of *S. aureus*, *E. coli* and *S. mutans* on ACMs were observed by SEM. As shown in Figure 4B, the morphologies of *S. aureus*, *E. coli* and *S. mutans* on the surface of P4T6 are intact and independent, contrastively, three types of bacterial cells on the surface of P4T6 (1%) membrane rupture, partially collapse and fuse together, indicating that P4T6 (1%) exhibits a destructive effect on the bacterial cells, which finally cause bacterial death as PHMG containing positively charged and hydrophobic alkyl groups can act on negatively charged bacterial membranes, leading to bacterial lysis and death (Jiang et al., 2018). Furthermore, with increasing the content of PHMG-SS, the number of bacteria adhered to the surface of the membrane also decrease, demonstrating that the ability of ACMs on preventing bacterial adhesion. Also, the surface electronegativity of ACMs may benefit the reduction of antibacterial adhesion owing to the electrostatic repulsion interaction.

In addition, the antibacterial activity of the ACMs was analyzed by fluorescence staining experiment. Syto 9 can label all bacteria with intact and damaged membranes, while PI can only label damaged bacterial cells with high permeability (Yang et al., 2020; Wang et al., 2023), and the introduction of PI will cause the decrease in the fluorescence intensity of Syto 9. Therefore, when dyed by the mixed solution of Syto 9 and PI, the bacteria with complete membrane structure will show green fluorescence, and the bacteria with damaged membrane structure will show red

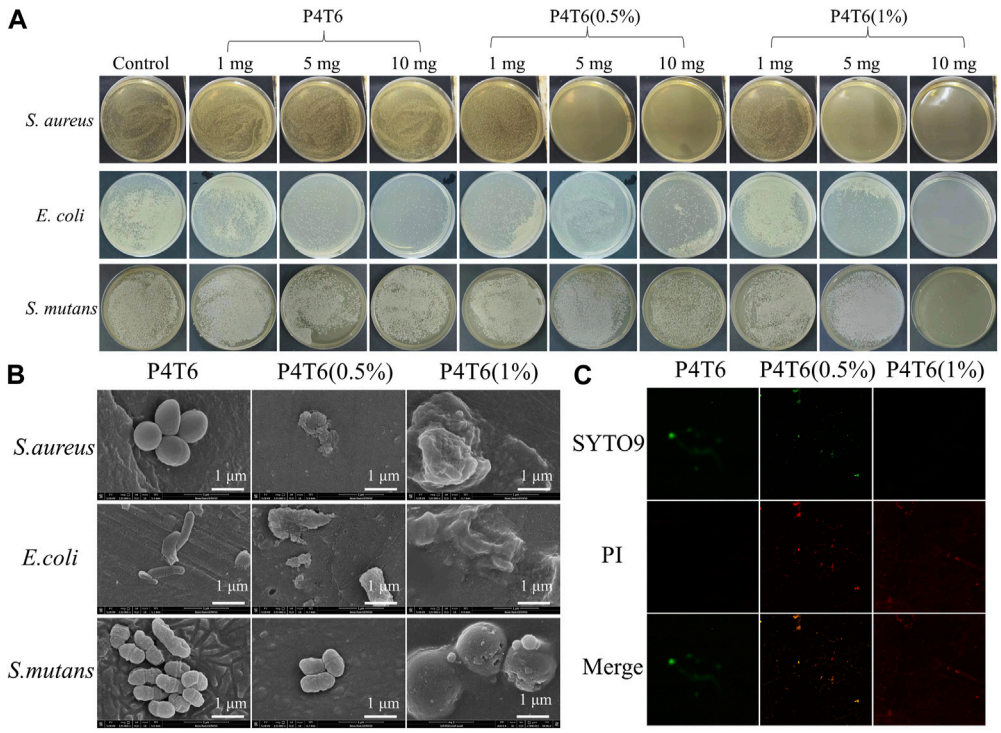

FIGURE 4
(A) Minimum inhibitory concentration of ACMs investigation; SEM **(B)** and CLSM **(C)** images of bacteria on ACMs.

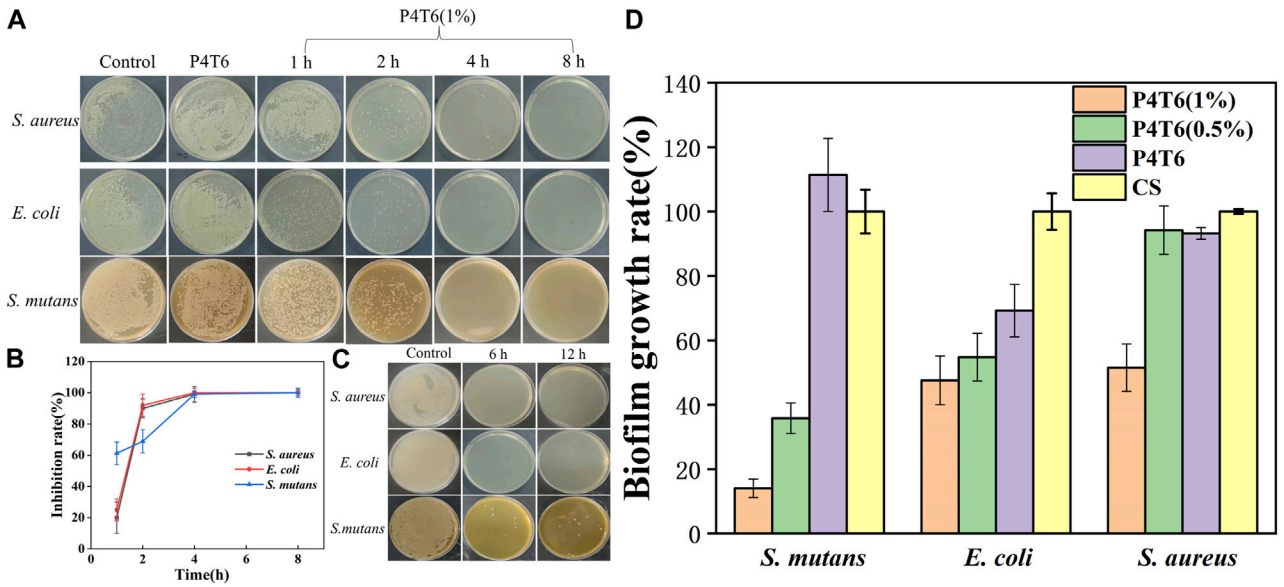

FIGURE 5
(A) Antibacterial kinetics of P4T6 (1%); **(B)** Sterilization curves with different contact periods; **(C)** Bactericidal ability after artificial saliva treatment (6, 12 h); **(D)** Biofilm growth ratios after crystal violet staining.

fluorescence. Images of bacteria after fluorescent staining are shown in Figure 4C. In the control group (P4T6), live *S. mutans* (green fluorescence) can be found presented in green color. With increasing the content of PHMG-SS, the number of live bacteria decreased and the number of dead bacteria presented in red color increased, and there is almost no green fluorescence on P4T6 (1%) membrane, which means that *S. mutans* were all killed. Meanwhile, with the introduction of PHMG-SS, the fluorescence intensity decreases,

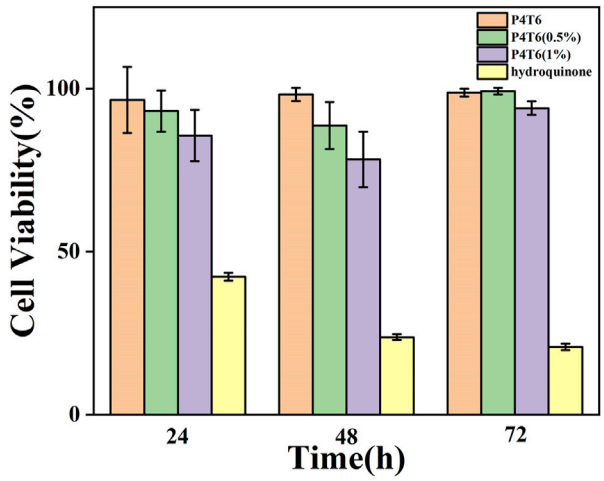

FIGURE 6
Cytotoxicity test results at P4T6, P4T6 (0.5%), P4T6 (1%) and hydroquinone (positive control).

which is consistent with the above antibacterial adhesion observed by SEM. Moreover, the photos of fluorescent stained *S. aureus* and *E. coli* treated by P4T6 (1%) are shown in Supplementary Figure S6.

3.5 Antibacterial kinetics and antibiofilm performance

The sterilization rates of ACMs against *S. aureus*, *E. coli* and *S. mutans* at different contact periods are shown in Figure 5A, P4T6 exhibits no antibacterial effect, but as expected, P4T6 (1%) membrane exhibits an antibacterial ability which is positively correlated with contact time (Figure 5B). After 4 h of contact, >99% bacterial were killed. In addition, after the treatment with artificial saliva for 6 and 12 h, the antibacterial ability of P4T6 (1%) still remains above 90% against three types of bacteria (Figure 5C), indicating the antibacterial property of P4T6 (1%) is relatively stable which may benefit the practical application needs of orthodontic patients and can ensure the oral health.

The antibiofilm performance of the ACMs are summarized in Figure 5D; Supplementary Figure S7. Taking the commercial sample as a comparison, with increasing the content of PHMG-SS, the biofilm growth ratios are significantly reduced, and the biofilm growth ratios of the three bacteria after the treatment by P4T6 (1%) (14.05% for *S. mutans*, 47.55% for *E. coli*, 51.47% for *S. aureus*) are much lower than those by the control group. On the one hand, the guanidine group on the surface of ACMs kill bacteria and inhibit the formation of biofilms; on the other hand, the hydrophobic surface also prevents the adhesion of bacteria. In brief, P4T6 (1%) can effectively inhibit the formation of biofilms on its surface.

3.6 Cytotoxicity

In addition, in order to further evaluate the safety of the ACMs on the human body, cytotoxicity experiments are conducted using the extracts of P4T6, P4T6 (0.5%), P4T6 (1%) and hydroquinone, respectively. The experimental results (Figure 6) show that the cell viability of all ACMs groups are above 80%, and the relative growth ratio of the P4T6 (1%) group is the lowest, but still higher than 75%. According to the standard toxicity class (GB/T16886.5-2003), their cytotoxicity belongs to class 1, which means ACMs meet the biosafety requirements.

4 Conclusion

In this study, ACMs with favorable transparency and excellent antibacterial performance were prepared by one-step hot-pressing membrane forming technology. The bactericidal rates against *S. aureus*, *E. coil* and *S. mutans* can reach 99.999%, 99.999%, and 99.997%, respectively. In addition, study have also revealed that ACMs had great antifouling property, which can effectively prevent the adhesion and growth of bacteria, and excellent biocompatibility (the cell viability was above 75%). Therefore, the ACMs designed and prepared in this study can be a potential alternative product to commercial IO.

Data availability statement

The original contributions presented in the study are included in the article/Supplementary Material, further inquiries can be directed to the corresponding author.

Author contributions

RS and LT proposed the idea. FY did the experiments. FY and CW analyzed the experiment data. FY draft the manuscript. LT and YJ helped review the manuscript. All authors contributed to the article and approved the submitted version.

Funding

This work was financially supported by the National Natural Science Foundation of China (52073186), Natural Science Foundation of Sichuan Province (2023NSFSC0569), and Clinical Research Project of West China School of Stomatology (21H1161, 21H0900, and 22Z0075).

Conflict of interest

The authors declare that the research was conducted in the absence of any commercial or financial relationships that could be construed as a potential conflict of interest.

Publisher's note

All claims expressed in this article are solely those of the authors and do not necessarily represent those of

their affiliated organizations, or those of the publisher, the editors and the reviewers. Any product that may be evaluated in this article, or claim that may be made by its manufacturer, is not guaranteed or endorsed by the publisher.

Supplementary material

The Supplementary Material for this article can be found online at: https://www.frontiersin.org/articles/10.3389/fbioe.2023.1233398/full#supplementary-material

References

Bakare, I. O., Pavithran, C., Okieimen, F. E., and Pillai, C. K. S. (2008). Synthesis and characterization of rubber-seed-oil-based polyurethanes. *J. Appl. Polym. Sci.* 109 (5), 3292–3301. doi:10.1002/app.28391

Bichu, Y. M., Alwafi, A., Liu, X., Andrews, J., Ludwig, B., Bichu, A. Y., et al. (2023). Advances in orthodontic clear aligner materials. *Bioact. Mater* 22, 384–403. doi:10.1016/j.bioactmat.2022.10.006

Burden, D. J. (2007). Oral health-related benefits of orthodontic treatment. *Semin. Orthod.* 13 (2), 76–80. doi:10.1053/j.sodo.2007.03.002

Cao, G., Lin, H., Kannan, P., Wang, C., Zhong, Y., Huang, Y., et al. (2018). Enhanced antibacterial and food simulant activities of silver nanoparticles/polypropylene nanocomposite films. *Langmuir* 34 (48), 14537–14545. doi:10.1021/acs.langmuir.8b03061

Chaturvedula, B. B., Muthukrishnan, A., Bhuvaraghan, A., Sandler, J., and Thiruvenkatachari, B. (2021). Dens invaginatus: A review and orthodontic implications. *Br. Dent. J.* 230 (6), 345–350. doi:10.1038/s41415-021-2721-9

Chen, J., Fan, L., Yang, C., Wang, S., Zhang, M., Xu, J., et al. (2020). Facile synthesis of Ag nanoparticles-loaded chitosan antibacterial nanocomposite and its application in polypropylene. *Int. J. Biol. Macromol.* 161, 1286–1295. doi:10.1016/j.ijbiomac.2020.07.151

Cheng, Q., Guo, X., Zou, J., Shi, X., Ding, S., Shi, Z., et al. (2019). A photo-crosslinked hybrid interpenetrating polymer network (IPN) for antibacterial coatings on denture base materials. *New J. Chem.* 43 (42), 16647–16655. doi:10.1039/c9nj02609f

Gardner, G. D., Dunn, W. J., and Taloumis, L. (2003). Wear comparison of thermoplastic materials used for orthodontic retainers. *Am. J. Orthod. Dentofac. Orthop.* 124 (3), 294–297. doi:10.1016/s0889-5406(03)00502-x

Huang, J., Murata, H., Koepsel, R. R., Russell, A. J., and Matyjaszewski, K. (2007). Antibacterial polypropylene via surface-initiated atom transfer radical polymerization. *Biomacromolecules* 8 (5), 1396–1399. doi:10.1021/bm061236j

Jiang, S., Wang, W., Ding, Y., Yu, Q., and Yao, L. (2018). Preparation and characterization of antibacterial microporous membranes fabricated by poly(AMS-co-DMAEMA) grafted polypropylene via melt-stretching method. *Chin. Chem. Lett.* 29 (3), 390–394. doi:10.1016/j.cclet.2018.01.006

Kolenbrander, P. E., Palmer, R. J., Jr., Periasamy, S., and Jakubovics, N. S. (2010). Oral multispecies biofilm development and the key role of cell-cell distance. *Nat. Rev. Microbiol.* 8 (7), 471–480. doi:10.1038/nrmicro2381

Kuramitsu, H. K., He, X., Lux, R., Anderson, M. H., and Shi, W. (2007). Interspecies interactions within oral microbial communities. *Microbiol. Mol. Biol. Rev.* 71 (4), 653–670. doi:10.1128/mmbr.00024-07

Kwon, J. S., Lee, Y. K., Lim, B. S., and Lim, Y. K. (2008). Force delivery properties of thermoplastic orthodontic materials. *Am. J. Orthod. Dentofac. Orthop.* 133 (2), 228–234. doi:10.1016/j.ajodo.2006.03.034

Liu, X., Guo, C., Zhuang, K., Chen, W., Zhang, M., Dai, Y., et al. (2022). A recyclable and light-triggered nanofibrous membrane against the emerging fungal pathogen Candida auris. *PLoS Pathog.* 18 (5), e1010534. doi:10.1371/journal.ppat.1010534

Lombardo, L., Martines, E., Mazzanti, V., Arreghini, A., Mollica, F., and Siciliani, G. (2017). Stress relaxation properties of four orthodontic aligner materials: A 24-hour *in vitro* study. *Angle Orthod.* 87 (1), 11–18. doi:10.2319/113015-813.1

Milionis, A., Tripathy, A., Donati, M., Sharma, C. S., Pan, F., Maniura-Weber, K., et al. (2020). Water-Based scalable methods for self-cleaning antibacterial ZnO-nanostructured surfaces. *Ind. Eng. Chem. Res.* 59 (32), 14323–14333. doi:10.1021/acs.iecr.0c01998

Regev, C., Jiang, Z., Kasher, R., and Miller, Y. (2022). Critical surface density of zwitterionic polymer chains affect antifouling properties. *Appl. Surf. Sci.* 596, 153652. doi:10.1016/j.apsusc.2022.153652

Richert, A., Olewnik-Kruszkowska, E., Adamska, E., and Tarach, I. (2019). Enzymatic degradation of bacteriostatic polylactide composites. *Int. Biodeterior. Biodegrad.* 142, 103–108. doi:10.1016/j.ibiod.2019.04.010

Schlafer, S., Meyer, R. L., Sutherland, D. S., and Stadler, B. (2012). Effect of osteopontin on the initial adhesion of dental bacteria. *J. Nat. Prod.* 75 (12), 2108–2112. doi:10.1021/np300514z

Sims, K. R., Jr., Maceren, J. P., Liu, Y., Rocha, G. R., Koo, H., and Benoit, D. S. W. (2020). Dual antibacterial drug-loaded nanoparticles synergistically improve treatment of Streptococcus mutans biofilms. *Acta Biomater.* 115, 418–431. doi:10.1016/j.actbio.2020.08.032

Wang, X., Wang, H., Cheng, J., Li, H., Wu, X., Zhang, D., et al. (2023). Initiative ROS generation of Cu-doped ZIF-8 for excellent antibacterial performance. *Chem. Eng. J.* 466, 143201. doi:10.1016/j.cej.2023.143201

Worreth, S., Bieger, V., Rohr, N., Astasov-Frauenhoffer, M., Töpper, T., Osmani, B., et al. (2021). Cinnamaldehyde as antimicrobial in cellulose-based dental appliances. *J. Appl. Microbiol.* 132 (2), 1018–1024. doi:10.1111/jam.15283

Xie, Y., Zhang, M., Zhang, W., Liu, X., Zheng, W., and Jiang, X. (2020). Gold nanoclusters-coated orthodontic devices can inhibit the formation of Streptococcus mutans biofilm. *ACS Biomater. Sci. Eng.* 6 (2), 1239–1246. doi:10.1021/acsbiomaterials.9b01647

Yang, T., Li, N., Wang, X., Zhai, J., Hu, B., Chen, M., et al. (2020). Dual functional AgNPs-M13 phage composite serves as antibacterial film and sensing probe for monitoring the corrosion of chromium-containing dental alloys. *Chin. Chem. Lett.* 31 (1), 145–149. doi:10.1016/j.cclet.2019.07.026

Yang, X., Wang, B., Sha, D., Liu, Y., Liu, Z., Shi, K., et al. (2021). PVA/Poly(hexamethylene guanidine)/gallic acid composite hydrogel films and their antibacterial performance. *ACS Appl. Polym. Mater* 3 (8), 3867–3877. doi:10.1021/acsapm.1c00447

Yuan, H., Xue, C., Zhu, J., Yang, Z., and Lan, M. (2021). Preparation and antifouling property of polyurethane film modified by PHMG and HA using layer-by-layer assembly. *Polym. (Basel)* 13 (6), 934. doi:10.3390/polym13060934

Zhang, J., Luo, H., Yin, X., Shi, Y., Zhang, Y., and Tan, L. (2021). Surface coating on aluminum substrate with polymeric guanidine derivative to protect jet fuel tanks from microbial contamination. *Surf. Coat. Technol.* 422, 127521. doi:10.1016/j.surfcoat.2021.127521

Zhang, M., Liu, X., Xie, Y., Zhang, Q., Zhang, W., Jiang, X., et al. (2020). Biological safe gold nanoparticle-modified dental aligner prevents the porphyromonas gingivalis biofilm formation. *ACS Omega* 5 (30), 18685–18692. doi:10.1021/acsomega.0c01532

Zhang, N., Bai, Y., Ding, X., and Zhang, Y. (2011). Preparation and characterization of thermoplastic materials for invisible orthodontics. *Dent. Mater J.* 30 (6), 954–959. doi:10.4012/dmj.2011-120

Zhao, W., Kumar Kundu, C., Li, Z., Li, X., and Zhang, Z. (2021). Flame retardant treatments for polypropylene: Strategies and recent advances. *Compos. Part A Appl. Sci. Manuf.* 145, 106382. doi:10.1016/j.compositesa.2021.106382

Zheng, L., Li, S., Luo, J., and Wang, X. (2020). Latest advances on bacterial cellulose-based antibacterial materials as wound dressings. *Front. Bioeng. Biotechnol.* 8, 593768. doi:10.3389/fbioe.2020.593768

Zhong, X., Li, R., Wang, Z., Wang, Y., Wang, W., and Yu, D. (2021). Highly flexible, transparent film prepared by upcycle of wasted jute fabrics with functional properties. *Process Saf. Environ. Prot.* 146, 718–725. doi:10.1016/j.psep.2020.12.013

Zhou, Y., Jiang, Y., Zhang, Y., and Tan, L. (2022). Improvement of antibacterial and antifouling properties of a cellulose acetate membrane by surface grafting quaternary ammonium salt. *ACS Appl. Mater. Interfaces* 14 (33), 38358–38369. doi:10.1021/acsami.2c09963

frontiers | Frontiers in Bioengineering and Biotechnology

TYPE Review
PUBLISHED 17 August 2023
DOI 10.3389/fbioe.2023.1249753

OPEN ACCESS

EDITED BY
Meng Tian,
Sichuan University, China

REVIEWED BY
Rui Zhong,
Chinese Academy of Medical Sciences and Peking Union Medical College, China
Zeng He,
Hospital of Chengdu Office of People's Government of Tibetan Autonomous Region, China

*CORRESPONDENCE
Gwenyth Newman,
g.newman@campus.unimib.it

†These authors have contributed equally to this work and share last authorship

RECEIVED 29 June 2023
ACCEPTED 07 August 2023
PUBLISHED 17 August 2023

CITATION
Newman G, Leclerc A, Arditi W, Calzuola ST, Feaugas T, Roy E, Perrault CM, Porrini C and Bechelany M (2023), Challenge of material haemocompatibility for microfluidic blood-contacting applications. *Front. Bioeng. Biotechnol.* 11:1249753. doi: 10.3389/fbioe.2023.1249753

Challenge of material haemocompatibility for microfluidic blood-contacting applications

Gwenyth Newman[1,2]*, Audrey Leclerc[3,4], William Arditi[2,5], Silvia Tea Calzuola[2,6], Thomas Feaugas[1,2], Emmanuel Roy[2], Cécile M. Perrault[2], Constance Porrini[2†] and Mikhael Bechelany[3,7†]

[1]Department of Medicine and Surgery, Università degli Studi di Milano-Bicocca, Milan, Italy, [2]Eden Tech, Paris, France, [3]Institut Européen des Membranes, IEM, UMR 5635, Univ Montpellier, ENSCM, Centre National de la Recherche Scientifique (CNRS), Place Eugène Bataillon, Montpellier, France, [4]École Nationale Supérieure des Ingénieurs en Arts Chimiques et Technologiques, Université de Toulouse, Toulouse, France, [5]Centrale Supélec, Gif-sur-Yvette, France, [6]UMR7648—LadHyx, Ecole Polytechnique, Palaiseau, France, [7]Gulf University for Science and Technology (GUST), Mubarak Al-Abdullah, Kuwait

Biological applications of microfluidics technology is beginning to expand beyond the original focus of diagnostics, analytics and organ-on-chip devices. There is a growing interest in the development of microfluidic devices for therapeutic treatments, such as extra-corporeal haemodialysis and oxygenation. However, the great potential in this area comes with great challenges. Haemocompatibility of materials has long been a concern for blood-contacting medical devices, and microfluidic devices are no exception. The small channel size, high surface area to volume ratio and dynamic conditions integral to microchannels contribute to the blood-material interactions. This review will begin by describing features of microfluidic technology with a focus on blood-contacting applications. Material haemocompatibility will be discussed in the context of interactions with blood components, from the initial absorption of plasma proteins to the activation of cells and factors, and the contribution of these interactions to the coagulation cascade and thrombogenesis. Reference will be made to the testing requirements for medical devices in contact with blood, set out by International Standards in ISO 10993-4. Finally, we will review the techniques for improving microfluidic channel haemocompatibility through material surface modifications—including bioactive and biopassive coatings—and future directions.

KEYWORDS

haemocompatibility, microfluidics, surface modification, coating, medical devices, thrombosis, biomaterials

1 Introduction

Material haemocompatibility of blood-contacting medical devices poses a major challenge to their long-term implementation (Jaffer et al., 2015). The haemocompatibilty of a material is the evaluation of the effects experienced by blood when interfaced with said material. Interactions between blood components and biomaterials contributes heavily to the process of medical device-induced thrombosis, a process which is difficult to curb once initiated (Hilal et al., 2019). The application of coatings is a crucial step in protecting the blood from material-induced damage, however their performance can vary depending on the substrate material, device dimensions and method of application (Fotovvati et al., 2019). The

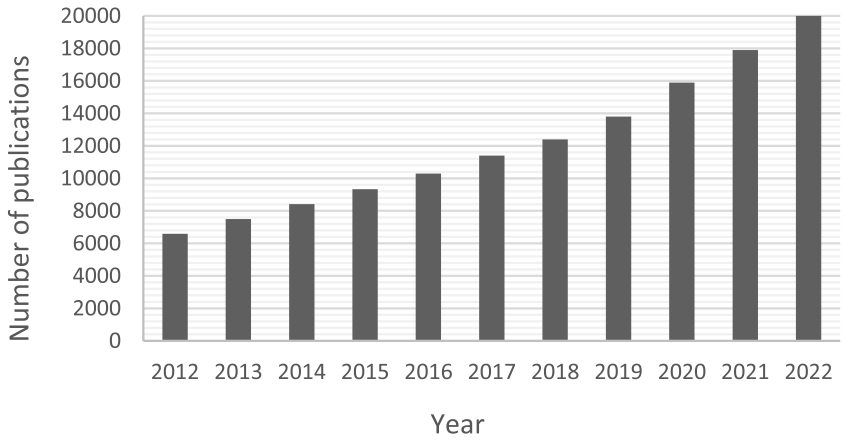

FIGURE 1
Number of publications (including patents) per year from 2012 until 2022 from searching Google Scholar with the term "microfluidics + blood –brain". The results including the word "brain" were removed to exclude irrelevant organ-on-chip papers focussing on the blood-brain barrier.

incorporation of new technologies—Such as microfluidics—In medical devices introduces new requirements and challenges to this process. Therefore, although previous reviews exist on the modes of action of haemocompatible coatings, there remains a lack of publications detailing microfluidic-specific applications. The growing interest in microfluidics for blood related applications can be observed by the increasing papers and patents published in this research area over the last decade, shown in Figure 1.

1.1 Microfluidics for blood-contacting applications

Microfluidics technology is based on the different phenomena experienced by fluid manipulated in microscale channels when compared to classical fluid dynamics. Under these geometrical constraints the surface area of the channel is much greater compared to the volume of fluid flowing through the channel, resulting in a shift in the force balance and a characteristically laminar flow profile (Beebe et al., 2002). In laminar flow regimes viscous forces dominate and particles follow precise streamlines without mixing across adjacent fluid layers, and hence mass transport processes are dominated by diffusion. The resulting system has highly predictable characteristics based on convection-diffusion equations and Fick's law, generating precise and tuneable gradients (Fan et al., 2018).

Microfluidics in the biomedical field has been dominated by diagnostics, cell and DNA analysis and organ-on-chip devices (Low et al., 2021). These platforms have the advantage of requiring less reagents, space and energy, minimising sample size. Therefore it may seem counter-intuitive for microfluidics to find use in high volume and high flow rate applications. Nonetheless, the precise control of diffusion gradients, short diffusion distances, and efficient fluidic transport in microfluidic channels have provided a window of opportunity for applications in another biomedical field: blood treatment. Research and development of microfluidic-based oxygenators and haemodialysers has grown in the past decade (Lee et al., 2008; Wei Hou et al., 2012; Potkay, 2014; Rochow et al., 2014; Kovach et al., 2015; D'Amico et al., 2017; Ausri et al., 2018; Yoon et al., 2019; Dabaghi et al., 2020; Luo et al., 2020; Gimbel et al., 2021; Lachaux et al., 2021; Santos et al., 2021).

A critical design consideration is haemocompatibility. In order to improve on current clinical devices, they must offer a less damageable experience for the blood over extended periods of time (from weeks to months). Microfluidic channels have an inherently high material surface-area to fluid volume ratio and therefore the blood-material interactions are even more pertinent. Furthermore, the small scale of microchannels means that even small thrombi can cause flow disruptions or blockage. This is therefore a key focus point to establish clinical feasibility of blood-contacting microfluidic medical devices, and a review of the literature in this field will support this research.

1.2 Common materials for microfluidic devices

Since the emergence of microfluidics for biomedical applications, the choice of device material—And related fabrication method—Has been a critical one. The most widely used materials for biomedical microfluidic devices are polymers, namely polydimethylsiloxane (PDMS) and thermoplastics, such as polystyrene (PS), polycarbonate (PC), cyclo-olefin copolymers (COC) and poly(methyl methacrylate) (PMMA). Multiple reviews have described the material properties in the context of microfluidic materials in depth (Tsao and DeVoe, 2009; Van Midwoud et al., 2012; Roy et al., 2016; Tsao, 2016; Gencturk et al., 2017; Voicu et al., 2017; Nielsen et al., 2020).

Briefly, although PDMS and thermoplastics—Particularly PS and PC, from which cell culture labware is made—Are acknowledged as biocompatible (Bélanger and Marois, 2001), this property is not evaluated in the same way as haemocompatibility (Picone et al., 2019). The definition of biocompatibility is the ability of a biomaterial to operate as intended without causing unwanted and inappropriate effects in the host (Williams, 2008). The focus of biocompatibility tests is generally in cell and tissue responses:

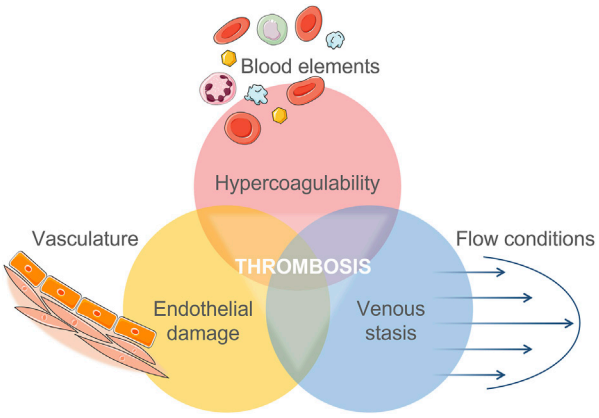

FIGURE 2
Virchow's Triad of interacting factors which contribute to an increased risk of thrombosis. Adapted from Wolberg et al. (2012) combined with Virchow's original translation.

viability, oxidative stress and enzymatic changes (Bélanger and Marois, 2001; Picone et al., 2019). A major downfall of PDMS and thermoplastics for blood-contacting applications is surface hydrophobicity (Mukhopadhyay, 2007; Tan et al., 2010; Van Midwoud et al., 2012; Gokaltun et al., 2017; Miranda et al., 2022) leading to adsorption of molecules to their surfaces and triggering coagulation pathways, as demonstrated in Figure 3. As well as absorbance concerns, PDMS is an unstable polymer with issues of unpolymerised oligomers leaching out of the material (Regehr et al., 2009; Berthier et al., 2012; Carter et al., 2020).

Gas permeability is an important consideration for blood-transporting channels to ensure blood gas levels remain between physiological limits (Beetham, 1982; Castro et al., 2022). PDMS has a high permeability to oxygen, with a coefficient of 600 Barrer (Evseev et al., 2019) or ~2000–4000 $\mu m^2 s^{-1}$ (Berthier et al., 2012), a value much greater than the other polymers. Changes in gas distributions risks bubble formation, potentially resulting in cell membrane rupture, embolism, or disruption to flow profiles (Heo et al., 2007; Berthier et al., 2012).

In this paper we will discuss material haemocompatibility, from the initial contact between blood and biomaterial, through the mounting of the coagulation cascade and formation of thrombi. The International Standards for testing haemocompatibilty will be reviewed, in the context of microfluidics and the common materials used in the fabrication of these devices. Following from this, the practical challenges of applying haemocompatible surface treatments to microchannels and the state of the research of microchannel coatings will be discussed, with brief reference to commercially-available coatings. We will finish by predicting the future direction of haemocompatible treatments for microfluidic channels.

2 Material haemocompatibility

Blood is a characteristically heterogenous fluid, comprised of plasma and cells. Cells—Red blood cells, white blood cells, and platelets—Constitute 45% of blood volume. The main role of platelets is in haemostasis, reducing loss of blood after vessel injury. Plasma is a complex mixture of water, fats, salts and a diverse proteome (Anderson and Anderson, 2002). The active nature of the blood means that interactions with foreign materials in the bloodstream can have far-reaching and detrimental effects. It is well-documented that blood coagulation is a complex, interrelated symphony of material, mechanical, and biological factors; first conceptualised by Virchow in the mid-19th century (Virchow, 1856; Kumar et al., 2010) and revisited throughout the years (Chung and Lip, 2003; Lowe, 2003; Wolberg et al., 2012). The Virchow Triad, represented in Figure 2, combines the original elements of Virchow's theory, adapted according to Wolberg et al. (2012). This section will focus on the interaction between the material and blood elements.

2.1 Protein adsorption

Immediately upon contact with a foreign material plasma proteins are adsorbed onto the surface, the initial step in the pathway which eventually results in thrombus formation (Figure 3). The composition of the protein layer depends on the biomaterial properties and individual protein concentration—Proteins with greater affinity will displace those less attracted in a process termed the Vroman effect (Simmonds et al., 2018). Mass spectrophotometry techniques have been employed to analyse these protein films and their development over time (Xia et al., 2002; Wagner and Castner, 2004). This method identifies molecules based on their mass-to-charge ratio, through ionisation of a surface by bombardment with electrodes, then collection and characterisation of these dispersed fragments. The adsorbed proteins form a monolayer of thickness 2–10 nm (Wilson et al., 2005; Jaffer et al., 2015). On adsorption to a surface, plasma proteins undergo a conformational change, allowing them to interact with coagulation factors and blood cells—Most notably platelets (Sivaraman and Latour, 2010; Zhang et al., 2017; Horbett, 2018). The interactions have been well-documented for the most prevalent, and problematic, proteins of the adsorbed layer: fibrinogen and albumin.

2.1.1 Albumin

Albumin comprises about 55% of the proteome (Anderson and Anderson, 2002), and rapidly diffuses and is one of the first proteins adsorbed to surfaces, however it soon becomes displaced by the Vroman effect, being replaced by proteins with a higher affinity for the surface (Leonard and Vroman, 1992; Wilson et al., 2005). Albumin does not contain binding sites for platelets and is generally considered to be inert, which promotes its use as an option in biopassive coatings, as will be discussed later (Hylton et al., 2005). Of these higher-affinity proteins, fibrinogen has the most significant effects.

2.1.2 Fibrinogen

Fibrinogen, a major coagulation factor in plasma, plays a critical role in material contact-initiated blood activation. Under physiological conditions, soluble fibrinogen circulates in the blood in an inactive form (Hylton et al., 2005) and only on vessel injury does it reveal its coagulation properties. Following

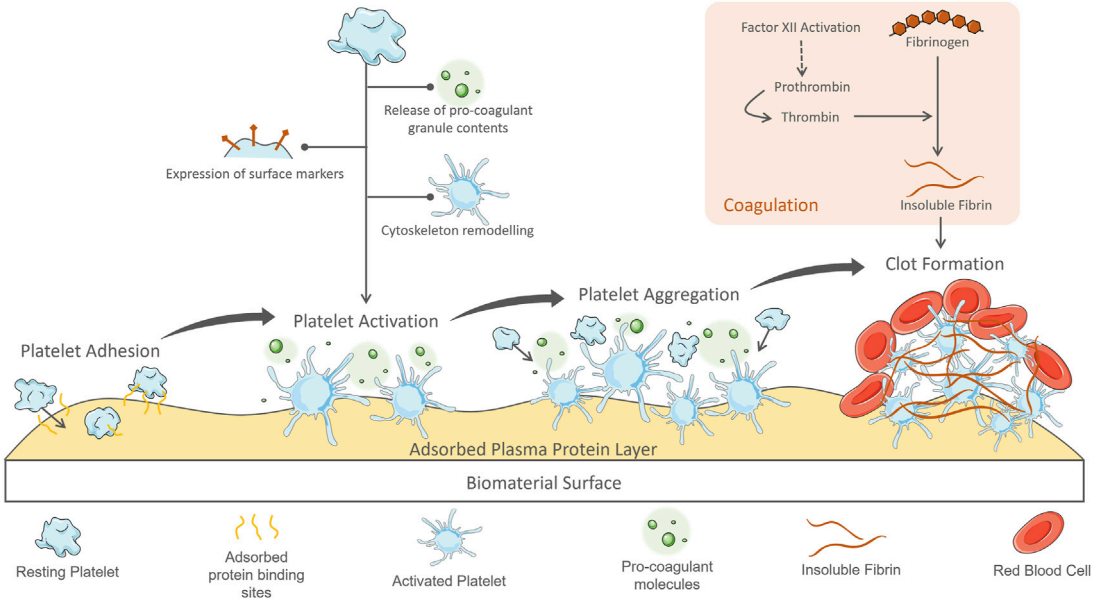

FIGURE 3
Process of plasma protein adsorption to a blood-contacting biomaterial surface and ensuing platelet activation and coagulation response leading to thrombus formation.

initiation, subsequent factors of the coagulation cascade are activated, leading to the generation of thrombin (Wolberg et al., 2012). Thrombin is an enzyme which catalyses the conversion of fibrinogen dissolved in plasma into fibrin fibres. These polymerise to form dense, branched networks which provide mechanical support to thrombi encompassing cells and clotting factors. In the physiological environment, these aggregates form at damage site to reduce bleeding and promote healing (Kalathottukaren and Kizhakkedathu, 2018). However, during material contact-initiated thrombosis this coagulation process contributes detrimentally. Firstly, fibrinogen is a surfactant (Horbett, 2018). It is a large molecule with many and varied side chains providing regions for bonding to biomaterial surfaces. This results in a rapid and wide-spread surface adsorption, only enhanced by conformational unfolding which increases available protein-surface interactions. This conformational change exposes platelet binding sites on fibrinogen which tethers circulating platelets to the surface—It is not the amount of adsorbed protein, but instead the shape change which mediates platelet adhesion (Sivaraman and Latour, 2010). Fibrinogen is over-represented in the adsorbed protein layer compared to its low concentration in plasma (5% of total protein content). Furthermore, fibrinogen can promote platelet adhesion even at very low concentrations on a material surface. Park et al. first identified the minimum adsorbed concentration of fibrinogen required for platelet activation on a glass-based substrate to be 20 ng/cm^2, or between 2%—15% surface coverage (Park et al., 1991). The maximal platelet adhesion was reported by Tsai et al. to occur with 5–10 ng/cm^2 of adsorbed fibrinogen to a polystyrene surface (Tsai et al., 1999). These values are extremely low considering that fibrinogen has been shown to adsorb from plasma to polymer surfaces between 100—200 ng/cm^2 (Horbett, 2013). Adsorption of fibrinogen can be used as a measure of material haemocompatibility.

2.2 Platelet Activation

Platelets adhered to the adsorbed protein layer on biomaterial surfaces exhibit similar pro-coagulant behaviour as during platelet plug formation following vessel injury. The extrinsic coagulation pathway initiates at sites of vessel damage where tissue factor, collagen and other proteins usually contained below the vascular endothelium have become exposed to the blood (Thomas, 2019; Neubauer and Zieger, 2021). These proteins bind and activate clotting factors and circulating platelets, triggering the coagulation cascade. In normal physiology, adhered platelets must withstand the shear forces exerted by flowing blood to maintain their position at the site of vessel damage (Kamath et al., 2001). To achieve this, platelets utilise many binding points specific for extracellular matrix proteins. In the case of biomaterial contact, the adsorbed protein layer provides these docking points for platelets, leading to a similar stubborn adhesion. Once adhered, the platelets become activated, undergoing a morphological change as occurs in the formation of the platelet plug during haemostasis (Kalathottukaren and Kizhakkedathu, 2018; Thomas, 2019). Cytoskeleton remodelling dramatically alters the platelet shape to facilitate their haemostatic functions of spreading and aggregation. Through the polymerisation of actin filaments, the resting disc shape spreads with finger-like filopodial extensions, reaching up to 420% of its resting surface area (Daimon and Gotoh, 1982; Thomas, 2019). This extended morphology catches other circulating blood cells. The resulting structure rapidly covers the surface forming aggregates structurally supported by fibrin.

Another important feature of platelets is their α-granules, dense granules and lysosomes, which are rapidly released into the extracellular space on activation (Kamath et al., 2001; Blair and Flaumenhaft, 2009; Flaumenhaft and Sharda, 2018; Thomas, 2019).

TABLE 1 Features of common polymers used in the fabrication of microfluidic devices for biomedical applications.

Polymer	Biocompatibility (according to ISO 10993 or USP class VI)	Hemocompatibility	Gas permeability to O2 (Barrer)
PDMS	Biocompatible Victor et al. (2019)	Not haemocompatible Van Oeveren et al. (2002)	600 Potkay (2014)
PS	Biocompatible Vesel et al. (2011)	Limited data available	4.75 ± 0.2 Compton et al. (2010)
PC	Biocompatible Gómez-Gras et al. (2021)	Not haemocompatible Krishnamoorthi et al. (2023)	1.68 Lai et al. (1993)
COC	Biocompatible Bernard et al. (2017)	Limited data available	0.72–2.39 Hu et al. (2006)
PMMA	Biocompatible Pituru et al. (2020), Díez-Pascual (2022)	Limited data available	0.26 Borandeh et al. (2019)

Granule contents include coagulants, adhesion proteins, growth factors, bioactive amines, immune mediators, chemokines, proinflammatory molecules and angiogenic factors (Flaumenhaft and Sharda, 2018). Activated platelet surface markers, such as P-selectin, initiate interactions with other cells and the material surface (Blair and Flaumenhaft, 2009). Adhesion proteins (such as fibrinogen and von Willebrand Factor) released from granules enhance these interactions. Released prothrombin contributes to the coagulation cascade in the formation of insoluble fibrin. High concentrations of pro-inflammatory chemokines are released from granules, propagating further platelet activation in a positive-feedback loop (Blair and Flaumenhaft, 2009; Thomas, 2019; Labarrere et al., 2020).

These responses of the blood on contact with biomaterials can be markers for testing of material haemocompatibility.

2.3 Evaluating material haemocompatibility with ISO 10993-4

The common polymers used for microfluidics in biomedical applications, their biocompatibility, haemocompatibility and gas permeability are summarised in Table 1.

Regarding the haemocompatibility of polymers, there is lack of published data to confirm their status. In addition, even when some companies develop regulated products, they do not always disclose all the tests carried out to obtain their certification. This lack of transparency reveals the need for further research in this field, in order to produce a robust evaluation of polymer haemocompatibility. Investigations into material haemocompatibility have fallen behind those for biocompatibility, perhaps revealing a complacency in medical device research to accept biocompatibility approval as sufficient for blood-contacting applications. However, specific haemocompatibility tests are required—Listed in International Standard (ISO) 10993-4.

ISO 10993 details the biological evaluation of medical devices, with part 4 dedicated to the selection of tests for interactions with blood. The types of devices discussed in this review fall into the categories of external communicating devices directly contacting circulating blood. The standard defines a haemocompatible device or material as: "*able to come into contact with blood without any appreciable clinically-significant adverse reactions*". The listed test categories check for these adverse reactions: haematology, haemolysis, platelet response, thrombosis, coagulation, and immune response. It is critical to carry out these tests under specific conditions in order to achieve relevant results.

2.3.1 Test operating conditions

According to the standard, the pre-treatment and analysis of blood samples are critical for correct interpretation of *in vitro* testing. Haematocrit, anticoagulant treatment, sample origins, sample preparation and storage, aeration, pH, temperature, contact surface area to sample volume ratio are listed as important variables to consider. Under dynamic test conditions, the list of variables extends to include flow rate, wall shear rate and pressure drop. The delay between blood sample collection and testing should be limited as much as possible (less than 4 h) in order to reduce non-physiological changes in blood properties.

These tests are simulated under *in vitro* operating conditions, replicating the blood-device interaction as closely as possible. Contact time, exposure ratio (surface area of material or device to blood volume ratio), temperature, sterility, and dynamic conditions (flow rate, shear rate, and pressure drop) should be specified to achieve this. Since the conditions in microfluidic channels are very specific, this is a crucial consideration when testing these devices.

2.3.2 Haematology

A Complete Blood Count (CBC) assesses the haematology of a blood sample. This is a standard clinical assessment carried out in medical laboratories. It returns the cell population counts, haematocrit and haemoglobin content from a blood sample via a series of tests run through a haematology analyser (Buttarello and Plebani, 2008). When compared to standard or control values this test can identify the loss of cells, either through retention on a material surface or destruction.

2.3.3 Haemolysis

Haemolysis is the rupture of the erythrocyte cell membrane. This can be biochemically-induced due to contact with the device material or changes in blood pH, temperature or nutritional factor content. Mechanical effects such as non-physiological shear stresses, turbulent flow paths or osmotic pressure differentials can induce haemolysis (Köhne, 2020). When the erythrocyte membrane ruptures haemoglobin is released into the surrounding plasma and can be detected. The level is reported as the percentage of free haemoglobin to the total haemoglobin concentration (Shin et al., 2021). Clinically, haemolysis is a concern due the loss of

erythrocytes which can result in anaemia. Excessive levels of haemoglobin can induce toxic effects on organs and may also contribute to thrombotic processes. ISO 10993-4 states that it is not possible to assign a general value for pass or fail of haemolysis assessment, the situation is more nuanced. The duration of exposure to the device, consistency of haemolysis throughout its use, and comparison to alternative treatments must be considered in risk-benefit analysis.

2.3.4 Platelet status

The attachment of platelets to the surfaces of medical devices can be quantified by various techniques. Running a platelet count before and after interaction with the device quantifies total reduction in platelets. Alternatively, direct counting of adhered cells per unit area can be completed by scanning electron microscopy of the surface. This method also allows for the cell morphology to be assessed. Platelets can be labelled prior to testing and the intensity of signal (fluorescence or radiation) can be used to determine the surface-bound cells (Weber et al., 2018; Braune et al., 2019). A similar method indirectly quantifies the platelet adhesion through apoptosis assays, such as LDH (lactate dehydrogenase). However, it must be noted that for these indirect tests platelet-rich plasma should be used rather than whole blood, otherwise the cell type is not certain.

Flow cytometry analysis is the most common method for determining the active state of a platelet population through detection of the membrane markers P-selectin (CD62) or CD42b which are expressed only when activated (Braune et al., 2019). Assays can be carried out to quantify soluble granule contents released by activated platelets, such as the amount of Platelet Factor 4 (PF4) or β-thromboglobulin (Braune et al., 2019). Alternative methods include qualitative investigation of platelet morphology with scanning electron microscopy.

2.3.5 Coagulation

The coagulation status of blood after contact with materials can be investigated through the generation of thrombin and fibrin, the major proteins of the pathway. This can be achieved by conducting ELISA for thrombin-antithrombin complex and fibrinopeptide A respectively (Braune et al., 2019).

2.3.6 Immune response

According to ISO 10993-4 the immune response takes into account the complement system and leukocyte functions (Weber et al., 2018; Braune et al., 2019). The number of leukocytes in a blood sample is reported in the CBC, and their adhesion to the material surface can be quantified by the same approach as for platelets. The active state of leukocytes is confirmed through the detection of PMN elastase, an enzyme secreted by activated leukocytes as part of the inflammatory response (Lee and Downey, 2001). The complement system activity is determined by the presence of proteins which are activated in a cascade during an immune response (Dunkelberger and Song, 2010). Since there are different pathways by which the complement system can be triggered, either protein C3a—Which is common to all pathways—Or the terminal product SC5b-9 is investigated. Their detection can determine if the complement system is active and the immune response has been mounted.

2.3.7 Limitations of haemocompatibility tests

Due to the micron scale dimensions, microfluidic channels are less tolerant to blockages and even minimal surface deposition can dramatically affect the hydrodynamic forces and therefore the device operation. There is a need to develop microfluidic-specific tests, or adapt the current ISO test recommendations to the operation of these devices, in order to ensure appropriately haemocompatible devices. The testing method outlined in this standard is only sufficient in investigating blood-biomaterial interaction and are limited in their ability to predict a device's holistic effect on the blood.

When considering erythrocytes, haemolysis is the standard ISO test to confirm material haemocompatibility, however it represents a high level of destruction to red blood cells which occurs in extreme conditions (Gusenbauer et al., 2018). The measurement does not consider the damages imposed prior to membrane rupture: pore formation, tether formation, changes to cell shape and membrane flexibility (Grigioni et al., 2005). This sublethal damage can result in early removal of cells from the bloodstream and consequently low haematocrit can result in anaemia (Olia et al., 2016). Although not included in ISO 10993-4, these effects can be identified by investigating red blood cell deformability through micropipette aspiration, viscometry or optical methods (Olia et al., 2016). The inclusion of sublethal damage tests would improve on current haemolysis detection techniques.

In extracorporeal devices, the entire blood volume will pass through before re-entering the vasculature and continuing circulation in the body. Therefore the damage to the blood will not be equivalent to the same volume of blood being repeatedly circulated through the device. However, it must also be noted that these devices are intended for long term use and therefore any deposition of blood products on the channel surfaces will contribute to a build-up over time.

The flow element part of Virchow's triad provides another avenue for design optimisation and testing through computational modelling. This is particularly interesting in microfluidic devices where the flow conditions are highly specific, predictable, and can be manipulated with close precision. The methods by which this can be achieved have been summarised in a recent review (Feaugas et al., 2023).

3 Blood-protective coatings

Coating of biomedical materials is standard practice for devices in contact with blood: from basic tubing to heart valves, stents and ECMO circuits. However, this remains a hurdle for new devices seeking clinical approval and development of haemocompatible coatings is an area of active research (Hedayati et al., 2019). This section will cover the unique challenges when coating microfluidic channels, pre-treatment of surfaces with plasma exposure, the haemocompatible coatings which have been applied to microchannels, and finally commercially-available coatings.

3.1 Challenges in coating microchannels

Typical well-established surface coating methods include dip-coating, spray-coating and physical/chemical vapour deposition

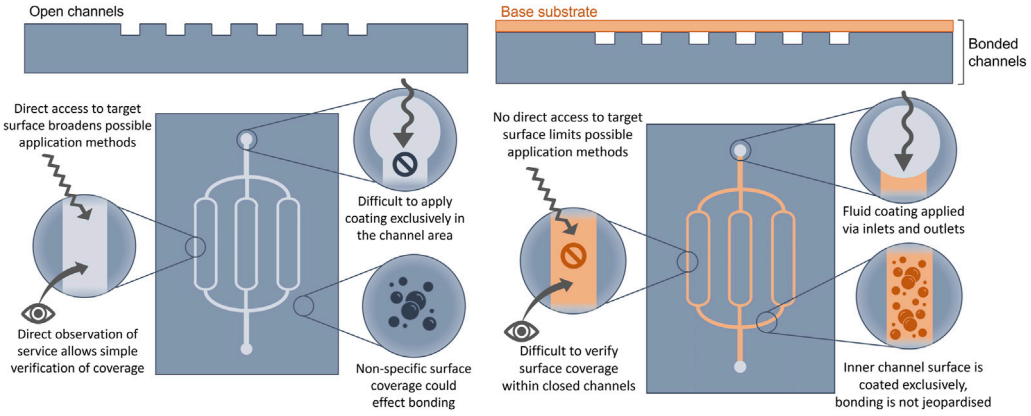

FIGURE 4
Differing coating applications to open (left side) and sealed (right side) microchannels, with practical features of each: benefits and challenges.

(Fotovvati et al., 2019). Microfluidic channels pose unique challenges which may deem these methods inappropriate, or else require substantial adaptions. Considering that most microfluidic chips are fabricated by the 'sandwich' method of creating open channels and then bonding them to a base substrate to seal (Convery and Gadegaard, 2019), coatings can be applied before or after this bonding step—With each approach bringing its own benefits and challenges, summarised in Figure 4.

Coating of open channels (prior to bonding) provides direct access to the target surface which is more likely to support the use of traditional techniques and equipment, and broadens the viable methods. Furthermore, verification of coating coverage can be carried out more reliably on an exposed surface where fluorescent and microscopy techniques can be employed. However, many traditional coating methods cover the material surface totally and non-specifically, but in microfluidics it is only the inner channel surface that requires coverage. Coatings applied to the substrate area around the channels is likely to alter bonding properties due to changed surface chemistry. Since sealing is already a major challenge further complications should be avoided (Tsao, 2016). In parallel, bonding often requires surface pre-treatment (Tsao and DeVoe, 2009; Sivakumar and Lee, 2020) which may interfere with the coating. To apply the coating only to the inner channel area requires microscale precision to deposit only on target areas.

To overcome this, microchannels may be coated after sealing. This approach, however, would require a fluidic coating method which can enter the channels via the inlets and outlets. As these devices have controlled operational conditions (such as hydraulic pressure and resistance) and the coatings often have their own requirements (such as exposure time and mode of reaction) and fluidic qualities (such as viscosity and chemical composition) it can be difficult to achieve a reliable coverage. Many surface treatment methods require direct interaction with the surface and are incompatible with a closed channel approach, such as plasma treatment (Sundriyal et al., 2020). Additionally, evaluation of coverage is difficult to achieve without opening the channels.

3.2 Plasma treatment

An initial step in polymer surface treatment is to increase the hydrophilicity. Plasma treatment (with either oxygen or air) can achieve this by degrading contaminants on the surface and introducing oxygen-containing functional groups (Lai et al., 2006). Plasma treatment directs high energy ions towards the surface, breaking organic bonds which are free to react with oxygen species in the gas to result in a negatively-charged surface with increased hydrophilicity (Yu et al., 2015; Iqbal et al., 2019; Primc, 2020; Jiang et al., 2022). However this method alone does not provide sufficient haemocompatibility (Recek et al., 2014), mainly due to hydrophobic recovery of the material or incomplete coverage of oxygen-containing groups (Mukhopadhyay, 2007; Zhou et al., 2012; Zahid et al., 2017). Therefore it is often used in combination with other haemocompatible coatings. The free radicals on the material surface after plasma treatment can be reacted with other molecules to cover the surface (Sharma et al., 2007; Shakeri et al., 2019; Özgüzar et al., 2022). Since plasma treatment is already a crucial step in microfluidic device fabrication, it positions this as a convenient and accessible option for surface pre-treatment. A plasma machine is a fundamental piece of equipment in microfabrication laboratories and its effects can be utilised simultaneously for bonding, cleaning and surface treatment purposes (Zhou et al., 2012; Sundriyal et al., 2020; Hassanpour-Tamrin et al., 2021).

3.2.1 Polymer stability

As previously mentioned, PDMS stability is a major concern when used in biomedical applications. Low molecular weight chains migrate from the interior of the PDMS to the surface by diffusion (Bodas and Khan-Malek, 2007), resulting in a return of the material's original hydrophobic properties (Lillehoj and Ho, 2010; Long et al., 2017; Trantidou et al., 2017). This can occur rapidly, from hours to days after surface modification, questioning its suitability for longer term biomedical use. It has been reported that after surface hydrophilisation by plasma treatment, the hydrophobic surface returns after 30 min to 2 h—Depending on the plasma parameters used (Stauffer, 2014; Long et al., 2017). As

already discussed, PEGylation of the PDMS surface improves its hydrophilic stability (Lai and Chung, 2020), but the polymer can be further stabilised through modification of its structure with PEG. The addition of PEG to uncured PDMS results in a stable surface hydrophilicity for up to 20 months (Gökaltun et al., 2019).

COC polymers also have stability issues. After plasma oxygenation, they are only stable for a few hours before returning to their hydrophobic character due to the reorganization of the polymer or contamination by air (Lee et al., 2015).

PC, a polymer, that is, neither strongly hydrophilic nor hydrophobic, is also one of those polymers whose hydrophilic nature can be improved by treatments, but not permanently. On the other hand, it is possible to stabilize it for at least 1 year by modifying its surface by reaction with branched polyethyleneimine as well as with a poly(ethylene-alt-maleic anhydride) anhydride and then by the hydrolysis of the anhydride groups (Jankowski and Garstecki, 2016). The PC surface thus contains a large amount of carboxyl groups.

Increasing the power intensity of the oxygen plasma treatment improves the stability time of PC and PS. Following treatment with a self-polarization voltage between 480 and 600 V, the polymers are still hydrophilic even after 6 months of storage (Larsson and Dérand, 2002).

The stability of PMMA surface hydrophilicity is improved this time by plasma treatment followed by fixation of polyvinylalcohol (PVA). In dry storage conditions, the PMMA could keep a contact angle between 10° and 20° for at least 1 month post-treatment. Tests were only conducted after 30 days so the stability beyond this period is still to be investigated (Yu et al., 2015).

3.3 Types of coating

3.3.1 Heparin

Bioactive haemocompatible coatings harness the pharmacological properties of anticoagulant molecules to intervene with thrombotic pathways. Heparin is a very common and widely used anti-coagulant drug in clinical medicine and is the gold-standard coating of medical devices, from general tubing to vascular stents and extracorporeal devices (Olsson and Larm, 1991; Biran and Pond, 2017; Jaffer and Weitz, 2019). It is a molecule based on heparan sulphate expressed on the surface of endothelial cells where it binds with anti-thrombin to counteract thrombin's platelet stimulation (Kuchinka et al., 2021). The catalytic mode of action of heparin is the same, it binds anti-thrombin at a specific active site (Casu, 1985). It is therefore crucial that this active penta-saccharide sequence found at the end of the heparin molecule is freely available for bonding with anti-thrombin. This adds further challenge to the method by which heparin can be attached to a substrate. Heparin has been immobilised on polymer surfaces by different methods, requiring initial activation or surface functionalisation which includes polymer brush spacers, protein layers or amination (Magoshi and Matsuda, 2002; Michanetzis et al., 2003; Olander et al., 2003; Chen et al., 2005; Linhardt et al., 2008; Du et al., 2011; Kolar et al., 2015; Biran and Pond, 2017; Özgüzar et al., 2022). These will be covered in the following sections.

Heparin treatment, however, does have drawbacks. The most severe is heparin-induced thrombocytopenia (HIT), a condition whereby the patient's immune cells are triggered to activate platelets on contact with heparin (Hilal et al., 2019). This has a rapid, pro-coagulant effect on the blood, forming clots which can have severe effects. HIT occurs in approximately 2.5% of patients, with a greater risk during recurring heparin treatments (Maul et al., 2016)—Such as during extra-corporeal therapies. It must also be noted that heparin operates by thinning the blood, therefore there is the associated risk of uncontrolled bleeding.

3.3.2 Albumin

Biopassive coatings aim to eliminate protein adsorption to the surface from first contact with blood, stopping initiation of coagulation cascade. They act through "stealth" techniques—Rendering the material surface inert. One such method is blocking by albumin (Sweryda-Krawiec et al., 2004; Hylton et al., 2005; Yamazoe et al., 2010; Zhang et al., 2013; Krajewski et al., 2015; Park et al., 2017). Albumin is the most abundant plasma protein and its structure does not possess platelet-binding sites. Intentional saturation of the material surface with albumin creates a protective layer which blocks binding of other proteins and the ensuing activation of coagulation pathways (Hylton et al., 2005). It can be applied as a solution through sealed channels making it well-suited for coating of microfluidic networks (Schrott et al., 2009; Convert et al., 2012; Azizipour et al., 2022). Furthermore, surface pre-treatment is not required for this method of coating (Guha Thakurta and Subramanian, 2011; Park et al., 2017). However, albumin can denature, dissolve or be displaced by fibrinogen over time, triggering the pathways described earlier (Amiji et al., 1992; Zelzer et al., 2012; Buddhadasa et al., 2018; Hasan et al., 2018). Albumin alone is considered better suited to short term applications, but can be used in combination with other strategies to improve its durability.

3.3.3 Polymer brushes

Polymer layers can be added to surfaces to limit protein adsorption, often referred to as polymer brushes because of their adhesion to the surface at one end of the chain (Buhl et al., 2020). Polymers based on the ethylene glycol unit, such as polyethylene glycol (PEG) and Poly (ethylene oxide) (PEO) (Leckband et al., 1999), are commonly bonded to surfaces as coatings to prevent non-specific protein fouling (Israelachvili, 1997; Wei et al., 2014; Fischer et al., 2018). This process is often referred to as PEGylation and has been achieved on the channels of PDMS microfluidic devices by plasma pre-treatment (Sharma et al., 2007) or integration as a copolymer additive (Gökaltun et al., 2019). PEGylated PDMS microchannels exhibit improved haemocompatibility—With reduced fibrinogen adsorption, platelet adhesion and platelet activation when compared to bare surfaces (Yeh et al., 2012; Kovach et al., 2014; Plegue et al., 2018; Gökaltun et al., 2019). This is accredited to the hydrophilic properties of PEG-based materials, whereby hydrogen bonds to the surface, creating a steric repulsion and a physical water barrier to reduce surface fouling (Chen et al., 2010; Long et al., 2017; Thon et al., 2017; Plegue et al., 2018).

Polymer brushes have also found application as spacers through immobilisation of specific molecules to the free end of the polymer chain, exposing it to the contacting blood (Wong and Ho, 2009; Wei et al., 2014; Kolar et al., 2015). PEG has reactive terminal hydroxyl groups which provide a platform for grafting of bioactive molecules or with other polymers to improve the coating properties. When used in this way, polymer brushes provide a secure grafting to the material surface and an end-point which can interact with the desired molecule. The bio-inspired polydopamine (PDAM) has gained interest for having great potential as a method of surface functionalisation by this approach (Liu et al., 2014; Madhurakkat Perikamana et al., 2015; Ding et al., 2016; Kanitthamniyom and Zhang, 2018; Ryu et al., 2018; Lee et al., 2019).

Originally inspired by the ability of mussels to securely adhere to multiple surfaces in harsh environmental conditions, PDAM-based coatings have been applied to polymers to improve their haemocompatibility (Yang et al., 2012; Ye et al., 2015; Li et al., 2020; Tan et al., 2021). Microfluidic channel surfaces have been functionalised with PDAM through self-polymerising methods in closed channels (Shen et al., 2015; Kanitthamniyom and Zhang, 2018; Khetani et al., 2020; Park et al., 2022). The current overriding application of PDAM is as a spacer to create a very secure and simple anchor point for other molecules (Luo et al., 2013), including bioactive anticoagulants, such as heparin (Leung et al., 2015).

3.3.4 Zwitterionic polymers

Zwitterionic polymers have both positive and negative charges, from cation and anion-containing groups respectively, while the overall charge is neutral (Sin et al., 2014; Blackman et al., 2019). The incentive to apply these polymers as a biocompatible surface layer comes from the similar dual-charge of the phospholipid membrane of mammalian cells (Schlenoff, 2014). Zwitterionic groups—Most commonly sulfobetaine, carboxybetaine, phosphobetaine and phosphorylcholine—Can be integrated to polymers referred to as polybetaines or polyzwitterionic materials (Chen et al., 2010; Schlenoff, 2014; Sin et al., 2014; Blackman et al., 2019). These polymers can be grafted to material surfaces and exert anti-fouling properties, increasing the surface hydrophilicity and forming a hydrated boundary layer—The same phenomenon which occurs at PEGylated surfaces (Chen et al., 2010; Schlenoff, 2014). Grafting of zwitterionic polymers on PDMS surfaces has exhibited improved haemocompatible properties: reducing fibrinogen adsorption, platelet deposition and haemolysis (Leigh et al., 2019; Kim et al., 2020; Jensen et al., 2021; McVerry et al., 2022; Mercader et al., 2022). Furthermore, grafting has been achieved on the inner surfaces of microfluidic channels (Plegue et al., 2018; Mercader et al., 2022) which suggests their applicability as a coating in microfluidic blood-contacting devices.

3.4 Commercial coatings

There are various blood-protective coatings commercially available, developed by medical device companies for use in coating of their medical devices such as cardiopulmonary bypass circuits (CPB). These commercial coatings, their mechanism of action (as biopassive, bioactive or combination), the molecular components, and the current applications are summarised in Table 2.

The coatings from Medtronic (*Balance*™ *Biosurface* & *Trillium*® *Biosurface*) differ only in the presence of heparin. They both consist of a primer layer on which is fixed polyethylene oxide (PEO) chains which deems the surface hydrophilic. The addition of sulphonate and sulphate groups contributes a negative-charge to repel platelets and also binds antithrombin to reduce thrombin production. Heparin, present only on the *Trillium*® *Biosurface* coating, increases the anti-coagulant activity (Medtronic, 2020).

The Maquet Getinge group uses three coatings: *SAFELINE*, *SOFTLINE*, and *BIOLINE*. The SAFELINE and SOFTLINE coatings do not contain heparin and their mechanism of operation is passivation. For SOFTLINE, this is particularly unique, utilising the hydrophilic polymer glycerol-poly(ethylene glycol)-ricinoleate with hydrophilic polymers. SAFELINE and BIOLINE are albumin-based, with BIOLINE being the bioactive option combining the addition of heparin (Getinge, 2018).

Xcoating™ and *PHISIO*, from the companies Terumo and LivaNova respectively, are both heparin-free coatings, of which only the hydrophilic nature prevents blood coagulation. However, they achieve this with two different polymers: PMEA poly(2-methoxyethylacrylate) for *Xcoating*™ and phosphorylcholine for PHISIO. Both of which reduce protein denaturation and platelet adhesion (Terumo, 2018; LivaNova, 2023).

3.5 Future prospects for haemocompatible coatings of microchannels

3.5.1 Endothelialisation

The future direction of haemocompatible coatings in microfluidic channels is following a biomimetic approach. One highly anticipated method is lining channels with endothelial cells. Within the body, the inner surface of the vascular network is lined with endothelial cells to form an inherently haemocompatible monolayer (Neubauer and Zieger, 2021). Vascular endothelial cells regulate blood haemostasis through multiple anticoagulant, antithrombotic and procoagulant mechanisms. The biologically-relevant dimensions of microfluidic channels places them as a potential candidate for endothelialisation (Hesh et al., 2019).

The aspiration is such that the blood will not recognise a change in environment from exiting the vessels of the body to the lined channels of the device (Hesh et al., 2019). The use of patient-derived cells to create a personalised device would reduce the risk of adverse reactions and further improve haemocompatibility. However major challenges face this approach. Since endothelial cells are very reactive to shear stress and hydrodynamic conditions the operational flow conditions must be closely controlled to avoid cellular detachment or disturbing the integrity of the monolayer (Roux et al., 2020). Furthermore, the attachment surface must be prepared for long-term cell culture (Jana, 2019). Depending on the substrate material it will require some kind of base coating to encourage cell adhesion and to support the culture. Maintenance of the culture is also an important consideration. Controlled removal and renewal of dead cells is required to ensure an operational and

TABLE 2 Commercial blood-protective coatings, their mechanism of action and the molecular components employed to achieve this, and the devices on which they are currently applied.

Company	Commercial name	Mechanism of action	Coating component	Current applications	References
Medtronic	Balance™ Biosurface	Combination	Polyethylene oxide (PEO); sulphate and sulphonate groups	CPB circuits	Teligui et al. (2014), Willers et al. (2021)
	Trillium® Biosurface	Combination	Heparin; PEO; sulphate and sulphonate groups	CPB circuits	Biran and Pond (2017), Hong and Waterhouse (2023)
Terumo	Xcoating™	Biopassive	Poly(2-methoxyethylacrylate) (PMEA)	CPB circuits, haemodialysers, catheters	Biran and Pond (2017)
Maquet Getinge group	BIOLINE	Bioactive	Heparin; albumin	CPB circuits, vascular graft	Hoshia et al. (2013), Biran and Pond (2017)
	SAFELINE	Biopassive	Albumin	CPB circuits	Preston et al. (2010), Zhang et al. (2021)
	SOFTLINE	Biopassive	Glycerol-poly(ethylene glycol)-ricinoleate	CPB circuits	Zhang et al. (2021)
LivaNova	PHISIO	Biopassive	Phosphorylcholine	CPB circuits, oxygenators	De Somer et al. (2000), Hei et al. (2023)

complete coating. The regulatory pathway to bring a cell-based coating to market will be challenging. Some characteristics of endothelium anti-coagulant activity has inspired research into new approaches for haemocompatible coatings. Although some microfluidic networks have been endothelialised (Burgess et al., 2009; Hellmann et al., 2020; Lachaux et al., 2021) significant progress is required before it is a feasible clinical option.

3.5.2 NO-releasing

Nitric Oxide (NO) is a soluble gas continuously produced and released into the blood by endothelial cells to regulate platelet activity, reducing their adhesion and aggregation to play a crucial anti-thrombotic role (Radomski et al., 1987; Emerson et al., 1999; Tousoulis et al., 2011; Porrini et al., 2020; Neubauer and Zieger, 2021). NO also modulates the inflammatory response (Kobayashi, 2010), T-cell mediated immunity (Bogdan, 2015; García-Ortiz and Serrador, 2018) and exhibits antibiotic properties (Wang et al., 2002). This response has been replicated in NO-releasing materials (Wu Y. et al., 2007b; Wu et al., 2007a; Seabra et al., 2010; Yang et al., 2015; Liu et al., 2017; Simon-Walker et al., 2017; Luo et al., 2018; Qiu et al., 2019; Sadrearhami et al., 2019; Devine et al., 2020; Lyu et al., 2020; Hosseinnejad et al., 2021; Mondal et al., 2021). Although their application to microchannels is limited so far, such coatings have been investigated for other biomedical applications, the use of polymers as base substrate means they are still relevant in the development of microfluidic devices. These approaches generally operate through the inclusion of a NO donor integrated into the coating matrix or immobilised on the material surface, the most common being S-Nitroso-N-acetylpenicillamine (SNAP) (Liu et al., 2017; Devine et al., 2020; Mondal et al., 2021), S-nitrosothiols (RSNOs) (Yang et al., 2015; Luo et al., 2018; Qiu et al., 2019; Hosseinnejad et al., 2021) or N-diazeniumdiolate precursors of NO (Wu B. et al., 2007a; Sadrearhami et al., 2019). Immobilisation can be achieved by grafting to protein spacers, as previously discussed (Liu et al., 2017). In attempts to further replicate the antithrombotic properties of the endothelium, these methods are often integrated with immobilised heparin (Wu B. et al., 2007a; Simon-Walker et al., 2017; Devine et al., 2020), which takes the place of endothelial heparan sulphate. However, the ability to control the release of NO over time is limited by the fact the molecule is highly reactive with a very short half-life. In the blood this is within the range of seconds (Weller, 2009; Fleming et al., 2017). This is also the case with the release of NO from N-diazeniumdiolate, where the half-life is only a few minutes, introducing technical difficulties with its manipulation (Jeong et al., 2018).

In an attempt to overcome this unstable release there is the alternative approach of introducing NO, instead in gaseous form. This is particularly relevant for microfluidics due to the efficient gas exchange capabilities in these devices (Thompson et al., 2020). The inclusion of NO in the sweep gas blend in oxygenators has previously gained interest in clinical settings, particularly in patients with severe respiratory conditions where there is some evidence that it improves oxygenation capabilities and reduces platelet activation (Mellgren et al., 1996; Keh et al., 1999; Skogby et al., 2003). However, more recent studies have called these results into question, revealing negligible effects or minimal improvements to blood condition after the addition of NO to the sweep gas during ECMO (Adhikari et al., 2007; Rossidis et al., 2020; Niebler et al., 2021; Fallon et al., 2022). Furthermore these therapies require further definition regarding the release flux of NO into the blood [the *in vivo* range for vascular endothelium is $0.5–4 \times 10^{-10}$ mol cm^{-2} min^{-1} (Vaughn et al., 1998)], since excessive levels can lead to detrimental effects including heart failure, blood pressure changes and neural defects (Khazan and Hdayati, 2014).

4 Discussion

Coatings are a critical part of improving haemocompatibility of blood-contacting devices. Since the emergence of polymeric microfluidic devices as new platforms for manipulating blood under predictable hydraulic conditions, the application of coatings to these devices must be considered. Until now the focus has been primarily on the mechanical experience of the blood and blood-processing functionalities, with the material interactions remaining an afterthought. Although it is true that

haemodynamic forces contribute hugely to damage experienced by blood in microfluidic networks, and the methods of protective design have been previously reviewed (Szydzik et al., 2020; Astor and Borenstein, 2022; Feaugas et al., 2023), devices will not achieve acceptable haemocompatibility without appropriate coating of microchannel surfaces. This review provides a foundational understanding of the significance of material-blood interactions in microfluidic channels and the formation of thrombi, and how coatings can improve haemocompatibility.

Since their conception, materials and fabrication of microfluidic devices have represented a major bottleneck to their commercialisation (Roy et al., 2011; Temiz et al., 2015; Nielsen et al., 2020). In the context of blood-contacting microfluidics this is even more pertinent since the most common materials—Polymers hailed for their improved fabrication qualities—Promote thrombogenic pathways. However, as noted in the lack of publications and data in Table 1, haemocompatibility is not a priority during testing with the focus being biocompatibility instead. The two characteristics are not interchangeable, they have very different parameters and requirements. It is clear that there is more research needed to verify the haemocompatibility of these polymers—Not only for microfluidics but for blood-contacting medical devices in general.

The multi-step fabrication processes of microfluidic devices require pre-treatment or surface modification steps which challenge the application or introduction of coatings. This represents a major limitation to the methods by which coatings can be applied to the microchannels, and must be considered before selecting the coating. From a fabrication perspective, it is more simple to apply the coating after sealing the microchannels in order to preserve bonding integrity. However, for this to work the coating must be fluidic and applicable through the inlet and outlet ports.

In general, haemocompatible coatings take inspiration from the endothelium. Heparin remains the gold standard for clinical blood protective coatings, positioning it as the first port-of-call for coating microfluidic channels too. However, trends in research are moving away from this coating method and towards "heparin-free" options which, as discussed, are showing promising results.

Microfluidic devices offer new platforms where diffusion gradients can be closely controlled. This has incentivised their application to blood processing medical devices, such as oxygenators or dialysers. The most common microfluidic materials are polymers, such as PDMS, which are poorly suited to this application since their surfaces promote thrombogenic processes. Furthermore, the geometry of microchannels is such that the surface area to volume ratio is shifted: there is a high contact between the flowing fluid and material walls. It is therefore critical that the surface be altered to protect the blood and improve device haemocompatibilty.

Coatings applied to blood-contacting medical devices have been shown to greatly reduce blood trauma during their use and is standard clinical practice. However, the process of coating microfluidic channels is not without challenges. The coating application method is limited by the fabrication and assembly process, or *vice versa*. In addition, the shear forces exerted by fluids on microchannel surfaces can challenge the integrity of the coating and it must be ensured to withstand the dynamic environment. Plasma cleaning is a crucial step in the fabrication of microfluidic devices, mostly in order to activate the surface for bonding but critically to remove debris or impurities. Activation of the material surface by plasma is often also the first step in the coating process by freeing functional groups for bonding with the coating molecules.

Heparin is considered the gold standard in anti-coagulant coatings, it is a bioactive molecule which is often immobilised on surfaces via polymers or protein anchors. One such protein is albumin. This readily available protein can be adsorbed rapidly to hydrophobic polymer surfaces to block unwanted adsorption of plasma proteins, however it is displaced over time. A major method of biopassive coatings is the grafting of polymers. The most common being PEG-based, hydrophilic polymers which create a hydrated layer at the surface which reduces blood-material interactions. Polymer brushes, including PDAM, can also function as spacers to attach molecules—Such as heparin—To material surfaces to render them haemocompatible. Zwitterionic polymer coatings mimic the dual-charge phenomenon of the cell membrane to repel protein and cells from surfaces.

The ideal coating would of course be the endothelial layer itself. Some progress has been made to coat networks of microchannels with cells but further research is required to support this approach in clinical devices of the future. Recently, haemocompatible coatings have employed other biomimetic approaches which replicate the activity of the endothelium, one focus being NO-releasing coatings. It is clear that future haemocompatible coating developments will integrate protective features of the natural endothelium in order to provide a truly biomimetic, inert surface for interaction with blood.

The evolution of microfluidics technology towards high volume blood processing involves new considerations and challenges to achieve surface haemocompatibility.

Author contributions

GN conceived and wrote the manuscript. AL contributed in writing the manuscript. WA, TF, SC, and ER contributed in reviewing the manuscript. CP, WA, CMP, and MB reviewed and structured the manuscript, and managed the project. All authors contributed to the article and approved the submitted version.

Conflict of interest

Authors GN, WA, SC, TF, ER, CMP, and CP were employed by the company Eden Tech.

The remaining authors declare that the research was conducted in the absence of any commercial or financial relationships that could be construed as a potential conflict of interest.

Publisher's note

References

Adhikari, N. K. J., Burns, K. E. A., Friedrich, J. O., Granton, J. T., Cook, D. J., and Meade, M. O. (2007). Effect of nitric oxide on oxygenation and mortality in acute lung injury: systematic review and meta-analysis. *Br. Med. J.* 334, 779–782. doi:10.1136/bmj.39139.716794.55

Amiji, M., Park, H., and Park, K. (1992). Study on the prevention of surface-induced platelet activation by albumin coating. *J. Biomater. Sci. Polym. Ed.* 3, 375–388. doi:10.1163/156856292x00196

Anderson, N. L., and Anderson, N. G. (2002). The human plasma proteome: history, character, and diagnostic prospects. *Mol. Cell. Proteomics* 1, 845–867. doi:10.1074/mcp.R200007-MCP200

Astor, T. L., and Borenstein, J. T. (2022). The microfluidic artificial lung: mimicking nature's blood path design to solve the biocompatibility paradox. *Artif. Organs* 46, 1227–1239. doi:10.1111/aor.14266

Ausri, I. R., Feygin, E. M., Cheng, C. Q., Wang, Y., Lin, Z. Y. W., and Tang, X. S. (2018). A highly efficient and antifouling microfluidic platform for portable hemodialysis devices. *MRS Commun.* 8, 474–479. doi:10.1557/mrc.2018.43

Azizipour, N., Avazpour, R., Sawan, M., Rosenzweig, D. H., and Ajji, A. (2022). Uniformity of spheroids-on-a-chip by surface treatment of PDMS microfluidic platforms. *Sensors Diagnostics* 1, 750–764. doi:10.1039/d2sd00004k

Beebe, D. J., Mensing, G. A., and Walker, G. M. (2002). Physics and applications of microfluidics in biology. *Annu. Rev. Biomed. Eng.* 4, 261–286. doi:10.1146/annurev.bioeng.4.112601.125916

Beetham, R. (1982). A review of blood pH and blood-gas analysis. *Ann. Clin. Biochem.* 19, 198–213. doi:10.1177/000456328201900402

Bélanger, M. C., and Marois, Y. (2001). Hemocompatibility, biocompatibility, inflammatory and *in vivo* studies of primary reference materials low-density polyethylene and polydimethylsiloxane: a review. *J. Biomed. Mat. Res.* 58, 467–477. doi:10.1002/jbm.1043

Bernard, M., Jubeli, E., Bakar, J., Tortolano, L., Saunier, J., and Yagoubi, N. (2017). Biocompatibility assessment of cyclic olefin copolymers: impact of two additives on cytotoxicity, oxidative stress, inflammatory reactions, and hemocompatibility. *J. Biomed. Mat. Res. - Part A* 105, 3333–3349. doi:10.1002/jbm.a.36199

Berthier, E., Young, E. W. K., and Beebe, D. (2012). Engineers are from PDMS-land, biologists are from polystyrenia. *Lab. Chip* 12, 1224–1237. doi:10.1039/c2lc20982a

Biran, R., and Pond, D. (2017). Heparin coatings for improving blood compatibility of medical devices. *Adv. Drug Deliv. Rev.* 112, 12–23. doi:10.1016/j.addr.2016.12.002

Blackman, L. D., Gunatillake, P. A., Cass, P., and Locock, K. E. S. (2019). An introduction to zwitterionic polymer behavior and applications in solution and at surfaces. *Chem. Soc. Rev.* 48, 757–770. doi:10.1039/c8cs00508g

Blair, P., and Flaumenhaft, R. (2009). Platelet α-granules: basic biology and clinical correlates. *Blood Rev.* 23, 177–189. doi:10.1016/j.blre.2009.04.001

Bodas, D., and Khan-Malek, C. (2007). Hydrophilization and hydrophobic recovery of PDMS by oxygen plasma and chemical treatment-An SEM investigation. *Sensors Actuators, B Chem.* 123, 368–373. doi:10.1016/j.snb.2006.08.037

Bogdan, C. (2015). Nitric oxide synthase in innate and adaptive immunity: an update. *Trends Immunol.* 36, 161–178. doi:10.1016/j.it.2015.01.003

Borandeh, S., Abdolmaleki, A., Zamani Nekuabadi, S., and Sadeghi, M. (2019). Methoxy poly(ethylene glycol) methacrylate-TiO2/poly(methyl methacrylate) nanocomposite: an efficient membrane for gas separation. *Polym. Technol. Mat.* 58, 789–802. doi:10.1080/03602559.2018.1520255

Braune, S., Latour, R. A., Reinthaler, M., Landmesser, U., Lendlein, A., and Jung, F. (2019). *In vitro* thrombogenicity testing of biomaterials. *Adv. Healthc. Mater* 8, 1900527. doi:10.1002/adhm.201900527

Buddhadasa, M., Lerouge, S., and Girard-Lauriault, P. L. (2018). Plasma polymer films to regulate fibrinogen adsorption: effect of pressure and competition with human serum albumin. *Plasma process. Polym.* 15, 1800040. doi:10.1002/ppap.201800040

Buhl, K. B., Agergaard, A. H., Lillethorup, M., Nikolajsen, J. P., Pedersen, S. U., and Daasbjerg, K. (2020). Polymer brush coating and adhesion technology at scale. *Polym. (Basel)* 12, 1475. doi:10.3390/polym12071475

Burgess, K. A., Hu, H. H., Wagner, W. R., and Federspiel, W. J. (2009). Towards microfabricated biohybrid artificial lung modules for chronic respiratory support. *Biomed. Microdevices* 11, 117–127. doi:10.1007/s10544-008-9215-2

Buttarello, M., and Plebani, M. (2008). Automated blood cell counts: state of the art. *Am. J. Clin. Pathol.* 130, 104–116. doi:10.1309/EK3C7CTDKNVPXVTN

Carter, S.-S. D., Atif, A.-R., Kadekar, S., Lanekoff, I., Engqvist, H., Varghese, O. P., et al. (2020). PDMS leaching and its implications for on-chip studies focusing on bone regeneration applications. *Organs-on-a-Chip* 2, 100004. doi:10.1016/j.ooc.2020.100004

Castro, D., Patil, S. M., and Keenaghan, M. (2022). *Arterial blood gas*. Treasure Island, FL: StatPearls Publishing.

Casu, B. (1985). Structure and biological activity of heparin. *Adv. Carbohydr. Chem. Biochem.* 43, 51–134. doi:10.1016/S0065-2318(08)60067-0

Chen, H., Chen, Y., Sheardown, H., and Brook, M. A. (2005). Immobilization of heparin on a silicone surface through a heterobifunctional PEG spacer. *Biomaterials* 26, 7418–7424. doi:10.1016/j.biomaterials.2005.05.053

Chen, S., Li, L., Zhao, C., and Zheng, J. (2010). Surface hydration: principles and applications toward low-fouling/nonfouling biomaterials. *Polym. Guildf.* 51, 5283–5293. doi:10.1016/j.polymer.2010.08.022

Chung, I., and Lip, G. Y. H. (2003). Virchow's triad revisited: blood constituents. *Pathophysiol. Haemost. Thromb.* 33, 449–454. doi:10.1159/000083844

Compton, O. C., Kim, S., Pierre, C., Torkelson, J. M., and Nguyen, S. T. (2010). Crumpled graphene nanosheets as highly effective barrier property enhancers. *Adv. Mat.* 22, 4759–4763. doi:10.1002/adma.201000960

Convert, L., Chabot, V., Zermatten, P. J., Hamel, R., Cloarec, J. P., Lecomte, R., et al. (2012). Passivation of KMPR microfluidic channels with bovine serum albumin (BSA) for improved hemocompatibility characterized with metal-clad waveguides. *Sensors Actuators, B Chem.* 173, 447–454. doi:10.1016/j.snb.2012.07.061

Convery, N., and Gadegaard, N. (2019). 30 Years of microfluidics. *Micro Nano Eng.* 2, 76–91. doi:10.1016/j.mne.2019.01.003

Dabaghi, M., Saraei, N., Fusch, G., Rochow, N., Brash, J. L., Fusch, C., et al. (2020). Microfluidic blood oxygenators with integrated hollow chambers for enhanced air exchange from all four sides. *J. Memb. Sci.* 596, 117741. doi:10.1016/j.memsci.2019.117741

Daimon, T., and Gotoh, Y. (1982). Cytochemical evidence of the origin of the dense tubular system in the mouse platelet. *Histochemistry* 76, 189–196. doi:10.1007/bf00501921

D'Amico, L., Ajami, N. J., Adachi, J. A., Gascoyne, P. R. C., and Petrosino, J. F. (2017). Isolation and concentration of bacteria from blood using microfluidic membraneless dialysis and dielectrophoresis. *Lab. Chip* 17, 1340–1348. doi:10.1039/c6lc01277a

De Somer, F., Ëois, K. F., Van Oeveren, W., Poelaert, J., De Wolf, D., Ebels, T., et al. (2000). Phosphorylcholine coating of extracorporeal circuits provides natural protection against blood activation by the material surface. *Eur. J. Cardiothorac. Surg.* 18, 602–606. doi:10.1016/s1010-7940(00)00508-x

Devine, R., Goudie, M. J., Singha, P., Schmiedt, C., Douglass, M., Brisbois, E. J., et al. (2020). Mimicking the endothelium: dual action heparinized nitric oxide releasing surface. *ACS Appl. Mat. Interfaces* 12, 20158–20171. doi:10.1021/acsami.9b22277

Díez-Pascual, A. M. (2022). PMMA-based nanocomposites for odontology applications: a state-of-the-art. *Int. J. Mol. Sci.* 23, 10288. doi:10.3390/ijms231810288

Ding, Y. H., Floren, M., and Tan, W. (2016). Mussel-inspired polydopamine for bio-surface functionalization. *Biosurface Biotribology* 2, 121–136. doi:10.1016/j.bsbt.2016.11.001

Du, Y. J., Berry, L. R., and Chan, A. K. C. (2011). Chemical-physical characterization of polyurethane catheters modified with a novel antithrombin-heparin covalent complex. *J. Biomater. Sci. Polym. Ed.* 22, 2277–2294. doi:10.1163/092050610X538227

Dunkelberger, J. R., and Song, W. C. (2010). Complement and its role in innate and adaptive immune responses. *Cell Res.* 20, 34–50. doi:10.1038/cr.2009.139

Emerson, M., Momi, S., Paul, W., Alberti, P. F., Page, C., and Gresele, P. (1999). Endogenous nitric oxide acts as a natural antithrombotic agent *in vivo* by inhibiting platelet aggregation in the pulmonary vasculature. *Thromb. Haemost.* 81, 961–966. doi:10.1055/s-0037-1614607

Fallon, B. P., Lautner-Csorba, O., Thompson, A. J., Lautner, G., Kayden, A., Johnson, M. D., et al. (2022). A pumpless artificial lung without systemic anticoagulation: the Nitric Oxide Surface Anticoagulation system. *J. Pediatr. Surg.* 57, 26–33. doi:10.1016/j.jpedsurg.2021.09.015

Fan, J., Li, S., Wu, Z., and Chen, Z. (2018). "Diffusion and mixing in microfluidic devices," in *Microfluidics for pharmaceutical applications* (Elsevier Inc). doi:10.1016/B978-0-12-812659-2.00003-X

Feaugas, T., Newman, G., Calzuola, S. T., Domingues, A., Arditi, W., Porrini, C., et al. (2023). Design of artificial vascular devices: hemodynamic evaluation of shear-induced thrombogenicity. *Front. Mech. Eng.* 9, 1060580. doi:10.3389/fmech.2023.1060580

Fischer, M., Maitz, M. F., and Werner, C. (2018). "7-Coatings for biomaterials to improve hemocompatibility," in *Hemocompatibility of biomaterials for clinical applications* (Elsevier Ltd). doi:10.1016/B978-0-08-100497-5.00007-0

Flaumenhaft, R., and Sharda, A. (2018). The life cycle of platelet granules. *F1000Research* 7, 236. doi:10.12688/f1000research.13283.1

Fleming, G., Aveyard, J., Fothergill, J. L., McBride, F., Raval, R., and D'Sa, R. A. (2017). Nitric oxide releasing polymeric coatings for the prevention of biofilm formation. *Polym. (Basel)* 9, 601. doi:10.3390/polym9110601

Fotovvati, B., Namdari, N., and Dehghanghadikolaei, A. (2019). On coating techniques for surface protection: a review. *J. Manuf. Mat. Process.* 3, 28. doi:10.3390/jmmp3010028

García-Ortiz, A., and Serrador, J. M. (2018). Nitric oxide signaling in T cell-mediated immunity. *Trends Mol. Med.* 24, 412–427. doi:10.1016/j.molmed.2018.02.002

Gencturk, E., Mutlu, S., and Ulgen, K. O. (2017). Advances in microfluidic devices made from thermoplastics used in cell biology and analyses. *Biomicrofluidics* 11, 051502. doi:10.1063/1.4998604

Getinge (2018). Getinge Maquet. Available at: https://www.getinge.com/int/ (Accessed June 26, 2023).

Gimbel, A. A., Hsiao, J. C., Kim, E. S., Lewis, D. J., Risoleo, T. F., Urban, J. N., et al. (2021). A high gas transfer efficiency microfluidic oxygenator for extracorporeal respiratory assist applications in critical care medicine. *Artif. Organs* 45, E247–E264. doi:10.1111/aor.13935

Gökaltun, A., Kang, Y. B., Abraham)Yarmush, M. L., Usta, O. B., and Asatekin, A. (2019). Simple surface modification of poly(dimethylsiloxane) via surface segregating smart polymers for biomicrofluidics. *Sci. Rep.* 9, 7377. doi:10.1038/s41598-019-43625-5

Gokaltun, A., Yarmush, M. L., Asatekin, A., and Usta, O. B. (2017). Recent advances in nonbiofouling PDMS surface modification strategies applicable to microfluidic technology. *Technol. Singap. World Sci.* 5, 1–12. doi:10.1142/s2339547817300013

Gómez-Gras, G., Abad, M. D., and Pérez, M. A. (2021). Mechanical performance of 3D-printed biocompatible polycarbonate for biomechanical applications. *Polym. (Basel)* 13, 3669. doi:10.3390/polym13213669

Grigioni, M., Morbiducci, U., D'Avenio, G., Di Benedetto, G., and Del Gaudio, C. (2005). A novel formulation for blood trauma prediction by a modified power-law mathematical model. *Biomech. Model. Mechanobiol.* 4, 249–260. doi:10.1007/s10237-005-0005-y

Guha Thakurta, S., and Subramanian, A. (2011). Evaluation of *in situ* albumin binding surfaces: a study of protein adsorption and platelet adhesion. *J. Mat. Sci. Mat. Med.* 22, 137–149. doi:10.1007/s10856-010-4169-3

Gusenbauer, M., Tóthová, R., Mazza, G., Brandl, M., Schrefl, T., Jančigová, I., et al. (2018). Cell damage index as computational indicator for blood cell activation and damage. *Artif. Organs* 42, 746–755. doi:10.1111/aor.13111

Hasan, A., Waibhaw, G., and Pandey, L. M. (2018). Conformational and organizational insights into serum proteins during competitive adsorption on self-assembled monolayers. *Langmuir* 34, 8178–8194. doi:10.1021/acs.langmuir.8b01110

Hassanpour-Tamrin, S., Sanati-Nezhad, A., and Sen, A. (2021). A simple and low-cost approach for irreversible bonding of polymethylmethacrylate and polydimethylsiloxane at room temperature for high-pressure hybrid microfluidics. *Sci. Rep.* 11, 4821. doi:10.1038/s41598-021-83011-8

Hedayati, M., Neufeld, M. J., Reynolds, M. M., and Kipper, M. J. (2019). The quest for blood-compatible materials: recent advances and future technologies. *Mat. Sci. Eng. R. Rep.* 138, 118–152. doi:10.1016/j.mser.2019.06.002

Hei, F., Guan, Y., and Yu, K. (2023). *Extracorporeal life support*. Singapore: Springer Nature.

Hellmann, A., Klein, S., Hesselmann, F., Djeljadini, S., Schmitz-Rode, T., Jockenhoevel, S., et al. (2020). EndOxy: mid-term stability and shear stress resistance of endothelial cells on PDMS gas exchange membranes. *Artif. Organs* 44, E419–E433. doi:10.1111/aor.13712

Heo, Y. S., Cabrera, L. M., Song, J. W., Futai, N., Tung, Y. C., Smith, G. D., et al. (2007). Characterization and resolution of evaporation-mediated osmolality shifts that constrain microfluidic cell culture in poly(dimethylsiloxane) devices. *Anal. Chem.* 79, 1126–1134. doi:10.1021/ac061990v

Hesh, C. A., Qiu, Y., and Lam, W. A. (2019). Vascularized microfluidics and the blood–endothelium interface. *Nature* 388, 18–547. doi:10.3390/mi11010018

Hilal, T., Mudd, J., and DeLoughery, T. G. (2019). Hemostatic complications associated with ventricular assist devices. *Res. Pract. Thromb. Haemost.* 3, 589–598. doi:10.1002/rth2.12226

Hong, J. K., and Waterhouse, A. (2023). Bioinspired approaches to engineer antithrombogenic medical devices for vascular intervention. *Arterioscler. Thromb. Vasc. Biol.* 43, 797–812. doi:10.1161/ATVBAHA.122.318238

Horbett, T. A. (2013). *Adsorbed proteins on biomaterials*. Third Ed. Elsevier. doi:10.1016/B978-0-08-087780-8.00036-X

Horbett, T. A. (2018). Fibrinogen adsorption to biomaterials. *J. Biomed. Mat. Res.* 106, 2777–2788. doi:10.1002/jbm.a.36460

Hoshia, R. A., Litha, R. V., Jena, M. C., Allen, J. B., Lapidosa, K. A., and Ameer, G. (2013). The blood and vascular cell compatibility of heparin-modified ePTFE vascular grafts. *Biomaterials* 34, 30–41. doi:10.1016/j.biomaterials.2012.09.046

Hosseinnejad, A., Fischer, T., Jain, P., Bleilevens, C., Jakob, F., Schwaneberg, U., et al. (2021). Enzyme mimetic microgel coating for endogenous nitric oxide mediated inhibition of platelet activation. *J. Colloid Interface Sci.* 601, 604–616. doi:10.1016/j.jcis.2021.05.143

Hu, C. C., Lee, K. R., Ruaan, R. C., Jean, Y. C., and Lai, J. Y. (2006). Gas separation properties in cyclic olefin copolymer membrane studied by positron annihilation, sorption, and gas permeation. *J. Memb. Sci.* 274, 192–199. doi:10.1016/j.memsci.2005.05.034

Hylton, D. M., Shalaby, S. W., and Latour, R. A. (2005). Direct correlation between adsorption-induced changes in protein structure and platelet adhesion. *J. Biomed. Mat. Res. - Part A* 73, 349–358. doi:10.1002/jbm.a.30295

Iqbal, M., Dinh, D. K., Abbas, Q., Imran, M., Sattar, H., and Ul Ahmad, A. (2019). Controlled surface wettability by plasma polymer surface modification. *Surfaces* 2, 349–371. doi:10.3390/surfaces2020026

Israelachvili, J. (1997). The different faces of poly(ethylene glycol). *Proc. Natl. Acad. Sci.* 94, 8378–8379. doi:10.1073/pnas.94.16.8378

Jaffer, I. H., Fredenburgh, J. C., Hirsh, J., and Weitz, J. I. (2015). Medical device-induced thrombosis: what causes it and how can we prevent it? *J. Thromb. Haemost.* 13, S72–S81. doi:10.1111/jth.12961

Jaffer, I. H., and Weitz, J. I. (2019). The blood compatibility challenge. Part 1: blood-contacting medical devices: the scope of the problem. *Acta Biomater.* 94, 2–10. doi:10.1016/j.actbio.2019.06.021

Jana, S. (2019). Endothelialization of cardiovascular devices. *Acta Biomater.* 99, 53–71. doi:10.1016/j.actbio.2019.08.042

Jankowski, P., and Garstecki, P. (2016). Stable hydrophilic surface of polycarbonate. *Sensors Actuators, B Chem.* 226, 151–155. doi:10.1016/j.snb.2015.11.100

Jensen, M. J., Peel, A., Horne, R., Chamberlain, J., Xu, L., Hansen, M. R., et al. (2021). Antifouling and mechanical properties of photografted zwitterionic hydrogel thin-film coatings depend on the cross-link density. *ACS Biomater. Sci. Eng.* 7, 4494–4502. doi:10.1021/acsbiomaterials.1c00852

Jeong, H., Park, K., Yoo, J. C., and Hong, J. (2018). Structural heterogeneity in polymeric nitric oxide donor nanoblended coatings for controlled release behaviors. *RSC Adv.* 8, 38792–38800. doi:10.1039/c8ra07707j

Jiang, B., Guo, H., Chen, D., and Zhou, M. (2022). Microscale investigation on the wettability and bonding mechanism of oxygen plasma-treated PDMS microfluidic chip. *Appl. Surf. Sci.* 574, 151704. doi:10.1016/j.apsusc.2021.151704

Kalathottukaren, M. T., and Kizhakkedathu, J. N. (2018). "2-Mechanisms of blood coagulation in response to biomaterials: extrinsic factors," in *Hemocompatibility of biomaterials for clinical applications*. Editor C. A. Siedlecki (Elsevier Ltd). doi:10.1016/B978-0-08-100497-5.00003-3

Kamath, S., Blann, A. D., and Lip, G. Y. H. (2001). Platelet activation: assessment and quantification. *Eur. Heart J.* 22, 1561–1571. doi:10.1053/euhj.2000.2515

Kanitthamniyom, P., and Zhang, Y. (2018). Application of polydopamine in biomedical microfluidic devices. *Microfluid. Nanofluidics* 22, 24–13. doi:10.1007/s10404-018-2044-6

Keh, D., Gerlach, M., Kürer, I., Spielmann, S., Kerner, T., Busch, T., et al. (1999). Nitric oxide diffusion across membrane lungs protects platelets during simulated extracorporeal circulation. *Eur. J. Clin. Invest.* 29, 344–350. doi:10.1046/j.1365-2362.1999.00459.x

Khazan, M., and Hdayati, M. (2014). The role of nitric oxide in health and diseases. *Scimetr* 3, e87393. doi:10.5812/scimetr.20987

Khetani, S., Yong, K. W., Ozhukil Kollath, V., Eastick, E., Azarmanesh, M., Karan, K., et al. (2020). Engineering shelf-stable coating for microfluidic organ-on-A-chip using bioinspired catecholamine polymers. *ACS Appl. Mat. Interfaces* 12, 6910–6923. doi:10.1021/acsami.9b20826

Kim, S., Ye, S. H., Adamo, A., Orizondo, R. A., Jo, J., Cho, S. K., et al. (2020). A biostable, anti-fouling zwitterionic polyurethane-urea based on PDMS for use in blood-contacting medical devices. *J. Mat. Chem. B* 8, 8305–8314. doi:10.1039/d0tb01220c

Kobayashi, Y. (2010). The regulatory role of nitric oxide in proinflammatory cytokine expression during the induction and resolution of inflammation. *J. Leukoc. Biol.* 88, 1157–1162. doi:10.1189/jlb.0310149

Köhne, I. (2020). Haemolysis induced by mechanical circulatory support devices: unsolved problems. *Perfus. (United Kingdom)* 35, 474–483. doi:10.1177/0267659120931307

Kolar, M., Mozetič, M., Stana-Kleinschek, K., Fröhlich, M., Turk, B., and Vesel, A. (2015). Covalent binding of heparin to functionalized PET materials for improved haemocompatibility. *Mater. (Basel)* 8, 1526–1544. doi:10.3390/ma8041526

Kovach, K. M., Capadona, J. R., Gupta, A. Sen, and Potkay, J. A. (2014). The effects of PEG-based surface modification of PDMS microchannels on long-term hemocompatibility. *J. Biomed. Mat. Res. - Part A* 102, 4195–4205. doi:10.1002/jbm.a.35090

Kovach, K. M., Labarbera, M. A., Moyer, M. C., Cmolik, B. L., Van Lunteren, E., Sen Gupta, A., et al. (2015). *In vitro* evaluation and *in vivo* demonstration of a biomimetic, hemocompatible, microfluidic artificial lung. *Lab. Chip* 15, 1366–1375. doi:10.1039/c4lc01284d

Krajewski, S., Neumann, B., Kurz, J., Perle, N., Avci-Adali, M., Cattaneo, G., et al. (2015). Preclinical evaluation of the thrombogenicity and endothelialization of bare metal and surface-Coated neurovascular stents. *Am. J. Neuroradiol.* 36, 133–139. doi:10.3174/ajnr.A4109

Krishnamoorthi, R., Anbazhagan, R., Thankachan, D., Thuy Dinh, V. T., Tsai, H. C., Lai, J. Y., et al. (2023). Antiblood cell adhesion of mussel-inspired chondroitin sulfate- and caffeic acid-modified polycarbonate membranes. *Langmuir* 39, 717–727. doi:10.1021/acs.langmuir.2c01688

Kuchinka, J., Willems, C., Telyshev, D. V., and Groth, T. (2021). Control of blood coagulation by hemocompatible material surfaces—a review. *Bioengineering* 8, 215–226. doi:10.3390/bioengineering8120215

Kumar, D. R., Hanlin, E. R., Glurich, I., Mazza, J. J., and Yale, S. H. (2010). Virchow's contribution to the understanding of thrombosis and cellular biology. *Clin. Med. Res.* 8, 168–172. doi:10.3121/cmr.2009.866

Labarrere, C. A., Dabiri, A. E., and Kassab, G. S. (2020). Thrombogenic and inflammatory reactions to biomaterials in medical devices. *Front. Bioeng. Biotechnol.* 8, 123. doi:10.3389/fbioe.2020.00123

Lachaux, J., Hwang, G., Arouche, N., Naserian, S., Harouri, A., Lotito, V., et al. (2021). A compact integrated microfluidic oxygenator with high gas exchange efficiency and compatibility for long-lasting endothelialization. *Lab. Chip* 21, 4791–4804. doi:10.1039/d1lc00356a

Lai, C. C., and Chung, C. K. (2020). Hydrophilicity and optic property of polyethylene glycol coating on polydimethylsiloxane for fast prototyping and its application to backlight microfluidic chip. *Surf. Coatings Technol.* 389, 125606. doi:10.1016/j.surfcoat.2020.125606

Lai, J., Sunderland, B., Xue, J., Yan, S., Zhao, W., Folkard, M., et al. (2006). Study on hydrophilicity of polymer surfaces improved by plasma treatment. *Appl. Surf. Sci.* 252, 3375–3379. doi:10.1016/j.apsusc.2005.05.038

Lai, J. Y., Jien, J. M., and Lin, S. H. (1993). Gas permeation in polycarbonate membranes prepared by the wet-phase inversion method. *Chem. Eng. Sci.* 48, 4069–4074. doi:10.1016/0009-2509(93)80251-K

Larsson, A., and Dérand, H. (2002). Stability of polycarbonate and polystyrene surfaces after hydrophilization with high intensity oxygen RF plasma. *J. Colloid Interface Sci.* 246, 214–221. doi:10.1006/jcis.2001.8032

Leckband, D., Sheth, S., and Halperin, A. (1999). Grafted poly(ethylene oxide) brushes as nonfouling surface coatings. *J. Biomater. Sci. Polym. Ed.* 10, 1125–1147. doi:10.1163/156856299x00720

Lee, H. A., Ma, Y., Zhou, F., Hong, S., and Lee, H. (2019). Material-independent surface chemistry beyond polydopamine coating. *Acc. Chem. Res.* 52, 704–713. doi:10.1021/acs.accounts.8b00583

Lee, J. H., Kim, S. K., Park, H. H., and Kim, T. S. (2015). TiO2 coated microfluidic devices for recoverable hydrophilic and hydrophobic patterns. *J. Micromechanics Microengineering* 25, 035032. doi:10.1088/0960-1317/25/3/035032

Lee, J. K., Kung, H. H., and Mockros, L. F. (2008). Microchannel technologies for artificial lungs: (1) theory. *ASAIO J.* 54, 372–382. doi:10.1097/MAT.0b013e31817ed9e1

Lee, W. L., and Downey, G. P. (2001). Leukocyte elastase: physiological functions and role in acute lung injury. *Am. J. Respir. Crit. Care Med.* 164, 896–904. doi:10.1164/ajrccm.164.5.2103040

Leigh, B. L., Cheng, E., Xu, L., Derk, A., Hansen, M. R., and Guymon, C. A. (2019). Antifouling photograftable zwitterionic coatings on PDMS substrates. *Langmuir* 35, 1100–1110. doi:10.1021/acs.langmuir.8b00838

Leonard, E. F., and Vroman, L. (1992). Is the Vroman effect of importance in the interaction of blood with artificial materials? *J. Biomater. Sci. Polym. Ed.* 3, 95–107. doi:10.1163/156856292X00105

Leung, J. M., Berry, L. R., Atkinson, H. M., Cornelius, R. M., Sandejas, D., Rochow, N., et al. (2015). Surface modification of poly(dimethylsiloxane) with a covalent antithrombin-heparin complex for the prevention of thrombosis: use of polydopamine as bonding agent. *J. Mat. Chem. B* 3, 6032–6036. doi:10.1039/c5tb00808e

Li, L., Yang, L., Liao, Y., Yu, H., Liang, Z., Zhang, B., et al. (2020). Superhydrophilic versus normal polydopamine coating: a superior and robust platform for synergistic antibacterial and antithrombotic properties. *Chem. Eng. J.* 402, 126196. doi:10.1016/j.cej.2020.126196

Lillehoj, P. B., and Ho, C. M. (2010). "A long-term, stable hydrophilic poly(dimethylsiloxane) coating for capillary-based pumping," in Proc. IEEE Int. Conf. Micro Electro Mech. Syst., Hong Kong, China, 24-28 January 2010, 1063–1066. doi:10.1109/MEMSYS.2010.5442393

Linhardt, R., Murugesan, S., and Xie, J. (2008). Immobilization of heparin: approaches and applications. *Curr. Top. Med. Chem.* 8, 80–100. doi:10.2174/156802608783378891

Liu, Q., Singha, P., Handa, H., and Locklin, J. (2017). Covalent grafting of antifouling phosphorylcholine-based copolymers with antimicrobial nitric oxide releasing polymers to enhance infection-resistant properties of medical device coatings. *Langmuir* 33, 13105–13113. doi:10.1021/acs.langmuir.7b02970

Liu, Y., Ai, K., and Lu, L. (2014). Polydopamine and its derivative materials: synthesis and promising applications in energy, environmental, and biomedical fields. *Chem. Rev.* 114, 5057–5115. doi:10.1021/cr400407a

LivaNova (2023). LivaNova. Available at: https://www.livanova.com/cardiopulmonary/en-us (Accessed June 26, 2023).

Long, H. P., Lai, C. C., and Chung, C. K. (2017). Polyethylene glycol coating for hydrophilicity enhancement of polydimethylsiloxane self-driven microfluidic chip. *Surf. Coatings Technol.* 320, 315–319. doi:10.1016/j.surfcoat.2016.12.059

Low, L. A., Mummery, C., Berridge, B. R., Austin, C. P., and Tagle, D. A. (2021). Organs-on-chips: into the next decade. *Nat. Rev.* 20, 345–361. doi:10.1038/s41573-020-0079-3

Lowe, G. D. O. (2003). Virchow's triad revisited: abnormal flow. *Pathophysiol. Haemost. Thromb.* 33, 455–457. doi:10.1159/000083845

Luo, J., Fan, J. B., and Wang, S. (2020). Recent progress of microfluidic devices for hemodialysis. *Small* 16, 1904076. doi:10.1002/smll.201904076

Luo, R., Tang, L., Wang, J., Zhao, Y., Tu, Q., Weng, Y., et al. (2013). Improved immobilization of biomolecules to quinone-rich polydopamine for efficient surface functionalization. *Colloids Surfaces B Biointerfaces* 106, 66–73. doi:10.1016/j.colsurfb.2013.01.033

Luo, R., Zhang, J., Zhuang, W., Deng, L., Li, L., Yu, H., et al. (2018). Multifunctional coatings that mimic the endothelium: surface bound active heparin nanoparticles with: *in situ* generation of nitric oxide from nitrosothiols. *J. Mat. Chem. B* 6, 5582–5595. doi:10.1039/c8tb00596f

Lyu, N., Du, Z., Qiu, H., Gao, P., Yao, Q., Xiong, K., et al. (2020). Mimicking the nitric oxide-releasing and glycocalyx functions of endothelium on vascular stent surfaces. *Adv. Sci.* 7, 2002330. doi:10.1002/advs.202002330

Madhurakkat Perikamana, S. K., Lee, J., Lee, Y. B., Shin, Y. M., Lee, E. J., Mikos, A. G., et al. (2015). Materials from mussel-inspired chemistry for cell and tissue engineering applications. *Biomacromolecules* 16, 2541–2555. doi:10.1021/acs.biomac.5b00852

Magoshi, T., and Matsuda, T. (2002). Formation of polymerized mixed heparin/albumin surface layer and cellular adhesional responses. *Biomacromolecules* 3, 976–983. doi:10.1021/bm0200377

Maul, T. M., Massicotte, M. P., and Wearden, P. D. (2016). "ECMO biocompatibility: surface coatings, anticoagulation, and coagulation monitoring," in *Extracorporeal membrane oxygenation: advances in therapy*. Editor M. S. Firstenberg (Rijeka, Croatia: IntechOpen), 27–61. doi:10.5772/63888

McVerry, B., Polasko, A., Rao, E., Haghniaz, R., Chen, D., He, N., et al. (2022). A readily scalable, clinically demonstrated, antibiofouling zwitterionic surface treatment for implantable medical devices. *Adv. Mat.* 34, 2200254. doi:10.1002/adma.202200254

Medtronic (2020). Balance™ biosurface. Available at: https://europe.medtronic.com/xd-en/healthcare-professionals/products/cardiovascular/cardiopulmonary/balance-biosurface.html (Accessed June 26, 2023).

Mellgren, K., Friberg, L. G., Mellgren, G., Hedner, T., Wennmalm, Å., and Wadenvik, H. (1996). Nitric oxide in the oxygenator sweep gas reduces platelet activation during experimental perfusion. *Ann. Thorac. Surg.* 61, 1194–1198. doi:10.1016/0003-4975(96)00017-3

Mercader, A., Ye, S. H., Kim, S., Orizondo, R. A., Cho, S. K., and Wagner, W. R. (2022). PDMS-zwitterionic hybrid for facile, antifouling microfluidic device fabrication. *Langmuir* 38, 3775–3784. doi:10.1021/acs.langmuir.1c03375

Michanetzis, G. P. A., Katsala, N., and Missirlis, Y. F. (2003). Comparison of haemocompatibility improvement of four polymeric biomaterials by two heparinization techniques. *Biomaterials* 24, 677–688. doi:10.1016/S0142-9612(02)00382-4

Miranda, I., Souza, A., Sousa, P., Ribeiro, J., Castanheira, E. M. S., Lima, R., et al. (2022). Properties and applications of PDMS for biomedical engineering: a review. *J. Funct. Biomater.* 13, 2. doi:10.3390/jfb13010002

Mondal, A., Singha, P., Douglass, M., Estes, L., Garren, M., Griffin, L., et al. (2021). A synergistic new approach toward enhanced antibacterial efficacy via antimicrobial peptide immobilization on a nitric oxide-releasing surface. *ACS Appl. Mat. Interfaces* 13, 43892–43903. doi:10.1021/acsami.1c08921

Mukhopadhyay, R. (2007). When PDMS isn't the best. *Anal. Chem.* 79, 3248–3253. doi:10.1021/ac071903e

Neubauer, K., and Zieger, B. (2021). Endothelial cells and coagulation. *Cell Tissue Res.* 387, 391–398. doi:10.1007/s00441-021-03471-2

Niebler, R. A., Chiang-Ching, H., Daley, K., Janecke, R., Jobe, S. M., Mitchell, M. E., et al. (2021). Nitric oxide added to the sweep gas of the oxygenator during cardiopulmonary bypass in infants: a pilot randomized controlled trial. *Artif. Organs* 45, 22–28. doi:10.1111/aor.13788

Nielsen, J. B., Hanson, R. L., Almughamsi, H. M., Pang, C., Fish, T. R., and Woolley, A. T. (2020). Microfluidics: innovations in materials and their fabrication and functionalization. *Anal. Chem.* 92, 150–168. doi:10.1021/acs.analchem.9b04986

Olander, B., Wirsén, A., and Albertsson, A. C. (2003). Silicone elastomer surface functionalized with primary amines and subsequently coupled with heparin. *Biomacromolecules* 4, 145–148. doi:10.1021/bm025654+

Olia, S. E., Maul, T. M., Antaki, J. F., and Kameneva, M. V. (2016). Mechanical blood trauma in assisted circulation: sublethal RBC damage preceding hemolysis. *Int. J. Artif. Organs* 39, 150–159. doi:10.5301/ijao.5000478

Olsson, P., and Larm, O. (1991). Biologically active heparin coating in medical devices. *Int. J. Artif. Organs* 14, 453–456. doi:10.1177/039139889101400801

Özgüzar, H. F., Evren, E., Meydan, A. E., Kabay, G., Göçmen, J. S., Buyukserin, F., et al. (2022). Plasma-Assisted surface modification and heparin immobilization: dual-functionalized blood-contacting biomaterials with improved hemocompatibility and antibacterial features. *Adv. Mat. Interfaces* 10, 2202009. doi:10.1002/admi.202202009

Park, J. H., Sut, T. N., Jackman, J. A., Ferhan, A. R., Yoon, B. K., and Cho, N. J. (2017). Controlling adsorption and passivation properties of bovine serum albumin on silica surfaces by ionic strength modulation and cross-linking. *Phys. Chem. Chem. Phys.* 19, 8854–8865. doi:10.1039/c7cp01310h

Park, K., Kim, S., Jo, Y., Park, J., Kim, I., Hwang, S., et al. (2022). Lubricant skin on diverse biomaterials with complex shapes via polydopamine-mediated surface functionalization for biomedical applications. *Bioact. Mater* 25, 555–568. doi:10.1016/j.bioactmat.2022.07.019

Park, K., Mao, F. W., and Park, H. (1991). The minimum surface fibrinogen concentration necessary for platelet activation on dimethyldichlorosilane-coated glass. *J. Biomed. Mat. Res.* 25, 407–420. doi:10.1002/jbm.820250311

Picone, P., Sabatino, M. A., Ajovalasit, A., Giacomazza, D., Dispenza, C., and Di Carlo, M. (2019). Biocompatibility, hemocompatibility and antimicrobial properties of xyloglucan-based hydrogel film for wound healing application. *Int. J. Biol. Macromol.* 121, 784–795. doi:10.1016/j.ijbiomac.2018.10.078

Pituru, S. M., Greabu, M., Totan, A., Imre, M., Pantea, M., Spinu, T., et al. (2020). A review on the biocompatibility of PMMA-Based dental materials for interim prosthetic restorations with a glimpse into their modern manufacturing techniques. *Mater. (Basel)* 13, 2894. doi:10.3390/ma13132894

Plegue, T. J., Kovach, K. M., Thompson, A. J., and Potkay, J. A. (2018). Stability of polyethylene glycol and zwitterionic surface modifications in PDMS microfluidic flow chambers. *Langmuir* 34, 492–502. doi:10.1021/acs.langmuir.7b03095

Porrini, C., Ramarao, N., and Tran, S. L. (2020). Dr. NO and Mr. Toxic - the versatile role of nitric oxide. *Biol. Chem.* 401, 547–572. doi:10.1515/hsz-2019-0368

Potkay, J. A. (2014). The promise of microfluidic artificial lungs. *Lab. Chip* 14, 4122–4138. doi:10.1039/c4lc00828f

Preston, T. J., Ratliff, T. M., Gomez, D., Olshove, V. F., Nicol, K. K., Sargel, C. L., et al. (2010). Modified surface coatings and their effect on drug adsorption within the extracorporeal life support circuit. *J. Extra. Corpor. Technol.* 42, 199–202. doi:10.1051/ject/201042199

Primc, G. (2020). Recent advances in surface activation of polytetrafluoroethylene (PTFE) by gaseous plasma treatments. *Polym. (Basel)* 12, 2295–2297. doi:10.3390/polym12102295

Qiu, H., Qi, P., Liu, J., Yang, Y., Tan, X., Xiao, Y., et al. (2019). Biomimetic engineering endothelium-like coating on cardiovascular stent through heparin and nitric oxide-generating compound synergistic modification strategy. *Biomaterials* 207, 10–22. doi:10.1016/j.biomaterials.2019.03.033

Radomski, M. W., Palmer, R. M. J., and Moncada, S. (1987). Endogenous nitric oxide inhibits human platelet adhesion to vascular endothelium. *Lancet* 330, 1057–1058. doi:10.1016/S0140-6736(87)91481-4

Recek, N., Mozetic, M., Jaganjac, M., Milkovic, L., Zarkovic, N., and Vesel, A. (2014). Adsorption of proteins and cell adhesion to plasma treated polymer substrates. *Int. J. Polym. Mat. Polym. Biomater.* 63, 685–691. doi:10.1080/00914037.2013.854243

Regehr, K. J., Domenech, M., Koepsel, J. T., Carver, K. C., Ellison-Zelski, S. J., Murphy, W. L., et al. (2009). Biological implications of polydimethylsiloxane-based microfluidic cell culture. *Lab. Chip* 9, 2132–2139. doi:10.1039/b903043c

Rochow, N., Manan, A., Wu, W. I., Fusch, G., Monkman, S., Leung, J., et al. (2014). An integrated array of microfluidic oxygenators as a neonatal lung assist device: *in vitro* characterization and *in vivo* demonstration. *Artif. Organs* 38, 856–866. doi:10.1111/aor.12269

Rossidis, A. C., Lawrence, K. M., Mejaddam, A. Y., Kim, A. G., Baumgarten, H. D., Coons, B. E., et al. (2020). The effects of nitric oxide in oxygenator sweep gas during extracorporeal circulation in a neonatal ovine model. *ASAIO J.* 66, 671–676. doi:10.1097/MAT.0000000000001047

Roux, E., Bougaran, P., Dufourcq, P., and Couffinhal, T. (2020). Fluid shear stress sensing by the endothelial layer. *Front. Physiol.* 11, 861. doi:10.3389/fphys.2020.00861

Roy, E., Galas, J. C., and Veres, T. (2011). Thermoplastic elastomers for microfluidics: towards a high-throughput fabrication method of multilayered microfluidic devices. *Lab. Chip* 11, 3193–3196. doi:10.1039/c1lc20251k

Roy, E., Pallandre, A., Horny, M. C., Delapierre, F. D., Horny, M. C., Delapierre, F. D., et al. (2016). "Overview of materials for microfluidic applications," in *Advances in microfluidics - new applications in biology, energy, and materials Sciences*. Editor X. Yu (Rijeka, Croatia: IntechOpen), 422.

Ryu, J. H., Messersmith, P. B., and Lee, H. (2018). Polydopamine surface chemistry: a decade of discovery. *ACS Appl. Mat. Interfaces* 10, 7523–7540. doi:10.1021/acsami.7b19865

Sadrearhami, Z., Shafiee, F. N., Ho, K. K. K., Kumar, N., Krasowska, M., Blencowe, A., et al. (2019). Antibiofilm nitric oxide-releasing polydopamine coatings. *ACS Appl. Mat. Interfaces* 11, 7320–7329. doi:10.1021/acsami.8b16853

Santos, J., Vedula, E. M., Lai, W., Isenberg, B. C., Lewis, D. J., Lang, D., et al. (2021). Toward development of a higher flow rate hemocompatible biomimetic microfluidic blood oxygenator. *Micromachines* 12, 888. doi:10.3390/mi12080888

Schlenoff, J. B. (2014). Zwitteration: coating surfaces with zwitterionic functionality to reduce nonspecific adsorption. *Langmuir* 30, 9625–9636. doi:10.1021/la500057j

Schrott, W., Slouka, Z., Červenka, P., Ston, J., Nebyla, M., Přibyl, M., et al. (2009). Study on surface properties of PDMS microfluidic chips treated with albumin. *Biomicrofluidics* 3, 44101. doi:10.1063/1.3243913

Seabra, A. B., Martins, D., Simões, M. M. S. G., Da Silva, R., Brocchi, M., and De Oliveira, M. G. (2010). Antibacterial nitric oxide-releasing polyester for the coating of blood-contacting artificial materials. *Artif. Organs* 34, 204–214. doi:10.1111/j.1525-1594.2010.00998.x

Shakeri, A., Imani, S. M., Chen, E., Yousefi, H., Shabbir, R., and Didar, T. F. (2019). Plasma-induced covalent immobilization and patterning of bioactive species in microfluidic devices. *Lab. Chip* 19, 3104–3115. doi:10.1039/c9lc00364a

Sharma, V., Dhayal, M., GovindShivaprasad, S. M., and Jain, S. C. (2007). Surface characterization of plasma-treated and PEG-grafted PDMS for micro fluidic applications. *Vacuum* 81, 1094–1100. doi:10.1016/j.vacuum.2007.02.004

Shen, B., Xiong, B., and Wu, H. (2015). Convenient surface functionalization of whole-Teflon chips with polydopamine coating. *Biomicrofluidics* 9, 044111. doi:10.1063/1.4927675

Shin, D. A., Lee, J. C., Shin, H., Cho, Y. J., and Kim, H. C. (2021). Point-of-care testing of plasma free hemoglobin and hematocrit for mechanical circulatory support. *Sci. Rep.* 11, 3788–3789. doi:10.1038/s41598-021-83327-5

Simmonds, M. J., Watanabe, N., Nandakumar, D., and Horobin, J. (2018). "Blood-device interaction," in *Mechanical circulatory and respiratory support* (Elsevier Inc). doi:10.1016/B978-0-12-810491-0.00019-9

Simon-Walker, R., Romero, R., Staver, J. M., Zang, Y., Reynolds, M. M., Popat, K. C., et al. (2017). Glycocalyx-inspired nitric oxide-releasing surfaces reduce platelet adhesion and activation on titanium. *ACS Biomater. Sci. Eng.* 3, 68–77. doi:10.1021/acsbiomaterials.6b00572

Sin, M. C., Chen, S. H., and Chang, Y. (2014). Hemocompatibility of zwitterionic interfaces and membranes. *Polym. J.* 46, 436–443. doi:10.1038/pj.2014.46

Sivakumar, R., and Lee, N. Y. (2020). Microfluidic device fabrication mediated by surface chemical bonding. *Analyst* 145, 4096–4110. doi:10.1039/d0an00614a

Sivaraman, B., and Latour, R. A. (2010). The relationship between platelet adhesion on surfaces and the structure versus the amount of adsorbed fibrinogen. *Biomaterials* 31, 832–839. doi:10.1016/j.biomaterials.2009.10.008

Skogby, M., Friberg, L. G., Adrian, K., and Mellgren, K. (2003). Pharmacological inhibition of plasma coagulation and platelet activation during experimental long-term perfusion. *Scand. Cardiovasc. J.* 37, 222–228. doi:10.1080/14017430310002185

Stauffer, F. (2014). La préparation d'émulsions doubles par un système microfluidique. Available at: https://hal.univ-lorraine.fr/hal-01732016/document.

Sundriyal, P., Pandey, M., and Bhattacharya, S. (2020). Plasma-assisted surface alteration of industrial polymers for improved adhesive bonding. *Int. J. Adhes. Adhes.* 101, 102626. doi:10.1016/j.ijadhadh.2020.102626

Sweryda-Krawiec, B., Devaraj, H., Jacob, G., and Hickman, J. J. (2004). A new interpretation of serum albumin surface passivation. *Langmuir* 20, 2054–2056. doi:10.1021/la034870g

Szydzik, C., Brazilek, R. J., and Nesbitt, W. S. (2020). A review of design considerations for hemocompatibility within microfluidic systems. *Semin. Thromb. Hemost.* 46, 622–636. doi:10.1055/s-0040-1710340

Tan, S. H., Nguyen, N. T., Chua, Y. C., and Kang, T. G. (2010). Oxygen plasma treatment for reducing hydrophobicity of a sealed polydimethylsiloxane microchannel. *Biomicrofluidics* 4, 32204–32208. doi:10.1063/1.3466882

Tan, X., Gao, P., Li, Y., Qi, P., Liu, J., Shen, R., et al. (2021). Poly-dopamine, poly-levodopa, and poly-norepinephrine coatings: comparison of physico-chemical and biological properties with focus on the application for blood-contacting devices. *Bioact. Mat.* 6, 285–296. doi:10.1016/j.bioactmat.2020.06.024

Teligui, L., Dalmayrac, E., Mabilleau, G., Macchi, L., Godon, A., Corbeau, J. J., et al. (2014). An *ex vivo* evaluation of blood coagulation and thromboresistance of two extracorporeal circuit coatings with reduced and full heparin dose. *Interact. Cardiovasc. Thorac. Surg.* 18, 763–769. doi:10.1093/icvts/ivu011

Temiz, Y., Lovchik, R. D., Kaigala, G. V., and Delamarche, E. (2015). Lab-on-a-chip devices: how to close and plug the lab? *Microelectron. Eng.* 132, 156–175. doi:10.1016/J.MEE.2014.10.013

Terumo (2018). Xcoating™ surface coating. Available at: https://www.terumocv.com/doc/876640_Xcoating-Brochure_JULY2018_FINAL_LowRes.pdf (Accessed June 26, 2023).

Thomas, S. G. (2019). *The structure of resting and activated platelets*. 4th ed. Elsevier Inc. doi:10.1016/B978-0-12-813456-6.00003-5

Thompson, A. J., Ma, L. J., Major, T., Jeakle, M., Lautner-Csorba, O., Goudie, M. J., et al. (2020). Assessing and improving the biocompatibility of microfluidic artificial lungs. *Acta Biomater.* 112, 190–201. doi:10.1016/j.actbio.2020.05.008

Thon, J. N., Dykstra, B. J., and Beaulieu, L. M. (2017). Platelet bioreactor: accelerated evolution of design and manufacture. *Platelets* 28, 472–477. doi:10.1080/09537104.2016.1265922

Tousoulis, D., Kampoli, A.-M., Tentolouris Nikolaos Papageorgiou, C., and Stefanadis, C. (2011). The role of nitric oxide on endothelial function. *Curr. Vasc. Pharmacol.* 10, 4–18. doi:10.2174/157016112798829760

Trantidou, T., Elani, Y., Parsons, E., and Ces, O. (2017). Hydrophilic surface modification of pdms for droplet microfluidics using a simple, quick, and robust method via pva deposition. *Microsystems Nanoeng.* 3, 16091. doi:10.1038/micronano.2016.91

Tsai, W. B., Grunkemeier, J. M., and Horbett, T. A. (1999). Human plasma fibrinogen adsorption and platelet adhesion to polystyrene. *J. Biomed. Mat. Res.* 44, 130–139. doi:10.1002/(SICI)1097-4636(199902)44:2<130::AID-JBM2>3.0.CO;2-9

Tsao, C. W., and DeVoe, D. L. (2009). Bonding of thermoplastic polymer microfluidics. *Microfluid. Nanofluidics* 6, 1–16. doi:10.1007/s10404-008-0361-x

Tsao, C. W. (2016). Polymer microfluidics: simple, low-cost fabrication process bridging academic lab research to commercialized production. *Micromachines* 7, 225. doi:10.3390/mi7120225

Van Midwoud, P. M., Janse, A., Merema, M. T., Groothuis, G. M. M., and Verpoorte, E. (2012). Comparison of biocompatibility and adsorption properties of different plastics for advanced microfluidic cell and tissue culture models. *Anal. Chem.* 84, 3938–3944. doi:10.1021/ac300771z

Van Oeveren, W., Haan, J., Lagerman, P., and Schoen, P. (2002). Comparison of coagulation activity tests *in vitro* for selected biomaterials. *Artif. Organs* 26, 506–511. doi:10.1046/j.1525-1594.2002.06872.x

Vaughn, M. W., Kuo, L., and Liao, J. C. (1998). Estimation of nitric oxide production and reaction rates in tissue by use of a mathematical model. *Am. J. Physiol.* 274, H2163–H2176. doi:10.1152/ajpheart.1998.274.6.H2163

Vesel, A., Mozetic, M., Jaganjac, M., Milkovic, L., Cipak, A., and Zarkovic, N. (2011). Biocompatibility of oxygen-plasma-treated polystyrene substrates. *EPJ Appl. Phys.* 56, 24024–24027. doi:10.1051/epjap/2011110169

Victor, A., Ribeiro, J., and Araújo, F. F. (2019). Study of PDMS characterization and its applications in biomedicine: a review. *J. Mech. Eng. Biomech.* 4, 1–9. doi:10.24243/jmeb/4.1.163

Virchow, R. (1856). *Gesammelte Abhandlungen zur Wissenschaftlichen Medicin*. Frankfurt am Main, Germany: Meidinger.

Voicu, D., Lestari, G., Wang, Y., DeBono, M., Seo, M., Cho, S., et al. (2017). Thermoplastic microfluidic devices for targeted chemical and biological applications. *RSC Adv.* 7, 2884–2889. doi:10.1039/c6ra27592c

Wagner, M. S., and Castner, D. G. (2004). Analysis of adsorbed proteins by static time-of-flight secondary ion mass spectrometry. *Appl. Surf. Sci.* 231–232, 366–376. doi:10.1016/j.apsusc.2004.03.100

Wang, P. G., Xian, M., Tang, X., Wu, X., Wen, Z., Cai, T., et al. (2002). Nitric oxide donors: chemical activities and biological applications. *Chem. Rev.* 102, 1091–1134. doi:10.1021/cr000040l

Weber, M., Steinle, H., Golombek, S., Hann, L., Schlensak, C., Wendel, H. P., et al. (2018). Blood-contacting biomaterials: *in vitro* evaluation of the hemocompatibility. *Front. Bioeng. Biotechnol.* 6, 99. doi:10.3389/fbioe.2018.00099

Wei Hou, H., Gan, H. Y., Bhagat, A. A. S., Li, L. D., Lim, C. T., and Han, J. (2012). A microfluidics approach towards high-throughput pathogen removal from blood using margination. *Biomicrofluidics* 6, 24115–2411513. doi:10.1063/1.4710992

Wei, Q., Becherer, T., Angioletti-Uberti, S., Dzubiella, J., Wischke, C., Neffe, A. T., et al. (2014). Protein interactions with polymer coatings and biomaterials. *Angew. Chem. - Int. Ed.* 53, 8004–8031. doi:10.1002/anie.201400546

Weller, R. B. (2009). Nitric oxide-containing nanoparticles as an antimicrobial agent and enhancer of wound healing. *J. Invest. Dermatol.* 129, 2335–2337. doi:10.1038/jid.2009.149

Willers, A., Arens, J., Mariani, S., Pels, H., Maessen, J. G., Hackeng, T. M., et al. (2021). New trends, advantages and disadvantages in anticoagulation and coating methods used in extracorporeal life support devices. *Membr. (Basel)* 11, 617. doi:10.3390/membranes11080617

Williams, D. F. (2008). On the mechanisms of biocompatibility. *Biomaterials* 29, 2941–2953. doi:10.1016/j.biomaterials.2008.04.023

Wilson, C. J., Clegg, R. E., Leavesley, D. I., and Pearcy, M. J. (2005). Mediation of biomaterial-cell interactions by adsorbed proteins: a review. *Tissue Eng.* 11, 1–18. doi:10.1089/ten.2005.11.1

Wolberg, A. S., Aleman, M. M., Leiderman, K., and Machlus, K. R. (2012). Procoagulant activity in hemostasis and thrombosis: virchow's triad revisited. *Anesth. Analg.* 114, 275–285. doi:10.1213/ANE.0b013e31823a088c

Wong, I., and Ho, C. M. (2009). Surface molecular property modifications for poly(dimethylsiloxane) (PDMS) based microfluidic devices. *Microfluid. Nanofluidics* 7, 291–306. doi:10.1007/s10404-009-0443-4

Wu, B., Gerlitz, B., Grinnell, B. W., and Meyerhoff, M. E. (2007a). Polymeric coatings that mimic the endothelium: combining nitric oxide release with surface-bound active thrombomodulin and heparin. *Biomaterials* 28, 4047–4055. doi:10.1016/j.biomaterials.2007.06.002

Wu, Y., Zhou, Z., and Meyerhoff, M. E. (2007b). *In vitro* platelet adhesion on polymeric surfaces with varying fluxes of continuous nitric oxide release. *J. Biomed. Mat. Res. Part A* 81A, 956–963. doi:10.1002/jbm.a.31105

Xia, N., May, C. J., McArthur, S. L., and Castner, D. G. (2002). Time-of-Flight secondary ion mass spectrometry analysis of conformational changes in adsorbed protein films. *Langmuir* 18, 4090–4097. doi:10.1021/la020022u

Yamazoe, H., Oyane, A., Nashima, T., and Ito, A. (2010). Reduced platelet adhesion and blood coagulation on cross-linked albumin films. *Mat. Sci. Eng. C* 30, 812–816. doi:10.1016/j.msec.2010.03.015

Yang, Z., Tu, Q., Zhu, Y., Luo, R., Li, X., Xie, Y., et al. (2012). Mussel-inspired coating of polydopamine directs endothelial and smooth muscle cell fate for re-endothelialization of vascular devices. *Adv. Healthc. Mat.* 1, 548–559. doi:10.1002/adhm.201200073

Yang, Z., Yang, Y., Xiong, K., Li, X., Qi, P., Tu, Q., et al. (2015). Nitric oxide producing coating mimicking endothelium function for multifunctional vascular stents. *Biomaterials* 63, 80–92. doi:10.1016/j.biomaterials.2015.06.016

Ye, W., Shi, Q., Hou, J., Gao, J., Li, C., Jin, J., et al. (2015). Fabricating bio-inspired micro/nano-particles by polydopamine coating and surface interactions with blood platelets. *Appl. Surf. Sci.* 351, 236–242. doi:10.1016/j.apsusc.2015.05.108

Yeh, P. Y., Zhang, Z., Lin, M., and Cao, X. (2012). Nonfouling hydrophilic poly(ethylene glycol) engraftment strategy for PDMS/SU-8 heterogeneous microfluidic devices. *Langmuir* 28, 16227–16236. doi:10.1021/la303196m

Yoon, T., Moon, H. S., Song, J. W., Hyun, K. A., and Jung, H. Il (2019). Automatically controlled microfluidic system for continuous separation of rare bacteria from blood. *Cytom. Part A* 95, 1135–1144. doi:10.1002/cyto.a.23909

Yu, H., Chong, Z. Z., Tor, S. B., Liu, E., and Loh, N. H. (2015). Low temperature and deformation-free bonding of PMMA microfluidic devices with stable hydrophilicity via oxygen plasma treatment and PVA coating. *RSC Adv.* 5, 8377–8388. doi:10.1039/c4ra12771d

Zahid, A., Dai, B., Hong, R., and Zhang, D. (2017). Optical properties study of silicone polymer PDMS substrate surfaces modified by plasma treatment. *Mat. Res. Express* 4, 105301–105308. doi:10.1088/2053-1591/aa8645

Zelzer, M., Albutt, D., Alexander, M. R., and Russell, N. A. (2012). The role of albumin and fibronectin in the adhesion of fibroblasts to plasma polymer surfaces. *Plasma process. Polym.* 9, 149–156. doi:10.1002/ppap.201100054

Zhang, C., Jin, J., Zhao, J., Jiang, W., and Yin, J. (2013). Functionalized polypropylene non-woven fabric membrane with bovine serum albumin and its hemocompatibility enhancement. *Colloids Surfaces B Biointerfaces* 102, 45–52. doi:10.1016/j.colsurfb.2012.08.007

Zhang, L., Casey, B., Galanakis, D. K., Marmorat, C., Skoog, S., Vorvolakos, K., et al. (2017). The influence of surface chemistry on adsorbed fibrinogen conformation, orientation, fiber formation and platelet adhesion. *Acta Biomater.* 54, 164–174. doi:10.1016/j.actbio.2017.03.002

Zhang, M., Pauls, J. P., Bartnikowski, N., Haymet, A. B., Chan, C. H. H., Suen, J. Y., et al. (2021). Anti-thrombogenic surface coatings for extracorporeal membrane oxygenation: a narrative review. *ACS Biomater. Sci. Eng.* 7, 4402–4419. doi:10.1021/acsbiomaterials.1c00758

Zhou, J., Khodakov, D. A., Ellis, A. V., and Voelcker, N. H. (2012). Surface modification for PDMS-based microfluidic devices. *Electrophoresis* 33, 89–104. doi:10.1002/elps.201100482

Frontiers in
Bioengineering and Biotechnology

Accelerates the development of therapies, devices, and technologies to improve our lives

A multidisciplinary journal that accelerates the development of biological therapies, devices, processes and technologies to improve our lives by bridging the gap between discoveries and their application.

Discover the latest Research Topics

See more →

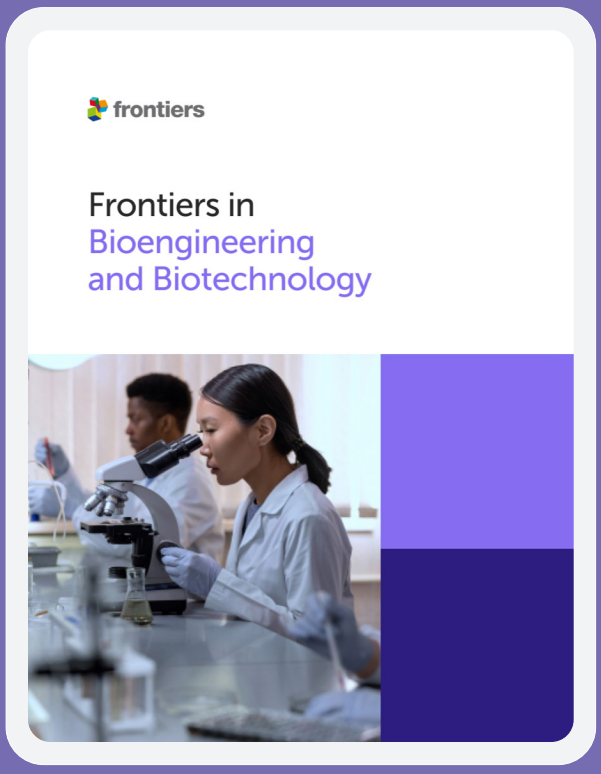

Frontiers

Avenue du Tribunal-Fédéral 34
1005 Lausanne, Switzerland
frontiersin.org

Contact us

+41 (0)21 510 17 00
frontiersin.org/about/contact